UNIVERSITY OF BIRMINGHAM

SCHOOL OF METALLURGY AND MATERIALS

ON THE CHARACTERISATION AND DETECTION OF ROLLING CONTACT FATIGUE (RCF) TYPE CRACKS IN RAILWAY VEHICLE WHEELS USING AN ALTERNATING CURRENT FIELD MEASUREMENT (ACFM) TECHNIQUE

BY

ANWAR PERVEZ JUNA

A THESIS SUBMITTED FOR THE DEGREE OF

DOCTOR OF PHILOSOPHY

2017

CONTENTS

DECLARATION **I**

ACKNOWLEDGEMENT **II**

ABSTRACT **III**

LEGENDS TO FIGURES **VIII**

CHAPTER 1 **1**

INTRODUCTION **1**

1.1 THE NECESSITY OF EFFICIENT, SAFE, RELIABLE AND COST-EFFECTIVE RAILWAY SERVICES 1

1.2 THE IMPORTANCE OF RAILWAY ROLLING STOCK RELIABILITY 1

1.3 INDUSTRIAL CHALLENGES 7

1.3.1 WHEELSET RELATED DEFECTS 7

1.3.2 MAINTENANCE ISSUES 8

1.3.3 THE GENERAL INSPECTION APPROACH 14

1.4 THE AIM OF THE PHD PROJECT 19

1.5 THE STRUCTURE OF THE PHD THESIS 21

CHAPTER 2 **24**
RAILWAY ROLLING STOCK

2.1 COMPONENTS OF RAILWAY ROLLING STOCK: ON WHEELSET, SUSPENSION AND BRAKING SYSTEM 24

2.2 COMMON FAULTS AND STRUCTURAL DEFECTS AFFECTING STRUCTURAL PERFORMANCE 30

2.3 MAINTENANCE REQUIREMENTS FOR DIFFERENT TYPES OF RAILWAY ROLLING STOCK: URBAN, SUBURBAN, INTERCITY AND FREIGHT RAILWAY ROLLING STOCK 31

CHAPTER 3 **34**
THE WHEEL-RAIL INTERFACE

3.1 THE IMPORTANCE OF THE WHEEL-RAIL INTERFACE AND 34

ADHESION

3.2 STRUCTURAL DEFECTS AFFECTING RAILWAY WHEELS 36

3.2.1 SPALLING 36

3.2.2 SHELLING 36

3.2.3 SCALING 37

3.2.4 CORRUGATION 38

3.2.5 WHEEL FLATS 38

3.2.6 CIRCULATORY AND GEOMETRIC DEFECTS 39

3.2.7 WHEEL TREAD ROLL-OVER 40

3.2.8 DEFECTS SPECIFIC TO MONOBLOC RAILWAY WHEELS 41

3.3 TYPICAL STEEL GRADES USED FOR THE MANUFACTURE OF RAILWAY WHEELS AND RAILWAY TRACK 43

3.3.1THE MICROSTRUCTURE OF STEEL MATERIAL 43

3.3.2 MATERIAL REQUIREMENTS AND MANUFACTURE OF RAILWAY WHEELS 45

3.4 THE ROLLING CONTACT FATIGUE (RCF) PHENOMENON IN RAILWAY WHEELS 48

3.5 MAINTENANCE METHODOLOGY 55

CHAPTER 4 61
INSPECTION OF RAILWAY WHEELSETS

4.1 AUTOMATED VISUAL INSPECTION SYSTEMS 61

4.2 ULTRASONIC NDE TECHNIQUES 61

4.3 ACOUSTIC EMISSION (AE) 64

4.4 RADIOGRAPHY 65

4.5 THERMOGRAPHY 66

4.6 MAGNETIC FLUX LEAKAGE (MFL) 67

4.7 EDDY CURRENT ELECTROMAGNETIC TECHNIQUE 67

4.8 ALTERNATING CURRENT FIELD MEASUREMENT (ACFM) TECHNIQUE 69

4.9 CONTRASTING ELECTROMAGNETIC NDE SYSTEMS 70

CHAPTER 5 72
FUNDAMENTALS OF THE ALTERNATING CURRENT FIELD MEASUREMENT (ACFM) TECHNIQUE

5.1 THE DEVELOPMENT OF THE THIN SKIN THEORY 72

5.2 THE INDUSTRIAL APPLICATION OF THE THIN SKIN EFFECT 75

5.3 ALTERNATING CURRENT FIELD MEASUREMENT (ACFM) TECHNIQUE 76

5.3.1 ACFM THEORY AND ELECTROMAGNETIC PRINCIPLES 76

5.3.2 FINITE ELEMENT ANALYSIS (FEA) MODELLING OF ACFM SENSOR RESPONSE TO IDEAL AND REAL RCF CRACKS FOUND IN RAILWAY WHEELS AND TRACK 79

5.3.3 ACFM FOR DEFECTS 80

5.4 INDUSTRIAL APPLICATIONS FOR THE ACFM TECHNIQUE 82

5.4.1 ACFM FOR THE RAILWAY INDUSTRY 82

5.4.2 AUTOMATED ROBOTIC DEPLOYMENT OF ACFM 83

5.4.3 ACFM FOR THREAD INSPECTION 83

5.4.4 APPLICATIONS FOR OTHER INDUSTRIAL SECTORS 84

CHAPTER 6 85
ON THE ASSESSMENT OF FAULTY RAILWAY WHEELS REMOVED FROM SERVICE

6.1 INTRODUCTION 85

6.2 MATERIALS AND EXPERIMENTAL TECHNIQUES 86

6.2.1 MATERIALS 88

6.2.1.1 RAILWAY WHEELS REMOVED FROM SERVICE 88

6.2.2 EXPERIMENTAL TECHNIQUES 92

6.2.2.1 THE MINI-PROFILE TECHNIQUE 92

6.2.2.2 OPTICAL METALLOGRAPHY 92

6.2.2.2.1 SAMPLE PREPARATION 92

6.2.2.2.2 OPTICAL MICROSCOPY 93

6.2.2.3 HARDNESS MEASUREMENTS 93

6.2.2.4 X-RAY TOMOGRAPHY (OR COMPUTED TOMOGRAPHY (CT)) 94

6.3 RESULTS AND DISCUSSION 94

6.3.1 MINI-PROFILES FOR THE HSR1, HSR2 AND HSR3, RAILWAY WHEELS REMOVED FROM SERVICE 94

6.3.2 RCF-TYPE CRACKS OBSERVED IN RAILWAY WHEELS REMOVED FROM SERVICE 97

6.3.2.1 RCF CRACKS OBSERVED IN WORN AND NEW (I.E. WITHOUT VISIBLE DEFECTS) RAILWAY WHEELS 97

6.3.2.2 3-D REPRESENTATION OF RCF-TYPE CRACKS OBSERVED IN RAILWAY WHEELS REMOVED FROM SERVICE 108

6.3.3 HARDNESS AND MICROSTRUCTURAL CHANGE WITH DEPTH FROM TREAD SURFACE FOR WORN (HSR1 AND HSR2) AND NEW (HSR3) RAILWAY WHEELS 117

6.3.3.1 HARDNESS CHANGE WITH DEPTH FROM TREAD SURFACE 117

6.3.3.2 MICROSTRUCTURAL CHANGE WITH DEPTH FROM TREAD SURFACE 132

6.4 CONCLUSION 146

CHAPTER 7 148
ON THE SENSITIVITY AND DETECTABILITY OF THE ACFM TECHNIQUE IN DETECTING AND PREDICTING DEFECT SIZES IN RAILWAY WHEELS

7.1 INTRODUCTION 148

7.2 MATERIALS AND EXPERIMENTAL TECHNIQUES 156

7.2.1 CALIBRATION PLATES TO SIMULATE CRACKS OBSERVED IN RAILWAY WHEELS REMOVED FROM SERVICE 157

7.2.2 ALTERNATING CURRENT FIELD MEASUREMENT (ACFM) TECHNIQUE 159

7.2.3 MAGNETIC PARTICLE INSPECTION (MPI) 162

7.3 RESULTS AND DISCUSSION 163

7.3.1 FACTORS AFFECTING ACFM SENSOR SIGNAL RESPONSE TO 163

CRACKS

7.3.1.1 INFLUENCE OF ACFM SENSOR ANGLE RELATIVE TO CRACK SURFACE ANGLE AND CRACK PROPAGATION ANGLE ON ACFM SIGNAL 163

7.3.1.2 INFLUENCE OF ACFM SENSOR LIFT-OFF AND OPERATIONAL SPEED ON ACFM SIGNAL 172

7.3.1.3 INFLUENCE OF CRACK SEPARATION AND CRACK CLUSTER NUMBER ON ACFM SIGNAL 178

7.3.1.4 INFLUENCE OF INDUCING FREQUENCY ON ACFM SIGNAL 188

7.3.1.5 ASSESSING THE CAPABILITY OF THE ACFM TECHNIQUE TO DETECT A SEVERELY CRITICAL DEFECT IN A CLUSTER OF SHALLOW DEFECTS AS COMMONLY FOUND IN RAILWAY WHEELS IN SERVICE 190

7.3.2 INFLUENCE OF RAILWAY WHEEL TREAD POSITION AND THE SEVERITY OF CRACKS ON THE ACFM SENSOR BACKGROUND SIGNAL FOR RAILWAY WHEELS IN SERVICE 196

7.3.3 THE CAPABILITY OF THE ACFM SENSOR TO DETECT AND SIZE (LENGTH AND DEPTH) CRACKS AND THUS ASSESS THE SEVERITY OF DAMAGE IN RAILWAY WHEELS IN SERVICE 200

7.4 CONCLUSION 241

CHAPTER 8 247
CONCLUSIONS, FUTURE WORK AND IMPORTANCE TO THE RAILWAY INDUSTRY

8.1 CONCLUSIONS 247

8.2 IMPORTANCE TO THE RAILWAY INDUSTRY AND FUTURE WORK 254

CHAPTER 9 257
APPENDICES

9.1 APPENDIX A 257

9.2 APPENDIX B 260

9.3 APPENDIX C 266

9.4 APPENDIX D 273

9.5 APPENDIX E 281

9.6 APPENDIX F 287

DECLARATION

I confirm that this is my own work and the use of all material from other sources has been properly and fully acknowledged.

ACKNOWLEDGEMENT

I would like to thank my supervisor, namely, Professor Paul Bowen (Head of School of Metallurgy and Materials) for personally arranging the purchase and, thus, provision of a calibration plate for the purposes of my work on this PhD project; this calibration plate consists of artificially created defects for the work presented in this PhD thesis which is identified as: CP_APJ_PHDPROJECT_2013 consisting of artificially created defects (or “notches”) by spark erosion which I had designed to simulate the types of RCF cracks found in railway wheels in service and then arranged to be manufactured by a local manufacturer in Birmingham and was then arranged to be purchased on my behalf through the University of Birmingham by Professor Paul Bowen for the purposes of my work on my PhD project.

I would also like to extend my thanks to the University of Birmingham for funding the PhD project through the EPSRC Doctoral Training (DTA) award. Furthermore, I would like to take this opportunity to extend my thanks to the Rail Technology Unit (RTU) at Manchester Metropolitan University in collaboration with other railway companies (confidential) for supplying the railway wheels for the work on the PhD project.

ABSTRACT

The following salient points have emerged from this work. X-ray tomography in conjunction with reconstruction techniques and also the multi-sectioning in conjunction with optical metallography approach are viable techniques to create 3-D images of cracks. Cracks initiate at pro-eutectoid (PE) ferrite boundaries and PE ferrite is flattened near the tread surface due to the very high strains and stresses in this region. Hardness for all wheels investigated decreases steeply with tread depth for approximately 1 mm below the tread surface and then the hardness decreases more slowly with tread depth. The results show that a 50 kHz ACFM probe provides higher sensitivity than the standard 5 kHz probe on ferrous and non-ferrous materials. Thus, a 50 kHz ACFM sensor is optimal for the detection and sizing of cracks in railway wheels and components in service; it is also found that the mean background signal is significantly lower for the ACFM system operating at the higher frequency than at the lower frequency of 50 and 5 kHz, respectively. As most RCF type cracks occur at +/- 45° to the circumferential direction, a sensor system with orthogonal fields at +/- 45° would be most appropriate. Contrary to former studies, this work has shown that crack propagation angle influences the ACFM signal and demonstrates that the ACFM sensor is most sensitive to cracks that propagate at higher angles between 60-90^0 in contrast to shallow angles of propagation of about 25^0 and less. Defects can still be detected at a lift-off of 5 mm above the surface of the material under inspection, although the signal strength is significantly depleted; the sensitivity is higher for the 50 kHz ACFM sensor. Therefore, in principle, the work presented here shows that any possible lift-off variations during inspection may be inferred and evaluated by determining the decrease in the sensor's signal strength which is in agreement with previous work conducted on similar systems [43, 86, 88, 117, 132]. Furthermore, even though appropriate high–speed inspection experiments could not be carried out using the current ACFM probe for the purpose of the PhD project due to the fact that the inspection system used for this study is inappropriate for inspections other than for slow manual speed due to limitations of the data acquisition board employed, thus, limiting the sampling rate to only a few kHz, previous work on similar systems [43, 86, 88, 117, 132] has shown that the signal response to cracks is significantly reduced at high operational speeds. The maximum change in the B_x signal is greater for closely spaced cracks which would thus significantly oversize the cracks. These

results also demonstrate that at a crack spacing of 20 mm the cracks can be sized resonabley accurately, whereas, for spacings of 15 mm the outer cracks, for example, in the four crack cluster would yield resonably good estimates for the crack pocket depths, however, the two inner cracks would significantly undersize the defects because these inner cracks in the crack cluster would yield higher values for the maximum change in the B_x signal; and the results also show that for crack spacing less than 15 mm the cracks thus estimated using the normalised change in the B_x signal would be significantly higher than the actual crack pocket depths. Furthermore, this effect needs to be taken into account when using the ACFM system on the railway network as the RCF cracks found in railway wheel tread surfaces are closely spaced and in most cases closer than 5 mm apart and thus it is difficult to size such defects using the present ACFM system when the cracks within a cluster have a inter-crack spacing of 5 mm or less. It is not possible at present to detect a deep crack within a cluster of shallow cracks using the current ACFM system. However, scans conducted with the probe oriented at 90^0 to the cluster of cracks consisting of a deep central crack surrounded by shallow cracks results in a distinct central sensor B_x signal that is a peak instead of a trough as observed in the case of the probe which is parallel to the crack orientation during a scan, thus, identifying the critical crack in the centre of the cluster which is significantly greater than the sensor signals for the individual shallow defects and thus suggesting that this method is capable of detecting a deep and critical crack in a cluster of shallow cracks, however, it is not possible to accurately size the deep crack in the cluster at present, nevertheless, this is a promising result and a way forward. Furthermore, in order to explain the above result obtained from this experiment the following explanation is presented in light of the current understanding of this phenomena about the leakage of magnetic flux in the scenario as shown in these results as demonstrated by the ACFM scans obtained from this experiment when the ACFM probe is oriented perpendicular to the direction of the cracks that with a transverse defect the induced current will flow parallel to the defect and be little affected by the presence of the defect. However, the direction of the magnetic field is now normal to the defect and, thus, it is expected that there would be a small flux leakage effect in the area of the defect. This is of course the field direction and driving mechanism of MPI. If there is a flux leakage effect it explains the signal response, namely an increase in B_x level and a sharp peak-trough in the B_z signal. It would be very much localised to the vicinity of the defect and would be

affected by defect depth and crack opening and this effect has previously been observed and the above interpretation is supported by research in the field as reported in [206,207]. The background ACFM signal varies with position across the railway wheel tread. Furthermore, the results show that the current ACFM system is capable of detecting and sizing cracks near the tread surface which are superimposed upon each other. However, it is found that the ACFM sensor, in its present state, is incapable of distinguishing between and, thus, detecting and sizing (length and depth) individual closely spaced (< 5 mm) surface breaking cracks in the treads of railway wheels in service investigated; at best the ACFM system in its current form can provide an estimate of crack sizes for a multiple stack of cracks which are superimposed upon each other in wheels in service. Furthermore, due to variations in the lift-off that occur during inspection of the rail wheels removed from service as a result of roughness of the tread surface and in the case of the normalised results obtained for the main calibration plate discussed in the earlier section above at different lift-off distances the ACFM system cannot provide correct rankings for the crack depths under these conditions which is also in agreement with previous work in this field [43, 86, 88, 117, 132], nevertheless, all the artificial cracks (or "notches) and most RCF cracks found in the railway wheels removed from service and investigated using the ACFM probe were detected. The results obtained from this study show that the ACFM sensor operating at a frequency of 50 kHz provides good estimates for the crack pocket depth for a crack propagation angle of 25^0 and under sizes the crack by 10%, whereas, the sensor at this frequency of operation significantly over sizes the crack by 70% for crack propagation angles of 60^0 and 90^0. Whereas, the ACFM sensor operating at a lower frequency of 5 kHz provides accurate estimates for the crack pocket depths for crack propagation angles between 60^0 and 90^0 but also provides a reasonable estimate for the crack pocket depth at a propagation angle of 25^0 and under sizes the crack depth by 40%. The results obtained demonstrate that for closely spaced cracks the normalised maximum change in the B_x signal component (i.e. $\Delta B_{xmax}/B_{x0}$) is relatively larger than for an isolated individual crack of the same size as shown by the results in this present work. Results obtained show that using an ACFM sensor operating at an inducing frequency of 50 kHz to detect the artificial cracks (notches) in the calibration plate on a four crack cluster shows that the ACFM system operating at this higher frequency yields significantly higher $\Delta B_{xmax}/B_{x0}$ values and thus over sizes the defects for all cracks investigated and all cracks could not be

sized as a result using the UK Network Rail sizing diagram shown in figure 7.4. However, in the case of the ACFM sensor operating at an inducing frequency of 5 kHz the sensor is found to be capable of providing reasonable estimates of the crack pocket depths at inter-crack spacing distances of 15 and 20 mm for the crack clusters consisting of two and four cracks and even though these crack pocket depth estimates are oversized by 36% in both of these cases at these inter-crack spacing distances these results are in line with previous similar studies reported in the literature [164,165]. However, at lower inter-crack spacing distances of 5 and 10 mm the ACFM techniques is not capable of distinguishing between individual cracks and considerably over sizes the cracks in agreement with former studies on similar systems [164,165]. The results also show that the estimate for the crack pocket depth is the same for two and four crack clusters at inter-crack-spacing distances of 15 and 20 mm but for a two crack cluster at an inter-crack spacing distance of 10 mm and an ACFM inducing frequency of 50 kHz the value of the normalised B_x obtained, i.e. $\Delta B_{xmax}/B_{x0}$, is too large using the ACFM sensor operating at 50 kHz than for the 5 kHz sensor employed to detect the same defects at the same inter-crack spacing distances and thus the 50 kHz sensor is incapable of sizing the defects at this inter-crack spacing using the sizing diagram shown in figure 7.4. However, the best results obtained from this study is found to be when the ACFM is operated at a lower frequency of 5 kHz on a cluster of two cracks with inter-crack-spacing distances at and above 15 mm, i.e. at inter-crack spacing distances of 15 and 20 mm, where the defects investigated are sized within reasonable estimates with an estimate for the crack pocket depth that is oversized by 20% of the actual depth of the defect at these two inter-crack spacing distances. This result is better and thus in line with that reported in the literature using an ACFM sensor operating at the same lower frequency. Therefore, these results demonstrate that the ACFM technique operating at lower frequencies (5 kHz) is much better suited at sizing (length and depth) cracks in railway track and railway wheels and components than an ACFM system operating at higher frequencies (50 kHz) and, thus, provides reasonable estimates for crack pocket depths. Furthermore, the results obtained demonstrate that a similar trend and features in the ACFM signal by using the ACFM technique on detecting and sizing the artificial cracks in the calibration plates investigated and on the RCF cracks identified in the three railway wheels removed from service and investigated, namely, railway wheels: HSR1, HSR2 and HSR3 which were provided by three different

manufacturers in conjunction with Manchester Metropolitan University (MMU) for the purposes of my work on my PhD research project at School of Metallurgy and Materials, University of Birmingham.

LEGENDS TO FIGURES

Figure 2.1 shows a schematic of the main wheelset components (the original of the above schematic is shown in reference [128] and has been reproduced and appropriately referenced here for the purpose of this PhD thesis).

Figure 2.2 a schematic showing additional wheelset components (the original of the above schematic is shown in reference [128] and has been reproduced and appropriately referenced here for the purpose of this PhD thesis).

Figure 2.3 shows a schematic of the axle for all types of wheelset; note, axles may be solid or hollow (the original of the above schematic is shown in reference [128] and has been reproduced and appropriately referenced here for the purpose of this PhD thesis).

Figure 2.4 shows a schematic of a typical monobloc wheel (the original of the above schematic is shown in reference [128] and has been reproduced and appropriately referenced here for the purpose of this PhD thesis).

Figure 2.5 shows a schematic of the base axle box (the original of the above schematic is shown in reference [128] and has been reproduced and appropriately referenced here for the purpose of this PhD thesis).

Figure 2.6 the above is a schematic diagram of the wheel tread region showing the relative dimensions of the different parts of the tread (the original of the above schematic is shown in reference [32] and has been reproduced and appropriately referenced here for the purpose of this PhD thesis).

Figure 3.1 shows damage caused by spalling resulting from thermal cracks on the wheel tread surface (the original of the above photographic image is shown in reference [11] and has been reproduced and appropriately referenced here for the purpose of this PhD thesis).

Figure 3.2 shows the presence of shelling and cavities on the wheel tread surface (the original of the above photographic image is shown in reference [11] and has been reproduced and appropriately referenced here for the purpose of this PhD thesis).

Figure 3.3 shows the presence of scaling damage on the wheel tread surface (the original of the above photographic image is shown in reference [11] and has been reproduced and appropriately referenced here for the purpose of this PhD thesis).

Figure 3.4 shows a wheel flat (the original of the above photographic image is shown in reference [11] and has been reproduced and appropriately referenced here for the purpose of this PhD thesis).

Figure 3.5(a) Local tread collapse.

Figure 3.5(b): Figures 3.5(a) and (b) show a schematic and photograph, respectively, of local tread collapse in a railway wheel (the originals of the above schematic and photographic image are shown in reference [11] and have been reproduced and appropriately referenced here for the purpose of this PhD thesis).

Figure 3.6 shows a schematic of polygonisation (the original of the above schematic is shown in reference [11] and has been reproduced and appropriately referenced here for the purpose of this PhD thesis).

Figure 3.7 shows a schematic and a photograph of wheel tread roll-over (the originals of the above schematic and photographic image are shown in reference [11] and have been reproduced and appropriately referenced here for the purpose of this PhD thesis).

Figure 3.8 shows deep sub-surface tread defect (the original of the above photographic image is shown in reference [11] and has been reproduced and appropriately referenced here for the purpose of this PhD thesis).

Figure 3.9 shows a schematic and a photographic image of damage caused by overheating affecting the rim-web transition (the originals of the above schematic and photographic image are shown in reference [11] and have been reproduced and appropriately referenced here for the purpose of this PhD thesis).

Figure 3.10 shows the Iron-Iron Carbon Phase Diagram.

Figure 5.1 shows an image of the ACFM defect indication data screen showing a typical ACFM sensor response to the presence of a defect in the material under inspection (the original of the above image is shown in reference [118] and has been reproduced, presented and appropriately referenced here for the purpose of this PhD thesis).

Figure 5.2 shows the different components of the current induced by the ACFM into the material under inspection flowing around the defect including field direction definitions and co-ordinate system (the original of the above schematic diagram is shown in reference [118] and has been reproduced and appropriately referenced here for the purpose of this PhD thesis).

Figure 6.1 railway wheel HSR1 at the minimum run-out tread position.

Figure 6.2 railway wheel HSR1 at the maximum run-out tread position.

Figure 6.3 photograph of the HSR1 railway wheel tread surface at the maximum and minimum run-out tread position segments A and B, respectively.

Figure 6.4 photograph of the HSR2 railway wheel tread surface showing the two circumferential bands of RCF cracks: first band consists of shallow and fine cracks oriented at approx. 600 to the circumferential direction of the tread found near the flange and the second circumferential band of cracks are oriented almost perpendicular (900 +/-0.50) to the circumferential direction of the tread and are found at approx. 3 cm from the non-flange end of the tread.

Figure 6.5 high magnification photographs of the HSR2 railway wheel tread surface showing the two circumferential band of RCF cracks: first band consists of shallow and fine cracks oriented at approx. 600 to the circumferential direction of the tread found near the flange and the second circumferential band of cracks are oriented almost perpendicular (900 +/-0.50) to the circumferential direction of the tread and are found at approx. 3 cm from the non-flange end of the tread. These two bands of RCF

cracks are regions of interest for the 3-D reconstruction of cracks using the multi-sectioning in conjunction with optical metallography approach and ACFM scans across these cracks as presented in chapters 4 and 6, respectively.

Figure 6.6 another high magnification photographs of the HSR2 railway wheel tread surface showing the two circumferential band of RCF cracks: first band consists of shallow and fine cracks oriented at approx. 600 to the circumferential direction of the tread found near the flange and the second circumferential band of cracks are oriented almost perpendicular (900 +/-0.50) to the circumferential direction of the tread and are found at approx. 3 cm from the non-flange end of the tread. These two bands of RCF cracks are regions of interest for the 3-D reconstruction of cracks using the multi-sectioning in conjunction with optical metallography approach and ACFM scans across these cracks as presented in chapters 4 and 6, respectively.

Figure 6.7 railway wheel HSR3 (wheel without visible defects).

Figure 6.8 shows the mini-profile for the HSR1 rail wheel segments at the position of maximum and minimum tread damage, i.e. maximum and minimum run-out, respectively, in comparison to the mini-profile for a new P8 rail wheel.

Figure 6.9 shows the mini-profile for the HSR2 rail wheel in comparison to the mini-profile for a new P8 rail wheel. The figure also shows the mini-profile for the new HSR3 rail wheel without visible defects.

Figure 6.10 Image of as-polished sectioned HSR1 wheel sample showing sub-surface cracking in the railway wheel HSR1 at the position of maximum run-out.

Figure 6.11 Image of as-polished sectioned HSR1 wheel sample showing sub-surface cracking in the railway wheel HSR1 at the position of minimum run-out.

Figure 6.12 A montague of optical micrographs from an etched sample of HSR1 wheel showing sub-surface cracking at position of maximum run-out.

Figure 6.13 A montague of optical micrographs from an etched HSR1 wheel sample showing sub-surface cracking at position of minimum run-out.

Table 6.1 shows rolling contact fatigue crack dimensions including angles of propagation relative to tread surface for HSR1 wheel at positions of maximum and minimum run-out.

Figure 6.14 shows fine crack near flange end of HSR2 rail wheel. These cracks grow at an angle of approximately 450 to the tread surface into the material and towards the flange end of the wheel. Their orientation on the tread surface is about 600 with respect to the circumferential line.

Figure 6.15 shows a crack at about 3 cm from the non-flange end of the HSR2 rail wheel (note: this crack is at the position on the tread surface as the closely spaced fine cracks at 900 on the tread surface which run across the entire circumferential length of the rail wheel). These cracks grow at an angle of about 450 to the tread surface into the material and towards the non-flange end of the wheel.

Figure 6.16 shows reconstructed 3-D images of cracks found on the tread of wheel HSR1 at the maximum run-out position using the X-ray tomography technique. Crack A can clearly be seen extending deep into the material at this tread position, whereas, the result shows that crack B is a more shallow crack and with a shorter surface length than crack A.

Figure 6.17 shows further reconstructed 3-D images of cracks found on the tread of wheel HSR1 at the maximum run-out position using the X-ray tomography technique; these are significantly deep cracks.

Figure 6.18 shows further reconstructed 3-D images of cracks found on the tread of wheel HSR1 at the maximum run-out position using the X-ray tomography technique; these are significantly deep cracks. The lower image shows a 2-D image slice (frame 8 in figure 9.8 in the Appendices chapter 9 where the crack is at its greatest depth of 11.2 mm) obtained from the X-ray tomography experiment in the RCF region of the railway wheel HSR1 at the maximum run-out position on the tread.

Figure 6.19 shows a schematic drawing of typical shallow and closely spaced cracks that are oriented at approximately 600 to the circumferential direction of the wheel found near the flange end of the worn railway wheel HSR2 using the optical images shown in figure 9.81 in the Appendices chapter 9 obtained using the multi-sectioning in conjunction with optical metallography approach.

Figure 6.20 shows a schematic drawing of typical shallow and closely spaced cracks that are oriented almost perpendicular to the circumferential direction of the wheel found at approximately 3 cm from the non-flange end of the worn railway wheel HSR2 using the optical images shown in figure 9.82 in the Appendix chapter 9 obtained using the multi-sectioning in conjunction with optical metallography approach.

Figure 6.21 shows 2-D image slices from frames: 1-15 incl. for the schematic of the crack reconstructed from these 2-D image slices obtained from the X-ray tomography (CT) experiment on the RCF region of the railway wheel HSR1 at the maximum run-out position on the tread as shown earlier in the chapter above; the crack is at its maximum depth of 11.2 mm as determined from the 8th 2-D slice image of the CT scan above.

Figure 6.22 shows optical exposure micrographs of a typical shallow and closely spaced crack found near the flange end of railway wheel HSR2 at different stages in the multi-stage in conjunction with optical metallography experiment carried out to reconstruct a three-dimensional (3-D) image of the above crack as shown above in figure 6.19.

Figure 6.23 shows optical exposure micrographs of a typical shallow and closely spaced crack found at approximately 3 cm from the non-flange end of railway wheel HSR2 at different stages in the multi-stage in conjunction with optical metallography experiment carried out to reconstruct a three-dimensional (3-D) image of the above crack as shown earlier in figure 6.20.

Figure 6.24 Hardness contour maps for railway wheels: HSR1 (both at the min. and max. run-out positions of the tread), HSR2 and HSR3.

Figure 6.25 Hardness contour maps for railway wheels: HSR1 (both at the min. and max. run-out positions of the tread), HSR2 and HSR3.

Figure 6.26 shows the hardness versus depth measurements carried out (both micro- and macro- hardness measurements were conducted here) at the "running line" position (measured: 70 mm from the flange end) on the treads for railway wheels: HSR1 (hardness measurements were carried out both at the maximum and minimum run-out positions on the tread of this wheel), HSR2 and HSR3. The data for the above graphs are shown in figure 8.5 of Appendix A in the appendices chapter 9.

Figure 6.27 Graph showing the change in hardness with depth for position 5 cm from the non-flange end of the HSR1 worn railway wheel at the min. run-out position on the tread.

Figure 6.28 Microhardness versus Depth for Flange Face Region of HSR1 Rail Wheel Tread at Position of Maximum Run-Out.

Figure 6.29 Microhardness versus Depth for Flange Root Region of HSR1 Rail Wheel Tread at Position of Maximum Run-Out.

Figure 6.30 Microhardness versus Depth for Running Band Region of HSR1 Rail Wheel Tread at Position of Maximum Run-Out.

Figure 6.31 Microhardness versus Depth for RCF Band Region of HSR1 Rail Wheel Tread at Position of Maximum Run-Out.

Figure 6.32 Microhardness versus Depth for Field Side Region of HSR1 Rail Wheel Tread at Position of Maximum Run-Out.

Figure 6.33 Microhardness versus Depth for Flange Face Region of HSR1 Rail Wheel Tread at Position of Minimum Run-Out.

Figure 6.34 Microhardness versus Depth for Flange Root Region of HSR1 Rail Wheel Tread at Position of Minimum Run-Out.

Figure 6.35 Microhardness versus Depth for Running Band Region of HSR1 Rail Wheel Tread at Position of Minimum Run-Out.

Figure 6.36 Microhardness versus Depth for RCF Band Region of HSR1 Rail Wheel Tread at Position of Minimum Run-Out.

Figure 6.37 Microhardness versus Depth for Field Side Region of HSR1 Rail Wheel Tread at Position of Minimum Run-Out.

Figure 6.38 Microhardness versus Depth for Flange Face Region of HSR2 Rail Wheel Tread.

Figure 6.39 Microhardness versus Depth for Flange Root Region of HSR2 Rail Wheel Tread.

Figure 6.40 Microhardness versus Depth for Running Band Region of HSR2 Rail Wheel Tread.

Figure 6.41 Microhardness versus Depth for RCF Band Region of HSR2 Rail Wheel Tread.

Figure 6.42 Microhardness versus Depth for Field Side Region of HSR2 Rail Wheel Tread.

Figure 6.43 Microhardness versus Depth for Flange Face Region of HSR3 Rail Wheel Tread.

Figure 6.44 Microhardness versus Depth for Flange Root Region of HSR3 Rail Wheel Tread.

Figure 6.45 Microhardness versus Depth for Running Band Region of HSR3 Rail Wheel Tread.

Figure 6.46 Microhardness versus Depth for RCF Band Region of HSR3 Rail Wheel Tread.

Figure 6.47 Microhardness versus Depth for Field Side Region of HSR3 Rail Wheel Tread.

Figure 6.48 shows the strained and unstrained microstructure of the worn railway wheel HSR1 near the tread surface and in the bulk of the material, respectively.

Figure 6.49 Optical micrograph showing the unstrained core matrix away from the tread surface at the minimum run-out position of railway wheel HSR1.

Figure 6.50 Optical micrograph showing the unstrained core matrix away from the tread surface at the maximum run-out position of railway wheel HSR1.

Figure 6.51 Optical micrograph showing an overview of crack and strained matrix at a distance of about 450 □m from the tread surface at the minimum run-out position of railway wheel HSR1.

Figure 6.52 Optical micrograph showing an overview of the crack and strain matrix near the tread surface at the minimum run-out position of railway wheel HSR1.

Figure 6.53 Optical micrograph showing an overview of crack and strained matrix at a distance of about 500 □m from the tread surface at the maximum run-out position of railway wheel HSR1.

Figure 6.54 The optical micrograph above appears to show that the cracks initiate along pro-eutectoid ferrite at prior austenite grain boundaries at the minimum run-out position of railway wheel HSR1.

Figure 6.55 shows the distribution of manganese sulphide (MnS) inclusions in steel at different temperatures (Etching: KLEMM Na2S2O3-K2SO4 x200 (the original of the above photographic image is shown in reference [135] and has been reproduced and appropriately referenced here for the purpose of this PhD thesis).

Figure 6.56 shows a low magnification optical micrograph showing the change in the microstructure with depth at a distance of 5.5 cm from the non-flange end of the tread surface of rail wheel HSR1 at the minimum run-out position.

Figure 6.57 shows the microstructure of wheel HSR2 near the tread surface at the running region (image taken at 6 cm from the non-flange end) showing no shearing in this region, as expected due to the reasons discussed above.

Figure 6.58 shows the sheared microstructure near the tread surface of wheel HSR1 in the RCF region.

Figure 6.59 shows the sheared microstructure near the tread surface of wheel HSR2 in the RCF region.

Figure 6.60 shows the microstructure near the tread surface of the new wheel HSR3 in the same region as the RCF region for wheels HSR1 and HSR2.

Figure 6.61 shows the sheared microstructure near the tread surface of wheel HSR1 at max. Run-out in the field side region where plastic flow has also been observed in the worn wheels investigated.

Figure 6.62 shows the sheared microstructure near the tread surface of wheel HSR2 in the field side region demonstrating that plastic flow has occurred in this tread position as expected.

Figure 6.63 shows the sheared microstructure near the tread surface of the new wheel HSR3 in the field side region.

Table 6.2 shows the depth at which microstructural change occurs at different positions from the non-flange edge along the treads of the worn railway wheel HSR1 at the maximum run-out position of the tread and the new railway wheel HSR3.

Figure 7.1 shows the steel calibration plate with artificially created cracks and crack clusters to simulate crack clusters found in railway wheels in service for the purposes of the experiments designed and work presented in this chapter.

Figure 7.2 a digital photograph showing the steel calibration plate: CP_APJ_PHDPROJECT_2013.

Figure 7.3 shows a schematic diagram for calibration plate: CP_2 including the dimensions and type of artificial cracks (or notches) found on the calibration plate.

Figure 7.4 shows the normalised maximum change in B_x value against crack surface length at zero lift-off for semi-elliptical cracks of elliptical ratios 1:1, 1.25:1, 1.5:1 and 1.75:1; the diagram is based on Network Rail UK (formerly Railtrack) visual length-depth guidance diagram for RCF cracks (modified from Railtrack manual) [148]. Thus the above diagram has been used for the purposes of the work carried out on this PhD project, and presented in this chapter on railway wheels removed from service, to determine estimates for the crack pocket depths.

Figure 7.5 a digital photograph showing the ACFM system in the bottom left hand corner of the above image together with the probe (inset in the bottom right hand corner of the image).

Figure 7.6 shows an image of the ACFM defect indication data screen showing a typical ACFM sensor response to the presence of a defect in the material under inspection [118].

Figure 7.7 a digital photograph showing the magnetic particle inspection (MPI) system.

Figure 7.8 shows the influence of ACFM sensor angle relative to crack surface angle.

Figure 7.9 Influence of crack propagation angle (between 25 and 900) on ACFM (5 kHz) signal response to isolated semi-elliptical artificial cracks of surface length and pocket depth of 10 mm and 5 mm, respectively.

Figure 7.10 Influence of crack propagation angle (between 25 and 900) on ACFM (50 kHz) signal response to isolated semi-elliptical artificial cracks of surface length and pocket depth of 10 mm and 5 mm, respectively.

Table 7.1 shows the mean maximum change in the ACFM signal (ΔB_{xmax}) for each calibration crack in the calibration steel plate CP_2; the ACFM scans across these artificial defects are shown in Appendix B in the appendices chapter 9.

Table 7.2 shows the normalised Mean $\Delta B_{xmax}/B_{x0}$ values for the ACFM sensor signal response for cracks of surface length and pocket depth of 10 mm and 5 mm, respectively, and for propagation angles of 250, 600 and 900, and for ACFM operating frequencies of 5 and 50 kHz.

Table 7.3 shows the comparison of estimated crack pocket depths (DEST), using figure 7.4, with the actual crack depth (i.e. oversized or undersized (%)), for the ACFM sensor signal response for cracks of surface length and pocket depth of 10 mm and 5 mm, respectively, and for propagation angles of 250, 600 and 900, and for ACFM operating frequencies of 5 and 50 kHz.

Figure 7.11 Influence of sensor lift-off between 0-5 mm on ACFM (5 kHz) signal for clusters of 4 cracks with an inter-crack spacing distance of 20 mm and, surface length and pocket depth of 10 mm and 5 mm, respectively.

Figure 7.12 Influence of sensor lift-off between 0-5 mm on ACFM (50 kHz) signal for clusters of 4 cracks with an inter-crack spacing distance 20 mm and, surface length and pocket depth of 10 mm and 5 mm, respectively.

Table 7.4 Influence of lift-off and ACFM frequency on ACFM signal for cracks spaced 20 mm apart and, surface length and pocket depth of 10 mm and 5 mm, respectively.

Table 7.5 shows the comparison of estimated crack pocket depths (DEST), using figure 7.4, with the actual crack depth (i.e. oversized or undersized (%)), for the ACFM sensor signal response for cracks spaced 20 mm apart and, surface length and pocket depth of 10 mm and 5 mm, respectively, for probe lift-off distances in the range: 0-5 mm above the specimen being investigated at inducing frequencies of 5 and 50 kHz.

Figure 7.13 Influence of crack spacing and crack cluster number on ACFM (5 kHz) signal response to clusters of 2 cracks with inter-crack spacings between 5 and 20 mm and, surface length and pocket depth of 10 mm and 5 mm, respectively.

Figure 7.14 Influence of crack spacing and crack cluster number on ACFM (5 kHz) signal response to clusters of 4 cracks with inter-crack spacings between 5 and 20 mm and, surface length and pocket depth of 10 mm and 5 mm, respectively.

Figure 7.15 Influence of crack spacing and crack cluster number on ACFM (50 kHz) signal response to clusters of 2 cracks with inter-crack spacings between 5 and 20 mm and, surface length and pocket depth of 10 mm and 5 mm, respectively.

Figure 7.16 Influence of crack spacing and crack cluster number on ACFM (50 kHz) signal response to clusters of 4 cracks with inter-crack spacings between 5 and 20 mm and, surface length and pocket depth of 10 mm and 5 mm, respectively.

Table 7.6 shows the normalised Mean $\Delta B_{xmax}/B_{x0}$ values for the ACFM sensor signal response for crack clusters of 2 and 4 cracks of surface length and pocket depth of 10 mm and 5 mm, respectively, with inter-crack spacing between 5 and 20 mm and for the ACFM operating at a frequency of 5 kHz.

Table 7.7 shows the normalised Mean $\Delta B_{xmax}/B_{x0}$ values for the ACFM sensor signal response for crack clusters of 2 and 4 cracks of surface length and pocket depth of 10

mm and 5 mm, respectively, with inter-crack spacing between 5 and 20 mm and for the ACFM operating at a frequency of 50 kHz.

Table 7.8 shows the comparison of estimated crack pocket depths (DEST), using figure 7.4, with the actual crack depth (i.e. oversized or undersized (%)), for the ACFM sensor signal response for a cluster of two cracks with each crack having an actual surface length and pocket depth of 10 mm and 5 mm, for inter-crack spacing distances between 5 and 20 mm at ACFM operating frequency of 5 kHz.

Table 7.9 shows the comparison of estimated crack pocket depths (DEST), using figure 7.4, with the actual crack depth (i.e. oversized or undersized (%)), for the ACFM sensor signal response for a cluster of four cracks with each crack having an actual surface length and pocket depth of 10 mm and 5 mm, for inter-crack spacing distances between 5 and 20 mm at ACFM operating frequency of 5 kHz.

Figure 7.17 shows ACFM (5 kHz) scan with the sensor oriented at 450 to cracks showing sensor signals for a cluster of 4 cracks spaced 5 mm apart.

Figure 7.18 shows ACFM (50 kHz) scan with the sensor oriented at 450 to cracks showing sensor signals for a cluster of 4 cracks spaced 5 mm apart.

Figure 7.19 shows ACFM (5 kHz) scan with the sensor oriented at 450 to cracks showing sensor signals for a cluster of 4 cracks spaced 20 mm apart.

Figure 7.20 shows ACFM (50 kHz) scan with the sensor oriented at 450 to cracks showing sensor signals for a cluster of 4 cracks spaced 20 mm apart.

Figure 7.21 shows the ACFM scans for crack clusters with and without a central deep crack with the ACFM sensor aligned parallel to the cracks and operating at a frequency of 5 kHz.

Figure 7.22 shows the ACFM scans for crack clusters with and without a central deep crack with the ACFM sensor aligned parallel to the cracks and operating at a frequency of 50 kHz.

Figure 7.23 shows the ACFM scans for crack clusters with and without a central deep crack with the ACFM sensor oriented at 900 to the cracks and operating at a frequency of 5 kHz.

Figure 7.24 shows the ACFM scans for crack clusters with and without a central deep crack with the ACFM sensor oriented at 900 to the cracks and operating at a frequency of 50 kHz

Figure 7.25 shows the variation in the background ACFM signal B_{x0} with tread position for the worn wheel HSR1 at tread positions of maximum and minimum run-out with and without cracks present. Note: that the above B_x data are not normalised in order to clearly show the variation in the background signal with and without defects.

Table 7.10 shows the variation in ACFM signal with Tread Position for Railway Wheels HSR1 (mean value taken for the maximum and minimum run-out wheel tread positions) and HSR3 for the sensor operating at a frequency of 5 kHz.

Table 7.11 shows the variation in ACFM signal with Tread Position for Railway Wheel HSR2 for the sensor operating at a frequency of 5 kHz.

Table 7.12 shows the variation in ACFM signal with Tread Position for Railway Wheels HSR1, HSR2 and HSR3 for the sensor operating at a frequency of 50 kHz.

Figure 7.26 shows sample ACFM scans for the worn HSR1 wheel at the position of maximum run-out on the tread and at a position of 7 cm from the non-flange end.

Figure 7.27 shows sample ACFM scans for the worn HSR1 wheel at the position of maximum run-out on the tread and at a position of 8 cm from the non-flange end.

Figure 7.28 shows sample ACFM scans for the worn HSR1 wheel at the position of minimum run-out on the tread and at a position of 6 cm from the non-flange end.

Figure 7.29 shows sample ACFM scans for the worn HSR1 wheel at the position of minimum run-out on the tread and at a position of 7 cm from the non-flange end.

Figure 7.30 shows sample ACFM scans for the new HSR3 wheel (without visible defects) at a position of 2.5 cm from the non-flange end of the tread.

Figure 7.31 shows sample ACFM scans for the new HSR3 wheel (without visible defects) at a position of 8 cm from the non-flange end of the tread.

Figure 7.32 shows an image of the RCF prone region on the tread of wheel HSR1 showing the severe level of surface RCF damage that has occurred between 4 and 6 cm from the non-flange end of this wheel. Locations at which the subsequent ACFM scans (shown in the figures below) conducted on this wheel tread have been clearly labelled on the photograph.

Figures7.33 (a)-(c) incl, above show ACFM scans carried out in the RCF prone region on the tread of wheel HSR1 at the maximum run-out tread position demonstrating that the sensor is capable of detecting severely critical defects in railway wheels in service, however, the cracks are superimposed on one another and it is difficult to distinguish between the individual cracks due to the limits on the ACFM sensitivity.

Figure 7.34 shows another image of the RCF prone region on the tread of wheel HSR1 showing the severe level of surface RCF damage that has occurred between 4 and 6 cm from the non-flange end of this wheel. Locations at which the subsequent ACFM scans (shown in the figures below) conducted on this wheel tread have been clearly labelled on the photograph.

Figures 7.35 (a)-(c) incl. above show ACFM (5 kHz) scans carried out in the RCF prone region on the tread of wheel HSR1 at the maximum run-out tread position as shown above in figure 7.34 demonstrating that the sensor is capable of detecting severely critical defects in railway wheels in service, however, the cracks are superimposed on one another and it is difficult to distinguish between the individual cracks due to the limits on the ACFM sensitivity.

Figure 7.36 ACFM (5 kHz) scan across closely spaced cracks near the flange end of railway wheel HSR2.

Figure 7.37 ACFM (50 kHz) scan across closely spaced cracks near the flange end of railway wheel HSR2.

Figure 7.38 shows ACFM scans of shallow closely spaced cracks (spacing < 3 mm) found close to the flange end of the worn HSR2 wheel tread using the ACFM sensor operating at frequencies of 5 and 50 kHz.

Figure 7.39 ACFM (5 kHz) sensor scan on hsr1 rail wheel at the 70 mm running position (Note: 8 cm from non-flange end chosen here for the 70 mm running position).

Figure 7.40 ACFM (50 kHz) sensor scan on hsr1 rail wheel at the 70 mm running position.

Figure 7.41 shows the influence of the inducing frequency on the ACFM signal.

Figure 7.42 shows ACFM scans of shallow closely spaced cracks (spacing < 3 mm) found close to the flange end of the worn HSR2 wheel tread using the ACFM sensor operating at frequency of 5 kHz.

Table 7.13 shows estimated pocket depths for selected cracks from all wheels removed from service and investigated using the crack sizing diagram shown in the previous chapter. All crack surface length and pocket depth range values calculated for all wheels are shown in table 7.14 (below).

Figure 7.43 shows mean estimated crack pocket depths (DEST) (mm) for railway wheels: HSR1, HSR2 and HSR3 using the ACFM technique.

Table 7.14 Estimated Crack Pocket Depths at Different Positions along the Tread Surface of Wheels HSR1, HSR2 and HSR3, using the Network Rail based Crack Sizing Plot by evaluating the maximum change in the ACFM (5 kHz) Signal and

using this value to determine the range possible range of Crack Surface Lengths and thus the range of Crack Pocket Depths from the four Ellipse Ratios Presented on the Sizing Diagram.

Table 9.1 Hardness measurements with depth below the tread surface for railway wheel HSR1 at the minimum run-out position of the tread and at different positions of 1 cm intervals along the tread.

Table 9.2 Hardness measurements with depth below the tread surface for railway wheel HSR1 at the maximum run-out position of the tread and at different positions of 1 cm intervals along the tread.

Table 9.3 Hardness measurements with depth below the tread surface for railway wheel HSR2 and at different positions of 1 cm intervals along the tread.

Table 9.4 Hardness measurements with depth below the tread surface for railway wheel HSR3 and at different positions of 1 cm intervals along the tread.

Table 9.5 Hardness measurements with depth below the tread surface at the running position on the railway wheel tread 70 mm from the back of the flange for railway wheels HSR1 (maximum and minimum run-out), HSR2 and HSR3.

Figure 9.1 ACFM scan across calibration plate crack CC1 with the sensor aligned parallel to the surface angle of the crack.

Figure 9.2 ACFM scan across calibration plate crack CC1 with the sensor oriented at 450 to the surface angle of the crack.

Figure 9.3 ACFM scan across calibration plate crack CC4 with the sensor aligned parallel to the surface angle of the crack.

Figure 9.4 ACFM scan across calibration plate crack CC4 with the sensor at 450 to the surface angle of the crack.

Figure 9.5 ACFM scan across calibration plate crack CC2 with the sensor aligned parallel to the surface angle of the crack.

Figure 9.6 ACFM scan across calibration plate crack CC2 with the sensor oriented at 450 to the surface angle of the crack.

Figure 9.7 ACFM scan across calibration plate crack CC5 with the sensor aligned parallel to the surface angle of the crack.

Figure 9.8 ACFM scan across calibration plate crack CC5 with the sensor oriented at 450 to the surface angle of the crack.

Figure 9.9 ACFM scan across calibration plate crack CC3 with the sensor aligned parallel to the surface angle of the crack.

Figure 9.10 ACFM scan across calibration plate crack CC3 with the sensor oriented at 450 to the surface angle of the crack.

Figure 9.11 ACFM scan across calibration plate crack CC6 with the sensor aligned parallel to the surface angle of the crack.

Figure 9.12 ACFM scan across calibration plate crack CC6 with the sensor oriented at 450 to the surface angle of the crack.

Figure 9.13 ACFM scan at position: 2.5 cm from the non-flange end of the HSR1 railway wheel tread at the maximum run-out position.

Figure 9.14 ACFM scan at position: 3 cm from the non-flange end of the HSR1 railway wheel tread at the maximum run-out position.

Figure 9.15 ACFM scan at position: 7 cm from the non-flange end of the HSR1 railway wheel tread at the maximum run-out position.

Figure 9.16 ACFM scan at position: 8 cm from the non-flange end of the HSR1 railway wheel tread at the maximum run-out position.

Figure 9.17 ACFM scan at position: 10 cm from the non-flange end of the HSR1 railway wheel tread at the maximum run-out position.

Figure 9.18 ACFM scan at position: 2.5 cm from the non-flange end of the HSR1 railway wheel tread at the minimum run-out position.

Figure 9.19 ACFM scan at position: 3 cm from the non-flange end of the HSR1 railway wheel tread at the minimum run-out position.

Figure 9.20 ACFM scan at position: 6 cm from the non-flange end of the HSR1 railway wheel tread at the minimum run-out position.

Figure 9.21 ACFM scan at position: 7 cm from the non-flange end of the HSR1 railway wheel tread at the minimum run-out position.

Figure 9.22 ACFM scan at position: 7 cm from the non-flange end of the HSR1 railway wheel tread at the minimum run-out position.

Figure 9.23 ACFM scan at position: 8 cm from the non-flange end of the HSR1 railway wheel tread at the minimum run-out position.

Figure 9.24 ACFM scan at position: 10 cm from the non-flange end of the HSR1 railway wheel tread at the minimum run-out position.

Figure 9.25 ACFM scans at positions: 2.5 and 3 cm from the non-flange end of the HSR1 railway wheel tread at the maximum (MMU_OW_2DOTS) and minimum (MMU_OW) run-out tread positions showing the variation in the background sensor signal at these tread positions.

Figure 9.26 ACFM scans at positions: 4 and 5 cm from the non-flange end of the HSR1 railway wheel tread at the maximum (MMU_OW_2DOTS) and minimum

(MMU_OW) run-out tread positions showing the variation in the background sensor signal at these tread positions.

Figure 9.27 ACFM scans at positions: 6 and 7 cm from the non-flange end of the HSR1 railway wheel tread at the maximum (MMU_OW_2DOTS) and minimum (MMU_OW) run-out tread positions showing the variation in the background sensor signal at these tread positions.

Figure 9.28 ACFM scan at position: 2.5 cm from the non-flange end of the HSR2 railway wheel tread.

Figure 9.29 ACFM scan at position: 3 cm from the non-flange end of the HSR2 railway wheel tread.

Figure 9.30 ACFM scan at position: 4 cm from the non-flange end of the HSR2 railway wheel tread.

Figure 9.31 ACFM scan at position: 5 cm from the non-flange end of the HSR2 railway wheel tread.

Figure 9.32 ACFM scan at position: 5 cm from the non-flange end of the HSR2 railway wheel tread.

Figure 9.33 ACFM scan at position: 6 cm from the non-flange end of the HSR2 railway wheel tread.

Figure 9.34 ACFM scan at position: 7 cm from the non-flange end of the HSR2 railway wheel tread.

Figure 9.35 ACFM scan at position: 8 cm from the non-flange end of the HSR2 railway wheel tread.

Figure 9.36 ACFM scan at position: 8 cm from the non-flange end of the HSR2 railway wheel tread.

Figure 9.37 ACFM scan at position: 9 cm from the non-flange end of the HSR2 railway wheel tread.

Figure 9.38 ACFM scan at position: 9 cm from the non-flange end of the HSR2 railway wheel tread.

Figure 9.39 ACFM scans at positions: 2 and 2.5 cm from the non-flange end of the HSR2 railway wheel tread showing the variation in the background sensor signal at these tread positions.

Figure 9.40 ACFM scans at positions: 3 and 4 cm from the non-flange end of the HSR2 railway wheel tread showing the variation in the background sensor signal at these tread positions.

Figure 9.41 ACFM scans at positions: 5 and 6 cm from the non-flange end of the HSR2 railway wheel tread showing the variation in the background sensor signal at these tread positions.

Figure 9.42 ACFM scans at positions: 7 and 8 cm from the non-flange end of the HSR2 railway wheel tread showing the variation in the background sensor signal at these tread positions.

Figure 9.43 ACFM scans at positions: 9 and 10 cm from the non-flange end of the HSR2 railway wheel tread showing the variation in the background sensor signal at these tread positions.

Figure 9.44 ACFM scan at position: 2.5 cm from the non-flange end of the HSR3 railway wheel tread.

Figure 9.45 ACFM scan at position: 6 cm from the non-flange end of the HSR3 railway wheel tread.

Figure 9.46 ACFM scan at position: 3 cm from the non-flange end of the HSR3 railway wheel tread.

Figure 9.47 ACFM scan at position: 2.5 cm from the non-flange end of the HSR3 railway wheel tread.

Figure 9.48 ACFM scan at position: 8 cm from the non-flange end of the HSR3 railway wheel tread.

Figure 9.49 ACFM scan at position: 2.5 cm from the non-flange end of the HSR3 railway wheel tread.

Figure 9.50 ACFM scan at position: 8 cm from the non-flange end of the HSR3 railway wheel tread.

Figure 9.51 ACFM scan at position: 9 cm from the non-flange end of the HSR3 railway wheel tread.

Figure 9.52 ACFM scan at position: 9 cm from the non-flange end of the HSR3 railway wheel tread.

Figure 9.53 ACFM scans at positions: 2.5 and 3 cm from the non-flange end of the HSR3 railway wheel tread showing the variation in the background sensor signal at these tread positions.

Figure 9.54 ACFM scans at positions: 4 and 5 cm from the non-flange end of the HSR3 railway wheel tread showing the variation in the background sensor signal at these tread positions.

Figure 9.55 ACFM scans at positions: 6, 8 and 9 cm from the non-flange end of the HSR3 railway wheel tread showing the variation in the background sensor signal at these tread positions.

Figure 9.56 Fine cracks found near the flange end and across most of the entire circumferential length of the HSR2 railway wheel at a position of 9.0 cm from the non-flange end.

Figure 9.57 HSR2 Rail Wheel ACFM (5 kHz) Scan across the Tread at position 9.0 cm from non-flange end.

Figure 9.58 HSR2 Rail Wheel ACFM (5 kHz) Scan across the Tread at position 9.0 cm from the non-flange end.

Figure 9.59 shows closely spaced and shallow cracks found near the flange of the HSR2 railway wheel and oriented approx. at 600 to the circumference of the wheel tread surface and present across most of the entire circumferential length of the wheel.

Figure 9.60 HSR2 Rail Wheel ACFM (5 kHz) Scan across Feature shown in A in figure 9.57.

Figure 9.61 shows fine cracks found near the non-flange end of the HSR2 railway wheel and oriented approx. at 900 to the circumference of the wheel tread surface and present across most of the entire circumferential length of the wheel at a position of 3 cm from the non-flange end.

Figure 9.62 Feature B on railway wheel HSR2 scanned by ACFM.

Figure 9.63 HSR2 Rail Wheel ACFM (5 kHz) Scan across Feature B.

Figure 9.64 Feature D found on the tread of railway wheel HSR2 scanned by ACFM.

Figure 9.65 HSR2 Railway Wheel ACFM (5 kHz) Scan across Feature D.

Figure 9.66 shows an image of the RCF prone region on the tread of wheel HSR1 showing the severe level of surface RCF damage that has occurred between 4 and 6 cm from the non-flange end of this wheel. Locations at which the subsequent ACFM scans (shown in the figures 9.65 and 9.66 below) conducted on this wheel tread have

been clearly labelled on the photograph. Note that this figure is shown as figure 7.31 in chapter 7 of the PhD thesis above and has been reproduced here to keep it in context as it is part of this report and for the ease of the reader.

Figure 9.67 HSR1 Railway Wheel ACFM (5 kHz) Scan across Region C. Note that this figure is shown as figure 7.32(a) in chapter 7 of the PhD thesis above and has been reproduced here to keep it in context as it is part of this report and for the ease of the reader.

Figure 9.68 HSR1 Rail Wheel ACFM (5 kHz) Scan across Feature E (an ‘E’ shaped feature at an angle of approximately 450 to the circumferential direction of the railway wheel). Note that this figure is shown as figure 7.32(b) in chapter 7 of the PhD thesis above and has been reproduced here to keep it in context as it is part of this report and for the ease of the reader.

Figure 9.69 HSR1 Rail Wheel ACFM (5 kHz) Scan across Feature L; shows two separate troughs corresponding to adjacent individual cracks. Note that this figure is shown as figure 7.32(c) in chapter 7 of the PhD thesis above and has been reproduced here to keep it in context as it is part of this report and for the ease of the reader.

Figure 9.70 shows another image of the RCF prone region on the tread of wheel HSR1 showing the severe level of surface RCF damage that has occurred between 4 and 6 cm from the non-flange end of this wheel. Region Y across which the subsequent ACFM scan (shown in figure 9.69 below) conducted on this wheel tread has been labelled on the photograph.

Figure 9.71 HSR1 Rail Wheel ACFM (5 kHz) Scan across Region Y.

Figure 9.72 shows another image highlighting specific areas of the RCF prone region on the tread of wheel HSR1 showing the severe level of surface RCF damage that has occurred between 4 and 6 cm from the non-flange end of this wheel. Locations at which the subsequent ACFM scans (figures 9.71-9.73 incl. below) conduct+ed on this wheel tread have been clearly labelled on the photograph. Note that this figure is shown as figure 7.33 in chapter 7 of the PhD thesis above and has been reproduced here to keep it in context as it is part of this report and for the ease of the reader.

Figure 9.73 ACFM (5 kHz) scan across feature R in the downward direction, showing a large primary and an adjacent smaller subsidiary trough, corresponding to clusters of large and small cracks, respectively. Note that this figure is shown as figure 7.34(a) in chapter 7 of the PhD thesis above and has been reproduced here to keep it in context as it is part of this report and for the ease of the reader.

Figure 9.74 HSR1 railway wheel ACFM (5 kHz) scan across region X. Note that this figure is shown as figure 7.34(b) in chapter 7 of the PhD thesis above and has been reproduced here to keep it in context as it is part of this report and for the ease of the reader.

Figure 9.75 HSR1 railway wheel ACFM (5 kHz) scan across region Z. Note that this figure is shown as figure 7.34(c) in chapter 7 of the PhD thesis above and has been reproduced here to keep it in context as it is part of this report and for the ease of the reader.

Figure 9.76 HSR1 rail wheel ACFM (5 kHz) scan along the 70 mm tread running position of the railway wheel.

CHAPTER 1
INTRODUCTION

1.1 THE NECESSITY OF EFFICIENT, SAFE, RELIABLE AND COST-EFFECTIVE RAILWAY SERVICES

The increasingly higher volume of trains running on the railway networks in Britain, Europe and throughout the world, combined with greater axle loads and increasing vehicle speeds are an ever increasing burden on the railway infrastructure and, therefore, can cause catastrophic failure due to derailments such as the major one that occurred at Hatfield in 2000 and, unfortunately, resulted in a loss of life including disruption to the rail network, increased maintenance costs and a loss of confidence in the industry. Therefore, it is of utmost importance to maintain a reliable, efficient and cost-effective railway network by developing and employing non-destructive evaluation methods, including developing and implementing high speed inspection systems, such as the alternating current field measurement (ACFM) technique which is currently under development, for the inspection of railway vehicle and components and railway track in order to ensure the integrity of railway assets and the continued safety of commuters. The main goal at present for the railway industry in Europe, in order to meet the current challenges facing the industry is first and foremost to improve railway safety and then to provide more efficient, reliable and sustainable, both financially and environmentally-friendly, railway systems. Thus, research and development of new and efficient technologies needs to be made a priority and, thus, advances in technologies have to be implemented and taken advantage of efficiently in the right manner. Currently, safety of railway assets is ensured by a combination of online monitoring and inspections at the production and maintenance stages including reducing the extent of wheelset related failures which, in turn, lowers the costs incurred during maintenance.

1.2 THE IMPORTANCE OF RAILWAY ROLLING STOCK RELIABILITY

During the past, freight and passenger traffic has increased at a rapid rate. Therefore, the railway network has had to cope with this challenge by employing certain appropriate measures and strategies to overcome such critical issues. These imposed

measures include re-timetabling, increased train lengths, demand management, introducing new rolling stock and infrastructure including the provision of more efficient engineering resources in order to reduce the possibility of down time in the network which can severely hamper the smooth running of the UK-wide rail network if appropriate provisions are not made in a timely manner to resolve the issues and, thus, rectify the situation. Furthermore, the substantial increase in passenger traffic has been accommodated by the supply of additional electrical multiple units (EMUs) and diesel multiple units (DMUs) to the railway network. According to a report by network rail [129] the average age of passenger rolling stock has been steadily declining from 21 to 13 years in 1999/2000 and 2005/2006, respectively. EMUs comprise most of the fleet (including the Pendolino fleet of vehicles) at approximately 63%, whereas, DMUs make up about 24% of the total fleet with the locomotive hauled vehicles that include HST trailers making up the rest of the fleet at approximately 13%. The EMU and DMU railway vehicles are more environmentally friendly and much quieter, faster and safer than their predecessors. In addition, their braking systems and acceleration capabilities including their operation in-service are superior than was the case for previous generations of railway rolling stock. Furthermore, coupled with a broad range of facilities for commuters as well as air-conditioning systems including more reliable growth these vehicles make a promising suite of passenger trains for the railway network moving forward. However, these vehicles still do pose certain challenges to the network and, therefore, some important issues need to be ironed out in order to achieve the above goal. Such issues include the significant increase the overall weight of the new type of rolling stock, a substantial increase in their annual mileage due to the increase in their functionality and the higher availability of the rolling stock, respectively. Furthermore, the maintenance costs and energy usage has significantly risen as a result of these factors together with sub-optimal bogie characteristics on some classes of vehicles. At present, the UK rail network is working alongside manufacturers, owners and operators to encourage the industry to further make use of track-friendly bogies and, thus, to make these systems more industrially widespread.

The primary issues faced by the railway industry at present as noted by relevant organisations [128] include wheel flats, out-of-round wheels, RCF damage, damage to bearings and sub-surface damage in the form of defects. The advantages provided by

automated wheelset condition monitoring systems are provision of prior warning of impending structural failure, the identification of trends, wear patterns including the provision of more efficient and cost-effective monitoring processes for structural assets. However, the main disadvantages of such systems at present which need to be immediately addressed and, thus, overcome to effectively implement these technologies in the rail industry are the substantially high initial costs involved in their implementation including the complex nature and, in certain cases, the loss of confidence in some systems. At present, wheel impact, out-of-round and hot axle bearing detectors (HABD) are employed by the rail industry for the condition monitoring of wheelsets. Manual and automated visual inspection systems are currently employed to assess wheel tread damage, monitoring of wheel profiles amongst other issues. However, the reason that has been identified as the main hindrance to the implementation of wheelset condition monitoring (WCM) systems thus far is due to their lack of proven success and confidence, including, as a result, that these systems have on the negative impact on the normal operational performance of wheelset components. Nevertheless, the impetus for conducting investigations of WCM systems for industrial applications has been provided by the strong business case offered by implementing these WCM systems for applications in the railway industry as identified and presented by the primary industrial manufacturers. It should also be ensured that WCM systems are deployed ensuring limited hindrance to the railway network and operations together with implementation of the vehicles on a regular basis. Effective decision-making on maintenance issues can be realised with the use of automated systems and it is generally believed that current standards and practices would not obstruct a move in this direction. Furthermore, even though some automatic vehicle identification (AVI) systems have been installed on the network for certain types of applications it is generally agreed upon within the industry that the development and deployment of a standard AVI system would be beneficial in terms of the full realisation of the potential of employing WCM technologies for industrial applications on the UK rail network.

In order to successfully implement automated WCM systems throughout the network it is of utmost importance to develop and integrate a standard AVI system into all WCM inspection stations and, thus, tag each vehicle that is to be monitored. Such a standard AVI system installed across the board on the railway network will enable

inspections which are carried out on vehicles and wheelset components to be systematically associated with specific vehicles and will also log the time and location of the specific inspections that were conducted. The provision of such information to all the stakeholders is important for trend analysis, determination of wear patterns for components and thus storing vital information on the history of every vehicle in service. Furthermore, a central database needs to be set up together with trained personnel acting as a support team to effectively manage and store the information acquired from the different WCM detectors. In addition, in order for such a database to properly function and action its tasks with the above intended aim it must have the following capabilities:

- Able to access data from all WCM inspection systems on the network.
- Possess the capacity to store large volumes of data received from all WCM inspection sites.
- Have an appropriate mechanism in place to identify and assign vehicle specific data to the right vehicle.
- Ensure that the system is user friendly such that relevant and useful vehicle specific information is provided to users by effectively organising, processing, analysing and reporting the information and making the data easily accessible to potential users from the various stakeholders and, thus, ensuring that every report generated is specifically tailored to the requirements of each specific type of stakeholder.
- Another important requirement to be met to successfully implement an automated WCM inspection system on the network is developing the right type of infrastructure for communication purposes to enable data to be routed from every inspection site to the database. This infrastructure can be constructed based on the currently available communication systems and that can, therefore, route the information to the database using a link via the internet.
- In addition, revisions may be required of existing specifications and formats or the creation of new ones may be needed, for instance, to standardise the data formats for the transfer of information to the central database. Additional standards and procedures might be required for the purposes of calibration and testing of inspection stations after installation. Therefore, wheelset

maintenance practices are also anticipated to move towards and, thus, considered in the light of condition based maintenance regimes.

- A further need is a cost-benefit analysis to be conducted, possibly by various stakeholders in a coordinated manner to ensure efficiency of purpose, because newly developed technologies are often rather expensive to develop and implement and, therefore, it is important to justify to the industry whether the subsequent implementation of a proposed new system is not only required for the specific purpose at hand but also economically viable.
- Appropriate strategies may also be needed to ensure a smooth transition to an intelligence based automated wheelset condition monitoring maintenance regime.
- Change-over from time/mileage to condition/performance based maintenance practices.
- Provision of adequate training for personnel to enable them to perform maintenance duties in order to maintain equipment instead of just inspecting equipment.
- Implementing a standard AVI system across the entire railway network.
- Ensuring that all the costs incurred and the benefits yielded by implementing a WCM regime network-wide are equally shared among all the relevant stakeholders.
- Strengthen the trust and confidence of users in newly installed technologies and systems for automated condition monitoring and maintenance regimes.
- Capable of effectively handling former and outdated WCM technologies and systems.

Furthermore, according to the RSSB report on wheelset monitoring [32], at present, the available automated WCM systems are able to meet most of the wheelset component monitoring requirements, however, not every inspection need is currently being met by these systems and, therefore, further work is ongoing in this area both within academia and industry to research and develop new technologies and strategies to address these pertinent issues. Some of the technological gaps to address these issues include assessing cracks found in the rail wheel tread, rim, flange and plate; wheel flange parameters can currently be determined using wheel profile systems, such as the mini-profile system, which can also be employed to determine the

thickness of the wheel's rim, out-of-roundness, including assessing other wheel parameters such as out-of-gauge and hollow wear; wheel impact detectors are currently used to identify and assess wheel parameters such as high impact and flats caused by sliding. There is currently an urgent requirement to fill the gap in automated technologies to detect and assess damage to axles; such axle parameters that need to be monitored include defects found in axles or, in the extreme case, cracked axles, wheel seat damage and have become severely deformed or bent. In the case of bearings the present spectrum of available inspection techniques are capable of detecting most of the types of defects which are commonly found in bearings. However, loose components are still manually inspected for the presence of potential defects, for example, loose backing rings and loose or damaged seats for the bearings, and the process has not been automated for this purpose thus far. Detectors such as acoustic bearing defect detectors and hot axle box detectors (HABD) are currently used to detect damage caused to the cone and roller of bearings and also to locate and investigate a cracked or shattered cup of the bearing. The parameters associated with bogies, such as, hunting and warped bogies are currently detected and monitored using bogie performance detectors, however, there is currently a gap in inspection technologies for detecting broken or missing springs and damage to dampers. Nevertheless, the monitoring of bogie springs can potentially be carried out using machine vision technologies, though, no such system has thus far been developed for this purpose. Furthermore, in the case of brake inspections, parameters such as ineffective and stuck brakes are at present inspected using cold and hot wheel detectors, respectively; whereas, detecting worn, broken or missing brake pads (or, alternatively, shoes) is currently carried out by employing brake pad/shoe condition monitoring techniques. However, at present there is a lack of available automated detection technologies for the inspection of the brake's beam.

Therefore, as discussed above, even though currently available wheelset condition monitoring systems are capable of meeting the majority of the present wheelset inspection needs for maintenance purposes, it is by no means all encompassing, as there are still technological gaps which need to be immediately addressed in this regard and, thus, work is ongoing in this field to develop appropriate technologies for the detection and investigation of other important railway wheelset parameters;

research and development is currently being conducted in industry in coordination and partnership with academia towards this end.

1.3 INDUSTRIAL CHALLENGES

1.3.1 WHEELSET RELATED DEFECTS

In general, railway wheels are removed from service due to the occurrence of RCF type defects such as out-of-roundness, spalling, shelling, flats and built-up treads. Currently deployed track-based wheelset inspection systems can monitor the condition of components, such as, axle bearings, braking systems, wheels damaged by spalling or due to sliding on the track, including hunting which is a transient motion in the lateral direction. However, due to the unreliability of current detectors and, thus, the potential for misinterpretation of data, combined with the fact that the present range of detection systems can altogether miss critical defects, such existing systems, therefore, are not regarded as a substitute for maintenance procedures. The majority of these detectors are connected to the central computer network for the railway system in order to feed information to the system for subsequent use, as required for the assessment of railway wheelsets. The main wheelset monitoring systems currently used in the British railway industry to monitor and inspect railway vehicles and components are discussed in detail in the following sections 1.3.2 and 1.3.3 below. However, the primary aim of implementing such systems is to be able to detect potential critical damage to the assets before catastrophic failure occurs. For example, the thermal energy emanating from a bearing can be detected using a hot box detector which can then relay any relevant and vital information on the bearing's standing structural condition to the central authority for command and control in order to address the issue and, thus, take any necessary precautions and measures to avert any possibility of imminent failure. However, as bearings are prone to rapidly heat-up and then immediately stop functioning before the train moves past an inspection point where a hot box might be stationed, there is, therefore, insufficient time for a warning signal to be relayed to the centralised database before remedial action can be implemented or a potential disaster, such as derailment, can be thwarted. Wheel impact monitors are able to identify defective out-of-round wheels due to, for instance, the presence of flats or spalling related damage on the wheel tread surface, these types of detectors are incapable of detecting any form of critical surface breaking defects and internal defects that might be present deep within the structure,

for example, a railway wheel, being inspected. Therefore, such types of defects will not be identified and, thus, overlooked by the system until inspection and maintenance is carried out on the damaged wheelset when it is, subsequently, removed from service. It is of utmost importance to be able to detect severe defects in the wheel in time to avoid critical failure such as the deterioration of the structural integrity of the wheel to critical levels which may lead to high probability of derailment. The drawbacks of currently available track-based inspection detection systems is their unreliability in terms of their limited functionality which is only to do with identifying rolling stock that requires inspection and/or maintenance prior to its leaving the depot. Also, the application of wheel impact detectors for wheelset inspection is constrained by the currently imposed threshold levels on such systems.

1.3.2 MAINTENANCE ISSUES

Railway wheels and track are regarded as major assets for the railway industry and, therefore, employing the correct maintenance procedure in a timely manner is of utmost importance in ensuring the reliability and integrity of the rolling stock structural assets including the safety of the commuters and commodities that are transported on the passenger and freight vehicles, respectively. Wheel and rail profiles that do not conform to each other and worn wheels which are hollow result in the loss of the vehicle' performance during the negotiation of curves by steering which, therefore, results in higher fuel consumption. As a result, the vehicles somewhat warp, thus, making the vehicle bolster rotate horizontally relative to the side frames; this causes the rails to develop prominently large angles of attack resulting in flange contact with the outer rail. Furthermore, a mismatch between the wheel and rail profiles leads to an increase the rolling resistance and, therefore, significant improvements in the design and maintenance can yield significant savings in terms of the overall fuel consumption. Furthermore, this impact on fuel consumption influences the stability of the vehicle and, thus, increases the risk of possible derailment which can lead to unwanted catastrophic consequences. To sum up, the significantly high amount of energy expended, the higher costs involved, for example, for actions such as transportation and installation, the subsequent adverse impact on the environment, the greater amount of resources required in order to replace worn wheels and rails, all have a considerable cumulative impact on the environment and the energy consumption to carry out the tasks involved such as the resources required

to produce new wheels and rails, for example, raw materials, transport and energy, together with the logistics involved in the transportation of damage worn wheels and rails and then install the new wheels and rails [130].

Presently, wheelset maintenance is carried out using visual inspection methods supplemented by some automated inspection systems, such as, wheel impact load detectors and HABD and the inspections are generally conducted on a periodic basis on vehicles and components on reaching the threshold for inspection or at the point of structural failure. At present, the provision of information by automated condition monitoring systems specifically concerning vehicles is limited in the majority of cases. Currently, available automated inspection systems provide early warnings of impending failure in machinery and, thus, provide useful information concerning the performance of components and, thus, alert when they begin to perform below par due to a major deterioration in functionality, for example, as a result of flat or out-of-round wheels, or the presence of hot axle bearings and changes in the condition of other such components that indicate an impending structural failure. However, in order to ensure the efficient use of such automated condition monitoring systems certain present practices will have to change and, thus, improved to become more efficient; for example, currently, information gathered from WCM systems which is not utilised fully and only to the extent of using the acquired data for the purposes of providing an alert to an impending critical failure. In addition, information gathered on non-alerting components is not fully used and also the alarm rates for certain systems are found to exceed the normal level which is regarded as acceptable in the industry and, therefore, can result in unwelcome delays for trains. Therefore, to counteract this current state of affairs the railway industry is having a re-think of its overall philosophy on maintenance and is moving towards a strategy which is reliant upon intelligent-based condition monitoring comprised of an integrated network of wheelset condition monitoring techniques that relay information concerning the condition of vehicles and components which is subsequently stored in a central database which acts as an ‘information hub’ which can, thus, be used to generate reports and provide useful alerts for impending catastrophic failure to components; these reports and alerts are tailored to the specific requirements of each stakeholder. The development and use of such intelligent and proactive condition monitoring systems for the automated monitoring of wheelset components can yield trends and

patterns in the performance of vehicles and components during the passage of time, ultimately, effectively control and minimise or prevent the occurrence of catastrophic failures during service.

The primary advantages and disadvantages of implementing wheelset condition monitoring systems industry-wide are as follows. An important benefit derived by the industry by effectively implementing the proactive WCM strategy as described above is that such a strategy ensures that the potential infrastructure and vehicle damage that may otherwise be caused is minimised and that track availability is increased, thus, reducing train delays and enhancing the efficiency of planned maintenance programs, hence reducing maintenance costs. Data obtained from automated condition monitoring systems including historical information and data obtained from other inspection regimes are together used to report on and, thus, judge the condition and the structural integrity of wheelset components in service. As a result of this wide-ranging information obtained from various sources patterns and trends in the wear behaviour of vehicle components can be ascertained and analysed and, therefore, appropriate preventative measures may be taken to pre-empt any form of failure and, thus, ensure that vehicles are maintained to the standards required by the industry in accordance with industrial standards in order to reduce the likelihood of wheelset components degrading to such an extent that the level of wear has reached a stage where their performance has deteriorated to unacceptable threshold levels.

The main advantages of implementing automated WCM systems in the railway industry include the following: improved safety, enhanced reliability and efficiency, an increase in the frequency of inspection, maintaining consistency of inspections, more availability of trains in operation on track, lower count of false alarms, prioritised maintenance activities focusing on vehicles and/or wheelset components that require immediate attention, thus, improving the efficiency of maintenance actions, limit the amount of train delays on the UK railway network, significantly increasing the service life of vehicles, resulting in significant cost-savings for the industry such as in the case of maintenance costs and, finally, the provision of central database with information on the service life history of all the vehicles and their components running on the UK rail network for the subsequent reporting on general trends for eventual predictive maintenance purposes. However, the main

disadvantages to the industry on the implementation of automated inspection systems are the following: high initial costs involved up-front to implement the automated inspection systems including the reliability issues associated with these systems and the costs involved in maintaining these systems, more complex systems, gaining confidence and trust in the data acquired from these WCM systems, there is also the potential for too much information being obtained from such automated inspection systems and, furthermore, the successful implementation for an efficient network of integrated automated WCM inspection systems on the railway network will require a change in the present railway practices. Two of the above mentioned benefits of implementing an automated WCM regime on the rail network, namely, an increase in the frequency of inspections and greater train availability are due to the fact that with the existence of automated WCM inspection systems for wheelset components the monitoring of the structural integrity of components can be carried out on every occasion that the vehicle passes an inspection station on the track and, thus, inspections may be conducted on multiple occasions every day.

Furthermore, the resultant effect of utilising WCM regimes in conjunction with making informal decisions concerning the overall performance of vehicles in service based on multiple inspections instead of a single inspection approach would be a significant reduction in the number of false alarms and, as a consequence, leading to a reduction in the frequency and occurrence of train delays and, thus, limit the negative impact which might otherwise occur on the railway network due to train delays in terms of the excessive financial costs incurred by the industry and, consequently, the negative impact that this may have on passenger satisfaction. The existence of a centralised database of information (or an information hub) gathered from various WCM systems and stored in the database can allow the maintenance regimes to be prioritised and specifically tailored to each type of vehicle and, thus, ensure that the maintenance procedures are made more efficient and cost-effective. This is realised as the information acquired from different detectors on a vehicle's performance clarifies the maintenance requirements of each type of vehicle. Prioritisation of maintenance is achieved by a scoring process where a score is assigned to each type of vehicle on the basis of the results obtained from each detector and, subsequently, generating a report which is then sent to relevant organisations advising on which vehicles need to be prioritised for urgent maintenance and also informing the relevant parties concerned

on the specific maintenance measures that need to be undertaken for immediate remedial action. Furthermore, the provision of feedback to maintenance depots by reports generated by a centralised database on information derived from an automated WCM system on the effectiveness of maintenance procedures on the performance of the vehicle and wheelset components would, thus, allow maintenance actions to be analysed, evaluated and, therefore, adjusted if required. As a result, maintenance actions would become more cost-effective and efficient; thus, potentially extending the service life of vehicles. The financial gains, in terms of cost-savings, provided by the implementation of an industry-wide automated WCM regime are due to various important factors which arise as a consequence of this change-over to a more automated condition monitoring system and include the following:

- Less manual inspections.
- Discarding unnecessary maintenance actions.
- More availability of vehicles.
- Less train delay.
- Vehicle and rail infrastructure are less likely to suffer damage induced by wheelsets that are faulty and damaged by the introduction of an automated WCM regime.
- The efficiency and accuracy of inspections and the WCM process is considerably enhanced.
- The service life of railway rolling stock is extended.

Therefore, the present and uppermost goal for the railway industry is to make the transition from the current management and monitoring of railway assets by manual inspection and auditing practice to a more intelligent and automated condition monitoring (CM) and/or structural health monitoring (SHM) system that will assess the structural health and, thus, integrity of railway assets by employing a more proactive approach using wide-ranging and focused information provided by various automated WCM detectors in order to investigate trends and changes in the functioning of the vehicles and wheelset components by determining the root causes of any issues that may arise concerning poor asset health and, thus, rectifying the situation before the system fails. This prevents vehicle components from degrading beyond acceptable threshold levels which, in turn, prevents wear and damage to components from unnecessarily occurring; thus, enhancing the performance levels of

railway vehicles improves the overall quality of rail network-wide which, in turn, yields cost benefits for the industry in terms of significantly lowering operational and maintenance (O&M), including replacement, costs for railway infrastructure. Train operators can also benefit from the information ascertained from the WCM centralised database to make more informed decisions on maintenance issues as an enhanced maintenance capability provided by an automated WCM system would naturally make changes to practices in the industry inevitable for monitoring and assessing the performance of vehicles and, thus, enable vehicle operators to well-maintain their fleet of vehicles at optimal levels and, therefore, reduce the risk of causing unnecessary damage to the rail infrastructure by the presence of damaged vehicles and components. Another important benefit for the railway network provided which is provided by the information ascertained on the performance of different vehicles from the database are the so-called threshold exception reports that highlight which vehicles are poorly performing on the track and, therefore, might degrade the structural integrity of of the track and, thus, ensuring that appropriate remedial action can be taken sooner rather than later to prevent the potential degradation of track and, subsequent, failure. Train operators also benefit from embracing such a preventative maintenance regime as this would potentially lead to a reduction in the costs associated with maintenance, enhance commuter satisfaction by improving the quality of the ride and reduce train delays for commuters; this last point is directly due to defective components being identified well in advance of any critical failure occurring and, thus, enabling corrective action to be undertaken to tackle and resolve any potential issues from arising. As such, faulty wheelset components can be maintained or removed if necessary whenever required and at the appropriate time as judged by the train operator so as to minimise any subsequent impact that may occur on the running of the trains on the track, thus, limiting the number of trains that are out of service at any given time and also to ensure that the periods during which these vehicles are missing from service is as short as possible to limit the impact on the railway network. The information on trends also makes the scheduling of maintenance procedures much more efficient including assessing the performance of fleets of the same type or different fleets running on different routes on the railway network in order to make informed decisions on, for example, which fleets perform better than others and, thus, design new fleets. Furthermore, maintaining components at their optimal state would also limit any potential consequential damage to other

components. In addition, rolling stock companies are able to maintain their vehicles at optimal levels to extend their service life by prioritising maintenance based on risk analysis carried out in the light of important information provided by reports generated by the central database. Furthermore, trends identified from an automated WCM system can pre-empt any potential wheelset failure as the implementation of such a system can identify wheelsets which might require such preventative maintenance measures as described above in contrast to solely identifying wheelsets that have already failed. Information acquired on general trends can be used to diagnose other important issues such as changes occurring in the patterns of wear which can indicate further potential problems that are associated with wheelsets such as faulty brakes. Therefore, data analysis can yield vital information concerning other related issues with vehicle components that have not been monitored which will also help in diagnosing and preventing possible critical failure to railway vehicle assets from occurring in the future. However, it must be stressed that the implementation of an automated WCM regime on the railway network is considered as an aid to conduct more specific, focused and efficient inspections and is not anticipated to replace inspections carried out manually altogether. Furthermore, trending data can be used by vehicle manufacturers to improve and modify future vehicle design based on information obtained from the WCM system's central database. Details on wera rates can show which components wear at higher rates and those that frequently exceed the acceptable threshold, as well as determining the likelihood of components failing and their service life including investigating the influence of different types of fleet of trains on various components and, finally, determining the performance of a specific type of fleet of vehicles performs on different routes. As a result, improvements in the design of vehicles can be made based on the performance of wheelsets during service over a period of time. This can also eventually manifest itself in appropriate changes being made to the standards in the industry from the information gathered by stakeholders which would thus inform, as appropriate, the regulatory bodies in the railway industry to address any relevant issues and concerns, thus, auctioning appropriate changes to the standards.

1.3.3 THE GENERAL INSPECTION APPROACH

The current state-of-the-art for the inspection of railway assets includes the employment of the main techniques listed below to detect damage caused to the

railway infrastructure and, thus, assess the structural integrity of the assets. Thus, develop strategies for maintenance purposes for remedial action. The current focus is on the development of viable cost-effective methodologies for the fast and efficient automated inspection of railway assets. Ultrasonic based inspection systems currently bear most of the burden of evaluating the structural integrity of railway assets, however, it is postulated in the available literature [128-130, 145-147] that a system comprised of conventional ultrasonic probes and an integrated network of electromagnetic non-destructive evaluation (NDE) sensors and automated visual inspection techniques combined with data control and appropriate software deployed for data analysis can provide a more rapid and efficient condition monitoring regime for high-speed applications in the future for the railway industry. The following is a list of the currently available non-destructive testing methods which may be used for wheelset maintenance [128].

- Visual Examination
- Magnetic Particle Examination (or Magnetic Particle Inspection (MPI))
- Eddy-Current Examination
- Alternating Current Field Measurement Technique (ACFM)
- Ultrasonic Testing (UT)
- Dye-Penetrant Examination
- Magnetic Flux Leakage (MFL) Technique
- Acoustic Emission (AE)

These and some other not so widely used techniques such as radiography are discussed in more depth in chapter 4. However, ultrasonic axle testing (UAT) is used to inspect the rim and disk of the wheel. Wheelsets are visually examined prior to repair or overhaul [32]. Only the parts that can be seen without removing components are to be examined. Ultrasonic testing is also used to detect discontinuities on the surface of the wheel tread. Such defects include cracks, wheel flats, dents, and alterations in the wheel material. Research is currently in progress to develop a laser-based ultrasonic NDE technique for the purpose of cracked axle detection.

All solid axles are also to be examined using magnetic particle inspection (MPI) during manufacture and wheelset overhaul. MPI is an inspection procedure used to

detect surface, or near surface, imperfections in magnetisable materials. MPI is not carried out on axles where bearings are fitted which cannot be demagnetised in situ. General surfaces, seats for wheels, gear wheels, suspension tubes and other interference fit components are to be subject to MPI when exposed.

Eddy-current examination is primarily focused on the detection of surface defects such as head checks that are commonly found to occur at the gauge corner of rails as well as for detecting wheel burns, short-pitch corrugations, amongst others [104].

The ACFM system is an electromagnetic non-destructive testing (NDT) technique and is an extension on the eddy-current method providing one pass inspection with a high tolerance to lift off [43, 114-118, 144]. No electrical contact is required and thus can be used through coatings providing crack detection and sizing (length and depth). Furthermore, there is no reliance on operator calibration; manual, automated and semi-automated systems are available. To summarise, the applications and the theoretical and practical limitations of the technique are as follows. The technique is currently used to inspect a wide range of materials including: carbon steels, stainless steels, duplex, super duplex, titanium, aluminium, including the inspection of welds and threads. The ACFM system can be employed in high temperature, air and sub-sea applications. However, the technique can only be used for surface breaking cracks. Grinding and weld repairs can cause spurious signals. Multiple defects reduce the ability to estimate defect depth; crack length needs to be greater than 5 mm. And complex signals can arise from tight geometries, edge effects and interconnected (branched) cracks. Radiography has been used for the assessment of welds but this has been employed to a limited extent due to the dangerous health risks which are associated with the use of this system and, therefore, the technique has, thus far, not been widely employed for the inspection of railway infrastructure for the reason mentioned above [109, 110]. Magnetic particle inspection can give an indication of the presence of surface breaking or near surface cracks which are approximately 1-2 mm deep, however, deeper defects cannot be detected and the technique does not provide information on the depth of cracks. Inspection by ultrasonic testing can be carried out using a walking stick or a portable system and also at higher speed by mounting the testing equipment onto test trains or hi-rail vehicles. The former require the line to be closed to rolling stock whilst the inspection is being carried out on the track; the railway industry relies heavily on this type of inspection because the results

provide a good approximation to the size and severity of the defects, even though such a process is logistically inefficient. Another common drawback which is associated with manual inspection by conventional UT of this kind is that the system can miss near surface or shallow defects and also very small defects which might be on the surface of the structure under inspection can obstruct the ultrasonic beam in its path and, thus, prevent the beam from reaching more critical defects which might be present in the material much deeper in the structure under test and, therefore, impairing the technique's ability in assessing the structural integrity of the critical railway assets and, thus, significantly underestimate the condition of such assets [43]. The latter system utilising UT at high speed is also limited in its ability to assess RCF damage on railway wheels and track as a result of the balance required between judging and setting the right threshold level and window of time to restrict the occurrence of false alarms and also be able to detect critically large defects at the same time. Another drawback at present which is associated with high speed inspection systems is the decrease in the signal to noise ratio with increasing speed; as a result, certain types of defects can be under estimated or even missed altogether at high speed. In addition, it is found that with the current state-of-the-art systems the resolution of UT systems decreases with increasing speed, even though such systems which are currently available can operate at a high speed of 100 km/hr; however, it is found that at this high speed the resolution is to a depth of 6 mm and, therefore, moderately sized defects can go undetected. Therefore, for this reason, inspection speeds are considerably lowered to facilitate the detectability of defects and, thus, enhance the probability of detection. As a result, high rail vehicles are operated at speeds of about 15 Km/hr even though their maximum running speed is approximately 35 km/hr for inspection purposes. Whereas, test trains that can operate at higher speeds of up to 100 km/hr are usually run at speeds between 40-80 km/hr for inspection purposes using on-board ultrasonic testing equipment [43, 114-118, 144]. Furthermore, magnetic flux leakage and eddy current sensors can be used in conjunction with UT systems and, thus, deployed on test trains and hi-rail vehicles in order to complement UT systems and, thus, increase the probability of detection of surface breaking and near-surface breaking RCF cracks. However, MFL sensors suffer from a significant loss of resolution at high vehicle running speeds; this is because the structure under test by this technique needs to be sufficiently magnetised so that an enough amount of flux can leak out of a potential discontinuity which might be

present in the structure to be subsequently detected by the system; however, the amount of flux leakage from a defect will decrease with increasing speed and, therefore, the detectability of the MFL system will be lower at high speed. Though MFL sensors do enhance the overall reliability of the inspection process when integrated and working in conjunction with UT systems, however, as a result, they also tend to decrease the maximum speed of inspection. Also, MFL sensors are more effective in detecting transverse rather than longitudinal defects. On the other hand, currently available state-of-the-art eddy current sensors are much better at detecting surface defects at high speed than MFL detectors in order to complement UT systems and speeds of inspection as high as 100 km/hr are reported in the literature [43, 114-118, 144] using such systems. However, even though eddy current systems are reasonably good for detecting surface breaking cracks at high speed these detectors are incapable of detecting near-surface defects which are greater than a depth of 2 mm from the surface of the structure under test and the presence of grinding marks on the structure's surface can significantly impair the ability of the eddy current sensor to detect very small RCF type cracks.

Automated visual inspection techniques are widely used for railway applications for the assessment of the structural integrity of railway assets; the degree of wear amongst other parameters can be assessed by using this technique including to a somewhat limited extent these systems can be used to detect RCF damage, however, the latter application is dependent on the speed of operation; portable systems are available and can be deployed on test trains to be used for high speed applications, as well as being installed on some passenger vehicles to inspect specific routes of interest for either single or multiple inspections of the same route. Even though the maximum speed at which visual inspection can be carried out is reported to be 320 km/hr for the detection of RCF damage the speed must not exceed 30 km/hr [43] for optimum image resolution and results. Again, as in the case of eddy current sensors, the presence of grinding marks on the structure's surface can significantly impair the ability of visual inspection systems in detecting RCF defects even at such low speeds. Recent research and development activities in the industry have resulted in the integration of automated vision technologies with ultrasonic systems in order to enable the inspection of both the surface of rails and internal defects which may be present in the structure, simultaneously [43, 114-118, 144].

Conventional UT inspection systems are inefficient at assessing rail welds due to extensive scattering of the high frequency ultrasonic energy beam which occurs at grain boundaries in the material under inspection, thus, inhibiting the penetration of the interrogating beam and yielding low signal-to-noise ratio values and resulting in low resolution. Therefore, alternative inspection techniques are necessary for inspecting defects in welds for which radiography has been used in the past [109, 110], however, employing this technique is hazardous to personnel and, therefore, is not commonly used in the railway industry for the inspection of structural assets. Furthermore, the determination of residual stress present in structural components, including their stress free temperature (SFT), can be carried out using a magnetic anisotropy and permeability system (MAPSTM) developed by MAPS Technology (UK). Manual inspections can be conducted using the MAPS portable system without line closure and, thus, not affecting railway operations in any significant manner.

Acoustic Emission is a passive and non-quantitative technique, but, gives a qualitative assessment of the internal condition of a component, such as a large tank that might contain hazardous liquid. The system consists of an array of acoustic sensors which are then attached around the structure under test at appropriate and strategic positions. The acoustic sensors then listen in on signals above a certain threshold arising from flaws and damage, such as growing cracks or corrosion and leaks emanating from the structure. Subsequently, the damage can be identified and located using triangulation techniques. However, in the case of the detection of crack growth the technique suffers from the challenge of distinguishing signals emanating from the growth of a crack and operating noise.

1.4 THE AIM OF THE PHD PROJECT

Rolling contact fatigue (RCF) cracks in rail wheels are complex in terms of their propagation angles and three-dimensional shape. In order to provide accurate non-destructive testing (NDT) quantification of the cracks their size and shape, and how this relates to any NDT signal outputs, needs to be understood. In this work NDT quantification using an alternating current field measurement (ACFM) sensor has been considered. ACFM sensors generate magnetic lines of flux and induced eddy currents in the target material and detect changes in these due to the presence of

surface breaking defects. The signal output is dependent on the magnetic lines of flux pathway, which is dependent on the crack size, shape and complexity (branching etc). Computer modelling (via finite element method based software; COMSOL Multiphysics) can be used to investigate the sensitivity of the ACFM signal to crack shape, size etc. However, the present PhD project is focused primarily on the experimental measurement of RCF type defects in rail wheels and has been carried out to quantify their size and shape including the associated microstructural and hardness changes in the wheel steel, which can also affect the ACFM sensor signal. ACFM sensor signal analysis has been undertaken to develop an understanding of sensor signal - RCF defect relationship.

The work presented in this thesis is aimed at further understanding the influencing factors affecting the ACFM signal response to defects, primarily, on RCF cracks found in railway wheels. The work presented in this thesis in the following experimental chapters aims to build on the current level of understanding on the following:

- Influence of crack characteristics: size, shape, propagation angle, cluster number and spacing.
- Influence of ACFM system operational parameters: probe lift-off, operational frequency (5 and 50 kHz), probe angle relative to crack surface direction, inspection speed.

Influence of material characteristics: type of steel material under inspection, permeability of the material under inspection, degree of material degradation and/RCF crack type(s), degree of hardness and work hardening of the material under inspection, change in the microstructure and hardness with depth below the tread surface of the railway wheel under inspection.

As a result of rolling contact fatigue type damage (RCF) caused by the presence stresses and strains at the rail-wheel interface railway systems are increasingly experiencing high levels of rail surface failure, for example, in the form of surface cracks and spalling. Thus, if left untreated the surface cracking will typically grow in length and depth leading to severe reductions in the service life of the wheel. Surface cracking can be managed by the grinding of the rail wheel tread surface to remove

surface defects and re-shape the rail wheel profile. This is most effective early on in the life-cycle of the crack. Thus ensuring that the correct measures and procedures are in place to determine the presence and severity of RCF type cracks can significantly enhance the maintenance and management of rail wheels in service and ultimately reduce maintenance costs and avoid unnecessary disruption to rail services. The work presented in this thesis investigates the influence of crack characteristics: size, shape, propagation angle, crack cluster number and crack spacing. Furthermore, the influence of ACFM system operational parameters: probe lift-off, operational frequency (5 and 50 kHz), probe angle relative to crack surface direction and inspection speed are also investigated.

In addition, studies on the influence of material characteristics and properties on ACFM signal response have been carried out; these include the type of steel material under inspection, material permeability, the degree of material degradation and the types of RCF cracks observed on the rail wheel tread, the degree of hardness and work hardening of the material under inspection, including the change in the microstructure and hardness with depth beneath the tread of the rail wheel under inspection.

1.5 THE STRUCTURE OF THE PHD THESIS

Following on from this introductory chapter the next four chapters are literature review chapters (chapters 2-5 inclusive) before moving on to the main experimental chapters (chapters 6 and 7) and the concluding chapter including a discussion on the importance to the industry and suggestion for future work (chapter 8). The different experimental techniques and materials used for the purposes of this PhD project are discussed at the beginning of each of the experimental chapters 7 and 8 as appropriate. Chapter 2 discusses the components of railway rolling stock, mainly, the wheelset, suspension and braking system, including common faults and structural defects affecting operational performance. The chapter further discusses the maintenance requirements for different types of rolling stock: urban, suburban, intercity and freight rolling stock. Again, emphasis here is on wheelsets, suspension and the braking system; the relationship among these components is also discussed, together with highlighting some reasons for possible delays and accidents that might occur on the railway network. Chapter 3 introduces the wheel-rail interface and discusses at length

its importance together with other crucial factors to the railway industry such as adhesion, structural defects affecting wheels and rails, typical steel grades used and the processes employed for the manufacture of wheels and rails, and an in depth discussion of the rolling contact fatigue phenomenon including the current maintenance methodology used to preserve the structural integrity and, thus, prolong the life of critical structural industrial assets. Chapter 4 discusses in more depth the main non-destructive evaluation (NDE) techniques that are currently commonly used in various sectors of industry, in particular the railway industry, to detect damage including cracks which are found on and near the surface including deep internal damage in ferrous and non-ferrous structural components in order to assess the structural integrity of material assets. Furthermore, chapter 5 presents an in-depth discussion on the fundamentals of the alternating current field measurement technique (ACFM); here the thin skin theory including the principles explaining ACFM inspection and relevant research carried out on ACFM applications for the railway industry including finite element (FE) modelling are discussed in more detail.

The first experimental chapter, namely, chapter 6, investigates the influence of the properties of as manufactured railway wheel material, for example, microstructure and hardness, on the susceptibility of the wheels to rolling contact fatigue damage and wear. The chapter considers the initial work which was carried out to determine the level of tread damage on the two worn railway wheels, namely, HSR1 and HSR2, including the relatively new railway wheel HSR3. This work presented in chapter 4 includes an analysis of the wheel samples in terms of the hardness and microstructural changes with depth from the tread surface and the type, size and spacing etc., of the cracks present and along different positions and different regions, for example, flange face, flange root, running band, rolling contact fatigue damage (RCF) band and field side, of the rail wheel treads for the three railway wheels with different levels of RCF damage on the tread surface have been investigated as part of the work on the PhD project.

The work present in chapter 7 initially discusses a study carried out, in a controlled manner using a calibration plate personally designed and arranged to have it manufactured by myself through a local manufacturer based in Birmingham, consisting of artificial defects (or “notches) created by spark erosion using the EDM

procedure to simulate cracks and crack cluster found in railway wheels in service in order to investigate the ACFM signal response to defects in relation to their size, shape, propagation angle, crack spacing and cluster number, including considering the influence of ACFM sensor parameters on the signal response to cracks such: as probe lift-off, frequency and speed of operation, probe angle relative to crack surface angle and, finally, an experiment designed and conducted to determine whether a critically deep crack present in the centre of a cluster of shallow cracks, as commonly found in railway wheels in service, can be detected using the ACFM system is presented. The chapter then considers and, analyses in depth, the ACFM results on the railway wheels removed from service with different level of wheel tread damage (HSR1 and HSR2) including the new wheel without visible defects (HSR3) which acts as a control; this study investigates the effect of changing background conditions including the influence of material properties such as hardness and microstructural changes with tread depth and thus the level of tread damage on the ACFM signal as well as considering the role played by other material properties such as permeability and residual stress. Furthermore, together with making concluding remarks and salient points emerging from the work presented in the PhD thesis including providing suggestions for future work, chapter 8 also discusses the sensitivity and, thus, detectability of the current ACFM system for railway wheels in service; thus modelling ACFM and predicting defect sizes using the system and considering its viability as a complementary non-destructive evaluation technique to be used in conjunction with other techniques, for example, ultrasonic, eddy-current, magnetic particle inspection, acoustic emission, amongst other techniques described in more detail in chapter 5 of the PhD thesis.

Imperfections on the tread of railway wheels can have a detrimental influence on railway and railway wheel components, causing severe impact loads, thus, leading to higher wheel/rail impact forces, resulting in impact noise and/or increased rolling noise and thus impacting on the environment. Therefore, to limit repair and maintenance costs and to meet noise legislation there is a large economic incentive to for detecting and replacing non-round wheels in time. As a result, the removal of railway wheels from service that cause additional damage to trains and tracks requires new criteria and defect detection methods to be developed.

CHAPTER 2
RAILWAY ROLLING STOCK

2.1 COMPONENTS OF RAILWAY ROLLING STOCK: ON WHEELSET, SUSPENSION AND BRAKING SYSTEM

Railway wheels of the solid type, as opposed to tired wheels, are predominantly used in the railway industry. The safe operation of a railway vehicle is heavily dependent on the structural integrity of the railway wheel and axle as the wheels support the entire weight of the vehicle. Therefore, wheels are vital structural assets for the railway industry and, thus, need to be maintained appropriately and efficiently in a timely manner and/or immediately removed from service if the structural damage reaches a critically unsafe level which can otherwise compromise their structural integrity and, thus, lead to catastrophic failure. Therefore, the strength of a wheel is of utmost importance and must be taken into consideration during the design of railway wheels. Furthermore, prolonging the lifetime of wheels is a significant factor that can be a prominent cost-saving measure for ensuring that the costs incurred for maintenance are minimal. To this end, as well as strength other important factors must be considered when designing rail wheels from the point of achieving enhanced and optimal operational performance; these include the wheel's resistance to wear, thermal crack initiation and propagation including the occurrence of noise due to the vehicle's and, thus, wheel's, vibrational motion that can have adverse implications for the surrounding environment. The correct choice of material design and configuration that is appropriate for the vehicle can significantly enhance the performance of the wheel.

The most common wheelsets which are currently employed in the UK rail network are comprised of two wheels that are fixed to a common axle. The axle is inserted in the wheel's hub, the rim contacts the rail and these two components of the wheel are connected to each other by the web. The axle is inserted in the wheel's hub. The rim's circumferential outer surface, which is referred to as the wheel tread, makes contact with the rail and the region at the back of the wheel tread which protrudes is referred to as the flange. The main requirements for solid wheels are strength, anti-wear, anti-thermal damage, low vibration (i.e. noise) characteristics limit the impact on the environment. The solid wheel is comprised of three parts, namely, a hub, wheel web

and rim. The structure of a typical monobloc wheel and a schematic diagram of the wheel tread region, are shown in figures 2.4 and 2.6, respectively [32] and, in the case of such a wheel the full wheel tread profile is manufactured from a single piece of steel as a single entity. Each of these parts has different characteristics and requirements; the web needs to have sufficient mechanical strength to withstand the high loads imposed on the wheel by the mass of the vehicle and its configuration is designed so as to allow the optimal distribution of the thermal stress. The choice of the steel grade for the manufacture of the rim is based on considerations to each other and, thus, the choice of the material composition, in particular, the carbon content of the material, needs to be properly and thoroughly thought through in order to produce an appropriate material based on a compromise between these two characteristics.

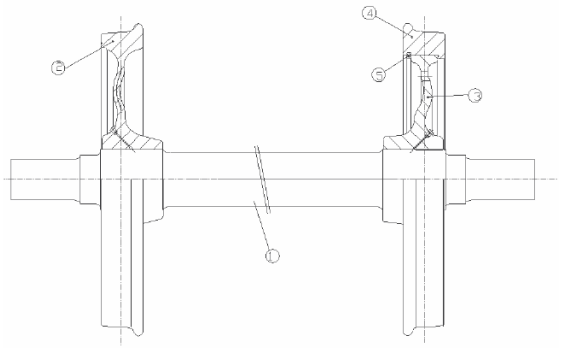

Key

1 Axle
2 Monobloc wheel
3 Wheel centre
4 Tyre
5 Retaining ring

Figure 2.1 shows a schematic of the main wheelset components (the original of the above schematic is shown in reference [128] and has been reproduced and appropriately referenced here for the purpose of this PhD thesis).

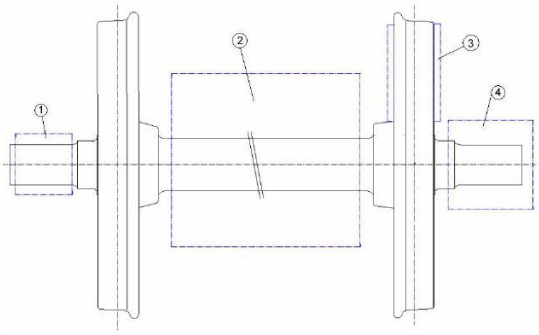

Key

1 Bearings
2 Brake disc, final drive or traction motor
3 Wheel- mounted brake disc
4 Axle box with bearings

Figure 2.2 a schematic showing additional wheelset components (the original of the above schematic is shown in reference [128] and has been reproduced and appropriately referenced here for the purpose of this PhD thesis).

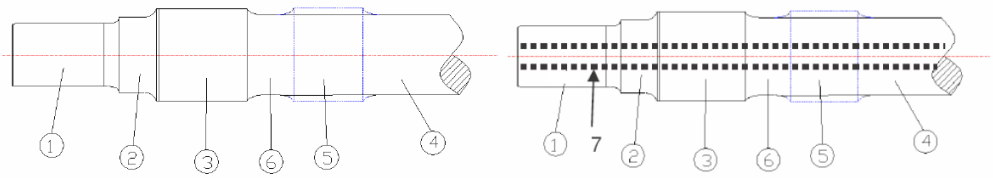

Key

1 Journal
2 Collar-bearing surface
3 Wheel seat
4 Axle body
5 Seat for disc, final drive or traction motor
6 Transition zone between seats
7 Hole for hollow axles

Figure 2.3 shows a schematic of the axle for all types of wheelset; note, axles may be solid or hollow (the original of the above schematic is shown in reference [128] and has been reproduced and appropriately referenced here for the purpose of this PhD thesis).

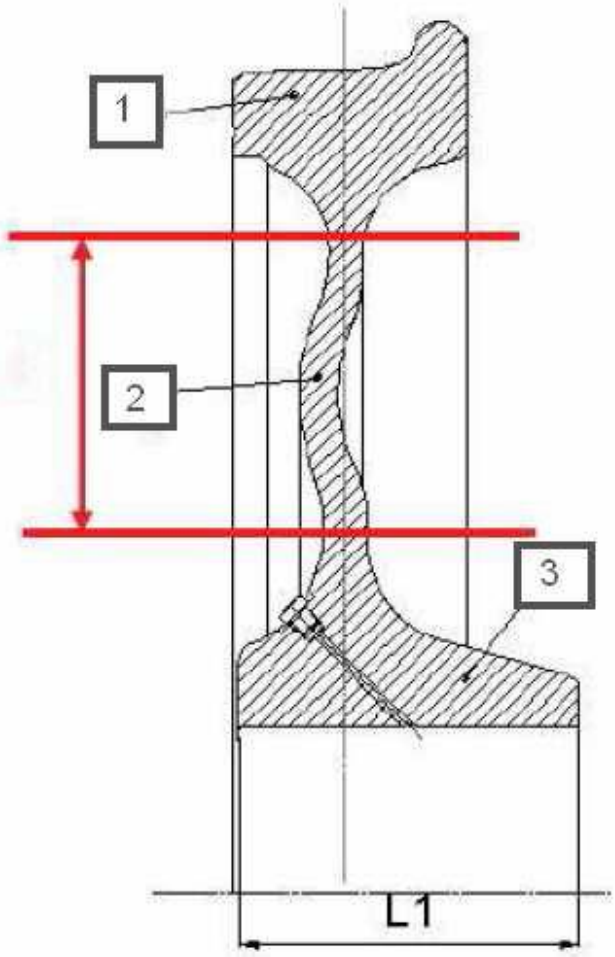

Key

1. Rim
2. Web
3. Hub
4. Hub-width

Figure 2.4 shows a schematic of a typical monobloc wheel (the original of the above schematic is shown in reference [128] and has been reproduced and appropriately referenced here for the purpose of this PhD thesis).

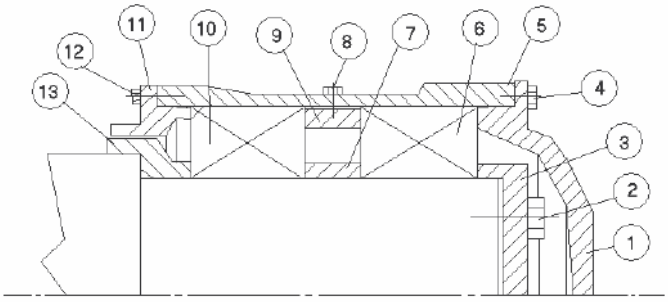

Key

1 Front cover
2 End cap bolts and locks
3 End cap
4 Front cover bolts and locks
5 Axle box body
6 Outer bearing
7 Internal spacer
8 Lubrication point
9 External spacer
10 Inner bearing
11 Rear cover
12 Rear cover bolts and locks
13 Abutment ring

NOTE 1 The components 6 – 7 – 9 and 10 may be replaced by a "cartridge" bearing

NOTE 2 The different types of sealing system shall be added in association with the corresponding types of bearing

Figure 2.5 shows a schematic of the base axle box (the original of the above schematic is shown in reference [128] and has been reproduced and appropriately referenced here for the purpose of this PhD thesis).

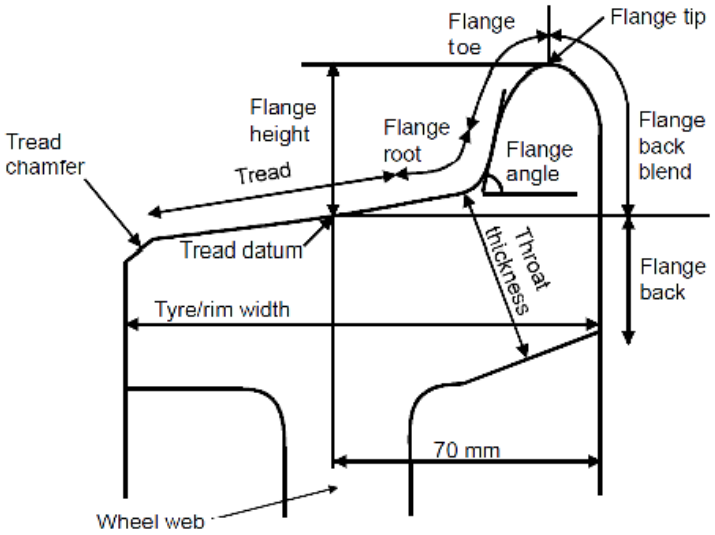

Diagrams identifying parts of the wheel

Figure 2.6 the above is a schematic diagram of the wheel tread region showing the relative dimensions of the different parts of the tread (the original of the above schematic is shown in reference [32] and has been reproduced and appropriately referenced here for the purpose of this PhD thesis).

During curving on railway lines the wheelset that leads tends to roll towards the outside of the curve, whereas, the trailing wheelset rolls towards the inside of the curve [32,121,128]. Due to the conicity of the wheels and their identical rotational speeds the radius of the outer wheel will become greater than the inner wheel during curving and the leading wheelset moves outwards. Thus, the wheel that leads will effectively have a larger radius of curvature and so tend to roll further than the wheel with a smaller radius of curvature and, thus, enabling the wheelset to steer in order to radially align itself [32,121,128] and thus successfully navigating the curve; the process is completely reversed in the case of the trailing wheelset. Furthermore, the process is assisted by the fact that the outer rail is made longer than the inner rail and, as such, the wheelsets curve easily over the equilibrium rolling line. The equilibrium rolling line is defined as the running line where the differences in the rolling radius and the length of the rails are balanced [32,121,128]. However, in actual in-service conditions, such radial alignment of wheelsets, are made harder to achieve by the suspension of the vehicle. This is related to the stiffness of the primary yaw suspension; as the stiffness increases, consequently, the forces thus required to achieve the necessary rotation of the wheelsets will also be higher. The creep force which is necessary to steer the wheelsets is the result of an excess of the difference in the rolling radius due to the leading wheelset moving outward beyond the limit of the equilibrium rolling line. In the same manner, the inward movement of the trailing wheelset beyond the equilibrium rolling line gives rise to the steering forces that are required for this wheelset. Furthermore, such forces depend on the effective conicity of the wheelset running on the rail. The difference in the rolling radius increases with increasing conicity for a specific lateral shift of the wheelset. In addition, wheel tread wear influences the conicity of railway wheelsets and it is found that increasing wear results in an increase in conicity. Furthermore, the adhesion between the wheel and rail region, including the wheel flange, both prevent the wheelset from producing sufficient difference in the rolling radius and, thus, limit the extent to which the required steering forces are generated. This leads to the wheelset making contact with the flange due to the contact points between the tread and the rail yielding forces that tend to force the running wheelset towards the flange; thus, resulting in the need for the emergence of the flange contact force to resist this occurrence and, therefore, this mechanism naturally leads to wear, and, as such, this process is a major cause of the occurrence of wear in railway wheels.

2.2 COMMON FAULTS AND STRUCTURAL DEFECTS AFFECTING OPERATIONAL PERFORMANCE

In general, maintenance of wheelsets encompasses in-service and off-vehicle (or, out-of-service) maintenance including overhaul following an incidence that might have occurred during service. Typical defects found in axles include the following. Axle protection defects (or, corrosion pit) can occur in an axle and are due to factors such as deficient adhesion, insufficient protection of parts or impact forces resulting from various sources [32,121,128], circumferential scoring/grooving defects, longitudinal defects resembling cracks and transverse defects (on body and journal sides), respectively. The latter defects are commonly found on disk seats, wheel seats or transmission gear. Furthermore, the primary axle box defects usually occur on weld fillets of manganese wear plates and on the axle box body (both cracking or failure). In addition, wheelsets are prone to damage and the main wheelset related defects are due to the displacement of components relative to the surface of their bearing which, as a consequence, results in the distortion or loosening etc. of railway wheels. Defects can also be found on the transmission gear or breaking equipment as well as on axle boxes and, therefore, these types of damage also need to be addressed as a matter of urgency whenever they occur. Wheel distortion defects are caused by an axial translational displacement of the wheel's rim section relative to its hub; such a distortion can occur either in the wheelset's external or internal parts [32,128]. In addition, fitted components on wheelsets are also prone to damage as a result of the loosening of wheelset components, for example, wheels or disks that have become loosened and, thus, may cause detrimental damage and thus present a potential hazard to the integrity and safety of the wheelset and, therefore, need to be immediately addressed to rectify the situation. The loosening of wheelset components in such a manner can take the form of either an axial or rotational displacement of the component. In the former case, the resulting displacement is due to a component's translation in the axial direction in relation to its bearing, whereas the latter case is caused by a displacement that is a consequence of the component's rotation which is relative to the surface of the bearing. Other types of wheelset defects that are commonly encountered are bent axle and brake disk defects. The former type of wheelset defect results from a permanent deflection along an unloaded axle's axis deflection, where, the maximum extent of the deflection is usually found to occur at

axle's central position. The latter can be classified as brake disc with cracks or brake disc failures [32,121,128].

2.3 MAINTENANCE REQUIREMENTS FOR DIFFERENT TYPES OF RAILWAY ROLLING STOCK: URBAN, SUBURBAN, INTERCITY AND FREIGHT RAILWAY ROLLING STOCK

Business, environmental and passenger considerations must be taken into account and addressed together with the constraints imposed on new railway rolling stock including strategies that will ensure the successful implementation and integration of new rolling stock on the railway network to happen as these are all important factors to be considered. The requirements for future rolling stock including the influencing and constraining factors as regards their development have to be considered and addressed in conjunction with the need to align the current rolling stock's physical attributes together with the routes on which these rolling stock designs are to be deployed. Network rail are working in collaboration with industrial partners and the government in order to find viable solutions to this end. The future rolling stock design requirements will be influenced and driven by factors such as passenger, environmental, industrial and network capacity requirements. Therefore, the industry needs to have a clear long term perspective on the different and distinct services that it needs to offer for the various industrial market sectors.

Described as follows, are the maintenance methodologies for the different emerging rolling stock families. In the case of suburban routes which are usually characterised by relatively higher densities than other types of routes the fleets designed to run on these routes consist of lightweight, high performance and high capacity electrified railway vehicles. As a result of the increased demand and heavy loads which are imposed on these types of fleet of trains there is a correspondingly strong business case for such fleets. The vehicles are, thus, optimised to cope with the forecasted increase in the loads imposed on these vehicles as a result of ever increasing passenger numbers. This demand is met by the functional requirements of the design of the vehicles; the rolling stock design for the electrified regions of the railway network needs to be lightweight, available and reliable due to frequent stopping and starting of vehicles on such routes. Due to limited and, often, awkward access to the infrastructure as well as limited and short amounts of time to carry out maintenance

on such fleets and routes the general strategy is to use intelligent condition monitoring and reporting systems on these fleet of trains. However, the business case for broad enhancement measures to be implemented for the infrastructure on lower density routes is not as strong as in the above case and, therefore, the rolling stock will need to be flexible, standard and optimised in line with the requirements of the route's infrastructure; the vehicles can either be electric or self-powered running vehicles on these routes. In the future, suburban metro fleet of trains are anticipated to be low-weight electrified multiple-unit vehicles with typically good characteristics as regards acceleration. These vehicles will need to be very reliable and optimised to regenerate the energy produced during braking and then transfer this energy back to the main power supply in the event of an increase in the frequency of stoppages in order to make these vehicles more environmentally friendly and economical an, thus, a viable solution. The trains will provide high capacity to accommodate greater passenger numbers maintaining good comfort levels which will be dictated by the specific route together with having optimised access and egress to ensure dwell times are kept as low as possible. Furthermore, good ventilation levels must be maintained at all times and the gangways should be spacious on-board these trains as appropriate for such routes to ensure the ease of passenger movement on-board these trains.

Furthermore, the business case of high speed routes which cater for inter-urban services on the UK railway network for high-speed trains (HST) such as Pendolino trains is strong due to their higher demand allowing high speed travel, stopping approximately every 30 minutes and reasonable dwelling times at stations. Therefore, these vehicles need to be maintained to provide the demands of passengers as regards requirements, particularly, the provision of seat availability including appropriate comfort levels during travel on these high speed and long journey routes; thus, intelligent automated condition monitoring regimes for inspection purposes and reporting are required to be implemented on these routes to satisfy passengers as regards ride quality and, therefore, appropriate functional design of HSTs further supports the business case to provide the necessary infrastructure needed to support the system's operation to meet the above objective. In addition, vehicles that service these high speed lines on the British railway network must have the following attributes: light on the track, efficient in terms of energy usage and track friendly. Furthermore, the current focus is on designing and developing a new fleet of HSTs

that will run on electrified track via overhead cables operated at 25 kV AC and, subsequently, these vehicles will re-supply energy that is generated during the braking process directly to the main power supply system; however, on routes where the track is not electrified generator cars will provide the necessary power required by these vehicles. In contrast, passenger journeys made on regional and rural routes are relatively short, therefore, connections at each end of the journey need to be made as efficient and as reliable as possible in order to make the prospect of travelling on these services more attractive to commuters by ensuring that such services are a viable and economical solution. Therefore, these types of railway rolling stocks, including the infrastructure, needs to be maintained relatively easily and also be robust.

CHAPTER 3

THE WHEEL-RAIL INTERFACE

3.1 THE IMPORTANCE OF THE WHEEL-RAIL INTERFACE AND ADHESION

The wheel-rail interface and adhesion are of utmost importance for the efficient operational performance of vehicles running on the railway network. Furthermore, the correct wheel and rail profiles help to easily and efficiently steer vehicles on track expending minimal energy and, thus, lowers the overall consumption of fuel by the vehicles in the process. The adhesion between the wheel and rail is extremely important for the safety of the vehicles during service and is reliant upon the friction that is generated between the wheel and rail during operational performance of the vehicle on the track. This friction, which is also referred to as traction, can be reduced by, for example, the presence of wet leaves on the track during wet weather conditions or oil being present which, therefore, results in the railway track becoming greasy and, thus, impairing the level of friction that is needed between the wheel and rail for the efficient functioning and running of trains on the railway track. Friction results in the loss of energy. In the case of metallic surfaces the frictional force is the result of the attractional forces which are generated at the contact patch between the surfaces as, for example, in the wheel/rail contact area and commonly referred to as adhesion between the contact region of the surfaces. At the microscopic level these forces of attraction between the metal surfaces in contact are irregular in form and when such surfaces are viewed under high magnification this is shown to be due to irregularities in the surface topography which resemble a terrain consisting of peaks, hills and valleys. Thus, under the strain of large loads such peaks on the irregular surface become welded to each other and/or inter-lock with the so-called valley's adjacent surface of the other metal object in the contact area. Thus, friction is due to the effective shearing of these welded regions and also from the irregularities which are present in the hard surface material making contact and, thus, ploughing the surface of the softer material. Therefore, this is one of the major reasons for choosing identical material steel grades for railway wheel and track in order to minimise and control the effect of such surface irregularities on the opposing surfaces of wheel and rail in the contact region and, thus, control and minimise friction and mitigate the occurrence of

wear and RCF. High and low frictional forces are required, for example, in traction and continuous motion scenarios, respectively, and finally, constant friction is necessary for the proper functioning of, for example, brakes and clutches in order to prevent the occurrence of undesired jerky movements. Furthermore, another important reason why the steel grades which are used to manufacture the wheel and rail should be of similar grade is to limit the occurrence of abrasive wear because abrasive wear occurs due to the material that abrades being much harder and having a greater degree of surface roughness than the surface which is to be abraded then it can be easily prevented or mitigated by either making the former's surface less rough and hard or by ensuring that the surface of the latter is harder in order to match the surface hardness and roughness of the former to act as protection against surface abrasion; This is the main reason for choosing similar or identical steel grades for the manufacture of wheels and rails in the railway industry.

Wheel and rail profiles that do not conform to one another have an adverse effect on the vehicle's operational performance and, thus, increase the vehicle's consumption of fuel during service and can result in structural damage to both the vehicle and rail such as fatigue related defects including an increase in the occurrence of wear and corrugation, amongst other types of defects, which would therefore require immediate attention to address any such issues that may arise by implementing appropriate maintenance procedures and/or replace the affected wheels and/or railway infrastructure, thus, incurring unwanted additional costs for maintenance and extra man-hours for professionally trained and skilled personnel to carry out the task of vital remedial action in order to address and rectify the situation. As a result of a misalignment between the wheel and rail the wheel will be misaligned to the track and is very likely to make hard contact with its flange on the railway track. In addition, a mismatch between the wheel and rail profiles can also destabilise a vehicle during service and, thus, may lead to derailment of the vehicle in the worst case scenario; misaligned wheel and rail profiles also have a bearing on the occurrence of surface fatigue damage which is directly related to an increase in the stress at the wheel-rail contact area.

3.2 STRUCTURAL DEFECTS AFFECTING RAILWAY WHEELS

3.2.1 SPALLING

Spalling (figure 3.1 [ref. 11]) is a defect caused by the instantaneous heating and the subsequent rapid cooling of the tread during and after block breaking and results in the detachment of material from the surface of the tread as a result of the coming together of thermally induced cracks; these cracks are thus likely to occur in martensite which is hard and brittle. In addition, classic RCF due to repeated loading and plastic deformation which leads to the initiation and growth of cracks, can also result in material loss from the wheel tread, thus, giving rise to spalling; such defects are usually short in length [12, 48, 89].

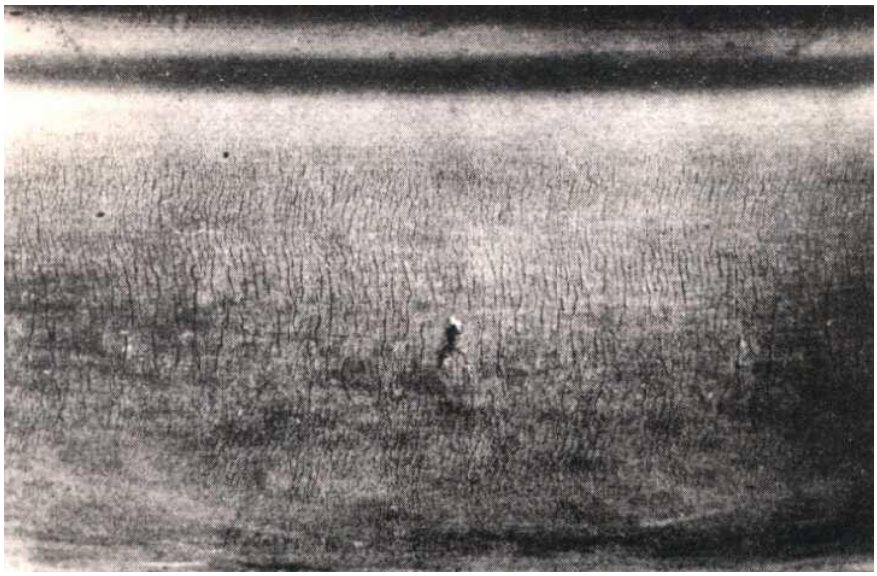

Figure 3.1 shows damage caused by spalling resulting from thermal cracks on the wheel tread surface (the original of the above photographic image is shown in reference [11] and has been reproduced and appropriately referenced here for the purpose of this PhD thesis).

3.2.2 SHELLING

Shelling (figure 3.2 [ref. 11]) is a cavity defect due to a local loss of material on the wheel and believed to be the result of RCF. Shelling [12, 18, 89] refers to all sub-surface cracks manifesting as flakes of material that is lost from the tread of a rail wheel. Such defects are primarily caused by excessive vertical wheel/rail contact forces with respect to the wheel diameter. However, it is difficult to distinguish between the phenomena of spalling and shelling simply by visual inspection.

Figure 3.2 shows the presence of shelling and cavities on the wheel tread surface (the original of the above photographic image is shown in reference [11] and has been reproduced and appropriately referenced here for the purpose of this PhD thesis).

3.2.3 SCALING

Scaling (figure 3.3 [ref.11]) is the build-up of metallic material on the surface of the wheel tread and thus results in a laminar metal flow across part of or, in some circumstances, the entire running surface of the wheel. It is usually attributed to sticking brakes which cause the wheel to slip or slide on the rail, thus heating it to the stage where the material becomes soft enough to flow on the tread surface. Mixing with dust from the brakes and other material it is then deposited onto the rail and subsequently cools in layer upon layer thus giving rise to a scaly appearance. The severity of scaling is determined by measuring its height from the wheel surface.

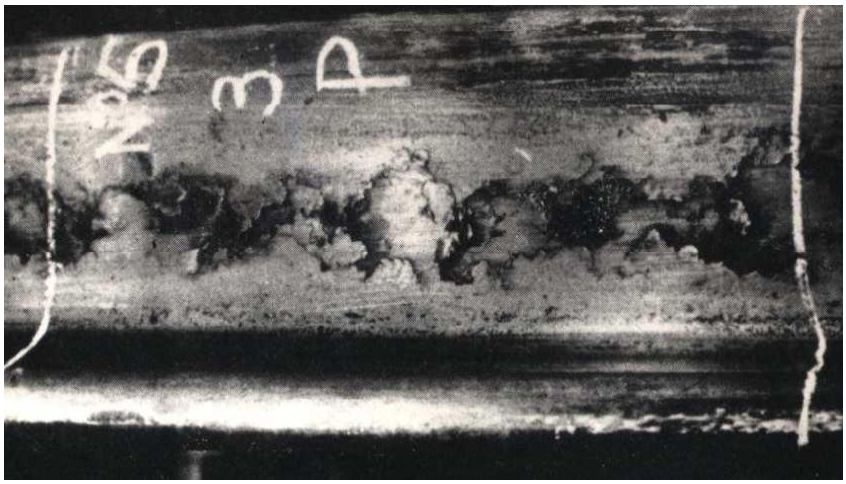

Figure 3.3 shows the presence of scaling damage on the wheel tread surface (the original of the above photographic image is shown in reference [11] and has been reproduced and appropriately referenced here for the purpose of this PhD thesis).

3.2.4 CORRUGATION

Corrugation is defined as an out-of-roundness (OOR) defect which is found on wheel treads that are block-braked. The dominating circumferential wavelength of this type of defect is 3-6 cm and the amplitude is <10 μm [49]. The proposed hypothesis that has been put forward for this type of defect is that block braking results in heating up of certain regions of the wheel tread and, as a result, some areas of the tread become warmer (formation of hot spots owing to thermo-elastic instability) than neighbouring regions. As a consequence, the heated regions protrude from the surface of the wheel due to thermal expansion and, thus, are subjected to more wear than the other parts of the wheel tread surface. However, as the wheel subsequently cools, the volume of material at these hot spots decreases, thus forming valleys, and, consequently, resulting in a corrugation pattern. Corrugation is the primary cause of rolling noise [120].

3.2.5 WHEEL FLATS

Wheel flats occur as a result of the sliding of the wheel on the rail without rolling and are primarily caused by the very high breaking force in relation to the wheel/rail friction. Common causes for this are poorly adjusted, defected or frozen brakes and/or the incidental and local reduction in wheel/rail friction due to the presence of ice or leaves on the railway line.

Figure 3.4 shows a wheel flat (the original of the above photographic image is shown in reference [11] and has been reproduced and appropriately referenced here for the purpose of this PhD thesis).

3.2.6 CIRCULATORY AND GEOMETRIC DEFECTS

Circulatory defects result in the shape of the wheel tread contact patch becoming permanently changed, for example, resulting in the local collapse of the wheel tread (see figures 3.5(a) and (b)) or polygonisation (figure 3.6) that causes defects to occur on the circumference of the rail wheel. Shelling Is evidently present in the central region of the collapse in the tread. The occurrence of local tread collapse damage is due to premature wheel tread turning which, in turn, is the result of wear, which includes flange wear, and the presence of thermal damage as a result of wheel slide in conjunction with tread braking mechanism. Furthermore, geometric defects occur at the flange tip and flange face and are usually discrete or continuous defects being caused by the flow or loss of material from the flange.

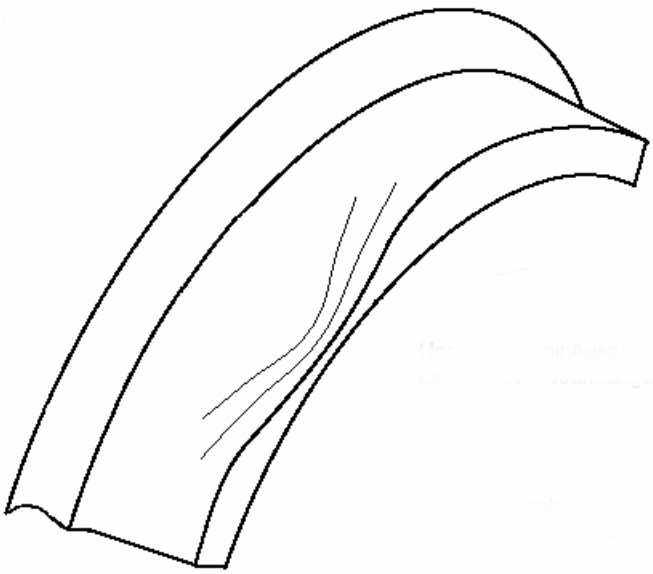

Figure 3.5(a) Local tread collapse.

Figure 3.5(b): Figures 3.5(a) and (b) show a schematic and photograph, respectively, of local tread collapse in a railway wheel (the originals of the above schematic and photographic image are shown in reference [11] and have been reproduced and appropriately referenced here for the purpose of this PhD thesis).

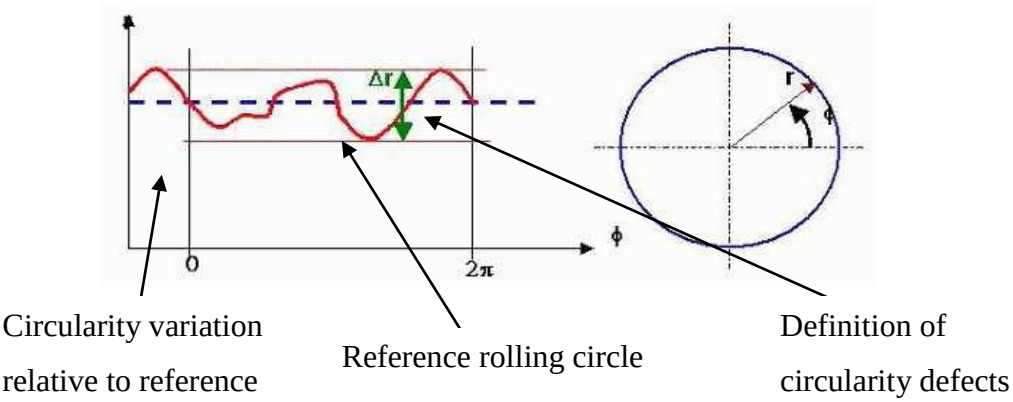

Figure 3.6 shows a schematic of polygonisation (the original of the above schematic is shown in reference [11] and has been reproduced and appropriately referenced here for the purpose of this PhD thesis).

3.2.7 WHEEL TREAD ROLL-OVER

Wheel tread roll-over (figure 3.7) is extruded material that has formed on the outer rim of the wheel during service by plastic deformation and is a continuous defect [50]. This defect is not expected to extend beyond 5 mm from the face of the wheel rim; neither should there be any cracks present. However, cracks that have initiated in the rolled over region of the material can readily propagate into the wheel rim with the potential for wheel fracture [119].

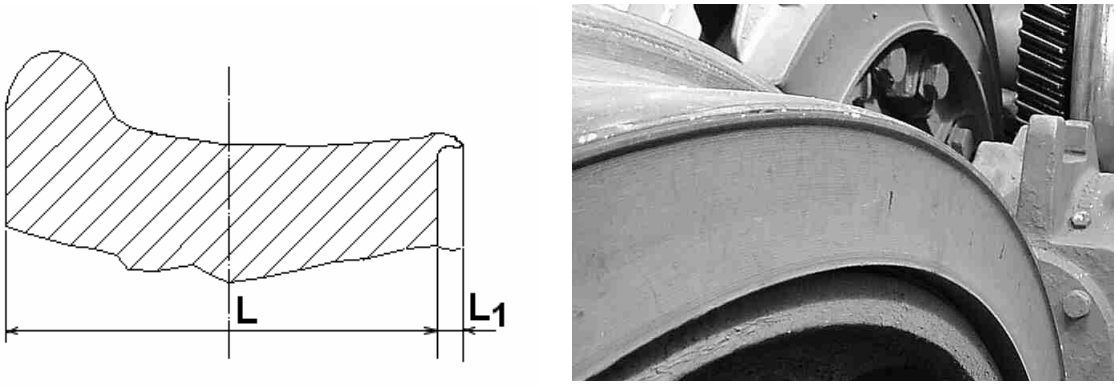

Figure 3.7 shows a schematic and a photograph of wheel tread roll-over (the originals of the above schematic and photographic image are shown in reference [11] and have been reproduced and appropriately referenced here for the purpose of this PhD thesis).

3.2.8 DEFECTS SPECIFIC TO MONOBLOC RAILWAY WHEELS

Defects that are specific to monobloc wheels include deep sub-surface tread defects (figure 3.8) which tend to grow parallel to the tread. Fatigue damage related rail wheel failures are characterised as either surface or sub-surface induced. The former is initiated due to gross plastic deformation of the material in close proximity to the wheel's surface as a consequence of increased loading and/or lower strength material in this near surface region of the tread, thus, leading to the growth of cracks in this region which extend within the material for several millimetres before returning to the surface and, subsequently, causing material to be detached from the tread surface. The latter type of failures occur below the tread surface and can initiate from the presence of macroscopic defects within the material or in defect free zones where the local stress might be extremely high. These defects can grow to a greater depth in the material, typically to a depth of about 30 mm beneath the tread surface before again returning to the surface and, thus, resulting in the loss of large amounts of material from the tread which can be very serious and, thus, become a potential safety hazard requiring the immediate removal of the wheel from surface for safety reasons. Furthermore, overheating can affect the transition between the rim and defects, thus, defects can form as a result of thermal contact with the web (figure 3.9).

Figure 3.8 shows deep sub-surface tread defect (the original of the above photographic image is shown in reference [11] and has been reproduced and appropriately referenced here for the purpose of this PhD thesis).

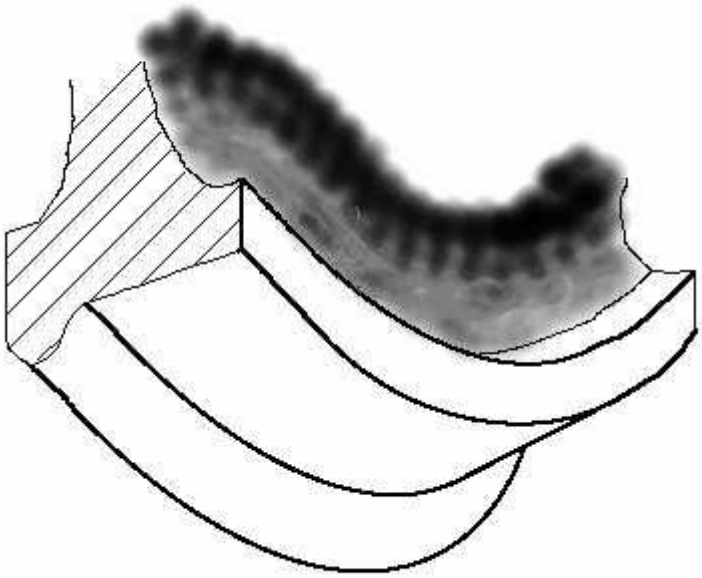

Figure 3.9 shows a schematic and a photographic image of damage caused by overheating affecting the rim-web transition (the originals of the above schematic and photographic image are shown in reference [11] and have been reproduced and appropriately referenced here for the purpose of this PhD thesis).

3.3 TYPICAL STEEL GRADES USED FOR THE MANUFACTURE OF RAILWAY WHEELS AND RAILWAY TRACK

3.3.1 THE MICROSTRUCTURE OF STEEL MATERIAL

The iron-iron carbon phase diagram shown in figure 3.10 represents the transformation of iron with respect to carbon content. The iron-iron carbide section of the phase diagram is of primary importance to structural engineers.

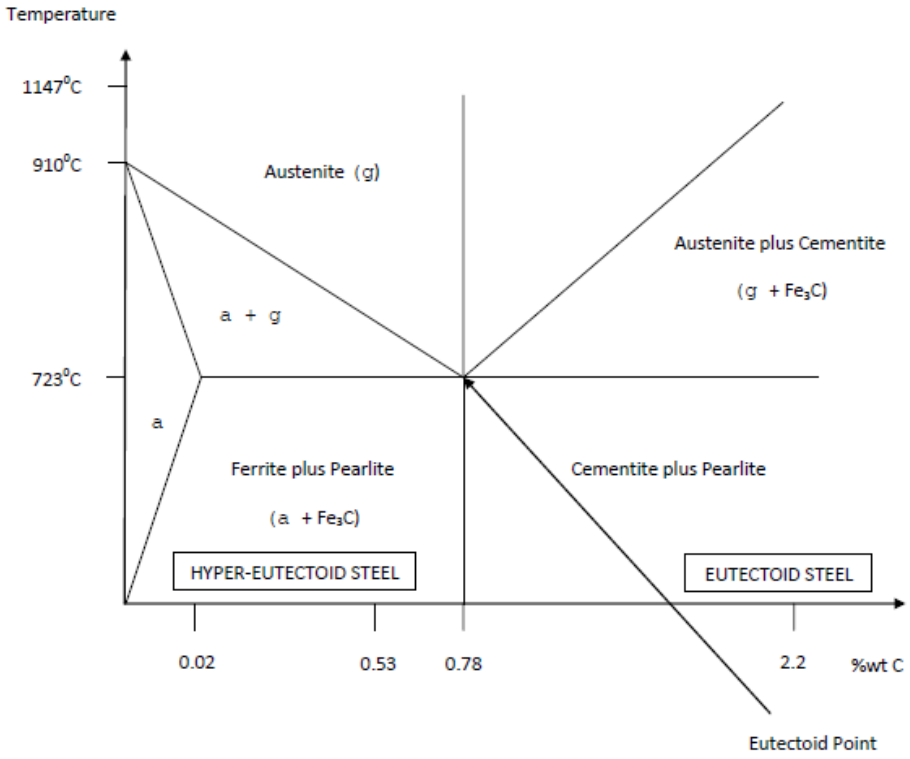

Iron-Iron Carbon Phase Diagram

Figure 3.10 shows the Iron-Iron Carbon Phase Diagram.

The microstructure of steel containing, for example, 0.53% weight carbon develops in the following manner. When steel solidifies it forms austenite. Upon slow cooling below 910 ^{0}C ferrite starts to form and the material transforms to a two-phase system consisting of ferrite and austenite. As more grains of ferrite start to form the remaining austenite becomes richer in carbon. The ferrite starts to nucleate around the grain boundaries of austenite, initially at the triple points. By slowly cooling further the ferrite grains gradually grow in size, particularly along the austenite grain boundaries, and the simultaneous diffusion of carbon takes place from the ferrite to the austenite regions since ferrite cannot retain more than 0.02% wt carbon. At this point the microstructure consists of a network of ferrite surrounding each austenite grain. Upon further slow cooling the remainder of the austenite transform into pearlite at the eutectoid temperature (723 °C). Pearlite has a microstructure comprised of alternate

lamellae of ferrite and cementite; at about 723^0C the remaining austenite, which now contains 0.78% carbon (eutectoid point) changes to pearlite. The resulting microstructure is a mixture consisting of white grains of ferrite together with dark grains of pearlite. The amount of pearlite for a given carbon content is calculated using the Lever Rule which states that: amount of ferrite = (0.78 – % wt carbon)/(0.78-0.02) assuming 0% wt carbon content in ferrite.

3.3.2 MATERIAL REQUIREMENTS AND MANUFACTURE OF RAILWAY WHEELS

The railway wheels and track are made by using high strength steel and in both cases the structure does not experience significant deformation under loading conditions in contrast to, for example, tires made of rubber that roll on asphalt. Thus, such rail wheels do not require much energy to roll on railway lines. Nominally, steel alloys for rail wheels are comprised of the following elements by weight percentages: carbon 0.67-0.77, manganese 0.60-0.85, silicon >0.15, phosphorus <0.05, sulphur <0.05, with only trace levels of molybdenum and chromium [21]. Railway wheels are usually composed of low alloyed steels with a high degree of purity. Tight tolerances for the alloying elements are desired in order to ensure low variation in material properties at elevated temperatures. The European standard EN13262 defines four different steel grades which mainly consist of up to 0.6 %wt carbon, up to 0.8 %wt manganese and up to 0.4 %wt silicon.

The microstructure of the wheel consists of ferrite and pearlite. Rail wheels have a conical shape of about 1 in 20; as a result, this conical shape has the effect of steering the wheelset around curves, so that the flanges rarely come into contact with the rail. The rails generally slant in at the same rate as the wheel conicity. As the wheels approach a curve, they will tend to follow a straighter path. This causes the wheelset to shift sideways on the track so that the effective diameter of the outer wheels is greater than that of the inner ones. Since the wheels are joined together rigidly by the axle the outer wheels will thus travel further, causing the train to naturally follow the curve. Ideally the choice of the alloy for rail wheels is dictated by choosing the right combination of hardness, wear resistance, and resistance to thermal cracking. Significant improvements in the mechanical strength of steel can be achieved by the addition of alloying elements such as chromium, manganese, and molybdenum. However, elements must be carefully chosen in order to balance the cost-effectiveness

and the enhancement of properties that may result as a consequence of addition of the elements to the material. Forging and casting are two of the main methods for rail wheel manufacture.

Single wheel quenching technology has proven to fulfil the increasing demands imposed on the modern rolling stock material for high speed railway wheel production. Railway wheels are one of the most stressed components of railway vehicles with axle loads of 25 tonnes and above [34, 35]. Railway wheels carry out various important functions, for example, guiding the train on the track navigating curves and switches on the track, and are constantly subjected to wear. The wheels also transfer acceleration and deceleration forces to the rail and are exposed to thermal stresses due to sliding and block breaking processes. Furthermore, in the case of high speed railway wheels very high centrifugal forces are generated. In addition, the different functional parts of the railway wheel, such as, the flange, rim, centre and hub, perform different tasks and therefore have different material properties. These properties are primarily determined /governed by the chemical composition of the material, however, other processes, for example, hot forming and heat treatment also play their part to varying degrees. Due to the railway wheel being the most critical component of railway vehicles and thus, a mass product and high safety part [36], the critical factors that need/which require close attention in order to produce wheels of the highest quality and a high level of automation are the reliability, availability and safety of the product [37] including the quality, reproducibility and cost efficiency of the production process. Railway wheels are usually manufactured from high purity unalloyed or low alloyed steels. The alloying elements used are under tight tolerance limits in order to minimise the variation of the material properties during the heating process. The wheel steel grades used and, to a certain extent, the process involved in their manufacture are defined by national and international standards, for example, UIC 812-3V [38], GOST 10791 [39], AAR M107-84 [40], or EN 13262 [41]. However, aside from these standards, several railway wheel manufacturers have created special steel grades for special applications [42]. Four different steel grades are defined by the European standard [41] which in general mainly consist of up to 0.6 % wt. carbon, 0.8 % wt. manganese and 0.4 % wt. silicon. Further, depending on the steel grade used the requirements for the wheels produced according to the European standard [35,41] can be summarised as follows:

- Tensile strength of the rim (between 780 and 1.050 MPa)
- Impact toughness of the rim (≥ 9 J, U-notch, measured at ambient temperatures)
- Residual stress (compression stresses are required in the as-manufactured wheel rim)
- Tensile strength of the centre (between 100 and 130 MPa lower than the rim strength)
- Fatigue strength of the centre (≥ 450 MPa, machined centre, 10^7 load cycles)

Furthermore, to control and thus achieve the above mentioned properties the control of the microstructure of the railway wheel is if utmost importance. To this end it has been found in industry that reaching an optimal compromise between having good mechanical properties, wear resistance and thermal stability is provided by fine-grain steels which have a microstructure comprised of fine-lamellar ferrite and pearlite [42]. As a result, steels consisting of ferrite and pearlite are extensively used in the manufacture of modern railway wheels, primarily high-speed railway wheels. However, recently bainitic steels have also been extensively studied for the purpose of rolling stock applications.

The appropriate heat treatment of wheels during manufacture is critical in determining the final properties of the wheel and thus providing a wheel with the required properties. This process is called rim-hardening and involves the following procedure. Initial austenitisation at temperatures of approximately 900 ^{0}C, however, only the wheel rim is rapidly cooled to a temperature of approximately 300 ^{0}C by usually a quick quench in water. Following the rim quench the centre and of the wheel are still close to the transition temperature. Therefore, further cooling is necessary in air to provide the rim with high strength and compressive residual stresses and to produce a wheel centre with a higher degree of flexibility. Finally, the wheel is annealed at about 500 ^{0}C in order to relieve stresses in the material, however, the annealing procedure has minimal impact on the microstructure and thus no significant changes to the microstructure or the mechanical properties of the railway wheel material are observed. Controlled cooling rates are essential for controlling the microstructure of the material and, as a result, lead to the different parts of the wheel having significantly different microstructures and thus allowing the engineering of the

material with respect to future service conditions of the railway wheel. The primary goal of the heat treatment process is to produce a rim with high microstructural homogeneity in both the radial and circumferential directions which is required for optimal uniform wear characteristics of the wheel tread to be realised. Thus, preventing wheel un-roundness and, as a result, providing the highest levels of comfort during travel and customer satisfaction. Furthermore, as a result of the above, damage due to rolling contact fatigue related failures to the railway wheel will be minimised. It is reported in the literature [35] that a typical wheel of diameter 920 mm reaches 107 load cycles after only 30,000 km in service. Requirements for the heat treatment facilities, cooling technology and the hardening and annealing facilities which are commonly used in the industry including the description of the widely automated production process is widely available in the literature [35].

Furthermore, generally in the UK rail wheel manufactures tend to use soft yaw suspensions to enable steering of the vehicle, however, on the continent manufacturers tend to choose stiffer yaw suspension designs. Therefore, the question has still not been adequately answered and thus put to rest and the jury is still out on which is the better design out of these two designs. It is also reported in the literature [121] that other solutions could include the use of, for instance, cross-braced or forced steering bogies in order to improve the vehicle's steering capability on curves, however, experience has shown that even though this results in very low curving forces, such systems suffer from hollow tread wear and false flanges being produced which can result in the occurrence of RCF when the rail vehicle passes over switches and crossings. Another solution that has been postulated by these authors is the use of freely rotating wheels to eliminate the longitudinal steering forces. Therefore, a system combining freely rotating wheels together with forced steering and efficient performance during curving on curves without producing any longitudinal creep forces could yield the ideal solution for the development of a low-RCF prone rail vehicle [121].

3.4 THE ROLLING CONTACT FATIGUE (RCF) PHENOMENON IN RAILWAY WHEELS

Rolling contact fatigue (RCF) in rails and rail wheels is the result of the inter-play between three major factors, namely, the contact stress, tangential creep forces and

creepage in the wheel-rail contact patch [121]. Recent work carried out by the authors of reference [121], namely, Evans and Iwnicki, on the computer modelling of vehicle dynamics and the wheel-rail interface has shown that the values of the above parameters can be estimated and, thus, predicted with relatively good accuracy under actual conditions by railway vehicle dynamic models. The above study conducted by these authors have demonstrated the use of powerful user-friendly and validated software computer packages which have been developed in collaboration with academia and the railway industry in order to simulate the motion of railway vehicles on track and under actual in-service conditions. One such widely used computer modelling software package is Vampire which has been extensively employed for validation purposes of different types of railway vehicles such as locomotives, freight and passenger carrier trains. In the first instance, in order to set up the computer model, equations of motion are set up to represent the dynamics of the vehicle. This can be achieved in two different two ways, either by being automatically generated by the software via a user interface or by entering a set of coordinates which describe the vital suspects concerning the suspension. The level of detail entered into the model will be dictated by the type of suspension including the result required from the modelling process; as such, the simulation process can yield a broad range of data concerning the railway vehicle such as displacements, accelerations and forces that may present at any specific point during the motion of the vehicle on the railway track. Vehicle inputs to the model include the following elements: springs, dampers, links, joints, friction surfaces or wheel-rail contact and these can be chosen from a library database and, subsequently, connected between locations referred to as nodes in a multi-body system model with variable complexity depending on the type of vehicle being analysed and the required output. Bodies are rigid but can be made flexible by changing the stiffness value. Furthermore, masses including moments of inertia must be specified in the model. Inputs for the track are specified for each wheelset and include parameters such as vertical and lateral alignment, gauge and cross-level; and further forces which may be acting, for example, wind loading and/or other powered actuators can also be specified in the computer model to simulate actual in-service conditions. The equations of motion can be analysed by various methods and yield different important information concerning the system being analysed. For example, an analysis based on the eigenvalues of matrices representing the equations of motion can yield the natural frequencies of the modes of oscillation

and, thus, the analysis by using this method can identify any form of instability which might occur in the system during motion and, therefore, the speed at which such a critical instability, referred more commonly as hunting, might occur. Other analysis methods include the quasi-static analysis and the time stepping integration of the equations of motion method. The former predicts the steady state parameters of all bodies in the system and the consequent suspension forces acting at the wheel-rail patch. The latter, is a highly powerful method of analysis which describes the scenario at curves of different radii or when a vehicle encounters a transition. Nonlinearities which may be present in the suspension and/or the wheel-rail contact patch as a result of flange contact and creep can be entered into the model. Further details on the current computer modes available can be found in references [121, 124-127]. The computer software packages currently available in industry enable the size and shape of contact patches including their points of contact and the magnitudes of the normal and tangential forces acting on the contact patch [121]. Furthermore, the challenge of modelling and thus better understanding the rolling contact fatigue phenomena at present is made more problematic because of the non-proportional stress state imposed on the mechanical components combined with the complex matter of describing the stress state under contact conditions. Multi-axial fatigue theory has been proposed to confront this issue, however, no such universally accepted model exists at present [22]. Currently, modelling rolling contact fatigue is generally carried out by employing Hertz theory or finite element analysis (FEA) are used to evaluate the stress response in mechanical rail and rail wheel components; to improve these simplified modelling approaches it is recommended to include in the models parameters such as the condition of the material's surface as well as its nonlinearity and wheel motion [21, 23-30].

The occurrence of RCF is governed by the correlation between the growth of cracks and the development of wear. The former is the result of the presence of contact stress and the tangential force at the wheel-rail contact area, and the latter is due to the creepage occurring at the contact area together with the tangential force. Furthermore, other factors also affect these parameters and these include: curve radius, wheel diameter, axle load, wheelbase, suspension yaw stiffness, wheel and rail profiles including their state of wear, the level of friction present at the wheel-rail interface, cant deficiency, traction and breaking forces, track geometry and properties of the

wheel and rail materials [121]. In contrast to shakedown theory which suggests that hardened rails are more resistant to cracking than normal grade steel rails, in practice, however, it is found that the opposite is the case and that such a state of affairs is a consequence of the presence of wear [122]. The occurrence of wear inhibits the development of RCF by gradually wearing down and, thus, altogether removing incipient cracks before an opportunity presents itself for them to grow to a critical level that can eventually undermine the integrity of the structure which may lead to unwanted catastrophic failure. In addition, wheel and rail wear is dependent on the rate of dissipation of energy in the rail-wheel contact area [123]. The rate of dissipation of energy at the contact patch is represented by the wear number $T\gamma$ which is given by the product of the tangential creep force and the creepage. It is shown by these authors [121] that there is a nonlinear relationship between the traction coefficient and wear and that wear increases quickly as the traction coefficient approaches the limiting value represented by the friction coefficient. Work is still ongoing in this field on vehicle dynamic simulations to better understand the correlation between crack growth and wear

Rolling contact fatigue damage (RCF) which is caused by the stresses incurred at the wheel-rail interface emanating in the form of surface cracks and spalling is thus observed in railway line and railway wheels. In rails, RCF is commonly found in high rail and in switches and crossings [121]. However, the work presented in this thesis will be focused on the types of RCF damage as observed on the tread of railway wheels. Rail wheel life depends largely on the resistance of the wheel to wear and its immunity to tread failures caused by thermal cracking and shelling as a result of RCF. Defects that are commonly found in all types of railway wheels are described in the next section and are discussed at length in the literature [89]. Due to trains nowadays experiencing increased levels of mechanical and thermal loading and higher speeds many railway systems are experiencing increased levels of rail and railway wheel surface failure. However, if the RCF damage remains untreated and reaches a severe level the cracks generated at the tread surface will typically grow in length and depth reaching a critical level leading to severe reductions in the service life of the railway wheel. Thus minimising and managing surface cracking at the tread is of utmost importance; this can be achieved by the regular and periodic process of grinding the rail wheel to remove surface defects and thus re-shape the profile of the wheel. This

process is most effective early stages of the life-cycle of cracks. Therefore, being able to determine the depth and severity of cracks in railway wheels with an effective maintenance programme in place to this end can significantly enhance the management and maintenance of railway wheels. Higher speeds and increasing weights result in rail wheels being constantly subjected to increasing amounts of loads. These loads are a combination of mechanical and thermal loads. The former are a consequence of axle loads and the latter result from, for example, braking, especially on block-braked wheels [1]. Thermal loads are affected by the Contact geometry and dynamics affect the thermal loads imposed on the rail wheels and these parameters are dependent upon the speed, spring stiffness, un-sprung mass, and evenness of the rail and rail wheels. During block-braking, friction against the brake blocks causes the surface layer of the rail wheel to be instantaneously heated at en elevated temperature and then immediately cooled in the wheel-rail contact area. As a consequence, cyclic thermal stresses are induced in the surface of the wheels which can give rise to thermal fatigue cracks [2]. The build-up of dynamic stress and strain fields in a rotating wheel during its lifetime in service can give rise to further fatigue phenomena, for example, the formation of cracks as a result of the presence of inclusions in the steel material, however, the process of plastic deformation will also cause the gradual degradation of the surface of a "pure" material, thus leading to crack initiation or so-called rolling contact fatigue (RCF) phenomena. As a result, the formation of RCF defects together with thermally induced cracks can lead to the occurrence of spalling and shelling that subsequently cause the detachment and loss of some of the material from the surface of the wheel. Consequently, this results in higher impact forces being imposed on the rail and/or rail wheel.

The normal braking action can sometimes be disturbed, for example, due to the presence of wet leaves, ice and/or dust on the surface of the rail. This can lead to wheel slide as a result of the significant reduction in the friction occurring between the rail and the wheel during braking under such uncontrolled conditions [3-5]. As a result, the temperature of the material that is close to the contact surface is rapidly increased and becomes high enough to transform a thin layer of the wheel steel material to austenite. Subsequently, on releasing the brakes, the austenitized material is quickly cooled and, consequently, transforms into martensite. Cracks may develop in this thin surface layer of the material that can subsequently grow by RCF

mechanisms. As in the case of rails, in railway wheels RCF cracks are surface breaking and typically grow at an angle to the running direction and propagate at a shallow angle until reaching a certain depth into the rail head (about 5 mm) [6,7] and subsequently extend deeper into the material and thus potentially grow to a critical size resulting in a detrimental break in the rail. These rolling contact fatigue type cracks extend in surface length as they grow within the material, however, no definitive relationship has thus far been found between the surface length and depth for RCF cracks. As a result, surface length measurements cannot be used in order to determine whether the defect has turned down and has become critical.

Fatigue damage in railway wheels is influenced by various factors; prominent amongst these is wheel diameter which will significantly affect the occurrence of fatigue damage on the wheel as reported by Liu et al [8]. These authors have suggested that the radius of the wheel will affect the internal stress in the wheel according to Hertz theory [8]. The above authors have demonstrated that the rate of accumulation of damage for different wheel sizes decreases as the wheel diameter increases and also increases as a result of increases in the vertical load imposed on the wheel. Furthermore, it has been found that the hardness of a material directly affects the contact stiffness and thus the stress response in the wheel [8,9]. The yield strength of the material increases as hardness increases and Liu et al. have also shown that the damage accumulation rate increases as the level of hardness of the material increases.

Furthermore, efforts have recently been made to optimise wheel and rail design. As a consequence, this tends to change the major wheel rim damage from wear to fatigue [8,10,11]. In contrast to wear which causes the material to deteriorate more slowly, fatigue causes abrupt fractures in wheels or loss of material from the tread surface. As a result, these failures may cause damage to rails and train suspensions, and in rare cases, lead to the derailment of the train. Therefore, an understanding of the underlying mechanism of RCF, which is caused by the repeated contact stress during the rolling motion, requires a detailed knowledge of the interaction between wheel and rim.

Furthermore, it has been postulated in the literature that various modes of failure exist for railway wheels [13,14,] and, according to Ekberg and Marais [15] there are

essentially three different types of failure mechanisms for wheels. These modes of rail wheel failure are classified by the above authors in terms of the different locations where these failure mechanisms originate, namely, at the structure's surface, sub-surface or deep within the material and are thus classified as: surface initiated, sub-surface initiated or deep surface initiated fatigue type failures, respectively. In general, two distinct types of cracks are commonly found to occur on wheel tread surfaces and these different crack formations arise due to different mechanical and thermal processes; these include cracks which are generated by the repeated mechanical contact stress arising as a result of the constantly recurring rolling motion of the wheel and due to the presence of thermal stresses which arise from friction occurring on the tread's surface as a result of braking, respectively. The latter appear as short cracks that are oriented in the tread's axial direction [15]. Furthermore, it is reported in the literature [16] that, in the majority of cases, railway wheels fail as a result of the shattering of rims, whereas, the least cause is attributed to thermally induced cracks and the rest are due to the occurrence of vertical split rim damage. Thermal cracks usually cause the detachment of some material from the wheel's tread surface, however, wheel failure caused by a broken rim is considered to be a far more dangerous proposition as it can damage the integrity of the railway wheel and, thus, impair the vehicle's standard of safety.

Fatigue crack growth parallel to the tread surface of railway wheels is considered to be the cause of shattered rim failures by Y. Liu et al. [17,18]. The initiation stage of this process is believed to be the result of high stress caused by the large forces acting on the wheel-rail patch or it might also be due to the material discontinuity. Furthermore, inclusions and/or voids present in the material in a highly stressed region of the tread may also lead to the failure of wheels, however, Ekberg et al. [21] also report that the initiation of such rim failures can be caused not only by the presence of inclusion but also by their absence in the material. Research has shown that newer wheels appear to be less prone to shattered rim failures and, thus, might be more resistant to this type of failure mechanism in wheels; nevertheless, this is not necessarily the case for numerous worn or so-called "old" wheels that are currently in-service. Adherence to tighter regulations imposed by the railway industry on wheel manufacture and inspection processes have thus far significantly improved the measures which have been taken to minimise or, preferably, ultimately prevent the

occurrence of rim failures due to shattering, however, the reality is that, unfortunately, all such failures cannot be eliminated at present and, thus, further work needs to be carried out in this field to improve the wheel manufacturing and maintenance processes further in order to realise the ultimate goal of permanently eliminating or further reducing the occurrence of such failures.

3.5 MAINTENANCE METHODOLOGY

An in-depth understanding of the RCF phenomena is vital in order to discover ways of eliminating or mitigating the effects of such damage to railway wheels and track and to find the most cost-effective, efficient and commercially viable routes to this end. Thus, a large amount of research has been carried out both within academia and industry and the results of this work have been well documented in the available literature and such work is continually being conducted to further understand the phenomena of RCF.

Grinding is a means by which RCF can be controlled by removing material and thus removing incipient cracks before they can grow to severe lengths and depths which can lead to catastrophic damage. However, this is generally a costly procedure and the life expectancy of the structure will be limited by the gradual loss of section due to the removal of material by grinding. Therefore, more cost-effective and efficient solutions must be sought in the long term to achieve the same ends and, thus, extensive research work is ongoing in this endeavour. One possible avenue to explore is to investigate the viability of using rail steels with higher rates of wear which would thus minimise the requirement to grind the material as artificial wear.

Furthermore, rail and wheel profiling is another method that is currently being explored in order to reduce contact stresses and/or traction coefficients to control and manage RCF. However, as a result of reducing the above parameters this is also found to reduce the ability to steer the vehicle on curves. Thus, changing the profile of the wheel and/or rail to control and manage RCF will most probably be at the expense of higher lubrication and/or more maintenance costs.

Furthermore, the wheel and rail profiles play an important part during the steering of the railway vehicle using minimal expenditure of energy and, thus, minimal

consumption of fuel. However, the disadvantages of having incorrect profiles that are ill-maintained are two-fold, namely, that the railway wheels become misaligned to the railway track and also the flange of the wheel makes contact against the rail in an identical manner to automobiles making contact with the curb. As a result of these factors the fuel consumption is significantly increased. In addition, incorrect wheel and rail profiles and their mismatch can lead to detrimental effects such as defects which would, therefore, require maintenance and also untimely replacement; such commonly occurring defects include wear, metal fatigue and corrugation, amongst other types of defects. Tus, all this entails the further expenditure of energy and cost to the railway industry in order to re-profile and/or re-manufacture the steel wheel and rail structural components. Furthermore, the wheel and rail profiles and their interaction with each other control the contact stress at the wheel/rail contact patch which, in turn, dictates the extent of the occurrence of the wear and the surface fatigue of both the wheel and the rail.

The inspection of brake pads is currently carried out by automated systems consisting of digital cameras which take exposures of the brake pads and, subsequently, employ machine vision technology to assess the condition and the degree of wear that has occurred on the brake pads during service. The process allows a full diagnosis of the condition of the brake pads and can determine parameters such as wear rates which can, thus, be further investigated in the event that the resulting wear rates are found to be either higher or lower than normal; thus, the system allows detection of non-uniform wear and any brake pads that might be missing. Furthermore, automatic vehicle identification systems (AVI) have been developed and are employed across the UK railway network to facilitate the process of analysing the data obtained from condition monitoring inspection systems that are based on the side of the track in order to ascertain general trends and, thus, wear patterns for vehicles on an individual basis.

Furthermore, the wheelset condition monitoring (WCM) RSSB report for task J607 [32] highlights some emerging technologies that are currently under development manufacturers and will be added to the condition monitoring repertoire in the future and these are as follows:

- Automated ultrasonic systems to detect cracked wheels including laser-ultrasonic systems to detect cracked axles.
- Train Fault Detection System (TFDS) Image Acquisition.
- Acoustic Systems designed for the on-board detection of defects which might be present in bearings.
- Bogie hunting detection systems that are based on displacement sensors

Furthermore, the railway wheelset maintenance standard in reference [122] specifies the following criteria for the maintenance of railway wheels in-service. The standard specifies limiting values for the lengths of wheel tread defects relative to the axle load, wheel diameter and speed; also, in certain cases, experience during service plays an important part in providing guidance on imposing restrictive values for these limits on defect lengths for tread defects such as cavities, metal build-up and wheel flats. Thermal cracks are altogether not allowed and wheel tread roll-over must not exceed 5 mm. In addition, the standard stipulates that the internal face of the wheel's rim and flange must be from defects such as radial cracks or sharp notches and that checks should be made to ensure that no grooves, which may be sharp-edged, are present on the wheel tread region. Also, there should be no friction between the flanging brake blocks and the rim's external face. Also, friction must be absent between the brake blocks and the wheel rim's external face and, therefore, flanging brake blocks are not allowed. Tooling marks such as sharp-edged notches and defects which might be present on the flange due to metal flow or have sharp edges are also to be addressed and not permitted. Furthermore, the above wheelset standard states that the wheel cannot be allowed to move in the radial or axial direction, however, any movement that is associated with any components which are assembled on the axle of the wheelset should be assessed and, thus, addressed in accordance with experience during service. The web of a wheel must be examined to ensure that there are no stress inducing defects present such as cracks or sharp-edged notches and also ensure that thermal or mechanical cracks are absent from the regions surrounding any holes, for example, on transmission gear and brake disk or anti-noise components which are usually mounted on, for example, the web. In addition, cracks are not permitted in the brake zone's central region neither in the border line of this area. In the event that the rim-web transition of the wheel experiences overheating then the standard stipulates that the dimensions and geometry of the wheel/rail interface must be assessed to

ensure that these are in line with and, thus, conform to the required standard as outlined in the above wheelset maintenance standard; if the geometry conforms to the standard then the assessment of potential thermally induced cracks shall ensue.

The above standard for wheelset maintenance requires that mandatory requirements and operations are met for in-service maintenance. Also, there should be a maintenance plan in place which must include the following:

- Periodicity of inspections by non-destructive means, including dimensional checks.
- The relevant criteria including the periodicity for on-vehicle maintenance operations that are deemed as mandatory must also be specified in line with the requirements; furthermore, the criteria and periodicity for maintenance procedures for domestic traffic must also be clearly specified for maintenance purposes.
- Special attention is required during the cleaning process undertaken for vehicles and bogies to prevent the ingress of cleaning fluid into components such as the bearings, axle-box and transmission, in order to protect the wheelset during the maintenance procedure.
- It is recommended that all relevant documented information regarding the proposed in-service maintenance procedures should be located on board the vehicles and be available at all times for practical reasons and ease of access to personnel so that maintenance actions can be performed in a fast and efficient manner.

Furthermore, the above mentioned standard requires that on the completion of off-vehicle maintenance the wheelset must be defect-free in order that it conforms to the maintenance requirements and operations deemed as appropriate by the standard. The off-vehicle maintenance plan as specified by the wheelset standard is as follows:

- The specific procedures and the periodicities for the necessary application of NDT tests should be specified in the plan, including, if necessary, other special actions to be implemented, for example, demagnetisation of components, etc.
- Instructions on the wheelset cleaning process and the criteria for the scrapping of bearings as well as guidance on how to protect against corrosion damage during overhaul.

- The tolerance limits for every type of component, such as for the dimensions of the components, must be specified in the maintenance plan.
- The provision of lists of maintenance tasks and applicable checks in order to ensure that the wheelset conforms to the standard required are also compulsory and, therefore, need to be included in the plan for off-service vehicle maintenance.
- Furthermore, information obtained from service experience is very beneficial moving forward and, thus, should be reflected upon and the beneficial factors appropriately assimilated in the maintenance plan in order to continuously improve upon the existing maintenance procedures.

The main maintenance operations for off-vehicle wheelset maintenance as described in the above mentioned wheelset maintenance standard are as highlighted below:

- General inspection including the cleaning of the wheelset; individual wheelset components should be protected if deemed necessary.
- All wheelset components, which include: bearings, lubrication systems, wheels, axle and axle-boxes, must be inspected.
- The re-profiling of wheelsets, if necessary, and the overhaul of axle-boxes are also mandatory measures.
- The assembly of bearings and wheels (in accordance with the EN13260 standard if these actions are judged as requirements.
- Appropriate measures must be in place and, thus, actioned upon whenever necessary to protect the wheelset components against the detrimental effects of damage caused by the presence of corrosion.
- A final check should be carried out to ensure that the wheelset conforms to the requirements of the standard and the provision of an overhaul auditable trail of operations including assembly or dismantling, also an important requirement.

Furthermore, the cleaning of wheelsets is to be carried out employing appropriate processes and using recommended products in conjunction with pressurised water, mechanical cleaning techniques or by using a brush; however, in the case of using mechanical methods it is important to ensure that such systems are not detrimental to the fatigue performance of the component beyond the recommended fatigue limit performance of the component being cleaned and care must also be taken to ensure

that the method does not mask any internal crack which might influence the sensitivity of the chosen methodology.

CHAPTER 4
INSPECTION OF RAILWAY WHEELSETS

4.1 AUTOMATED VISUAL INSPECTION SYSTEMS

The simplest and most widely used NDE technique is by visual inspection. The technique is capable of detecting damage and distortion on the surface of materials. However, its capability is reliant upon the level of illumination and on the eyesight of the inspector operating the system; thus, regular eyesight tests for personnel are mandatory and a necessary part of industry and are thus given at regular intervals to inspectors. Visual aids include magnifying glasses via endoscopes and borescopes, fully remote video systems and optimisation of signal processing of the image obtained is consequently required.

Increasingly, during the past decade, automated visual inspection systems incorporating cameras have been used for railway applications [43, 44]. These systems incorporate high-speed exposure digital cameras in order to capture in-situ images of the railway track and wheels in-service, including the ability to take photographs at such high-speeds of railway wheels and components and thus assess their condition in-service. Subsequently, image analysis is conducted employing appropriate software techniques. Inspection speeds are controlled dependent on the resolution required and/or type of inspection necessary, for example, surface damage like RCF and rail corrugation or, for instance, the investigation of the level of wear on rails or the determination of rail gap; the former is carried out at low speeds of about 4 km/h, whereas, the latter type of investigation can be conducted at much higher speeds of up to 320 km/h [43-48].

4.2 ULTRASONIC NDE TECHNIQUES

Systems used for the inspection of rails using conventional ultrasonic probes [44, 49-51] involve the following process: a piezoelectric element generates a beam of ultrasonic energy which is transmitted into the rail. An ensemble of transducers, correctly positioned, then detect the reflected or scattered beam and the resulting amplitude of such reflections combined with their position in time and space can provide important information on the location and type of defects present in the

material and, thus, an overall assessment of the structural integrity of the material under inspection being investigated.

The probability of detection (PoD) of defects that may be present in the material under inspection can be increased by transmitting the ultrasonic beam at different angles within the component since it is possible that such detrimental defects as can cause failure if not detected as soon as possible are most likely to be located at various angles within the material. Thus, in industry, the reflected angles that are normally chosen for the transmission of the ultrasonic beam are: 0^0, 37^0, 45^0 and 70^0. Ultrasonic transducers are positioned at appropriate locations around the component under investigation in order to optimise the detection of defects present in the material.

Test trains incorporating ultrasonic testing equipment are used in industry to detect surface breaking including deep internal defects and perform rather efficiently for this purpose. It is common practice for these test trains to use a water filled 'bag' or 'wheel' to provide the ultrasonic pathway into the rail. However, such high-speed systems are usually unable to detect RCF defects that are smaller than 4 mm deep. Such surface defects may mask critical internal defects and therefore make it more difficult to interpret and, thus, yielding a distorted analysis of the structural integrity of the material being inspected. Some drawbacks of ultrasonic inspection using test trains include the inspection of corrosion, for example, in the foot of the rail where only partial inspection of the rail is possible, and during the inspection of welds because it is normally difficult to obtain any sort of energy transfer from the locations at which defects generally initiate from these welds in order to perform an ultrasonic test.

Long-range ultrasonic and laser-based ultrasonic systems, references [54-61] and [62-73] respectively, are two ultrasonic NDE techniques that are promising NDE techniques which are promising complementary systems that are currently being investigated as future NDE techniques and are thus under development. The former technique involves the transmission of volumetric waves within the material under inspection and such waves can take the form of Lamb, Plate or Rayleigh wave modes which are transmitted in the material using piezoelectric transducers appropriately positioned and coupled onto the structure such that the required wave mode is

transmitted in the material being investigated. Reflections arising from reference points, attributed to, for example, welds and joints or reflections emanating from cracks or corrosion present within the material are subsequently detected, recorded and analysed; thus, yielding valuable information concerning the likelihood (or PoD) of a defect being present in the structure including its location and relative size (length and depth). An important requirement for the efficient execution of this technique is the necessity for a trained and skilled workforce to carry out the operation. However, stress inducing components that may be present in the structure under investigation can attenuate the signal, thus, significantly reducing the effective distance over which the technique is useful. Therefore, in order to address the issue of optimising the effective range over which inspection by this method is most effective consideration must be given to the choice of operating frequency and the mode of propagation of the ultrasonic wave into the material. Furthermore, the sensitivity of the technique to the cross-sectional area of the structure must also be taken into consideration when employing the technique to optimise the PoD of defects in the material under inspection.

The latter technique generates ultrasonic waves by using high-powered lasers to fire laser pulses onto the structure being investigated for defects or other types of sub-surface and deeper internal damage and, thus, create ultrasonic waves of various modes as required (e.g. shear, surface, compressional and plate waves) in the material by either laser ablation or a thermoelastic process. On the wave reaching the material's surface any surface displacement that may be present is then usually detected using an interferometer acting as the receiver for the signal. In addition, ultrasonic phase arrays have been developed consisting of multiple ultrasonic testing elements which are coupled with time delay electronic components to create phase shifts and, thus, ultrasonic beams by the process of constructive and destructive interference of the waves. Such an ultrasonic beam provides a valuable advantage over more conventional ultrasonic testing systems as the beam can be further controlled by steering, sweeping and focussing, the beam onto the target of interest by optimising the angle of the beam relative to the area of interest in the material under inspection; ideally, the projected beam should be perpendicular to the defects being investigated. Another advantage of this technique over the conventional method is that as a result of the presence of multiple ultrasonic elements in the array set-up the

ability to focus the beam is significantly enhanced and, thus, the beam can be made to efficiently penetrate deeper into the structure being inspected and, into more complex geometries such as in deep welds where otherwise with more conventional systems
It might be more difficult to penetrate and, thus, search for defects. By focussing the beam the energy of the ultrasonic beam can be significantly increased.

Another NDE technique which is used to detect flaws in ferromagnetic materials is the electromagnetic acoustic transducer (EMAT) [79-88]. In an EMAT system a high electrical current is passed through an induction coil which is placed close to the surface of the material under test in the vicinity of a strong magnetic field caused, for example by a permanent magnet. The nature of the resultant ultrasound is dictated by the magnetic field characteristics, coil geometry and the properties of the material under investigation. The main advantage that EMAT systems have over other NDE systems is that as a result of electromagnetic coupling a coupling medium is not required between the probe and the surface of the material under test. Furthermore, the technique is capable of detecting flaws and damage caused to rails by the mechanism of rolling contact fatigue; however, cracks which are smaller than 2 mm are difficult to detect by this method and inspection speeds must be kept low between 5 and 9 km/h. Therefore, in the recent past research has been carried out [43, 114-118, 144] on NDE systems incorporating EMATs and PEC probes in order to increase the sensitivity, and, thus, the detectability of the cracks present in railway and railway wheels using this technique.

4.3 ACOUSTIC EMISSION (AE)

Acoustic emission is used in industry to investigate and, thus, assess the structural integrity of large structures and is commonly employed to detect liquid and gas leakage occurring in such structures including the assessment of rotating machinery [92-94]. In essence, these sensors are piezoelectric transducers that are usually air-coupled onto the structure being investigated for possible damage. The detected signal is amplified and, subsequently, processed and analysed. Signal processing is regarded as the most important aspect of AE testing in order to distinguish between genuine signal emanating, for example, from crack growth or other types of damage within the material from signals arising from external factors, such as, noise that may be related to the environment, mechanics or electronics of the AE system. To this end the

received signal is filtered using appropriate electronics. The process of triangulation is commonly employed to gather information on the source's locality within the structure including the source type such as a growing crack. Various parameters are taken into consideration when analysing this information in order to determine the nature of the source; these include, the returning signal's amplitude, duration, rise-time, energy and frequency.

In contrast to the passive acoustic emission technique described above the acoustic emission pulsing (AEP) [95-105] technique is its active counterpart. Whereas the former detects signals arising from developing flaws in the structure being investigated the latter system consists of a transducer which generates ultrasound and a number of other transducers that act as sensors and are thus placed at strategically identified appropriate positions around the structure under inspection. Thus, due to the absence and presence of any defects present in the structure the original signal spectrum generated by the transmitting ultrasound transducer will be unchanged and changed, respectively. With proper calibration combined with the right signal analysis procedure the AEP system can provide valuable information on the type and severity of damage that may be present in the structure of interest. Work is currently underway in the railway industry to develop AEP inspection systems at high speed as, at present, only static systems are employed; to this end, laser ultrasonics including air-coupled acoustic emission systems are being explored.

4.4 RADIOGRAPHY

Radiography is extensively used in a wide range of industrial sectors and has found practical applications in the railway industry to detect flaws, discontinuities and to assess the general condition and, thus, the structural integrity of rail and rail wheel treads, as has been shown by the work presented in chapter 6 of this PhD thesis. Therefore, x-ray tomography, which is more commonly referred to as computed tomography (CT), is a useful and viable technique in detecting and sizing cracks observed in rail wheel treads and other such surface-breaking cracks in steel structural components. There are two types of CT scanners, namely, cone scanners and fan-like beam scanners [109,110]. The former rotate whereas the latter translate. In the case of the fan-like beam scanners a collimated x-ray beam is used to scan across the material under test, whereas, the cone beam scanner rotates the object being inspected which is

placed on a platform that is made to rotate, thus, resulting in over a thousand 2D images being produced. In both of these systems the resulting 2D images of the defects are subsequently reconstructed to create 3D visuals of the object under inspection using appropriate reconstruction software. Gamma or x-ray sources can be used for radiographic inspection, however, nowadays, due to the availability of more compact digital x-ray detectors, x-ray sources are generally favoured. The technique can provide valuable information on the characteristics of defects, for example, their size, length and propagation angles, as shown by the work presented in chapter 6 of this thesis, and also providing information concerning the location of the flaws present in the structure. However, together with its advantages, radiography presents with it some serious drawbacks, most notably, serious health and safety risks and hazards associated with the technique and, therefore, doses for the inspection of rail and rail wheel treads and components by this method need to be kept as low as is practically possible to ensure the safety as of the personnel. Another use for x-ray tomography is in determining the composition of the material under inspection; furthermore, a complementary technique, namely, x-ray diffraction (XRD) can be used to determine the residual stress near the wheel tread surface.

4.5 THERMOGRAPHY

Thermography is a non-destructive technique used to inspect parts of materials or systems by imaging the thermal patterns at the surface of the object under inspection and is a relatively safe technique that requires no contact with the object under inspection. The technique is computer controlled and detects and measures small temperature differences which are then downloaded and shown as an image, in colour or a grey scale map, on a computer. The infrared thermography system consists of an infrared detector and is employed in a wide range of industrial applications to non-destructively inspect materials and provide mapping of thermal patterns (or thermograms) of the surface of the object being inspected for material structural integrity in a non-intrusive manner [112]. There are two types of thermographic inspection techniques: passive and active. The former is based on the principle that the feature of interest is at a higher or lower temperature than the background as is used for surveillance purposes. The latter requires an external or internal energy source to provide thermal contrast between the object under inspection and the background; examples of external energy sources employed for this purpose are

photographic flashes (heat pulsed stimulation) or halogen lamps (periodic heating) and for an internal source the contrast is achieved by using a sonic or ultrasonic transducer for burst and amplitude modulated stimulation [113] in order to generate mechanical oscillations and, thus, internal excitations. This method can be used for the detection of shallow sub-surface defects (few millimeters in depth) in quick time and in materials with a large surface area. The technique is currently employed in various industrial sectors which include the aerospace, automotive and power sectors.

4.6 MAGNETIC FLUX LEAKAGE (MFL)

Magnetic flux leakage is a quantitative technique requiring a high level of set-up and is thus prone to human error during operation and requires well trained personnel to operate the system. Therefore, the standard operating procedures need to be clear and sufficiently detailed. However, the technique in itself is simple to understand and use. The principle relies on the detection of any leakage of magnetic flux from the component under test due to any damage to its structure that may be present. In order to achieve this,, the component being inspected is required to be magnetically saturated or be close to saturation; this is achieved by placing the component under test between the poles of a permanent magnet. In general, the amplitude of the obtained signal will be proportional to the volume of the material loss from the structure in the interrogated region, thus, indicating the presence of damage in the structure under test. Results, can be adversely affected by various factors such as an inhomogeneous surface due to surface roughness, distortion, corrosion that might be present on the surface being investigated, any build-up of debris on the magnets including any physical disturbance that might hinder the system's motion as it scans across the surface of the component under inspection.

4.7 EDDY CURRENT ELECTROMAGNETIC TECHNIQUE

Eddy current sensors, such as the pulsed eddy current technique (PEC) are used in the rail industry to detect surface defects. These sensors comprise one exciting and one sensing coil [43, 44, 49-51, 106-108]. The technique works by introducing an alternating current in an exciting coil placed in close proximity to the surface of the material under test, thus, generating a magnetic field near the material's surface. Subsequently, due to changes in the magnetic field, eddy currents are created and flow in a thin 'skin' layer near the material's surface. The skin depth is a function of the

frequency of operation of the eddy current system and of the permeability of the material under inspection. Furthermore, lift-off variations significantly affect the sensor's signal response to defects and, thus, for optimum results it has been verified and agreed upon by manufacturers and independent researchers in the field that the sensor must remain at a constant distance of no greater than 2 mm above the surface of the structure under test and it is of utmost importance to ensure that this lift-off distance is carefully maintained and does not exceed this limit throughout the inspection process. The eddy currents, in turn, result in a back electromagnetic field being produced; thus, the presence of any flaws in the material which impede the flow of eddy currents would, therefore, result in a difference and, thus, an in-balance between the applied and back electromagnetic fields and, thus, yield a defect signal which can be detected.

The pulsed eddy current (PEC) technique differs from conventional ultrasonic systems in that instead of measuring the wall thickness as in the case of the conventional technique it measures the average loss of wall thickness over an area (i.e. a 'footprint') of the component being investigated. The technique's principle is that a transmitter coil is used to produce a magnetic pulse which, in turn, induces eddy currents in the component under test and, as a result, these eddy currents produce a second magnetic pulse within the material under inspection which is subsequently detected by the system's receiving coil. The system then analyses the rate of decay of the eddy current pulse within the material and, thus, assesses the damage based on the comparison being made between the transient time of specific features against known calibrated signals from similar material components or parts. The system is relatively easy to use, however, for efficient operation and optimum results it is recommended that the operator is supplied with as much information concerning the component under test as possible in order for the equipment to be set up in the right way so as to assist in the proper analysis and interpretation of the results obtained. The technique is suitable for the inspection of damage in both conducting and non-conducting materials and for low alloy steel materials.

4.8 ALTERNATING CURRENT FIELD MEASUREMENT (ACFM) TECHNIQUE

An alternative to magnetic particle inspection (MPI) or dye-penetrant inspection techniques the alternating current field measurement (ACFM) technique is a non-contact and non-invasive electromagnetic technique which is used in various industrial sectors to detect surface defects in ferromagnetic materials; the technique also has the capability of somewhat detecting some near surface defects in non-ferrous materials due to the greater skin depth availability in non-ferrous materials than in ferrous structures as will be discussed in more detail in the next chapter where the theory and principles of operation behind the technique will be discussed in more depth. In general, as an overview, the principle behind the technique is that a uniform alternating current is induced into the surface of the component under investigation that results in a corresponding magnetic field which remains undisturbed in the absence of a defect, however, if the current encounters a defect in its path then it will be made to naturally flow down the sides of the defect and also across the face of the defect. The probes within the ACFM system have been developed in such a manner to enable the capture and recording of changes to the magnetic field disturbances. Crack sizing, i.e. length and depth estimates, are evaluated using appropriate software algorithms which are constantly being developed and improved by incorporating fresh data received from ongoing research in the field to determine crack shapes and sizes in the surfaces of structures using other non-invasive techniques such as computed tomography (CT) in conjunction with 3D reconstruction and modelling techniques. The technique can detect defects through coatings such as rust or paint and, thus, can cope with poor surfaces. Furthermore, the system has a better lift-off capability than eddy-current sensors as the signal diminishes with the square of lift-off distance in the former and with the cube of lift-off distance in the latter and, thus, can cope better with variations in lift-off.

Due to its simple methodology and ease of use ac field measurements are widely employed in a range of different industrial sectors in order to detect and size cracks at and near the surface of ferromagnetic and non-ferromagnetic structural components. Furthermore, the development of appropriate mathematical models of the electromagnetic fields has thus led to the elimination for the need for the calibration

of the system for practical applications. Determining the size of the crack and the service loading is of utmost importance in calculating the likelihood of failure.

the following is an overview of the main features and attributes of the ACFM system and then the standard operating procedure for the technique is described as below.

The alternating current field measurement (ACFM) system is an electromagnetic NDT technique providing one pass inspection and has the following attributes including an overview on ACFM for defects, applications, theoretical and practical limitations:

- High tolerance to lift-off
- No electrical contact requirement thus can be used through coatings.
- Provides crack detection and sizing (length and depth).
- No reliance on operator calibration.
- Manual, automated and semi-automated systems available.
- Used to inspect a wide range of ferrous and non-ferrous materials including: carbon steels, stainless steels, duplex, super duplex, titanium, aluminium.
- Inspection of welds and threads.
- High temperature, air and sub-sea applications.
- Can only be used for surface breaking cracks.
- Grinding and weld repairs can cause spurious signals.
- Multiple defects reduce the ability to estimate defect depth; crack length needs to be greater than 5 mm.
- Complex signals can arise from tight geometries, edge effects and interconnected (branched) cracks.

4.9 CONTRASTING ELECTROMAGNETIC NDE SYSTEMS

The combined use of conventional ultrasonic systems working in tandem with magnetic flux leakage (MFL), i.e. magnetic induction, sensors can significantly increase the probability of detection (PoD) of small near-surface and surface breaking defects in railway components [43]. The latter technique relies on magnetising the component under test to saturation, or as close to saturation as is practically possible, using a permanent magnet [90,91]. The magnetic flux is usually air-coupled into the material and the sensor detects any changes in the magnetic component due to the presence of any defects in the sample; this change in the magnetic field is the result of

the leakage of flux due to the presence of surface breaking defects such as RCF cracks that might be present in the component under test, thus indicating the presence of the defect. However, MFL cannot detect internal defects such as deep internal cracks and rail foot corrosion. Furthermore, as inspection speeds increase the technique's performance increasingly deteriorates due to a significant reduction in the magnetic flux density and, thus, its performance is significantly hampered at high speeds.

The three main electromagnetic non-destructive evaluation systems that are currently in use and under continued development are MFL, PEC and ACFM. MFL and PEC have been used as vehicle mounted systems and all three systems can be used as slow speed manual systems ('walking stick' type systems). The performance of MFL deteriorates as the speed is increased beyond 35 km/h, whereas, the PEC technique can potentially operate reliably up to a speed of 70 km/h.

All of the electromagnetic NDE techniques are most suited to detect surface defects, however, currently MFL sensors cannot detect cracks <4 mm in size. Nevertheless, the MFL and PEC techniques can detect near-surface internal defects. The PEC system is more strongly affected by lift-off variations (< 2 mm), whereas, the ACFM method is more reliable in this respect (~ 5 mm); as in the former case the signal decreases with the cube of the lift-off distance, whereas, for the latter technique, the strength of the signal decreases with the square of lift-off.

CHAPTER 5
FUNDAMENTALS OF THE ALTERNATING CURRENT FIELD MEASUREMENT (ACFM) TECHNIQUE

5.1 THE DEVELOPMENT OF THE THIN SKIN THEORY

It has been previously shown [131] that a time varying current flowing in a conductor tends to concentrate itself near the conductor's surface and, for very high frequencies, the alternating current is restricted near the surface of the material in a very thin layer; such phenomena of non-uniform distribution of time-varying currents in conducting materials is referred to as the *skin effect*. The skin effect in conducting materials is caused by the process of electromagnetic induction; the changing magnetic field as a result of the induced alternating current thus induces eddy currents in the conductor which in turn produce a secondary magnetic field. As a result of Lorentz's law the induced eddy currents produce this magnetic flux that opposes the external magnetic flux and, consequently, the total resultant flux is reduced. Higher conductivities induce larger currents in the conducting material and as the permeability of the material increases the subsequent reduction in magnetic flux becomes more pronounced. As a result, both the alternating magnetic flux and the induced currents which flow in the conducting materials are significantly reduced. All conductors exhibit the skin effect, however, the phenomena is more pronounced for ferromagnetic rather than non-ferromagnetic materials having identical conductivity values and, as a result, the current, and magnetic flux, tends to be more restricted in a thin layer near the surface of the conductor in the former case. Thus, the skin effect is extremely important in practical terms for industrial applications; for example, at very high frequencies an extremely thin layer of the conductor would transport most of the current. Therefore, in industrial applications the conductor is usually coated with the best available conductor and, thus, ensure that most of the current is made to flow through this conductive coating, ideally a silver coating would be used for such a purpose, however, as silver is prone to oxidation, a coating of gold is usually applied for this purpose as the metal is inert.

The following is the derivation of the skin depth (δ) for an idealised case of a sinusoidal alternating current (ac) with angular frequency ω, flowing in a conductor

with conductivity σ and permeability μ. Another assumption that needs to be made in this idealised case is that the current density vector J is parallel to the boundary surface and has a single component such that $J=J_z\mu_z$ with reference to the y-axis which represents the distance from the interface. The distribution of the alternating current in the conducting medium is derived as follows. The solution to the problem is not merely an academic one but is vitally important in practical terms. On solving the Maxwell equations it will be found that the intensity of the current density and field vectors decrease exponentially with distance from the boundary surface; the decrease is more pronounced at high frequency, conductivity and permeability values. For any conductor having a radius of curvature much larger than thickness of the current's layer the results thus obtained are applicable to everyday applications to a high degree of accuracy.

From Maxwell's equations in their complex form and assuming the medium to be a good conductor the displacement current density in the second of Maxwell's equations can be neglected. Thus,

$$\Delta x\boldsymbol{E}=-j\omega\boldsymbol{B} \qquad \Delta x\boldsymbol{H}=\boldsymbol{J} \quad (5.1)$$

Since, $\boldsymbol{E}=\boldsymbol{J}/\sigma$ and $\boldsymbol{H}=\boldsymbol{B}/\mu$ then the equations in 5.1 above thus yield:

$$\Delta x\boldsymbol{J}=-j\omega\sigma\boldsymbol{B} \quad \Delta x\boldsymbol{B}=\mu\boldsymbol{J} \qquad (5.2)$$

Assuming that the current density vector J has a z-component dependent on y and, from the Biot-Savart law and symmetry, thus the vector B has only an x-component. Thus,

$$dJ_z/d_y=-j\omega\sigma B_x \qquad -dB_x/d_y=\mu J_z \qquad (5.3)$$

From equations (5.3) above B_x can be eliminated in order to obtain an equation in terms of J_z as follows below.

$$d^2J_z/d_y^2=j\omega\mu\sigma J_z \qquad (5.4)$$

The solution to the above equation then becomes:

$$J_z(y)=J_1e^{ky}+J_2e^{-ky} \qquad (5.5)$$

where,

$$k=(j\omega\mu\sigma)^{-1/2} = (1+j)[(\omega\mu\sigma)/2)]^{-1/2}=(1+j)k \text{ and } k=[(\omega\mu\sigma)/2]^{-1/2} \qquad (5.6)$$

Now, making the assumption that for y = 0 the current density is Jz(0), then, for y approaching infinity the current density thus increases indefinitely and, therefore, J1=0, thus,

$$J_z(y)=J_z(0)e^{-ky}e^{-jky} \qquad (5.7)$$

As a result, this shows that the intensity of the current density vector decreases exponentially with increasing y. Therefore, at a distance known as the skin depth (d) given by:

$$\delta=1/k=(2/\omega\mu\sigma)^{-1/2}\ (m) \qquad (5.8)$$

Therefore, the amplitude of the current density vector decreases to 1/e of its value at the boundary surface (i.e. $J_z(0)$).

Furthermore, the above equation for the skin depth (δ) can also be expressed in terms of the ac frequency (f) and, thus, defined as:

$$\delta=(\pi\sigma\mu f)^{-1/2} \qquad (5.9)$$

It should be stressed that although the above analysis is derived for an idealised case it is also valid and, thus, applicable, for a current distribution in any conducting material having a radius of curvature which is much larger than the skin depth. Therefore, from the above equation it is evident that the skin depth is inversely proportional to the square root of the current's frequency and the conducting medium's conductivity and permeability.

Alternating currents flowing in conductors are non-uniformly distributed over their cross-section and at high frequencies the ac current tends to become more concentrated near the conductor's surface due to the skin effect derived above. Thus, at very high frequencies due to the highly pronounced skin effect in such a case as for any good metallic conductor the current flows in a very thin layer. The skin depth characterises the penetration of the current in a conductor and from the formula for the skin depth it is shown that the current density at the skin depth is 1/e (or 0.37) of its value at the conductor's surface.

Minshekar-Syahkal et.al. [136] have shown in their work on describing the distribution of the ac field around surface breaking cracks that a solution exists which accurately determines the crack depth from measurements of the voltage made using a crack micro-gauge device when the values for the skin depth (δ) and crack depth (d) are comparable. Furthermore, as a guiding principle, ease of operation, interpretation and reliability are high engineering qualities to strive for in this regard.

5.2 THE INDUSTRIAL APPLICATION OF THE SKIN EFFECT

The usefulness of the principle behind the skin effect in industrial applications is seen for the detection and sizing of surface breaking cracks in steel materials as it is found that high frequency and low current density yields variations in the surface voltages arising from the presence of these cracks that are measurable, thus, enabling the portability of the instrument. The frequency of operation of the crack micro-gauge, or more commonly known as the alternating current field measurement system (ACFM) is usually about 6 kHz in order to limit the skin depth for most steels to approximately 0.1 mm. During operation, the ac field is induced across the region under inspection to ensure that a uniform field is made to flow perpendicular to the plane containing the defect. Thus enabling the potential difference measurements to be made using the probe positioned at a constant contact separation distance (D) from the surface of the material under test; thus yielding measurements representing the potential difference just before the crack and over the crack itself as the probe is scanned across the region of interest, represented by V_1 and V_2, respectively. Thus, in the case of a uniform field, V_1 and V_2 are related as follows:

$$V_1/\Delta = V_2/(\Delta + 2d_1)$$

$$\text{thus, } d_1 = (\Delta/2)[V_2/(V_1 - 1)] \qquad (5.10)$$

The above equation yields the depth d_1 provided measurements of the local potential difference and contact spacing are made and is a value obtained whilst making the assumption that the field is uniform in the vicinity of the crack. However, in reality the structure and crack geometries give rise to non-uniform fields; nevertheless, it is found that these fields can be modelled using appropriate algorithms [131] in numerous cases to yield good results in line with experimental data. However, it should be borne in mind that the above equation to determine the depth d_1 is only a good approximation in relation to the true depth of the flaw (d) as research has shown that various important factors play a part to different extents in influencing the result; these factors include the following:

1. The Aspect ratio of actual cracks as found in in-service conditions produce non-uniform field distributions.
2. Electrical contacts which may be present and randomly distributed across the face of the crack would also be an influencing factor.
3. In non-magnetic components thin-skin effects are not prominent and, thus, irrelevant.
4. Field non-uniformity due to the geometry of the structure under test.
5. The presence of fluids, for example, in the use of the probes in sub-sea environments as in the detection of flaws in oil rig structures.
6. Changes in material properties.
7. The presence of mechanical stress in the structure under test.

5.3 ALTERNATING CURRENT FIELD MEASUREMENT (ACFM) TECHNIQUE

5.3.1 ACFM THEORY AND ELECTROMAGNETIC PRINCIPLES

Alternating current field measurement (ACFM) is an electro-magnetic non-destructive inspection technique capable of both detecting and sizing (i.e. length and depth) surface breaking defects in both ferritic and non-ferritic materials. The ACFM system consists of a probe that is connected to an ACFM instrument which is controlled by windows based software on a computer that runs the instrument and, displays and

stores the data. An integral field generator within the probe induces a current to flow in the surface of the material to be inspected. The action of a constant current generator in the instrument combined with an appropriately designed inducer present in the probe ensures that the current under the probe is uniform in direction and strength. The probe incorporates an encoder which, provided with a start location, tracks the absolute position of the probe along the area of inspection. Thus enabling checks to be made along the entire length to be inspected and control the speed of deployment together with accurately pin-pointing the defects [43, 114-118].

The concept behind ACFM is that an alternating current can be induced to flow in a thin skin near the surface of a conductor. On introducing a remote uniform current into the area of the specimen under investigation, the induced current will remain undisturbed provided the specimen is defect-free. However, if the current encounters any cracks that are present in the material this will, as a consequence, cause the otherwise uniform current to flow around the ends and down the faces of the crack. As a result, the change in the direction of the flow of current will cause the magnetic flux to become non-uniform. The magnetic flux is constantly monitored by two types of sensor which measure the magnetic field in two directions: B_z and B_x; the former measures the disturbance caused to the current that flows around the ends of a crack and, the latter, measures the reduction in density above the deepest part of the defect (see figures 5.1 and 5.2).

During the inspection process the ACFM software records and displays the results obtained from the B_x and B_z sensors. The defect is indicated by the distinct traces generated by the B_x and B_z signals. The B_x signal component shows a trough which is related to the defect depth: the larger the trough the deeper the defect. Analysis of the B_x signal is used to determine the depth of a defect by reference to a mathematical model which relates the observed deviation in the B_x signal to crack depth. As a consequence, no prior calibration of the system is required. However, this method of evaluating the depth of defects was developed for long shallow cracks such as those seen in welds, and for some elliptical shapes, therefore it will not be so good for complex RCF type cracks The shape of the B_z signal, which includes a peak and a trough, indicates the position of the defect along and across the area of the material under inspection, thus the surface length of the crack is determined.

The alternating current does not penetrate deep into the material but is maintained in a very thin skin (approximately <0.2 mm deep depending on the material and frequency of operation) in the surface of the material under investigation and is thus unaffected by the overall geometry of the component [34-37]. The technique is extensively used in the oil and gas industry for petrochemical applications and is being used in conjunction with other NDT techniques, for example, magnetic particle inspection (MPI).

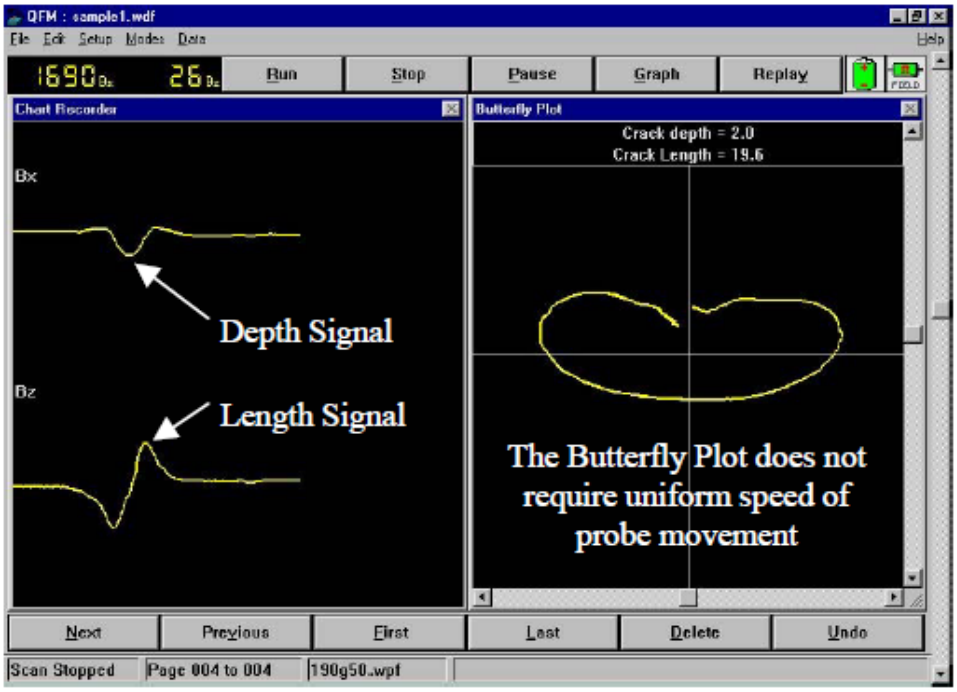

Figure 5.1 shows an image of the ACFM defect indication data screen showing a typical ACFM sensor response to the presence of a defect in the material under inspection (the original of the above image is shown in reference [118] and has been reproduced, presented and appropriately referenced here for the purpose of this PhD thesis).

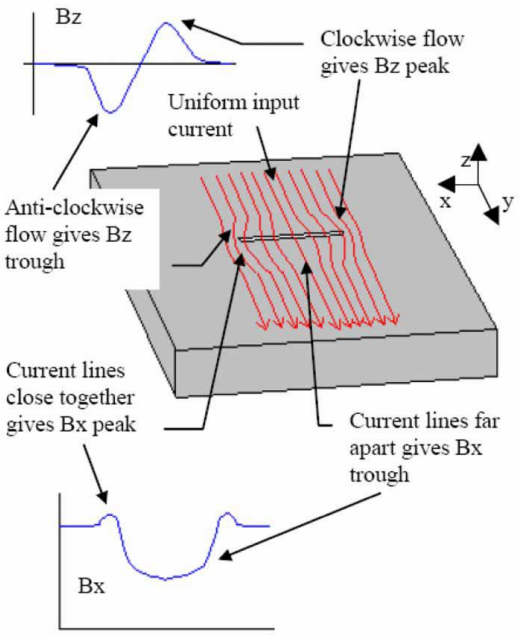

Figure 5.2 shows the different components of the current induced by the ACFM into the material under inspection flowing around the defect including field direction definitions and co-ordinate system (the original of the above schematic diagram is shown in reference [118] and has been reproduced and appropriately referenced here for the purpose of this PhD thesis).

5.3.2 FINITE ELEMENT ANALYSIS (FEA) MODELLING OF ACFM SENSOR RESPONSE TO IDEAL AND REAL RCF CRACKS FOUND IN RAILWAY WHEELS AND TRACK

Previous work reported in the literature by Nicholson et.al. [148] has investigated the relationship between the ACFM signal and RCF defects in rails and rail wheels employing a finite element analysis (FEA) method. The current Amigo software accompanying the ACFM system uses the estimates derived from the theory of regular cracks. Furthermore, in the case of the commercial walking stick ACFM system which is currently being widely used on the rail network has been fed with empirical corrections from the available experimental data that has been provided by destructive tests on RCF cracks, but it should be noted that this has only been done for crack pocket lengths that are greater than 4 mm. However, recent work reported in the literature has been carried out using COMSOL Multiphysics software in order to develop a finite element method (FEM) model to model the response of the ACFM sensor to both idealised artificial and actual cracks in rail and rail wheels [132, 148]. It is reported by these authors in their work that the model allows for both irregular types of cracks catering for a broad spectrum of shapes and sizes (i.e. crack pocket

and surface lengths) including cracks which might overlap each other to be accurately assessed. Their study also focused on making comparisons between idealised elliptical shaped cracks and real RCF crack shapes which are rather of a more complex nature in terms of their shape and size and this was done for light to moderate RCF cracks.

The general principle behind the modelling approach is as follows. A very fine mesh is created around the region of interest which consists of the defect being assessed including a layer above the rail where measurements are to be taken. Thus, in this way, three dimensional modelling of the cracks are carried out in conjunction with applying an impedance boundary condition to the model between the surface of the rail and the air medium. As a result, this assumes that the boundary forms the channel along which the current flows, thus, immensely simplifying both the FEM model and the task of finding solutions to crack shapes of a more complex nature. Due to the very small skin depth in steel at high ACFM operating frequencies the above assumption made is safe to use as any errors that may arise as a result are negligible and, thus, can be ignored. This study has shown good agreement between the experimental results and the results obtained from the FEM model for the elliptical crack shapes presented for the model that approximate the crack shapes for light to moderate RCF cracks. In general, the work conducted by these authors has demonstrated that the ACFM signal response to simplified semi-elliptical crack shapes which represent moderate RCF cracks found in rails in service as provided by the model result in good agreement with experimental ACFM signal response results obtained from actual cracks of similar dimensions.

5.3.3 ACFM FOR DEFECTS

The ACFM technique is a versatile non-contact electromagnetic inspection method for the detection and sizing (length and depth) of defects in structural assets and, as mentioned before, has been successfully employed for this purpose in a wide range of industrial sectors, most notably in the oil and gas industry in air and sub-sea environments but also more recently being developed for applications in the railway industry. The system allows inspection to be carried out at high speed (from a few centimetres per minute to a few metres per minute). ACFM arrays, consisting of various field inducers, are used in order to allow a field to be introduced within the inspected surface in different orientations. This is particularly useful in situations

where the crack orientation is unknown or variable. In this case, additional sensors are also incorporated in order to take full advantage of the additional input field directions.

The ACFM technique including the electromagnetic field modelling which is required for the quantification of the size of cracks was developed at UCL in the 1980s [40,41]. At present, the modelling is restricted to regularly shaped (including semi-elliptical) cracks, however, as a result of a series of recent destructive tests conducted on worn rail, empirical corrections to the sizing models have been incorporated into an ACFM walking stick for use on the UK rail network [38,43]. However, to my knowledge, no relationship has been reported in the literature between the ACFM signal and rail RCF crack size. This is due to the complex shape of cracks. Furthermore, cracks of pocket depth less than 4 mm were not apparently included in the study [40]. The requirements are four input parameters; the probe lift off, the x-component of the background magnetic field (B_{x0}), the minimum value of the x-component of the magnetic field, B_{Xmin}, and the linear distance between the minimum and maximum values of the z-component of the magnetic field B_{zd}. B_{zd} and $\delta B_{xmax}/B_{x0}$ are used to calculate a depth estimate for a given lift off, where: $B_{xmax} = B_{x0} - B_{xmin}$. The ACFM probe provides measurements with analogue to digital conversion (ADC) units, while the model reports results in SI units. Since $\delta B_{xmax}/B_{x0}$ is a dimensionless ratio and B_{zd} is independent of signal amplitude, a normalisation of the B_x and B_z data may be performed to allow a comparison of the experimental and theoretical results.

The three main electromagnetic (EM) NDE systems that are currently in use and under constant development are: MFL, PEC and ACFM. MFL and PEC have been used as vehicle mounted systems for rail inspection and all three systems can be used as slow speed manual systems (‘walking stick’ type systems). The performance of MFL deteriorates as the speed is increased beyond 35 km/h, whereas the PEC technique can potentially operate reliably up to a speed of 70 km/h. However, PEC is adversely affected by grinding marks and lift-off variations. All of the electromagnetic NDE techniques are most suited to detect surface defects, however, currently MFL sensors cannot detect cracks <4 mm in size. Nevertheless, the MFL and PEC techniques can detect near-surface internal defects [44], as a result the above

techniques can also be applied to the inspection of surface breaking and near surface rail wheel defects.

5.4 INDUSTRIAL APPLICATIONS FOR THE ACFM TECHNIQUE

5.4.1 ACFM FOR THE RAILWAY INDUSTRY

The ACFM technique has been extensively employed in the railway industry, in particular, to inspect railway track, bogies and wheelsets. The inspection of bogies for possible damage is not too complicated because these structures are welded and, in their case, inspection speeds do not usually present a problem. Former extensive trials on critical assets, such as wheelsets and particularly on axles using the ACFM method has demonstrated that the ACFM system outperforms the MPI technique, not only in terms of PoD but also in the provision of consistent data [134]. As a consequence, ACFM has been extensively employed to detect and size (length and depth) RCF cracks found in rail and rail wheels. Previously, the more non-invasive means of visual inspection and ultrasonic testing in the form of "walking stick" probes were extensively employed to inspect the above railway assets; however, the former provides no information regarding the depth of defects, whereas, the latter is incapable of sizing a critical crack in terms of its depth which is embedded in a cluster of shallow defects that closely surround the critical defect, a situation which is commonly encountered in railway track and railway wheels in-service. Furthermore, as the original ACFM probe was developed for standard fatigue cracks which are in sharp contrast to RCF defects in terms of their morphology this, therefore, means that the theoretical sizing models which were developed in the 1980s for standard types of fatigue cracks are, thus, inappropriate for sizing RCF cracks. Therefore, extensive research work was carried out on actual RCF cracks present in rails using destructive means and the results thus obtained were then compared with other defective rails which showed good agreement between the calibration test results and the results obtained from actual rails [137]. As a result of this work systems incorporating appropriate sizing algorithms were developed, thus, resulting in the manufacture of a "walking stick" ACFM probe comprised of an Amigo ACFM instrument and a portable laptop computer developed by TSC Inspection Systems Ltd. for rail inspection. Work has continued in collaboration with academia and industry in order to develop an ACFM probe for high speed inspection of critical railway assets to be deployed on test trains for this purpose.

5.4.2 AUTOMATED ROBOTIC DEPLOYMENT OF ACFM

Furthermore, automated inspection systems include remotely-operated vehicles (ROVs) for deployment in underwater environments instead of using the services of professional diving personnel [137] and also in top-side applications where using humans would be costly, difficult and hazardous; such applications include the use of robotic systems for the inspection of damage in the linings of storage tanks for waste from nuclear waste [138] and for the detection of defects in the internal walls of coke-drums [139-144] where such walls consist of carbon steel and a layer of cladding made from standard steel which are welded together. Such robots consist of cameras and lasers for initial visual inspection and location of damage on the structure under inspection and then the areas of interest can be inspected for regional damage by the ACFM array probe which is incorporated into the arm of the robotic system. Such probes are designed and developed incorporating an air-coolant system as, for such applications, the probe needs to operate at elevated temperatures close to 100^0 C and, thus, maintain the temperature of the electronics within operable conditions. The current trend of developing systems which are increasingly becoming smaller and faster due to the continued advancement in electronics together with ACFM array probes that get longer and, thus, the development of more complex and sophisticated automated systems for deployment in underwater and top-side environments means that the ACFM system will continually find applications for the inspection damage and, thus, assess the integrity and safety of structural assets in a wide range of industrial sectors.

5.4.3 ACFM FOR THREAD INSPECTION

Other applications of the ACFM technique include the inspection of welded structures, flaw detection in vessels including the inspection of threaded connections in drill-pipe and components; the latter application is usually carried out using MPI or dye-penetrant (for non-magnetic structures), however, employing such techniques is found to be rather problematic in the case of inspecting female box threads and combined with the well-known fact that these systems are prone to miss critical defects in such circumstances and, thus, lead to costly failure [133]. Therefore, in order to counter this problem ACFM was chosen to inspect drill-pipe as it offered an important advantage in contrast to the above techniques in that the ACFM's signal response increases with the depth of the defect and, thus, increasing the PoD of

critical defects. Due to uniform thread geometry background signal changes were found to be small which thus enabled the development of software in order to automate the ACFM system for the purpose of detecting defects in threaded drill-pipe connections and components. Furthermore, the development of ACFM sensor arrays has enabled a probe to be produced which consists of sensors that are present in the root of each thread and, therefore, the ACFM system can inspect the entire thread in a single 360^0 scan [134].

5.4.4 APPLICATIONS FOR OTHER INDUSTRIAL SECTORS

As a result of the proven versatility of ACFM the technique is now being used for a wide range of applications. For example, the technique has been successfully used to inspect the steel structures of roller coasters including the people carrying components and thus resulting in significant cost benefits to theme park owners. Furthermore, the ACFM method has extensively been employed to inspect bridges together with use of abseiling techniques to inspect the more difficult access areas as well as through coatings; the combination of ACFM and abseiling has also been used for the inspection of dockside and other large cranes, providing, once again, additional economic benefits to the industry.

The technique is still being extensively used in the oil and gas industry for petrochemical applications in conjunction with former methods, for example, magnetic particle inspection (MPI), which had been commonly used in the past for such purposes. As a result, the ACFM technique is gaining wide acceptance commercially throughout the world as a versatile NDE inspection method which is capable of reliably detecting and sizing surface defects and provide additional economic and time saving benefits.

CHAPTER 6
ON THE ASSESSMENT OF FAULTY RAILWAY WHEELS REMOVED FROM SERVICE

6.1 INTRODUCTION

The work presented in this chapter investigates the influence of the properties of as manufactured railway wheel material, for example, microstructure and hardness, on the susceptibility of the wheels to rolling contact fatigue damage and wear. These properties are in turn influenced by the manufacturing process, steel composition, and thermal and mechanical loading during operation. As a result, such properties are prone to vary with tread position and depth below the surface of the tread, as is shown in the work presented here on railway wheels removed from service. The stress and conditions at the wheel/rail contact patch, severity of observed RCF damage (such as RCF cracks and plastic flow) and, changes in microstructure and hardness with depth below the tread surface of worn and new (i.e. without visible defects) railway wheels, with different levels of tread surface damage, which were removed from service are investigated and discussed in this chapter. In the next chapter, the results presented in this chapter will be further discussed and correlated to the ACFM signal response to tread position, RCF-type crack size and spacing etc. including the influence of changing background conditions on the ACFM signal response: changes in microstructure and hardness near and below the tread surface and the role of residual stress including parameters related to the ACFM sensor.

To this end three standard high speed railway wheels which were removed from service from modern multiple-unit trains running in the UK with different severity levels of tread damage have thus been investigated. Two of these wheels contain visible defects and are of different levels of wheel tread damage; the wheel with the most severe level of tread damage containing the most visible defects will be referred to in this chapter as HSR1 and the wheel with the least level of tread damage is referred to as HSR2. The former has a history of being removed from service after 144,000 miles after overhaul, requiring tyre turning, and then again after a further 112,000 miles. This wheel was subsequently sectioned at positions of maximum and minimum run-out which are diametrically opposite to each other and the former is

referred to as the more defective tread position (tread B) and the latter as the less defective tread position (tread A) in this work, respectively. The former and latter positions correspond to the flange height maximum and minimum, respectively, thus indicating that the tread wear and damage were at their greatest and least at these points, respectively. The third wheel is a 'new' wheel removed from a similar train without visible RCF cracks and serves as a control for comparison purposes and identified as HSR3. All three railway wheels investigated as part of this PhD project are of the R8T steel grade, however, they have been manufactured by three different manufacturers and supplied in conjunction with Manchester Metropolitan University (MMU) for the purposes of the work carried out on the present PhD project. Images for all three rail wheels investigated have been shown in the previous chapter.

6.2 MATERIALS AND EXPERIMENTAL TECHNIQUES

Photographs for all railway wheels investigated, namely, wheels HSR1, HSR2 and HSR3, including images of their tread surfaces showing clearly the positions where RCF damage is most prominent on these rail wheels, are shown below. As informed by the suppliers of the railway wheels investigated for the purposes of my work on this PhD project, namely, the manufacturers in collaboration with Manchester Metropolitan University (MMU), the removal from service of the HSR1 rail wheel was due to high degree RCF damage present on the surface of the wheel relatively early in the life of the wheel. The HSR2 rail wheel is at the end of its life and, thus, immediately removed. All the railway wheels examined were initially sectioned and then investigated for changes in hardness and microstructure with depth below the surface of the tread.

Optical microscopy was employed, after appropriate sectioning of the material and employing standard mounting and polishing procedures to investigate and characterise the microstructure and the RCF cracks present in the rail wheel tread surface of the worn wheel sections and the new wheel. The sample preparation steps followed for the metallographic procedure include appropriate grinding and then polishing the sample to a micron finish using the appropriate reagents for each stage of the polishing process and, for subsequent microstructural examination, the specimen needs to be etched for appropriate times using Nital solution which can consist of either 2 or 5% Nitric acid in Ethanol; the former concentration has been preferred and

used to lightly etch the surface of the specimen when appropriate as the etching process is slower and thus yields better results in order to reveal the representative morphology (internal microstructure) of the material.

Vickers hardness tests as described in the previous chapter were conducted at regular intervals along the tread surface of the rail wheel segments sectioned at positions maximum and minimum run-out. Micro-hardness measurements, using a MVK-H1 Mitutoyo Hardness Testing Machine with a load of 300, were carried out on the worn wheel at different locations along the tread surface at 1 cm intervals from the non-flange end to determine the hardness values of the material with depth and to correlate the results with the ACFM measurements taken at these locations as presented in chapter 6. In addition, for practical purposes, macro-hardness tests were carried below a depth of 9 mm from the tread surface for all wheels studied.

X-ray tomography (or computed tomography (CT)) in conjunction with the reconstruction of the 2-D image slices obtained from the experiment has been used to generate 3-D visuals of the complex and deep cracks found in the RCF prone regions of the treads for railway wheels HSR1 at the maximum and minimum run-out positions of this wheel and HSR2. Due to the unavailability of a 3-D reconstruction/modelling imaging software for use on this work at the time within the department to be used in conjunction with X-ray tomography, Matlab software in conjunction with NRecon reconstruction software has been initially used to create the 3-D images of the cracks as shown in the results and discussion section (below). In addition to the results provided using this method 3-D images of the cracks observed using X-ray tomography were also generated by using the 2-D image slices showing the cracks at different equidistant depths beneath the tread surface in conjunction with NRecon reconstruction software thus providing multi sections of the cracks and then with careful “hand and eye co-ordination” using a standard drawing package such as found in Microsoft Word these 3-D visuals of the surface breaking cracks were generated; this method provided better shape information for such cracks as the curves of the cracks on each 2-D slice could better be followed with careful hand and eye coordination.

Furthermore, the now well established multi-sectioning in conjunction with optical metallography approach as described in the previous chapter and in the literature [20] has been employed to create 3-D images of the shallow and closely spaced cracks oriented at approximately 60^0 to the circumferential direction of the tread surface near the flange end and also the shallow and closely spaced cracks that are oriented at almost right angles (90^0 +/-5^0) to the circumferential direction found on the surface of the tread at a position of about 3 cm from the non-flange end of this wheel, as shown in the next section. This technique provided better results in terms of crack shapes due to the reasons discussed earlier, i.e. due to the unavailability of 3-D reconstruction software in conjunction with X-ray tomography in the department for use on this project at the time.

These experiments were carried out to determine the size and orientation of propagation of cracks in the worn railway wheels HSR1 and HSR2 and, thus, to compare these results with the actual crack size (length and depth) observations made on the three railway wheels that were investigated with different levels of railway wheel tread RCF damage by utilising optical microscopy.

6.2.1 MATERIALS

6.2.1.1 RAILWAY WHEELS REMOVED FROM SERVICE

The following are descriptions of the materials used for the purposes of the work carried out on this PhD project. Three railway wheels which were removed from service of varying degrees of RCF damage are investigated for the purposes of this work. These wheels were removed from high speed multiple unit trains and are referred throughout the PhD thesis as HSR1, HSR2 and HSR3. Railway wheels HSR1 and HSR2 are worn wheels showing higher and lower levels of railway wheel tread surface damage, respectively; with the former studied further at the maximum and minimum run-out tread positions. Railway wheel HSR3 is a relatively new wheel showing no (or minimal) signs of visible tread surface RCF damage. All three railway wheels were supplied by three different manufacturers through Manchester Metropolitan University (MMU) for the purposes of this PhD project. Due to the present confidentiality agreements between the University of Birmingham and the manufacturers I am not at liberty to currently disclose the identity of the railway

wheel manufacturers and have thus referred to the railway wheels investigated as high-speed railway wheels (HSRWs): HSR1, HSR2 and HSR3.

Figure 6.1 railway wheel HSR1 at the minimum run-out tread position.

Figure 6.2 railway wheel HSR1 at the maximum run-out tread position.

Figure 6.3 photograph of the HSR1 railway wheel tread surface at the maximum and minimum run-out tread position segments A and B, respectively.

Figure 6.4 photograph of the HSR2 railway wheel tread surface showing the two circumferential bands of RCF cracks: first band consists of shallow and fine cracks oriented at approx. 60^0 to the circumferential direction of the tread found near the flange and the second circumferential band of cracks are oriented almost perpendicular (90^0 +/-0.5^0) to the circumferential direction of the tread and are found at approx. 3 cm from the non-flange end of the tread.

Figure 6.5 high magnification photographs of the HSR2 railway wheel tread surface showing the two circumferential band of RCF cracks: first band consists of shallow and fine cracks oriented at approx. 60^0 to the circumferential direction of the tread found near the flange and the second circumferential band of cracks are oriented almost perpendicular (90^0 +/-0.5^0) to the circumferential direction of the tread and are found at approx. 3 cm from the non-flange end of the tread. These two bands of RCF cracks are regions of interest for the 3-D reconstruction of cracks using the multi-sectioning in conjunction with optical metallography approach and ACFM scans across these cracks as presented in chapters 4 and 6, respectively.

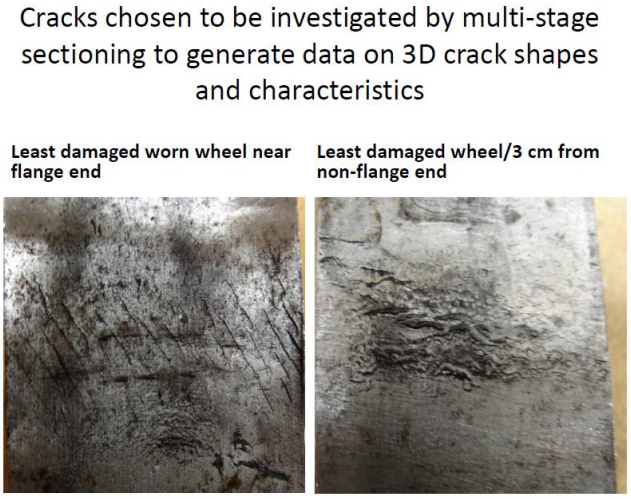

Figure 6.6 another high magnification photographs of the HSR2 railway wheel tread surface showing the two circumferential band of RCF cracks: first band consists of shallow and fine cracks oriented at approx. 60^0 to the circumferential direction of the tread found near the flange and the second circumferential band of cracks are oriented almost perpendicular (90^0 +/-0.5^0) to the circumferential direction of the tread and are found at approx. 3 cm from the non-flange end of the tread. These two bands of RCF cracks are regions of interest for the 3-D reconstruction of cracks using the multi-sectioning in conjunction with optical metallography approach and ACFM scans across these cracks as presented in chapters 4 and 6, respectively.

Figure 6.7 railway wheel HSR3 (wheel without visible defects).

6.2.2 EXPERIMENTAL TECHNIQUES

6.2.2.1 THE MINI-PROFILE TECHNIQUE

The mini-profiling system is employed in the railway industry to determine the condition and dimensions of components; as applied to railway wheels the technique is used to monitor the profiles of railway wheels in cross-section and to determine the flange height, flange width and the diameter of the railway wheel. The mini-prof rail wheel instrument is magnetically attached to the wheel tread on the back of the flange, thus, enabling the measurement and calculation of the above wheel parameters including degree of wear which might have occurred during service. Furthermore, the mini-profiling system is a user-friendly hand-held apparatus. The instrument is currently used to measure mini-profiles for different types of wheels currently employed in locomotives and trams. The system and process is computer controlled and data is automatically stored using a portable laptop computer.

6.2.2.2 OPTICAL METALLOGRAPHY

6.2.2.2.1 SAMPLE PREPARATION

Surfaces of the samples to be examined by optical microscopy were initially cut using a mechanical saw and/or a microtome cutting machine, in both the transverse and longitudinal directions of the railway wheel tread surface for subsequent investigations of the severity of cracks in the various regions of the tread in these directions and changes in the microstructure and hardness with depth below the tread

surface of railway wheels HSR1, HSR2 and HSR3. After the samples are cut to the appropriate dimensions for optical metallography they are then mounted in bakerlite with the surface under examination facing upwards in the mounting instrument. The sample is then ground and polished to a 0.1 micron or, at least, a 1 micron polish finish using appropriate reagents for each stage of the grinding and polishing technique for subsequent investigation of the cracks by optical microscopy. For microstructural examination and thus in order to reveal the microstructure of the material in the transverse and longitudinal sections of the polished sample they are then etched in 2 % or 5 % Nital solution; the former solution etches the sample slower than the latter and is thus preferred.

6.2.2.2.2 OPTICAL MICROSCOPY

The optical microscope remains a fundamental tool for microstructural examination and phase investigation of materials. The standard optical microscope consists of the following components: projector lens, objective lens, specimen holder, condenser lens and the light source. The image is magnified by the light source by passing a beam of light through the object to be examined. Subsequently, the condenser lens focuses the light onto the sample under inspection and then the objective lens can magnify the beam and thus provide different magnifications, for example, 5x, 10x, 20x, 50x and 100x as in the case of the optical microscope employed for the present work; the magnified image is then viewed by the observer via the projector lens. For optimum results the sample needs to be initially carefully prepared for subsequent examination under the microscope as discussed in the previous section.

6.2.2.3 HARDNESS MEASUREMENTS

Vickers hardness tests as described in the previous chapter were conducted at regular intervals along the tread surface of the rail wheel segments sectioned at positions maximum and minimum run-out. Micro-hardness measurements, using a MVK-H1 Mitutoyo Hardness Testing Machine with a load of 300, were carried out on the worn wheel at different locations along the tread surface at 1 cm intervals from the non-flange end to determine the hardness values of the material with depth and to correlate the results with the ACFM measurements taken at these locations as presented in chapter 6. In addition, for practical purposes, macro-hardness tests were carried below a depth of 9 mm from the tread surface for all wheels studied.

6.2.2.4 X-RAY TOMOGRAPHY (OR COMPUTED TOMOGRAPHY (CT))

X-ray tomography (CT) is a computer controlled imaging technique which uses irradiation, usually in the form of X-rays, to produce 3-D representations of the object being scanned and, thus, is an effective non-destructive technique initially designed for medical imaging and now also commonly used in industrial applications in various sections of industry, for example, metallurgy and materials, for the internal inspection of components to determine their state and structural integrity; flaw and failure analysis are some of the areas for which this technique has been applied.

There are two types of CT scanners, namely, cone scanners and fan-line beam scanners [1-3]. The former rotate whereas the latter translate. In the case of the fan-like beam scanners the x-rays are produced and the beam is collimated to create a line. The x-ray line beam is then translated across the part and data is collected by the detector. The data is then reconstructed to create a 3-D volume rendering of the part. However, cone beam scanners rotate [3]. During the CT scan the part is placed on a rotary table. As the part rotates the cone of x-rays produce about 1300 2-D images which are collected by the detector. The 2-D images are then processed to create a 3-D volume rendering of the external and internal geometries of the part.

6.3 RESULTS AND DISCUSSION

6.3.1 MINI-PROFILES FOR THE HSR1, HSR2 AND HSR3, RAILWAY WHEELS REMOVED FROM SERVICE

Prior to carrying out mini-profiles on all the three railway wheels investigated for this work, measurements were initially conducted to assess the flange thickness and flange height of rail wheels HSR1, HSR2 and HSR3, in order to determine their wheel profiles. These measured mini-profiles were then compared to a P8 railway wheel profile which was supplied by the Rail Technology Unit (RTU), Manchester Metropolitan University (MMU), to serve as a comparison for the mini-profile measurements carried out on railway wheels HSR1, HSR2 and HSR3, for the purposes of this PhD project as shown in figures 6.8 and 6.9. The flange thickness and flange height for rail wheel HSR1 are 27 mm and 26 mm, respectively, and the flange thickness and flange height for rail wheel HSR3 are 32 mm and 31 mm, respectively. This information indicated that the worn rail wheels HSR1 and HSR2 are P8 rail wheel profiles, however, the flange thickness and height measurements for the new

rail wheel HSR3, or the wheel without visible defects which was chosen to serve as a control for this work, were slightly higher than for the former worn rail wheels and, thus, it was deduced from this result that wheel HSR3 is most probably to be a P10 profile. Following this min-profile measurements were carried out on all three rail wheels; the min-profiles of the worn wheels HSR1 and HSR2 have been superimposed upon a new P8 profile and shown in figures 6.8 and 6.9, respectively, to determine the amount of wear on each wheel which has taken place during its lifetime and, as will be seen in the section on hardness below, these results are in agreement with the hardness contour maps shown for these rail wheels below. However, as a profile for a P10 railway wheel was not available it was not possible to overlay the mini-profile obtained for the HSR3 new rail wheel over a new P10 rail wheel profile; nevertheless, the hardness contour map along the tread obtained for this wheel in conjunction with the level of RCF damage observed on the tread surface of the wheel agree well with the mini-profile and suggest that not much wear has occurred on the surface of this wheel as compared with the worn rail wheels HSR1 and HSR2. To this end, the mini-profile data should be aligned to the flange back, as this shows no significant change with use. Thus, overlaying the mini-profile data from the HSR1 and HSR2 rail wheels with a P8 profile has shown that the greatest degree of wear on the tread surface has occurred for wheel HSR1 at the position of maximum run-out, followed by wheel HSR2 and then HSR1 at the position of minimum run-out and these results agree with the hardness gradient contour maps for these rail wheels in figures 6.21 and 6.22 (below). The reason for the higher hardness values for the maximum run-out position compared with the minimum run-out position of wheel HSR1 is as a result of the greater unevenness of the former tread position and thus its greater out-of-roundness (OOR) which means that higher forces and thus stresses are imposed on the wheel tread at the position of maximum run-out which is clearly shown by the hardness contour maps for these tread positions. However, observations made of the surfaces of all wheels investigated do not show evidence of wear having occurred and/or rail contact in the flange tip region.

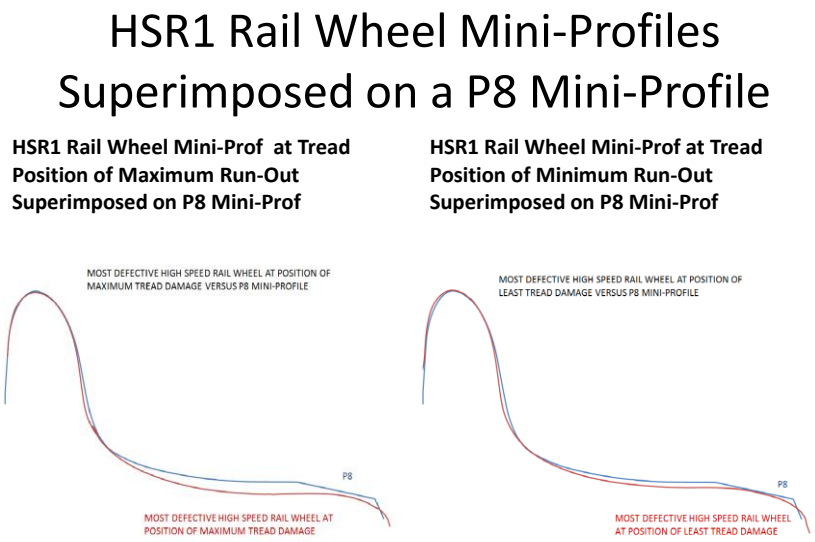

Figure 6.8 shows the mini-profile for the HSR1 rail wheel segments at the position of maximum and minimum tread damage, i.e. maximum and minimum run-out, respectively, in comparison to the mini-profile for a new P8 rail wheel.

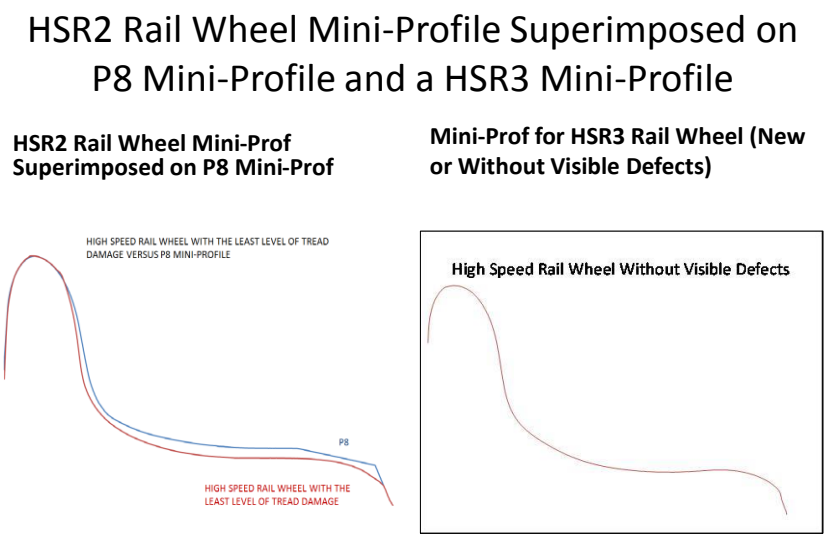

Figure 6.9 shows the mini-profile for the HSR2 rail wheel in comparison to the mini-profile for a new P8 rail wheel. The figure also shows the mini-profile for the new HSR3 rail wheel without visible defects.

6.3.2 RCF-TYPE CRACKS OBSERVED IN RAILWAY WHEELS REMOVED FROM SERVICE

6.3.2.1 RCF CRACKS OBSERVED IN WORN AND NEW (I.E. WITHOUT VISIBLE DEFECTS) RAILWAY WHEELS

Observations of all three railway wheels investigated show that all wheels have a degree of RCF damage in the field side region as is commonly found in this region of the wheel tread in railway wheels from similar fleets [9]. Furthermore, two of the rail wheels studied, namely, rail wheels HSR1 and HSR2, show a degree of shallower RCF cracks present near the flange, specifically, in the flange root region of these rail wheels.

Initial work has focused on the assessment of the severity of the defects on the railway wheels removed from service at positions maximum and minimum run-out corresponding to locations of maximum and minimum tread damage, respectively. Observations of the surface breaking RCF cracks and the microstructure of the wheels were carried out using an optical microscope after employing appropriate sample preparation techniques for metallography as described in the previous chapter. Table 6.1 shows the measured values for the different crack parameters, for example, crack surface length and depth including angles of propagation relative to tread surface of the worn wheel at positions of maximum and minimum run-out. Observations made on the orientation of RCF type cracks on the three railway wheels investigated including measurements carried out on their dimensions and propagation angles into the material including the degree and position of the cracks and crack clusters along the tread reveal the following.

Considering the symmetrical nature of the positioning of the wheels on a bogie then, as a result, the rail wheel tread surface damage on the worn rail wheels HSR1 and HSR2 show a symmetric presentation of RCF defects on these wheels, as would be expected. The most common presentation of RCF defects are typically at surface angles of 45° in the circumferential direction (or circumferential orientation) wheel tread, however, such cracks can occur at between 30-60°. Many cracks will appear curved, with a more transverse appearance closer to the running line which occurs at 70 mm from the back of the flange and more circumferential closer to the edge of the

rail wheel (or non-flange end) and this can yield surface crack angles between 0–90° in the circumferential direction.

Sections through the wheel tread have been taken and the depth of damage has been assessed. This study has found cracks propagating to a greater depth in the samples from the tread sections of the HSR1 rail wheel removed from service, which I have prepared and examined for this PhD project that has been previously reported in a private communication from Manchester Metropolitan University (MMU) [181,182]. The cracks present on the tread at the position of minimum run-out are shallow with a mean max. depth of approx. 1.5 mm from the surface (figure 6.11) whilst the cracks at the tread position of maximum run-out where the level of damage is at its highest for this wheel the cracks were much deeper with a mean maximum depth of approximately 5.5 mm and appeared to be unconnected with the surface in this plane with a propagation direction that was difficult to ascertain (figure 6.10).

In this work examining the same samples the cracks have been observed on metallographically prepared ground and polished samples. The depth and severity of damage has been investigated and the observed crack depth at the position of maximum run-out (figure 6.10), have a maximum mean depth of approximately 5.5 mm, whilst at the diametrically opposite minimum run-out position on the wheel (figure 6.11), they have a maximum depth of approximately 1.5 mm. Thus, optical metallography provides good resolution which enables deep cracks to be seen.

Observations made on HSR1 wheel tread segments A and B show that RCF cracks are present on the tread around the entire circumference of the wheel in a region generally between 30 and 65 mm from the rim face. Cracks present at the position of minimum run-out (tread segment A) are closely spaced and oriented at an angle of approximately 50.6^0 to the wheel axis; some shelling has occurred. However, at the position of maximum run-out (tread segment B) there was no obvious orientation to the cracking, but similar to the position of minimum run-out, some shelling had occurred. In addition, many ‘tongues’ of deformed surface material are observed. Sectioning of the wheel through the rim at positions of maximum and minimum run-out showed that the tread at the former position was slightly hollow, which is indicative of wear at this position, compared to that at the latter position.

Observations of the tread damage on rail wheel HSR2 show a significantly lower concentration of RCF-type cracks on the surface as compared to the HSR1 worn rail wheel where the damage is much greater. Furthermore, the crack spacing is greater than the crack depth in the former wheel as shown in figures 6.14 and 6.15. The reasons underlying this phenomena needs to be investigated further and is beyond the remit and scope of the current PhD project and, thus, is a suggestion for work to be undertaken in the future.

Thus observations made on the HSR2 rail wheel have revealed two distinct bands of cracks, but which present with different angles of orientation on the surface of the wheel as shown in section 6.2.1.1 above. The band of cracks which develop in tightly spaced clusters that is located near the flange end consists of cracks which grow at a wheel surface angle of approximately 60° and have a surface length of several millimetres and a crack spacing of about 2-3 mm, whereas, the cluster of cracks that are found in the second band near the non-flange end are much smaller in size and grow a few millimetres in surface length at most with a crack spacing that is much smaller than the former band of cracks of about 1 mm or less occurring within a rough band and at an approximate surface angle of 90° +/-5^0. These cracks can present with the same surface angle with respect to the circumferential orientation. However they can propagate into the wheel in opposite directions as shown in figures 6.14 and 6.15. The former figure shows an optical micrograph taken of such a crack in the transverse direction of the tread found near the flange end of wheel HSR2 propagating at an approximate angle of 45^0 into the material to the vertical in relation to the tread surface; these cracks grow towards the flange end of the rail wheel with an approximate tread surface angle of orientation on of 60^0 with respect to the circumferential direction of the wheel. The latter optical exposure again taken in the transverse tread direction shows a similar crack found in the other band near the non-flange end of the rail wheel propagating in the opposite direction at the same propagation angle of approximately 45^0 to the vertical.

In general, toward the end of the lifetime of a rail wheel the rate of growth of RCF-type cracks can be twice the normal rate, for example, when the wheel has been turned and thus the diameter has subsequently been reduced by approximately 10 % of its original diameter. Typically, lifetime of a railway wheel is 4 years; this is based

on a running distance of 140,000 miles between each complete turning activity per year.

Results obtained from the HSR2 rail wheel show that after the first 140,000 miles RCF cracks of approximately 1 mm depth had formed (see figures 6.14 and 6.15 below). These shallow but closely spaced cracks (spaced approximately 2-3 mm apart) and extending for several millimetres in surface length oriented at a surface angle of approximately 60^0 along the circumference of this worn rail wheel near the flange end in the flange root region of the wheel are indicative of fine surface breaking RCF-type cracks usually found in worn rail wheels in the flange root region of the tread. These cracks are likely due to the leading wheel coming into contact with the outer rail on moderate and sharp curves [2]. Furthermore, as the flange root is normally not lubricated this can result in significantly high normal tangential stresses being imposed in this area of the rail wheel tread. As shown by this work, these fine closely spaced clusters of cracks do not tend to propagate deep into the material; this effect is most probably the result of the specific direction of the tangential forces in this area not promoting the propagation of these cracks further into the material by fluid entrapment [3]. Also, at the running line of all the wheels studied which lies in the running region of the wheel tread and is about 70 mm from the back of the rail wheel for all wheels investigated the trailing wheelset is made to contact the rail in this region on curves. Consequently, many wheel cycles occur with relatively low or moderate stresses imposed on the wheel. The tangential forces and, thus, stresses which result are relatively low due to traction and/or breaking and this means that the peak stress occurs below the surface of the tread. This might be the reason why one does not see many cracks on the surface of this region of the tread near this “70 mm running line” as observed on the HSR1 and HSR2 wheels by visual inspection, but some light level of wear is seen here; however, as will be shown in chapter 6 the ACFM sensor does register signals from cracks near this area which would suggest the possibility of the existence of cracks below the tread surface here. It is reported in the literature that in contrast to the other regions of the tread the running band experiences a similar number of stress cycles in each rolling direction [2]. Observations conducted in this region on the rail wheels studied indicate that the surface damage in this area of the tread is usually due to wear. In the region of the treads of the worn wheels where RCF damage is most prominent, referred to as the

RCF band, which as observed in wheels HSR1 and HSR2 to extend from the central region of the tread to the field side, the results show an increase in surface hardness (see section 6.3.3 below) and the presence and concentration of a greater number of surface breaking and deeper RCF cracks (see figures 6.1-6.4 incl.). This is caused by the leading wheel contacting the inner rail on curves whilst simultaneously the opposite wheel makes direct contact with either the flange face or the route of the flange. Thus, under these conditions the frequency of contacts made are considerably less, nevertheless, the stresses are much higher and, thus, results in higher material hardness and an increase in the level of surface damage, as observed in these worn rail wheels, as well as an increase in the concentration and severity of RCF-type cracks present in this region of the wheel tread. Furthermore, as seen from this work, cracks in this region can be angled as observed in the HSR1 rail wheel, however, the cracks can also be oriented almost circumferentially, i.e. close to 90^0 along the running direction, as observed in wheel HSR2 due to the occurrence and influence of traction forces.

As initially informed by Manchester Metropolitan University (MMU) when the three rail way wheels were initially supplied for the purposes of my work on the PhD project 2.5 mm of the rail wheel tread from HSR2 was removed on turning in order to restore the required rail wheel profile. Thus, it has been seen from this work that for the same mileage significantly more RCF crack growth occurs towards end of life. Explanations of why this might occur including factors that may influence this are as follows. Higher contact stresses may result due to a decrease in the diameter of the rail wheel by 10 %. Furthermore, a 10% loss in the diameter of the rail wheel and a rail wheel mileage of 140,000 miles would result in more wheel revolutions due to the significant reduction in the circumference of the rail wheel. Also, the braking / anti-stick would consequently become less effective for the worn rail wheel than for a new wheel diameter for which it was originally designed. Changes in microstructure with depth below the tread might also be a significant factor to consider in this regard. In addition, higher rail wheel tread surface hardness may be the result of forging process. As a result, this might induce differences in prior austenite grain size due to, for example, variations in strain and temperature during forging. Furthermore, the balance in the resultant wear and RCF damage of the rail wheel would be affected by the pro-

eutectoid (PE) ferrite content including the pearlite lamellar spacing and the types of inclusions in the microstructure of the rail wheel material.

The new HSR3 rail wheel hardness contours appear to suggest that contact due to both left hand and right hand cornering has been seen as indicated by the higher hardness values near the tread surface of this wheel close to the flange and non-flange ends. It is found that the smaller the wheel (i.e. smaller diameter) the greater the contact stress, thus, RCF is found to be more severe when the wheel diameter is smaller. Possible reasons for this might include the following: (i) grain size variation, (ii) pearlite spacing variation, (iii) inclusions. All these factors affect RCF growth and wear rate. Systematic cracks are found on the treads of worn railway wheels in service both on the front and rear bogies as observed on the treads of railway wheels HSR1 and HSR2 in this work. These RCF-type cracks are found close to the field side of the wheel and mirror images of these cracks are present at each end of the wheel tread; these cracks are also observed around the circumference of the railway wheel. Observations made on the treads of the worn wheels HSR1 and HSR2 also reveal that, in general, such cracks are found to be oriented more transverse relative to the circumferential direction.

There are three stages that are involved in the process of initiation and growth of fatigue cracks in rail and rail wheels as follows. During the first stage of the process extremely high levels of plastic deformation (i.e. plastic flow) that occurs at and near the surface of the material results in the initiation of cracks. The plastic flow results in the hardening of the surface of the material and, thus, makes the material's surface in this region brittle; thus, leading to ratcheting of particles that may eventually become separated. As a result, voids are created in between these particles, thus, making the actual contact area significantly smaller than the theoretical elliptical elliptic area given by Hertz theory. Due to this the contact tresses will further be accentuated, thus, leading to further detachment of particles. At a later stage the particles that remain due to the fact that they are hard to wear out, subsequently, act as additional nuclei for crack initiation. Furthermore, as the crack grows and, thus, deepens within the material the initial high crack growth rate is attenuated rather rapidly. In the case of rails, and it is a similar scenario in the case of railway wheels, such cracks are inclined at a shallow angle of about 15^0 to the rail head and are oriented in the same direction

as the wheel motion. As a result, the extremely high levels of plastic strains which are experienced by the material in this region result in local changes to the microstructure of the material. During the second stage of the process the stress field that is produced by the wheel-rail contact ensures the continued propagation of cracks in the same direction of inclination. Furthermore, the reverse shear stresses that cause crack growth initially increase rapidly with depth, thus, accelerating crack growth, however, subsequently, as the crack grows and, thus, the distance from the contact area increases the reverse shear stresses then decrease, thus, eventually slowing down the process of crack growth. The influence of the contact stress field typically extends to a depth of about 10-15 mm below the surface of the material. In addition, the plastic flow that occurs beneath the surface of the material due to the effects of contact stresses and stresses that are locked within the material as a result of the occurrence of plastic deformation; surface cracking including in the case of rails the prevalence of shear stresses in the rail head results in metallurgical changes in the material due to the prevalence of inclusions within the material. Furthermore, during the third stage of the process, upward or downward branching of cracks can occur due to the influence of bulk and residual stresses in the material. The upward branching of cracks results in part of the surface of the material becoming detached due to the occurrence of material flakes. Whereas, branching in the downward direction that normally occurs in rails at about 70^0 at an orientation direction of about 70^0 to the horizontal surface can lead to a dangerous critical fracture of the material. Therefore, crack growth rates are initially high and then somewhat decrease followed by "handshaking" with increased growth rates that are prevalent during the second stage of the process described above and finally "handshaking" again with the third stage of the process. However, it should be noted that the handshake that occurs between each stage of the process is not an automatic occurrence and, thus, the arrest of cracks crack propagation may be stopped at any stage of the process if the conditions permit that to happen. Thus, it is not inevitable that every crack may lead to the failure of the material. Furthermore, fatigue and wear play an important part in this process because if the wear rate is high at the surface of the material then cracks will not have the time to form as any cracks that are initiated or present will be immediately worn away as the wear rate will be significantly higher than the rate of crack formation. The arrest of cracks is possible if the handshake growth rate between each of the three stages as discussed above is lower than the rate of wear of the material [171].

Furthermore, previous extensive studies on fatigue damage in rails caused by rolling contact fatigue have revealed the following as reported in [209]. RCF damage due to bodies in contact can cause damage to the railway wheel and track in different ways depending upon the severity of the contact pressure and the magnitude of the shear forces that act within the contact patch area where the wheel and rail are in contact with each other. For most trains that operate in Britain this contact area is small and of the order of a five pence coin. The forces which are produced and thus act between the wheel and rail in this contact patch during the motion of the vehicle over the track and that ultimately lead to RCF damage are characteristic of the behaviour in this contact patch. Damage due to RCF occurs in the form of surface cracks as a result of rail wear, or through plastic flow of the material. Initially, RCF results in the formation of short cracks that grow at a shallow angle which can suddenly turndown, i.e. sometimes grow by changing from a shallow to a steep angle. In rails it is generally found that such a turndown occurs when cracks are of the order of 30 mm in surface length, at which stage the probability of rail fracture is considerably increased. Extensive investigations that have been carried out over the years in the field have revealed at least three separate modes of RCF initiation and growth, namely, steady state, bi-stable and convergent motion. These three RCF modes that are postulated in the literature [209] are described as follows. The bi-stable contact mode is believed to occur in curves with radii of the order of 1200 to 2000 m, although the same behaviour might occur on tighter or shallower curves. This mode describes RCF damage that occurs in the event that the wheel-rail interface operates in a region of instability in which small changes in lateral displacement in the wheels result in large changes in the rolling radius. The convergent motion mode is used to describe RCF damage that occurs when the railway track appears to slip sideways relative to the wheel as a direct consequence of changes in alignment and, therefore, the wheel flange is made to converge upon the gauge face of the rail even though the wheel flange may not come into contact with the gauge face. This mode of behaviour is thought to occur in moderate curves of radii in the region of 21000 m or more and also in straight track. However, it is also possible that this type of behaviour might occur on tighter curves where one would normally expect the bi-stable mode of RCF damage to occur. Furthermore, investigations have revealed that this mode is probably the primary cause of rolling contact fatigue in railway track except for plain track and switches and crossings (S&C). However, curving forces due to the steady state mode

are the probable cause of RCF related damage on the gauge corner of the tight radius area of switch blades. Furthermore, it is believed that the convergent motion mode is the most likely cause of fatigue damage for railway track components at switch entry and trailing points, switch transitions, at crossings and closure rails. Furthermore, it is generally understood that across the railway system network in the United Kingdom, rolling contact fatigue damage is caused by the prevalence of excess wheel-rail forces at the wheel-rail contact area. These forces are due to the relatively large displacement of the axle in relation to either side of the rail. This state of affairs is the same in the case for curves, straight railway track or at switches and crossings. The mechanism tends to be dominated by the steady-state mode in tight curves, whereas, the mechanism is transient in moderate curves, switches and crossings and straight railway track. Extensive research conducted by the British railway industry has demonstrated that the main factors which govern the initiation and growth of rolling contact fatigue are: wheel wear, track alignment and, bogie and yaw stiffness; the latter is the horizontal rotational stiffness between axles on a bogie.

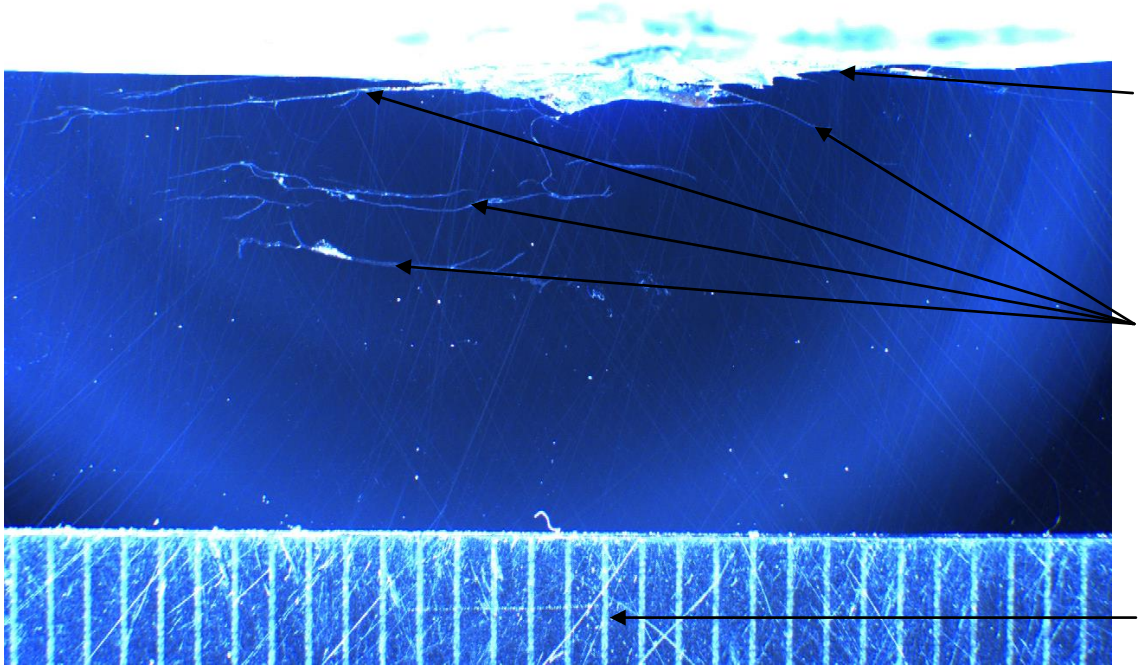

Figure 6.10 Image of as-polished sectioned HSR1 wheel sample showing sub-surface cracking in the railway wheel HSR1 at the position of maximum run-out.

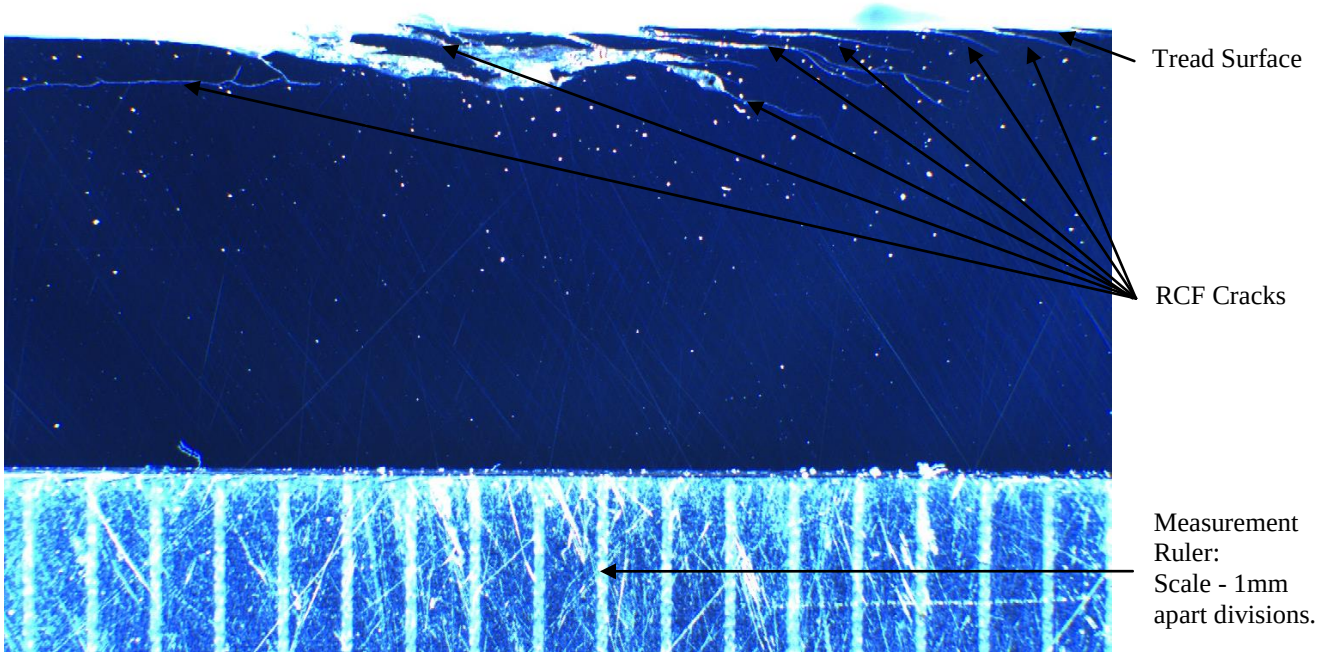

Figure 6.11 Image of as-polished sectioned HSR1 wheel sample showing sub-surface cracking in the railway wheel HSR1 at the position of minimum run-out.

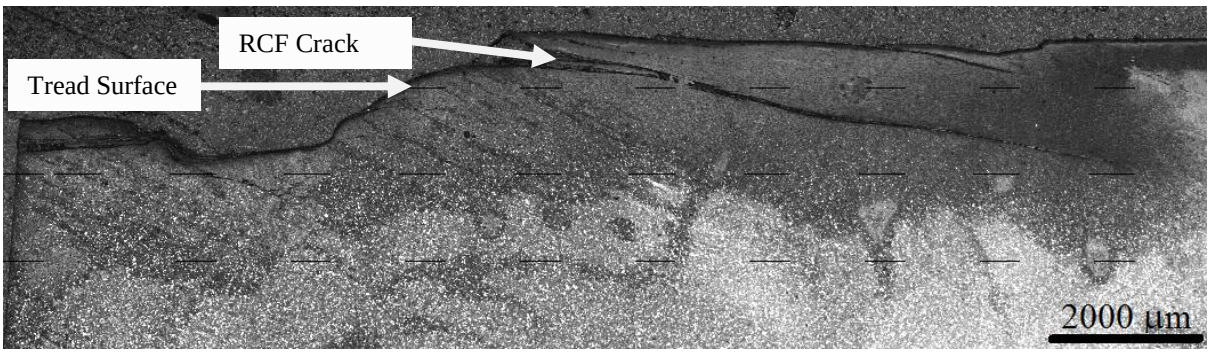

Figure 6.12 A montague of optical micrographs from an etched sample of HSR1 wheel showing sub-surface cracking at position of maximum run-out.

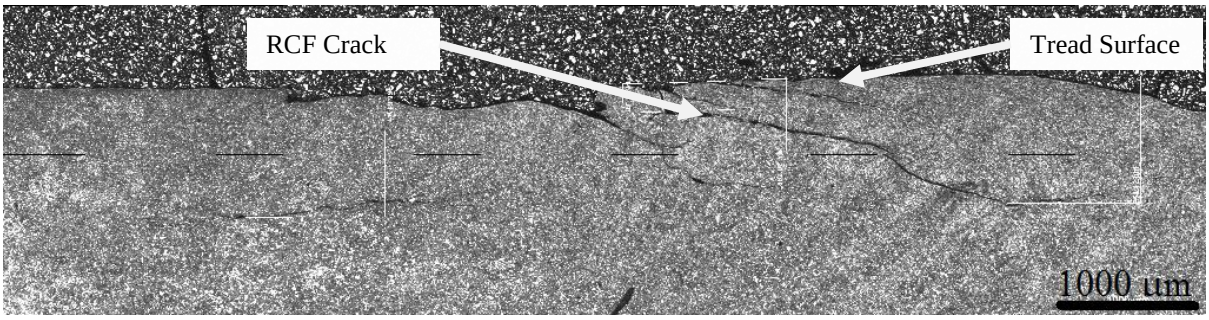

Figure 6.13 A montague of optical micrographs from an etched HSR1 wheel sample showing sub-surface cracking at position of minimum run-out.

Table 6.1 shows rolling contact fatigue crack dimensions including angles of propagation relative to tread surface for HSR1 wheel at positions of maximum and minimum run-out.

Parameter	Tread surface position of maximum run-out	Tread surface position of minimum run-out
Surface length	Mean 5.4 mm, Max. 11.3 mm Standard deviation 3.5 mm Variance 12.2	Mean 2.3 mm, Max. 5.4 mm Standard deviation 1.8 mm Variance 3.2
Mean Max. depth	5.5 mm	1.5 mm
Angle of propagation	Mean 14.3^0, Min. 3.5^0, Max. 60.0^0 Standard deviation 17.3^0	Mean 15.9^0, Min. 3.0^0, Max. 68.0^0 Standard deviation 17.4^0
Angle of RCF defects to wheel circumference	Mean 50.6^0, Min. 43.0^0, Max. 55.0^0	Mean 38.5^0, Min. 33.0^0, Max. 46.0^0

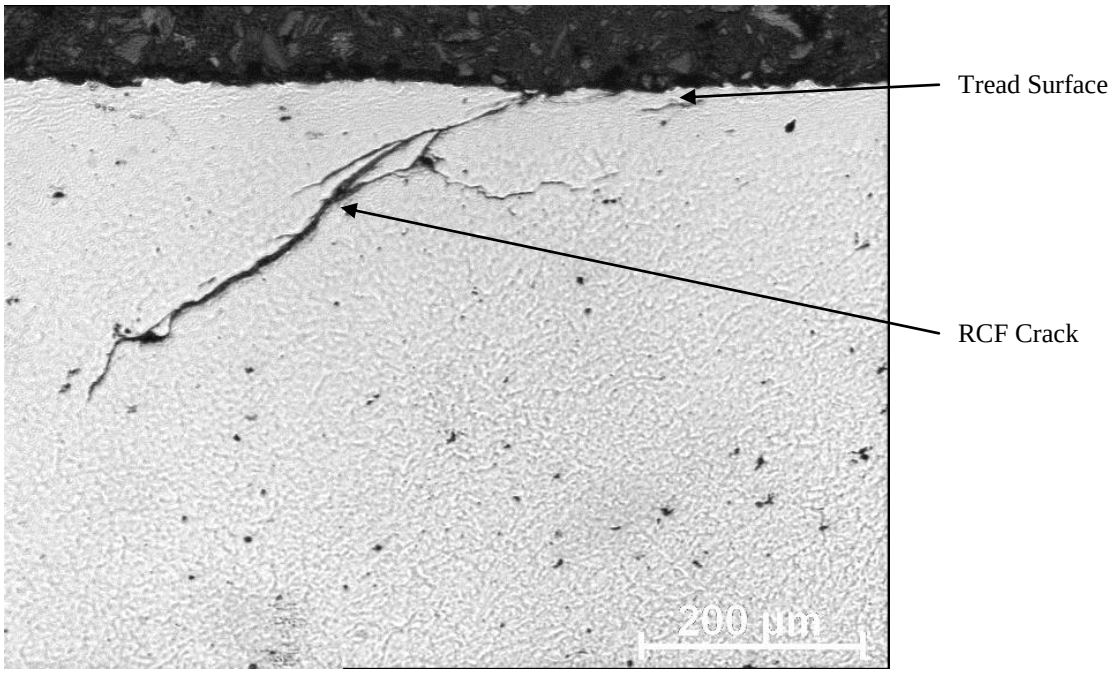

Figure 6.14 shows fine crack near flange end of HSR2 rail wheel. These cracks grow at an angle of approximately 45^0 to the tread surface into the material and towards the flange end of the wheel. Their orientation on the tread surface is about 60^0 with respect to the circumferential line.

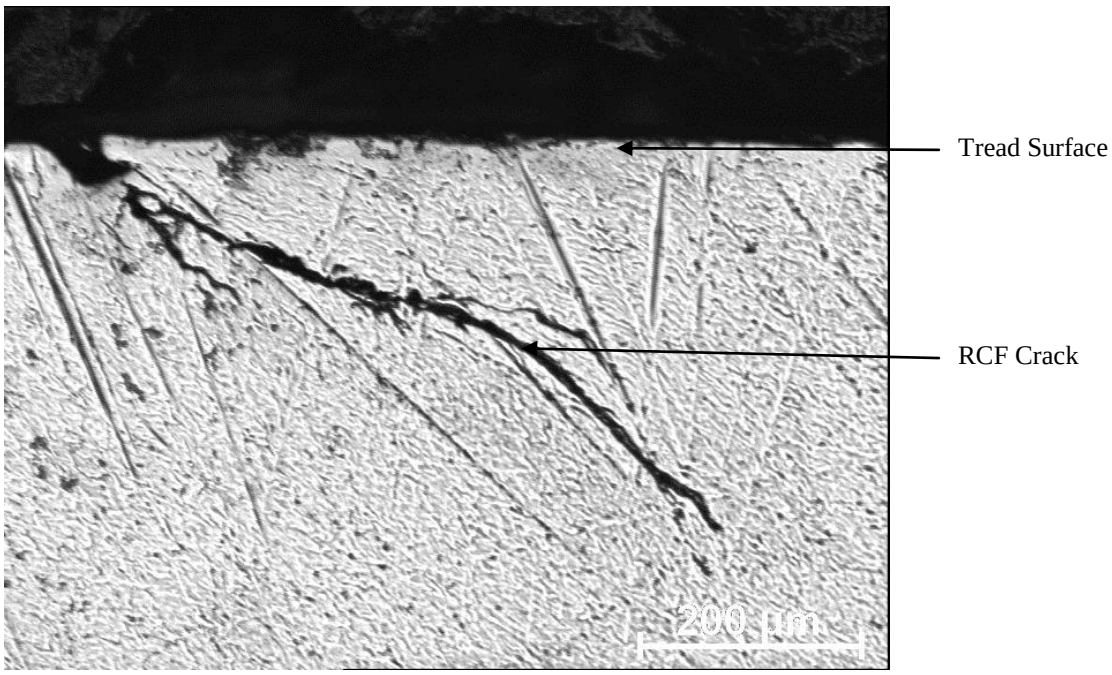

Figure 6.15 shows a crack at about 3 cm from the non-flange end of the HSR2 rail wheel (note: this crack is at the position on the tread surface as the closely spaced fine cracks at 90^0 on the tread surface which run across the entire circumferential length of the rail wheel). These cracks grow at an angle of about 45^0 to the tread surface into the material and towards the non-flange end of the wheel.

6.3.2.2 3-D REPRESENTATION OF RCF-TYPE CRACKS OBSERVED IN RAILWAY WHEELS REMOVED FROM SERVICE

X-ray tomography (or computed tomography (CT)) in conjunction with the reconstruction of the 2-D image slices obtained from the experiment has been used to generate 3-D visuals of the complex and deep cracks found in the RCF prone regions of the treads for railway wheels HSR1 at the maximum and minimum run-out positions of this wheel. However, due to the unavailability of 3-D modelling and imaging software within the department for this purposes of the work on this PhD project, Matlab software in conjunction with NRecon reconstruction software has been initially used to create the 3-D images of the cracks as shown in the results and discussion section (below), this provided reasonably good estimates for crack sizes (length and depth), that agree with the results obtained using optical microscopy, and reasonably representative shapes for these complex cracks. In addition to the results provided using this method 3-D images of the cracks observed using X-ray tomography were also generated by using the 2-D image slices showing the cracks at different equidistant depths beneath the tread surface in conjunction with NRecon reconstruction software and creating multi sections of the cracks and then with careful "hand and eye co-ordination" using a standard drawing package such as found in

Microsoft Word these 3-D visuals of the surface breaking cracks were created; this method provided better image and shape information for such cracks and these results are also shown below.

However, due to the unavailability of a 3-D reconstruction/modelling imaging software to be used in conjunction with X-ray tomography on this work at the time within the department the multi-sectioning in conjunction with optical metallography approach was used for the purposes of generating 3-D crack shapes found in the tread of worn wheel HSR2. Therefore, the well-established multi-sectioning in conjunction with optical metallography approach has been employed to create 3-D images of the shallow and closely spaced cracks oriented at approximately 60^0 to the circumferential direction of the tread surface near the flange end and also the shallow and closely spaced cracks that are oriented at almost right angles (90^0 +/-5^0) to the circumferential direction found on the surface of the tread at a position of about 3 cm from the non-flange end of this wheel, as shown in the next section. This technique provided better results in terms of crack shapes due to the reasons discussed earlier, i.e. due to the unavailability of 3-D reconstruction software in conjunction with X-ray tomography in the department for use on this project at the time. These experiments were carried out to determine the size and orientation of propagation of cracks in the worn railway wheels HSR1 and HSR2 and, thus, to compare these results with the actual crack size (length and depth) observations made on the all three railway wheels investigated with different levels of rail tread RCF damage by utilising optical microscopy. Furthermore, these results will also be compared to the crack sizes estimated using the ACFM sensor on the worn wheels in chapter 6 where the sensitivity of the ACFM technique operating at 5 and 50 kHz to detect and accurately size defects found in railway wheels in service is analysed and discussed. Furthermore, previous studies [148] have also used X-ray tomography (i.e. computed tomography) as a complementary and an effective technique for the quantification of reconstructed RCF cracks and thus using the data obtained from the CT technique to determine the size and morphological shape of actual RCF cracks.

The results obtained by X-ray tomography in terms of crack shape, size and orientation, are compared with the results from observations made using optical microscopy. Three-dimensional modelling of these reconstructed images for the X-ray

tomography (CT) scan provides information on the shape of these RCF cracks. Figure 6.16 shows a reconstructed image from the CT scan on the more defective sample at the position of maximum run-out on the tread showing two distinct cracks, labelled A and B, that extend downwards into the material from the tread surface. Cracks A and B propagate at shallow angles of 17^0 and 10^0, respectively, that gives a mean value of about 14^0, which is in agreement with the observed mean value for the propagation angle of these cracks as obtained by optical metallography for this tread position on the worn wheel. Furthermore, the measured average maximum surface lengths and depths of cracks A and B as determined from X-ray tomography experiments (figure 4.9) are as follows. The estimated average maximum surface length and depth of cracks A are 15 mm and 12 mm, respectively, and for crack B the estimated average maximum surface length and depth are 1 mm and 2 mm, respectively; these results are in close agreement with measurements made by optical microscopy, thus, demonstrating that the X-ray tomography (CT) technique is a viable procedure to use in non-destructively testing railway wheels and components for defect detection and sizing, complementing other techniques used for this purpose as shown by the work presented here. Figure 6.17 shows further reconstructed 3-D images of cracks found on the tread of wheel HSR1 at the maximum run-out position using the X-ray tomography technique; these are significantly deep cracks with complex geometries in line with RCF-type crack geometries in other similar steel railway line and wheel material as reported in the literature [20].

Figure 6.18 shows a schematic (not drawn to scale) of the 3-D crack shape for the crack seen in the 2-D image slice obtained from the X-ray tomography experiment in the RCF region of the railway wheel HSR1 at the maximum run-out position on the tread. The figure clearly the complex shape of the crack, however, an outline of the semi-elliptical nature of the RCF crack can be seen from the above image. Figure 6.18 also shows one of the 2-D image slices used to construct the schematic of the crack, namely, the image slice identified as frame 8 shown here as well as shown together with the other 2-D image scans in the relevant appendix section in the Appendices chapter at the end of the PhD thesis, where the crack is at its greatest depth of 11.2 mm obtained from the X-ray tomography experiment in the RCF region of the railway wheel HSR1 at the maximum run-out position on the tread. Figure 6.19 shows a schematic drawing of typical shallow and closely spaced cracks that are oriented at

approximately 60^0 to the circumferential direction of the wheel found near the flange end of the worn railway wheel HSR2 using the optical images shown in figure 6.22 in Appendix G of the Appendices chapter 8 obtained using the multi-sectioning in conjunction with optical metallography approach. From the multi-sectioned optical micrographs obtained the results show that this crack has mean surface length and depth dimensions of 7 mm and 713 μm, respectively. Figure 6.20 shows a schematic drawing of typical shallow and closely spaced cracks that are oriented almost perpendicular to the circumferential direction of the wheel found at approximately 3 cm from the non-flange end of the worn railway wheel HSR2 using the optical images shown in figure 6.23 in Appendix H of the Appendices chapter 8 obtained using the multi-sectioning in conjunction with optical metallography approach. From the multi-sectioned optical micrographs obtained the results show that this crack has mean surface length and depth dimensions of 6 mm and 743 μm (approx. 0.7 mm), respectively.

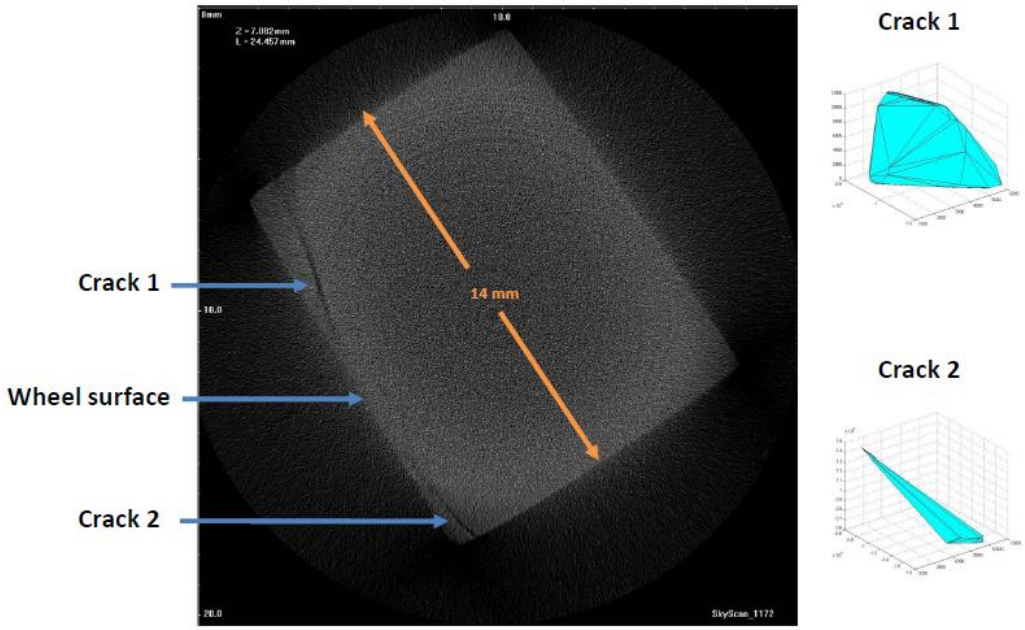

Figure 6.16 shows reconstructed 3-D images of cracks found on the tread of wheel HSR1 at the maximum run-out position using the X-ray tomography technique. Crack A can clearly be seen extending deep into the material at this tread position, whereas, the result shows that crack B is a more shallow crack and with a shorter surface length than crack A.

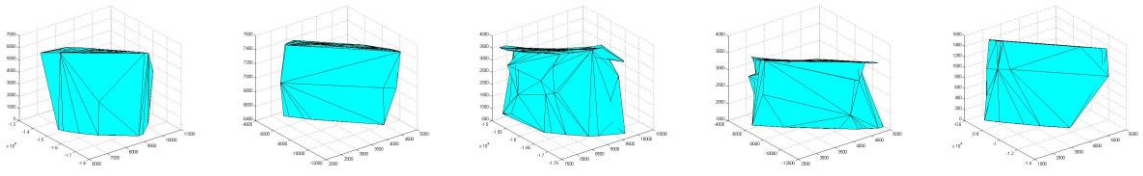

Figure 6.17 shows further reconstructed 3-D images of cracks found on the tread of wheel HSR1 at the maximum run-out position using the X-ray tomography technique; these are significantly deep cracks.

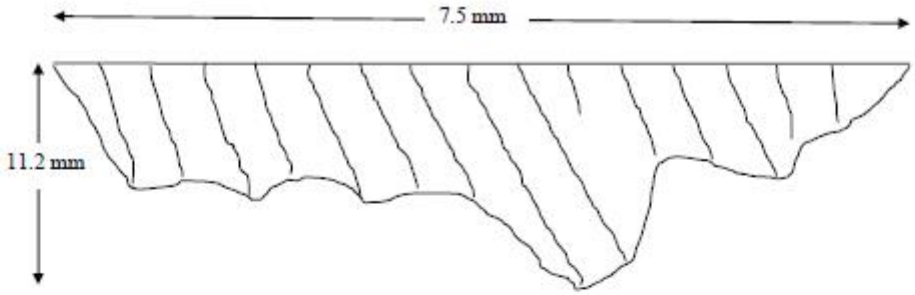

The above figure shows a schematic (not drawn to scale) of the 3-D crack shape for the crack seen in the 2-D image slice obtained from the X-ray tomography experiment in the RCF region of the railway wheel HSR1 at the maximum run-out position on the tread. The figure shows clearly the complex shape of the crack, however, an outline of the semi-elliptical nature of the RCF crack can be seen from the above image.

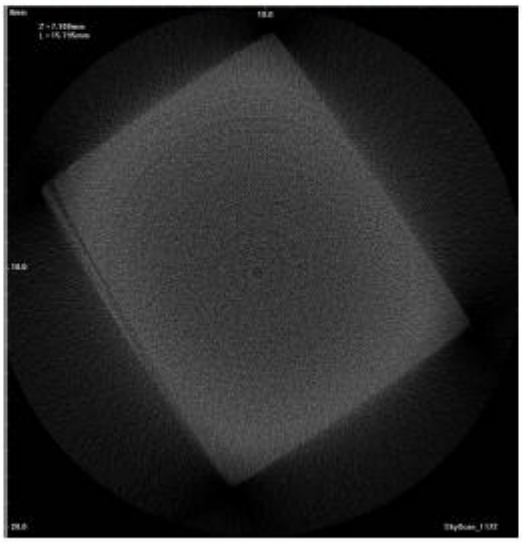

Figure 6.18 shows further reconstructed 3-D images of cracks found on the tread of wheel HSR1 at the maximum run-out position using the X-ray tomography technique; these are significantly deep cracks. The lower image shows a 2-D image slice (frame 8 in figure 9.8 in the Appendices chapter 9 where the crack is at its greatest depth of 11.2 mm) obtained from the X-ray tomography experiment in the RCF region of the railway wheel HSR1 at the maximum run-out position on the tread.

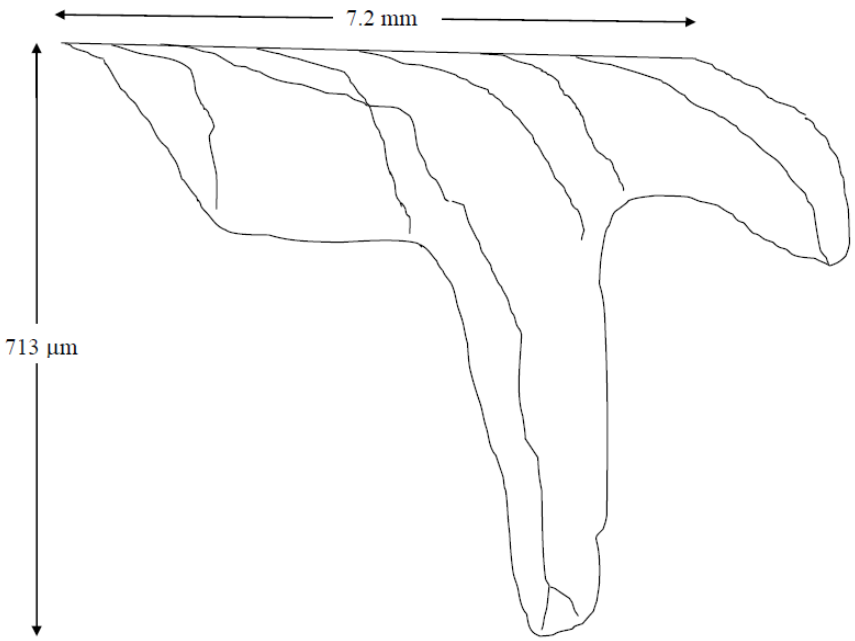

Figure 6.19 shows a schematic drawing of typical shallow and closely spaced cracks that are oriented at approximately 60^0 to the circumferential direction of the wheel found near the flange end of the worn railway wheel HSR2 using the optical images shown in figure 9.81 in the Appendices chapter 9 obtained using the multi-sectioning in conjunction with optical metallography approach.

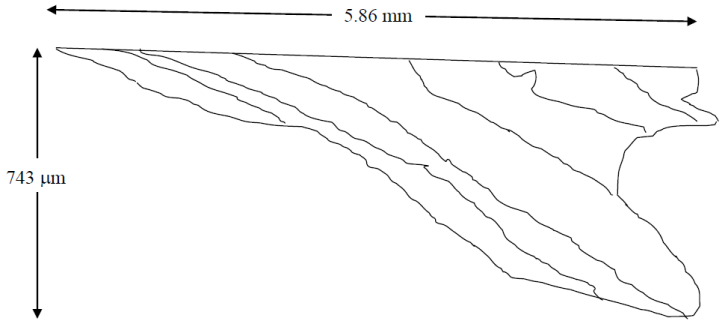

Figure 6.20 shows a schematic drawing of typical shallow and closely spaced cracks that are oriented almost perpendicular to the circumferential direction of the wheel found at approximately 3 cm from the non-flange end of the worn railway wheel HSR2 using the optical images shown in figure 9.82 in the Appendix chapter 9 obtained using the multi-sectioning in conjunction with optical metallography approach.

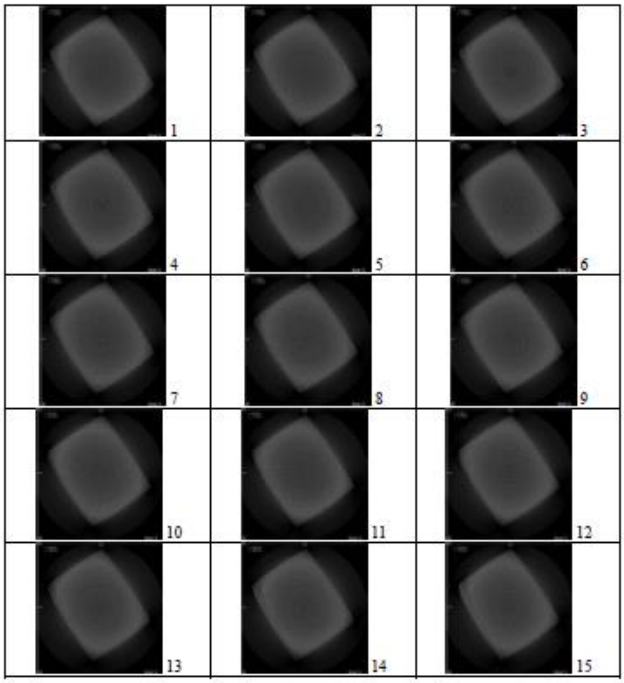

Figure 6.21 shows 2-D image slices from frames: 1-15 incl. for the schematic of the crack reconstructed from these 2-D image slices obtained from the X-ray tomography (CT) experiment on the RCF region of the railway wheel HSR1 at the maximum run-out position on the tread as shown earlier in the chapter above; the crack is at its maximum depth of 11.2 mm as determined from the 8th 2-D slice image of the CT scan above.

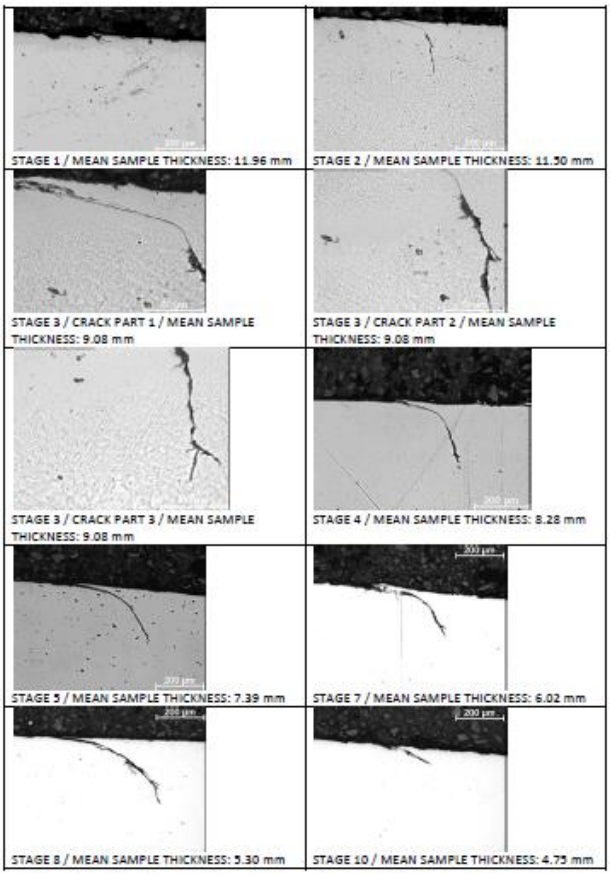

Figure 6.22 shows optical exposure micrographs of a typical shallow and closely spaced crack found near the flange end of railway wheel HSR2 at different stages in the multi-stage in conjunction with optical metallography experiment carried out to reconstruct a three-dimensional (3-D) image of the above crack as shown above in figure 6.19.

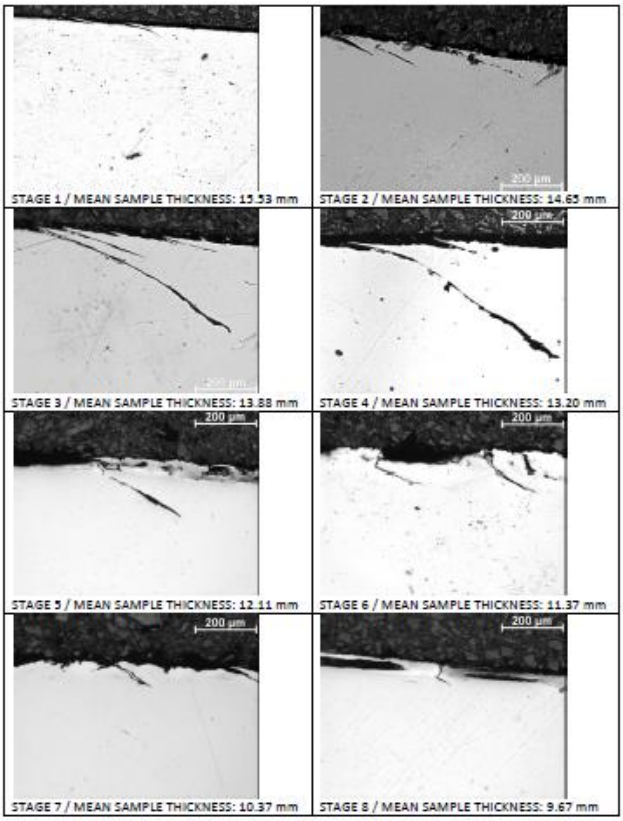

Figure 6.23 shows optical exposure micrographs of a typical shallow and closely spaced crack found at approximately 3 cm from the non-flange end of railway wheel HSR2 at different stages in the multi-stage in conjunction with optical metallography experiment carried out to reconstruct a three-dimensional (3-D) image of the above crack as shown earlier in figure 6.20.

The material properties of the wheel steel material influence the degree to which the wheels experience RCF damage; the rail wheels are more prone to such damage towards the end of their lifetime. The prominent influencing factors in this regard are the change in material properties such as hardness and microstructure with depth below the as-manufactured tread surface. Change in the microstructure and hardness with depth beneath the tread surface, thus variations in the imposed stress on the wheel, may result in the occurrence of localised damage on the rail wheel. Former studies have revealed a correlation between the pro-eutectoid ferrite content in the material and its resistance to RCF damage [16].

6.3.3 HARDNESS AND MICROSTRUCTURAL CHANGE WITH DEPTH FROM TREAD SURFACE FOR WORN (HSR1 AND HSR2) AND NEW (HSR3) RAILWAY WHEELS

6.3.3.1 HARDNESS CHANGE WITH DEPTH FROM TREAD SURFACE

The results obtained from this study are representative of these three rail wheels as at least two segments of these wheels after being appropriately cut were examined for the purposes of this work. Results show similar trends in hardness and microstructural change with tread depth, as presented and discussed in this section and the following section, respectively, and thus representative and selected results are shown for the purposes of identifying and understanding general trends and thus to draw meaningful conclusions. Vickers micro- and macro-hardness tests were conducted across the entire rail wheel tread for the three wheels studied at positions of 1 cm apart in order to create the hardness contour maps showing the change in hardness levels with tread depth for all rail wheels investigated as shown in figures 6.24 and 6.25. Micro-hardness measurements provide higher resolution which is primarily important in gauging the level of hardness at and near the tread surface. Micro-hardness tests on all wheels studied were carried out to a maximum depth of 9 mm below the tread, whereas, at the “running line” for all wheels which lies 70 mm from the back of the flange macro-hardness measurements were also carried out to a depth of at least 50 mm at greater intervals of 5 mm after reaching a depth of about 10 mm below the tread surface as shown in figure 6.26. This result shows a general trend of decreasing hardness values with depth below the surface of the tread to a nominal mean hardness value of approximately 250 for worn and new rail wheels investigated as would be expected for such rail wheels manufactured from R8T steel grade material. The position 70 mm from the back of the flange end is denoted as the nominal running position; here there are relatively low tangential forces (but lots of running).

The results show that the hardness levels for the worn and new railway wheels investigated are highest near the tread surface and across the entire tread in all its regions. The greater level of hardness in this near surface area of the tread is due to work hardening and high stresses imposed on the material in this layer close to the surface of the wheel, thus, resulting in a change in the microstructure of the rail wheels and, as a consequence, leading to plastic flow in the regions that are in close proximity to the wheel tread.

Steel material inhomogeneity including the accuracy of indentations made by the user during measurements contribute to the errors and the resultant accuracy of the measurements. Nevertheless, general and meaningful trends can be drawn from the work presented here. Results show that the degree of hardness is significantly high near the running surface and that the level of hardness decreases with depth below the tread surface for all wheels investigated and in all regions of the tread.

From this work the significantly higher micro-hardness values observed between 8-9 cm from the non-flange end of the worn and new wheel tread segments suggests that the hardness is most likely due to cornering at curves. Furthermore, from the hardness contour maps for all wheels studied it can be seen that high surface hardness is present in all the three rail wheels, even in the new wheel HSR3 near the flange and non-flange ends, i.e. in the flange face and field side regions, respectively. This is most probably due to cornering as the flange of the leading wheelset makes contact with the outer rail during motion on sharp curves. The resultant stresses, primarily the tangential forces, can be high, especially if the rail/wheel contact is not properly lubricated. As a result, the surface damage in this area of the surface of the tread is usually due to the process of wear.

The measured micro-hardness values at positions 2, 3, 8 and 9 cm, from the non-flange end for the “new” HSR3 rail wheel are higher (> 350) than the nominal value (approx. 300) in the bulk of this material which suggests that the greater work hardening at the surface at these positions could be the result of the wheel running on curves at these locations. Also, cracks are present at positions 2 cm and 3 cm from the non-flange end for the worn HSR1 and HSR2 rail wheels and the new HSR3 rail wheel investigated.

Furthermore, the same wheel having higher hardness values than nominal values at different locations along the tread surface might possibly be due to manufacturing changes which will result in different properties; the geometry of the wheel will also be an influencing factor.

Figures 6.24 show contour maps of micro-hardness measurements with depth for the worn wheel HSR1 at the position of maximum and minimum run-out for the tread

made at different positions along the tread surface from the non-flange end of the tread. The results show that the maximum hardness values are found at approximately 5.0 cm from the non-flange end of the tread indicating that this is the main position of contact between the wheel and rail. Figure 6.27 shows the change in hardness with depth graph at the minimum tread run-out location for position 5 cm from the non-flange end. It is expected that the maximum contact stress position between the wheel and rail will vary across the tread during service as it depends on the rail profile and whether contact is being made on straight or curved rail. However, the hardness value seems to be higher than expected at a position of 9.0 cm from the non-flange end, therefore this is believed to be due to the effect of cornering of the vehicle and thus the motion of the wheel at curves on the railway track. It is clear from these results that the depth of hardening is quite severe until a depth of about 300 μm beneath the surface at this tread position, with micro-hardness values of 356.2 and 355.5 as compared with an average value in the un-strained region of about 300 for this material. This compares well with similar micro-hardness surveys that are reported in the literature [152] on rail steels with sub-surface depth at two rail head transverse section locations where the reported data shows a micro-hardness value of about 350 at a depth of about 250 μm and a nominal value of about 300 in the unstrained region beyond a depth of about 500 μm below the surface. This is in close agreement with the results obtained by my work on worn rail wheel steel as demonstrated in the present chapter here and in the next section where it is also demonstrated that the change in the microstructure from the strained to the unstrained regions and, thus, the depth of damage, occurs at about 600 μm below the tread surface.

The results obtained from the hardness measurements conducted in the different regions of the tread of the relatively new HSR3 rail wheel shown in figures 6.43-6.47 incl. below show that the hardness of the rail wheel material decreases linearly with depth below the tread surface which is believed to be as a consequence of the manufacturing process and these results are in agreement with similar studies conducted on railway wheels manufactured from similar steels. Material properties of new wheels of wheel steel grades similar to R8T steels that are of the type of rail wheel steel grades used for the purposes of the present work have been previously investigated [7, 8].These authors report changes in hardness and microstructure with depth of the rail wheel rim and have also reported that the hardness of the material

decreases linearly with depth below the tread surface for a new railway wheel due to the manufacturing process, thus, in line with the finding from the current work. Furthermore, the findings reported in this chapter from the present work are in line with that reported in the literature [2] that hardness is present in both types of surface defects – thermally affected and fatigue cracking surfaces and that the hardness is highest in the wheel tread surfaces (reported hardness value: 750) in the location where martensitic transformation has occurred (thermal affect), whereas, in the RCF region the highest hardness value reported in the above reference is 430. This is in agreement with my work presented in this chapter as shown in the hardness results below. Increased micro-hardness values in the RCF region (without thermal effect) reflects the intensity of plastic flow deformation as can be seen in the optical micrographs shown in the section on the change in the microstructure with tread depth below.

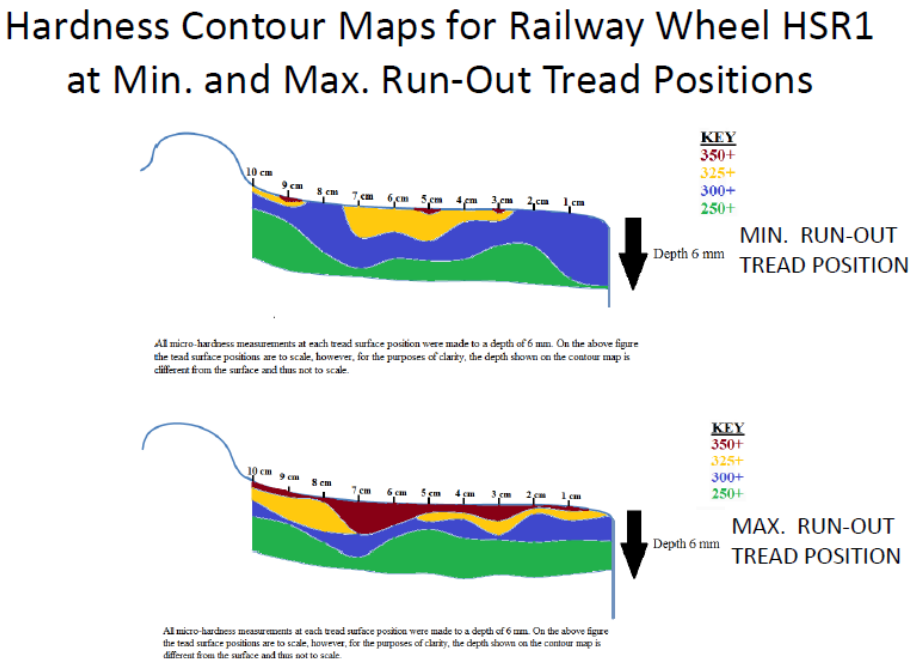

Figure 6.24 Hardness contour maps for railway wheels: HSR1 (both at the min. and max. run-out positions of the tread), HSR2 and HSR3.

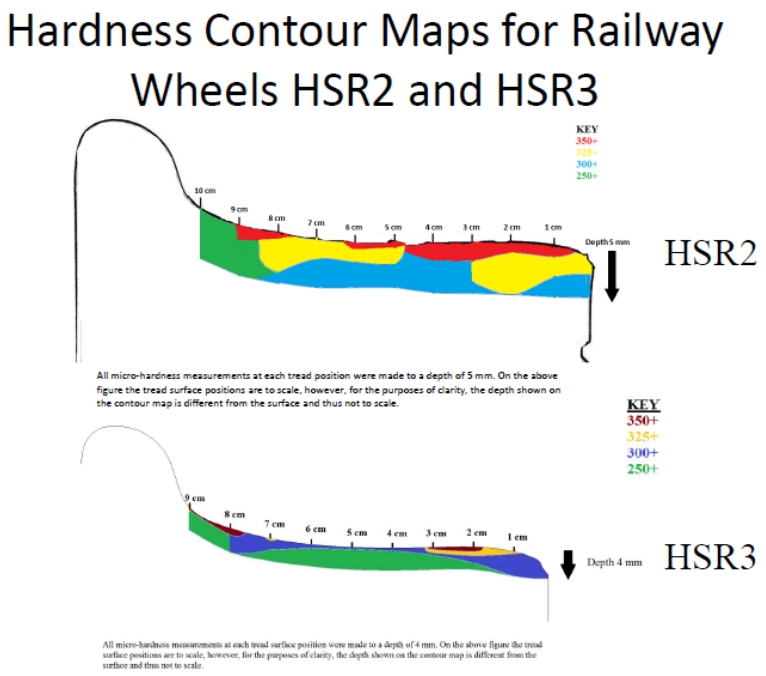

Figure 6.25 Hardness contour maps for railway wheels: HSR1 (both at the min. and max. run-out positions of the tread), HSR2 and HSR3.

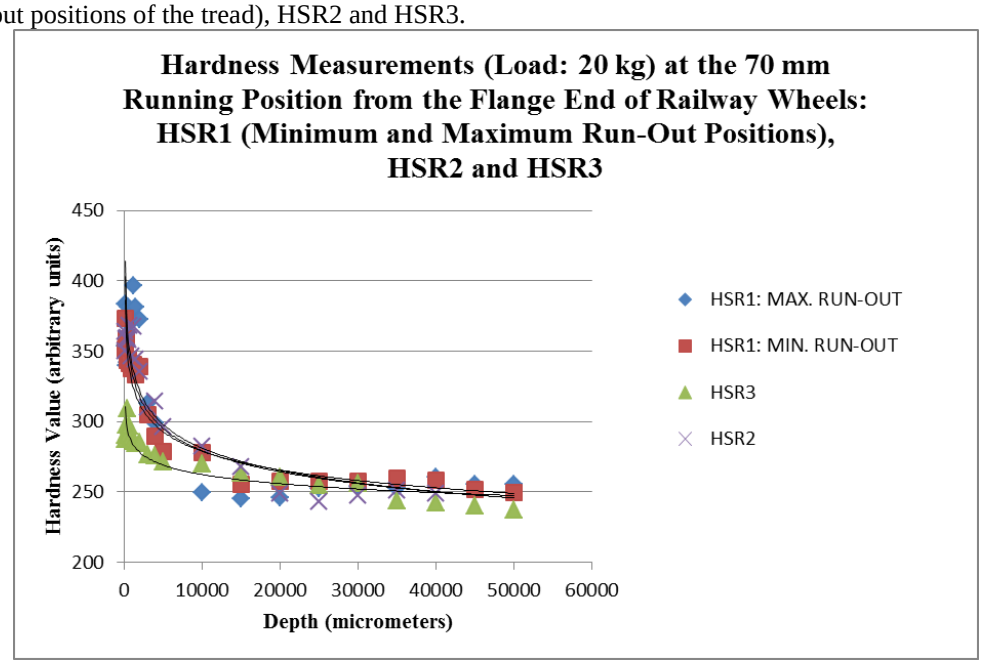

Figure 6.26 shows the hardness versus depth measurements carried out (both micro- and macro- hardness measurements were conducted here) at the "running line" position (measured: 70 mm from the flange end) on the treads for railway wheels: HSR1 (hardness measurements were carried out both at the maximum and minimum run-out positions on the tread of this wheel), HSR2 and HSR3. The data for the above graphs are shown in figure 8.5 of Appendix A in the appendices chapter 9.

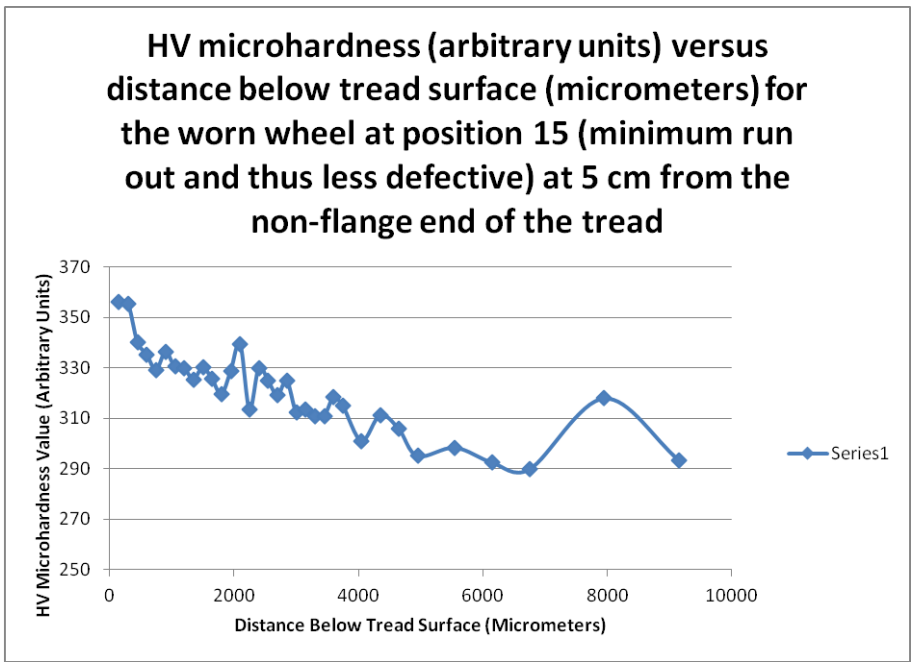

Figure 6.27 Graph showing the change in hardness with depth for position 5 cm from the non-flange end of the HSR1 worn railway wheel at the min. run-out position on the tread.

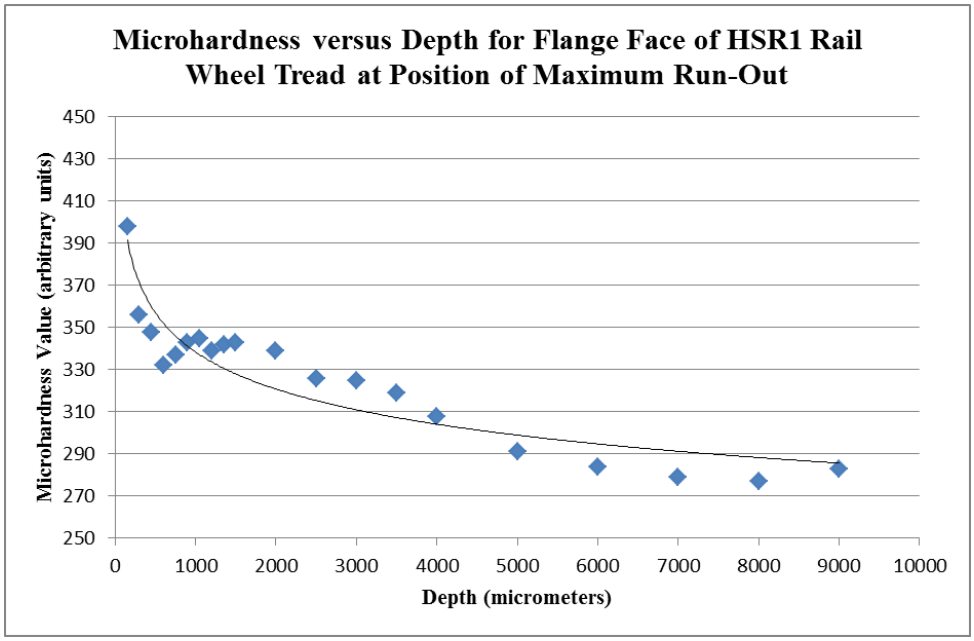

Figure 6.28 Microhardness versus Depth for Flange Face Region of HSR1 Rail Wheel Tread at Position of Maximum Run-Out.

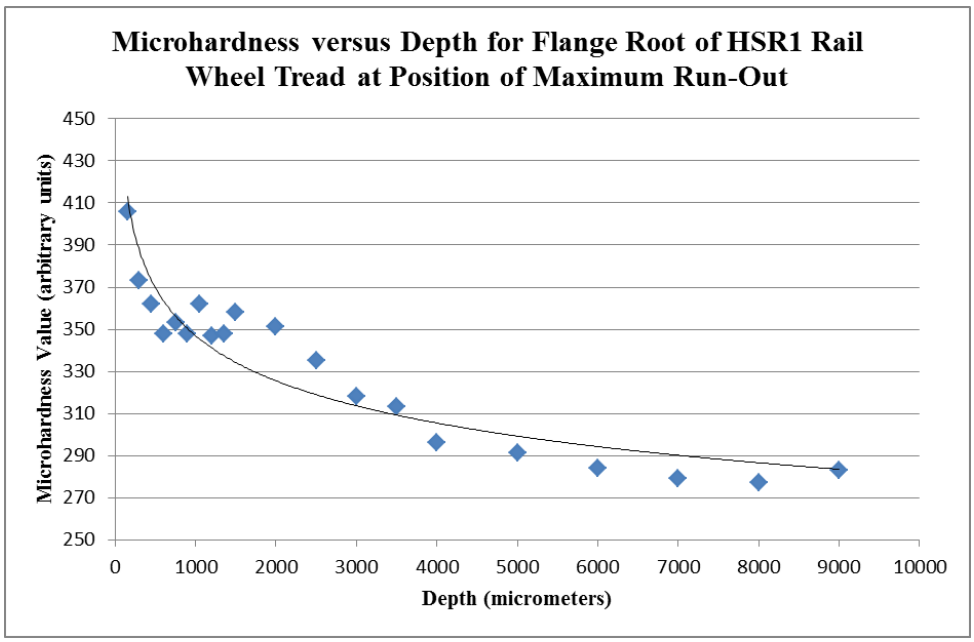

Figure 6.29 Microhardness versus Depth for Flange Root Region of HSR1 Rail Wheel Tread at Position of Maximum Run-Out.

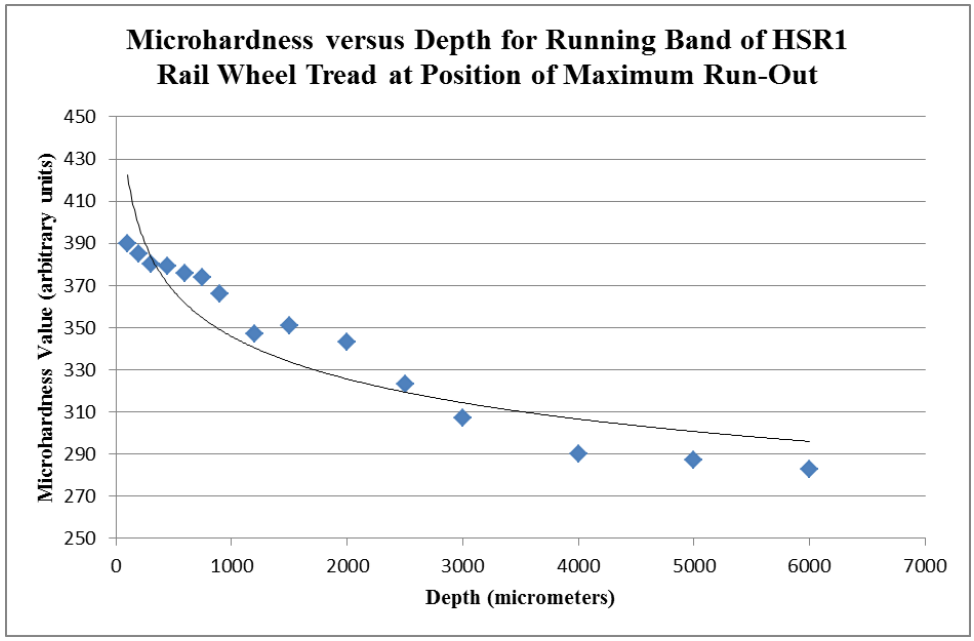

Figure 6.30 Microhardness versus Depth for Running Band Region of HSR1 Rail Wheel Tread at Position of Maximum Run-Out.

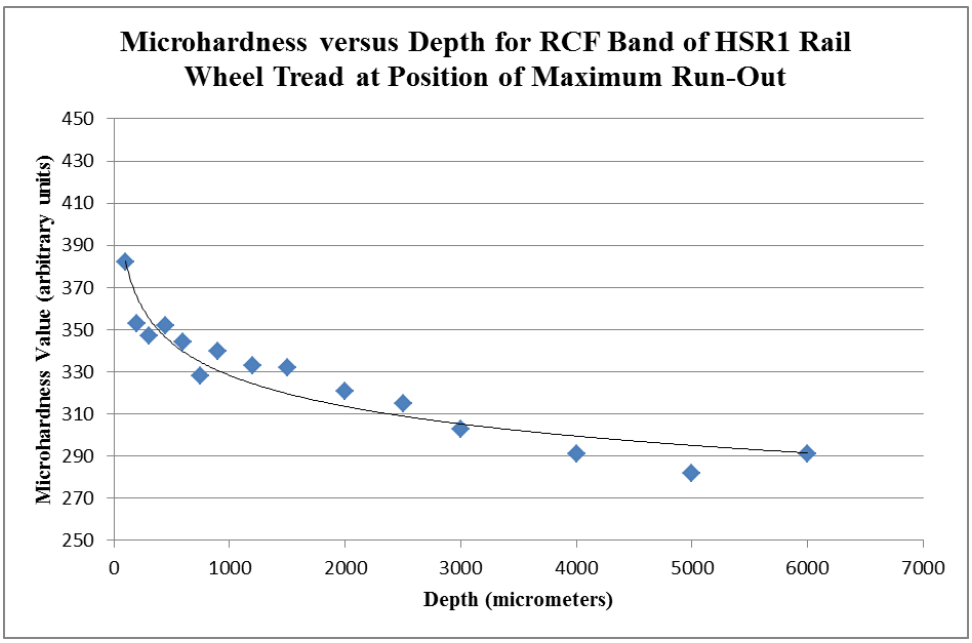

Figure 6.31 Microhardness versus Depth for RCF Band Region of HSR1 Rail Wheel Tread at Position of Maximum Run-Out.

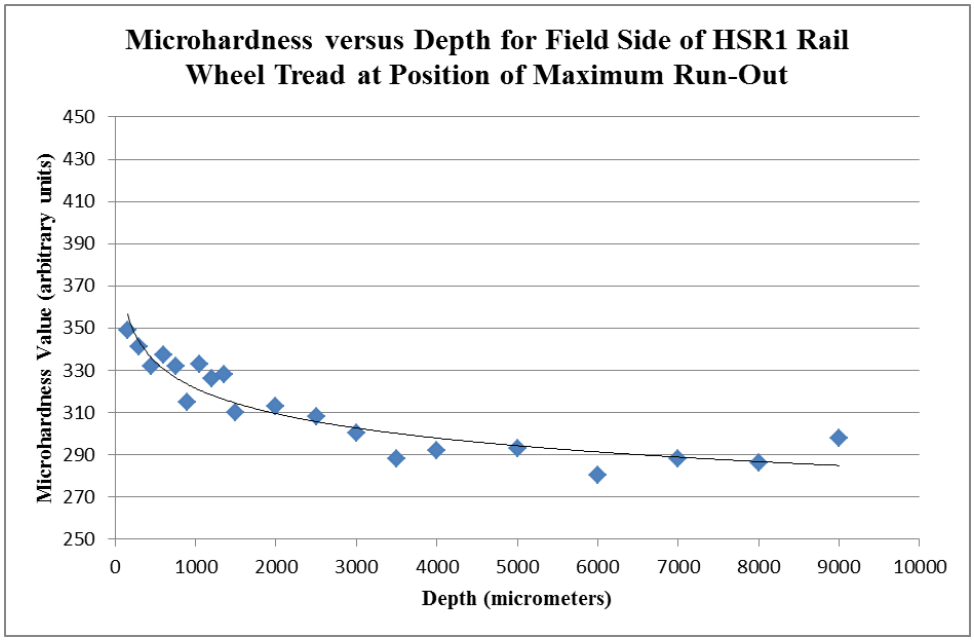

Figure 6.32 Microhardness versus Depth for Field Side Region of HSR1 Rail Wheel Tread at Position of Maximum Run-Out.

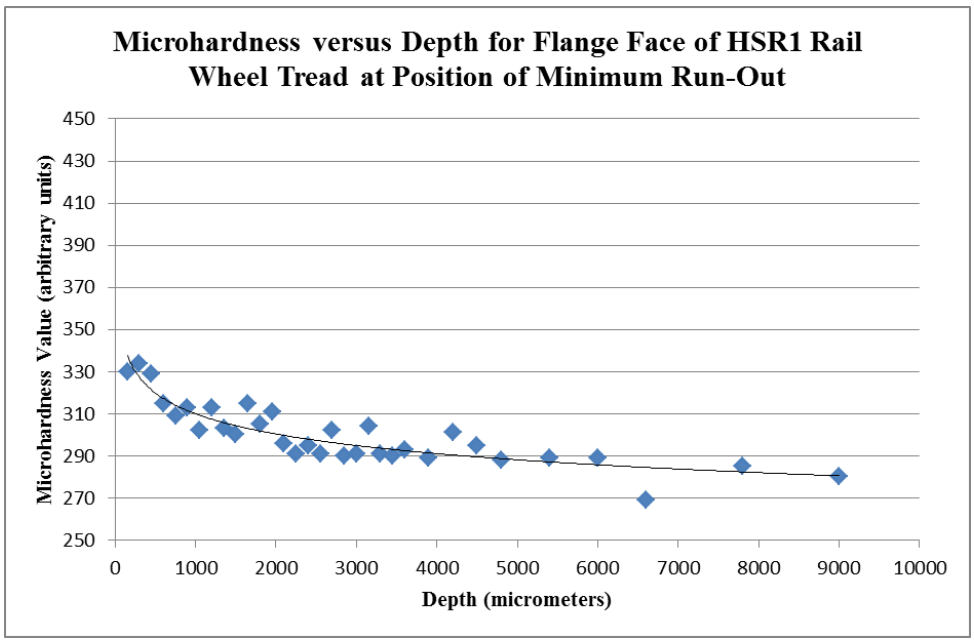

Figure 6.33 Microhardness versus Depth for Flange Face Region of HSR1 Rail Wheel Tread at Position of Minimum Run-Out.

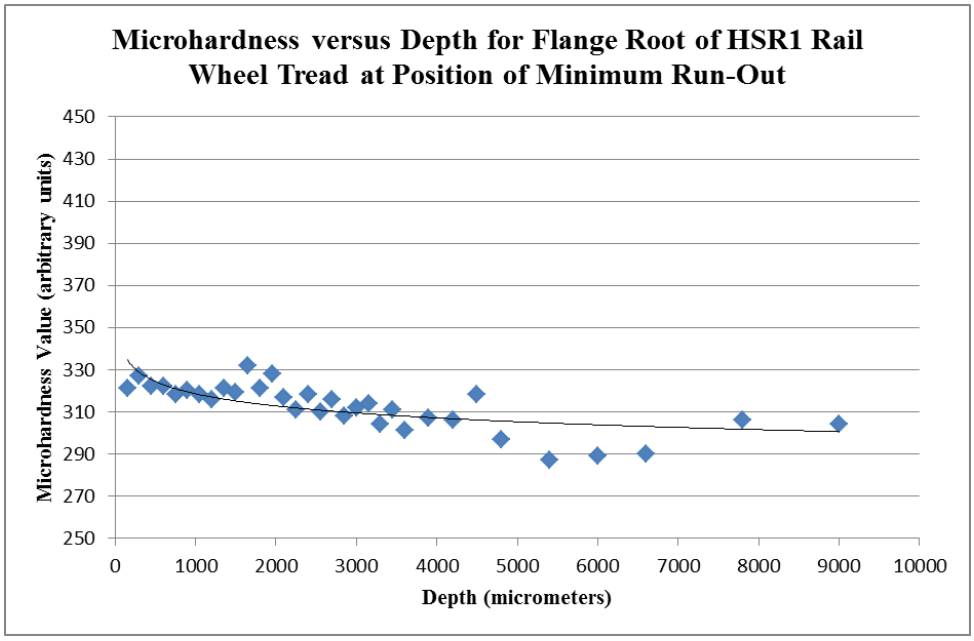

Figure 6.34 Microhardness versus Depth for Flange Root Region of HSR1 Rail Wheel Tread at Position of Minimum Run-Out.

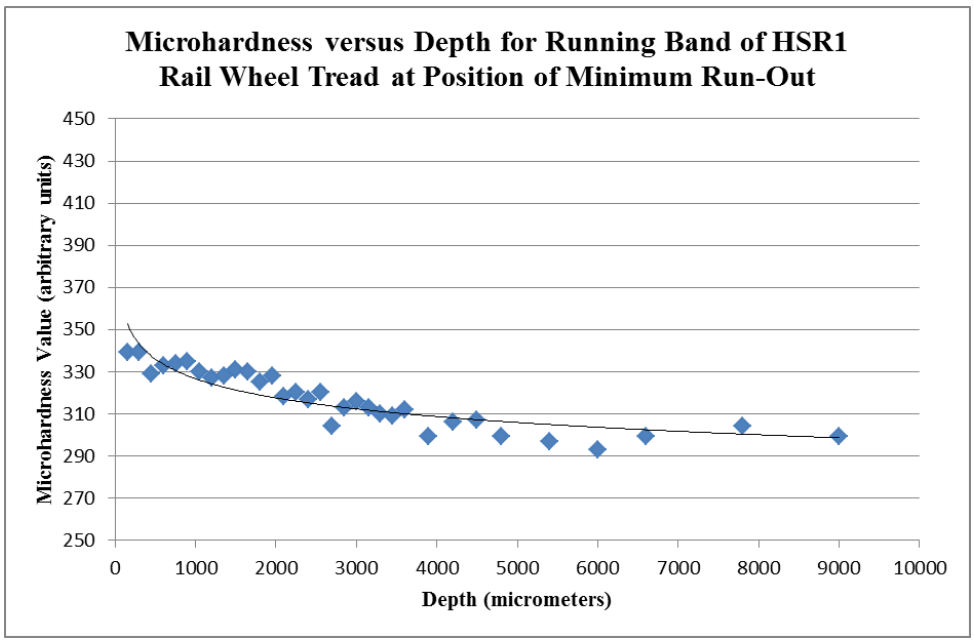

Figure 6.35 Microhardness versus Depth for Running Band Region of HSR1 Rail Wheel Tread at Position of Minimum Run-Out.

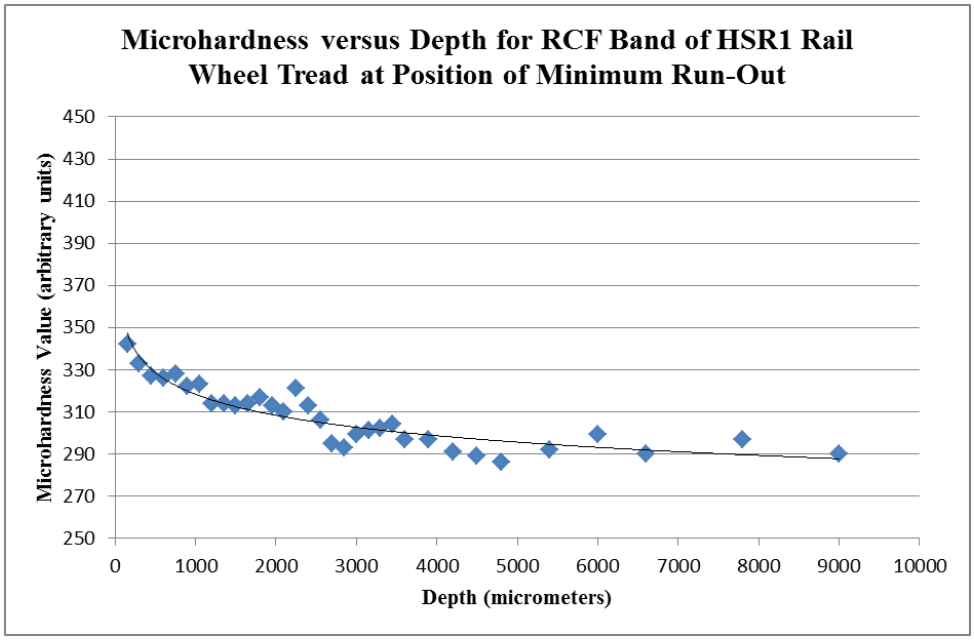

Figure 6.36 Microhardness versus Depth for RCF Band Region of HSR1 Rail Wheel Tread at Position of Minimum Run-Out.

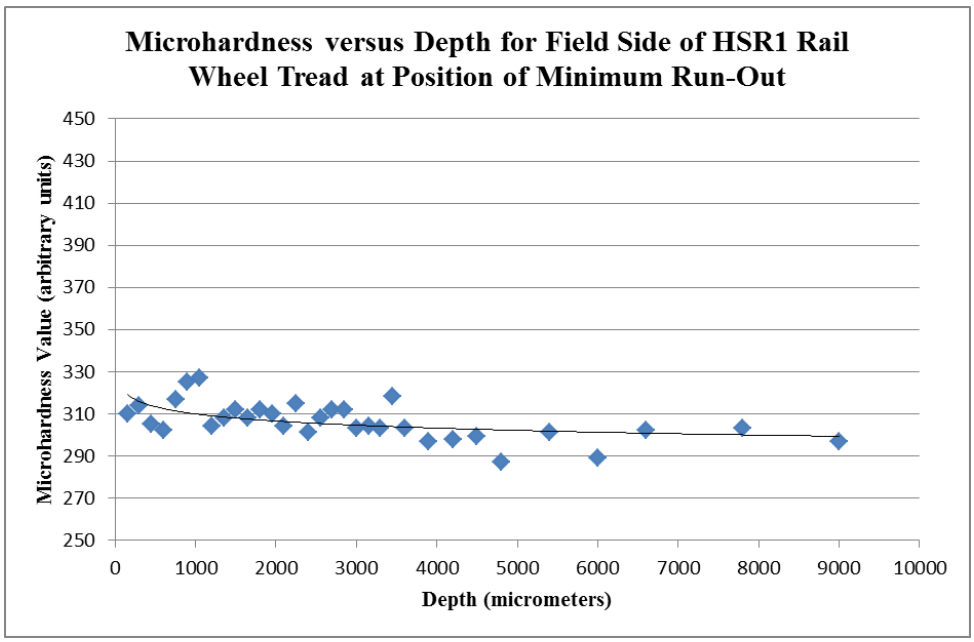

Figure 6.37 Microhardness versus Depth for Field Side Region of HSR1 Rail Wheel Tread at Position of Minimum Run-Out.

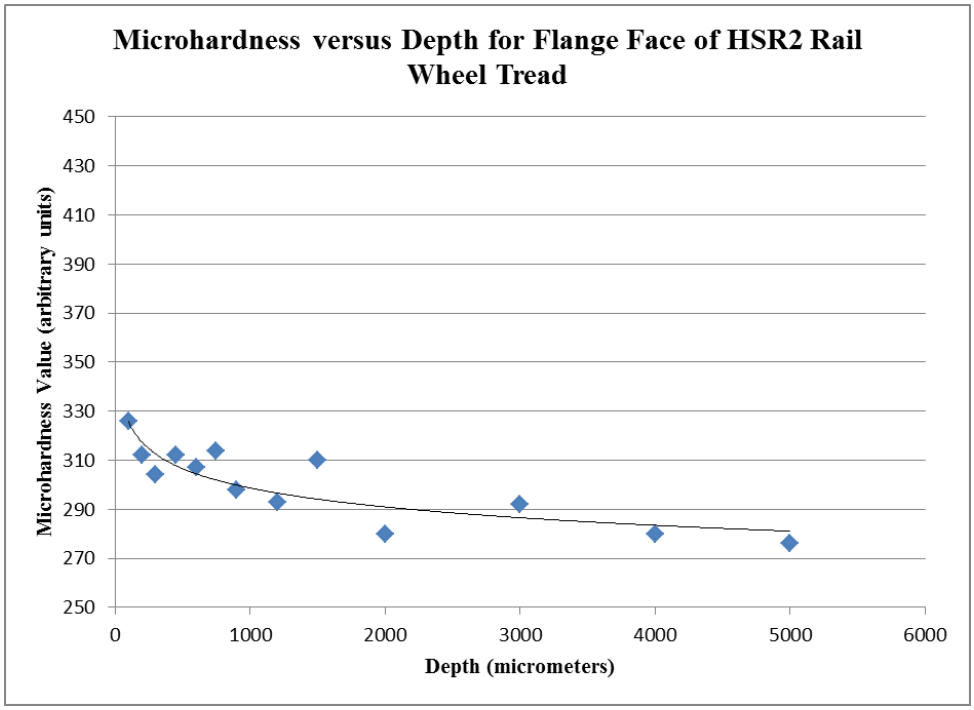

Figure 6.38 Microhardness versus Depth for Flange Face Region of HSR2 Rail Wheel Tread.

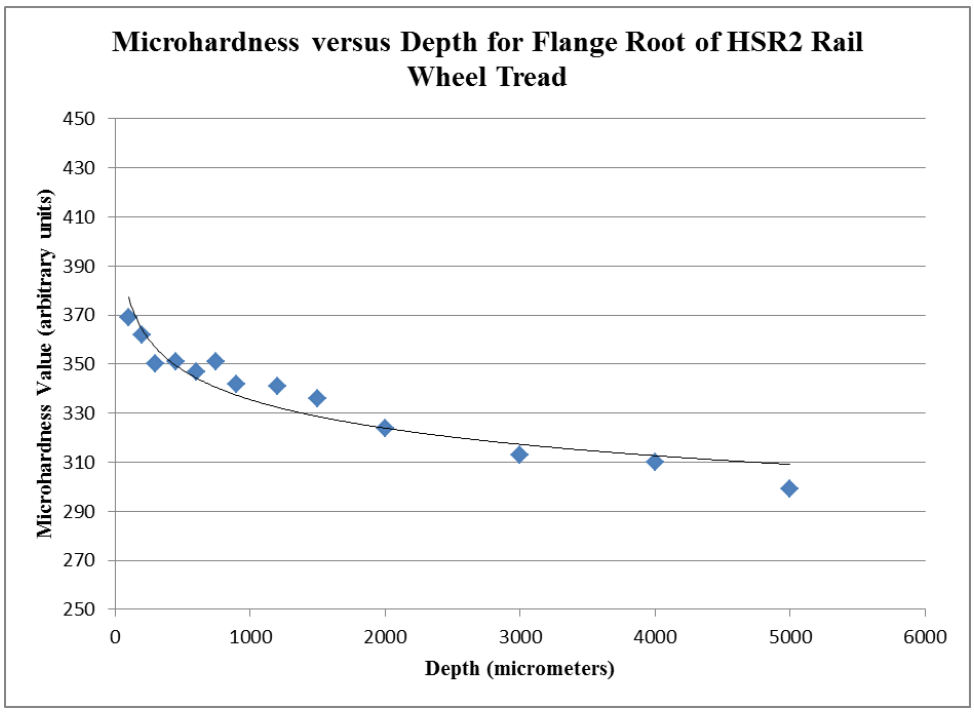

Figure 6.39 Microhardness versus Depth for Flange Root Region of HSR2 Rail Wheel Tread.

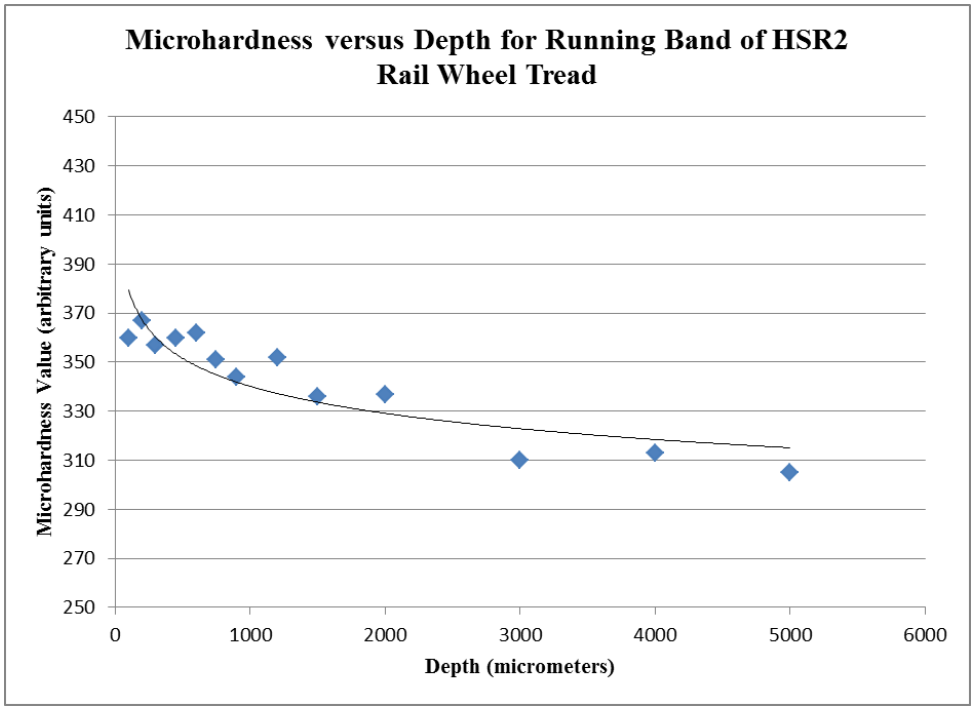

Figure 6.40 Microhardness versus Depth for Running Band Region of HSR2 Rail Wheel Tread.

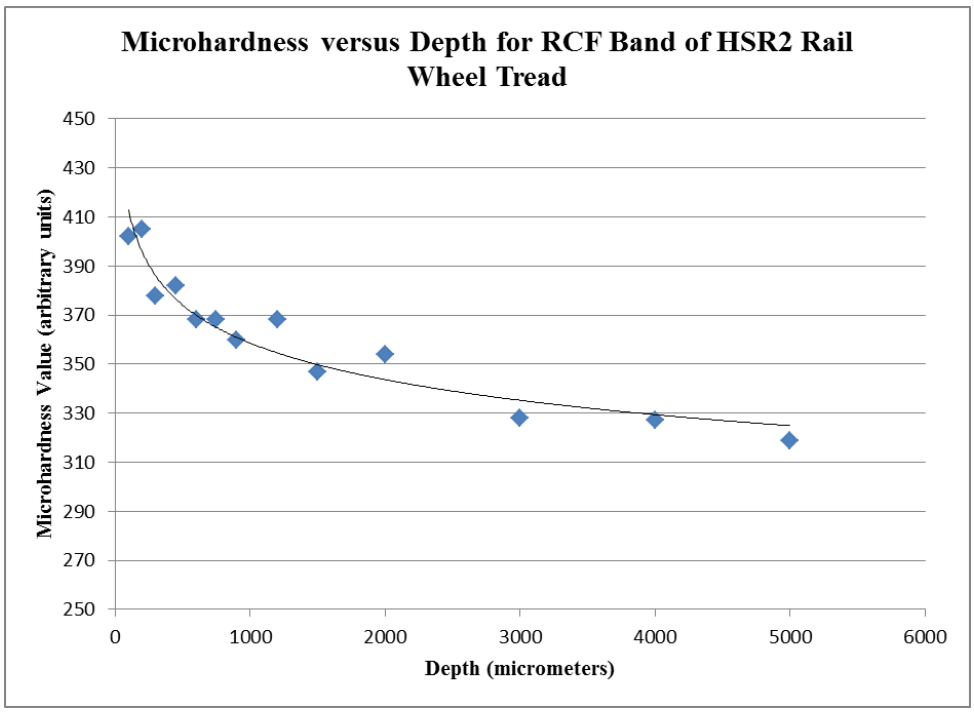

Figure 6.41 Microhardness versus Depth for RCF Band Region of HSR2 Rail Wheel Tread.

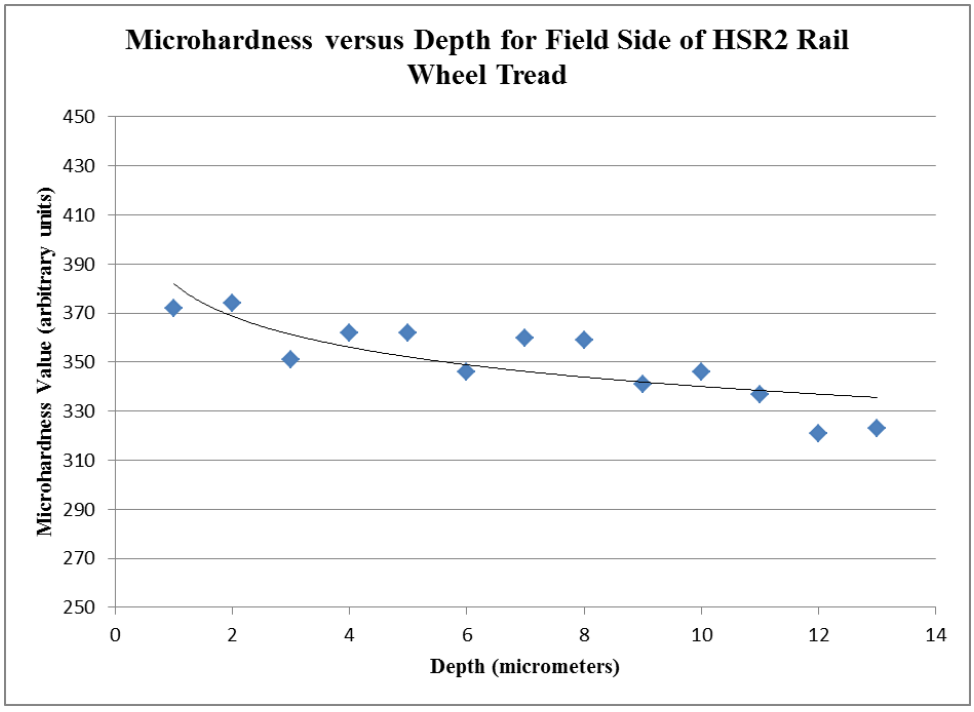

Figure 6.42 Microhardness versus Depth for Field Side Region of HSR2 Rail Wheel Tread.

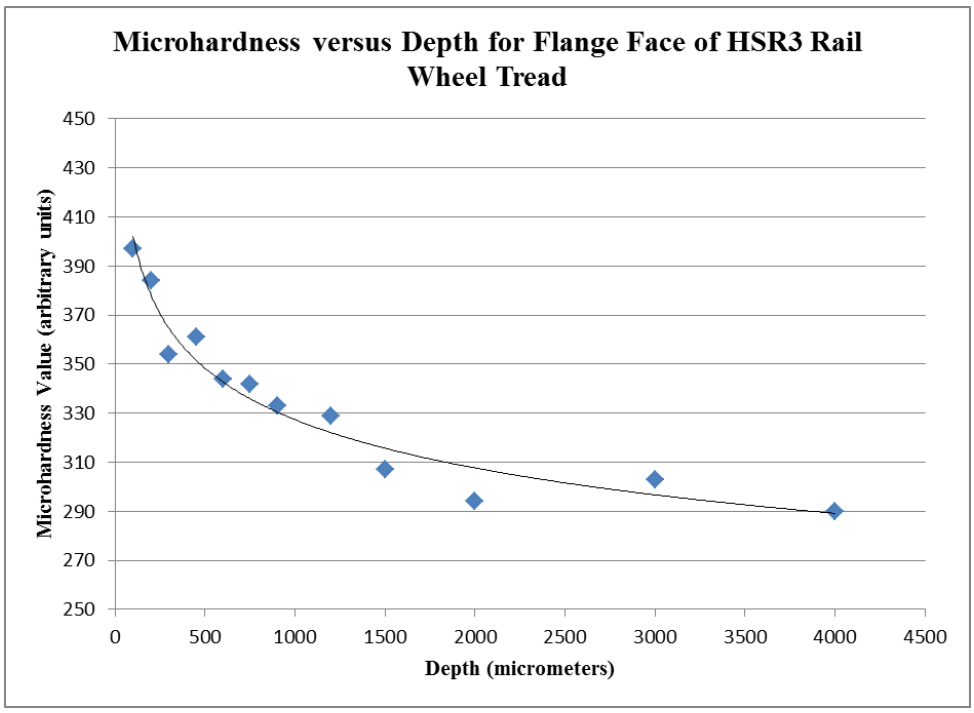

Figure 6.43 Microhardness versus Depth for Flange Face Region of HSR3 Rail Wheel Tread.

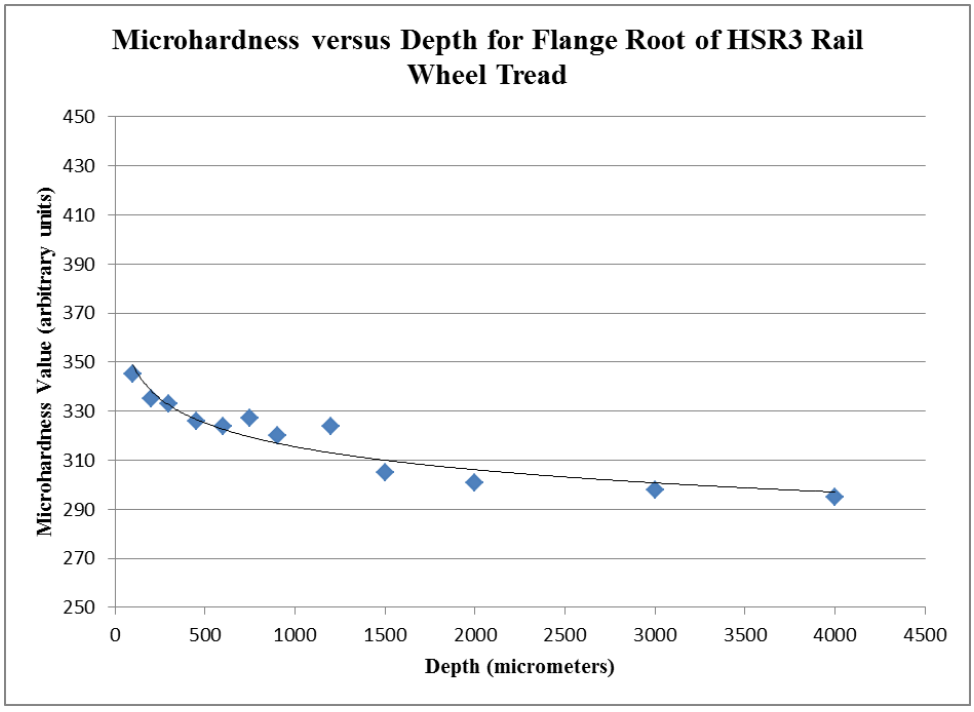

Figure 6.44 Microhardness versus Depth for Flange Root Region of HSR3 Rail Wheel Tread.

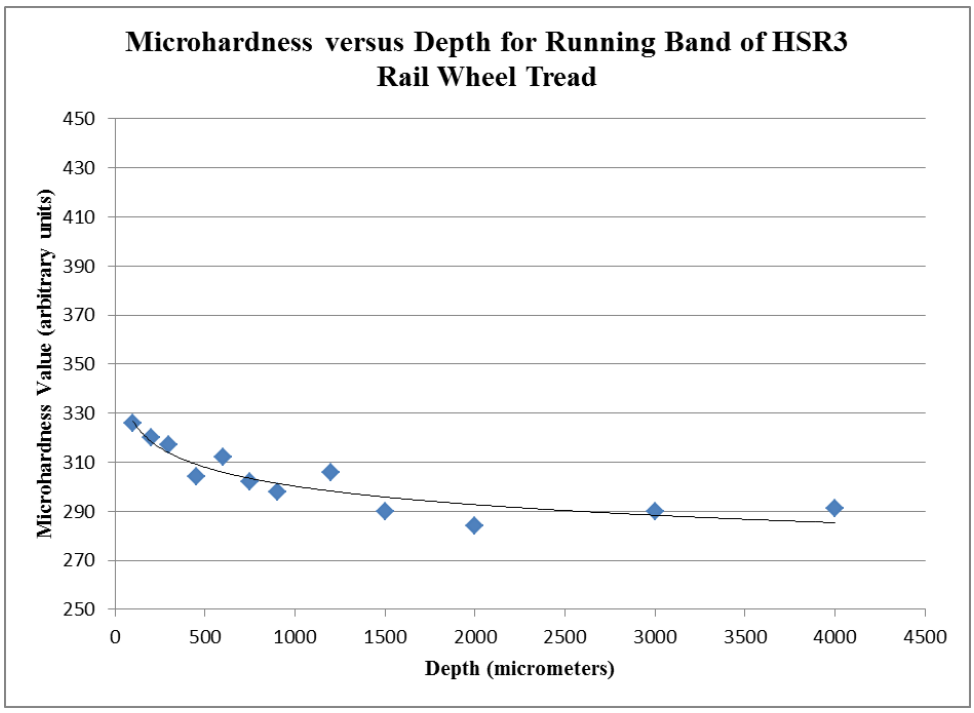

Figure 6.45 Microhardness versus Depth for Running Band Region of HSR3 Rail Wheel Tread.

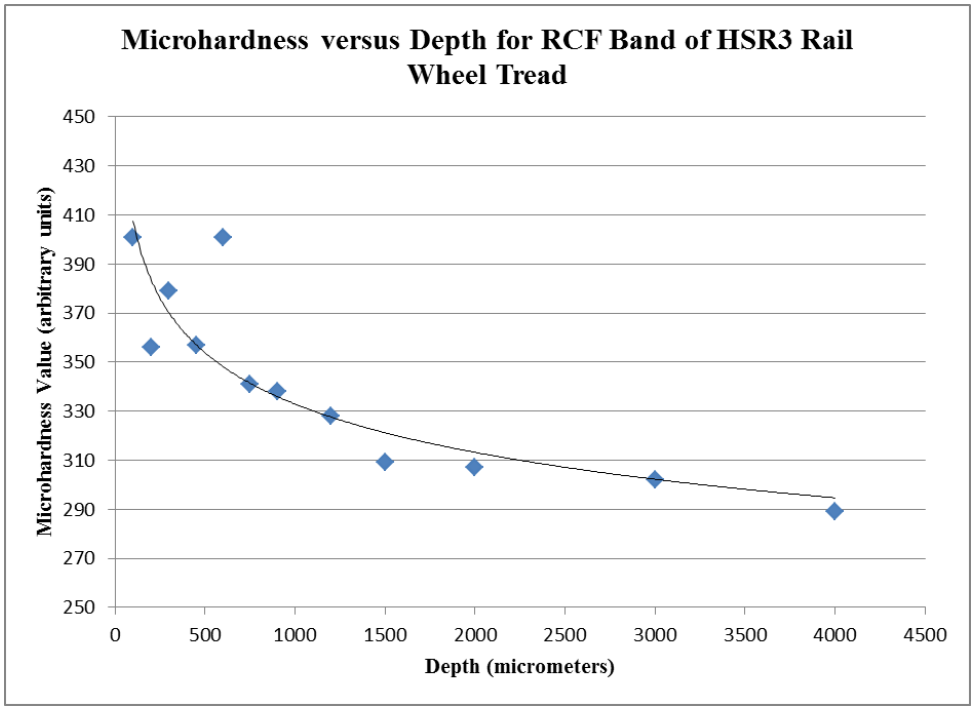

Figure 6.46 Microhardness versus Depth for RCF Band Region of HSR3 Rail Wheel Tread.

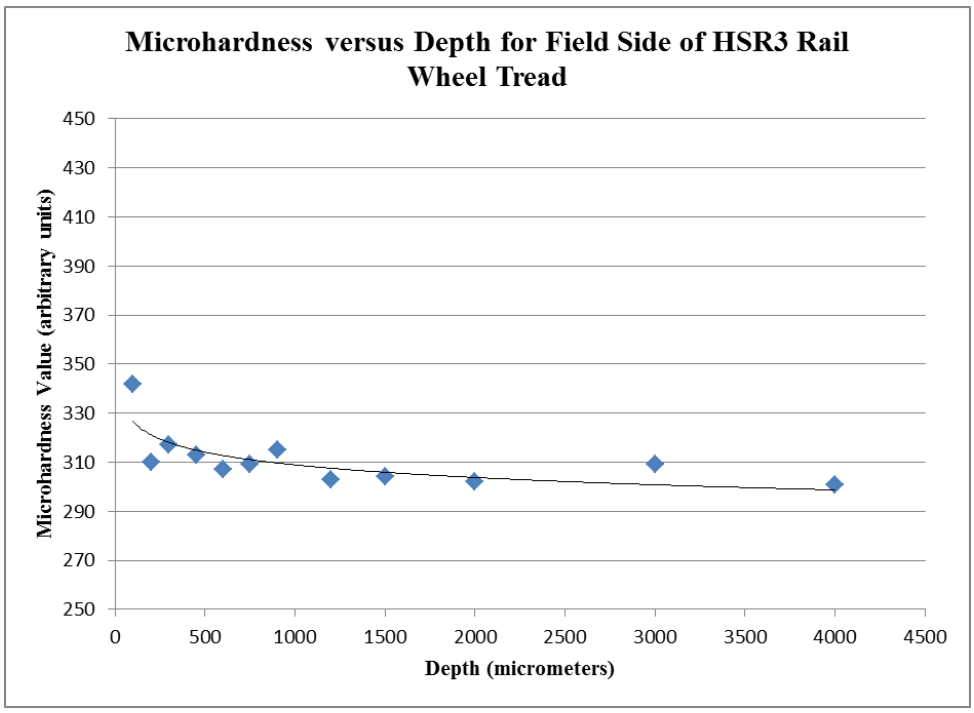

Figure 6.47 Microhardness versus Depth for Field Side Region of HSR3 Rail Wheel Tread.

The hardness data for all the hardness versus tread depth results presented in this chapter to generate the charts above are found in the Appendices chapter 9.

6.3.3.2 MICROSTRUCTURAL CHANGE WITH DEPTH FROM TREAD SURFACE

Figures 6.49 and 6.50 show the unstrained core matrix away from the tread surface at positions of minimum and maximum run-out, respectively, showing a small amount of discontinuous pro-eutectoid ferrite at prior austenite grain boundaries. Colonies of pearlite (optically dark) consisting of periodically spaced lamellae are surrounded by pro-eutectoid ferrite (optically light) at prior austenite grain boundaries. Figures 6.51 and 6.52 and show an overview of the crack and strained matrix near the surface at a position of minimum run-out and, figure 6.53 a crack and a strained matrix at a position of maximum run-out, on the tread for wheel HSR1; it is evinced from figures 6.51 and 6.52 that cracks can propagate parallel to the sheared grain boundaries near the tread surface. Figure 6.52 shows that RCF cracks initiate primarily at pro-eutectoid ferrite boundaries in highly strained regions. This is in agreement with previous work in the literature [16]. It is also reported by these authors that the pro-eutectoid content is higher than the pearlite fraction during cyclic loading and that twin-disc tests have revealed that the fatigue life is reduced as a result of an increase

in the amount of pro-eutectoid ferrite content present in the material. Thus, railway wheels are more prone to the initiation and subsequent growth towards the end of their working lifetime when constantly recurring wear and continued turning on the lathe has resulted in great degree of material being removed from the surface of the wheel during the course of its operational life.

Surface cracks which do not penetrate deep into the material such as the cluster of closely spaced and shallow cluster of cracks as are found near the flange end of the tread surface of wheel HSR2 do not pose a significant risk to the railway industry, in terms of maintenance costs and wheel tread damage and, thus, can generally be ignored when it comes to maintenance practices for practical reasons. However, deeper cracks as observed on the RCF region of railway wheel HSR1 do pose a significant threat and therefore need to be immediately addressed in terms of maintenance procedures applied to the railway industry.

Figure 6.43 is an optical micrograph showing an overview of the strained matrix near the tread surface at the minimum run-out position on the tread surface wheel HSR1. In addition, observations of the change in the microstructure of the material of the wheels investigated during this work with tread surface depth by optical metallography show that, as a consequence of the presence of such deep cracks in the material, these cracks appear to shield the microstructure of the material from excessive shear and, as a result, the material which is present above such cracks thus burdens more of the shear stress imposed on the material that lies directly under these cracks as has been observed from this work and evinced from the optical micrographs shown in figures 6.51 and 6.54; and these results are in line with similar findings reported in the literature [14, 15].

The pro-eutectoid ferrite bands are flattened near the tread surface due to the high stress and strain imposed on the microstructure in this region. Figure 6.43 clearly shows that the pro-eutectoid ferrite bands are oriented in the direction of the strain field. Furthermore, from figure 6.54 it is apparent that as the cracks are large thus the initiation stage will have been removed by wear. In figure 6.54 the matrix appears not to have been significantly affected by strain, thus, suggesting that this is some distance from the surface of the wheel. In that case the cracks would be driven more

by elastic stresses and therefore would not be controlled by the microstructure. Furthermore, in the literature [2] it is postulated that three phases of wheel tread damage exist as follows. Initially, cracks are created in the radial direction as martensitic transformation leads to compressive forces at at surface layers. Minimal ductility of martensite prevents the material from becoming plastically deformed at the tread's surface, thus, resulting in the branching of cracks only in the radial direction. Following this stage the stage of radial cracking is growth through austenitized material and these radial cracks then change direction and incline at small angles, thus, growing towards the material's surface; resulting in spalling at the surface which is typical of this type of surface damage. Finally, the cracks then grow towards the thermally unaffected regions of the material of the wheel; no structural orientation or the branching of cracks occurs here. Furthermore, manganese sulphide inclusions, which are reported in the literature to be commonly found in these wheel steel materials and are nominally of the order of about 10 μm in size or less [5,6] are shown in figure 6.55 below. Figure 6.56 is an optical micrograph of a lightly etched surface region of a longitudinally cut section of the tread surface at a position of 5.5 cm from the non-flange end. The micrograph shows the change in the microstructure of the material with depth. The change from the strained to the unstrained microstructure appears to occur at a depth of around 600 μm below the tread surface which is in line with similar studies that are reported in the literature [152].

Furthermore, in the previous section on the change in hardness with tread depth in the various regions of the tread for all three railway wheels investigated it is shown that a general trend of hardness decreasing with depth below the tread exists in all regions of the tread. It is also apparent from these results that the hardness is higher near the surface of the wheel tread due to work hardening and that initially the hardness abruptly drops with tread depth to a depth below the surface of about 1 mm in all wheels investigated and then decreases in a less steep gradient as can be seen in figures 6.28-6.47 incl. above. In this connection, it is reported in the literature [2,7,10,11,12.13] that the carbon content of R8T steel grade railway wheels and other similar grade steel wheels to the ones investigated for the purposes of this work is consistent throughout the wheel rim and the pro-eutectoid (PE) ferrite fraction increases with depth and it is postulated that pearlite lamellar spacing might be influenced by the local cooling rate of the material during the manufacturing process;

an increase in the hardness of the material is found to result in tighter lamellar spacing as evinced from the work presented here and supported by previous work cited above. However, due to time constraints and the scope of the present PhD project accurate measurements of the pro-eutectoid ferrite content and the lamellar spacing of pearlite in the railway wheels investigated for this work could not be carried out. However, visual inspection of the microstructure of samples analysed from the three railway wheels investigated shows that the pro-eutectoid ferrite content does appear to increase with depth below the tread surface and the lamellar spacing of pearlite becomes smaller, or tighter, with an increase in the hardness levels of the material near the surface of the wheel tread in all regions of the tread for wheels HSR1, HSR2 and HSR3. Thus, the results and salient points arising from this work are in line with the general trends reported in previous work on similar rail wheels reported in the literature. The change in hardness with depth below the tread surface can also influenced by the manufacturing process together with change in pro-eutectoid ferrite content with depth and the surface or near surface hardness levels thus resulting in the occurrence of a high degree of plastic flow in these near surface regions of the tread [2].

Furthermore, as shown by the studies presented and discussed in this chapter on the changes in hardness and microstructure with depth below the tread surface of all three railway wheels investigated and, in line with the literature [19], the depth of hardening as ascertained from the hardness contour maps for all three wheels shown in the previous section is greater than the depth of microstructural change, or deformation, as shown by the comparison of the depth of hardening from the hardness contour maps and the evaluation of the depth at which microstructural change occurs as shown in table 6.2 (below) for the worn railway wheel HSR1 at the maximum run-out tread position of this wheel and the new railway wheel HSR3; and also as evinced by visual inspection from the optical micrographs of the microstructure for all three railway wheels investigated with different levels of RCF tread wheel surface damage. Due to the vast amounts of results and optical images obtained from this study only some selected optical images are shown in this section. Factors influencing hardness, for example, an increase in the density of dislocation as a result of work hardening do not necessarily result in a change in the microstructure of the material. It is reported in the literature [2] that the extent of the depth of hardening correlates closely to the depth at

which the applied shear stress exceeds the shear stress of the unstrained bulk matrix of the microstructure of the material.

In addition, as observed from the present work the hardness level in the RCF prone region is greater than in the running region of the wheel tread due to an increase in the degree of applied stress in the former region. Furthermore, as can be seen from the optical micrographs showing the RCF cracks found in the RCF region shown earlier in section 6.3.2 and in the current section (below) the depths of cracks in this region are quite severe propagating deep into the material here. Thus, material properties, particularly in this region are of utmost importance as, on subsequently turning the wheelset on the lathe, this highly stressed and hardened material in this RCF prone region will become the surface of the re-profiled railway wheel.

Figure 6.47 shows the microstructure of wheel HSR2 near the tread surface at the running region (image taken at 6 cm from the non-flange end) showing no shearing in this region. This is expected due to the following reason. It is reported in the literature [2] that in the running region of the wheel tread the frequency of rail/wheel contacts are higher, however, the tangential forces are relatively low; these tangential forces are typically in the circumferential direction and are associated with traction and breaking. Also, equal number of stress cycles occur in each rolling direction including similar circumferential forces in each direction as well. Thus, figure 6.47 demonstrates that there is no shearing in this running region; this optical micrograph shows the microstructure near the tread surface in the transverse direction at a position of 6 cm from the non-flange end which is in the running region of the tread of wheel HSR2. Reasons postulated in the literature for the material not showing any shear here are, firstly, that the tangential forces which are usually associated with emanating from traction and breaking are simply insufficient to shear the microstructure [2], and, secondly, it might be probable that any amount of shear induced within the material whilst rolling in one direction is subsequently mitigated by the rolling action of the wheel over the rail in the opposite direction which thus results in a equal and opposite amount of shear and therefore the resultant shear is zero as the shear in both directions is cancelled [17, 18].

Figure 6,48 and 6.49 show the sheared microstructure near the tread surface of wheels HSR1 and HSR2, resepcetively, in the RCF region. Figure 6.50 shows the microstructure near the tread surface of the new wheel HSR3 in the same region of the wheel tread as the RCF regions for the worn wheels HSR1 and HSR2. Figures 6.61 and 6.62 show the sheared microstructure in the field side region near the tread surface of wheel HSR1 at max. run-out and wheel HSR2, respectively, showing minimal or no plastic flow having occured in this region of the wheel treads than in other regions of the treads of these worn wheels investigated, however, the microstructure of these figures do show that there is some difference in the microstriucture of wheel HSR2 than in HSR1 and that a significantly higher level of shear has occurred in the latter than in the former near the tread surface in this region of the treads which is in line with the hardness contour maps for these wheels shown earlier where the hardness is greater for wheel HSR1 than HSR2 in this region and is evinced from he microstructures of the wheel material for these wheels shown in figures 6.61 and 6.62 where the pro-eutectioid ferrite is flattened to a greater extent in wheel HSR1 near the field side than in wheel HSR2 at the same tread position. Figure 6.53 shows the microstructure near the tread surface of the new wheel HSR3 in the field side region; here there appears to be minimal shearing and no plastic flow as well.. The reasons postulated for there being no or minimal plastic flow in the field side region of the railway wheel tread than in other regions of the tread is as follows. The field side region experiences considerably less number of stress cycles than other regions of the tread and therefore the extent of plastic flow that occurs here and the level of hardness in this region of the wheel tread are significantly lower than in other regions of the tread. However, studies conducted utilising the twin-disc test methodology [16] suggest that the level of hardness and shear near the surface of the wheel tread are influenced by the number of stress cycles and that the relatively low amount of stress cycles which the field side region of the tread commonly experiences results in relatively low hardening of the material in this region of the tread.

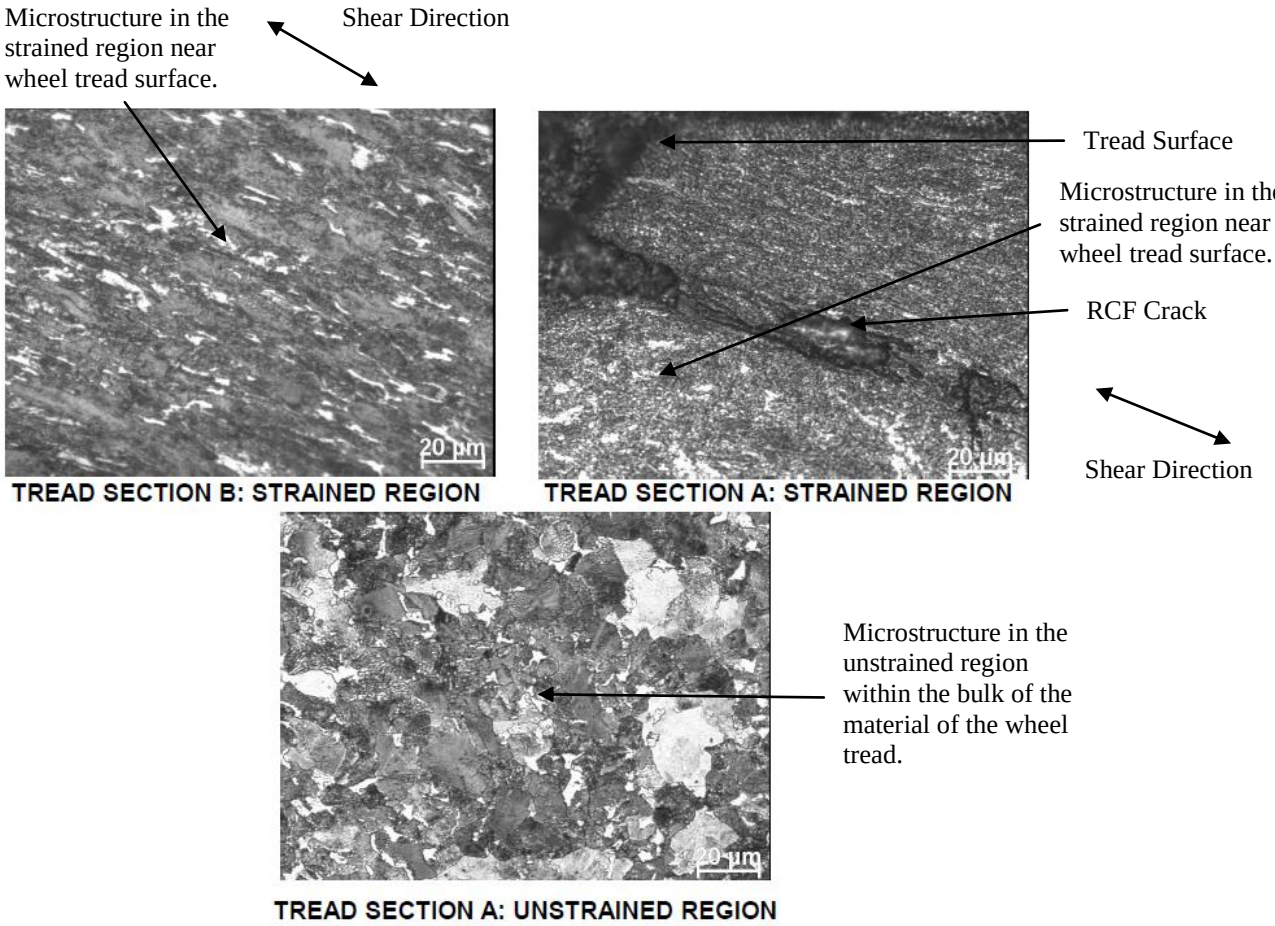

Figure 6.48 shows the strained and unstrained microstructure of the worn railway wheel HSR1 near the tread surface and in the bulk of the material, respectively.

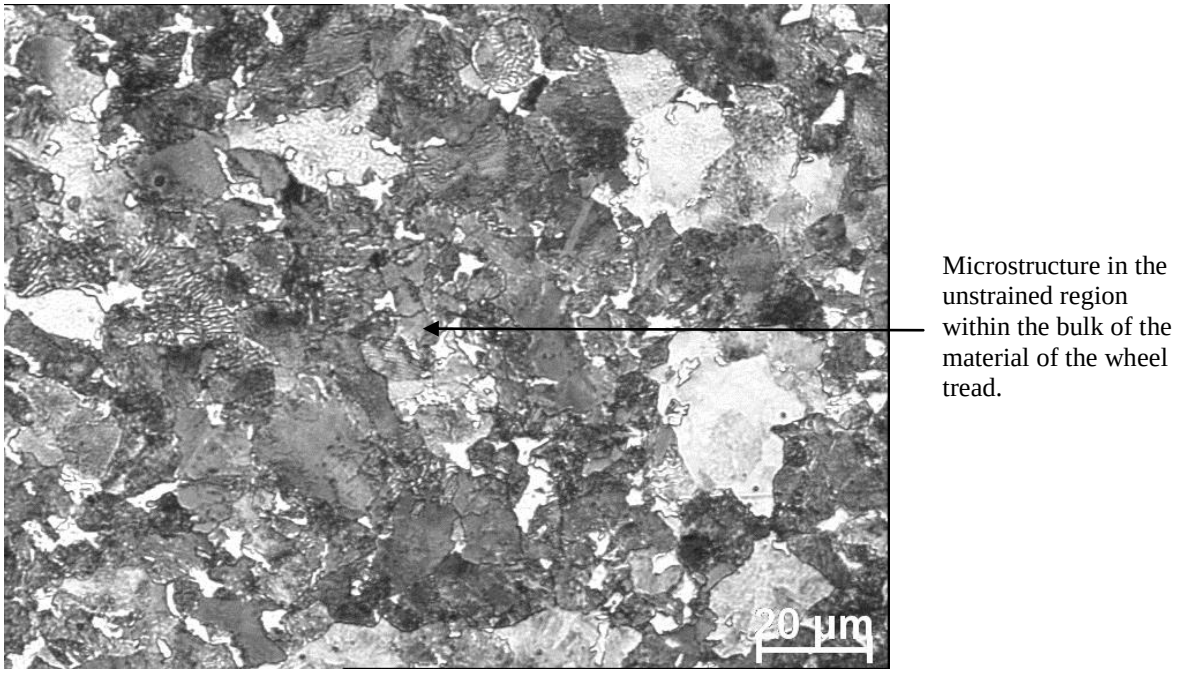

Figure 6.49 Optical micrograph showing the unstrained core matrix away from the tread surface at the minimum run-out position of railway wheel HSR1.

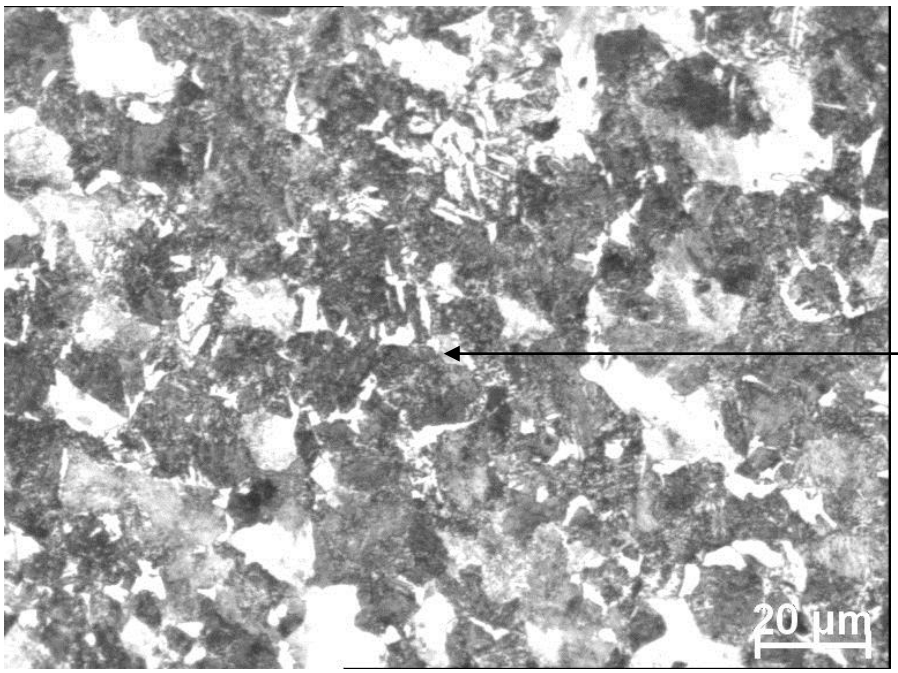

Figure 6.50 Optical micrograph showing the unstrained core matrix away from the tread surface at the maximum run-out position of railway wheel HSR1.

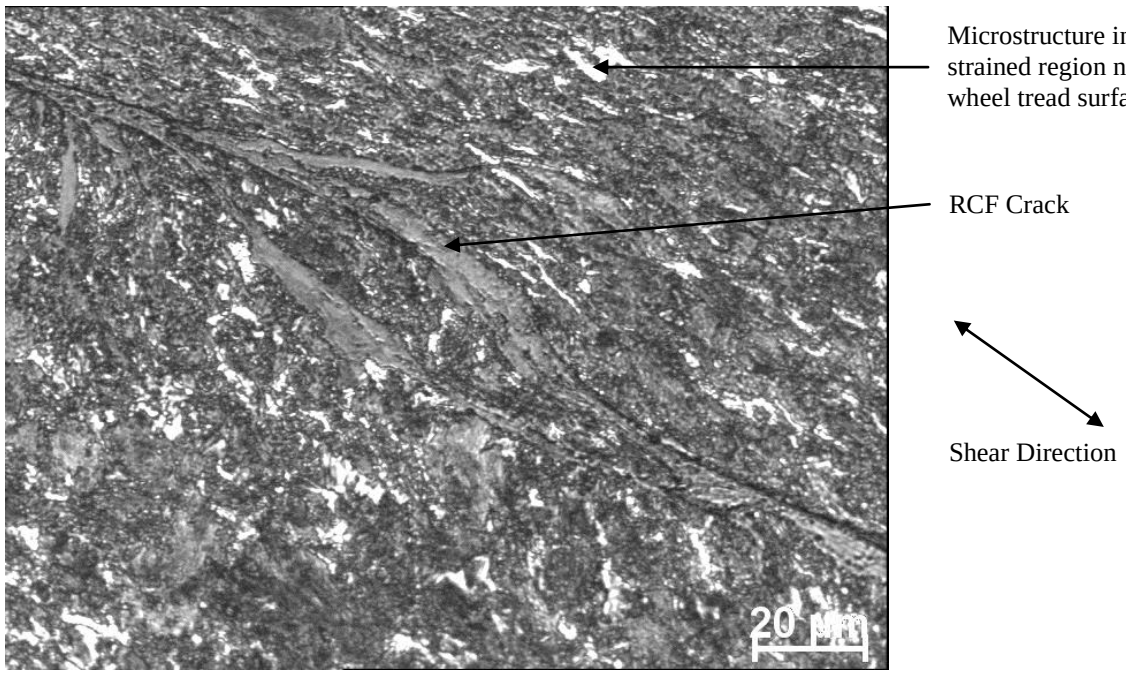

Figure 6.51 Optical micrograph showing an overview of crack and strained matrix at a distance of about 450 μm from the tread surface at the minimum run-out position of railway wheel HSR1.

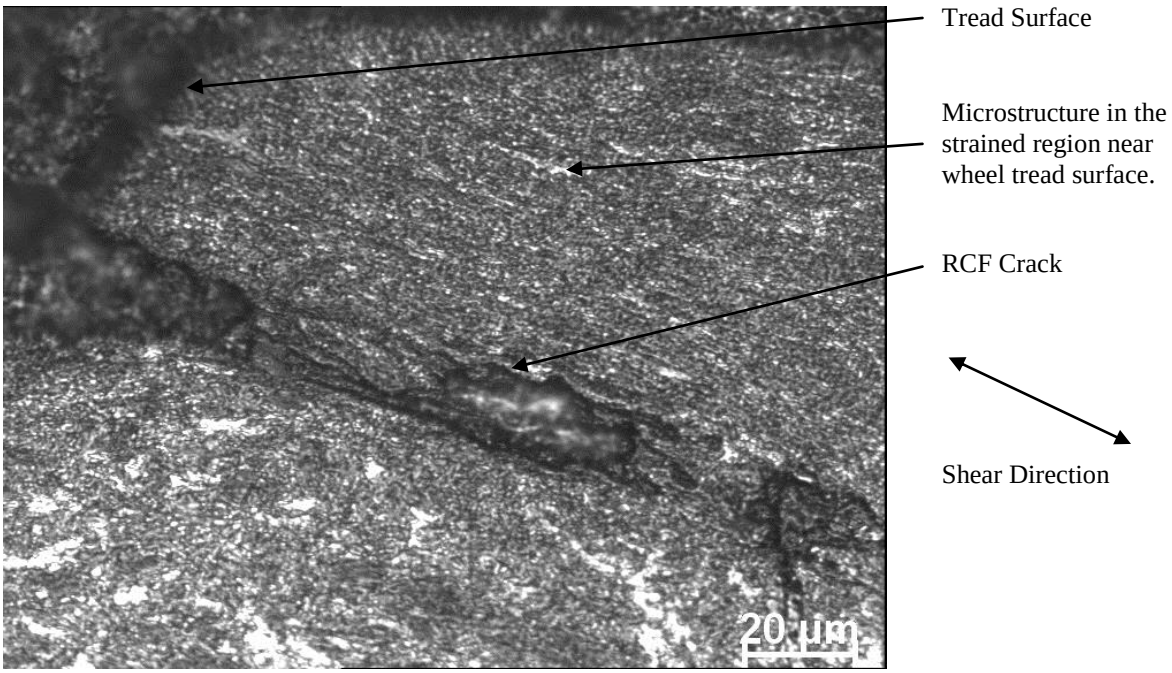

Figure 6.52 Optical micrograph showing an overview of the crack and strain matrix near the tread surface at the minimum run-out position of railway wheel HSR1.

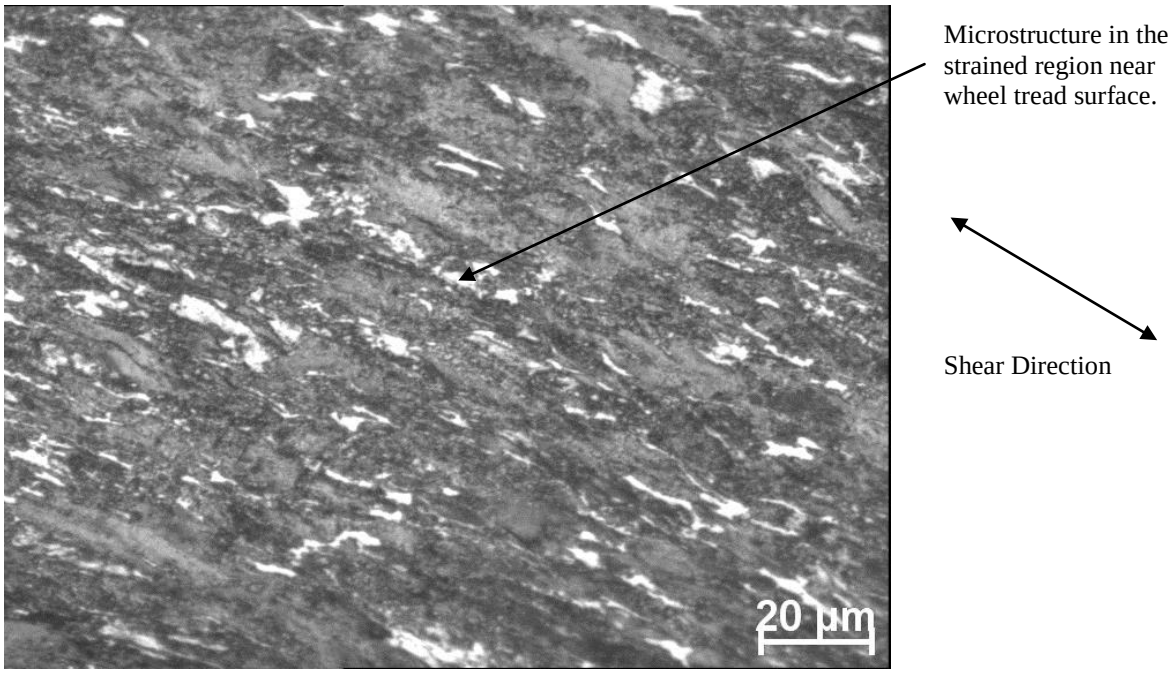

Figure 6.53 Optical micrograph showing an overview of crack and strained matrix at a distance of about 500 μm from the tread surface at the maximum run-out position of railway wheel HSR1.

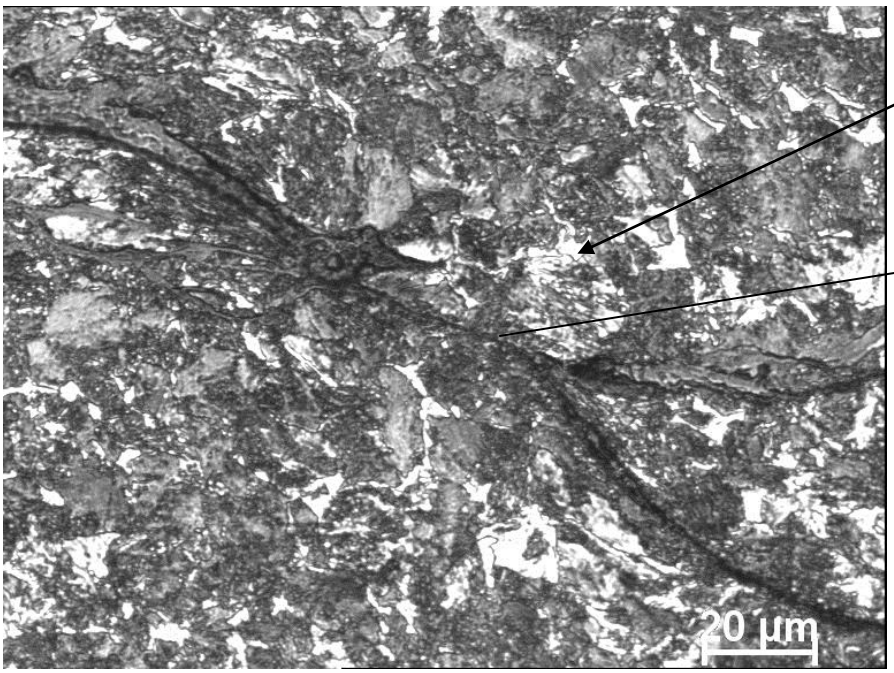

Figure 6.54 The optical micrograph above appears to show that the cracks initiate along pro-eutectoid ferrite at prior austenite grain boundaries at the minimum run-out position of railway wheel HSR1.

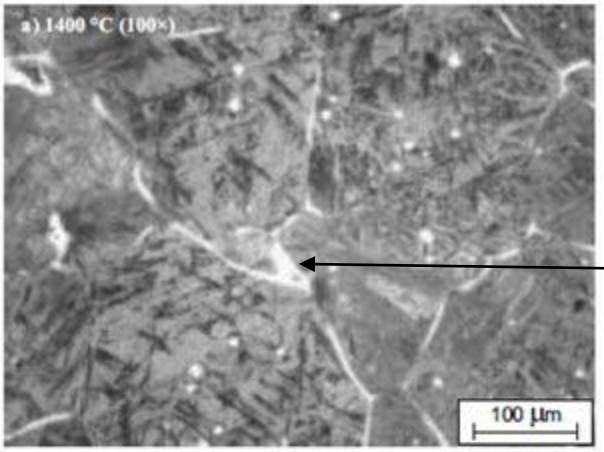

Manganese Sulphide (MnS) Inclusion

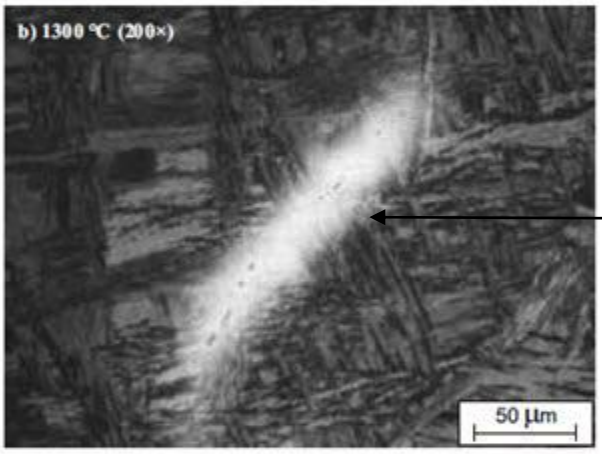

Manganese Sulphide (MnS) inclusion

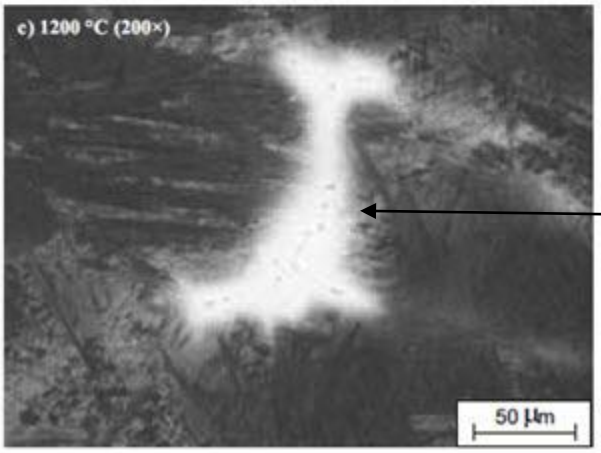

Manganese Sulphide (MnS) inclusion

Figure 6.55 shows the distribution of manganese sulphide (MnS) inclusions in steel at different temperatures (Etching: KLEMM Na2S2O3-K2SO4 x200 (the original of the above photographic image is shown in reference [135] and has been reproduced and appropriately referenced here for the purpose of this PhD thesis).

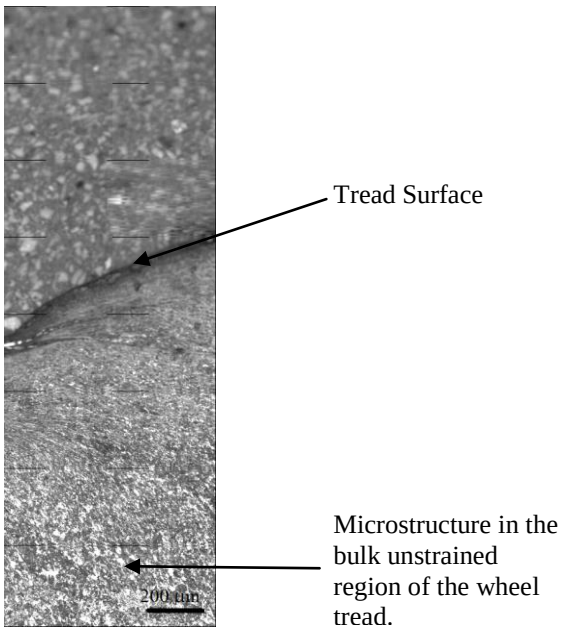

Figure 6.56 shows a low magnification optical micrograph showing the change in the microstructure with depth at a distance of 5.5 cm from the non-flange end of the tread surface of rail wheel HSR1 at the minimum run-out position.

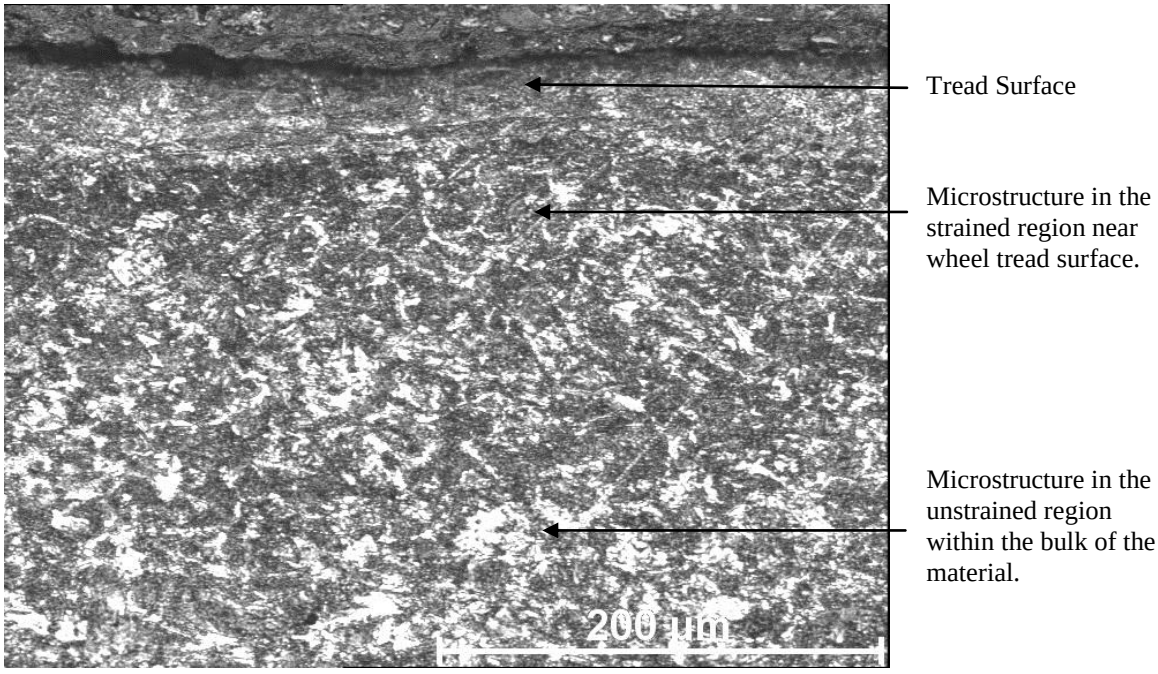

Figure 6.57 shows the microstructure of wheel HSR2 near the tread surface at the running region (image taken at 6 cm from the non-flange end) showing no shearing in this region, as expected due to the reasons discussed above.

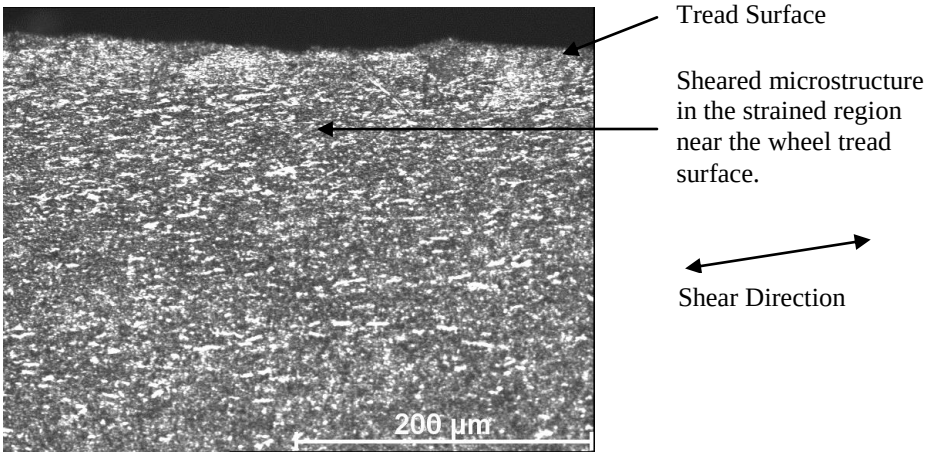

Figure 6.58 shows the sheared microstructure near the tread surface of wheel HSR1 in the RCF region.

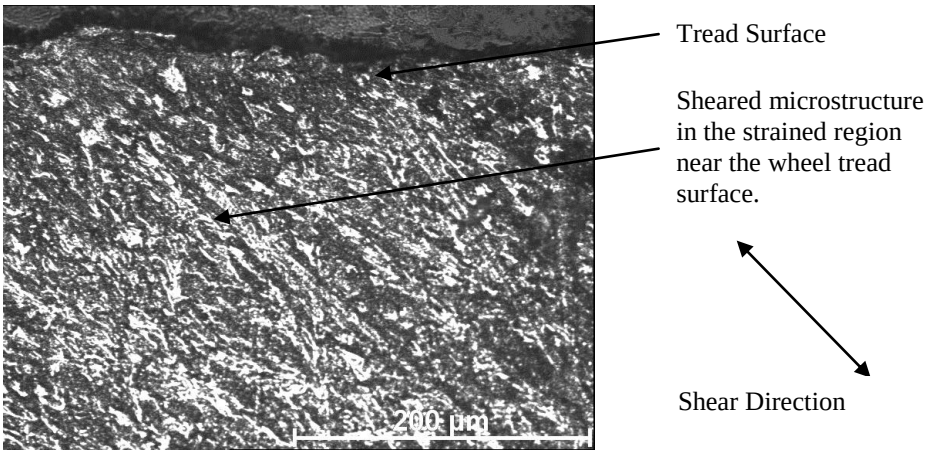

Figure 6.59 shows the sheared microstructure near the tread surface of wheel HSR2 in the RCF region.

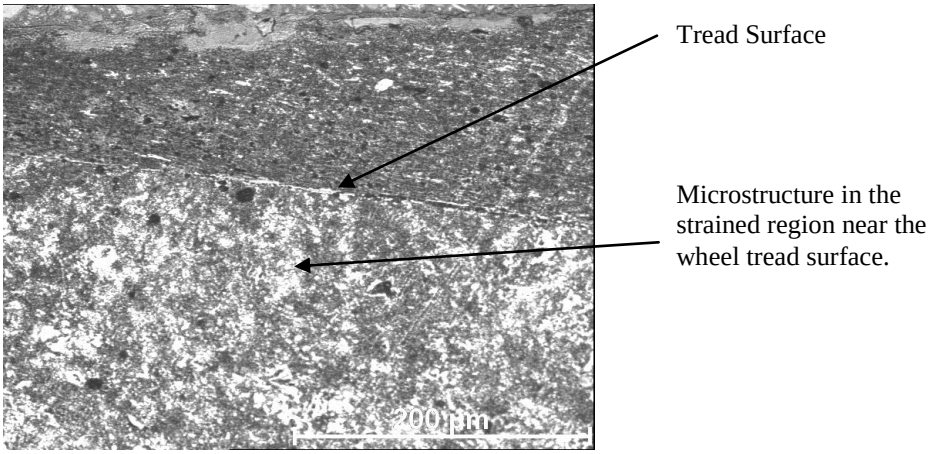

Figure 6.60 shows the microstructure near the tread surface of the new wheel HSR3 in the same region as the RCF region for wheels HSR1 and HSR2.

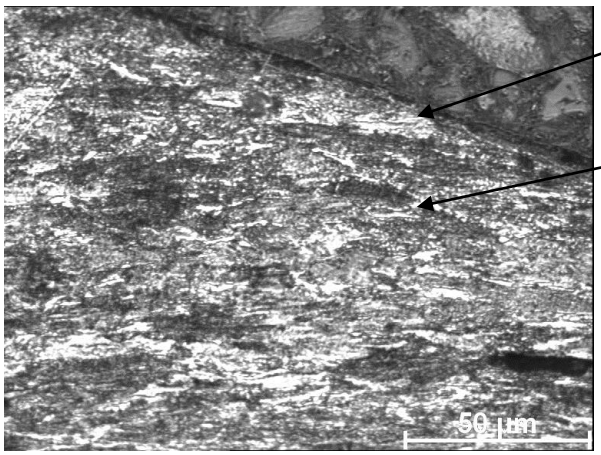

Figure 6.61 shows the sheared microstructure near the tread surface of wheel HSR1 at max. Run-out in the field side region where plastic flow has also been observed in the worn wheels investigated.

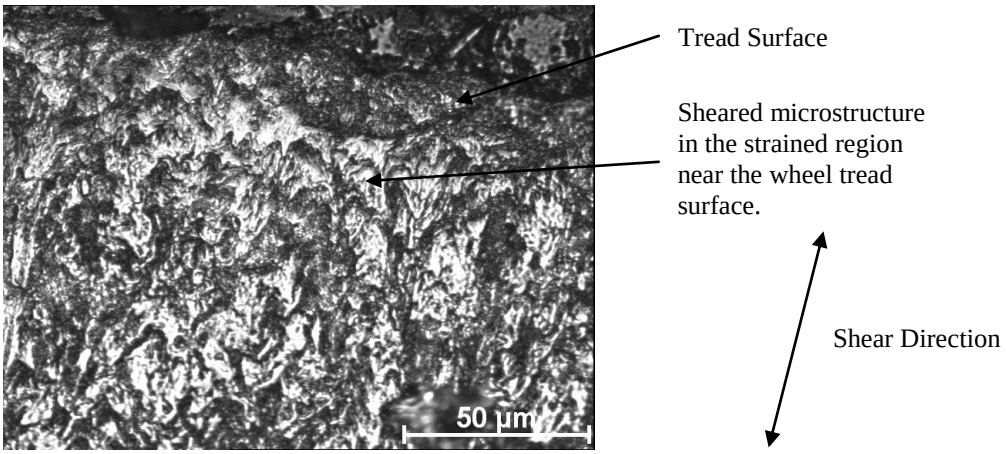

Figure 6.62 shows the sheared microstructure near the tread surface of wheel HSR2 in the field side region demonstrating that plastic flow has occurred in this tread position as expected.

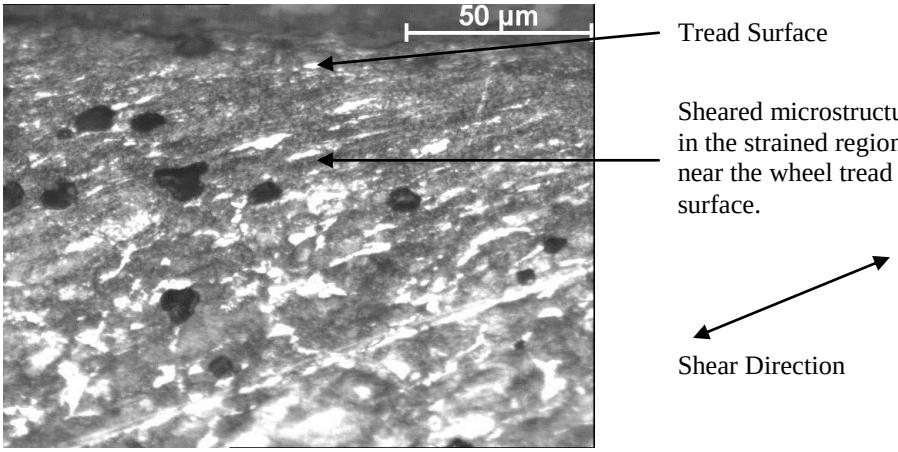

Figure 6.63 shows the sheared microstructure near the tread surface of the new wheel HSR3 in the field side region.

Table 6.7 shows the depth at which microstructural change occurs at different positions from the non-flange edge along the treads of the worn railway wheel HSR1 at the maximum run-out position of the tread and the new railway wheel HSR3.

Tread Position from Non-Flange Edge of Wheel (cm)	Depth of Microstructural Change Below Tread Surface (mm) for Worn Wheel HSR1 at Max. Run-out Position	Depth of Microstructural Change Below Tread Surface (μm) for New Wheel HSR3
1 cm	280 μm	60 μm
2 cm	200 μm	700 μm
3 cm	1510 μm	250 μm
4 cm	400 μm	125 μm
5 cm	1120 μm	117 μm
6 cm	2000 μm	100 μm
7 cm	3000 μm	140 μm
8 cm		1050 μm
9 cm	1000 μm	400 μm
10 cm	380 μm	

6.4 CONCLUSION

Observations made by optical microscopy reveal a greater crack depth (5.5 mm) in the more defective tread segment (position of maximum run-out) than in the less defective tread segment (position of minimum run-out) of the worn HSR1 rail wheel which thus implies a greater depth of hardening at the former tread position than in the latter in this material. In general, two bands of circumferential RCF cracks are found on worn wheel treads; one band of cracks is found near the flange end and the other in the RCF region and close to the field side. Circumferential RCF cracks and fine, closely, spaced shallow RCF cracks are found in the field side and flange root regions of railway wheel HSR2. The work shows that cracks initiate at pro-eutectoid ferrite boundaries and the pro-eutectoid is flattened near the tread surface due to the very high strains and stresses in this region. X-ray tomography in conjunction with reconstruction techniques and also the multi-sectioning in conjunction with optical metallography approach are viable techniques to create 3-D images of cracks

observed in railway wheels removed from service. Furthermore, in general, the hardness values for all wheels investigated decreases sharply with tread depth for approximately 1 mm below the tread surface and then the hardness gradually decreases more slowly with tread depth. The hardness contour maps obtained for all three wheels investigated showing the level of hardness with depth below the tread surface correlate well with the depth below the tread at which the microstructure change, however, the depth of hardening is generally greater than the microstructural change. The higher hardness levels near the tread surface of the worn railway wheels HSR1 and HSR2 near the flange end and field side are most likely due to cornering on curves. The hardness trend observed is likely as a result of changes in the pro-eutectoid ferrite content and changes in lamellar spacing of pearlite. In addition to the correlation between changes in hardness and microstructure with tread depth other factors that contribute to the observed change in hardness with tread depth include the contact stresses and strains imposed on the material during service and the railway wheel manufacturing process employed. This trend would be expected to result in an increased likelihood of the occurrence of RCF-type cracks being initiated toward the end of the lifetime of the railway wheel. This correlates well with observations made of the wheels investigated for this work.

Plastic flow and the shearing of the microstructure of the material occur near the tread surface due to rail/wheel contact which might exceed the yield stress of the unstrained bulk material. As a result, the microstructure in such highly stressed regions near the tread surface of the railway wheels investigated show high levels of shear, thus, resulting in higher hardness values in these regions as a consequence of the presence of high tangential forces at railway curves. Furthermore, as expected, a greater concentration of cracks are found to occur in these regions which thus initiate due to the presence of higher stresses and strains in these regions of the tread, thus, resulting in the detachment of the material from the wheel tread surface due to wear. In addition, the central running region of the railway wheel experiences more frequent rail/wheel contacts than other regions in both running directions; however, the tangential forces are lower in these regions and thus results in a higher level of wear despite not significantly changing the microstructure in these regions of the wheel tread.

CHAPTER 7
ON THE SENSITIVITY AND DETECTABILITY OF THE ACFM TECHNIQUE IN DETECTING AND PREDICTING DEFECT SIZES IN RAILWAY WHEELS

7.1 INTRODUCTION

The work undertaken and presented in this chapter is focused on investigating in a controlled environment, the alternating current field measurement technique (ACFM) signal response to artificially created cracks and crack clusters created in a calibration plate to simulate crack clusters in railway wheels in service and those observed in railway wheels that have approached the end of their operational life and, thus, are subsequently removed from service for reasons of safety. The complex nature of RCF cracks and as a relationship between the surface length of the cracks and their pocket depths has thus far not been found, a planar semi-elliptical shape provides an approximation to their shape, in particular, during the early stages of the growth of RCF cracks, for example, in the case of light to moderate rail cracks [6, 7, 33, 43, 134, 148, 136-144, 158, 159]. Thus, the analysis of the response of the ACFM sensor to such semi-elliptical cracks of a similar size and ellipse ratios found in practice in the UK railway network on rail and rail wheels is appropriate in order to understand and draw meaningful conclusions on the sensitivity of the current ACFM system to be able to detect and size (length and depth) defects of the types and dimensions of RCF-type cracks commonly found in rail and railway wheels including components in service in the railway network. Thus, to this end, the calibration plate identified as: CP_APJ_PHDPROJECT_2013 consisting of artificially created defects (or “notches”) by spark erosion was designed by myself with the appropriate crack sizes (length and depth), crack spacing, crack cluster numbers, crack propagation angles, including the cluster of shallow defects (the control) and the cluster of shallow defects surrounding a more severe and critically deep defect, and then arranged through the department to be manufactured by a local EDM manufacturer for the purposes of my PhD project.

The focus of the study carried out and discussed in this chapter attempts to answer and shed further light, in a controlled environment, on the following:

- Influence of ACFM sensor angle relative to crack surface angle on signal.
- Influence of ACFM sensor lift-off on the signal.
- Influence of the crack propagation angle on the signal.
- Influence of ACFM sensor operational speed on signal.
- Influence crack spacing and the number of cracks within a cluster on signal.
- Influence of ACFM frequency of operation (5 and 50 kHz) on signal.
- Assessing the capability of the ACFM technique to detect a severely critical defect within a cluster of shallow defects as commonly found in railway wheels in service.

To this end, a calibration plate consisting of "notches" has been designed and developed as shown below representing artificial cracks in order to simulate cracks and conditions observed in railway wheels in a controlled environment within the laboratory. These artificially created cracks (or "notches") are of semi-elliptical shapes with crack width of 0.5 mm and crack surface lengths of 10 mm and crack depths ranging from 1.5 mm to 5 mm including propagating angles ranging from 0-90^0 with isolated defects and crack cluster numbers of 2-4 with crack spacing ranging from 5-20 mm as shown in chapter 2 to simulate the early stages of crack growth as observed in rail wheels removed from service since it is found that such cracks are of a semi-elliptical nature in the early stages of their growth in wheels in service. ACFM can be used to detect defects in railway and railway wheel components. As shown in the previous chapter rolling contact fatigue (RCF) type cracks are complex in form due to high wheel/rail contact stresses that result in the contact patch. The artificial defects created by the process of EDM on the steel plate: CB_APJ_PHDPROJECT2013 are less than 20 mm in surface length and, thus, simulate light to moderate RCF-type crack dimensions encountered on the UK Rail Network.

The assessment of the severity of a crack by employing the ACFM technique entails the recording and measurement of changes in the B_x and B_z components of the magnetic flux components of the sensor during operation which thus yields estimates for the crack pocket depth and length, respectively. It is possible to determine the length of a crack by visual inspection and/or by using the change determined in the B_z component of the magnetic flux from the signal, however, this is prone somewhat to

error in the result. A detailed analysis of the theory and principles of operation of the ACFM technique, including signal interpretation, has been provided in chapter 5 and for further reading it would be advisable, for example, to refer to references [6, 7, 33, 43, 117, 118, 132, 134, 147, 148, 136-144, 158, 159]. In order to assess the severity of defects the normalised maximum change in the B_x signal, i.e. $\Delta B_{xmax}/B_{x0}$ and the surface length of the crack need to be determined, where, ΔB_{xmax} and B_{x0} are the observed maximum change in the B_x signal and the background signal, respectively; $\Delta B_{xmax} = B_{xmax} - B_{xmin}$, where B_{xmin} is the minimum of the trace of the B_x signal relative to the background signal B_{x0}. This is a previously verified and established approach which has been successfully modelled on isolated RCF cracks measured experimentally using the ACFM sensor [6, 7, 33, 148]; previous work has shown that crack shapes reconstructed from known calibration crack size and/or data obtained by X-ray tomography (CT) and then modelled using COMSOL multi-physics software has shown that the model can be employed to represent the change in the normalised value of the B_x signal component, i.e. $\Delta B_{xmax}/B_{x0}$, both for artificial defects created in a calibration steel plate and actual cracks found in rails removed from service [6, 7, 33, 148]. Estimates for the crack pocket depths for all railway wheels investigated were calculated using the diagram shown in figure 7.4 below [148] for the purposes of the work carried out on this PhD project. If the surface length of a crack and the normalised maximum change in the B_x component ($\Delta B_{xmax}/B_{x0}$) of the ACFM signal are known it is then possible to use this diagram to determine the appropriate ellipse ratio and thus an estimate for the crack pocket depth.

Amigo ACFM probes were used for the work on this PhD project. ACFM pencil probes, operating at frequencies of 5 and 50 kHz, respectively, developed by TSC Inspection System based in Milton Keynes, United Kingdom. Furthermore, I would like to state here that the 50 kHz ACFM sensor was personally supplied by TSC Inspection Systems for the purposes of my work on my PhD project, which I have presented here in this chapter and in the next chapter, on my personal and direct request made to the company for the purposes of my work on the PhD project.

The ACFM sensor when positioned at zero-lift off is set to be aligned with the position of the sensing coils encapsulated in the probe. For optimum results the orientation of the ACFM sensor relative to the crack angle needs to be such that the

current is made to flow perpendicularly to the surface breaking component of the crack being inspected.

The aim of the work presented here is to investigate rolling contact fatigue (RCF) type cracks in worn rail wheels removed from service using an alternating current field measurement (ACFM) sensor. Modelling in the past thus far, as reported in the literature and to my knowledge, has been mainly focused on regularly shaped cracks, including semi-elliptical defects, and recently some destructive tests have been conducted on cracked worn railway wheels thus yielding further empirical corrections to the currently available sizing models which have subsequently been incorporated in the ACFM walking stick probe system for use on the UK Rail Network [6, 7, 43, 148]. However, research is currently ongoing in this area and recent work has been carried out and reported in the available literature on investigating the relationship between the ACFM signal and RCF defects in rails and rail wheels employing a finite element analysis (FEA) method [6, 7, 117, 132, 147, 148]. In [148] a study has been carried out using COMSOL Multiphysics software in order to develop a finite element method (FEM) model to model the response of the ACFM sensor to both idealised artificial and actual cracks in rail and rail wheels. It is reported by these authors that the model allows for both irregular types of cracks catering for a broad spectrum of shapes and sizes (i.e. crack pocket and surface lengths) including cracks which might overlap each other to be accurately assessed. Their study also focused on making comparisons between idealised elliptical shaped cracks and real RCF crack shapes which are rather of a more complex nature in terms of their shape and size and this was done for light to moderate RCF These studies are ongoing in order to understand the complex issue of correlating and thus finding a relationship between the ACFM signal response to actual cracks, with complex shapes and morphologies, that are commonly found in rail and rail wheels Thus, to this end, the current work on this PhD project has attempted to further investigate the ACFM signal response to actual cracks found in railway wheels removed from service and thus ascertain a correlation between the ACFM signal and RCF cracks by conducting in-depth investigations using the ACFM sensor on artificial cracks created in a calibration steel plate. This is to simulate actual cracks that are commonly found in rail wheels. In addition, a further in-depth complementary study has been carried out employing the ACFM sensor on detecting RCF cracks found in railway wheels removed from service in order to

compare and contrast the results obtained from these two investigations. Furthermore, cracks in the study conducted by the authors in the cited references: [6, 7, 43, 148] do not appear to have assessed cracks of pocket depths less than 4 mm [148]. Therefore, the work carried out for the purposes of this PhD project and presented in this chapter and in the previous chapter is aimed at attempting to understand and correlate the ACFM signal response to actual complex surface breaking RCF cracks found in railway wheels removed from service and modelling the ACFM signal response to artificially created defects in a steel calibration plate that simulates cracks and crack clusters found in railway wheels removed from service, respectively. ACFM is capable of detecting and sizing defects through various types of coatings including rust and paint and the influence of different types of coatings on the surface of railway components on ACFM signal including the principles of operation of the ACFM system have already been discussed in chapter 5 of this PhD thesis and can further be found in the literature [6, 7, 33, 43, 134, 148, 136-144, 158, 159].

In line with the previous work carried out and presented in reference [148] where the authors have stated that they have determined estimates for crack pocket depths of RCF type cracks found in rail and rail wheels by using the diagram which is shown in this chapter as figure 7.4 estimates for the crack pocket depths for all railway wheels investigated for the purposes of the current work were calculated using the diagram shown in figure 7.4. This shows the normalised maximum change in B_x value against crack surface length at zero lift-off for semi-elliptical cracks of elliptical ratios 1:1, 1.25:1, 1.5:1 and 1.75:1. The diagram is based on Network Rail UK (formerly Railtrack) visual length-depth guidance diagram for RCF cracks (modified from Railtrack manual) [148]. Figure 7.4 shows plots for each semi-ellipse with their particular elliptical ratios where the maximum change in the normalised B_x value, i.e. B_{xmax}/B_{x0} is plotted against the surface length of the crack. It can be seen from the curves that initially the values for $\Delta B_{xmax}/B_{x0}$ increase more linearly and steeply with crack surface length for each of the four elliptical ratios chosen for investigation. Therefore, this suggests that the ACFM is clearly capable of differentiating between cracks of different sizes with cracks that have pocket lengths within this region of the curves. Therefore, this suggests that the ACFM system is able to accurately quantify and size such cracks that are classified as light to moderate according to the UK Network Rail guidance diagram (figure 7.4). As a result, for a crack with a known

surface length and a corresponding normalised B_x signal, it is possible to use figure 7.4 in order to determine an estimate for the crack pocket length that is based on the elliptical ratio that best fits the value for the maximum change in the normalised B_x signal (i.e. B_{xmax}/B_{x0}).

Thus, the UK Network Rail guidance diagram shown below (figure 7.4) has been used for the purposes of the work carried out on this PhD project, and presented in this chapter on railway wheels removed from service, to determine estimates for the crack pocket depths. Therefore, if the surface length of a crack and the normalised maximum change in the B_x component ($\Delta B_{xmax}/B_{x0}$) of the ACFM signal are known it is then possible to use this diagram to determine the appropriate ellipse ratio and thus an estimate for the crack pocket depth. Therefore, in the case of the calibration plates shown in figures 7.1 and 7.2 below estimates for the crack pocket depths (D_{EST}) for the artificial cracks (i.e. "notches") by using the ACFM technique were evaluated first by reading off an estimate for the crack surface length (SL_{EST}) using the curve in figure 7.4 corresponding to the ellipse ratio of 1.75:1 as this is the curve in this figure which has the closest ellipse ratio to all the artificial defects in both calibration plates presented that all have an actual ellipse ratio of 2:1. Then, from this estimate of the crack surface length (SL_{EST}) the estimate for the crack depth is given by:

$$D_{EST} = SL_{EST}/2$$

Finally, in order to ascertain the percentage discrepancy in the result obtained by using the ACFM technique and thus determine whether the result is accurate, oversized or undersized, a comparison is made of the estimated defect size, i.e. calculated pocket depth (D_{EST}) by using the ACFM system and the actual defect depth. Furthermore, as shown by the results in this chapter, in the event that the actual surface lengths of the cracks are unknown, as in the case of wheels in service, this diagram can be used to determine the range of possible crack pocket depths for cracks observed in rail wheels in service by measuring the ACFM signal response to these cracks and/or crack clusters and by using the diagram to then determine the range of possible surface lengths for such cracks based on the possible four ellipse ratio curves provided on the diagram. Then from the result obtained for the range of possible crack surface lengths and by using the four ellipse ratios presented in the Network Rail

diagram corresponding to their respective four surface lengths obtained from the normalised ACFM B_{xmax} signal value it is then possible to evaluate the range of possible crack pocket depths corresponding to the ACFM signal obtained for the crack or crack cluster, including a minimum, maximum and average possible estimates for the crack pocket depth to determine these estimates. This is based on the RCF-type cracks of different surface lengths and ellipse ratios and their corresponding normalised values for the ACFM B_x signal response to these cracks found on the UK Rail Network and thus used to determine estimates for the crack pocket depths in this work. These results are then correlated to the actual depth for cracks determined at the appropriate tread positions on the appropriate railway wheel from optical metallography results that are shown in the previous chapter and also comparing these results with the crack pocket depths as obtained using x-ray tomography in conjunction with reconstruction techniques including by using the other method of determining 3-D crack shapes using the multi-sectioning in conjunction with optical metallography approach, as also shown in the previous chapter. This is what has been done to determine estimates for the cracks found in the treads of the wheels investigated for the work presented here as, for example, the results shown in table 7.4 in section 7.3.2 (below). However, it should be noted that the method of determining the crack pocket depth using the model described above can only provide an estimate for the crack pocket depth and not the actual depth of the crack which will depend on the angle of propagation of such cracks [6].

The regular monitoring and recording of cracks in rail wheel treads is of utmost importance and, as such, a necessary requirement for maintenance purposes in the railway industry to ensure the continued safety and integrity of the railway infrastructure, track and vehicles and, thus, ensure safe and reliable travel for the satisfaction of passengers with comfort. Thus, in so doing, this helps to maintain a record of RCF cracks in wheel treads as regards their size (length and depth) and shapes in order to subsequently employ appropriate maintenance procedures to rectify and mitigate the occurrence of potential rolling contact fatigue damage that may arise on the wheel tread during the lifetime of the railway wheels in service conditions. As a result, the Railway Group Standard (GM/RT2466, Issue: Three, Date: February 2010) [208] has stipulated the following strategy in regard to the monitoring and recording of cracks and the agreed strategy that is currently in place and thus

employed and acted upon in the British railway industry in order to deal with railway wheels that may be encountered during service which have RCF cracks present in the wheel tread. The maintenance criteria are derived from the safe operating experience of wheelsets that are designed and manufactured to the British Rail (BR) bogie and suspension section (BASS) design codes and the associated British Standards that operate on the BR network. It is stipulated in the above standard that in the event that any cracks which may be found in the transition between the tread and rim, on the outside face of the rim, in the flange or in any roll-over then the wheelset shall immediately be removed from service. However, any move that may be made to a repair facility shall be at a speed restricted to 40 mile/hr or less that does not exceed 45 mile/hr. In the case of multiple small cracks being found on the wheel tread and one of the cracks exceeds 40 mm in length then the wheelset is required to be removed from service within 24 hours of the fault being identified. Furthermore, in the case of an isolated crack that is longer than 30 mm in length being found in the tread it is mandatory that the vehicle is removed from service immediately. However, where an isolated crack that is longer than 20 mm is found in the tread then the wheelset is required to be removed from service within 24 hours of the fault being located within a 24 hour period of the fault being found. However, according to the above standard there are no limits that are currently set for permissible cracks for wheelsets which are designed and manufactured to any other design codes rather than BASS design codes. Therefore, it is recommended by the above standard that limits shall be derived by comparison with the limits that are set for wheelsets which are designed to BASS design codes, taking into consideration the specific characteristics of the wheelset concerned. Furthermore, the wheelset is also required to be removed from service within 24 hours of either of the following faults related to the presence of wheel tread cavities are found:

i. The presence of any single cavity which is greater than 15 mm long circumferentially around the wheel.
ii. The presence of any two cavities that are separated by less than 50 mm and having a total length which is in excess of 15 mm circumferentially around the wheel.

7.2 MATERIALS AND EXPERIMENTAL TECHNIQUES

The calibration plate identified as CP_APJ_PHDPROJECT_2013 used for the purposes of the work presented in this chapter is shown in chapter 3. Information concerning the cracks and their dimensions are shown in these figures including the dimensions for the surface length, propagation depth (or so-called pocket depth), propagation angle, crack spacing and crack cluster number for all artificial defects (or notches) created by the EDM process on this steel calibration plate; all these defects are of width 0.5 mm. Also, the diagram for the calibration plate identified as CP_2 used initially for preliminary investigations for the purposes of the work presented in this chapter can be found in chapter 3. Information on the cracks (or notches) found on this plate including their dimensions are provided on this diagram.

ACFM measurements were carried out using an Amigo instrument developed by TSC Inspection Systems (UK). Two ACFM probes with different operating frequencies of 5 and 50 kHz were used for the present study including the work discussed in the next chapter. The measurements were carried out with the ACFM probe oriented parallel to the crack to ensure that the current flow is perpendicular to the length of the crack [6, 148]. Measurements were made at zero lift off (pencil probe touching the wheel surface) and at different positions along the tread surface from the non-flange end (the "tread position" refers to the distance from the non-flange edge for the worn HSR1 and HSR2 rail wheels removed from service and the new rail wheel segments which act as a control. At least four scans were made at each tread position for all the rail wheels investigated and the results are found to be reproducible.

7.2.1 CALIBRATION PLATES TO SIMULATE CRACKS OBSERVED IN RAILWAY WHEELS REMOVED FROM SERVICE

Calibration Plate: CP_APJ_PHDPROJECT_2013

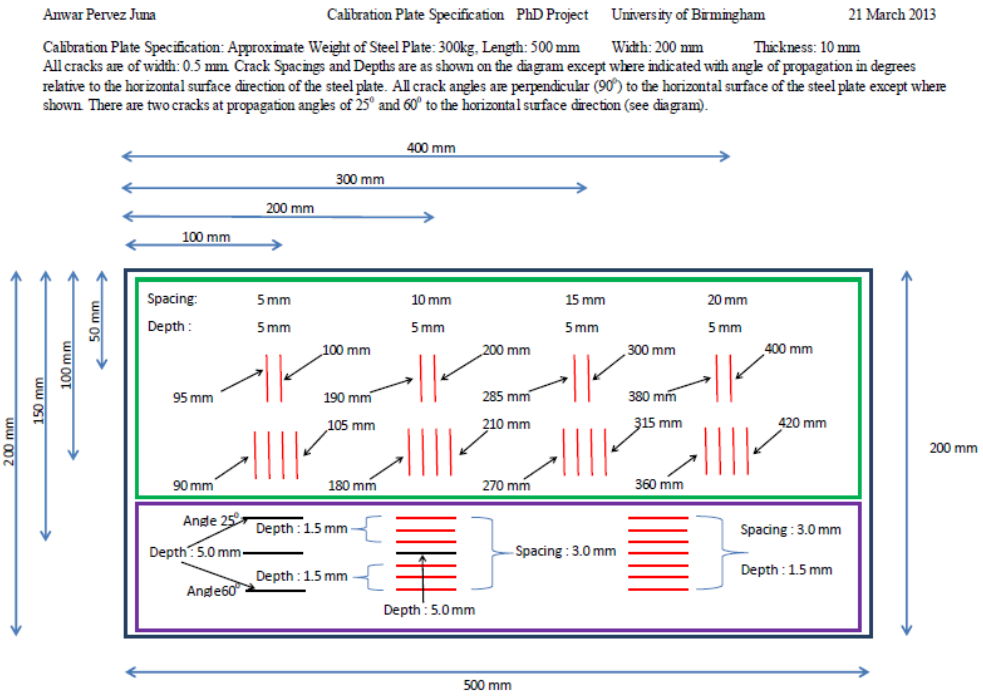

Figure 7.1 shows the steel calibration plate with artificially created cracks and crack clusters to simulate crack clusters found in railway wheels in service for the purposes of the experiments designed and work presented in this chapter.

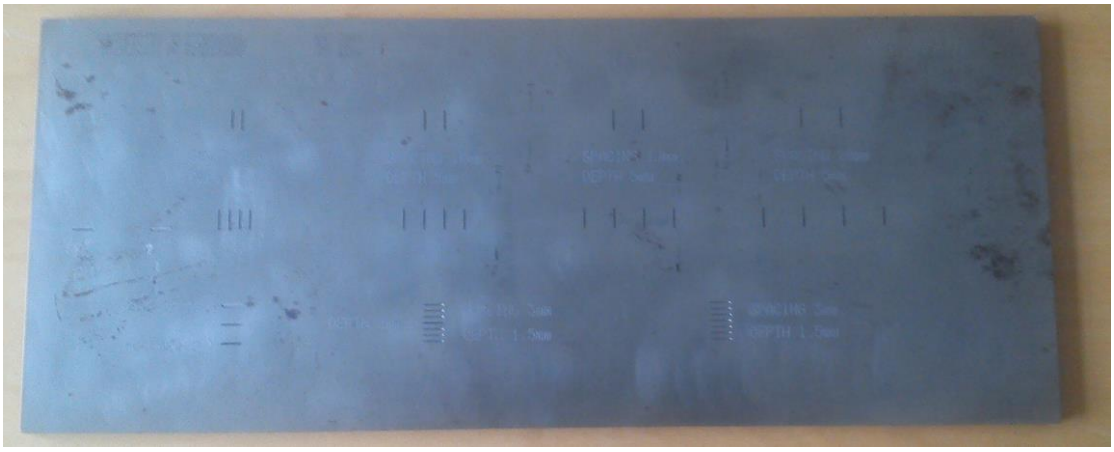

Figure 7.2 a digital photograph showing the steel calibration plate: CP_APJ_PHDPROJECT_2013.

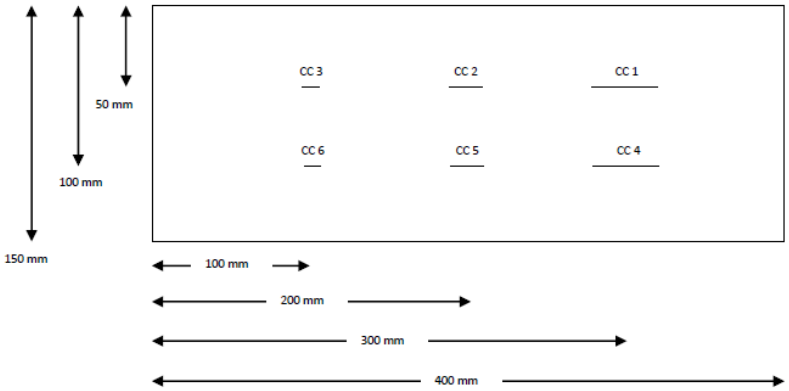

Calibration Crack ID	Crack Type and Dimensions
Crack 1 (CC1)	10 x 5 mm semi-elliptical
Crack 2 (CC2)	5 x 2.5 mm semi-elliptical
Crack 3 (CC3)	2 x 1 mm semi-elliptical
Crack 4 (CC4)	10 x 5 mm rectangular
Crack 5 (CC5)	5 x 2.5 mm rectangular
Crack 6 (CC6)	2 x 1 mm rectangular

Figure 7.3 shows a schematic diagram for calibration plate: CP_2 including the dimensions and type of artificial cracks (or notches) found on the calibration plate.

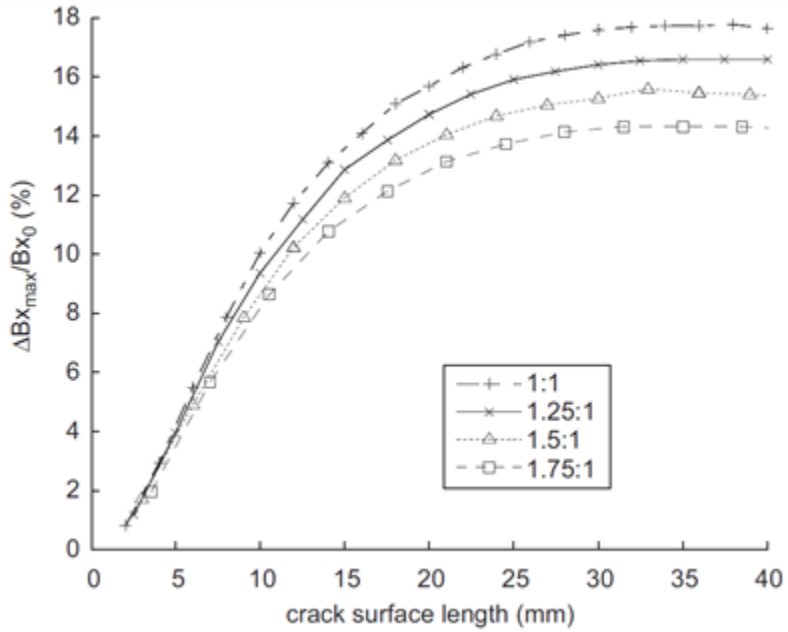

Figure 7.4 shows the normalised maximum change in B_x value against crack surface length at zero lift-off for semi-elliptical cracks of elliptical ratios 1:1, 1.25:1, 1.5:1 and 1.75:1; the diagram is based on Network Rail UK (formerly Railtrack) visual length-depth guidance diagram for RCF cracks (modified from Railtrack manual) [148]. Thus the above diagram has been used for the purposes of the work carried out on this PhD project, and presented in this chapter on railway wheels removed from service, to determine estimates for the crack pocket depths.

Furthermore, for the work presented below on railway wheels HSR1, HSR2 and HSR3 removed from service that have different levels of tread damage which were shown and discussed at length in the previous chapter the ACFM measurements were carried out using an Amigo instrument developed by TSC Inspection Systems (UK) with two probes operating at different frequencies of 5 and 50 kHz. The measurements were carried out with the ACFM probe oriented parallel to the crack to ensure that the current flow is perpendicular to the length of the crack and thus obtain optimum signal to detect and size cracks [6, 148]. Measurements were made at zero lift off (pencil probe touching the wheel surface) and at different positions along the tread surface from the non-flange end ("tread position" refers to the distance from the non-flange edge of the wheel) for the worn standard high-speed rail wheel removed from service and the new rail wheel segments which act as a control. At least four scans were made at each tread position (1 cm apart) and for all rail wheel regions for the three wheels which were investigated as part of this study and the results are found to be reproducible.

7.2.2 ALTERNATING CURRENT FIELD MEASUREMENT (ACFM) TECHNIQUE

The theory, concept and electromagnetic principles of the ACFM technique have been discussed at length earlier in chapters 4 and 5 and, thus, the same ground will not be covered here, however, the standard operating procedure for the ACFM technique is as follows. The ACFM unit is connected to the computer via a communication cable which is attached to the connector on the front panel of the system. The portable computer consists of an internal battery and thus can be used remotely, however, the system can be operated on 110/240 V AC (50/60 Hz) through a mains pack and/or a battery charger. After connecting all the appropriate leads to the ACFM system and the computer including the mains switch on the mains supply to the lead. Then, press the "reset" button and verify that the "red" indicator is on. Next, press the "test" button to remove the "red" indicator. Once again press the "reset" button in order to re-activate the "red" indicator and confirm that the indicating light remains on. Then select the appropriate probe for the scans to be conducted and connect the probe to the ACFM system and create a directory in order to store the inspection data. Connect the probe to the instrument and select the correct probe configuration. Then create a new data file via the "function check data file" option. Next, position the ACFM probe on

the material under inspection and start the scan and the data collection process. The data should be displayed in a similar manner to that shown below which has been reproduced here from chapter 5 to make it easier for the reader. Finally, save the data files to be subsequently analysed. Refer to the TSC operational manual for the ACFM system for further details [114].

During inspection the ACFM system software records and displays the results obtained from the B_x and B_z sensors. The defect is indicated by the distinct traces generated by the B_x and B_z signals. The B_x signal component shows a trough which is related to the defect depth: the larger the trough the deeper the defect. Analysis of the B_x signal is used to determine the depth of a defect by reference to a mathematical model which relates the observed deviation in the B_x signal to crack depth. As a consequence, no prior calibration of the system is required. The shape of the B_z signal, which includes a peak and a trough, indicates the position of the defect along and across the area of the material under inspection, thus the surface length of the crack is determined. The alternating current does not penetrate deep into the material but is maintained in a very thin skin (approximately <0.2 mm deep depending on the material and frequency of operation) in the surface of the material under investigation and is thus unaffected by the overall geometry of the component [34-37].

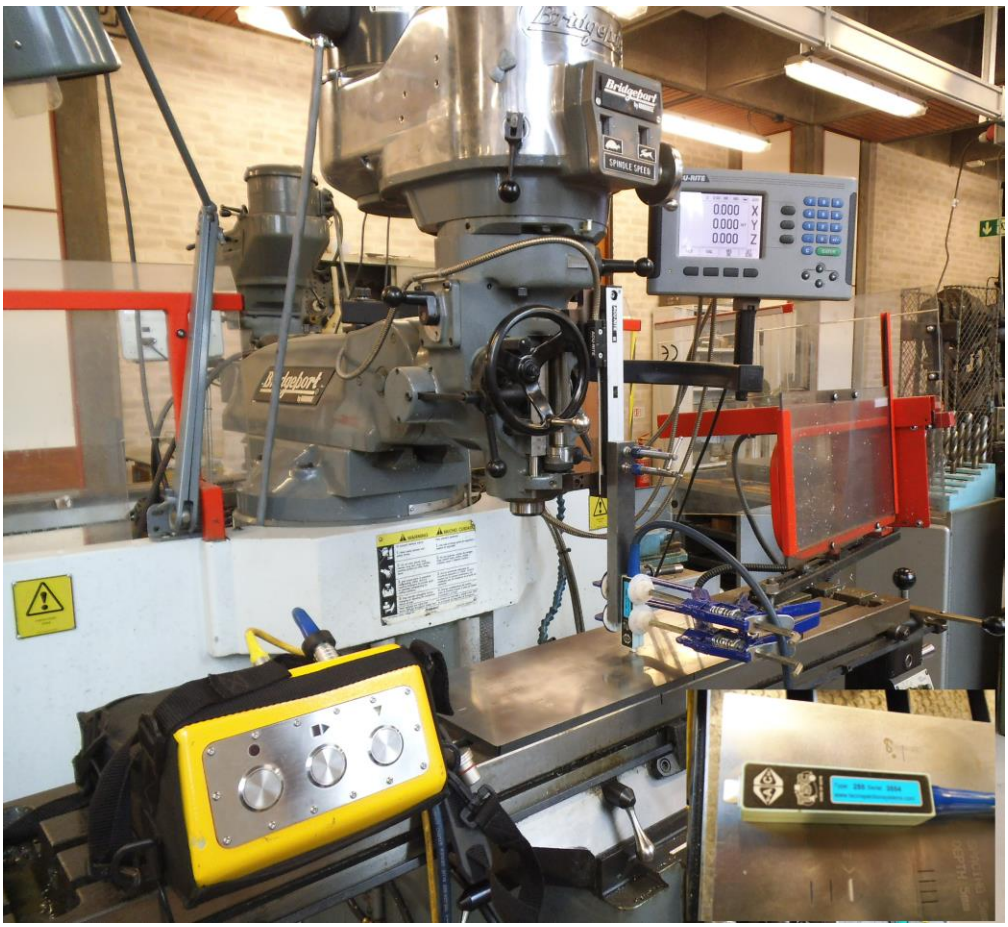

Figure 7.5 a digital photograph showing the ACFM system in the bottom left hand corner of the above image together with the probe (inset in the bottom right hand corner of the image).

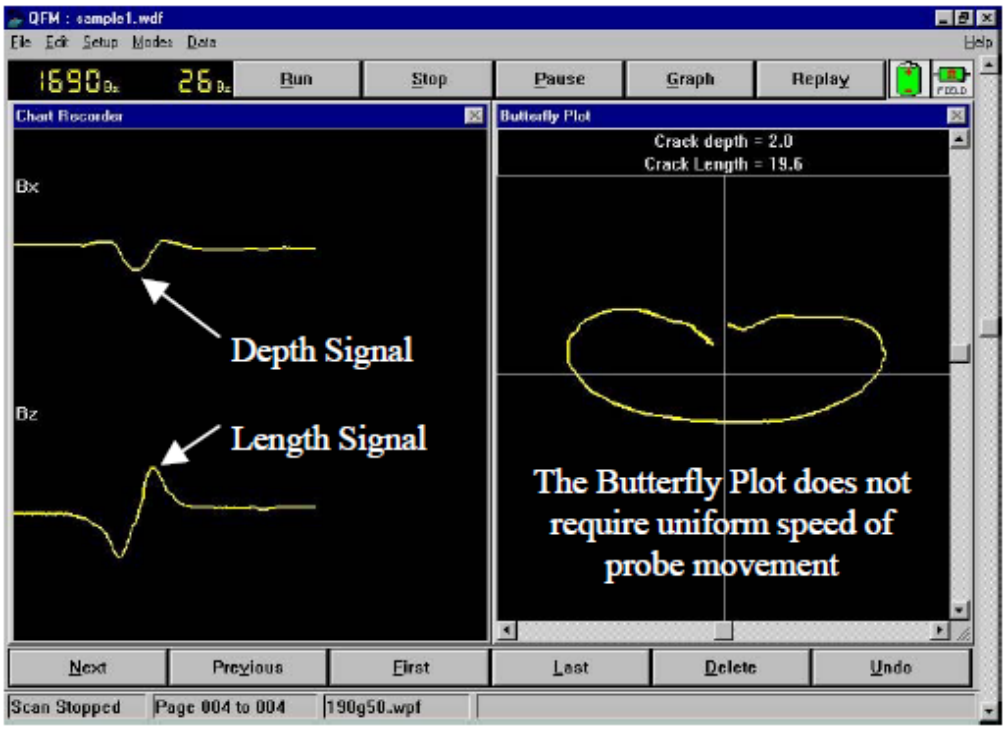

Figure 7.6 shows an image of the ACFM defect indication data screen showing a typical ACFM sensor response to the presence of a defect in the material under inspection [118].

7.2.3 MAGNETIC PARTICLE INSPECTION (MPI)

The magnetic particle inspection (MPI) method is a widely used as a non-destructive technique in various industries that is a fast, efficient and user friendly, inspection method utilised for the detection of defects in ferromagnetic materials. The system employs magnetic fields in conjunction with very small magnetic particles in order to detect defects in materials. The concept behind the MPI technique is that the material under inspection is initially magnetised and in the event that there is a crack present on and/or near the surface the defect will thus result in a leakage field [100-102]. Once the component has been magnetised then iron particles are applied onto the surface of the material's magnetised part under test either in a dry or wet suspended state by a sprinkling or spraying method. Consequently, the particles will be attracted and cluster at the flux leakage fields, thus forming a visible indication that can be inspected and analysed.

Figure 7.7 a digital photograph showing the magnetic particle inspection (MPI) system.

7.3 RESULTS AND DISCUSSION

7.3.1 FACTORS AFFECTING ACFM SENSOR SIGNAL RESPONSE TO CRACKS

7.3.1.1 INFLUENCE OF ACFM SENSOR ANGLE RELATIVE TO CRACK SURFACE ANGLE AND CRACK PROPAGATION ANGLE ON ACFM SIGNAL

As RCF cracks may grow at various angles relative to the rail or wheel running direction it is of utmost importance to assess the influence of a mismatch between the crack and probe angle; hence, the reason for conducting the present study. Furthermore, for the purposes of the model in reference [148], as discussed above and in more depth in chapter 5, the assumptions that are made by the authors in [148] include that the rail or wheel (i.e. high carbon steel materials, for example rail 260 grade) has a relative permeability (μ_0) and an electrical conductivity (σ) of 50 and $5x10^6$ S/m, respectively. These values are based on the microstructure for near fully pearlitic steel material.

The influence of changes in the ACFM probe angle relative to the crack surface angles, discussed here, and variations in sensor lift-off, as discussed in the next section, on the signal response and, thus, sensitivity of the ACFM sensor are investigated as part of this work and the results and salient points arising from this study are presented in this chapter, as these would be very important considerations to take on board when designing and developing systems that are based on fixed sensor and/or high speed industrial applications to be effectively utilised in the UK Rail Network. Also, it is reported in the literature that the magnitude of the change in the B_x signal relative to the background signal B_0 is sensitive to any mismatch between the optimum angle of the sensor relative to the crack [6, 7, 148]

The ACFM system is capable of detecting defects presented in any orientation relative to the crack surface angle, however, the signal strength is significantly influenced by the orientation of the ACFM sensor relative to the crack surface angle and as the results in figure 7.8 for the probe positioned parallel and at 45^0 to the crack surface angle, respectively, demonstrate, the $\Delta B_{xmax}/B_{x0}$ value and thus the strength of the signal is optimum and greatest when the ACFM sensor is aligned and scanned parallel to the defect under inspection across its centre and in a direction parallel to the

running direction of the wheel/rail, i.e. positioned at 0^0 relative to the crack surface angle; at this probe orientation relative to the crack angle the ac current induced by the ACFM probe within the thin layer of the material containing the crack under inspection is made to flow in a perpendicular direction to the surface breaking component of the crack. However, as a result of the ACFM sensor angle relative to the crack angle being changed from the optimal angle of 0^0 and thus becoming offset the current flowing beneath the crack is significantly reduced and thus flows more easily across the face of the crack. As a result, the normalised value in the signal strength, determined by the normalised value of the maximum change in B_{xmax} (i.e. $\Delta B_{xmax}/B_{x0}$), decreases with increasing offset as shown by these results in agreement with former studies [7, 148]. In addition, in reference [7] it is reported that as a result of an offset angle of $+/-25^0$ the value of $\Delta B_{xmax}/B_{x0}$ does not correspond directly to above the mid-point of the crack but instead this results in two local minimum B_x/B_{x0} values to either side of the crack. As a result, at offset angles which are greater than $+/-25^0$ a double trough is observed in the B_x signal rather than the single trough that is typically observed for crack and probe angles that are closely matched. In line with their work the present work conducted for the purposes of this PhD project has also demonstrated this effect. Furthermore, the authors in reference [7] have demonstrated that as a result of offset angles greater than 25^0 such a geometry yields an asymmetrical presentation of $\Delta B_{xmax}/B_{x0}$ values, i.e. an offset angle of -25^0 yields a different (lower) $\Delta B_{xmax}/B_{x0}$ value to that of an offset value of $+25^0$. It is also stated in [7] that for probe offset angles of $+/-10^0$ the subsequent change in $\Delta B_{xmax}/B_{x0}$ values is relatively small. Therefore, the different offset angles will produce different values and, thus, different magnitudes of errors in the estimated crack pocket lengths as compared to the actual crack depths and, thus, these findings need to be taken into consideration when sizing cracks using the ACFM technique. Furthermore, this phenomenon is particularly important for non-handled ACFM systems in which case the ACFM sensors are mounted in a carrier and, as a result, the angles of the sensors are fixed relative to the running direction of the rail/wheel. In addition, RCF cracks can occur at various angles to the rail/wheel running direction and these can range between about $30\text{-}75^0$ as have been reported in the literature and have been observed for rail [151-153,156,157]. As a result, for fixed angle ACFM probes it is in general reasonable to assume that an offset angle of the order of at least $+/-15^0$ can occur. In this regard, it should be noted that at present the ACFM walking stick that is

accredited for use on the UK rail network [158] including the ACFM probes that are currently attached to inspection trains that are currently being investigated and developed as part of the INTERAIL project [147,159] are at present mounted at fixed angles. RCF cracks are formed on railway wheels due to the wheel running on the low rail in a curve in a direction perpendicular to the resultant of the longitudinal and tangential forces that act on the wheel at curves. As a result, different angles of presentation of cracks are observed on the wheel tread surface and that are usually found to be between 30^0 and 60^0 [148]. These different presentations of crack angles are dependent upon various factors, such as, the wheel profile, bogie primary yaw stiffness and the curvature of the rail [160]. As shown in the previous chapter and in agreement with similar studies reported in the literature [161,162] RCF cracks in railway wheels are usually found to occur in two different bands located at specific regions across the wheel tread. These are comprised of cracks that are oriented at an angle of approximately 60^0 to the running surface in a band which is near the flange end that lies at a position of approximately 50 mm from the back of the flange and also much smaller cracks that are almost circumferentially oriented in a band that is found to be closest to the non-flange end of the railway wheel (i.e. near the end of the wheel) and is approximately 80-100 mm from the back of the flange [161,162]. Furthermore, at present the EU Superail project is attempting to develop an ACFM array probe for wheelset inspection. However, even though the benefits provided by the large uniform field that is created by the array system and, thus, the greater coverage and, as a result, the faster inspection of the wheel running surface, must be considered together with bearing in mind and addressing the potential that currently exists between the probe and crack angles; as this is an important issue that needs to be addressed in order to accurately size cracks. To this end, an automated robotic ACFM system is currently being developed that allows the probe to be moved and rotated in a controlled manner. The primary aim of this automated system is to address the issue of changing RCF crack horizontal angle. A fine grid of scans is conducted over a known RCF crack and the software that is built into the system then uses the B_z component of the signal to determine the crack angle [7,159]. Using this method a maximum error in the detection of the crack angle of 13.2^0 is reported in the literature and, thus, this will significantly affect the ability of the system to accurately size cracks, bearing in mind that the extent of the mismatch between the ACFM probe and

the angle of the crack would not be known beforehand by the system's in-built software [116]: Saferail, EU Collaborative Project [147,159,166].

Furthermore, during growth the cracks extend in surface length, however, no correlation between the surface length and pocket depth for such cracks has thus far been found and therefore the search is still on and research in this area needs to continue to find a relationship between the above parameters for RCF cracks present in rail and rail wheels. As a result, surface length measurements of such cracks cannot be used to determine whether the crack has become severe enough to be classified as critical and, thus, warranty special measures to be undertaken to address this issue. To my knowledge no relationship has been reported in the literature to relate the B_x signal to the crack depth based on the crack length; as the relationship will depend on the crack shape. The existing methods use either complex signal inversion algorithms, for example, using a neural network approach or by reference to a database containing different crack geometries that relate the B_x signal to the depth profile for a crack surface length [6, 7, 136-144, 148, 158, 159]; these former studies have demonstrated that the accuracy of the data will be influenced by the spacing between the ACFM scan lines. The above authors [7] have also reported that the signal will be affected by the ACFM probe angle by the variation in signal to noise ratio. Therefore, the probe angle needs to be maintained at the crack surface angle to obtain maximum field perturbations, thus leading to an optimisation of the signal to noise ratio. Furthermore, in line with my work presented here, the results presented by these authors do not show any clear indication of multiple cracks they have also reported that as there is no differentiation of the separate cracks, crack surface length and angle gives significant error.

The propagation angle of RCF cracks in rail materials reported in the literature [104, 150-155] to initially lie between $10\text{-}30^0$ and the crack is deemed to propagate in the direction of motion. Therefore, as the depth of propagation of a crack is dependent upon the vertical angle of the crack, in order to evaluate the crack's depth it is necessary to ascertain the propagation angle of the crack by using an alternative method or, alternatively, an appropriate assumption needs to be made. As discussed in the previous chapter RCF cracks occur in rails and rail wheels due to high stresses experienced by the material during service; and these cracks are complex in shape and

initially, typically, grow at a relatively shallow angle into the material until they reach a critical depth (for rails this depth is beyond about 5 mm [7]), after which they turn and, then, potentially grow to a critical size and, eventually, lead to detrimental and dangerous break in the railway wheel material which can have major safety implications and lead to disastrous consequences. Thus, the early detection of damage caused rolling contact fatigue on rail and railway wheels is of utmost importance. Furthermore, as shown by the results in figures 7.9 and 7.10 and table 7.2 on the influence of the angle of propagation of cracks on ACFM signal the crack propagation angle does significantly affect the ACFM signal and yields higher normalised maximum B_x change values relative to the background signal which would, as a result, significantly influence the estimated measurements for the crack pocket depth and length, for propagation angles greater than 25^0; these normalised values are highest and optimum for propagation angles of 60 and 90^0 which therefore demonstrates that the ACFM sensor is most sensitive to cracks that propagate at higher angles between 60-90^0 in contrast to shallow angles of propagation of about 25^0 and less. Therefore, the results obtained from the work presented here are in contrast to previous studies in this area and reported in the literature [6, 7, 148] where it is reported by these authors that the propagation angles of cracks between 5^0 and 90^0 do not affect the ACFM signal, whereas, the work presented here clearly shows that the angle of propagation of cracks in the material significantly influences the normalised maximum change in the B_x ACFM signal and, thus, this work suggests that it is of utmost importance that the angle of propagation of cracks in the material need to be taken into consideration in order to accurately size the cracks. The results obtained from this study show that the ACFM sensor operating at a frequency of 50 kHz provides good estimates for the crack pocket depth for a crack propagation angle of 25^0 and under sizes the crack by 10%, whereas, the sensor at this frequency of operation significantly over sizes the crack by 70% for crack propagation angles of 60^0 and 90^0. Whereas, the ACFM sensor operating at a lower frequency of 5 kHz provides accurate estimates for the crack pocket depths for crack propagation angles between 60^0 and 90^0 but also provides a reasonable estimate for the crack pocket depth at a propagation angle of 25^0 and under sizes the crack depth by 40%. Therefore, these results show that the correlation between the ACFM signal and crack propagation angle is different from that previously reported in the literature [6, 7, 148] where it is stated that crack propagation angle has not been found to affect the ACFM

signal response (i.e. B_x and B_z signal components) to cracks which is contrary to the findings from the current work presented in this chapter as these results show that the signal is significantly affected by the crack propagation angle.

In general, the current understanding, as reported in the literature [27], is that one of the primary requirements in order to be able to successfully detect defects using electromagnetic non-destructive methods in ferromagnetic materials is that a magnetic field which is induced in the part being tested must intercept the defect at a 45 to 90^0 angle. Therefore, defects that are normal (90^0) relative to the magnetic field will produce the strongest and, thus, optimum indications as in such an orientation the flaws would disrupt more of the magnetic flux. This is in line with the work carried out on this PhD project and the results presented in this chapter on the influence of crack propagation angle on the ACFM signal strength where it is shown here that the optimum and, thus, high signal is obtained when the crack propagation angle exceeds 25^0 and is at 60-90^0, i.e. at high propagation angles. Therefore, for the proper inspection of components by electromagnetic non-destructive means it is important to be able to establish a magnetic field in at least two directions.

In line with previous studies the work presented in this chapter demonstrates that the ACFM system is capable of accurately sizing and is thus appropriate for RCF cracks that are classified as light to moderate in the degree of severity according to the UK Network Rail guidance diagram and that can be assumed to be semi-elliptical in shape and have not turned down into the material (i.e. propagation angles between 10-30^0) and where the corresponding B_x signal of the ACFM is significantly affected by changes in crack pocket length.

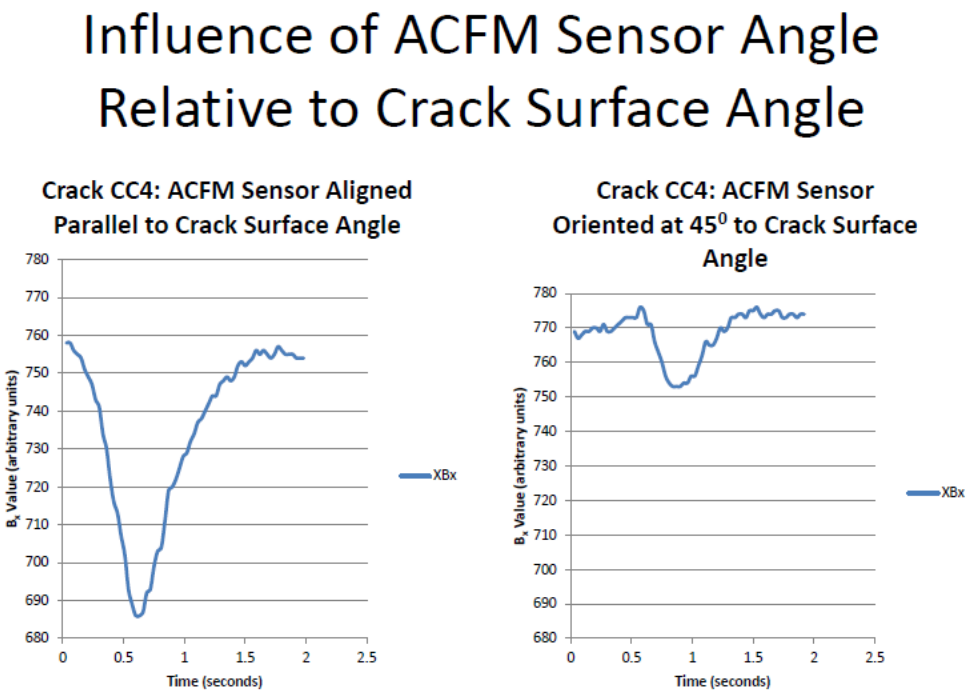

Figure 7.8 shows the influence of ACFM sensor angle relative to crack surface angle.

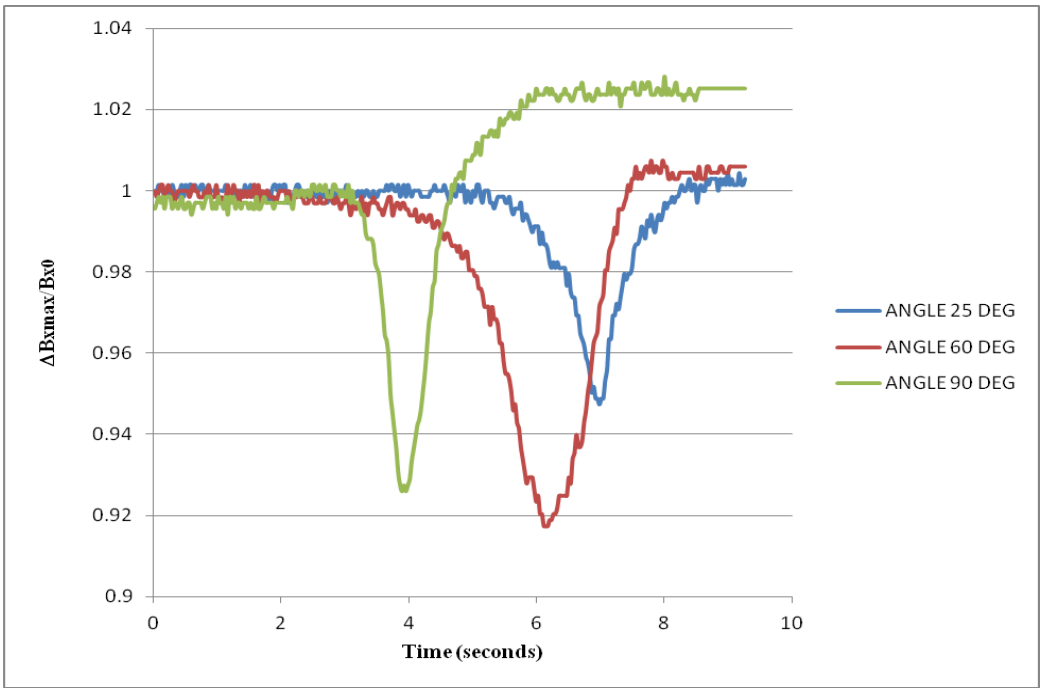

Figure 7.9 Influence of crack propagation angle (between 25 and 90^0) on ACFM (5 kHz) signal response to isolated semi-elliptical artificial cracks of surface length and pocket depth of 10 mm and 5 mm, respectively.

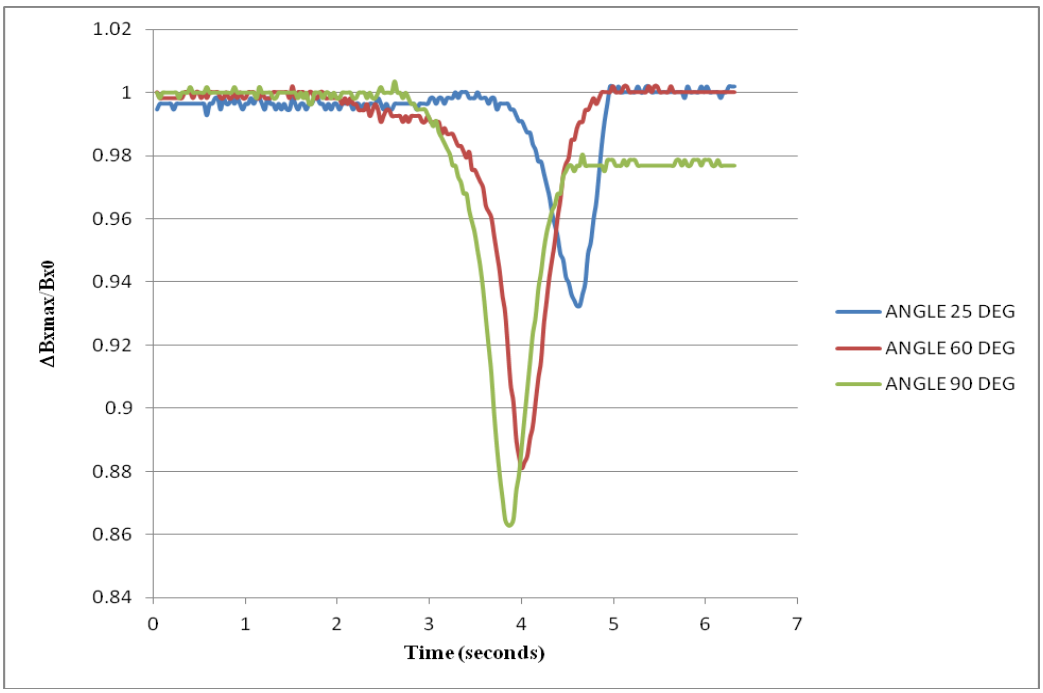

Figure 7.10 Influence of crack propagation angle (between 25 and 90^0) on ACFM (50 kHz) signal response to isolated semi-elliptical artificial cracks of surface length and pocket depth of 10 mm and 5 mm, respectively.

Table 7.1 shows the mean maximum change in the ACFM signal (ΔB_{xmax}) for each calibration crack in the calibration steel plate CP_2; the ACFM scans across these artificial defects are shown in Appendix B in the appendices chapter 9.

Calibration Crack ID	Crack Type and Dimensions	Mean Maximum Change in ACFM B_x Signal (ΔB_{xmax}) / Normalised Value (N)
Crack 1 (CC1)	10 x 5 mm semi-elliptical	ΔB_{xmax}: 70 / N: 0.091 (9.1%) for sensor aligned parallel to the crack surface angle. ΔB_{xmax}: 35 / N: 0.045 (4.5%) for sensor oriented at angle of 45^0 to the crack surface angle.
Crack 2 (CC2)	5 x 2.5 mm semi-elliptical	ΔB_{xmax}: 35 / N: 0.045 (4.5%) for sensor parallel to crack surface angle. ΔB_{xmax}: 15 / N: 0.019 (1.9%) for sensor oriented at angle of 45^0 to the crack surface angle.
Crack 3 (CC3)	2 x 1 mm semi-elliptical	ACFM sensor not sensitive enough to identify or distinguish between cracks within experimental uncertainty due to the large scatter in the observed data with the sensor either aligned parallel or oriented at an angle of 45^0 to the crack surface angle.
Crack 4 (CC4)	10 x 5 mm rectangular	ΔB_{xmax}: 70 / N: 0.091 (9.1%) for sensor aligned parallel to the crack surface angle. ΔB_{xmax}: 20 / N: 0.026 (2.6%) for sensor oriented at angle of 45^0 to the crack surface angle.
Crack 5 (CC5)	5 x 2.5 mm rectangular	ΔB_{xmax}: 35 / N: 0.045 (4.5%) for sensor aligned parallel to the crack surface angle.

		ΔB_{xmax}: 15 / N: 0.019 (1.9%) for sensor oriented at angle of 45^0 to the crack surface angle.
Crack 6 (CC6)	2 x 1 mm rectangular	ACFM sensor not sensitive enough to identify, or distinguish between, cracks within experimental uncertainty due to the large scatter in the observed data with the sensor either aligned parallel or oriented at an angle of 45^0 to the crack surface angle.

Table 7.2 shows the normalised Mean $\Delta B_{xmax}/B_{x0}$ values for the ACFM sensor signal response for cracks of surface length and pocket depth of 10 mm and 5 mm, respectively, and for propagation angles of 25^0, 60^0 and 90^0, and for ACFM operating frequencies of 5 and 50 kHz.

Crack Propagation Angle	ACFM: 5 kHz Mean $\Delta B_{xmax}/B_{x0}$ Value	ACFM: 50 kHz Mean $\Delta B_{xmax}/B_{x0}$ Value
25^0	0.05 (5.0%)	0.065 (6.5%)
60^0	0.08 (8.0%)	0.12 (12.0%)
90^0	0.08 (8.0%)	0.12 (12.0%)

Table 7.3 shows the comparison of estimated crack pocket depths (D_{EST}), using figure 7.4, with the actual crack depth (i.e. oversized or undersized (%)), for the ACFM sensor signal response for cracks of surface length and pocket depth of 10 mm and 5 mm, respectively, and for propagation angles of 25^0, 60^0 and 90^0, and for ACFM operating frequencies of 5 and 50 kHz.

Inducing Frequency (kHz)	Crack Propagation Angle	Mean $\Delta B_{Xmax}/B_{x0}$ Value	Estimated Surface Length (SL_{EST}) (mm)	Estimated Crack Pocket Depth (D_{EST}) (mm)	Comparison of D_{EST} with Actual Crack Depth: Oversized or Undersized (%)
5 kHz	25^0	0.05 (5.0%)	6.0 mm	3.0 mm	Undersized: 40.0%
5 kHz	60^0	0.08 (8.0%)	10.0 mm	5.0 mm	Accurate D_{EST}
5 kHz	90^0	0.08 (8.0%)	10.0 mm	5.0 mm	Accurate D_{EST}
50 kHz	25^0	0.07 (7.0%)	9.0 mm	4.5 mm	Undersized: 10.0%
50 kHz	60^0	0.12 (12.0%)	17.0 mm	8.5 mm	Oversized: 70.0%
50 kHz	90^0	0.12 (12.0%)	17.0 mm	8.5 mm	Oversized: 70.0%

7.3.1.2 INFLUENCE OF ACFM SENSOR LIFT-OFF AND OPERATIONAL SPEED ON ACFM SIGNAL

Another important factor that needs to be considered when deploying the ACFM technique especially for high-speed applications such as in the case of the proposed INTERAIL integrated inspection system [147,159], is the variation in the probe lift-off which will have a significant influence on the accurate sizing of cracks. Therefore, even though the ACFM technique fares better than the eddy current sensors in this regard as the signal's strength decreases with the square of the lift-off distance in contrast to the cube of the lift-off as in the case of the eddy current sensors and, thus, the ACFM system is relatively insensitive to variations in lift-off, this parameter must be taken into consideration and, thus, quantified in order to correctly determine crack estimates. Although, this does not rank that high in terms of being critical for low-speed applications such as in the case of hand held ACFM inspection systems, for example, the ACFM walking stick system including the automated ACFM robotic system currently under development where controlling variations in lift-off is relatively simple.

The sensitivity of the ACFM sensor to lift-off is important in determining the size of cracks in terms of their length and depths as it is reported in the literature [6, 7, 148] that the sensitivity of the ACFM signal response to defects decreases with increasing lift-off. Therefore, in order to assess the sensitivity of the present ACFM system to variations in lift-off of the probe above the material under investigation experiments were carried out on the calibration plate denoted as CP_APJ_PHDPROJECT_2013 using the ACFM probe operating at 5 kHz and 50 kHz, i.e. low and high frequencies to also investigate the influence of operating frequency on the ACFM signal response to cracks, and the results are presented in figures 7.11 and 7.12 below for scans carried out using the ACFM sensor at operating frequencies of 5 kHz and 50 kHz, respectively, at lift-offs between 0-5 mm across a cluster of four semi-elliptical cracks each of surface length 10 mm and depth 5 mm (elliptical ratio: 2:1) with the ACFM probe positioned parallel to the surface angle of the cracks for attaining optimum signal strength.

These results show that the normalised $\Delta B_{xmax}/B_{x0}$ decreases significantly with lift-off. The results also show that the background signal significantly increases with lift-

off which has not been previously observed and/or reported, to my knowledge, in the literature. The decrease in the change in $\Delta B_{xmax}/B_{x0}$ values with lift-off for this cluster of cracks scanned using the ACFM sensor operating at frequencies of 5 kHz and 50 kHz are shown in table 5.1 below. As can be seen the percentage decrease in the normalised $\Delta B_{xmax}/B_{x0}$ values is also slightly but significantly greater for the probe operating at a higher frequency of 50 kHz. Thus the results are in agreement with the general trend reported in the literature on the variation of the ACFM signal response to defects with variations in probe lift-off [6, 7, 148]. As a result, a significant decrease in the ACFM signal response to cracks with increasing lift-off is observed as shown by the decrease in the $\Delta B_{xmax}/B_{x0}$ with lift-off values obtained from this experiment. These results become critical for high speed applications, for example, in the case of the high speed deployment in the Inter-rail integrated inspection system [6, 7, 148, 211-216] where some degree of variation in lift-off is expected due to the occurrence of high g-force when the ACFM system is attached to a train for inspection purposes. Whereas, in low speed ACFM inspection applications, as in the case of the present hand held ACFM sensor used for the purposes of this PhD project and in the case of other ACFM systems such as the walking stick and the automated robotic ACFM systems [7], one can control the lift-off of the probe with much ease; furthermore, the results presented in this work show that the accuracy between the results obtained using the hand held probe in conjunction with the rail network normalised $\Delta B_{xmax}/B_{x0}$ versus surface length diagram for different semi-elliptical cracks of various elliptical ratios and the actual crack pocket depths (depth 5 mm for the artificial cracks created in calibration plate CP_2) are closer in value to the actual crack depths and therefore match better to the actual values than the accuracy reported by using the automated robotic ACFM system as shown by the lower percentage mismatch in these results obtained using the hand held ACFM probe in contrast to the mismatch in the results from similar experiments reported in the literature [6, 7, 148] using the automated robotic ACFM system, as would be expected as one would naturally have more control over the handling of the probe when it is hand held in contrast to the automated ACFM system which would follow a single path over the rail or rail wheel under inspection and therefore the fluctuation in lift-off would be expected to be greater, whereas, in the case of the hand held probe one can follow the contour of the rail wheel and/or rail more closely, thus, limiting the fluctuation and thus variability in lift-off that might otherwise occur.

The results in figure 7.11 and 7.12 also show that defects can still be detected at a lift-off of 5 mm above the surface of the material under inspection, although the signal strength is significantly depleted; the strength of the signal is higher for the ACFM operating at the higher frequency of 50 kHz. This is in agreement with similar work carried out using a 5 kHz ACFM sensor reported in the literature [6, 7, 148] where it is stated that defects can be detected at this lift-off position. Even though the ACFM signal strength and response to cracks decreases with the square of the lift-off, in contrast to eddy-current sensors where the signal strength decreases with the cube of lift-off, and thus is relatively less sensitive to lift-off variations than eddy-current sensors, the variation in the signal strength with lift-off is, nevertheless, an important factor to take on board when considering estimating the size of defects as this factor will significantly affect the estimations of the size of cracks using the appropriate crack sizing algorithms. Furthermore, it is reported in the literature [43, 86, 88, 117, 132, 159] on work carried out on similar systems that the data obtained at different inspection speeds and at a constant probe lift-off of 0.8 mm demonstrated that there is no change in the signal's amplitude or in its level of noise within the inspection speed range investigated during the tests; their work also showed, which is in agreement with my work presented in this chapter, that the probe lift-off during the inspection procedure is an important factor which must be controlled and, thus, taken into consideration during the inspection process in order to quantify RCF cracks correctly. Therefore, in principle, the work presented here shows that any possible lift-off variations during inspection may be inferred and evaluated by determining the decrease in the sensor's signal strength which is in agreement with previous work conducted on similar systems [43, 86, 88, 117, 132, 159]. Furthermore, even though appropriate high–speed inspection experiments could not be carried out using the current ACFM probe for the purpose of the PhD project due to the fact that the inspection system used for this study is inappropriate for inspections other than for slow manual speed due to limitations of the data acquisition board employed, thus, limiting the sampling rate to only a few kHz, previous work on similar systems [43, 86, 88, 117, 132] has shown that the signal response to cracks is significantly reduced at high operational speeds. Furthermore, as in the case with the use of arrays of sensors for fast inspection of rail wheel surfaces on the rail network the descrepency

that may arise between the sensor angle relative to the crack surface angle due to high running speeds needs to be addressed for the accurate sizing of cracks.

Furthermore, in [159] it is demonstrated that the signal for a notch of depth 2 mm at 0.8 mm lift-oo is comparable to the signal for a notch of depth 4 mm at a lift-off distance of 2 mm above the specimen under test and the signal as a result of a notch of depth 4 mm at a probe lift-off of 3 mm is comparable to the signal for a notch of depth 2 mm at a lift-off distance above the sample of 2 mm. Therefore, the probe lift-off distance is a critical parameter which needs to be taken into consideration during the inspection process under actual in-service conditions in order to be able to accurately quantify RCF cracks. Furthermore, the work presented in this chapter, in agreement with previous work such as that which is reported in reference [159], has demonstrated that the ACFM signal in the raw non-normalised ACFM data decreases with increasing lift-off distance from the sample being inspected. Thus, this suggests that it might be possible to determine any lift-off variations that that may arise during the actual inspection procedure by quantifying the decrease in the overall ACFM signal strength.

Furthermore, in reference [159] findings from a study on the influence of inspection speed on the ACFM signal response to RCF cracks are reported; high-speed inspection tests were carried out using an ACFM pencil probe on a specially built rig to achieve high inspection speeds. It is reported in [159] that initial tests that were carried out on a controlled rotary test piece containing notches simulating defects demonstrated and, thus, verified that the ACFM system is capable of detecting defects at speeds of up to 121.5 km/hr at constant probe lift-off and that the intensity of the signal remained effectively unaffected by lift-off variations and reduced with the square of the lift-off as is expected and in line with the current work presented in this chapter. Subsequently, tests reported in refernece [159] to simulate actual inspection conditions for rail inspections at high speed which were carried out on a spinning rail rig at the University of Birmingham with the ACFM probe installed on a specially designed trolley syatem demonstrated that it ia difficult to control variations in probe lift-off and, thus, difficult to compensate for the variations in lift-off that occurred during the spinning rail rig tests as a consequence of the limitations in the design of the trolley system employed for these tests. Data analysis showed that it was possible

to detect all the defects, however, it was found that the variations in the lift-off that occurred made it impossible to correctly size the defects and, thus, were not conducive in ranking the defects investigated in their study. The study presented in [159] further demonstrated that the signal remained largely unaffected at speeds up to 48 km/hr, however, due to lift-off variations their study could not proceed further in order to assess the capability of the ACFM technique to inspect defects at higher speeds under actual conditions. Nevertheless, their investigation has shown that the implication arising from their study which suggests that there is virtually no loss of signal with increasing speed is of utmost importance for the use of the ACFM technique as an alternative non-destructive method for the high speed inspection of rails. Therefore, in line with the work presented in this chapter previous similar studies [159] have demonstrated that the ACFM technique is capable of detecting RCF defects at high speeds of inspection even though measurable probe lift-off may occur.

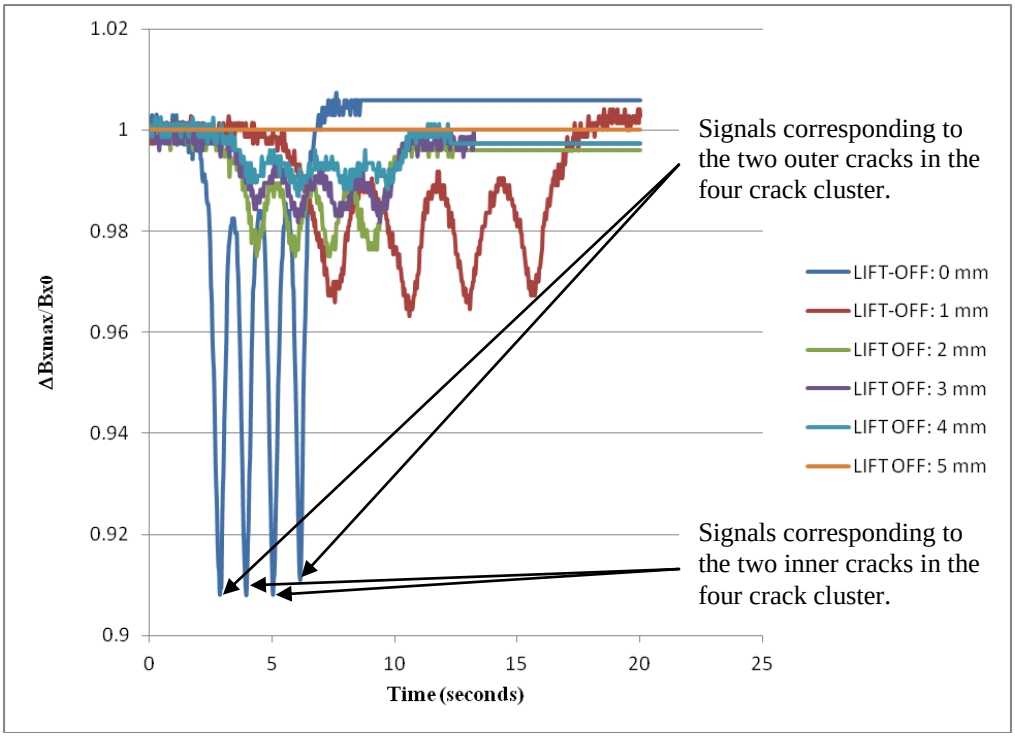

Figure 7.11 Influence of sensor lift-off between 0-5 mm on ACFM (5 kHz) signal for clusters of 4 cracks with an inter-crack spacing distance of 20 mm and, surface length and pocket depth of 10 mm and 5 mm, respectively.

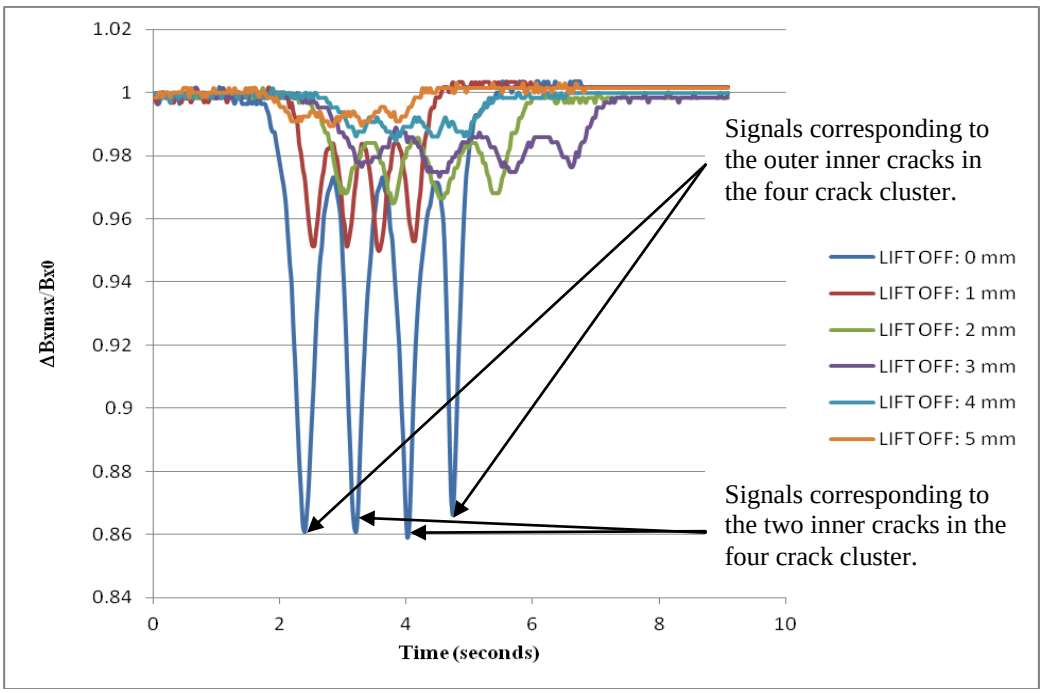

Figure 7.12 Influence of sensor lift-off between 0-5 mm on ACFM (50 kHz) signal for clusters of 4 cracks with an inter-crack spacing distance 20 mm and, surface length and pocket depth of 10 mm and 5 mm, respectively.

Table 7.4 Influence of lift-off and ACFM frequency on ACFM signal for cracks spaced 20 mm apart and, surface length and pocket depth of 10 mm and 5 mm, respectively.

ACFM Inducing Frequency: 5 kHz	ACFM Inducing Frequency: 50 kHz
Lift-off: 0 mm Change in $\Delta B_{xmax}/B_{x0}$: 0.09 (9.0%)	Lift-off: 0 mm Change in $\Delta B_{xmax}/B_{x0}$: 0.14 (14.0%)
Lift-off: 1 mm Change in $\Delta B_{xmax}/B_{x0}$: 0.03 (3.0%)	Lift-off: 1 mm Change in $\Delta B_{xmax}/B_{x0}$: 0.05 (5.0%)
Lift-off: 2 mm Change in $\Delta B_{xmax}/B_{x0}$: 0.025 (2.5%)	Lift-off: 2 mm Change in $\Delta B_{xmax}/B_{x0}$: 0.03 (3.0%)
Lift-off: 3 mm Change in $\Delta B_{xmax}/B_{x0}$: 0.015 (1.5%)	Lift-off: 3 mm Change in $\Delta B_{xmax}/B_{x0}$: 0.025 (2.5%)
Lift-off: 4 mm Change in $\Delta B_{xmax}/B_{x0}$: 0.01 (1.0%)	Lift-off: 4 mm Change in $\Delta B_{xmax}/B_{x0}$: 0.013 (1.3%)
Lift-off: 5 mm Change in $\Delta B_{xmax}/B_{x0}$: 0 (0%)	Lift-off: 5 mm Change in $\Delta B_{xmax}/B_{x0}$: 0.01 (1.0%)

Table 7.5 shows the comparison of estimated crack pocket depths (D_{EST}), using figure 7.4, with the actual crack depth (i.e. oversized or undersized (%)), for the ACFM sensor signal response for cracks spaced 20 mm apart and, surface length and pocket depth of 10 mm and 5 mm, respectively, for probe lift-off distances in the range: 0-5 mm above the specimen being investigated at inducing frequencies of 5 and 50 kHz.

Inducing Frequency (kHz)	Lift-off Distance (mm)	Mean $\Delta B_{Xmax}/B_{x0}$ Value (%)	Estimated Surface Length (SL_{EST}) (mm)	Estimated Crack Pocket Depth (D_{EST}) (mm)	Comparison of D_{EST} with Actual Crack Depth: Oversized or Undersized (%)
5 kHz	0 mm	0.09 (9.0 %)	12.0 mm	6.0 mm	Oversized: 20.0%
50 kHz	0 mm	0.14 (14.0%)	26.0 mm	13.0 mm	Oversized: 160.0%
5 kHz	1.0 mm	0.03 (3.0%)	4.0 mm	2.0 mm	Undersized: 60.0%
50 kHz	1.0 mm	0.05 (5.0%)	6.0 mm	3.0 mm	Undersized: 40.0%
5 kHz	2.0 mm	0.025 (2.5%)	4.0 mm	2.0 mm	Undersized: 60.0%
50 kHz	2.0 mm	0.03 (3.0%)	4.0 mm	2.0 mm	Undersized: 60.0%
5 kHz	3.0 mm	0.015 (1.5%)	3.5 mm	1.8 mm	Undersized: 64.0%
50 kHz	3.0 mm	0.025 (2.5%)	4.0 mm	2.0 mm	Undersized: 60.0%
5 kHz	4.0 mm	0.01 (1.0%)	2.7 mm	1.4 mm	Undersized: 70.0%
50 kHz	4.0 mm	0.013 (1.3%)	3.0 mm	1.5 mm	Undersized: 70.0%
5 kHz	5.0 mm	0 (0%)	Unsolvable	Unsolvable	Unsolvable
50 kHz	5.0 mm	0.01 (1.0%)	2.7 mm	1.4 mm	Undersized: 72.0%

7.3.1.3 INFLUENCE OF INTER-CRACK SEPARATION AND CRACK CLUSTER NUMBER ON ACFM SIGNAL

The inter-crack spacing is defined as the length of the region between two adjacent defects in the running direction of the rail/wheel. It is reported in the available literature that the growth rate and inter-crack spacing of RCF cracks is influenced by the grade of the rail material [163]. It is found that the inter-crack spacing values vary and are dependent upon various parameters, for example, rail type, radius of curvature and traffic conditions; as a result, the inter-crack spacing of RCF cracks can vary over a wide range and have been reported in [37] to be between 0.8 mm and 1.7 mm and in more widely spaced cracks with inter-crack spacing as large as 20 mm have been reported in references [164,165]. In agreement with the work presented here in this

chapter previous similar studies [148] have demonstrated that the ACFM signal is affected by the presence of closely spaced clustering of defects in such a manner that the signal associated with a cluster of defects appears to be elongated in the direction in which the scan is carried out in comparison to the signal associated with a single isolated defect, thus, suggesting that multiple defects are present even though multiple troughs associated with each defect in the cluster cannot be seen. In [148] it is reported that at crack spacing of 1 mm and 3 mm individual troughs are not present, however, in agreement with and shown in the figures presented in the current work in this chapter the authors of reference [148] also report that the indications of the beginnings of individual troughs associated with each crack in the cluster can be seen to be emerging. However signal noise may make such indications of troughs rather more difficult to identify and distinguish during experiment. In the literature it is reported that typically a +/-10% experimental variation can occur [7], however, as shown in the present study at wider inter-crack spacing, for example at an inter-crack spacing distance of 20 mm, individual troughs corresponding to each crack within the cluster become more distinct and, thus, identifiable. Thus, for closely spaced cracks the normalised maximum change in the B_x signal component (i.e. $\Delta B_{xmax}/B_{x0}$) is relatively larger than for an isolated individual crack of the same size as shown by the results in this present work. Results obtained show that using an ACFM sensor operating at an inducing frequency of 50 kHz to detect the artificial cracks (notches) in the calibration plate on a four crack cluster shows that the ACFM system operating at this higher frequency yields significantly higher $\Delta B_{xmax}/B_{x0}$ values and thus over sizes the defects for all cracks investigated and all cracks could not be sized as a result using the UK Network Rail sizing diagram shown in figure 7.4. However, in the case of the ACFM sensor operating at an inducing frequency of 5 kHz the sensor is found to be capable of providing reasonable estimates of the crack pocket depths at inter-crack spacing distances of 15 and 20 mm for the crack clusters consisting of two and four cracks and even though these crack pocket depth estimates are oversized by 36% in both of these cases at these inter-crack spacing distances these results are in line with previous similar studies reported in the literature [164,165]. However, at lower inter-crack spacing distances of 5 and 10 mm the ACFM techniques is not capable of distinguishing between individual cracks and considerably over sizes the cracks in agreement with former studies on similar systems [164,165]. The results also show that the estimate for the crack pocket depth is the same for two and four crack clusters

at inter-crack-spacing distances of 15 and 20 mm but for a two crack cluster at an inter-crack spacing distance of 10 mm and an ACFM inducing frequency of 50 kHz the value of the normalised B_x obtained, i.e. $\Delta B_{xmax}/B_{x0}$, is too large using the ACFM sensor operating at 50 kHz than for the 5 kHz sensor employed to detect the same defects at the same inter-crack spacing distances and thus the 50 kHz sensor is incapable of sizing the defects at this inter-crack spacing using the sizing diagram shown in figure 7.4. However, the best results obtained from this study is found to be when the ACFM is operated at a lower frequency of 5 kHz on a cluster of two cracks with inter-crack-spacing distances at and above 15 mm, i.e. at inter-crack spacing distances of 15 and 20 mm, where the defects investigated are sized within reasonable estimates with an estimate for the crack pocket depth that is oversized by 20% of the actual depth of the defect at these two inter-crack spacing distances. This result is better and thus in line with that reported in the literature using an ACFM sensor operating at the same lower frequency. Therefore, these results demonstrate that the ACFM technique operating at lower frequencies (5 kHz) is much better suited at sizing (length and depth) cracks in railway track and railway wheels and components than an ACFM system operating at higher frequencies (50 kHz) and, thus, provides reasonable estimates for crack pocket depths. However, it should be noted that even though the troughs yield the same $\Delta B_{xmax}/B_{x0}$ values at an inter-crack spacing of 20 mm giving accurate and, thus, yielding, accurate crack estimates the B_x/B_{x0} value does not return to the background level between each crack at every different inter-crack spacing distance considered in the current work presented in this chapter. It is necessary to use an accurate background estimate for crack sizing purposes in order to provide correct estimates for the length and depth of cracks. This is the reason why an appropriate estimate for the background value has been chosen from the obtained ACFM result and used to estimate crack sizes for the three railway wheels removed from service and investigated as part of this study using the ACFM technique as discussed below as this is based on the $\Delta B_{xmax}/B_{x0}$ value. The study has shown that very closely spaced defects result in a single trough that would inevitably significantly oversize the defects present within the cluster of cracks if the presence of multiple defects is unknown beforehand. Further studies are at present being carried out to investigate the response of the ACFM system to RCF crack clusters that are primarily focused on the development of theoretical models for differently sized multiple defects that are oriented at various angles in relation to each other. Figures 7.13-7.16

incl. and the results shown in tables 5.4 and 5.5 show the following general trends. The maximum change in the B_x ACFM signal increases significantly with a decrease in crack separation; the maximum change in the B_x signal is greater for closely spaced cracks which would thus significantly oversize the cracks using figure 7.1 (above). Furthermore, the results show a significant increase in the change in the B_x signal with an increase in the ACFM sensor frequency and therefore the sensitivity of the sensor in detecting and sizing defects is enhanced by increasing the operational frequency of the ACFM sensor. These results also demonstrate that at a crack spacing of 20 mm the cracks can be sized resonabley accurately, whereas, for spacings of 15 mm the outer cracks, for example, in the four crack cluster would yield resonably good estimates for the crack pocket depths, however, the two inner cracks would significantly undersize the defects because these inner cracks in the crack cluster would yield higher values for the maximum change in the B_x signal as shown by these results; and the results also show that for crack spacing smaller than 15 mm the cracks thus estimated using the normalised change in the B_x signal would be significantly higher than the actual crack pocket depths. These results are in line with previous studies [6, 7, 148]. Furthermore, as will be shown in the next chapter this effect needs to be taken into account when using the ACFM system on the railway network as the RCF cracks found in railway wheel tread surfaces, as shown in the previous chapter are, in general, closely closely spaced and in most cases closer than 5 mm apart as shown in wheel HSR2 in the RCF crack circumferential bands observed near the flange end and at approximately 3 cm from the non-flange end of this wheel where the spacing between the cracks are about 2-3 mm and 1 mm, respectively. Therefore, it is difficult to size such defects using the present ACFM system when the cracks within a cluster have a crack spacing of about 5 mm or smaller inter-crack spacing Previous work [6, 7, 148] has reported that it is difficult to size defects using the ACFM sensor that are spaced closer than about 5 mm as also shown by the work presented here in this chapter. Figures 7.17 and 7.18 show ACFM scans carried out with the sensor oriented at 45^0 to cracks showing signals for a cluster of 4 cracks spaced 5 and 20 mm apart. These figures show sensor signals and are interesting results because they appear to show that crack clusters with crack spacing of 5 mm and smaller which cannot be distinguished with the probe parallel to the cracks during the scan can be detected with the probe oriented at an angle of 45^0 (or higher angle of 90^0 as shown in the next section) to the cluster of closely spaced cracks, however, this method cannot be used

to accurately size the defects at present as further work needs to be done in this area to understand this phenomena. However, these results are reproducible and a significant way forward in further developing the ACFM system in order to dectect and size cracks within a cluster of closely spaced cracks as are found in railway wheels in service.

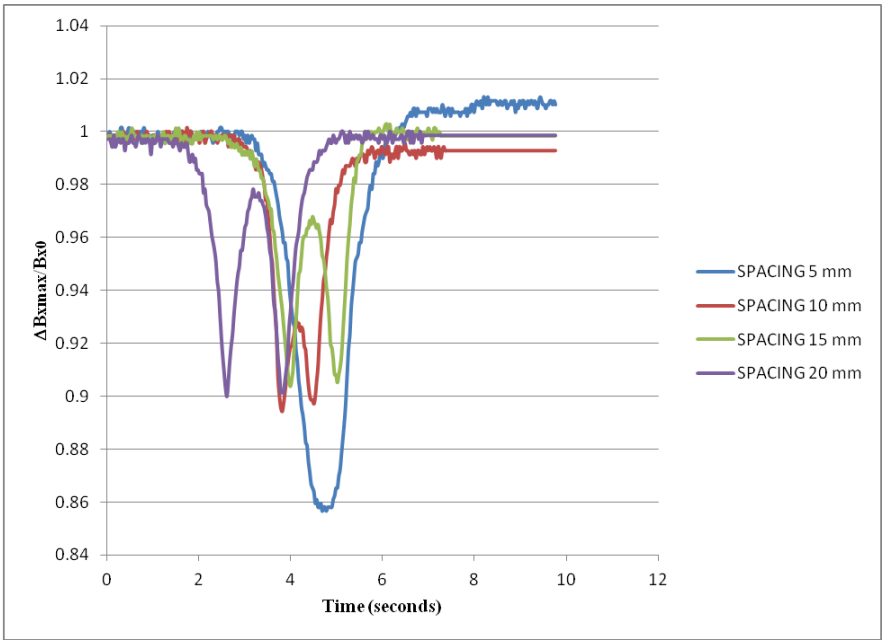

Figure 7.13 Influence of crack spacing and crack cluster number on ACFM (5 kHz) signal response to clusters of 2 cracks with inter-crack spacings between 5 and 20 mm and, surface length and pocket depth of 10 mm and 5 mm, respectively.

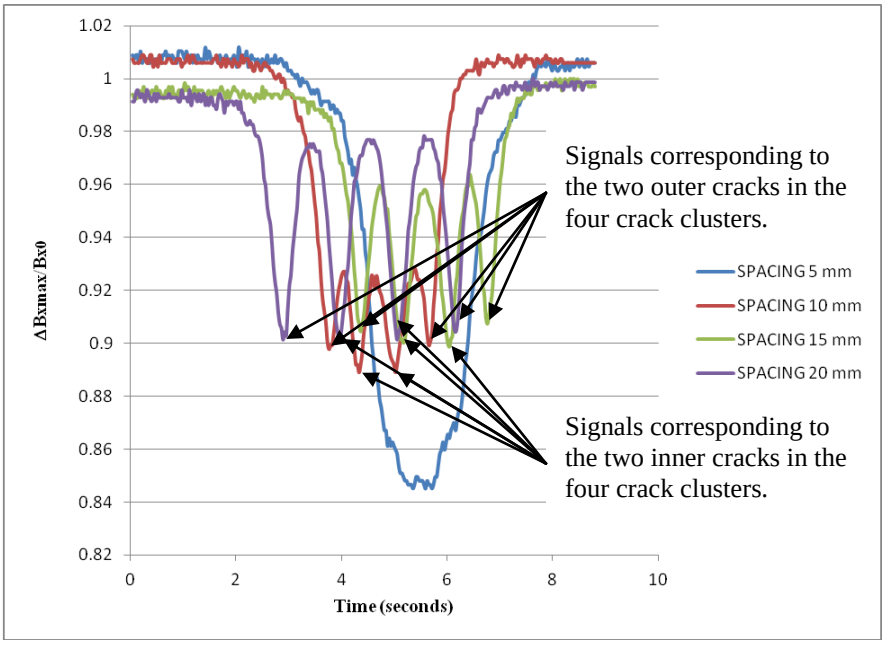

Figure 7.14 Influence of crack spacing and crack cluster number on ACFM (5 kHz) signal response to clusters of 4 cracks with inter-crack spacings between 5 and 20 mm and, surface length and pocket depth of 10 mm and 5 mm, respectively.

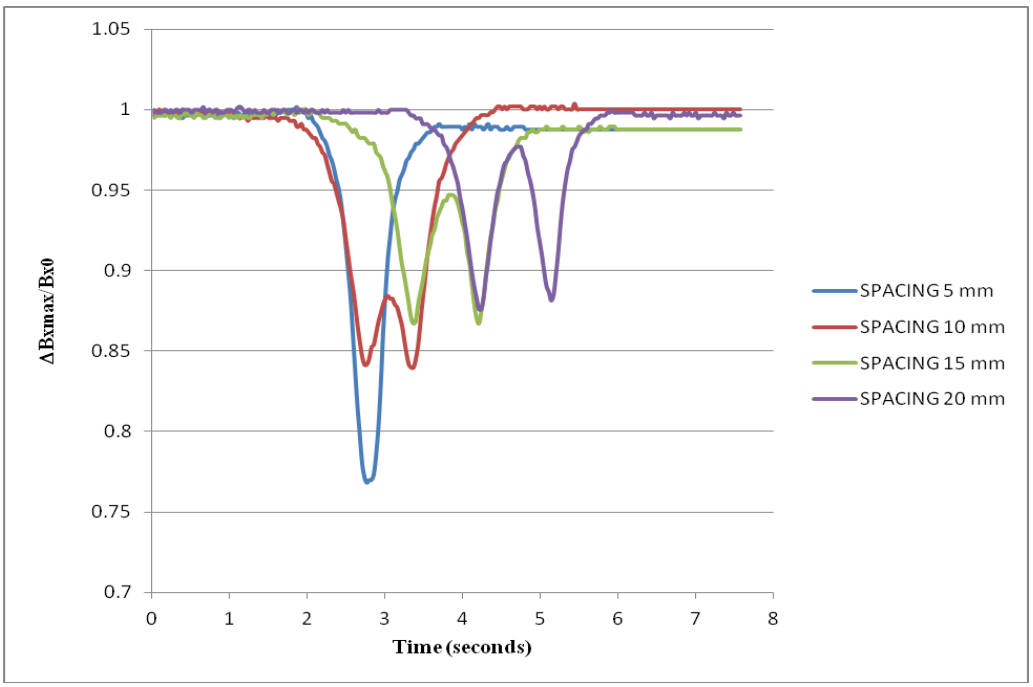

Figure 7.15 Influence of crack spacing and crack cluster number on ACFM (50 kHz) signal response to clusters of 2 cracks with inter-crack spacings between 5 and 20 mm and, surface length and pocket depth of 10 mm and 5 mm, respectively.

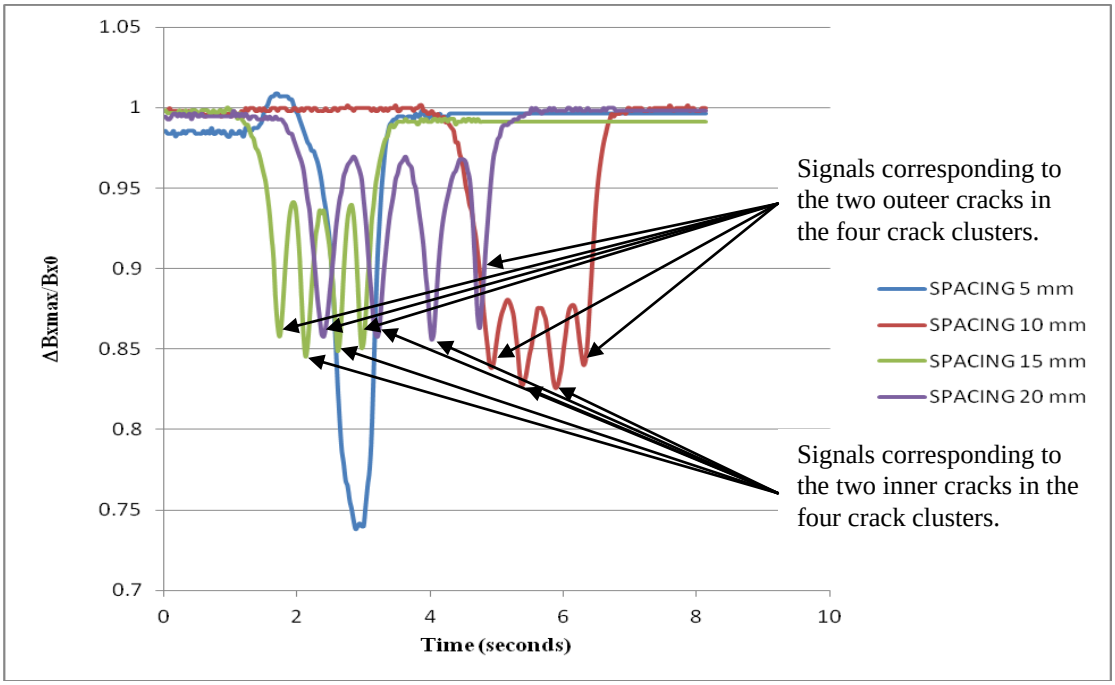

Figure 7.16 Influence of crack spacing and crack cluster number on ACFM (50 kHz) signal response to clusters of 4 cracks with inter-crack spacings between 5 and 20 mm and, surface length and pocket depth of 10 mm and 5 mm, respectively.

Table 7.6 shows the normalised Mean $\Delta B_{xmax}/B_{x0}$ values for the ACFM sensor signal response for crack clusters of 2 and 4 cracks of surface length and pocket depth of 10 mm and 5 mm, respectively, with inter-crack spacing between 5 and 20 mm and for the ACFM operating at a frequency of 5 kHz.

Inter-crack Spacing (mm)	ACFM: 5 kHz Mean $\Delta B_{xmax}/B_{x0}$ Value for a Crack Cluster of Two Cracks	ACFM: 5 kHz Mean $\Delta B_{xmax}/B_{x0}$ Value for a Crack Cluster of Four Cracks
5 mm	0.14 (14.0%)	0.16 (16.0%)
10 mm	0.10 (10.0%)	0.11 (11.0%)
15 mm	0.09 (9.0%)	0.10 (10.0%)
20 mm	0.10 (10.0%)	0.095 (9.5%)

Table 7.7 shows the normalised Mean $\Delta B_{xmax}/B_{x0}$ values for the ACFM sensor signal response for crack clusters of 2 and 4 cracks of surface length and pocket depth of 10 mm and 5 mm, respectively, with inter-crack spacing between 5 and 20 mm and for the ACFM operating at a frequency of 50 kHz.

Inter-crack Spacing (mm)	ACFM: 50 kHz Mean $\Delta B_{xmax}/B_{x0}$ Value for a Crack Cluster of Two Cracks	ACFM: 50 kHz Mean $\Delta B_{xmax}/B_{x0}$ Value for a Crack Cluster of Four Cracks
5 mm	0.23 (23.0%)	0.25 (25.0%)
10 mm	0.16 (16.0%)	0.17 (17.0%)
15 mm	0.13 (13.0%)	0.15 (15.0%)
20 mm	0.12 (12.0%)	0.14 (14.0%)

Table 7.8 shows the comparison of estimated crack pocket depths (D_{EST}), using figure 7.4, with the actual crack depth (i.e. oversized or undersized (%)), for the ACFM sensor signal response for a cluster of two cracks with each crack having an actual surface length and pocket depth of 10 mm and 5 mm, for inter-crack spacing distances between 5 and 20 mm at ACFM operating frequency of 5 kHz.

Inducing Frequency (kHz)	Inter-crack Spacing Distance (mm)	Mean $\Delta B_{Xmax}/B_{x0}$ Value (%)	Estimated Surface Length (SL_{EST}) (mm)	Estimated Crack Pocket Depth (D_{EST}) (mm)	Comparison of D_{EST} with Actual Crack Depth: Oversized or Undersized (%)
5 kHz	5 mm	0.14 (14.0 %)	26.0 mm	13.0 mm	Oversized: 160%
50 kHz	5 mm	0.23 (23.0%)	Unsolvable	Unsolvable	Unsolvable

5 kHz	10 mm	0.1 (10%)	13.5 mm	6.8 mm	Oversized: 36%
50 kHz	10 mm	0.16 (16.0%)	Unsolvable	Unsolvable	Unsolvable
5 kHz	15 mm	0.09 (9.0%)	12.0 mm	6.0 mm	Oversized: 20.0%
50 kHz	15 mm	0.13 (13.0%)	26.0 mm	13.0 mm	Oversized: 160.0%
5 kHz	20 mm	0.09 (9.0%)	12.0 mm	6.0 mm	Oversized: 20.0%
50 kHz	20 mm	0.12 (12.0%)	17.0 mm	8.5 mm	Oversized: 70.0%

Table 7.9 shows the comparison of estimated crack pocket depths (D_{EST}), using figure 7.4, with the actual crack depth (i.e. oversized or undersized (%)), for the ACFM sensor signal response for a cluster of four cracks with each crack having an actual surface length and pocket depth of 10 mm and 5 mm, for inter-crack spacing distances between 5 and 20 mm at ACFM operating frequency of 5 kHz.

Inducing Frequency (kHz)	Inter-crack Spacing Distance (mm)	Mean $\Delta B_{Xmax}/B_{x0}$ Value (%)	Estimated Surface Length (SL_{EST}) (mm)	Estimated Crack Pocket Depth (D_{EST}) (mm)	Comparison of D_{EST} with Actual Crack Depth: Oversized or Undersized (%)
5 kHz	5 mm	0.16 (16.0%)	Unsolvable	Unsolvable	Unsolvable
50 kHz	5 mm	0.25 (25.0%)	Unsolvable	Unsolvable	Unsolvable
5 kHz	10 mm	0.11 (11.0%)	15.5 mm	7.8 mm	Oversized: 56.0%
50 kHz	10 mm	0.17 (17.0%)	Unsolvable	Unsolvable	Unsolvable
5 kHz	15 mm	0.1 (10.0%)	13.5 mm	6.8 mm	Oversized: 36.0%
50 kHz	15 mm	0.15 (15.0%)	Unsolvable	Unsolvable	Unsolvable
5 kHz	20 mm	0.1 (10.0%)	13.5 mm	6.8 mm	Oversized: 36.0%
50 kHz	20 mm	0.14 (14.0%)	26.0 mm	13.0 mm	Oversized: 160.0%

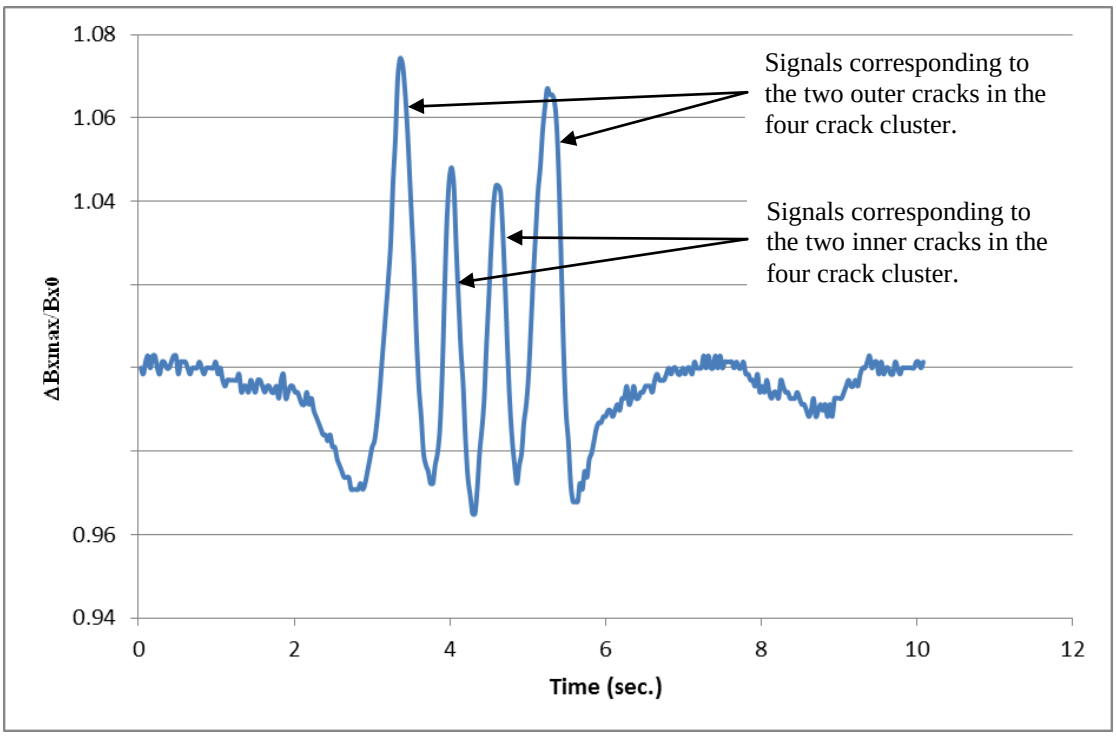

Figure 7.17 shows ACFM (5 kHz) scan with the sensor oriented at 45^0 to cracks showing sensor signals for a cluster of 4 cracks spaced 5 mm apart.

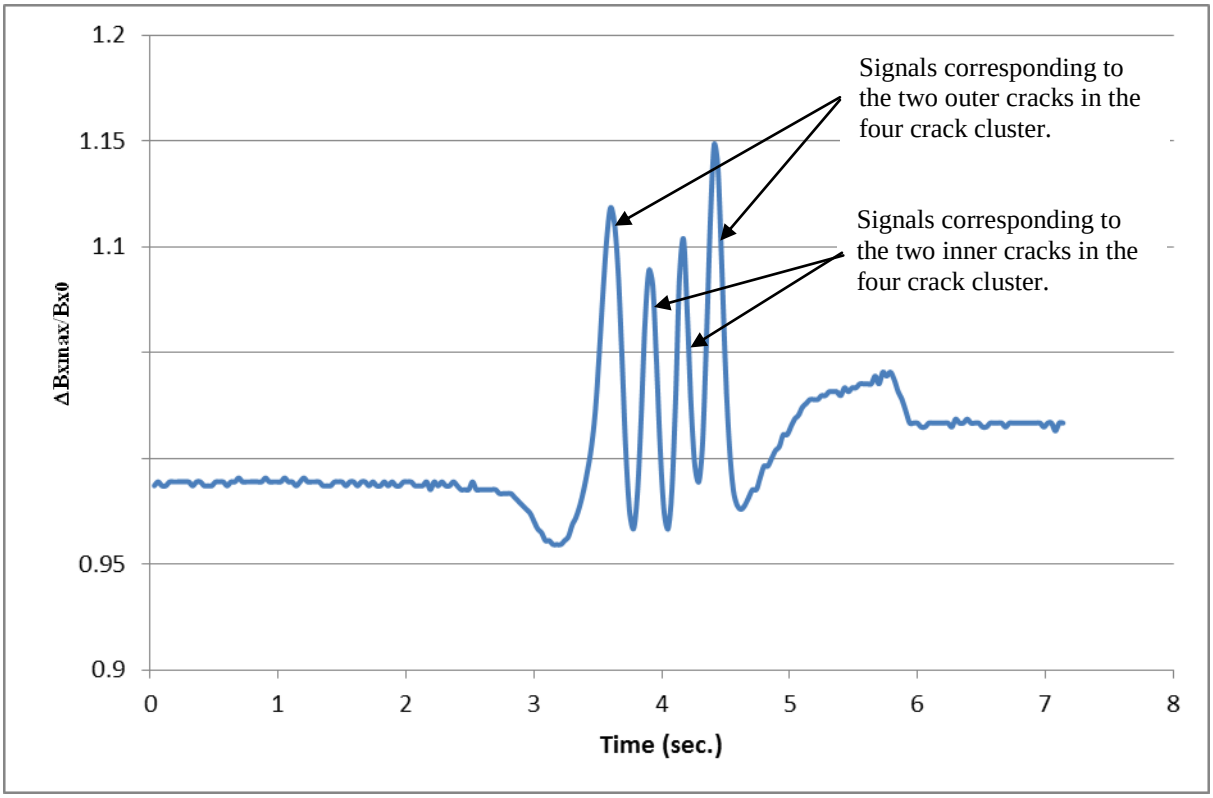

Figure 7.18 shows ACFM (50 kHz) scan with the sensor oriented at 45^0 to cracks showing sensor signals for a cluster of 4 cracks spaced 5 mm apart.

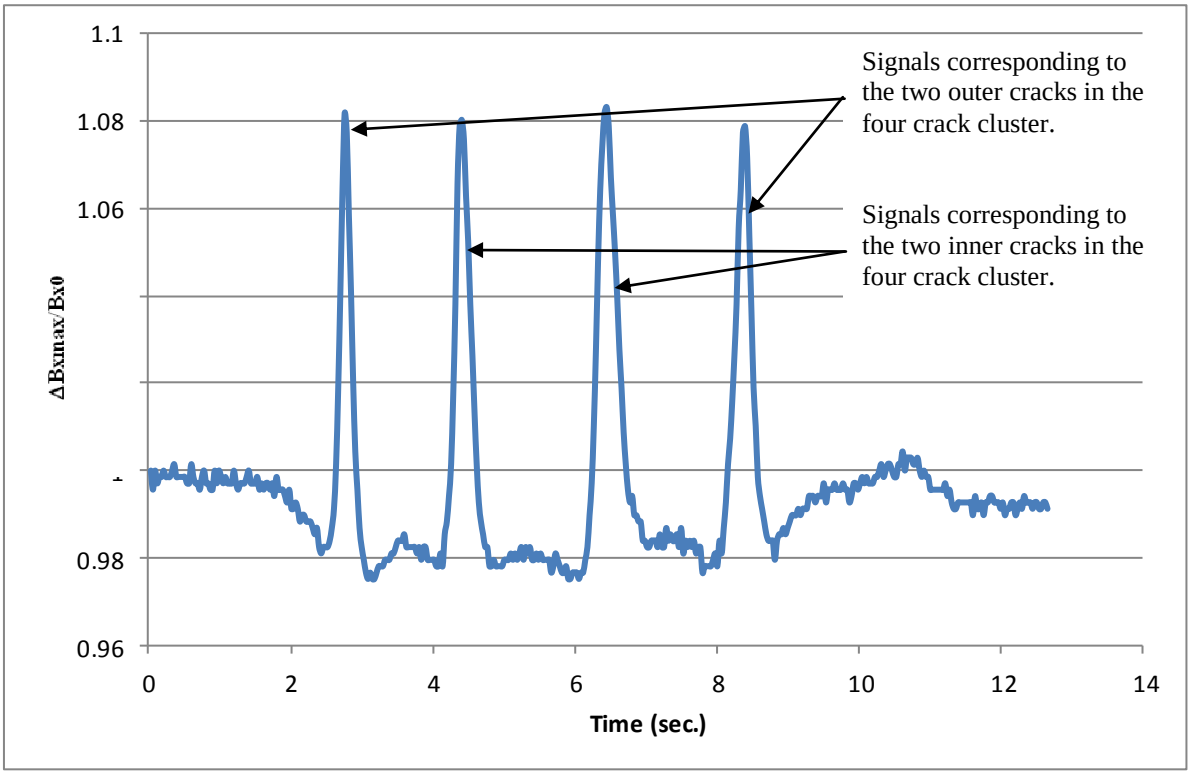

Figure 7.19 shows ACFM (5 kHz) scan with the sensor oriented at 45^0 to cracks showing sensor signals for a cluster of 4 cracks spaced 20 mm apart.

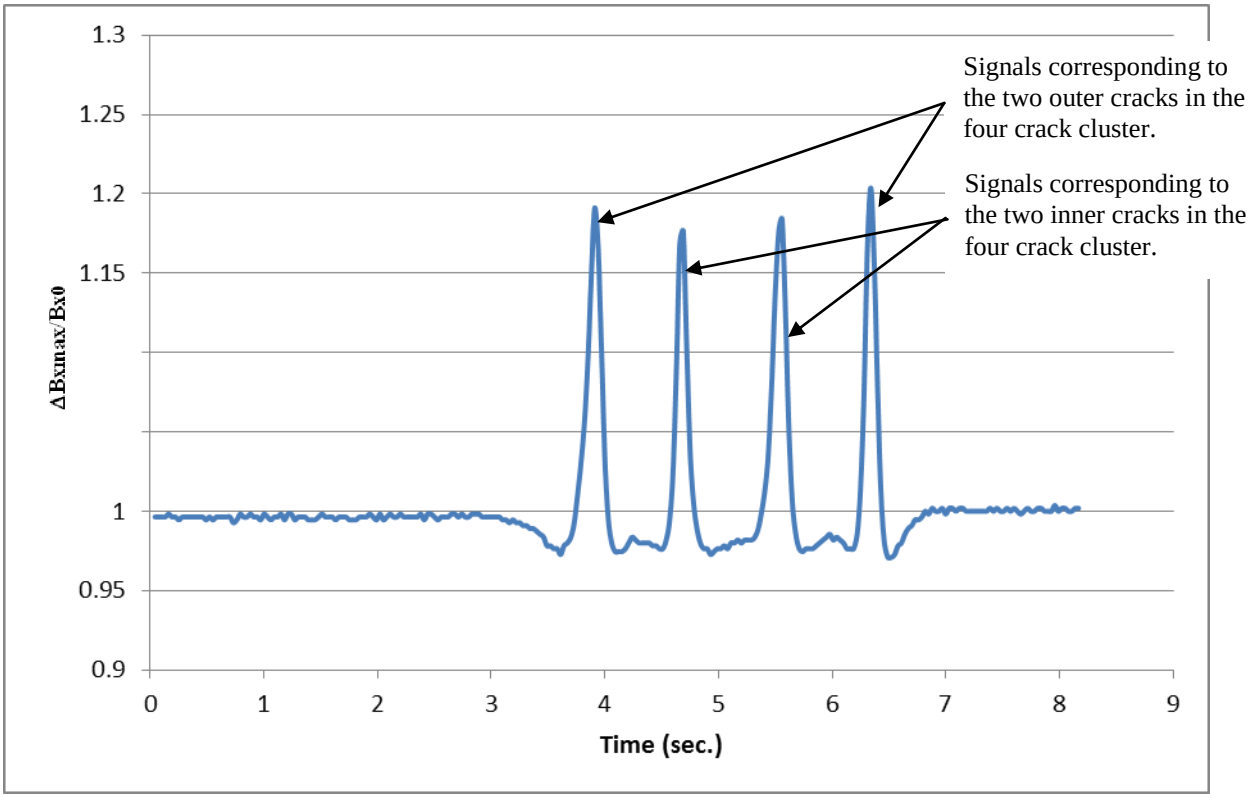

Figure 7.20 shows ACFM (50 kHz) scan with the sensor oriented at 45^0 to cracks showing sensor signals for a cluster of 4 cracks spaced 20 mm apart.

7.3.1.4 INFLUENCE OF INDUCING FREQUENCY (5 AND 50 KHZ) ON ACFM SIGNAL

The results presented in the above sections demonstrate that the inducing frequency of the ACFM sensor significantly influences signal acquisition and, thus, the accuracy of the measurement made by the ACFM system. Therefore, it is of utmost importance to determine the appropriate inducing frequency in order to further design and develop the ACFM system. The results obtained from the work presented in this chapter are in line with previous work on various simulations designed to study the influence of inducing frequency on the induction electromagnetic field [26] which demonstrated that the magnitude of the induced magnetic field in the material under inspection decreases with increasing frequency; whereas, the sensitivity of the magnetic field and, thus, the sensitivity of the ACFM sensor for the detection of defects increases with increasing frequency. Furthermore, it is reported by these authors that for low operating frequencies the error in quantification is very large and thus cannot meet the criteria and requirements for inspection. This is in line with the work and results that are presented and discussed in the current chapter which shows that the sensitivity of the ACFM sensor in the detection and sizing of cracks is enhanced by an increase in inducing frequency as a 50 kHz ACFM probe provides higher sensitivity than the standard 5 kHz probe on ferrous and non-ferrous materials. Thus, a 50 kHz ACFM sensor is optimal for the detection and sizing of cracks in railway wheels and components in service. Thus, for optimum results an array of such higher frequency ACFM probes positioned at different orientations relative to the wheel tread surface is likely to be more capable of detecting cracks in railway wheels which might be orientated at different angles relative to the tread surface circumferential direction, in order to take into account the different crack surface angles that might be present on the surface of the wheel tread.

In reference [167] a study has been carried out to investigate the influence of the ACFM operating frequency on the defect characteristic vectors accordingly, as the distortions in the B_x and B_z components of the signal that are caused by the presence of defects are analysed in order to obtain the defect information. For parameters are selected to describe the shape and the size of the crack after performing a comparative analysis with a large number of experiments, namely, the distance between the peak and valley of the B_z component (B_L), the amplitude of the B_x signal without the defect

(M_{x0}), the maximum distortion of the B_x component above the defect (MX_{max}), and the maximum distortion of the B_z component above the defect (MZ_{max}). A parameter to characterise sensitivity has been introduced in order to describe the parameter variations which reduce detection error and improve the signal-to-noise ratio (SNR) [168]. Thus, the sensitivities of the B_x and B_z components of the signal, i.e., S_x and S_z, respectively, are given as follows:

$$S_x = M_{Xmax}/M_{X0} \text{ and } S_z = MZ_{max}/M_{X0} \qquad (7,1)$$

According to the ACFM principle and the quantification algorithm [169,170], L_z is directly related to the length of the defect and S_x and S_z are related to the depth of the defect. Therefore, the characteristic vectors as defined above, i.e. S_x, S_z and L_z, influence the accuracy of the measurement of the ACFM system. In agreement with the results presented here in this chapter, the work reported by the authors in reference [167] has demonstrated that the sensitivity of the ACFM system increases with increasing frequency. The sensitivity is defined so that it shows the proportion of defect signals in the total magnetic field signals detected by the ACFM probe (see equation 7.1). At low inducing frequencies, even with a larger magnetic field signal, the signal corresponding to the defect is still small and, thus, can be easily masked by the noise which results in a large quantification error. It is found that when the inducing frequency is less than 1200 Hz the quantification error is 100% due to the low sensitivity found to be approximately 18%, which, thus, meets the engineering requirement. The simulation results that are reported in reference [167] show that the induction magnetic field intensity on the work piece surface attenuate with an increase in the inducing frequency, whereas, the magnetic field sensitivity due to the presence of a defect increases and the quantification error decreases with an increase in the inducing frequency. Furthermore, at low inducing frequencies the quantification error is too large in order to meet the necessary requirements for inspection purposes.. Therefore, taking into consideration the principle of “fit for purpose” and “high accuracy”, the inducing frequency should be greater than 5000 Hz in order to achieve the desired accuracy of detection and sensitivity. However, in order to obtain a stronger induced magnetic field to guarantee the effectiveness of picking up signals the inducing frequency should not be too high. Therefore, the inducing frequency is of utmost importance since it has a significant effect on the performance of the entire

system to carry out the function of signal extraction and thus to enhance the accuracy of detection. Thus, the optimisation of the frequency is of utmost importance in order to further design and develop the ACFM system.

In order to be able to efficiently employ array ACFM systems it is necessary to be able to switch between the sensors in the array as fast as possible for conducting rapid inspection. However, it is reported in the available literature [159] that in the case of sensor operating at a frequency of 5 kHz certain limitations exist such as: switching settling times, data transfer rates and also limitations in the sampling rate of a 5 kHz sensor. Furthermore, for the above factors in the case of conventional analogue electronics the scan speed is restricted to about 0.15 m/s for a single field 16-channel array. However, these limitations have been overcome and, thus, scan speeds have been increased by between four to five times than is currently the case for conventional ACFM probes by increasing the energising frequency of the system from 5 kHz to 50 kHz coupled with some modifications that have also been made to the signal processing electronics [159].

7.3.1.5 ASSESSING THE CAPABILITY OF THE ACFM TECHNIQUE TO DETECT A SEVERELY CRITICAL DEFECT IN A CLUSTER OF SHALLOW DEFECTS AS COMMONLY FOUND IN RAILWAY WHEELS IN SERVICE

In addition, an experiment has been designed to determine whether the ACFM system can detect and potentially size a deep and critical crack present in the centre of a cluster of shallow cracks as is commonly found in railway and railway wheels and components. To this end the calibration plate was also designed as shown in figure 7.1 (above) in which were incorporated a set of seven shallow semi-elliptical cracks with a surface length 10 mm and crack pocket depth of 1.5 mm spaced 3 mm apart as well as another set of identical cracks but with a central deep crack replacing the shallow crack in the centre and this deep crack has dimensions of: surface length 10 mm, and pocket depth 5 mm; all these cracks propagate at 90^0 (perpendicular) to the surface of the material. Figures 7.18 and 7.19 show the ACFM scans for crack clusters with and without a central deep crack with the ACFM sensor aligned parallel to the cracks and operating at frequencies of 5 and 50 kHz, respectively. These results show that the maximum change in the B_x signal is significantly larger for the cluster of cracks which have a central deep crack and these results also show that the background

signal value (arbitrary units) is significantly lower for the ACFM sensor operating at the higher frequency of 50 kHz than for the system operating at the lower frequency of 5 kHz. Therefore, this result demonstrates that a deep crack within a cluster of shallow cracks can be inferred from the larger change in the B_x signal relative to the background signal if it is known that a deep and critical crack is present in the cluster of shallow cracks, however, if one does not know that a deep crack is present in the crack cluster then it is difficult to ascertain whether a deep and thus critical crack is present in the cluster. Therefore, the result demonstrates it is not possible at present to detect and size a deep crack within a cluster of shallow cracks using the ACFM sensor in its present state. Nevertheless, interestingly again as with the work shown in the previous section scans with different angles of ACFM sensor orientations with respect to the angle of the cluster of cracks were tried and interestingly it is found that with the angle of the probe at right angles (90^0), i.e. perpendicular, to the orientation of the cluster of cracks during the scan the resulting sensor signal from the sensor reveals a central sensor signal which is significantly greater than the sensor signals for the shallow defects and thus suggesting that this method is capable of detecting a deep and critical crack in a cluster of shallow cracks, however, it is not possible to accurately size the deep crack in the cluster at present, nevertheless, this is a promising result and a way forward.

Furthermore, in order to explain the above results obtained from this experiment the following discussion and explanation is presented in light of the current understanding of this phenomena about the leakage of magnetic flux in the scenario as shown in these results as demonstrated by the ACFM scans obtained from this experiment when the ACFM probe is oriented perpendicular to the direction of the cracks and this explanation is supported and confirmed by Dr. Mike Smith and Dr. Martin Lugg (TSC Inspection Systems based in Milton Keynes, United Kingdom, who have developed the ACFM system). According to Dr. Mike Smith and Dr. Martin Lugg as explained and discussed in depth by these authors in reference [206] it is their explanation of this phenomena that with a transverse defect the induced current will flow parallel to the defect and be little affected by the presence of the defect. However, the direction of the magnetic field is now normal to the defect and, thus, it is expected that there would be a small flux leakage effect in the area of the defect. This is of course the field direction and driving mechanism of MPI. If there is a flux leakage effect it

explains the signal response, namely an increase in B_x level and a sharp peak-trough in the B_z signal. It would be very much localised to the vicinity of the defect and would be affected by defect depth and crack opening which is what the above authors have observed as reported in [206,207]. Furthermore, this explanation is supported and expanded upon by the aforementioned authors in chapter 10 on Alternating Current Field Measurement (ACFM) in [206] where the following is stated. It is postulated by these authors that the simplistic view of current perturbations producing the measured signals would suggest that discontinuities that are oriented in a direction transverse to the probe scan direction, thus being parallel to the uniform currents, would not be detected. However, it is stated by these authors that, in fact, measurable signals corresponding to discontinuities which are oriented in the transverse direction to the probe scan are generally produced in ferrous steel materials that arise from flux leakage effects rather than current perturbation. The signals are relatively short and of the order of approximately the length of the sensor coils. The B_x signal consists of an upward peak which is caused by the increased flux density above the crack; whereas, the B_z signal assumes a close peak to trough pair that is due to the flux going up, out of and then down into the metal on either side of the crack. As a result, an upward shaped loop in a butterfly shaped plot is produced that is distinct from that produced due to a normal longitudinal discontinuity signal but which may be confused with the signal emanating from a seam weld. However, the distinguishing features in the signals from a transverse discontinuity and a seam weld are that the former yield shorter signals, whereas, the latter give a constant signal whenever the probe crosses the weld. Furthermore, the signals are found to be strongest when the probe is scanned across the deepest, or widest, part of the crack; the crack ends do not produce strong signals.

Furthermore, the above authors state in [206] that because the intensity of the signal is related to an equal extent to both the depth of the crack and the crack opening for that reason the signal intensity cannot be used in order to determine the depth of the discontinuity. Also, non-ferrous materials do not produce such signals. Therefore, for these reasons, in order to be able to positively detect transverse discontinuities it is recommended that the operator makes two sets of scans with the probe oriented in two orthogonal directions, or alternatively, to use an array probe that continually switches between two orthogonal current inputs [206]. For cracks that are oriented somewhere

between the purely longitudinal and the purely transverse directions the signals are found to lie between the two extremes. Discontinuities that lie within approximately 30^0 of the longitudinal direction result in signals which appear to be similar to a longitudinal discontinuity except that the B_x trough's amplitude is reduced and that the B_z signal is made to become more asymmetric, i.e. the peak (or trough) at the leading end of the crack is larger than the corresponding trough (or peak) at the trailing end. Furthermore, it is observed that for cracks that are oriented within 30^0 of the transverse direction the signals resemble those which are caused by a transverse discontinuity, except that the B_z signal becomes strongly asymmetric in shape. In addition, for cracks that are oriented at about 45^0 the B_x signal is generally found to practically disappear but B_z signals can be obtained from both the centre and the ends of the discontinuity [206].

Thus, further work needs to be done in this area to first better understand the phenomena and then build on models to achieve the goal of accurately sizing such deep critical cracks which are found in railway wheels in service. Furthermore, as most RCF type cracks occur at +/- 45° to the circumferential direction, a sensor system with orthogonal fields at +/- 45° would be most appropriate. Thus an array of ACFM sensors, specially placed in the system at orientations of $+/-45^0$ in either orientation direction as above and also at 90^0 to the crack angle can detect RCF-type cracks on railway and railway wheels. In the case of the MFL technique the material under inspection is magnetised close to saturation and, in the event that a defect is present at or near the surface of the material magnetic flux lines leak out from the area surrounding the defect. Also, stress variations influence the magnetic permeability of the material.

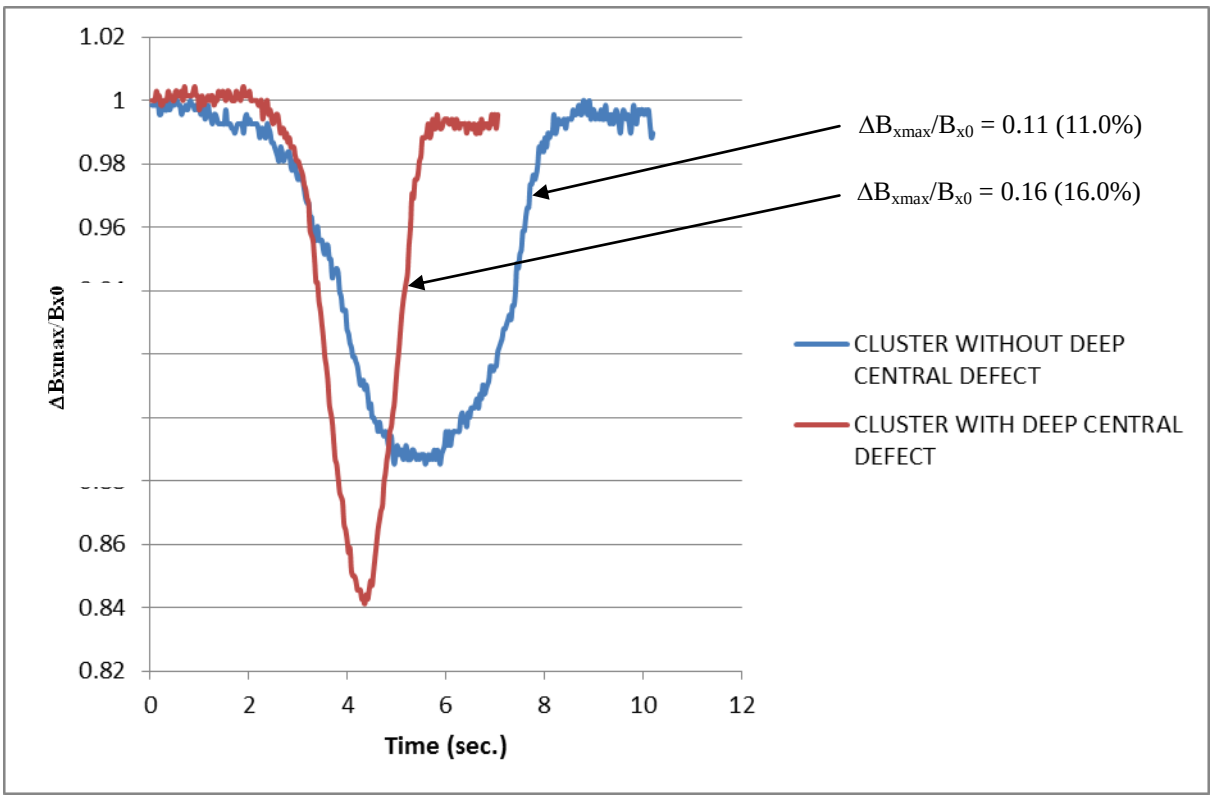

Figure 7.21 shows the ACFM scans for crack clusters with and without a central deep crack with the ACFM sensor aligned parallel to the cracks and operating at a frequency of 5 kHz.

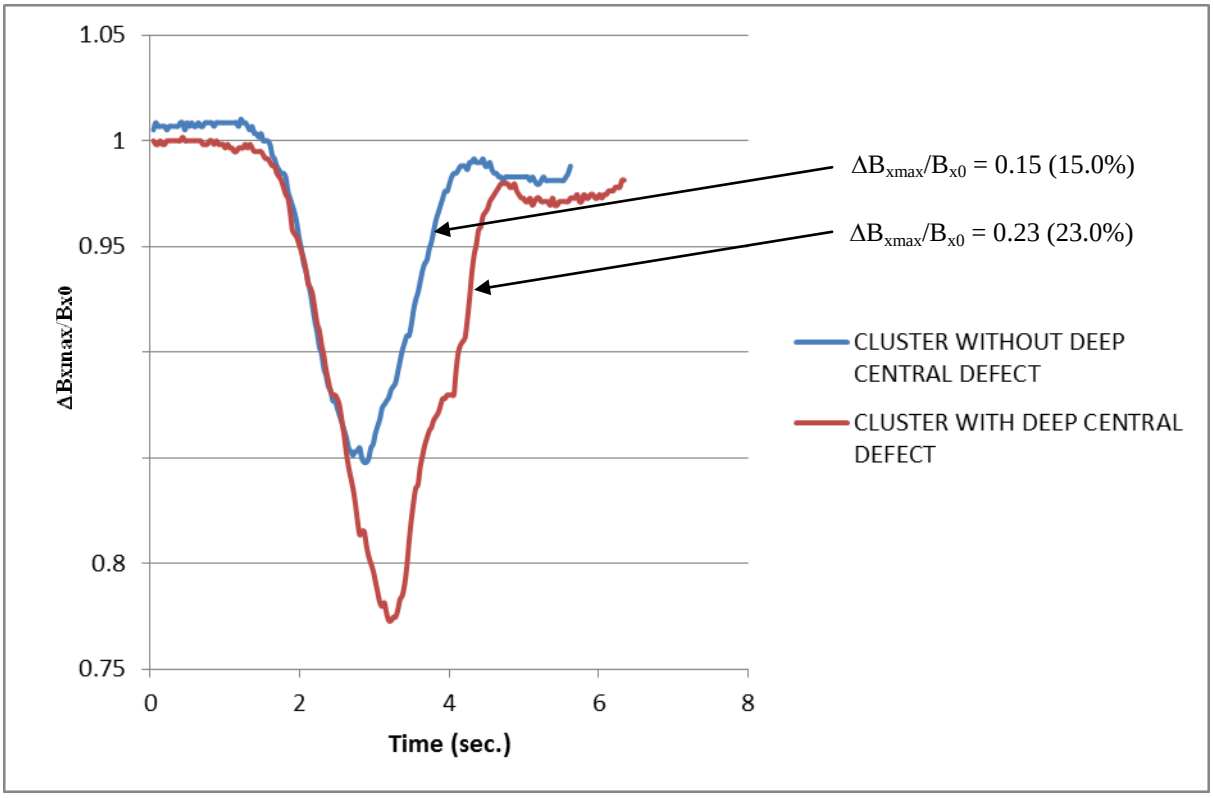

Figure 7.22 shows the ACFM scans for crack clusters with and without a central deep crack with the ACFM sensor aligned parallel to the cracks and operating at a frequency of 50 kHz.

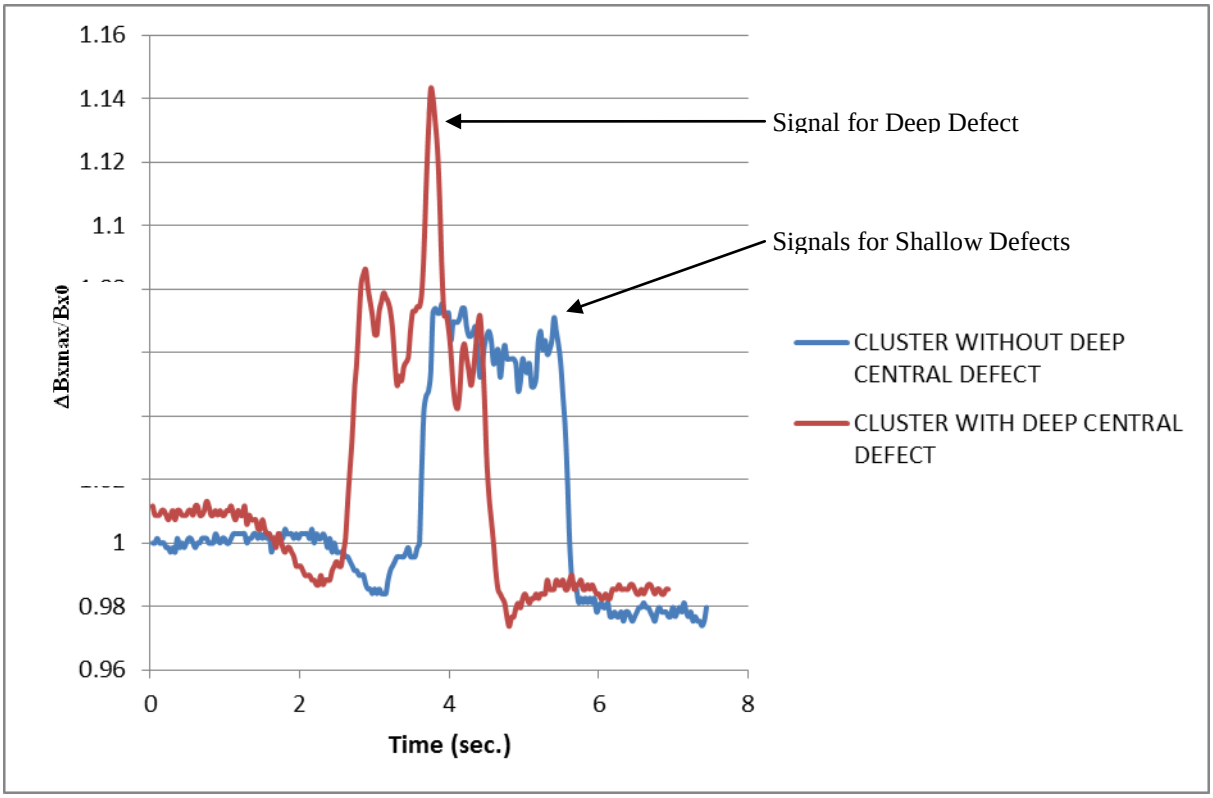

Figure 7.23 shows the ACFM scans for crack clusters with and without a central deep crack with the ACFM sensor oriented at 90^0 to the cracks and operating at a frequency of 5 kHz.

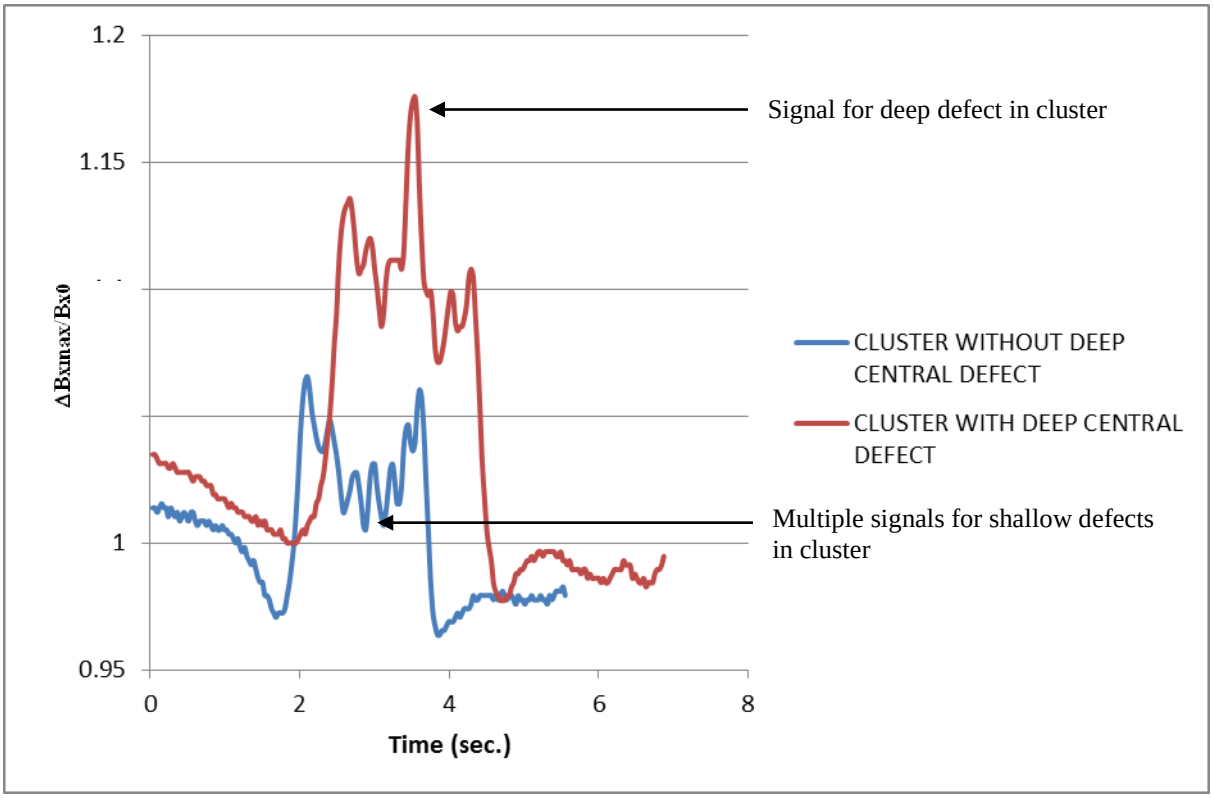

Figure 7.24 shows the ACFM scans for crack clusters with and without a central deep crack with the ACFM sensor oriented at 90^0 to the cracks and operating at a frequency of 50 kHz.

7.3.2 INFLUENCE OF RAILWAY WHEEL TREAD POSITION AND THE SEVERITY OF CRACKS ON THE ACFM SENSOR BACKGROUND SIGNAL FOR RAILWAY WHEELS IN SERVICE

The aim of the work presented here is to investigate rolling contact fatigue (RCF) type defects in worn rail wheels removed from service using an alternating current field measurement (ACFM) sensor. To this end railway wheels HSR1, HSR2 and HSR3, which were removed from service from modern multiple-unit trains running in the UK with different severity levels of tread damage have been investigated. ACFM measurements were carried out using an Amigo instrument with two different probes operating at frequencies of 5 and 50 kHz developed by TSC Inspection Systems (UK). The measurements were carried out with the ACFM probe oriented parallel to the crack to ensure that the current flow is perpendicular to the length of the crack [7,8]. Furthermore, measurements were made at zero lift off (pencil probe touching the wheel surface) and at different positions along the tread surface from the non-flange end ("tread position" refers to the distance from the non-flange edge) for the worn rail wheels HSR1 and HSR2 removed from service and the rail wheel HSR3 which is the 'new' wheel without showing no, or little, signs of visible damage or defects and that acts as a control. At least four scans were made at each tread position for all the rail wheels investigated and the results are found to be reproducible.

All crack size range estimates for the three rail wheels at different tread positions are evaluated using the UK Network Rail diagram, as shown in the previous chapter, and determining the maximum normalised change in each B_x signal, i.e. $\Delta B_{xmax}/B_{x0}$, for each crack signal and then using the diagram based on the UK Network Rail crack dimensions found in wheels in service on the rail network as shown in the previous chapter (figure 7.2) to determine the range of surface lengths for each normalised signal in conjunction with the different types of ellipse ratio curves on the diagram; and from the determined range of surface lengths ellipse ratios estimates have been determined for the crack pocket depths for the ACFM signals obtained for each observed and labelled crack in all ACFM traces presented in appendices C-E incl. in the appendices chapter 8. This is a simplified approach as the method is treating the cracks found in these rail wheels removed from service as semi-elliptical in shape, however, in reality, the nature of such cracks and their shapes which are found in the tread surfaces of the rail wheels under investigation are found to be more complex as

shown by the three-dimensional images of cracks present in wheels in service derived using the methods of multi-sectioning in conjunction with optical microscopy and x-ray tomography reconstructed images of the cracks observed in the defective worn rail wheels HSR1 and HSR2. ACFM scans were made over the wheel segments of the wheel without visible RCF cracks (HSR3). Four wheel segments were scanned each of approx. 60 cm in length.

Results obtained for the HSR1, HSR2 and HSR3, rail wheels show that the background ACFM signal varies with position across the tread as shown in figure 7.24 (note that in this figure the B_x data are not normalised in order to clearly show the variation in the background signal with and without defects) and the data in tables 6.2 and 6.3 (below) and in the figures shown in the figures in appendices C-E incl. in the appendices chapter 9. It is known that changes in microstructure and residual stresses can affect electromagnetic signals [2]. The ACFM values for the HSR3 wheel are consistent and show little scatter for positions 2.5 and 3.0 cm from the non-flange end.

Furthermore, ACFM scans were made over worn wheel segments sectioned from wheels HSR1 and HSR2 containing defects to a greater and lesser degree, respectively. Two wheel segments, of approximate segment length of 38 cm, from wheel HSR1 were examined, from the same wheel but at diametrically opposite positions around circumference of the wheel at the maximum and minimum run-out positions of the tread of this wheel as earlier discussed in chapter 4. Visual observation indicates surface breaking cracks approx. between tread positions 4 to 6 cm from the non-flange edge. No significant cracking has been observed at a tread position of 8 cm from the non-flange end of this worn wheel, however, scatter is still being seen in the ACFM signal (see table 6.1), which might mean that cracks exist beneath the surface. Once again, the results show that the background ACFM signal varies across the tread as shown in the figures in appendices C-E incl. in the appendices chapter 8 and these results correlate well with the wheel tread hardness contour maps shown earlier in chapter 4 for the more defective wheel section (tread B) and less defective wheel section (tread A) where the areas colour coded as red near the tread surface are the areas of interest where the cracks are found to be more prominent and the micro-hardness values are found to be the highest thus reducing the ACFM signal at these positions as shown in tables 6.1-6.3 incl. (below) and also

corresponds to the strained regions where the microstructure is significantly different from the unstrained region below the tread surface as discussed in chapter 4 which shows the microstructure of the worn wheel in the unstrained and strained regions, in the bulk and near the surface of the tread at positions of maximum and minimum run-out. Furthermore, it is also shown in chapter 6 that as the cracks are large in the RCF region of the worn wheel HSR1 the initiation stage will have been removed by wear and as demonstrated and discussed in that chapter the matrix appearing as if it has seen little strain here and thus suggesting that this is some way from the surface of the wheel. In that case the cracks will be driven more by elastic stresses and therefore will not be microstructurally controlled. As a result this would have detrimental implications for the sizing of surface breaking RCF cracks by the ACFM technique. This is because if the initiation stage of the crack is far removed from the tread surface this would yield significantly smaller B_x and B_z ACFM signals than would otherwise be expected if the crack initiation stage had not been worn away by the process of wear and thus would provide a misleading and erroneous measurement for the crack size (length and depth) because the ACFM signal would be reduced relative to the amount of the crack that had been removed from its initiation stage by wear.

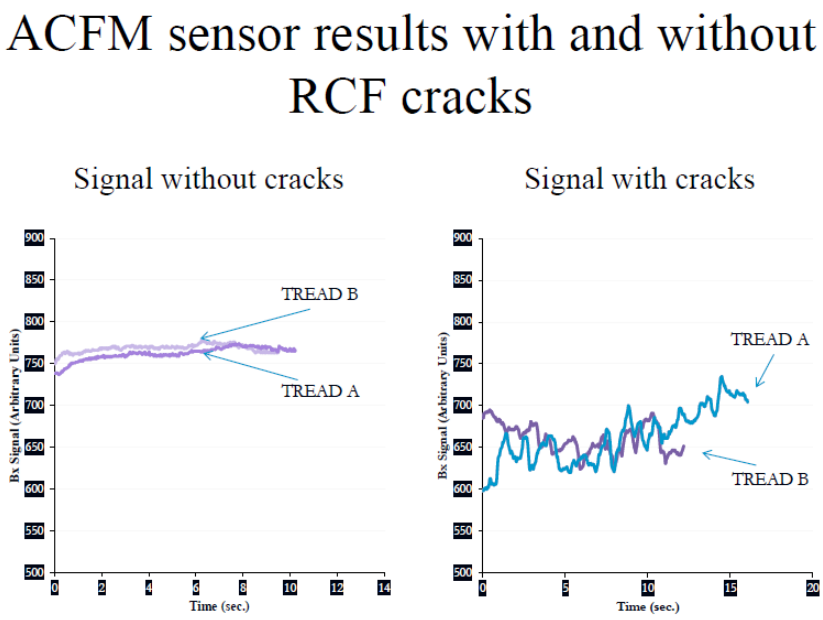

Figure 7.25 shows the variation in the background ACFM signal B_{x0} with tread position for the worn wheel HSR1 at tread positions of maximum and minimum run-out with and without cracks present. Note: that the above B_x data are not normalised in order to clearly show the variation in the background signal with and without defects.

Table 7.10 shows the variation in ACFM signal with Tread Position for Railway Wheels HSR1 (mean value taken for the maximum and minimum run-out wheel tread positions) and HSR3 for the sensor operating at a frequency of 5 kHz.

Wheel Tread Position from Non-Flange Edge (cm)	Mean B_x (New Wheel)	Mean Standard Deviation (New Wheel)	Mean B_x (Worn Wheel)	Mean Standard Deviation (Worn Wheel)
2.5	749.5	5.7	755.2	6.3
3.0	746.3	4.8	764.9	6.0
4.0	769.1	10.0	755.7	16.9
5.0	793.7	5.1	661.3	27.9
6.0	803.5	3.7	610.3	29.6
7.0	812.3	3.3	743.7	41.2
8.0	817.7	7.2	801.9	16.0
9.0	747.7	5.4	822.5	12.2
10.0			840.6	10.7

Table 7.11 shows the variation in ACFM signal with Tread Position for Railway Wheel HSR2 for the sensor operating at a frequency of 5 kHz.

Tread Wheel Tread Position from Non-Flange Edge (cm)	Mean B_x for wheel HSR2 with the ACFM probe positioned parallel to cracks/45^0 to the tread running direction	Mean Standard Deviation for wheel HSR2 with ACFM probe positioned parallel to cracks (45^0 to tread running direction)	Mean B_x for wheel HSR2 with ACFM probe at 90^0 to the running direction	Mean Standard Deviation for wheel HSR2 with with ACFM probe at 90^0 to the running direction
2.0	772.2	4.0	755.2	4.6
3.0	781.7	2.6	777.3	4.6
4.0	783.4	4.7	775.1	3.0
5.0	798.5	5.6	796.5	4.9
6.0	809.6	4.3	806.4	4.2
7.0	813.9	3.9	813.8	5.3
8.0	827.8	2.9	813.2	3.3
9.0	828.2	3.6	822.2	3.3
10.0	859.3	2.1	852.6	1.3

Table 7.12 shows the variation in ACFM signal with Tread Position for Railway Wheels HSR1, HSR2 and HSR3 for the sensor operating at a frequency of 50 kHz.

Wheel Tread Position from Non-Flange Edge (cm)	Mean B_x (arbitrary units) for Worn Wheel HSR1 (Max. Run-Out)	Mean B_x (arbitrary units) for Worn Wheel HSR1 (Min. Run-Out)	Mean B_x (arbitrary units) for Worn Wheel HSR2	Mean B_x (arbitrary units) for New Wheel HSR3
1 cm	640	650	645	640
2 cm	640	640	650	620
3 cm	580	640	650	680
4 cm	500	550	680	680
5 cm	650	660	700	690
6 cm	700	700	700	700
7 cm	700	700	700	700
8 cm	700	700	680	720
9 cm	730	730	730	720
10 cm	760	730	760	

7.3.3 THE CAPABILITY OF THE ACFM SENSOR TO DETECT AND SIZE (LENGTH AND DEPTH) CRACKS AND THUS ASSESS THE SEVERITY OF DAMAGE IN RAILWAY WHEELS IN SERVICE

Before proceeding to the discussion pertaining to the results obtained from this study it is, in my view, of utmost importance here to stress and make clear at this point that the wheel HSR1 which was supplied by Manchester Metropolitan University (MMU) for the purposes of my work was a fresh segment of the wheel which was not identified as having previously been magnetised by MMU for MPI examination as the confidential reports [181,182] accompanying the wheel that are in my possession and were supplied with the wheel do not suggest otherwise, as MMU had prepared separate sliced sections from the wheel for their MPI work as discussed in their confidential report which I have in my possession and have cited within the references section of the PhD thesis that was supplied together with the rest of the raw wheel HSR1 that had not been magnetised by MPI at the start of my PhD project. In addition, I have worked on two other wheels, namely HSR2 and HSR3, from different suppliers that had previously not been magnetised by MPI as no MPI had been carried out on these wheels prior to being supplied for the purposes of my work by the manufacturers. Therefore, the segment of the wheel HSR1 which I have used would not have been magnetised as it is a separate section of the tread position of the wheel that was supplied to University of Birmingham on my behalf for the purposes of my

work as discussed in the previous chapter and in this chapter. Therefore, the ACFM crack measurements and data obtained and presented in this chapter for wheels HSR1, HSR2 and HSR3, that were supplied by three different and independent railway manufacturers and that had not been previously magnetised are valid. Nevertheless, a discussion regarding the influence of residual magnetism on the ACFM signal based on recent research carried out by Mike Smith (TSC Inspection Systems Limited, Milton Keynes, United Kingdom) and Stephen Ford (Daimler Chrysler Rail Systems (UK) Limited) as reported in reference [207] on the effect of magnetisation on steel material that may occur, due to for example MPI, on the ACFM signal is now presented for such a scenario. The following is reported in the aforementioned report supplied by Dr. Mike Smith, for the purposes of my work presented here, on experimental laboratory tests that are intended to establish if a magnetic field in a work piece affects the detectability of defects using the ACFM technique. In theory, the ACFM technique operates by inducing an ac magnetic field into the work piece under test and, detecting changes in the fields around defects. Therefore, if a work piece has a residual or applied uniform magnetic field, only the base level will change and the changes to induced ac fields that are caused by the presence of defects in the work piece will remain unaffected. The above authors have stated in their report that these tests, whilst not conclusive, support this view for fields of 10 Gauss and probably 20 Gauss, and that to be mor conclusive, additional tests are required [181]. The experimental procedure employed for the purposes of the above test, that had been conducted by these authors in order to investigate the effect of uniform residual or induced magnetic fields on defect detection and sizing in a work piece, is as follows. The method involved placing a permanent magnet at different positions on a work plate, i.e. transverse and longitudinal to the defect, and subsequently scanning the defect with the ACFM probe. The magnetism at the defect was measured with a calibrated Gauss meter, serial number 28/0020, having a full scale deflection of 20 Gauss [181].

The results show an effect of the cracks in the HSR1 wheel sections on the ACFM sensor. However, it is not possible to separate out signals from individual cracks as they are severely overlapping each other. The figures presented in appendices C-E incl. in the appendices chapter 9 clearly show the presence of clusters of cracks of various sizes at different positions across the rail wheel tread of the worn wheel and

the wheel without visible RCF cracks, respectively, indicated by the change in the B_x signal (signified by a trough); these changes in the B_x signal are clearly labelled on each ACFM scan trace presented in the appendices and in the selected figures shown in this chapter (below). Furthermore, ACFM scans were carried out on the worn wheel HSR2 undertaken with the ACFM probe positioned at 90^0 to the tread running direction. Again, all positions where the measurements were taken are from the non-flange end of the tread and were conducted at positions between 2 and 10 cm and selected results are presented in this chapter and in appendices C-E incl. in the appendices chapter 9.

The results show that the present ACFM sensor is capable of detecting and sizing relatively large cracks which are superimposed upon each other. However, it is found that the ACFM sensor, in its current state, is incapable of distinguishing between individual surface breaking cracks in the treads of rail wheels investigated and thus is incapable of detecting and sizing individual cracks in these rail wheels. And as shown in the previous chapter clusters of closely spaced cracks would give a larger B_x signal than each of the isolated cracks in the cluster thus yielding a misleading result in the estimation of the cracks present in the cluster and with a significant error in the calculation of the crack size (length and depth) and therefore this needs to be taken into consideration when applying the ACFM in its current form to industrial applications for the sizing of surface breaking RCF-type cracks found on railway lines and railway wheels in service on the UK Railway Network. However, at best the ACFM system in its present state can detect the presence of cracks in railway wheels and components and provide an estimate of crack sizes for a conglomerate or a multiple stack of cracks which are superimposed upon each other.

Furthermore, the work has shown that the ACFM sensor is capable of detecting clusters of surface breaking RCF cracks in the worn railway wheels (HSR1 and HSR2); and in the case of the relatively ‘new’ railway wheel which does not show much sign of the presence of visible defects on the tread surface (HSR3) the results do however, indicate the presence of sub-surface defects present in this wheel just below the tread surface as can be inferred from the relatively small ACFM signals obtained at various positions along the tread of this wheel. Selected results obtained for the three railway wheels investigated for this work are shown in the ACFM scans in the

figures presented in appendices C-E incl. in the appendices chapter 9. The slight rise in the strength of the signal as the ACFM probe is passed over the tread during the scan as observed in some of the scans is most likely due to a combination of the effects of the unevenness (or out-of-roundness) of the tread surface and the slight change in the curvature of the tread along the line of the scan. At all times during each scan carried out the ACFM probe was hand held vertically at right angles to the tread surface and at zero lift-off and at a position oriented, at best, parallel to the surface cracks so as to ensure that the ACFM sensor is constantly maintained at the optimum position for obtaining a good ACFM signal and thus the detection of the cracks present near the tread surface.

In addition, the results shown in figures 9.33-9.48 incl. in appendix D and table 7.2 for the least defective wheel worn wheel HSR2 indicate the presence of small cracks near the tread surface of the rail wheel from the ACFM signals obtained within experimental uncertainty. This supports the results shown and discussed in chapter 4 which show the presence of small surface breaking RCF-type cracks present along the tread at different positions along the tread of this railway wheel, in particular, near the flange end where there are closely spaced shallow cracks oriented at an approximate angle of 60^0 to the circumferential direction across the entire circumference of the wheel and also at a position of about 3 cm from the non-flange end of this wheel where again there are shallow defects but which are oriented almost perpendicular to the circumferential direction.

The normalised B_x change is the measure that has been used for quantifying the cracks. The normalised change in the B_x signal is given by $\Delta B_x/B_{x0}$ where, ΔB_x and B_{x0} are the change in the B_x signal and the background B_x signal, respectively. In order to size the defects correctly it is necessary to estimate the background signal that should be subsequently used to determine the ΔB_x values and the normalised change for the defective wheels. To this end estimates were made for the background signal from the ACFM results obtained for all the rail wheels which were investigated. It is found that the mean estimates for the background B_x signal which should be used to subsequently determine the ΔB_x signal for the calibration plate cracks, wheel without visible RCF defects and the worn wheels, are 770, 780 and 800, respectively, and these estimates for the background ACFM signal for the wheels with different levels

of damage were then used appropriately to evaluate the crack pocket lengths shown in table 6.4 for all cracks and/or crack clusters identified from the ACFM scans presented here. However, it should be stated that the results obtained have shown that an appropriate value for the background signal to use for all similar rail wheels would be 800 because it is found that in every case the value obtained for the crack pocket length for all the cracks and/or crack clusters identified is the same to three significant figures whether the value used for the background ACFM signal lies between 770 and 800. Therefore, a background value of 800 has used as the mean estimate for the background signal for all similar rail wheels to determine the ΔB_x and the normalised change in order to quantify the cracks. Furthermore, it should be stated that this optimum mean background signal was chosen from the results obtained using the ACFM sensor operating at a frequency of 5 kHz for all three wheels investigated for this study in order to estimate crack pocket depths, however, it is found from this work that the background ACFM signal changes with the operating frequency of the sensor and is significantly lower for a higher frequency sensor operating at 50 kHz, however, as the background signal values (arbitrary units) are relatively large for the sensor operating at these frequencies in comparison to the maximum change in the B_x signal for the crack(s) then choosing either of the mean background signal values for the high or low frequency sensor (the value generally is lower by about 100 arbitrary units for the 50 kHz ACFM sensor than when the sensor is operating at a frequency of 5 kHz) the evaluated crack pocket depths are not significantly different from one another; therefore, it is safe to choose a value of 800 for the background signal to calculate an estimate for crack pocket depths in worn railway wheels in service. Furthermore, it is not possible at present to separate out signals from individual cracks as they are found to severely overlap each other on the railway wheels investigated as part of this study. The work has also shown that the range of crack pocket depths and surface lengths estimated, using the normalised maximum change in the B_x signal (i.e. $\Delta B_{xmax}/B_{x0}$) in conjunction with the diagram shown in figure 7.1 using the range of four semi-elliptical ratios shown on the diagram, from the ACFM sensor when scanned over the tread surface at different positions along the tread surface on wheels HSR1, HSR2 and HSR3, are between: 2 and 18 mm which agrees well with the crack depths and surface lengths found by using optical metallography, X-ray tomography in conjunction with reconstruction techniques and the multi-sectioning in conjunction

with optical microscopy approach, as shown and discussed earlier in this work presented in chapter 6.

ACFM scans were made over wheel segments of the worn HSR1 wheel segments at the positions of maximum and minimum run-out for this wheel. Visual observation indicates surface breaking cracks approx. between tread positions 4 to 6 cm from the non-flange end. No significant cracking has been observed at a tread position of 8 cm from the non-flange end of the worn wheel, however, scatter is still being seen in the ACFM signal which might mean that cracks exist beneath the surface. Furthermore, the results clearly show an effect of the cracks in wheel HSR1 on the ACFM sensor. However, it is not possible to separate out signals from individual cracks as they are overlapping quite severe. To my knowledge no relationship has been reported in the literature to relate the B_x signal to the crack depth based on the crack length; as the relationship will depend on the crack shape [7]. The existing methods use either complex signal inversion algorithms, for example, using a neural network approach [17] or by reference to a database containing different crack geometries that relate the B_x signal to the depth profile for a crack surface length [26]. Recent work carried out by [26] has demonstrated that the accuracy of the data will be influenced by the spacing between the ACFM scan lines. The above authors have also reported that the signal will be affected by the ACFM probe angle by the variation in signal to noise ratio. Therefore, the probe angle needs to be maintained at the crack surface angle to obtain maximum field perturbations, thus leading to an optimisation of the signal to noise ratio. Furthermore, in line with my work presented here, the results presented by these authors do not show any clear indication of multiple cracks they have also reported that as there is no differentiation of the separate cracks, crack surface length and angle gives significant error. Furthermore, figure 7.11 shows a signal indication for a cluster of cracks in the large trough for the B_x signal trace labelled “D”. This cluster of cracks is inferred from the work presented in the previous chapter where it is shown that a cluster of closely spaced cracks yield a large B_x signal and therefore this result suggests that this cluster of cracks are closely spaced and, bearing in mind the findings from the study on the influence of crack spacing and crack cluster number carried out by using the ACFM on artificially created semi-elliptical cracks (or “notches”) machined into a calibration steel plate by the EDM process for controlled experiments reported in the previous chapter, are thus likely to be closely

spaced cracks as inferred from the presence of a number of very small troughs found at the bottom of the deep resultant signature signal for this cluster of closely spaced cracks at “D”; there are possibly five cracks in this cluster as inferred from the five small troughs at the lower part of the main large trough. This is similar to the ACFM signal shown for the closely spaced and shallow cracks that are found near the flange end of railway wheel HSR2 in figure 7.42 (below). Thus, the results presented here obtained from the work conducted using the ACFM probe to detect cracks in the surface of railway wheels removed from service corroborate the findings from the study carried out using the ACFM system on artificial cracks in a steel calibration plate in a controlled environment as discussed in the previous chapter.

The results shown in figures 7.40 and 7.41 demonstrate that the ACFM sensor working at a frequency of 50 kHz ACFM sensor is more sensitive to detecting and distinguishing between individual cracks, albeit relatively; thus a higher frequency sensor is relatively better in detecting and distinguishing between cracks, however, it is still not possible to fully discriminate between individual cracks. To this end an array of ACFM sensors at different orientations, especially positioned at angles of +/- 45 degrees and at other angles to the crack surface angles should be incorporated within/into a system in order to detect cracks and size these cracks properly which may/might be oriented at different angles to the probe angle. Also, note that the background signal is lower for the ACFM system working at an operating frequency of 50 kHz as compared to the ACFM working at 5 kHz. This is a trend that has been seen in all the results obtained from this work on all railway wheels investigated: HSR1, HSR2 and HSR3, including in the ACFM signal response to artificially created cracks (or “notches”) in the calibration plate discussed in the previous chapter, and is lower by about/approximately 100 arbitrary units for all railway wheels studied / investigated.

Figure 7.42 shows ACFM scans of shallow closely spaced cracks (spacing < 3 mm) found close to the flange end of the worn HSR2 wheel tread using the ACFM sensor operating at frequency of 5 kHz. This shows that the ACFM cannot distinguish between individual cracks and gives a single large B_x signal with a deep trough as shown. This is in agreement with the results presented in the previous chapter which show that the ACFM produces a single large B_x signal for closely spaced cracks as

these cracks; from visual inspection of the tread these cracks are spaced by about 3 mm. However, the small ‘spikes’ which can be seen at the bottom of the trough suggest the presence of a cluster of closely spaced cracks in this figure as also shown by controlled experiments in the previous chapter where ACFM scans on closely spaced cracks show a similar effect. However, this large signal, as shown in chapter 5 would give an erroneous oversized estimate for these cracks due to their close spacing.

In addition, table 7.4 and figure 7.43 show calculated estimated values of crack pocket depths at different positions along the tread surface of wheels HSR1, HSR2 and HSR3, using the Network Rail based Crack Sizing Plot by evaluating the maximum change in the ACFM (5 kHz) Signal and using this value to determine the range possible range of crack surface lengths and thus the range of crack pocket depths from the four ellipse ratios presented on the sizing diagram. These results are in line with the range of crack depths as determined using optical microscopy, X-ray tomography and multi-sectioning in conjunction with optical metallography experiments.

Furthermore, due to variations in the lift-off that occur during inspection of the rail wheels removed from service as a result of roughness of the tread surface and in the case of the normalised results obtained for the main calibration plate discussed in the earlier section above at different lift-off distances the ACFM system cannot provide correct rankings for the crack depths under these conditions which is also in agreement with previous work in this field [43, 86, 88, 117, 132], nevertheless, all the artificial cracks (or “notches) and most RCF cracks found in the railway wheels removed from service and investigated using the ACFM probe were detected.

In actual service conditions it is generally well known that RCF cracks can depart from the simplistic assumed and approximated shape of such cracks as an ellipse. This is particularly the case for cracks that are classified as, in some cases, moderate, heavy and severe according to the Network Rail UK guidance diagram as described before. In reference [148] it has been demonstrated by a study carried out on moderately sized RCF cracks that the sub-surface portion of such cracks might extend to a significant extent beyond the surface breaking component. Thus, for the purpose maintain the integrity, safety and maintenance of railway track and railway wheels it is of utmost

importance to be able to accurately detect and size the deepest part of such a complex shaped crack in order to assess its severity. It is reported in the literature [148] that the ACFM technique is currently incapable of differentiating the above complex RCF crack shape with the part of the crack that extends beyond the surface breaking component and a smaller crack shape that has had the extended portion of the crack beyond the surface breaking component removed from the shape using the COMSOL Multiphysics software to model the response of the ACFM sensor to a simulated moderate sized RCF crack which extends beyond the surface breaking component.

It is believed that the presence of the deepest section of the complex crack that extends beyond the crack's surface breaking component results in the current being made to flow around the side of the defect instead of flowing under the defect when compared to the case of a semi-elliptical shaped crack of an identical pocket length size. As a result, the reduction in the B_x component of the magnetic field in the former is less in comparison to the latter. Therefore, for the accurate sizing of cracks the ACFM technique, in its present state, is more suited to be applied to the sizing of cracks classified as light to moderate sized RCF cracks on the UK Network Rail diagram classification diagram, albeit with some degree of error being introduced for the latter case dependent on the development of the complex shape of the crack.

Furthermore, a previous study reported in reference [172] that has been carried out in order to investigate factors that influence the skin depth during crack sizing experiments using the ACFM technique. This study was initiated in an attempt to account for approximately small (approximately 10%) differences between crack depths measured using the ACFM technique and measured by ultrasonic systems and, thus, investigate the factors that may influence the surface voltage readings as, in the case of the ACFM system, the A.C. field applied to a metal is confined to a skin layer of the surface and then the surface electric field is investigated employing a voltage-difference probe. A change in the voltage gradient along the surface is interpreted as being due to a change in the path length along a field line between the probe contacts, thus indicating the presence of a crack [172]. As the ACFM has a constant current output any change in the measured voltage that is not caused by the presence of a defect must therefore be the result of a change in the skin depth. The measured voltage is proportional to $(\sigma\delta)^{-1}$ and hence to $(\mu/\delta)^{1/2}$ [172], where, μ and σ are the

magnetic permeability and electrical conductivity of the material, respectively, and δ denotes the skin depth. The main theoretical analysis in the study reported in [172] has been confined to investigating the effects on magnetic permeability as any factor that influences electrical conductivity will have a much greater effect on magnetic permeability. Mechanical stress is known to be a major factor that affects magnetic permeability and thus, the study reported in [172] has focused on this aspect and on the influence of anisotropy in the surface of the material being inspected due to rolling or machining.

Magnetic materials are comprised of atoms that have uncompensated electron spins which give rise to a net magnetic dipole moment. The electrostatic interaction between atoms that determines the interatomic spacing coexists with an exchange interaction between the electron spins. The strength of this interaction in ferromagnetic materials is such that the total energy of the system is a minimum when all dipole moments are aligned parallel to each other and, particularly in the case of iron, in a direction parallel to the [100] crystal plane. However, in actual materials if all the spins were aligned in the same direction then there would be a large amount of magneto-static energy associated with the magnetic field closure lines. This is reduced as a result of the material being devolved into magnetic domains. Within each domain the spins are oriented parallel to each other, however, the direction of alignment changes from one domain to another, typically by 90^0 or 180^0. Furthermore, the presence of an inhomogeneity in the crystal lattice structure due to an applied stress thus introduces additional terms in the interaction energy [172,173]. For a tensile stress the domains that are oriented approximately parallel (or anti-parallel) to the stress grow, whereas in the presence of a compressive stress the domains that are oriented perpendicular to the direction of the applied stress grow. In the case of high stresses, or within single domains, the energy minima are somewhat displaced away from the crystal axes.

Permeability is a measure of the extent to which a material's net magnetisation has increased in the presence of an external magnetic field. The net magnetisation of the material is the vector sum of the individual magnetisations of every domains and is zero for an un-magnetised material. In the case of an external magnetic field (H) being applied an additional term, $MHcosX$ is introduced into the equation which yields the

interaction energy, developed by Kittel that can be found in references [172,173], between a magnetic dipole and the surrounding field for a cubic lattice in the presence of a uniaxial applied stress (T), where *M* denotes the magnetisation of each domain and *X* is the angle between *M* and *H*. Therefore, domains that are oriented approximately parallel to the magnetic field (H) will tend to grow at the expense of domains that are oriented anti-parallel to the field. The permeability of the material, which is given by $\mu=M/H$, is limited by the fact that in order to increase the net magnetisation domain walls need to move past obstacles such as dislocations, inclusions etc. which, thus, requires an expenditure of energy. As a result of the random nature of the distributions of dislocations, orientation of domain walls etc., it is essentially rather difficult to make quantitative predictions of the influence of stress on the permeability of the material, nevertheless, the qualitative effect may be demonstrated as in [172] where it is reported that in the case of an external magnetic field which is applied parallel to the direction of the applied stress permeability is increased with tension as in that case there will be more domain walls which are more favourably oriented and the permeability is decreased with compression. Whereas, the opposite is the case when the field is perpendicular to the stress. In principle, the ACFM system is used in a manner which ensures that the electric field is oriented parallel to the stress axis in order to ensure that the magnetic field is perpendicular to the stress. The study conducted in [172] has demonstrated that the relationship between the ACFM micro-gauge reading and stress is fairly linear with minimal hysteresis and good repeatability and that the stress influences permeability to a much greater extent than conductivity. It is reported by these authors in [172] that the micro-gauge voltage readings increase with tension as expected, even though the change is not as large as in the case of a parallel field. Furthermore, the plastic deformation of a material leads to most of the cross-section being under compressive residual micro-stress with small regions under higher tensile residual micro-stresses [172]. Thus, the specimen subsequently behaves as if it has an initial comprehensive stress superimposed on any applied stresses. Thus, it is reported in the literature [172] that the bulk of the increases observed in the micro-gauge readings appear to be due to the inherent internal micro-stresses in the material. Since the applied stress influences the permeability of the material it is therefore possible that rolling or a similar process may affect the permeability as well. Particularly, in the event that the grains become elongated in one specific direction then that direction will be a preferred axis of

magnetisation. Thus, an A.C. field that is subsequently applied in this direction will then experience a lower permeability and therefore produce a lower surface electric field strength. It is also reported in [172] that the surface conditions of the material had a greater effect on the micro-gauge readings than bulk anisotropy; and it is also demonstrated that in the elastic region, due to the small hysteresis observed in this region it, thus, makes it feasible to invert the experiment and predict surface stresses from the micro-gauge readings. However, in order to obtain absolute stress values a reference reading needs to be taken on a part of the specimen under test that is assumed to have zero stress; care must be taken though to ensure that any geometric effects during the experiment are eliminated that would otherwise result in a non-uniform field distribution over the specimen. It should be noted that if the region which is being tested has previously undergone plastic strain, then there is no unique relationship between the present stress level and the micro-gauge reading.

The magnetic properties of ferromagnetic steel material such as hysteresis loops, permeability, coercive force, remanence, etc., are dependent upon numerous material characteristics, for example, chemical composition, metallurgical structure (such as grain size, phase and texture), hardness and mechanical stress [175]. As a result, the study of the influence of each individual material characteristic has received widespread attention in the recent past because of its potential application to non-destructive characterisation materials including online monitoring of material properties. Thus, a comparison of the various pertinent material characteristics, as above, on the magnetic properties requires attention. Previous work carried out and reported by Kwan and Burkhardt [177] on studying the effects of grain size, hardness and stress, on the magnetic hysteresis loops of steel specimens has demonstrated that the mechanically harder materials exhibit a smaller magnetic induction (B), thus indicating that they are harder to magnetise. In general, it is found that the hardness effect is greatest when the magnetic field strength (H_m) is in the range where the maximum magnetic permeability occurs. It is also reported by these authors that there is no general relationship between the coercive force and hardness of materials. The applied stress significantly changes the shape and magnitude of the hysteresis loops. Qualitatively tensile stress is found to increase the magnetic induction (B) and the slope of the sides of the hysteresis loops, whereas, compressive stress has the opposite effect. Furthermore, these authors report from their findings that the ratio between

residual induction (B_r) and the maximum induction (B_m) increases during tension and decreases under compression. The above described qualitative behaviour of the influence of stress is typical for ferromagnetic materials that have positive magneto-striction coefficients and is based on the domain theory and the magneto-elastic interaction effect [173,175,176]. Quantitatively, the effects of stress are dependent on the material type, H_m value and the hardness of the material. Furthermore, as in the case of the hardness effect, the stress effect is found to be the greatest when H_m is in the range where the steepest change in the magnetic induction occurs and the mechanically harder material exhibits the least stress effect than a softer specimen, thus, indicating an inverse relationship between the effect of stress and hardness, as reported by the above authors in [177]. As there is no relationship between the effects of stress and grain size, thus, suggesting that the magneto-elastic interaction which produces the stress effect, is not influenced by grain size. Furthermore, as the magneto-elastic interaction energy is dependent upon the angle between the stress and magnetisation directions [175,176] the resulting stress effects on the hysteresis loops, thus, also depend upon this angle. As a result, on the application of a uniaxial stress to the material the hysteresis loops become anisotropic and, thus, exhibit a dependence on the magnetisation direction. Generally, a magnetic field applied perpendicular to the direction of the stress results in the behaviour of the stress effects on the hysteresis loops [178] or other magnetic properties such as Barkhausen noise [179] that is opposite to the case where the magnetic field is applied parallel to the direction of the stress. In summary, the hysteresis loops are sensitive to both hardness and stress but are insensitive to grain size within the material. Thus, hardness and stress may be determined by employing the dependence of the hysteresis loops on these parameters. Furthermore, the stress and hardness effects can be differentiated by utilising the stress induced anisotropy. However, due to the lack of sensitivity it would be rather difficult to determine the grain size by measuring the hysteresis loops [173,175-178].

Furthermore, Erdogan et al. [180] have studied the influence of epitaxial ferrite on yielding and plastic flow in dual phase steel in tension and compression. It is reported by the above authors that the elastic limits in tension and compression were found to be indistinguishable and very low, thus, suggesting that mobile dislocations are present in the ferrite as a result of stress relaxation processes. The mobile dislocations are believed to accommodate the increase volume that accompanies the

transformation of austenite to martensite during the heat treatment process. It is also reported by these authors that, in general, their observations revealed that the epitaxial ferrite had an effect on the average proof stresses which were found to be generally higher during compression than during tension due to the presence of residual stresses in the martensite and ferrite as a result of the heat treatment procedure. These proof stresses as evaluated from the asymmetry in the proof stresses were small because of the stress relaxation in the ferrite at the temperature at which the martensite formed. It is also reported by the above authors that epitaxial ferrite significantly increased the ductility of the material due to the influence of the epitaxial ferrite on the rate of work hardening between approximately 0.5 and 3% strain and it is also reported by these authors that the epitaxial ferrite is found to reduce the work hardening rate in this range of strain. In [180] it is suggested that mobile dislocations that are present in the ferrite due to stress relaxation processes that occur in order to accommodate the volume change that accompanies the austenite to martensite transformation during heat treatment of the steel material. As the applied stress is changed in either tension or compression the mobile dislocations would be expected to glide. However, subsequently exhaustion of the mobile dislocation density would then force the flow stress to rise to a level at which conventional work hardening by dislocation multiplication and interaction may occur. Any asymmetry in the proof stress has been interpreted by these authors in terms of composite theory to imply the presence of residual stresses in martensite and ferrite after heat treatment. Stress relaxation by plastic flow in ferrite is also reported in [180] to a cause a significant decrease in the residual stress of martensite in order to accommodate the above transformation volume change. The mechanisms of stress relaxation in the ferrite content of the material are believed to give rise to the mobile dislocation density that leads to the low elastic limits in tension and compression. Erdogan et al. [180] also report that increasing the epitaxial ferrite content results in a significant increase in uniform elongation in tension with some loss of stress, and also influenced the work hardening behaviour of the material strongly, However, the above two effects were not found in a coarser material comprised of 25% martensite content. It was also found by these authors that the coarser microstructure containing greater martensite content demonstrated the least asymmetry in its proof stress in tension and compression, the lowest (i.e. near zero) residual stress and, thus, the greatest amount of plastic deformation in ferrite during the transformation process of austenite to martensite,

work hardening rates have been found to vary due to due to the behaviour of ‘old’ ferrite which is present at the inter-critical annealing temperature and the ‘new’ epitaxial ferrite that is produced during cooling prior to the formation of martensite. The effect of epitaxial ferrite in reducing the hardening rate over the strain range investigated by these authors is found to be responsible for this effect of increasing the ductility of the material. Reducing the rate of work hardening at the earliest stage of plastic deformation is found to lower the flow stress of the material over the remainder of the process in order that the work hardening rate is equal to the true stress at a larger strain [180].

Furthermore, in [182] a study carried out in order to investigate the effect of ferrite fraction, in 0.17-0.8 wt.% C steels with ferrite-pearlite microstructures on multi-frequency electromagnetic sensor readings has found that it may be possible to measure the phase fraction of the ferrite content in dual phase steel materials by using an electromagnetic sensor. It has been found that due to an increase in pearlite content (up to 90%) the relative permeability and, hence inductance, decreases. The inductance of the electromagnetic sensor is affected by changes in relative permeability. The above method aids in achieving quality control by enabling the monitoring of the phse fraction in a non-destructive manner. The differences in magnetic properties, such as magnetic permeability and electrical conductivity, in specimens with different microstructural phases, are exploited by the electromagnetic sensors. In this regard, the change in the relative permeability of the material has a significant effect in ferromagnetic steel material. Previous studies have demonstrated that electromagnetic sensors are able to determine the levels of decarburisation (variation of ferrite content with depth) in steel rod [182-184]. Power lase models are extensively used when considering the effective electrical or magnetic properties of materials that consist of two components with contrasting properties [182,185-188]. The following power lase model equation is used to predict the effective permeability:

$$\mu_e^{\beta} - (1-f)\mu_1^{\beta} + f\mu_2^{\beta}$$

Where μ_1 and μ_2 denote the relative permeability values of the first and second phases, respectively, f denotes the fraction of the second phase and β is a dimensionless parameter. For example, previously the power law has been used to

predict the dielectric constant of mixtures such as the Looyenga formula (β = 1/3) [187] and the Birchak formula (β = 1/2) [188].

The magnetic properties of ferromagnetic materials are greatly influenced by the chemical composition and microstructure of the material. Therefore, the changes occurring in the microstructure can be monitored in steel materials during manufacture or the gradual degradation of the material can be assessed by measuring and monitoring any the changes that occur in the magnetic properties of the material [189]. To this end, various electromagnetic systems have been developed in order to monitor the processing of steel material; some of these systems as reported in the literature include the following: pulsed electromagnetic sensor for the automated sorting of scrap stainless steel [190], multi-frequency sensor for the measurement of ferrite/austenitic phase fraction and identification of phase transformation during the manufacture of strip steel material consisting of multiphase microstructures [191,192], the development of micro-magnetic sensors to evaluate pinholes and defects in steel sheets and rods [193], electromagnetic sensors used to determine the grain size of continuously moving steel sheet during the different phases of processing [194]. In [195] it is reported that the size of the magnetic domain is directly proportional to the square root of grain size for grain diameters in the range 0.05 and 1.0 mm. The influence of grain size on the magnetic properties of the material is due to the generation of closure domains at the grain boundaries that obstruct the domain wall movement during the magnetisation process. Furthermore, studies that have been carried out to investigate the influence of grain size on the hysteresis loop in commercial carbon steel material [196] have demonstrated that changes in grain size affect the hysteresis loop curves and that due to the coarsening of the grains and, thus, their size, induced magnetic saturation (B_{max}) is decreased as a result. In [204] it is reported that the coercivity {H_c) is inversely proportional to the grain size and a correlation between the coercivity and the presence of ferrite and pearlite content in the material has been postulated according to the following formula:

$$Hc = c_1(v_p/d_p) + c_2(v_f/d_f)$$

Where v_p and v_f denote the ferrite and pearlite volume fractions, respectively, and d_p and d_f refer to the pearlite colony size and ferrite grain size, respectively; c_1 and c_2 are

constants. Furthermore, the presence of an additional constituent to the microstructural composition of the material has been shown in [204] to tend to dominate the magnetic behaviour when the particular additional constituent is present in the carbon steel material in sufficient quantities. In addition, in [205] it is stated that at pearlite volume fractions less than 17% the coercivity (H_c) is not significantly affected by pearlite, however, for pearlite content that is greater than 60% the value of H_c is found to increase proportionally to the pearlite volume fraction independently of the grain size. Furthermore, H_c is strongly dependent upon the percentage martensite present rather than the grain size of ferrite in ferritic steels comprised of more than 15% martensite. It is also reported in [189,205] that in the case of austenised quenched and tempered plain-carbon steel materials the prior austenite grain size has a negligible effect on the characteristics of the hysteresis loop. Furthermore, because material degradation mechanisms, such as corrosion, creep and fatigue, change the area of the affected components, it is of utmost importance to properly evaluate the feasibility of using an electromagnetic sensor to detect changes in the cross-sectional area of steel materials.

In addition, in [189] it has been demonstrated that features of the microstructure of carbon steels such as ferrite content, grain size, inclusions, etc., have a significant effect on the magnetic properties of steel material. Furthermore, the electromagnetic sensor is reported to be able to detect changes in the magnetic properties of the material as a result of changes occurring in the cross-sectional area. Therefore, the electromagnetic sensor can potentially be used as a reliable non-destructive system for the detection and monitoring of changes in the microstructure and morphology of the material that occurs during the different steel manufacturing stages or changes due to the degradation of the material. In [189] it is reported that the carbon content present in the steel material influences the magnetic behaviour of the material as an increase in the amount of iron carbide (cementite) is found to reduce the magnetisation potential of the steel material. It is also reported by the authors in [189] that the induced magnetic saturation and the coercivity which is measured using an electromagnetic sensor can be reliably correlated to the percentage amount of ferrite content, grain size and hardness value of the steel material. Furthermore, it is shown that a reduction in the cross-sectional area of the steel rods used in the study in [189] leads to a significant corresponding reduction in both the induced saturated flux and

the magnetic retentivity (i.e. the ability of the material to retain or resist magnetisation) where both of these quantities were shown to have a linear correlation with the loss of the mass of the material. Thus, an electromagnetic sensor may be employed to identify microstructural features and evaluate changes occurring in the cross-sectional area in structural steel materials. In addition, before making the following comments as postulated in a private communication by email correspondence as cited in reference [210] it must be stressed again here at this point that the three railway wheels supplied by three different and independent railway manufacturers that have therefore been investigated for the purposes of the work presented in this PhD thesis were not magnetised prior to conducting ACFM scans on these wheels. This is supported by the fact that the confidential reports [181,182] accompanying the wheel identified as HSR1 that are in my possession and were supplied with the wheel do not suggest otherwise. Furthermore, the manufacturers of wheels HSR2 and HSR3 have not indicated that these wheels are magnetised by MPI or any other means nor provided any information in the form of supported documentation neither communicated by other means to suggest otherwise and therefore these wheels are presumed not to be magnetised by MPI or by way of any alternative method. Nevertheless, in the event of the presence of the magnetisation effect in these railway wheels and thus considering a scenario in which residual magnetism may exist in these wheels the following is postulated in [210]. As the optical micrographs presented in the previous chapter of the present thesis demonstrate the material has, to a certain extent, undergone the process of plastic deformation. Hence, this implies that residual stresses may have built up in the steel microstructure. As a result, the relative magnetic permeability will not be uniform and hence will lead to variable magnetisation. This will cause a non-steady background ACFM signal leading to an underestimation or overestimation of the cracks detected.

Furthermore, the most common faults that are found to occur on wheelsets are the result of wheel and axle bearing damages [199]. An ever increasing trend of railway vehicle speeds and traffic including currently increasing axle loads means that a potential failure of the axle bearing may result in catastrophic failure and, thus, lead to derailment of the vehicle resulting in the possible loss of life, extreme disruption to the operation of the railway network, increased maintenance costs associated with the railway infrastructure such as railway track damage and, thus, leading to a loss in

confidence and customer satisfaction in the railway industry. In this regard the authors of reference [199] have demonstrated that acoustic emission signal envelope analysis serves as an effective on-board condition monitoring system for the detection and evaluation of defective axle bearings including identifying and recording their characteristic defect frequencies under actual operating conditions. It is reported in [199] that the system is capable of detecting and identifying defects in slightly severely damaged bearings, however, in the case of the mildly damaged bearings the system can only detect the presence of a defect in the component. Damaged axle bearings cause an increase in the amplitude of the peaks in the power spectrum following Fast Fourier Transform (FFT) which, thus, indicates that a defect is present in the component. Using the characteristic frequencies including their respective harmonics as well as the knowledge of the kinematics of the particular bearing(s) in question being inspected it is then possible to establish the type of defect present using this method.

Wheelsets are continuously exposed to severe operating conditions whilst in service due to damage caused by rolling contact fatigue, thermal variations and impact [199,200]. As a result, deterioration of the structural integrity of wheels and axle bearings may lead to an increase in the level of vibration, noise and temperature that is produced by the axle bearing and, thus, these collectively act as signature for a defective axle bearing [201]. Defects that are present in axle bearings are usually accompanied by increased vibration, acoustic emission (AE) patterns and amplitude. Thus, vibration analysis and AE are generally considered as the most appropriate online condition monitoring techniques for the continuous and effective monitoring of axle bearings [202]. In general, defects that are commonly found in axle bearings are classified as either distributed or local defects [203]. The former which include such defects as surface roughness, waviness, including the variation in the contact force between the rolling elements can lead to an increase in vibration and noise intensities due to the axle bearings. Whereas, the latter include defects such as cracks, spalls and pits which can subsequently generate impulse that can yield vibration of short duration or AE signals [204]. Piezoelectric sensors can be used to detect stress waves generated by AE for structural health monitoring purposes. Previous work in this area has been carried out and reported in the available literature by C. Yi et al. where defective railway bearings have been investigated using vibration analysis employing

the Ensemble Empirical Mode Decomposition (EEMD) and the Hilbert marginal spectrum to analyse the vibration data [205]. The classic axle failure is a fatigue related issue as a result of high magnitude bending stresses that alternate between tension and compression. In [208] a study has been conducted to address axle life value related to reliability and to make a comparison with the realised life value up to fracture. The section that lies between the wheel and gear is the location where the fracture occurs. This study investigated wagon loading cases based on statistical data related to passenger numbers. Minimum axle life values can be determined by considering full load and, subsequently, the effective life values can be calculated by employing Palmgren-Miner's theorem for real loading conditions in the case of different distributions. Furthermore, in [208] it is reported that the minimum axle life value as determined for a wagon travelling with load is 1.4 years and, then, using statistical data and different distributions and taking into consideration actiual loading conditions and by using the aforementioned Palmgren-Miner cumulative damage theory the analysis performed and reported by the authors in [208] has realised an average axle life value of 12 years, as the axle life value is less in the case of heavy loading than in the case for light loading conditions. Furthermore, operational in-service conditions greatly influence the effective life of axles for wagon speeds less than 13 m/s even with maximum loads the life is infinite, however, at a vehicle speed of 40 m/s even with no passengers on board the vehicle the life of the axle is reported not to be less than 2 years.

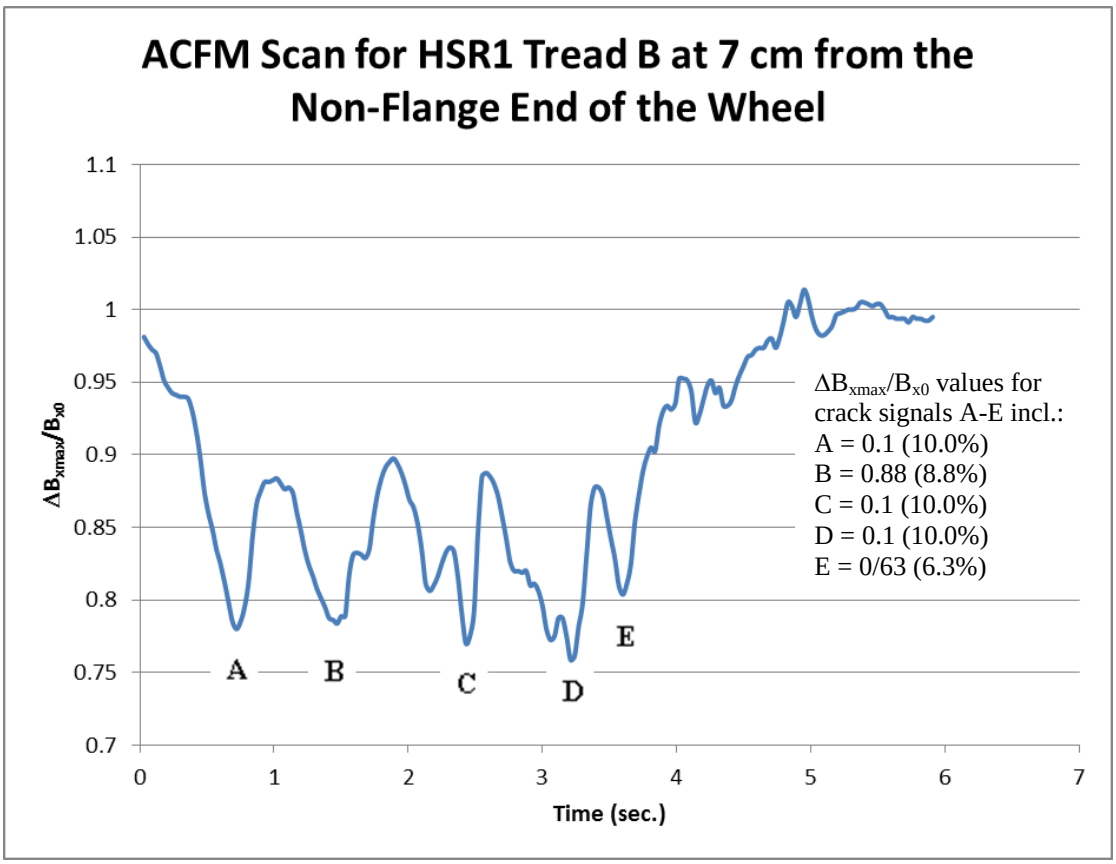

Figure 7.26 shows sample ACFM scans for the worn HSR1 wheel at the position of maximum run-out on the tread and at a position of 7 cm from the non-flange end.

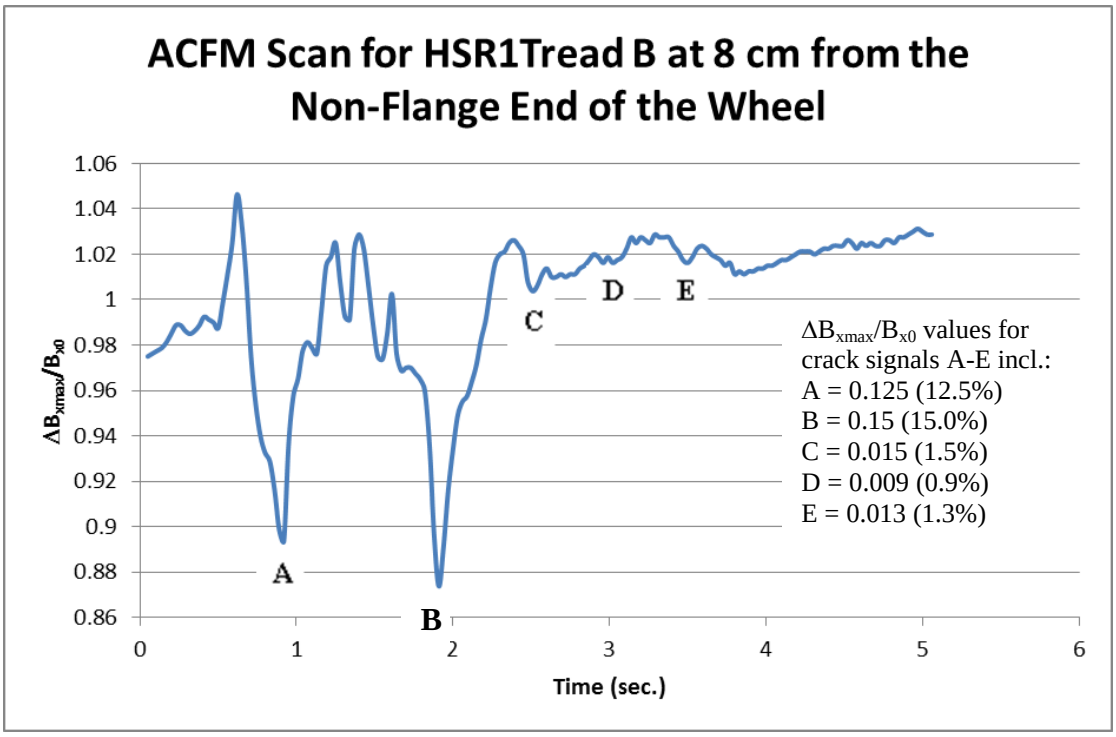

Figure 7.27 shows sample ACFM scans for the worn HSR1 wheel at the position of maximum run-out on the tread and at a position of 8 cm from the non-flange end.

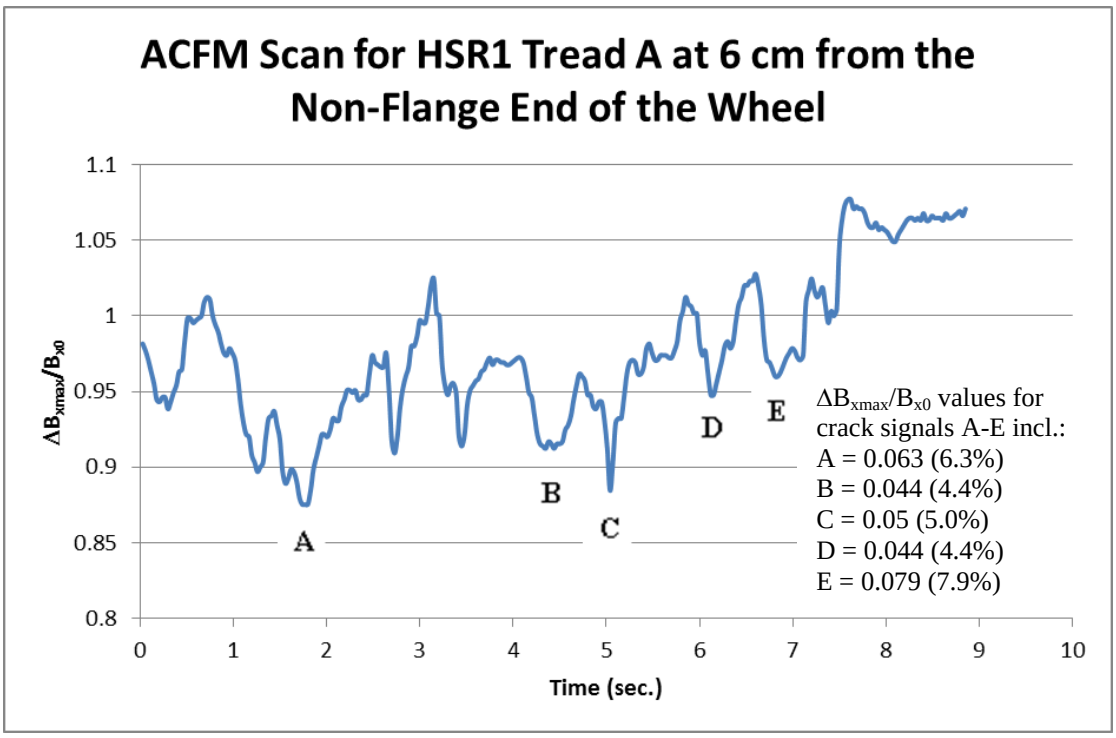

Figure 7.28 shows sample ACFM scans for the worn HSR1 wheel at the position of minimum run-out on the tread and at a position of 6 cm from the non-flange end.

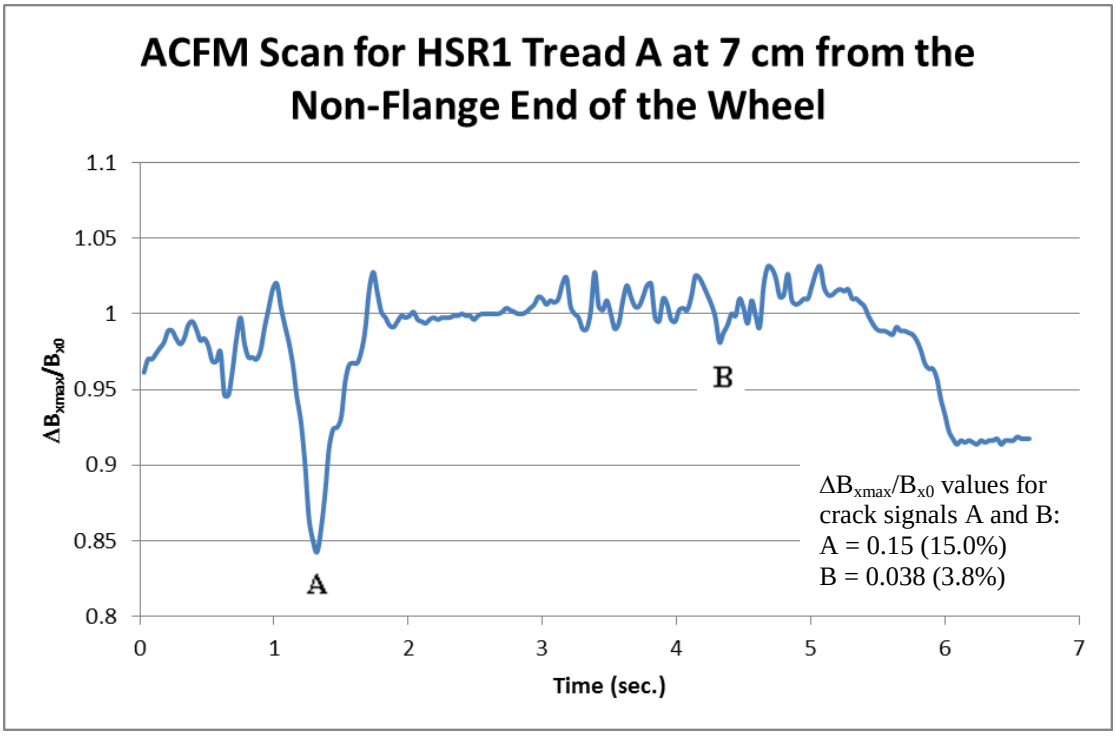

Figure 7.29 shows sample ACFM scans for the worn HSR1 wheel at the position of minimum run-out on the tread and at a position of 7 cm from the non-flange end.

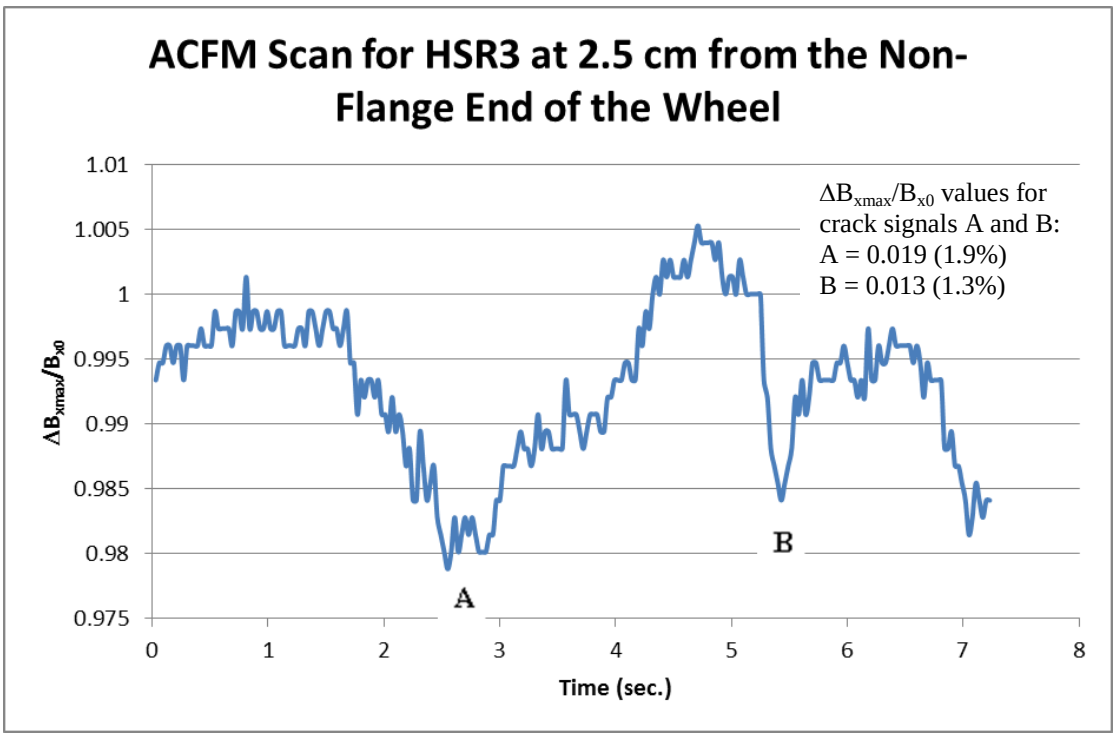

Figure 7.30 shows sample ACFM scans for the new HSR3 wheel (without visible defects) at a position of 2.5 cm from the non-flange end of the tread.

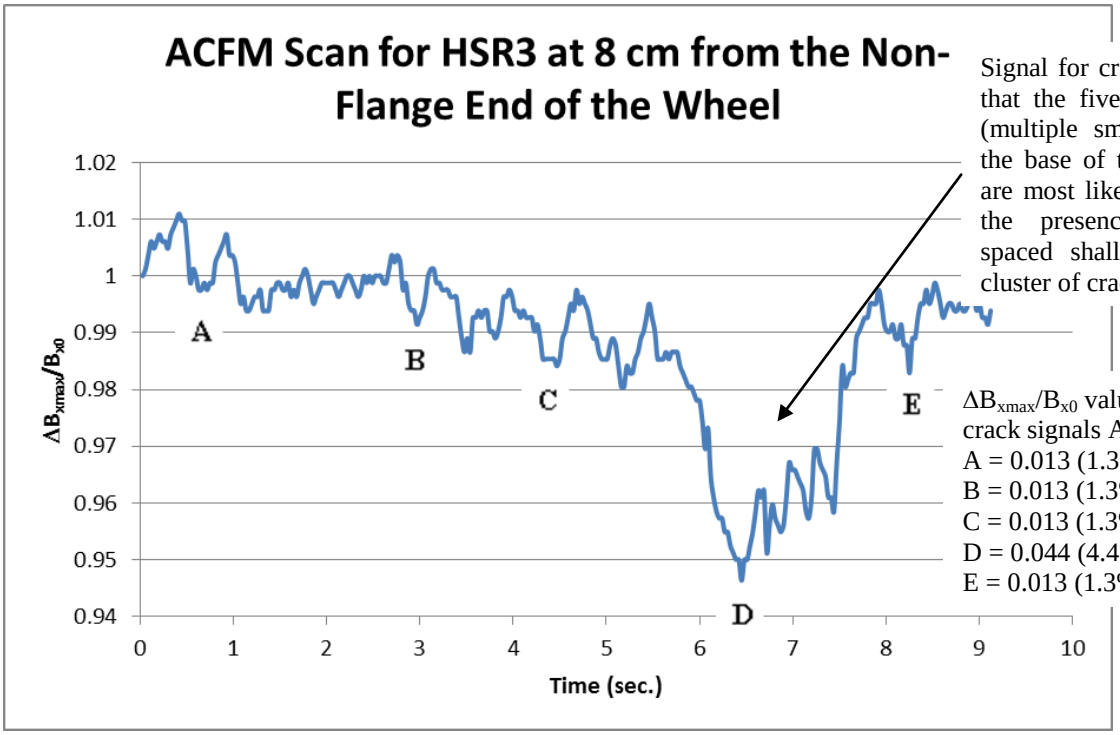

Figure 7.31 shows sample ACFM scans for the new HSR3 wheel (without visible defects) at a position of 8 cm from the non-flange end of the tread.

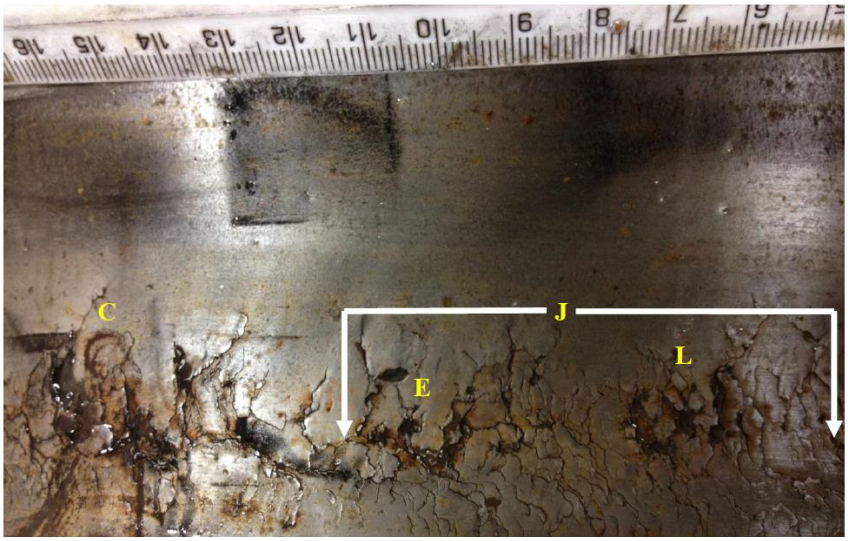

Figure 7.32 shows an image of the RCF prone region on the tread of wheel HSR1 showing the severe level of surface RCF damage that has occurred between 4 and 6 cm from the non-flange end of this wheel. Locations at which the subsequent ACFM scans (shown in the figures below) conducted on this wheel tread have been clearly labelled on the photograph.

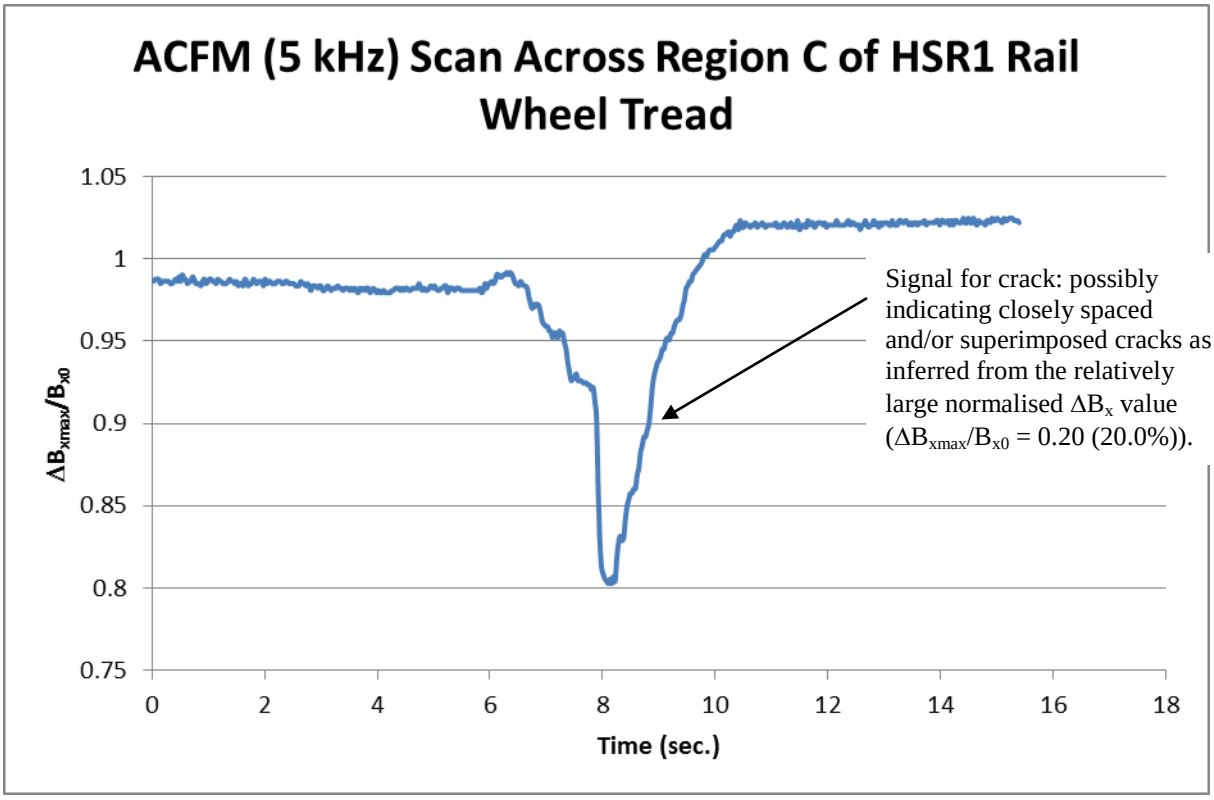

Figure 7.33 (a)

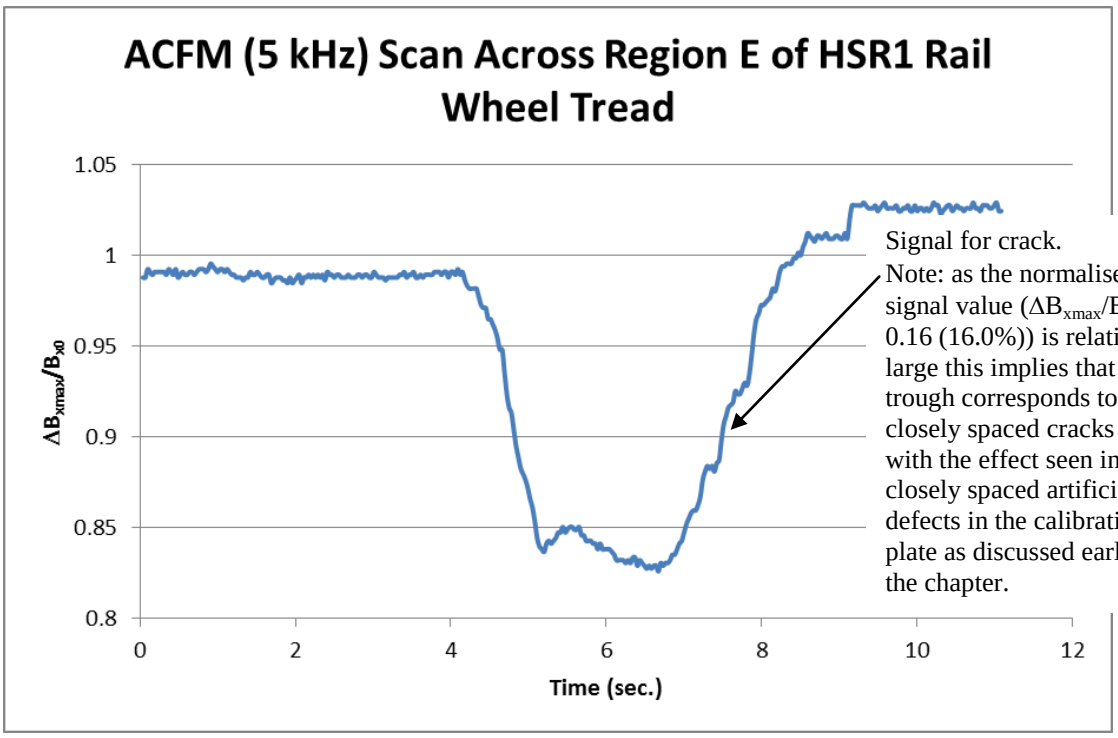

Figure 7.33 (b)

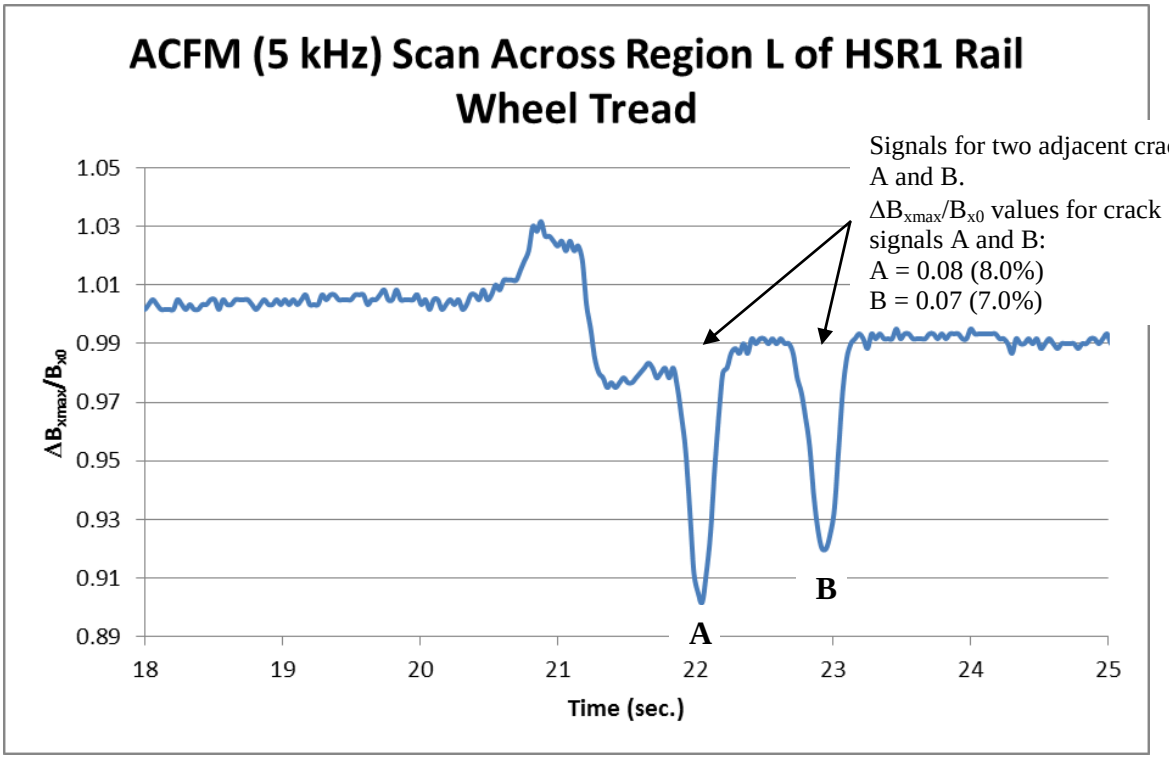

Figure 7.33 (c)

Figures7.33 (a)-(c) incl, above show ACFM scans carried out in the RCF prone region on the tread of wheel HSR1 at the maximum run-out tread position demonstrating that the sensor is capable of detecting severely critical defects in railway wheels in service, however, the cracks are superimposed on one another and it is difficult to distinguish between the individual cracks due to the limits on the ACFM sensitivity.

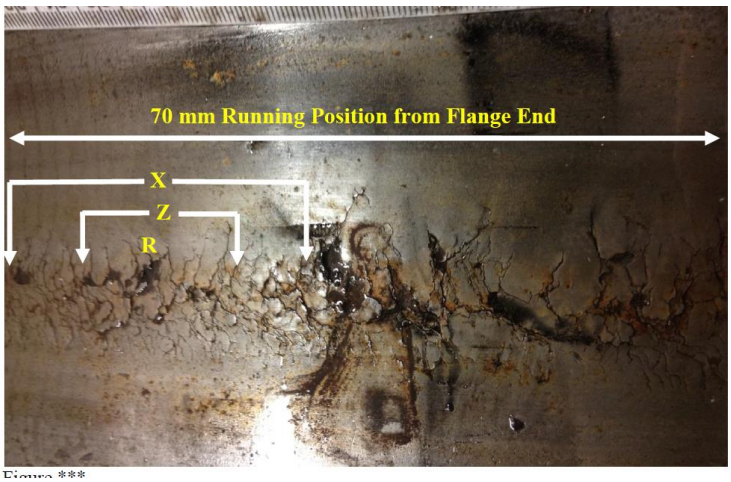

Figure 7.34 shows another image of the RCF prone region on the tread of wheel HSR1 showing the severe level of surface RCF damage that has occurred between 4 and 6 cm from the non-flange end of this wheel. Locations at which the subsequent ACFM scans (shown in the figures below) conducted on this wheel tread have been clearly labelled on the photograph.

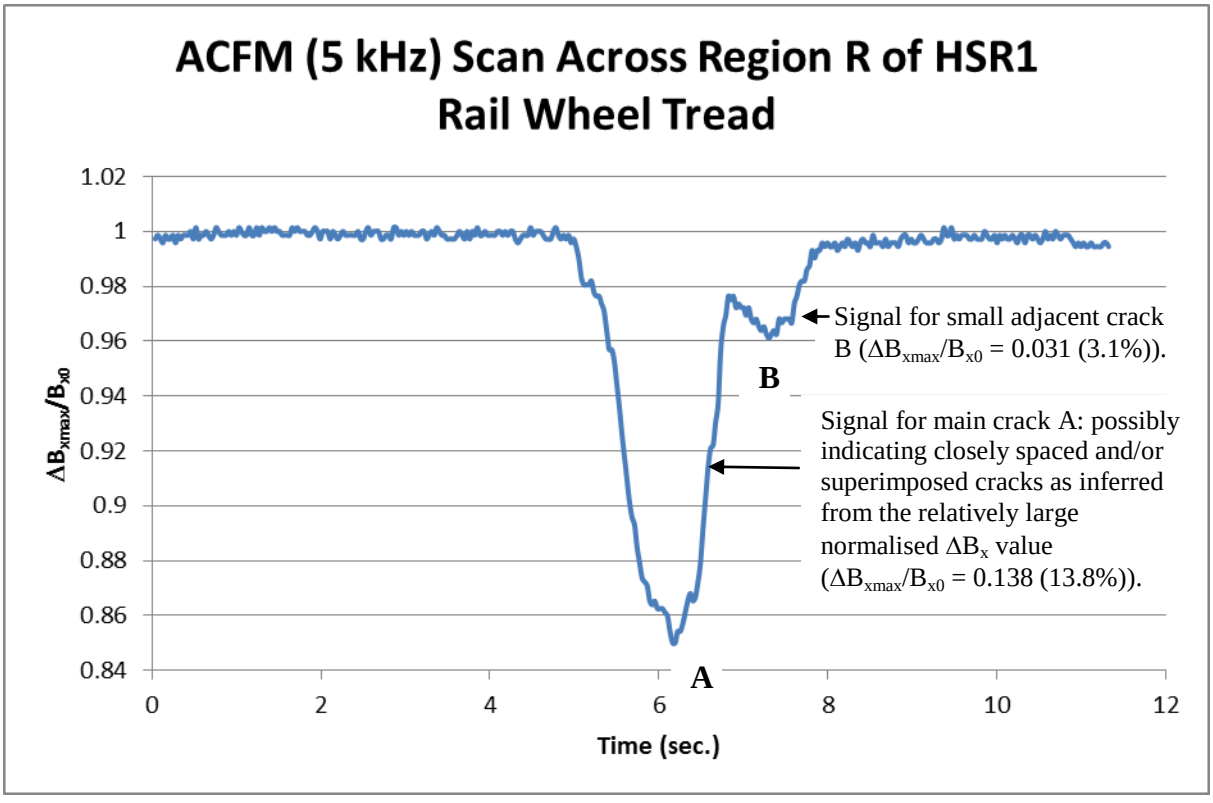

Figure 7.35 (a)

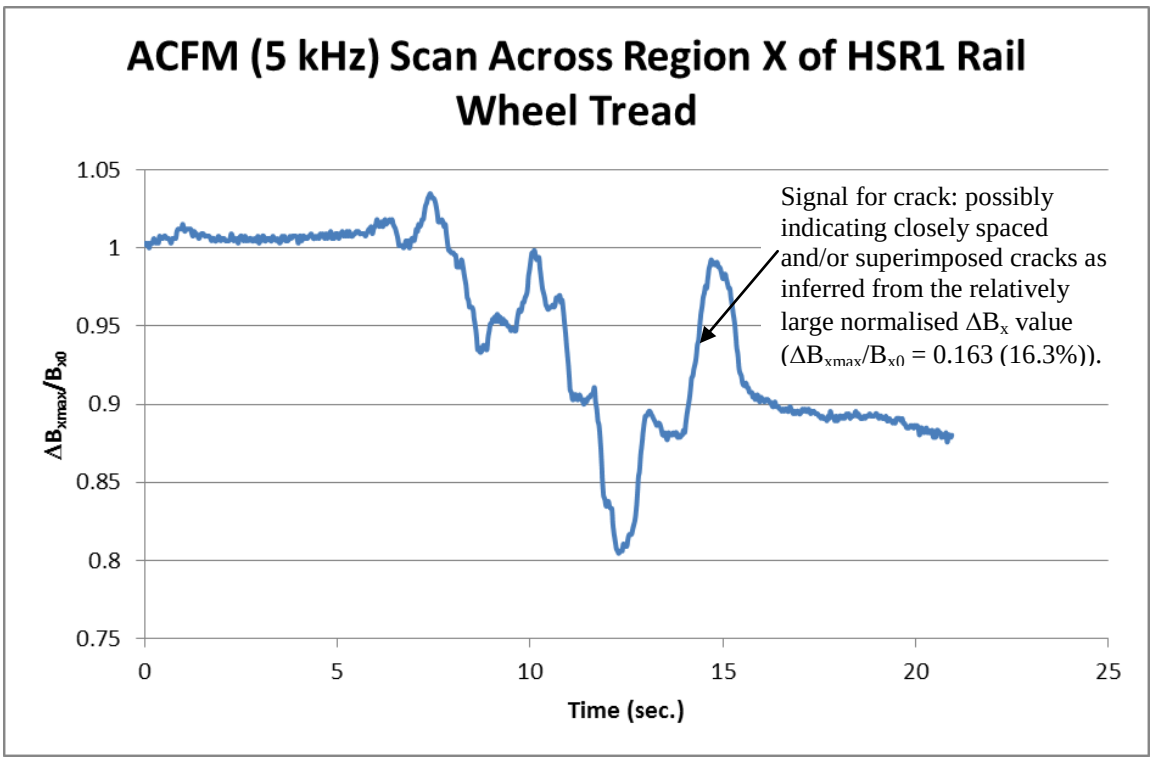

Figure 7.35 (b)

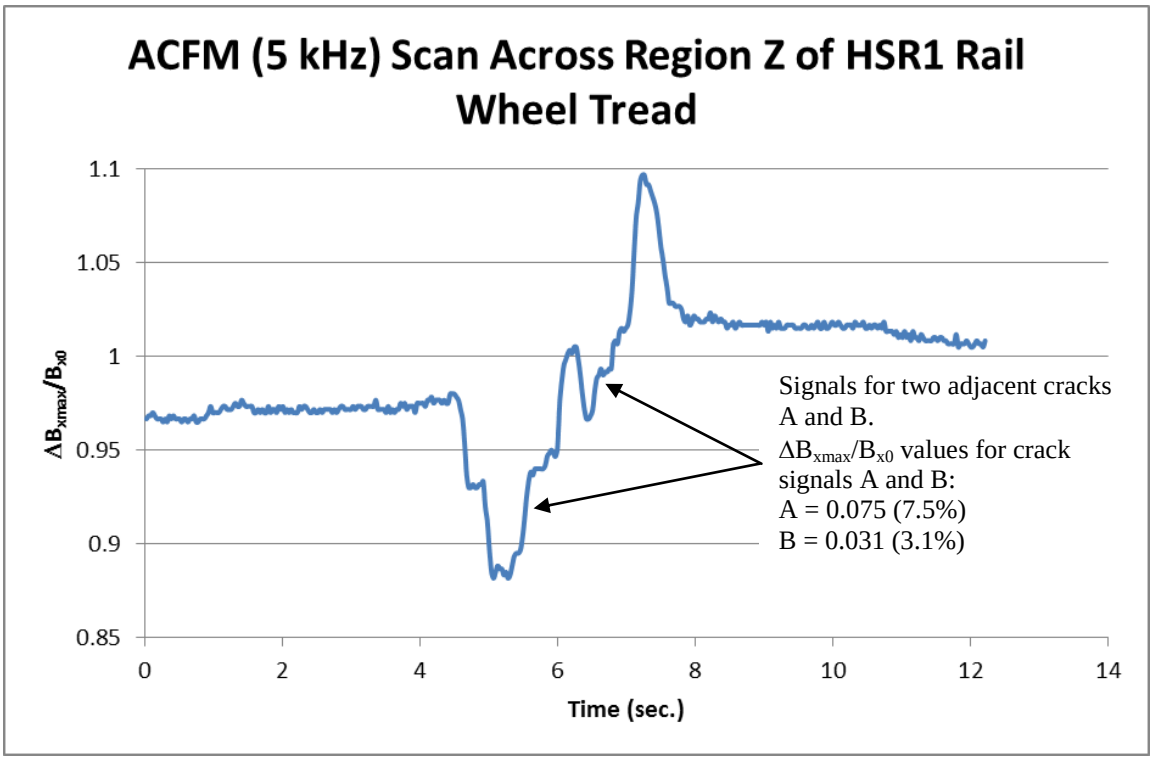

Figure 7.35 (c)

Figures 7.35 (a)-(c) incl. above show ACFM (5 kHz) scans carried out in the RCF prone region on the tread of wheel HSR1 at the maximum run-out tread position as shown above in figure 7.34 demonstrating that the sensor is capable of detecting severely critical defects in railway wheels in service, however, the cracks are superimposed on one another and it is difficult to distinguish between the individual cracks due to the limits on the ACFM sensitivity.

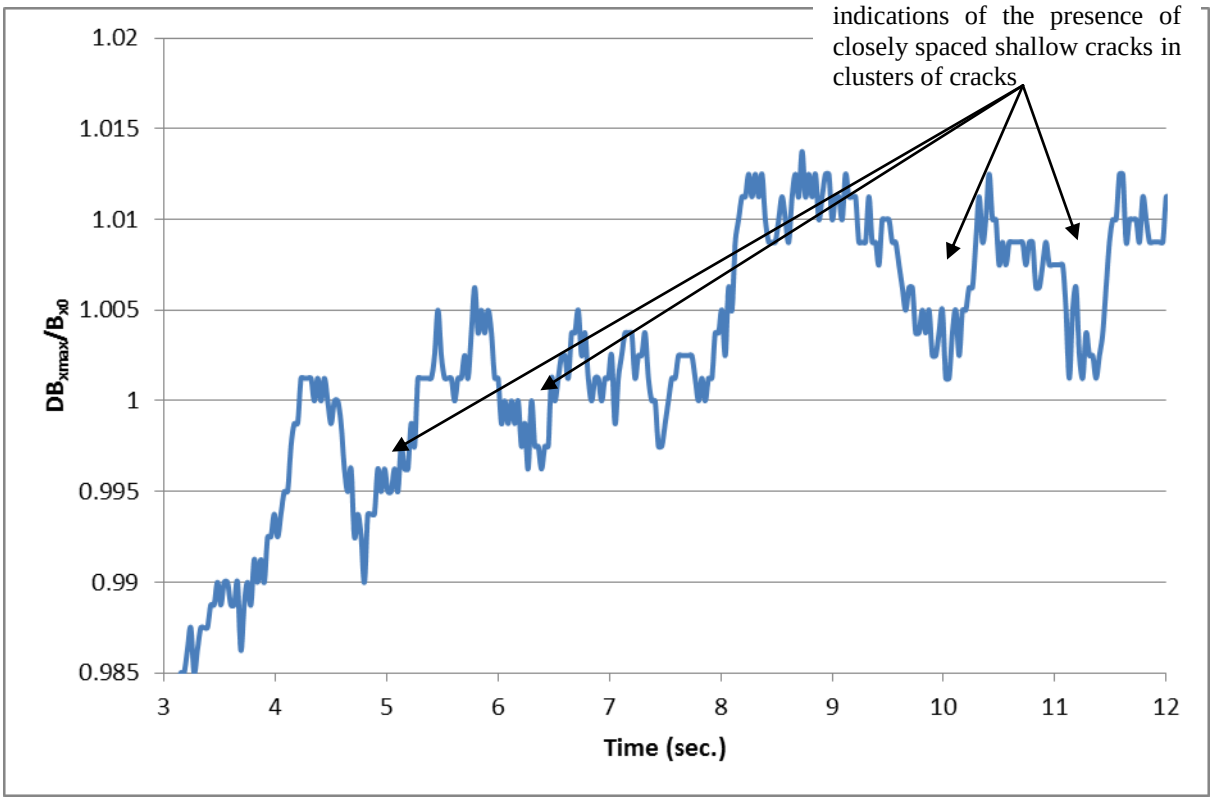

Figure 7.36 ACFM (5 kHz) scan across closely spaced cracks near the flange end of railway wheel HSR2.

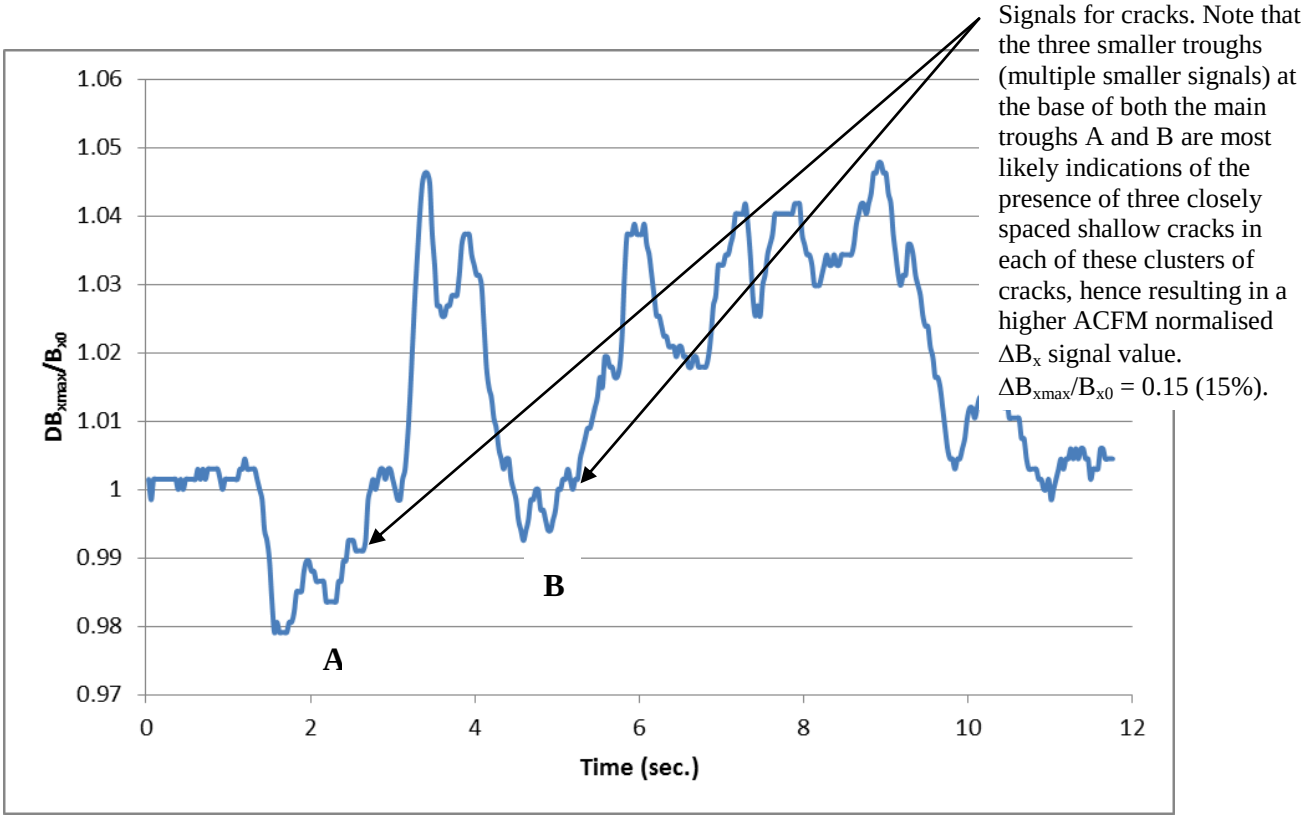

Figure 7.37 ACFM (50 kHz) scan across closely spaced cracks near the flange end of railway wheel HSR2.

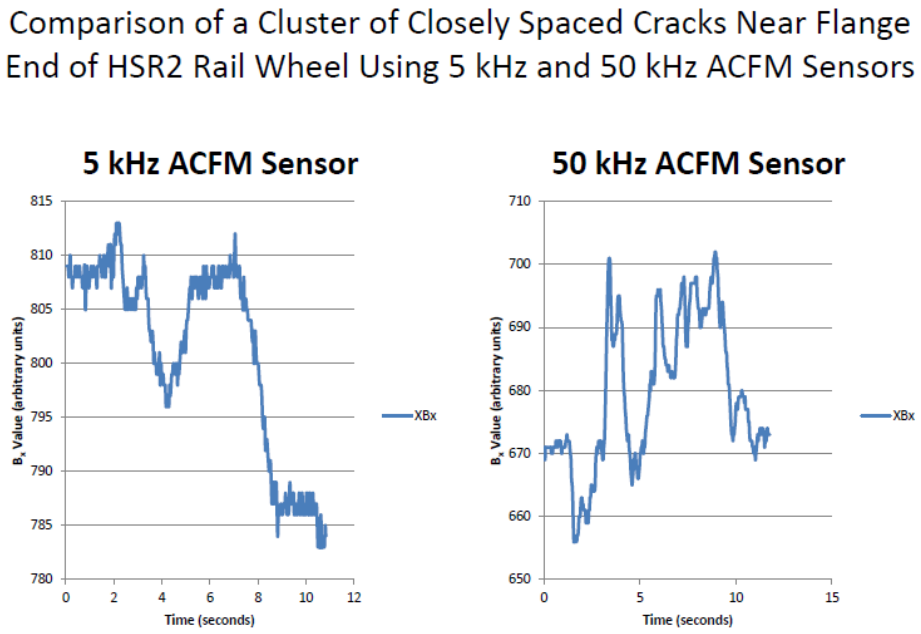

Figure 7.38 shows ACFM scans of shallow closely spaced cracks (spacing < 3 mm) found close to the flange end of the worn HSR2 wheel tread using the ACFM sensor operating at frequencies of 5 and 50 kHz.

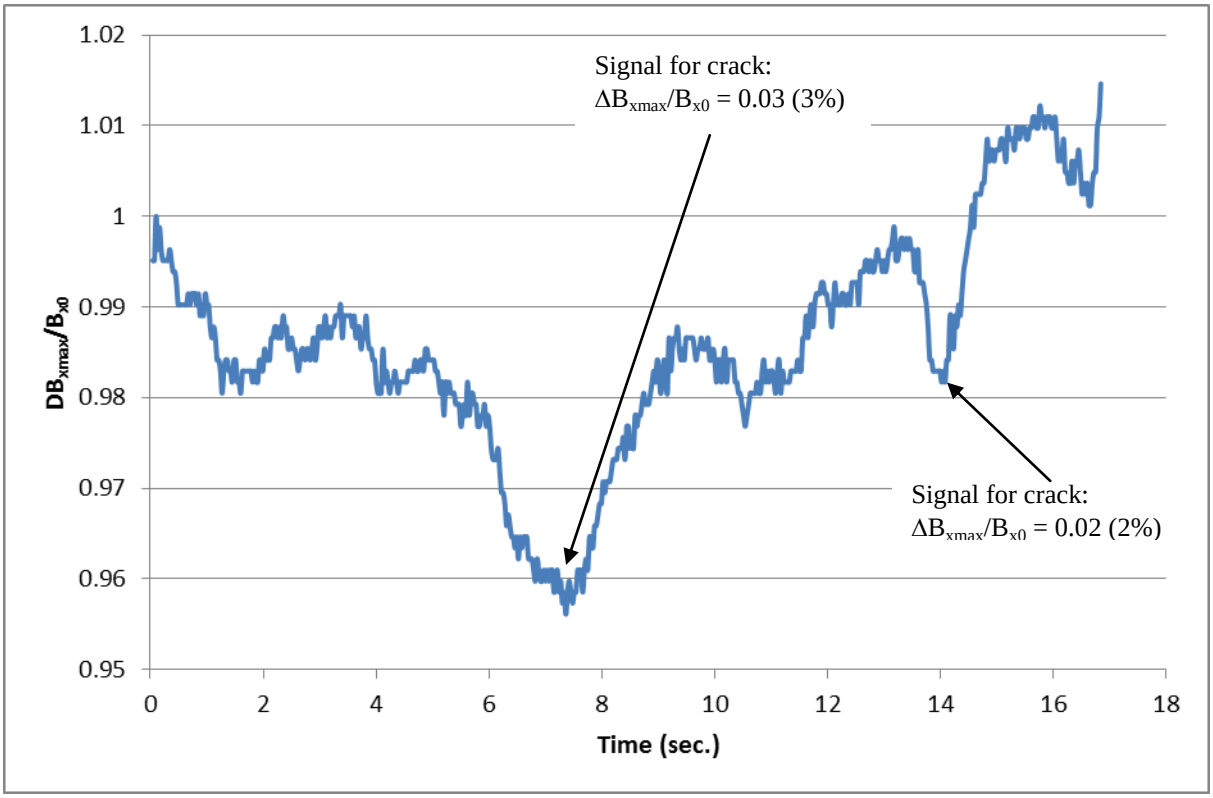

Figure 7.39 ACFM (5 kHz) sensor scan on hsr1 rail wheel at the 70 mm running position (Note: 8 cm from non-flange end chosen here for the 70 mm running position).

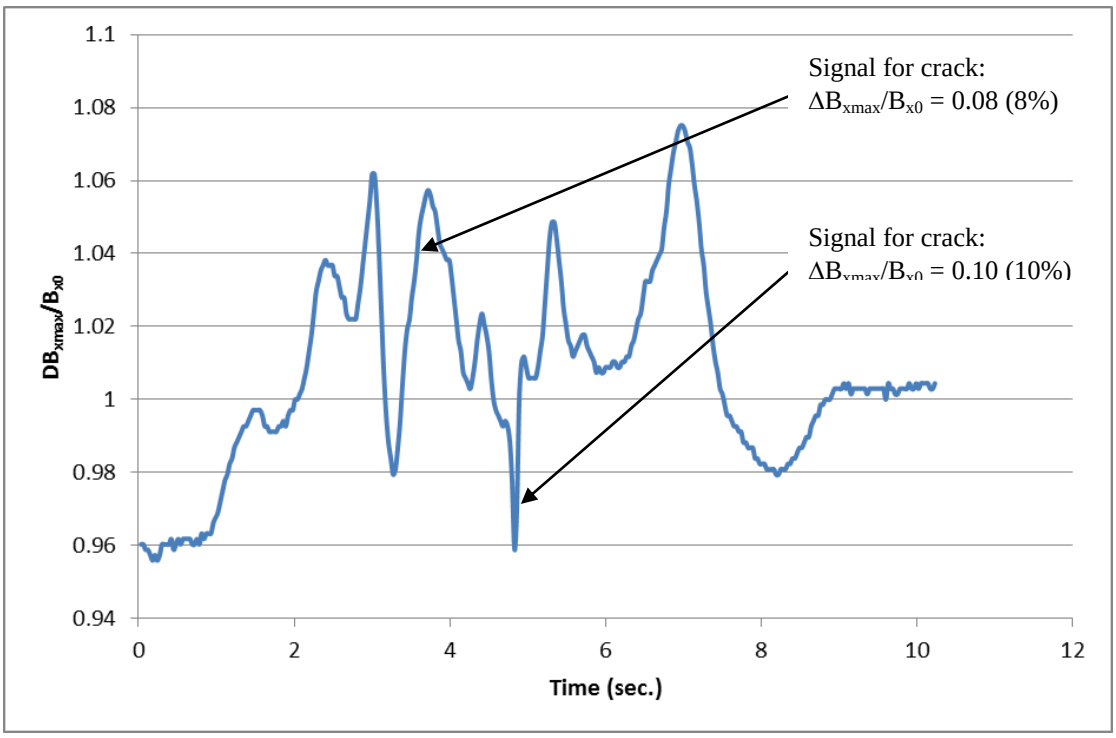

Figure 7.40 ACFM (50 kHz) sensor scan on hsr1 rail wheel at the 70 mm running position.

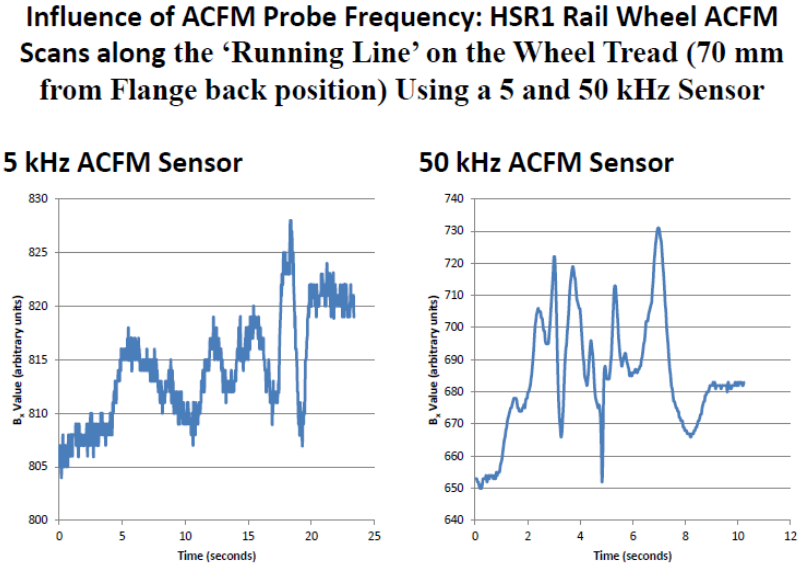

Figure 7.41 shows the influence of the inducing frequency on the ACFM signal.

Cracks at 60 degrees to circumferential direction near flange end of the least damaged worn wheel

Signals for closely spaced shallow cracks in a cluster of cracks

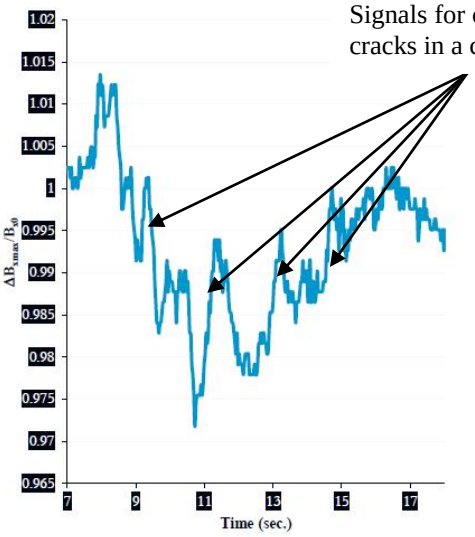

Figure 7.42 shows ACFM scans of shallow closely spaced cracks (spacing < 3 mm) found close to the flange end of the worn HSR2 wheel tread using the ACFM sensor operating at frequency of 5 kHz.

Table 7.13 shows estimated pocket depths for selected cracks from all wheels removed from service and investigated using the crack sizing diagram shown in the previous chapter. All crack surface length and pocket depth range values calculated for all wheels are shown in table 7.14 (below).

Estimated pocket depths (mm) for selected cracks from wheels in service

Tread Position from Non-flange End (cm)	Most defective worn wheel	Least defective worn wheel	Wheel without visible defects
3 cm	1.4 – 1.7 mm	1.6 - 1.8 mm	1.5 - 2.4 mm
4 cm		1.6 mm	
5 cm		1.5 mm	
6 cm	4.6 - 6.7 mm	1.4 – 1.6 mm	2.4 mm
7 cm	2.9 - 17.2 mm	1.4 – 1.5 mm	
8 cm	1.7 – 17.2 mm	1.7 – 1.8 mm	1.2 – 4.1 mm
9 cm		1.5 – 1.8 mm	
10 cm	1.2 – 2.9 mm		

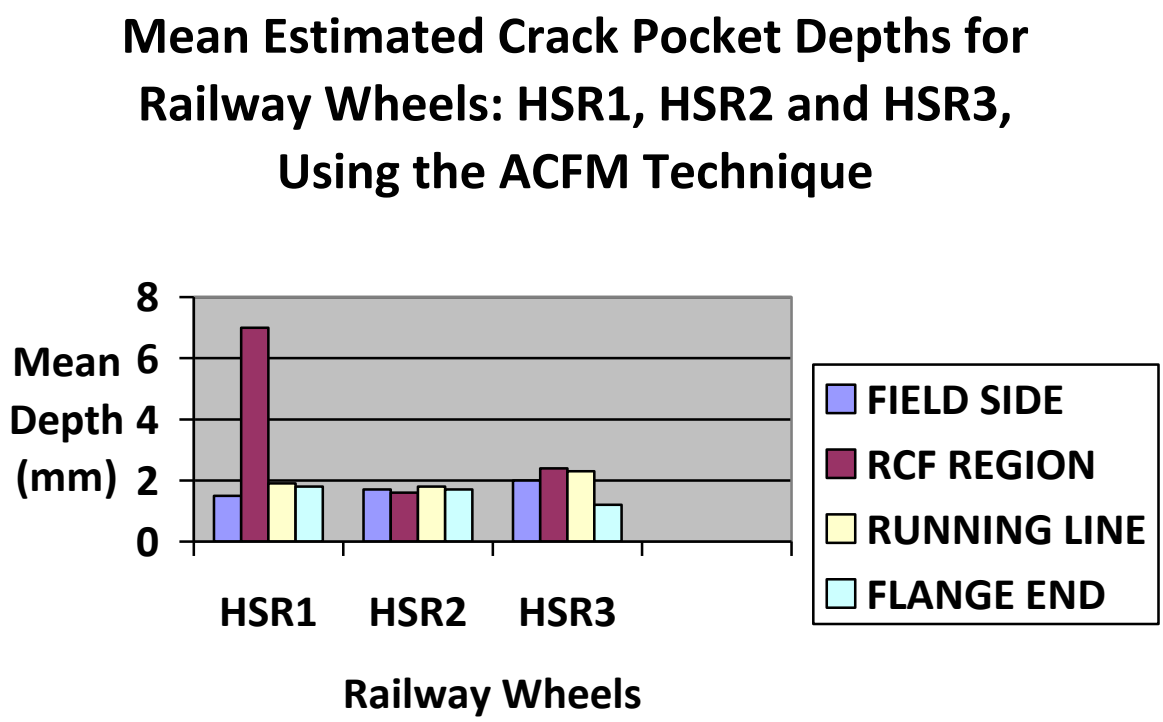

Figure 7.43 shows mean estimated crack pocket depths (DEST) (mm) for railway wheels: HSR1, HSR2 and HSR3 using the ACFM technique.

Table 7.14 Estimated Crack Pocket Depths at Different Positions along the Tread Surface of Wheels HSR1, HSR2 and HSR3, using the Network Rail based Crack Sizing Plot by evaluating the maximum change in the ACFM (5 kHz) Signal and using this value to determine the range possible range of Crack Surface Lengths and thus the range of Crack Pocket Depths from the four Ellipse Ratios Presented on the Sizing Diagram.

Railway Wheel ID / Figure No. / Tread Position from Non-flange End / Region	Crack ID /ΔB_x/ $\Delta B_{xmax}/B_{x0}$ (N) Value (%)	Estimated Crack Surface Length (SL_{EST}) (mm) for Different Semi-elliptical Shaped Crack Ellipse Ratios: 1:1, 1.25:1, 1.5:1 and 1.75:1 As An Approximation to Actual Cracks					Estimated Crack Pocket Depth (D_{EST}) (mm) for Different Semi-elliptical Shaped Crack Ellipse Ratios: 1:1, 1.25:1, 1.5:1 and 1.75:1 As An Approximation to Actual Cracks				
		Ellipse 1:1	Ellipse 1.25:1	Ellipse 1.5:1	Ellipse 1.75:1	Mean	Ellipse 1:1	Ellipse 1.25:1	Ellipse 1.5:1	Ellipse 1.75:1	Mean
HSR1 / 9.13 / 2.5 cm / Field Side Region	A / 5 / 0.6% B / 4 / 0.5% C / 7 / 0.9% D / 5 / 0.6%	2.0 mm 1.8 mm 2.2 mm 2.0 mm	2.0 mm 1.8 mm 2.2 mm 2.0 mm	2.0 mm 1.8 mm 2.2 mm 2.0 mm	2.0 mm 1.8 mm 2.2 mm 2.0 mm	2.0 mm 1.8 mm 2.2 mm 2.0 mm	2.0 mm 1.8 mm 2.2 mm 2.0 mm	1.6 mm 1.4 mm 1.8 mm 1.6 mm	1.3 mm 1.2 mm 1.5 mm 1.3 mm	1.1 mm 1.0 mm 1.3 mm 1.1 mm	1.5 mm 1.4 mm 1.7 mm 1.5 mm
HSR1 / 9.14 / 3.0 cm / Field Side Region	A / 4 / 0.5% B / 4 / 0.5%	1.8 mm 1.8 mm	1.8 mm 1.8 mm	1.8 mm 1.8 mm	1.8 mm 1.8 mm	1.8 mm 1.8 mm	1.8 mm 1.8 mm	1.4 mm 1.4 mm	1.2 mm 1.2 mm	1.0 mm 1.0 mm	1.4 mm 1.4 mm

HSR1 / 9.15 / 7.0 cm / RCF Region	A / 80 / 10.0% B / 70 / 8.8% C / 80 / 10.0% D / 80 / 10.0% E / 50 / 6.3%	10.0 mm 8.9 mm 10.0 mm 10.0 mm 6.7 mm	10.7 mm 9.6 mm 10.7 mm 10.7 mm 7.1 mm	11.3 mm 10.2 mm 11.3 mm 11.3 mm 7.6 mm	12.6 mm 11.3 mm 12.6 mm 12.6 mm 8.2 mm	11.2 mm 10.0 mm 11.2 mm 11.2 mm 7.4 mm	10.0 mm 8.9 mm 10.0 mm 10.0 mm 6.7 mm	8.6 mm 7.7 mm 8.6 mm 8.6 mm 5.7 mm	7.5 mm 6.8 mm 7.5 mm 7.5 mm 5.1 mm	7.2 mm 6.5 mm 7.2 mm 7.2 mm 4.7 mm	8.3 mm 7.5 mm 8.3 mm 8.3 mm 5.6 mm
HSR1 / 9.16 / 8.0 cm / Running Line Position	A / 100 / 12.5% B / 120 / 15.0% C / 12 / 1.5% D / 7 / 0.9% E / 10 / 1.3%	13.6 mm 17.7 mm 2.6 mm 2.2 mm 2.6 mm	14.9 mm 20.8 mm 2.6 mm 2.2 mm 2.6 mm	17.3 mm 26.1 mm 2.6 mm 2.2 mm 2.6 mm	20.1 mm Infinite 2.6 mm 2.2 mm 2.6 mm	16.5 mm 21.5 mm 2.6 mm 2.2 mm 2.6 mm	13.6 mm 17.7 mm 2.6 mm 2.2 mm 2.6 mm	11.9 mm 16.6 mm 2.1 mm 1.8 mm 2.1 mm	11.5 mm 17.4 mm 1.7 mm 1.5 mm 1.7 mm	11.5 mm Infinite 1.5 mm 1.3 mm 1.5 mm	12.1 mm 17.2 mm 2.0 mm 1.7 mm 2.0 mm
HSR1 / 9.17 / 10.0 cm / Flange End	A / 7 / 0.9% B / 20 / 2.5%	2.2 mm 3.6 mm	2.2 mm 3.8 mm	2.2 mm 4.0 mm	2.2 mm 4.2 mm	2.2 mm 3.9 mm	2.2 mm 3.6 mm	1.8 mm 3.0 mm	1.5 mm 2.7 mm	1.3 mm 2.4 mm	1.7 mm 2.9 mm
HSR1 / 9.18 / 2.5 cm / Field Side Region	A / 3 / 0.4% B / 6 / 0.8%	1.5 mm 2.1 mm	1.5 mm 2.1 mm	1.5 mm 2.1 mm	1.5 mm 2.1 mm	1.5 mm 2.1 mm	1.5 mm 2.1 mm	1.2 mm 1.7 mm	1.0 mm 1.4 mm	0.9 mm 1.2 mm	1.2 mm 1.6 mm
HSR1 / 9.19 / 3.0 cm / Field Side Region	A / 4 / 0.5% B / 7 / 0.9% C / 4 / 0.5%	1.8 mm 2.2 mm 1.8 mm	1.8 mm 2.2 mm 1.8 mm	1.8 mm 2.2 mm 1.8 mm	1.8 mm 2.2 mm 1.8 mm	1.8 mm 2.2 mm 1.8 mm	1.8 mm 2.2 mm 1.8 mm	1.4 Mm 1.8 mm 1.4 mm 1.4 mm	1.2 mm 1.5 mm 1.2 mm	1.0 mm 1.3 mm 1.0 mm	1.4 mm 1.7 mm 1.4 mm

	D / 4 / 0.5%	1.8 mm	1.8 mm	1.8 mm	1.8 mm	1.8 mm	1.8 mm		1.2 mm	1.0 mm	1.4 mm
HSR1 / 9.20 / 6.0 cm / RCF Region	A / 50 / 6.3%	6.7 mm	7.1 mm	7.6 mm	8.2 mm	7.4 mm	6.7 mm	5.7 mm	5.1 mm	4.7 mm	5.6 mm
	B / 35 / 4.4%	5.2 mm	5.2 mm	5.2 mm	5.9 mm	5.4 mm	5.2 mm	4.2 mm	3.5 mm	3.4 mm	4.1 mm
	C / 40 / 5.0%	5.6 mm	6.1 mm	6.2 mm	6.7 mm	6.2 mm	5.6 mm	4.9 mm	4.1 mm	3.8 mm	4.6 mm
	D / 35 / 4.4%	5.2 mm	5.2 mm	5.2 mm	5.9 mm	5.4 mm	5.2 mm	4.2 mm	3.5 mm	3.4 mm	4.1 mm
	E / 63 / 7.9%	8.3 mm	8.9 mm	9.1 mm	9.2 mm	8.9 mm	8.3 mm	7.1 mm	6.1 mm	5.3 mm	6.7 mm
HSR1 / 9.21 / 7.0 cm / RCF Region	A / 55 / 6.9%	7.4 mm	7.6 mm	8.1 mm	8.6 mm	7.9 mm	7.4 mm	6.1 mm	5.4 mm	4.9 mm	6.0 mm
	B / 30 / 3.8%	5.0 mm	5.0 mm	5.0 mm	5.3 mm	5.1 mm	5.0 mm	4.0 mm	3.3 mm	3.0 mm	3.8 mm
	C / 25 / 3.1%	4.3 mm	4.3 mm	4.9 mm	4.9 mm	4.6 mm	4.3 mm	3.4 mm	3.3 mm	2.8 mm	3.5 mm
	D / 20 / 2.5%	3.6 mm	3.8 mm	4.0 mm	4.2 mm	3.9 mm	3.6 mm	3.0 mm	2.7 mm	2.4 mm	2.9 mm
	E / 25 / 3.1%	4.3 mm	4.3 mm	4.9 mm	4.9 mm	4.6 mm	4.3 mm	3.4 mm	3.3 mm	2.8 mm	3.5 mm
HSR1 / 9.22 / 7.0 cm / RCF Region	A / 120 / 15.0%	17.7 mm	20.8 mm	26.1 mm	Infinite	21.5 mm	17.7 mm	16.6 mm	17.4 mm	Infinite	17.2 mm
	B / 30 / 3.8%	5.0 mm	5.0 mm	5.0 mm	5.3 mm	5.1 mm	5.0 mm	4.0 mm	3.3 mm	3.0 mm	3.8 mm
HSR1 / 9.23 / 8.0 cm / Running Line Position	A / 8 / 1.0%	2.4 mm	2.4 mm	2.4 mm	2.4 mm	2.4 mm	2.4 mm	1.9 mm	1.6 mm	1.4 mm	1.8 mm
	B / 8 / 1.0%	2.4 mm	2.4 mm	2.4 mm	2.4 mm	2.4 mm	2.4 mm	1.9 mm	1.6 mm	1.4 mm	1.8 mm
	C / 8 / 1.0%	2.4 mm	2.4 mm	2.4 mm	2.4 mm	2.4 mm	2.4 mm	1.9 mm	1.6 mm	1.4 mm	1.8 mm
HSR1 / 9.24 /	A / 6 / 0.8%	2.1 mm	2.1 mm	2.1 mm	2.1 mm	2.1 mm	2.1 mm	1.7 mm	1.4 mm	1.2 mm	1.6 mm

10.0 cm / Flange End	B / 15 / 1.9%	3.1 mm	3.1 mm	3.1 mm	3.3 mm	3.2 mm	3.1 mm	2.5 mm	2.1 mm	1.9 mm	2.4 mm
	C / 8 / 1.0%	2.4 mm	2.4 mm	2.4 mm	2.4 mm	2.4 mm	2.4 mm	1.9 mm	1.6 mm	1.4 mm	1.8 mm
	D / 3 / 0.4%	1.5 mm	1.5 mm	1.5 mm	1.5 mm	1.5 mm	1.5 mm	1.2 mm	1.0 mm	0.9 mm	1.2 mm
	E / 4 / 0.5%	1.8 mm	1.8 mm	1.8 mm	1.8 mm	1.8 mm	1.8 mm	1.4 mm	1.2 mm	1.0 mm	1.4 mm
	F / 4 / 0.5%	1.8 mm	1.8 mm	1.8 mm	1.8 mm	1.8 mm	1.8 mm	1.4 mm	1.2 mm	1.0 mm	1.4 mm
	G / 4 / 0.5%	1.8 mm	1.8 mm	1.8 mm	1.8 mm	1.8 mm	1.8 mm	1.4 mm	1.2 mm	1.0 mm	1.4 mm
HSR2 / 9.28 / 2.5 cm / Field Side Region	A / 6 / 0.8%	2.1 mm	2.1 mm	2.1 mm	2.1 mm	2.1 mm	2.1 mm	1.7 mm	1.4 mm	1.2 mm	1.6 mm
HSR2 / 9.29 / 3.0 cm	A / 8 / 1.0%	2.4 mm	2.4 mm	2.4 mm	2.4 mm	2.4 mm	2.4 mm	1.9 mm	1.6 mm	1.4 mm	1.8 mm
HSR2 / 9.30 / 4.0 cm	A / 6 / 0.8%	2.1 mm	2.1 mm	2.1 mm	2.1 mm	2.1 mm	2.1 mm	1.7 mm	1.4 mm	1.2 mm	1.6 mm
HSR2 / 9.31 / 5.0 cm	A / 12 / 1.5%	2.6 mm	2.6 mm	2.6 mm	2.6 mm	2.6 mm	2.6 mm	2.1 mm	1.7 mm	1.5 mm	2.0 mm
	B / 7 / 0.9%	2.2 mm	2.2 mm	2.2 mm	2.2 mm	2.2 mm	2.2 mm	1.8 mm	1.5 mm	1.3 mm	1.7 mm
HSR2 / 9.32 / 5.0 cm	A / 7 / 0.9%	2.2 mm	2.2 mm	2.2 mm	2.2 mm	2.2 mm	2.2 mm	1.8 mm	1.5 mm	1.3 mm	1.7 mm
	B / 6 / 0.8%	2.1 mm	2.1 mm	2.1 mm	2.1 mm	2.1 mm	2.1 mm	1.7 mm	1.4 mm	1.2 mm	1.6 mm
	C / 5 / 0.6%	2.0 mm	2.0 mm	2.0 mm	2.0 mm	2.0 mm	2.0 mm	1.6 mm	1.3 mm	1.1 mm	1.5 mm
HSR2 / 9.33 /	A / 4 / 0.5%	1.8 mm	1.8mm	1.8 mm	1.8 mm	1.8 mm	1.8 mm	1.4 mm	1.2 mm	1.0 mm	1.4 mm

6.0 cm	B / 6 / 0.8% C / 5 / 0.6%	2.1 mm 2.0 mm	2.1 mm 2.0 mm	2.1 mm 2.0 mm	2.1 mm 2.0 mm	2.1 mm 2.0 mm	2.1 mm 2.0 mm	1.7 mm 1.6 mm	1.4 mm 1.3 mm	1.2 mm 1.1 mm	1.6 mm 1.5 mm
HSR2 / 9.34 / 7.0 cm	A / 5 / 0.6% B / 4 / 0.5%	2.0 mm 1.8 mm	2.0 mm 1.8 mm	2.0 mm 1.8 mm	2.0 mm 1.8 mm	2.0 mm 1.8 mm	2.0 mm 1.8 mm	1.6 mm 1.4 mm	1.3 mm 1.2 mm	1.1 mm 1.0 mm	1.5 mm 1.4 mm
HSR2 / 9.35 / 8.0 cm	A / 8 / 1.0% B / 7 / 0.9%	2.4 mm 2.2 mm	2.4 mm 2.2 mm	2.4 mm 2.2 mm	2.4 mm 2.2 mm	2.4 mm 2.2 mm	2.4 mm 2.2 mm	1.9 mm 1.8 mm	1.6 mm 1.5 mm	1.4 mm 1.3 mm	1.8 mm 1.7 mm
HSR2 / 9.36 / 8.0 cm	A / 8 / 1.0%	2.4 mm	2.4 mm	2.4 mm	2.4 mm	2.4 mm	2.4 mm	1.9 mm	1.6 mm	1.4 mm	1.8 mm
HSR2 / 9.37 / 9.0 cm	A / 5 / 0.6%	2.0 mm	2.0 mm	2.0 mm	2.0 mm	2.0 mm	2.0 mm	1.6 mm	1.3 mm	1.1 mm	1.5 mm
HSR2 / 9.38 / 9.0 cm	A / 8 / 1.0%	2.4 mm	2.4 mm	2.4 mm	2.4 mm	2.4 mm	2.4 mm	1.9 mm	1.6 mm	1.4 mm	1.8 mm
HSR3 / 9.44 / 2.5 cm	A / 15 / 1.9%	3.1 mm	3.1 mm	3.1 mm	3.3 mm	3.2 mm	3.1 mm	2.5 mm	2.1 mm	1.9 mm	2.4 mm
HSR3 / 9.45 / 6.0 cm	A / 15 / 1.9%	3.1 mm	3.1 mm	3.1 mm	3.3 mm	3.2 mm	3.1 mm	2.5 mm	2.1 mm	1.9 mm	2.4 mm
HSR3 / 9.46 / 3.0 cm	A / 8 / 1.0%	2.4 mm	2.4 mm	2.4 mm	2.4 mm	2.4 mm	2.4 mm	1.9 mm	1.6 mm	1.4 mm	1.8 mm
HSR3 / 9.47 /	A / 15 / 1.9%	3.1 mm	3.1 mm	3.1 mm	3.3 mm	3.2 mm	3.1 mm	2.5 mm	2.1 mm	1.9 mm	2.4 mm

2.5 cm	B / 10 / 1.3%	2.6 mm	2.6 mm	2.6 mm	2.6 mm	2.6 mm	2.6 mm	2.1 mm	1.7 mm	1.5 mm	2.0 mm
HSR3 / 9.48 / 8.0 cm	A / 10 / 1.3%	2.6 mm	2.6 mm	2.6 mm	2.6 mm	2.6 mm	2.6 mm	2.1 mm	1.7 mm	1.5 mm	2.0 mm
	B / 10 / 1.3%	2.6 mm	2.6 mm	2.6 mm	2.6 mm	2.6 mm	2.6 mm	2.1 mm	1.7 mm	1.5 mm	2.0 mm
	C / 10 / 1.3%	2.6 mm	2.6 mm	2.6 mm	2.6 mm	2.6 mm	2.6 mm	2.1 mm	1.7 mm	1.5 mm	2.0 mm
	D / 35 / 4.4%	5.2 mm	5.2 mm	5.2 mm	5.9 mm	5.4 mm	5.2 mm	4.2 mm	3.5 mm	3.4 mm	4.1 mm
	E / 10 / 1.3%	2.6 mm	2.6 mm	2.6 mm	2.6 mm	2.6 mm	2.6 mm	2.1 mm	1.7 mm	1.5 mm	2.0 mm
HSR3 / 9.49 / 2.5 cm	A / 10 / 1.3%	2.6 mm	2.6 mm	2.6 mm	2.6 mm	2.6 mm	2.6 mm	2.1 mm	1.7 mm	1.5 mm	2.0 mm
	B / 5 / 0.6%	2.0 mm	2.0 mm	2.0 mm	2.0 mm	2.0 mm	2.0 mm	1.6 mm	1.3 mm	1.1 mm	1.5 mm
HSR3 / 9.50 / 8.0 cm	A / 22.5 / 2.8%	3.7 mm	3.7 mm	3.7 mm	3.7 mm	3.7 mm	3.7 mm	3.0 mm	2.5 mm	2.1 mm	2.8 mm
	B / 3 / 0.4%	1.5 mm	1.5 mm	1.5 mm	1.5 mm	1.5 mm	1.5 mm	1.2 mm	1.0 mm	0.9 mm	1.2 mm
HSR3 / 9.51 / 9.0 cm	A / 4 / 0.5%	1.8 mm	1.8 mm	1.8 mm	1.8 mm	1.8 mm	1.8 mm	1.4 mm	1.2 mm	1.0 mm	
	B / 4 / 0.5%	1.8 mm	1.8 mm	1.8 mm	1.8 mm	1.8 mm	1.8 mm	1.4 mm	1.2 mm	1.0 mm	
	C / 6 / 0.8%	2.1 mm	2.1 mm	2.1 mm	2.1 mm	2.1 mm	2.1 mm	1.7 mm	1.4 mm	1.2 mm	
	D / 8 / 1.0%	2.4 mm	2.4 mm	2.4 mm	2.4 mm	2.4 mm	2.4 mm	1.9 mm	1.6 mm	1.4 mm	1.8 mm
	E / 8 / 1.0%	2.4 mm	2.4 mm	2.4 mm	2.4 mm	2.4 mm	2.4 mm	1.9 mm	1.6 mm	1.4 mm	1.8 mm
HSR3 / 9.52 / 9.0 cm	A / 7 / 0.9%	2.2 mm	2.2 mm	2.2 mm	2.2 mm	2.2 mm	2.2 mm	1.8 mm	1.5 mm	1.3 mm	1.7 mm
	B / 7 / 0.9%	2.2 mm	2.2 mm	2.2 mm	2.2 mm	2.2 mm	2.2 mm	1.8 mm	1.5 mm	1.3 mm	1.7 mm
Feature B	B / 11 / 1.4 %	2.6 mm	2.6 mm	2.6 mm	2.6 mm	2.6 mm	2.6 mm	2.1 mm	1.7 mm	1.5 mm	2.0 mm
9.0 cm /	Mean: 10 /	2.6 mm	2.6 mm	2.6 mm	2.6 mm	2.6 mm	2.6 mm	2.1 mm	1.7 mm	1.5 mm	2.0 mm

Feature A	1.3%										
Feature C	C / 160 / 20.0 %	Infinite	Infinite	Infinite	Infinite	Infinite	Infinite	Infinite	Infinite	Infinite	Infinite
9.0 cm / Feature A (Cluster)	A / 12 / 1.5 % B / 15 / 1.9 % C / 10 / 1.3 %	2.6 mm 3.1 mm 2.6 mm	2.6 mm 3.1 mm 2.6 mm	2.6 mm 3.1 mm 2.6 mm	2.6 mm 3.3 mm 2.6 mm	2.6 mm 3.2 mm 2.6 mm	2.6 mm 3.1 mm 2.6 mm	2.1 mm 2.5 mm 2.1 mm	1.7 mm 2.1 mm 1.7 mm	1.5 mm 1.9 mm 1.5 mm	2.0 mm 2.4 mm 2.0 mm
Approx. 5.0 cm (near 70 mm running line) / ACFM Probe Across Feature H	H / 8 / 1.0 %	2.4 mm	2.4 mm	2.4 mm	2.4 mm	2.4 mm	2.4 mm	1.9 mm	1.6 mm	1.4 mm	1.8 mm
Approx. 5.0 cm (near 70 mm running line) / ACFM Probe Held Parallel to Feature H	H / 25 / 3.1 %	4.3 mm	4.3 mm	4.9 mm	4.9 mm	4.6 mm	4.3 mm	3.4 mm	3.3 mm	2.8 mm	3.5 mm
9.0 cm /	A / 10 / 1.3 %	2.6 mm	2.6 mm	2.6 mm	2.6 mm	2.6 mm	2.6 mm	2.1 mm	1.7 mm	1.5 mm	2.0 mm

Feature A	B / 12 / 1.5 %	2.6 mm	2.6 mm	2.6 mm	2.6 mm	2.6 mm	2.6 mm	2.1 mm	1.7 mm	1.5 mm	2.0 mm
9.0 cm / Feature A: Near Ends (RHS)	A / 35 / 4.4 %	5.2 mm	5.2 mm	5.2 mm	5.9 mm	5.4 mm	5.2 mm	4.2 mm	3.5 mm	3.4 mm	4.1 mm
Feature J	J / 5 / 0.6 %	2.0 mm	2.0 mm	2.0 mm	2.0 mm	2.0 mm	2.0 mm	1.6 mm	1.3 mm	1.1 mm	1.5 mm
Feature J / ACFM Probe Parallel to most of crack	J / 15 / 1.9 %	3.1 mm	3.1 mm	3.1 mm	3.3 mm	3.2 mm	3.1 mm	2.5 mm	2.1 mm	1.9 mm	2.4 mm
Feature J / ACFM Probe 45^0 to crack	J / 8 / 1.0 %	2.4 mm	2.4 mm	2.4 mm	2.4 mm	2.4 mm	2.4 mm	1.9 mm	1.6 mm	1.4 mm	1.8 mm
Across Dark Band Near 70 mm Running Position	A / 10/ 1.3 % B / 7 / 0.9 % C / 8 / 1.0 % D / 15 / 1.9 %	2.6 mm 2.2 mm 2.4 mm 3.1 mm	2.6 mm 2.2 mm 2.4 mm 3.1 mm	2.6 mm 2.2 mm 2.4 mm 3.1 mm	2.6 mm 2.2 mm 2.4 mm 3.3 mm	2.6 mm 2.2 mm 2.4 mm 3.2 mm	2.6 mm 2.2 mm 2.4 mm 3.1 mm	2.1 mm 1.8 mm 1.9 mm 2.5 mm	1.7 mm 1.5 mm 1.6 mm 2.1 mm	1.5 mm 1.3 mm 1.4 mm 1.9 mm	2.0 mm 1.7 mm 1.8 mm 2.4 mm
Feature Q	Q / 7 / 0.9 %	2.2 mm	2.2 mm	2.2 mm	2.2 mm	2.2 mm	2.2 mm	1.8 mm	1.5 mm	1.3 mm	1.7 mm
Feature R	R (Main Peak) /	16.0 mm	17.8 mm	20.7 mm	25.6 mm	20.0 mm	16.0 mm	14.2 mm	13.8 mm	14.6 mm	14.7 mm

	A: 110 / 13.8 % Subsidiary Peak B: 25 / 3.1 %	4.3 mm	4.3 mm	4.9 mm	4.9 mm	4.6 mm	4.3 mm	3.4 mm	3.3 mm	2.8 mm	3.5 mm
Area Z	A / 60 / 7.5 % B / 25 / 3.1 %	8.4 mm 4.3 mm	8.7 mm 4.3 mm	8.9 mm 4.9 mm	9.3 mm 4.9 mm	8.8 mm 4.6 mm	8.4 mm 4.3 mm	7.0 mm 3.4 mm	5.9 mm 3.3 mm	5.3 mm 2.8 mm	6.7 mm 3.5 mm
Area Y	A / 80 / 10.0 % B / 40 / 5.0 %	10.0 mm 5.6 mm	10.7 mm 6.1 mm	11.3 mm 6.2 mm	12.6 mm 6.7 mm	11.2 mm 6.2 mm	10.0 mm 5.6 mm	8.6 mm 4.9 mm	7.5 mm 4.1 mm	7.2 mm 3.8 mm	8.3 mm 4.6 mm
B (Across E Shaped Feature)	A / 100 / 12.5 % B / 110 / 13.8 %	13.6 mm 16.0 mm	14.9 mm 17.8 mm	17.3 mm 20.7 mm	20.1 mm 25.6 mm	16.5 mm 20.0 mm	13.6 mm 16.0 mm	11.9 mm 14.2 mm	11.5 mm 13.8 mm	11.5 mm 14.6 mm	12.1 mm 14.7 mm
Area X	A / 10/ 1.3 % B / 40 / 5.0 % C / 130 / 16.3 %	2.6 mm 5.6 mm 22.0 mm	2.6 mm 6.1 mm 28.5 mm	2.6 mm 6.2 mm Plot N/A	2.6 mm 6.7 mm Plot N/A	2.6 mm 6.2 mm 25.3 mm	2.6 mm 5.6 mm 22.0 mm	2.1 mm 4.9 mm 22.8 mm	1.7 mm 4.1 mm Plot N/A	1.5 mm 3.8 mm Plot N/A	2.0 mm 4.6 mm 22.4 mm
W Shaped Feature	A / 40 / 5.0 % B / 25 / 3.1 %	5.6 mm 4.3 mm	6.1 mm 4.3 mm	6.2 mm 4.9 mm	6.7 mm 4.9 mm	6.2 mm 4.6 mm	5.6 mm 4.3 mm	4.9 mm 3.4 mm	4.1 mm 3.3 mm	3.8 mm 2.8 mm	4.6 mm 3.5 mm
“WAVY” SHAPED FEATURE	A / 65 / 8.1 % B / 65 / 8.1 %	8.5 mm 8.5 mm	8.7 mm 8.7 mm	9.5 mm 9.5 mm	10.0 mm 10.0 mm	9.2 mm 9.2 mm	8.5 mm 8.5 mm	7.0 mm 7.0 mm	6.3 mm 6.3 mm	5.7 mm 5.7 mm	6.9 mm 6.9 mm

7.4 CONCLUSION

The work has shown that the background ACFM signal varies with position across the railway wheel tread for the wheels investigated with different levels of RCF tread surface damage. The optimum mean background signal chosen for all three wheels investigated for this study in order to estimate crack pocket depths for an ACFM sensor operating at a frequency of 5 kHz is 800. However, it is found from this work that the background ACFM signal changes with the operating frequency of the sensor and is significantly lower for a higher frequency sensor operating at 50 kHz, however, as the background signal values (arbitrary units) are relatively large for the sensor operating at these frequencies in comparison to the maximum change in the B_x signal for the crack(s) then choosing either of the mean background signal values for the high or low frequency sensor (the value generally is lower by about 100 arbitrary units for the 50 kHz ACFM sensor than when the sensor is operating at a frequency of 5 kHz) the evaluated crack pocket depths are significantly different from one another; therefore, it is safe to choose a value of 800 for the background signal to calculate an estimate for crack pocket depths in worn railway wheels in service.

Furthermore, the results show that the present ACFM sensor is capable of detecting and sizing cracks near the tread surface which are superimposed upon each other. However, it is found that the ACFM sensor, in its present state, is incapable of distinguishing between individual surface breaking cracks in the treads of rail wheels investigated and thus is incapable of detecting and sizing individual cracks in these rail wheels. However, at best the ACFM system in its current form can provide an estimate of crack sizes for a multiple stack of cracks which are superimposed upon each other. The work has also shown that the range of crack pocket depths and surface lengths estimated, using the normalised maximum change in the B_x signal (i.e. $\Delta B_{xmax}/B_{x0}$) in conjunction with the diagram shown in figure 7.4 using the range of four semi-elliptical ratios shown on the diagram, from the ACFM sensor when scanned over the tread surface at different positions along the tread surface on wheels HSR1, HSR2 and HSR3, are between: 2 and 18 mm which agrees well with the crack depths and surface lengths found by using optical metallography, X-ray tomography in conjunction with reconstruction techniques and the multi-sectioning in conjunction with optical microscopy approach, as shown and discussed earlier in this work in chapter 6.

Results show that a 50 kHz ACFM probe provides higher sensitivity than the standard 5 kHz probe on ferrous and non-ferrous materials. Thus, a 50 kHz ACFM sensor is optimal for the detection and sizing of cracks in railway wheels and components in service; it is also found that the mean background signal is significantly lower for the ACFM system operating at the higher frequency than at the lower frequency of 50 and 5 kHz, respectively. As most RCF type cracks occur at +/- 45° to the circumferential direction, a sensor system with orthogonal fields at +/- 45° would be most appropriate. Thus an array of ACFM sensors positioned in the system at different to the crack angle can significantly improve the probability of cracks in the material under inspection. Furthermore, the work demonstrates that crack propagation angle significantly affects the ACFM signal and, for propagation angles greater than 25^0, yields higher normalised maximum B_x change values relative to the background signal which would, thus, significantly influence the estimated measurements for the crack pocket depth and length,; these normalised values are highest and optimum for propagation angles of 60 and 90^0 which therefore demonstrates that the ACFM sensor is most sensitive to cracks that propagate at higher angles between 60-90^0 in contrast to shallow angles of propagation of about 25^0 and less. Therefore, for the proper inspection of components by electromagnetic non-destructive means it is important to be able to establish a magnetic field in at least two directions. The results also show that defects can still be detected at a lift-off of 5 mm above the surface of the material under inspection, although the signal strength is significantly depleted; the strength of the signal is higher for the ACFM operating at the higher frequency of 50 kHz. Furthermore, the work has shown that the probe lift-off during the inspection procedure is an important factor which must be controlled and, thus, taken into consideration during the inspection process in order to quantify RCF cracks correctly and this is in agreement with previous recent studies on similar systems. Therefore, in principle, the work presented here shows that any possible lift-off variations during inspection may be inferred and evaluated by determining the decrease in the sensor's signal strength which is in agreement with previous work conducted on similar systems [43, 86, 88, 117, 132]. The maximum change in the B_x ACFM signal increases significantly with a decrease in crack separation; the maximum change in the B_x signal is greater for closely spaced cracks which would thus significantly oversize the cracks using figure 7.4 (above). These results also demonstrate that at a

crack spacing of 20 mm the cracks can be sized resonabley accurately, whereas, for spacings of 15 mm the outer cracks, for example, in the four crack cluster would yield resonably good estimates for the crack pocket depths, however, the two inner cracks would significantly undersize the defects because these inner cracks in the crack cluster would yield higher values for the maximum change in the B_x signal; and the results also show that for crack spacing smaller than 15 mm the cracks thus estimated using the normalised change in the B_x signal would be significantly higher than the actual crack pocket depths. Furthermore, this effect needs to be taken into account when using the ACFM system on the railway network as the RCF cracks found in railway wheel tread surfaces, as shown in the previous chapter are, in general, closely closely spaced and in most cases closer than 5 mm apart as shown in wheel HSR2 in the RCF crack circumferential bands observed near the flange end and at approximately 3 cm from the non-flange end of this wheel where the spacing between the cracks are about 2-3 mm and 1 mm, respectively. Therefore, it is difficult to size such defects using the present ACFM system when the cracks within a cluster have a crack spacing of about 5 mm or smaller inter-crack spacing. Results from ACFM scans for crack clusters with and without a central deep crack with the ACFM sensor aligned parallel to the cracks and operating at frequencies of 5 and 50 kHz, respectively. These results show that the maximum change in the B_x signal is significantly larger for the cluster of cracks which have a central deep crack and these results also show that the background signal value (arbitrary units) is significantly lower for the ACFM sensor operating at the higher frequency of 50 kHz than for the system operating at the lower frequency of 5 kHz. Therefore, this result demonstrates that a deep crack within a cluster of shallow cracks can be inferred from the larger change in the B_x signal relative to the background signal if it is known that a deep and critical crack is present in the cluster of shallow cracks, however, if one does not know that a deep crack is present in the crack cluster then it is difficult to ascertain whether a deep and thus critical crack is present in the cluster. Therefore, the result demonstrates it is not possible at present to detect a deep crack within a cluster of shallow cracks using the ACFM sensor in its present state. Nevertheless, again as with the work shown in the previous section above scans with different angles of ACFM sensor orientations with respect to the angle of the cluster of cracks were tried and the following interesting and reproducible results are obtained. It is found that scans conducted with the probe oriented at 90^0 to the cluster of cracks consisting of a deep

central crack surrounded by shallow cracks results in a distinct central sensor B_x signal that is a peak instead of a trough as observed in the case of the probe which is parallel to the crack orientation during a scan, thus, identifying the critical crack in the centre of the cluster which is significantly greater than the sensor signals for the individual shallow defects and thus suggesting that this method is capable of detecting a deep and critical crack in a cluster of shallow cracks, however, it is not possible to accurately size the deep crack in the cluster at present, nevertheless, this is a promising result and a way forward. Furthermore, in order to explain the above result obtained from this experiment the following explanation is presented in light of the current understanding of this phenomena about the leakage of magnetic flux in the scenario as shown in these results as demonstrated by the ACFM scans obtained from this experiment when the ACFM probe is oriented perpendicular to the direction of the cracks that with a transverse defect the induced current will flow parallel to the defect and be little affected by the presence of the defect. However, the direction of the magnetic field is now normal to the defect and, thus, it is expected that there would be a small flux leakage effect in the area of the defect. This is of course the field direction and driving mechanism of MPI. If there is a flux leakage effect it explains the signal response, namely an increase in B_x level and a sharp peak-trough in the B_z signal. It would be very much localised to the vicinity of the defect and would be affected by defect depth and crack opening and this effect has previously been observed and the above interpretation is supported by research in the field as reported in [206,207].

Furthermore, due to variations in the lift-off that occur during inspection of the rail wheels removed from service as a result of roughness of the tread surface and in the case of the normalised results obtained for the main calibration plate discussed in the earlier section above at different lift-off distances the ACFM system cannot provide correct rankings for the crack depths under these conditions which is also in agreement with previous work in this field [43, 86, 88, 117, 132], nevertheless, all the artificial cracks (or “notches) and most RCF cracks found in the railway wheels removed from service and investigated using the ACFM probe were detected. The results obtained from this study show that the ACFM sensor operating at a frequency of 50 kHz provides good estimates for the crack pocket depth for a crack propagation angle of 25^0 and under sizes the crack by 10%, whereas, the sensor at this frequency

of operation significantly over sizes the crack by 70% for crack propagation angles of 60^0 and 90^0. Whereas, the ACFM sensor operating at a lower frequency of 5 kHz provides accurate estimates for the crack pocket depths for crack propagation angles between 60^0 and 90^0 but also provides a reasonable estimate for the crack pocket depth at a propagation angle of 25^0 and under sizes the crack depth by 40%. The results obtained demonstrate that for closely spaced cracks the normalised maximum change in the B_x signal component (i.e. $\Delta B_{xmax}/B_{x0}$) is relatively larger than for an isolated individual crack of the same size as shown by the results in this present work. Results obtained show that using an ACFM sensor operating at an inducing frequency of 50 kHz to detect the artificial cracks (notches) in the calibration plate on a four crack cluster shows that the ACFM system operating at this higher frequency yields significantly higher $\Delta B_{xmax}/B_{x0}$ values and thus over sizes the defects for all cracks investigated and all cracks could not be sized as a result using the UK Network Rail sizing diagram shown in figure 7.4. However, in the case of the ACFM sensor operating at an inducing frequency of 5 kHz the sensor is found to be capable of providing reasonable estimates of the crack pocket depths at inter-crack spacing distances of 15 and 20 mm for the crack clusters consisting of two and four cracks and even though these crack pocket depth estimates are oversized by 36% in both of these cases at these inter-crack spacing distances these results are in line with previous similar studies reported in the literature [164,165]. However, at lower inter-crack spacing distances of 5 and 10 mm the ACFM techniques is not capable of distinguishing between individual cracks and considerably over sizes the cracks in agreement with former studies on similar systems [164,165]. The results also show that the estimate for the crack pocket depth is the same for two and four crack clusters at inter-crack-spacing distances of 15 and 20 mm but for a two crack cluster at an inter-crack spacing distance of 10 mm and an ACFM inducing frequency of 50 kHz the value of the normalised B_x obtained, i.e. $\Delta B_{xmax}/B_{x0}$, is too large using the ACFM sensor operating at 50 kHz than for the 5 kHz sensor employed to detect the same defects at the same inter-crack spacing distances and thus the 50 kHz sensor is incapable of sizing the defects at this inter-crack spacing using the sizing diagram shown in figure 7.4. However, the best results obtained from this study is found to be when the ACFM is operated at a lower frequency of 5 kHz on a cluster of two cracks with inter-crack-spacing distances at and above 15 mm, i.e. at inter-crack spacing distances of 15 and 20 mm, where the defects investigated are sized within reasonable

estimates with an estimate for the crack pocket depth that is oversized by 20% of the actual depth of the defect at these two inter-crack spacing distances. This result is better and thus in line with that reported in the literature using an ACFM sensor operating at the same lower frequency. Therefore, these results demonstrate that the ACFM technique operating at lower frequencies (5 kHz) is much better suited at sizing (length and depth) cracks in railway track and railway wheels and components than an ACFM system operating at higher frequencies (50 kHz) and, thus, provides reasonable estimates for crack pocket depths. Furthermore, the results obtained demonstrate that a similar trend and features in the ACFM signal by using the ACFM technique on detecting and sizing the artificial cracks in the calibration plates investigated and on the RCF cracks identified in the three railway wheels removed from service and investigated, namely, railway wheels: HSR1, HSR2 and HSR3 which were provided by three different manufacturers in conjunction with Manchester Metropolitan University (MMU) for the purposes of my work on my PhD research project at School of Metallurgy and Materials, University of Birmingham.

CHAPTER 8
CONCLUSIONS, FUTURE WORK AND IMPORTANCE TO THE RAILWAY INDUSTRY

8.1 CONCLUSIONS

The following salient points arise from the investigation carried out on the characterisation of RCF-type cracks and influence of railway wheel damage on changes in hardness and microstructure with tread depth and position in railway wheels removed from service Observations made by optical microscopy reveal a greater crack depth (5.5 mm) in the more defective tread segment (position of maximum run-out) than in the less defective tread segment (position of minimum run-out) of the worn HSR1 rail wheel which thus implies a greater depth of hardening at the former tread position than in the latter in this material. In general, two bands of circumferential RCF cracks are found on worn wheel treads; one band of cracks is found near the flange end and the other in the RCF region and close to the field side. Circumferential RCF cracks and fine, closely, spaced shallow RCF cracks are found in the field side and flange root regions of railway wheel HSR2. The work shows that cracks initiate at pro-eutectoid ferrite boundaries and the pro-eutectoid is flattened near the tread surface due to the very high strains and stresses in this region. X-ray tomography in conjunction with reconstruction techniques and also the multi-sectioning in conjunction with optical metallography approach are viable techniques to create 3-D images of cracks observed in railway wheels removed from service. Furthermore, in general, the hardness values for all wheels investigated decreases sharply with tread depth for approximately 1 mm below the tread surface and then the hardness gradually decreases more slowly with tread depth. The hardness contour maps obtained for all three wheels investigated showing the level of hardness with depth below the tread surface correlate well with the depth below the tread at which the microstructure change, however, the depth of hardening is generally greater than the microstructural change. The higher hardness levels near the tread surface of the worn railway wheels HSR1 and HSR2 near the flange end and field side are most likely due to cornering on curves. The hardness trend observed is likely as a result of changes in the pro-eutectoid ferrite content and changes in lamellar spacing of pearlite. In addition to the correlation between changes in hardness and microstructure

with tread depth other factors that contribute to the observed change in hardness with tread depth include the contact stresses and strains imposed on the material during service and the railway wheel manufacturing process employed. This trend would be expected to result in an increased likelihood of the occurrence of RCF-type cracks being initiated toward the end of the lifetime of the railway wheel. This correlates well with observations made of the wheels investigated for this work.

Plastic flow and the shearing of the microstructure of the material occur near the tread surface due to rail/wheel contact which might exceed the yield stress of the unstrained bulk material. As a result, the microstructure in such highly stressed regions near the tread surface of the railway wheels investigated show high levels of shear, thus, resulting in higher hardness values in these regions as a consequence of the presence of high tangential forces at railway curves. Furthermore, as expected, a greater concentration of cracks are found to occur in these regions which thus initiate due to the presence of higher stresses and strains in these regions of the tread, thus, resulting in the detachment of the material from the wheel tread surface due to wear. In addition, the central running region of the railway wheel experiences more frequent rail/wheel contacts than other regions in both running directions; however, the tangential forces are lower in these regions and thus results in a higher level of wear despite not significantly changing the microstructure in these regions of the wheel tread.

In chapter 7 the results obtained from the study on the response of the ACFM sensor to artificial cracks (or “notches”) created in a calibration steel plate in order to simulate cracks and conditions found in railway wheels in services are shown and discussed. These results show that a 50 kHz ACFM probe provides higher sensitivity than the standard 5 kHz probe on ferrous and non-ferrous materials. Thus, a 50 kHz ACFM sensor is optimal for the detection and sizing of cracks in railway wheels and components in service; it is also found that the mean background signal is significantly lower for the ACFM system operating at the higher frequency than at the lower frequency of 50 and 5 kHz, respectively. As most RCF type cracks occur at +/- 45° to the circumferential direction, a sensor system with orthogonal fields at +/- 45° would be most appropriate. Thus an array of ACFM sensors positioned in the system at different to the crack angle can significantly improve the probability of cracks in

the material under inspection. Furthermore, the work demonstrates that crack propagation angle significantly affects the ACFM signal and, for propagation angles greater than 25^0, yields higher normalised maximum B_x change values relative to the background signal which would, thus, significantly influence the estimated measurements for the crack pocket depth and length,; these normalised values are highest and optimum for propagation angles of 60 and 90^0 which therefore demonstrates that the ACFM sensor is most sensitive to cracks that propagate at higher angles between 60-90^0 in contrast to shallow angles of propagation of about 25^0 and less. Therefore, for the proper inspection of components by electromagnetic non-destructive means it is important to be able to establish a magnetic field in at least two directions. The results also show that defects can still be detected at a lift-off of 5 mm above the surface of the material under inspection, although the signal strength is significantly depleted; the strength of the signal is higher for the ACFM operating at the higher frequency of 50 kHz. Furthermore, the work has shown that the probe lift-off during the inspection procedure is an important factor which must be controlled and, thus, taken into consideration during the inspection process in order to quantify RCF cracks correctly and this is in agreement with previous recent studies on similar systems. Therefore, in principle, the work presented here shows that any possible lift-off variations during inspection may be inferred and evaluated by determining the decrease in the sensor's signal strength which is in agreement with previous work conducted on similar systems [43, 86, 88, 117, 132]. Furthermore, even though appropriate high–speed inspection experiments could not be carried out using the current ACFM probe for the purpose of the PhD project due to the fact that the inspection system used for this study is inappropriate for inspections other than for slow manual speed due to limitations of the data acquisition board employed, thus, limiting the sampling rate to only a few kHz, previous work on similar systems [43, 86, 88, 117, 132] has shown that the signal response to cracks is significantly reduced at high operational speeds. The maximum change in the B_x ACFM signal increases significantly with a decrease in crack separation; the maximum change in the B_x signal is greater for closely spaced cracks which would thus significantly oversize the cracks using figure 7.4 (above). These results also demonstrate that at a crack spacing of 20 mm the cracks can be sized resonabley accurately, whereas, for spacings of 15 mm the outer cracks, for example, in the four crack cluster would yield resonably good estimates for the crack pocket depths, however, the two inner cracks would

significantly undersize the defects because these inner cracks in the crack cluster would yield higher values for the maximum change in the B_x signal; and the results also show that for crack spacing smaller than 15 mm the cracks thus estimated using the normalised change in the B_x signal would be significantly higher than the actual crack pocket depths. Furthermore, this effect needs to be taken into account when using the ACFM system on the railway network as the RCF cracks found in railway wheel tread surfaces, as shown in the previous chapter are, in general, closely closely spaced and in most cases closer than 5 mm apart as shown in wheel HSR2 in the RCF crack circumferential bands observed near the flange end and at approximately 3 cm from the non-flange end of this wheel where the spacing between the cracks are about 2-3 mm and 1 mm, respectively. Therefore, it is difficult to size such defects using the present ACFM system when the cracks within a cluster have a crack spacing of about 5 mm or smaller inter-crack spacing. Results from ACFM scans for crack clusters with and without a central deep crack with the ACFM sensor aligned parallel to the cracks and operating at frequencies of 5 and 50 kHz, respectively. These results show that the maximum change in the B_x signal is significantly larger for the cluster of cracks which have a central deep crack and these results also show that the background signal value (arbitrary units) is significantly lower for the ACFM sensor operating at the higher frequency of 50 kHz than for the system operating at the lower frequency of 5 kHz. Therefore, this result demonstrates that a deep crack within a cluster of shallow cracks can be inferred from the larger change in the B_x signal relative to the background signal if it is known that a deep and critical crack is present in the cluster of shallow cracks, however, if one does not know that a deep crack is present in the crack cluster then it is difficult to ascertain whether a deep and thus critical crack is present in the cluster. Therefore, the result demonstrates it is not possible at present to detect a deep crack within a cluster of shallow cracks using the ACFM sensor in its present state. Nevertheless, again as with the work shown in the results and discussion section in chapter 7 scans with different angles of ACFM sensor orientations with respect to the angle of the cluster of cracks were tried and the following interesting and reproducible results are obtained. It is found that scans conducted with the probe oriented at 90^0 to the cluster of cracks consisting of a deep central crack surrounded by shallow cracks results in a distinct central sensor B_x signal that is a peak instead of a trough as observed in the case of the probe which is parallel to the crack orientation during a scan, thus, identifying the critical crack in the

centre of the cluster which is significantly greater than the sensor signals for the individual shallow defects and thus suggesting that this method is capable of detecting a deep and critical crack in a cluster of shallow cracks, however, it is not possible to accurately size the deep crack in the cluster at present, nevertheless, this is a promising result and a way forward. Furthermore, in order to explain the above result obtained from this experiment the following explanation is presented in light of the current understanding of this phenomena about the leakage of magnetic flux in the scenario as shown in these results as demonstrated by the ACFM scans obtained from this experiment when the ACFM probe is oriented perpendicular to the direction of the cracks that with a transverse defect the induced current will flow parallel to the defect and be little affected by the presence of the defect. However, the direction of the magnetic field is now normal to the defect and, thus, it is expected that there would be a small flux leakage effect in the area of the defect. This is of course the field direction and driving mechanism of MPI. If there is a flux leakage effect it explains the signal response, namely an increase in B_x level and a sharp peak-trough in the B_z signal. It would be very much localised to the vicinity of the defect and would be affected by defect depth and crack opening and this effect has previously been observed and the above interpretation is supported by research in the field as reported in [206,207].

The work presented in chapter 6 on the investigation of capability of the ACFM system in detecting and sizing cracks, and thus assessing the level of RCF damage on the surface of railway wheels in service has shown that the background ACFM signal varies with position across the railway wheel tread for the wheels investigated with different levels of RCF tread surface damage. The optimum mean background signal chosen for all three wheels investigated for this study in order to estimate crack pocket depths for an ACFM sensor operating at a frequency of 5 kHz is 800. However, it is found from this work that the background ACFM signal changes with the operating frequency of the sensor and is significantly lower for a higher frequency sensor operating at 50 kHz, however, as the background signal values (arbitrary units) are relatively large for the sensor operating at these frequencies in comparison to the maximum change in the B_x signal for the crack(s) then choosing either of the mean background signal values for the high or low frequency sensor (the value generally is lower by about 100 arbitrary units for the 50 kHz ACFM sensor than when the sensor

is operating at a frequency of 5 kHz) the evaluated crack pocket depths are significantly different from one another; therefore, it is safe to choose a value of 800 for the background signal to calculate an estimate for crack pocket depths in worn railway wheels in service.

Furthermore, the results show that the present ACFM sensor is capable of detecting and sizing cracks near the tread surface which are superimposed upon each other. However, it is found that the ACFM sensor, in its present state, is incapable of distinguishing between individual surface breaking cracks in the treads of rail wheels investigated and thus is incapable of detecting and sizing individual cracks in these rail wheels. However, at best the ACFM system in its current form can provide an estimate of crack sizes for a multiple stack of cracks which are superimposed upon each other. The work has also shown that the range of crack pocket depths and surface lengths estimated, using the normalised maximum change in the B_x signal (i.e. $\Delta B_{xmax}/B_{x0}$) in conjunction with the diagram shown in figure 7.4 using the range of four semi-elliptical ratios shown on the diagram, from the ACFM sensor when scanned over the tread surface at different positions along the tread surface on wheels HSR1, HSR2 and HSR3, are between: 2 and 18 mm which agrees well with the crack depths and surface lengths found by using optical metallography, X-ray tomography in conjunction with reconstruction techniques and the multi-sectioning in conjunction with optical microscopy approach, as shown and discussed earlier in this work in chapter 6

Furthermore, due to variations in the lift-off that occur during inspection of the rail wheels removed from service as a result of roughness of the tread surface and in the case of the normalised results obtained for the main calibration plate discussed in the earlier section above at different lift-off distances the ACFM system cannot provide correct rankings for the crack depths under these conditions which is also in agreement with previous work in this field [43, 86, 88, 117, 132], nevertheless, all the artificial cracks (or “notches) and most RCF cracks found in the railway wheels removed from service and investigated using the ACFM probe were detected.

The results obtained from this study show that the ACFM sensor operating at a frequency of 50 kHz provides good estimates for the crack pocket depth for a crack

propagation angle of 25^0 and under sizes the crack by 10%, whereas, the sensor at this frequency of operation significantly over sizes the crack by 70% for crack propagation angles of 60^0 and 90^0. Whereas, the ACFM sensor operating at a lower frequency of 5 kHz provides accurate estimates for the crack pocket depths for crack propagation angles between 60^0 and 90^0 but also provides a reasonable estimate for the crack pocket depth at a propagation angle of 25^0 and under sizes the crack depth by 40%. The results obtained demonstrate that for closely spaced cracks the normalised maximum change in the B_x signal component (i.e. $\Delta B_{xmax}/B_{x0}$) is relatively larger than for an isolated individual crack of the same size as shown by the results in this present work. Results obtained show that using an ACFM sensor operating at an inducing frequency of 50 kHz to detect the artificial cracks (notches) in the calibration plate on a four crack cluster shows that the ACFM system operating at this higher frequency yields significantly higher $\Delta B_{xmax}/B_{x0}$ values and thus over sizes the defects for all cracks investigated and all cracks could not be sized as a result using the UK Network Rail sizing diagram shown in figure 7.4. However, in the case of the ACFM sensor operating at an inducing frequency of 5 kHz the sensor is found to be capable of providing reasonable estimates of the crack pocket depths at inter-crack spacing distances of 15 and 20 mm for the crack clusters consisting of two and four cracks and even though these crack pocket depth estimates are oversized by 36% in both of these cases at these inter-crack spacing distances these results are in line with previous similar studies reported in the literature [164,165]. However, at lower inter-crack spacing distances of 5 and 10 mm the ACFM techniques is not capable of distinguishing between individual cracks and considerably over sizes the cracks in agreement with former studies on similar systems [164,165]. The results also show that the estimate for the crack pocket depth is the same for two and four crack clusters at inter-crack-spacing distances of 15 and 20 mm but for a two crack cluster at an inter-crack spacing distance of 10 mm and an ACFM inducing frequency of 50 kHz the value of the normalised B_x obtained, i.e. $\Delta B_{xmax}/B_{x0}$, is too large using the ACFM sensor operating at 50 kHz than for the 5 kHz sensor employed to detect the same defects at the same inter-crack spacing distances and thus the 50 kHz sensor is incapable of sizing the defects at this inter-crack spacing using the sizing diagram shown in figure 7.4. However, the best results obtained from this study is found to be when the ACFM is operated at a lower frequency of 5 kHz on a cluster of two cracks with inter-crack-spacing distances at and above 15 mm, i.e. at inter-crack spacing

distances of 15 and 20 mm, where the defects investigated are sized within reasonable estimates with an estimate for the crack pocket depth that is oversized by 20% of the actual depth of the defect at these two inter-crack spacing distances. This result is better and thus in line with that reported in the literature using an ACFM sensor operating at the same lower frequency. Therefore, these results demonstrate that the ACFM technique operating at lower frequencies (5 kHz) is much better suited at sizing (length and depth) cracks in railway track and railway wheels and components than an ACFM system operating at higher frequencies (50 kHz) and, thus, provides reasonable estimates for crack pocket depths. Furthermore, the results obtained demonstrate that a similar trend and features in the ACFM signal by using the ACFM technique on detecting and sizing the artificial cracks in the calibration plates investigated and on the RCF cracks identified in the three railway wheels removed from service and investigated, namely, railway wheels: HSR1, HSR2 and HSR3 which were provided by three different manufacturers in conjunction with Manchester Metropolitan University (MMU) for the purposes of my work on my PhD research project at School of Metallurgy and Materials, University of Birmingham.

8.2 IMPORTANCE TO THE RAILWAY INDUSTRY AND FUTURE WORK

Observations of the tread damage on rail wheel HSR2 show a significantly lower concentration of RCF-type cracks on the surface as compared to the HSR1 worn rail wheel where the damage is much greater. Furthermore, the crack spacing is greater than the crack depth in the former wheel as discussed in chapter 4; the reasons underlying this phenomena need to be investigated further and is beyond the remit and scope of the current PhD project and, thus, is a suggestion for work to be undertaken in the future. The work carried out on this PhD project has shown the promise of the ACFM technique as a non-destructive evaluation (NDE) technique in evaluating the severity of RCF damage in railway track and railway wheels and components. Therefore, further research and development of the ACFM system in conjunction with a system that incorporates arrays of ACFM sensors placed within the system at different angles of orientation relative to the surface crack angles to have a better probability of detecting potential cracks present on and/or near the surface of the wheel tread including other complimentary NDE techniques in such a wide ranging system which also incorporates, for example, ultrasonic testing (UT) in order to detect

and evaluate internal defects amongst other appropriate NDE techniques such as automated visual systems, acoustic emission (AE), magnetic particle inspection (MPI) and magnetic flux leakage (MFL) [1-21]. Such a system will provide an efficient non-destructive inspection system to detect defects and, thus, determine and ensure the integrity of railway track and railway wheels and components. The goal should be to tailor such a system in order to enhance the level of automation of railway infrastructure maintenance and, thus, improve the cost-effectiveness, quality and reliability, of the maintenance procedure and, therefore, ensure the integrity of railway assets and the safety, comfort and quality ride of passengers. Thus, making the prospect journeying by train a viable economic, environmentally friendly, fast, comfortable and, most importantly, safe means of travel for commuters.

Furthermore, the work carried out on the INTERAIL project (www.interail project.eu) is a European collaboration of 13 countries and this collaborative research project is jointly coordinated by ISQ and the United Kingdom supported by the European commission. The aim of the research initiative is to successfully implement and, thus, demonstrate the operation of the INTERAIL high-speed inspection system under in-service conditions. Thus, the project's ultimate goal is to restrict the occurrence of rail related failures; in order to achieve this, the high-speed inspection system incorporates three novel semi-automated inspection methods, namely, ACFM, ultrasonic phased arrays and vibration analysis (high-frequency). ACFM is deployed for the detection and sizing of surface-breaking defects and the ultrasonic system to locate and assess the severity of potential internal defects. The findings by the above authors also suggest that no significant loss of signal occurs with increasing inspection speed; this implies that, more importantly, the ACFM technique is a viable and alternative option for implementation on the rail network for the high-speed autonomous inspection of railway track, and therefore, in light of the results presented in chapter 7 the ACFM system is a viable alternative technique to be added to the NDE toolbox for the high-speed inspection of railway wheels and components.

At present, further work on the theoretical modelling of complex non-standard RCF crack shapes is continuously being carried out to further understand the ACFM response to such cracks as are found in actual service conditions in rail and rail wheels in an attempt to verify the results obtained by theoretical means for such complex

shaped RCF cracks; this work will extend beyond just considering planar shaped cracks and extend to studying the simulations of s-shaped cracks which are typical of moderately sized and larger cracks, i.e. classified as heavy to severe cracks on the UK Network Rail standard diagram. In addition, further work is currently ongoing in order to understand the response of the ACFM sensor to clusters of RCF cracks, in particular, the present focus is on the theoretical modelling of multiple defects with various sizes and angles relative to each other. It is reported in the literature [159] that at present a study is being conducted tpo investigate the performance of the ACFM system at inspection speeds of up to 80 km/hr and maintaining a constant probe lift-off distance by also employing a newly designed trolley system for the experiment. Furthermore, modelling to evaluate the interaction of RCF cracks with the AC and electromagnetic fields induced is currently underway and further work is also planned in order to focus on the investigation of an ACFM module with the automated vision and ultrasonic module as part of the complete INTERAIL high speed inspection system. Further work also needs to focus on investigating the influence of using low-frequency probes in order to study the effects arising as a result of grain anisotropy.

CHAPTER 9

APPENDICES

9.1 APPENDIX A: HARDNESS VERSUS TREAD DEPTH DATA FOR RAILWAY WHEELS HSR1, HSR2 AND HSR3

Tables 9.1-9.5 inclusive below show the hardness data for all the hardness versus tread depth results for railway wheels HSR1, HSR2 and HSR3. These results are used for the charts generated and shown in chapter 6 of the PhD thesis.

Table 9.1 Hardness measurements with depth below the tread surface for railway wheel HSR1 at the minimum run-out position of the tread and at different positions of 1 cm intervals along the tread.

Depth (μm)	HV 1 cm	HV 2 cm	HV 3 cm	HV 4 cm	HV 5 cm	HV 6 cm	HV 7 cm	HV 8 cm	HV 9 cm	HV 10 cm
150	311	310	386	330	357	335	335	310	362	344
300	322	306	358	335	351	335	335	314	333	335
450	311	300	346	334	326	326	331	309	327	331
600	305	298	332	347	331	319	336	317	311	320
750	324	311	333	339	336	334	326	311	316	301
900	336	313	328	326	345	337	332	321	306	320
1050	331	323	341	306	344	336	336	316	303	302
1200	309	299	327	316	341	331	320	321	308	318
1350	309	307	324	310	340	331	331	327	303	303
1500	312	312	317	310	336	332	345	309	303	297
1650	312	305	322	314	347	325	336	334	326	304
1800	303		317	312	324	333	331	327	303	307
1950	315	305	326	308	326	329	349	334	300	321
2100	304	304	323	303	331	311	328	321	301	292
2250	311	320	328	316	321	312	330	312	292	290
2400	307	295	328	318	325	305	322	332	299	292
2550	308	308	311	300	338	317	325	308	297	285
2700	318	307	308	270	326	300	321	320	306	298
2850	318	305	289	285	325	324	317	315	292	288
3000	308	298	301	300	336	313	316	337	282	299
3150	310	299	308	296	322	311	321	319	302	305
3300	310	296	300	309	324	291	315	314	284	299
3450	321	316	305	292	328	296	319	334	280	300
3600	320	286	303	303	324	309	310	305	289	297
3900	311	283	308	299	298	285	315	324	282	295
4200	303	294	280	300	303	321	303	312	303	300
4500	313	285	285	298	310	293	326	333	295	296
4800	318	255	297	306	283	306	304	307	282	294

5400	304	290	285	293	294	296	303	283	274	303
6000	283	295	294	309	294	278	291	304	273	306
6600	317	287	292	291	284	291	329	274	266	272
7800	309	298	294	301	292	304	319	317	283	288
9000		291	299	281	307	297	310	305	297	263

Table 9.2 Hardness measurements with depth below the tread surface for railway wheel HSR1 at the maximum run-out position of the tread and at different positions of 1 cm intervals along the tread.

Depth (μm)	HV 1 cm	HV 2 cm	HV 2.5 cm	HV 3 cm	HV 4 cm	HV 5 cm	HV 6 cm	HV 7 cm	HV 8 cm	HV 9 cm	HV 10 cm
100		348	387	433	360	407	372	422			
150	349								396	400	414
200		330	343	380	360	411	362	406			
300	352	318	319	391	360	393	376	391	351	361	362
450	346	332	326	385	366	398	370	381	344	352	366
600	341	322	335	369	350	390	376	386		348	344
750	341	285	327	358	340	409	386	359	336	338	347
900	344	325	329	373	334	357	378	396	346	339	332
1050	341								349	341	327
1200	334	318	343	374	297	339	388	363	345	333	334
1350	323								347	337	332
1500	308	332	325	366	305	339	400	358	344	342	323
2000	303	311	324	345	305	319	357	389	341	336	314
2500	294	323	308	330	300	295	319	377	327	325	323
3000	305	321	311	307	272	298	307	352	331	318	310
3500	292								323	314	312
4000	281	294	292	290	288	277	290	304	321	294	295
5000	293	283	286	282	277	288	278	303	292	289	288
6000	280	302	284	295	284	278	296	272	282	286	283
7000	288								283	275	284
8000	286								276	277	286
9000	298								274	292	287

Table 9.3 Hardness measurements with depth below the tread surface for railway wheel HSR2 and at different positions of 1 cm intervals along the tread.

Depth (μm)	HV 1 cm	HV 2 cm	HV 3 cm	HV 4 cm	HV 5 cm	HV 6 cm	HV 7 cm	HV 8 cm	HV 9 cm	HV 10 cm
100	393	351	463	392	353	364	330	369	409	242
200	385	363	437	415	360	354	339	366	382	241
300	352	349	406	378	350	368	332	365	354	253
400	372						340			
450	353	352	397	397	352	352	340	357	267	267
600	383	340	388	375	370	358	343	339	360	254
750	342	350	367	386	337	334	348	349	357	270
900	371	349	356	375	324	343	335	336	354	241

1200	361	356	362	385	340	342	342	346	335	251
1500	346	336	352	354	331	329	329	337	341	279
2000	339	353	352	356	333	326	331	328	314	246
3000	340	333	324	326	302	300	311	323	306	278
4000	307	335	328	317	322	305	308	328	293	267
5000	319	327	320	309	302	305	302	310	285	266

Table 9.4 Hardness measurements with depth below the tread surface for railway wheel HSR3 and at different positions of 1 cm intervals along the tread.

Depth (μm)	HV 1 cm	HV 2 cm	HV 3 cm	HV 4 cm	HV 5 cm	HV 6 cm	HV 7 cm	HV 8 cm	HV 9 cm
100	342	406	395	322	303	285	347	402	392
200	310	355	357	318	302	301	333	372	397
300	317	403	355	320	291	300	322	376	
450	313	380	334	287	306	289	327	362	360
600	307	363	340	311	297	299	320	352	336
750	309	360	324	295	287	303	324	352	332
900	315	342	335	288	269	302	307	351	315
1200	303	340	317	325	294	289	317	365	294
1500	304	313	305	280	288	286	300	330	284
2000	302	320	293	273	296	275	322	307	282
3000	309	325	279	286	306	289	284	319	286
4000	301	299	279	291	301	295	285	306	273

Table 9.5 Hardness measurements with depth below the tread surface at the running position on the railway wheel tread 70 mm from the back of the flange for railway wheels HSR1 (maximum and minimum run-out), HSR2 and HSR3.

Depth (μm)	HSR1 (MAX. RUN-OUT) HV DATA	HSR1 (MIN. RUN-OUT) HV DATA	HSR2 HV DATA	HSR3 HV DATA
100	383	351	350	288
200	353	373	364	290
300	340	359	359	298
450	342	343	359	309
600	382	344	358	291
750	369	341	368	297
900	373	338	347	289
1200	397	340	368	286
1500	381	333	344	284
2000	373	339	335	285
3000	313	305	310	277
4000	299	290	314	276
5000	277	279	296	271
10000	249	278	282	270
15000	245	255	268	264
20000	246	258	249	260
25000	252	257	243	255

30000	254	257	247	256
35000	253	260	251	244
40000	260	258	249	242
45000	256	252		240
50000	256	250		237

9.2 APPENDIX B: CALIBRATION PLATE CP_2 ACFM SCANS

Note: all horizontal and vertical axes on all plots shown in this appendix are Time (seconds) and B_x Values (arbitrary units), respectively.

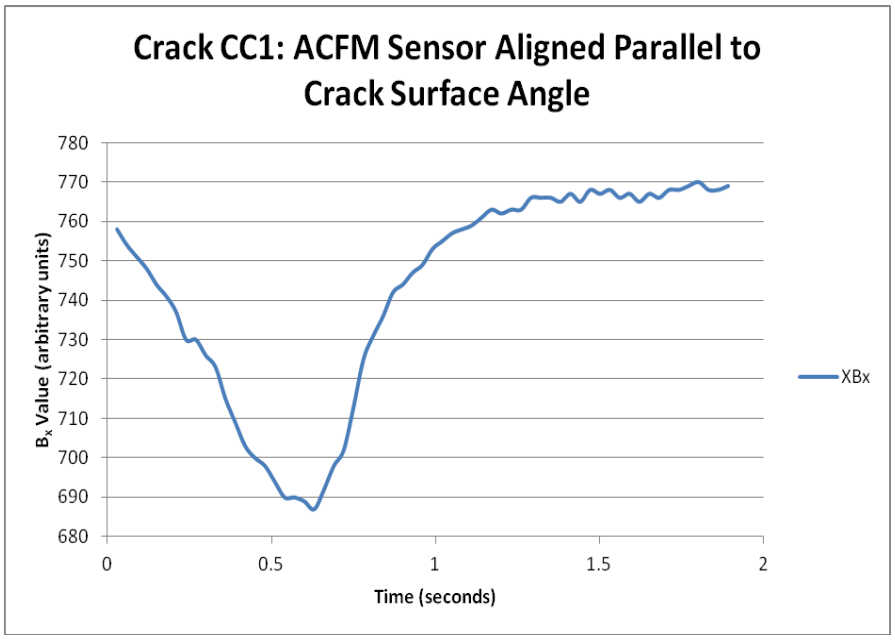

Figure 9.1 ACFM scan across calibration plate crack CC1 with the sensor aligned parallel to the surface angle of the crack.

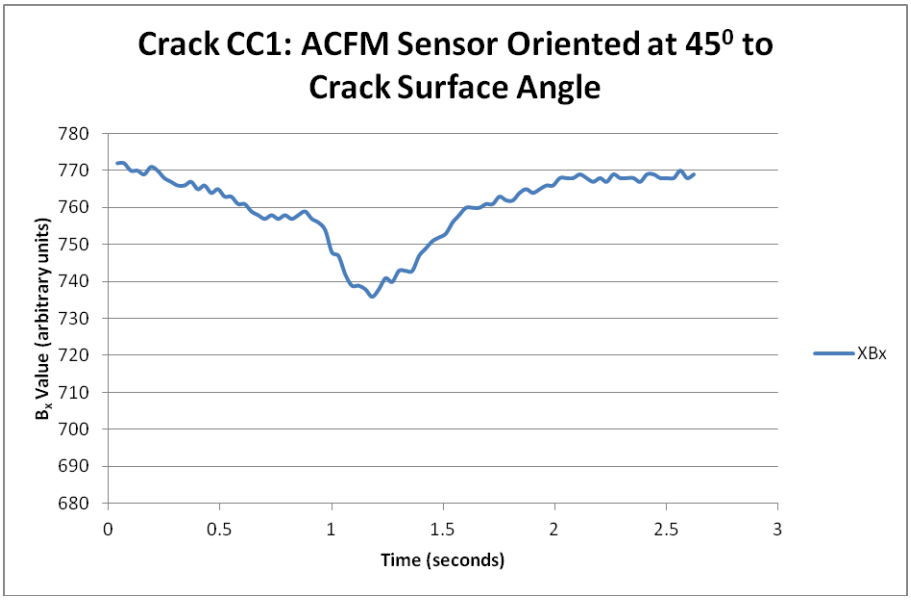

Figure 9.2 ACFM scan across calibration plate crack CC1 with the sensor oriented at 450 to the surface angle of the crack.

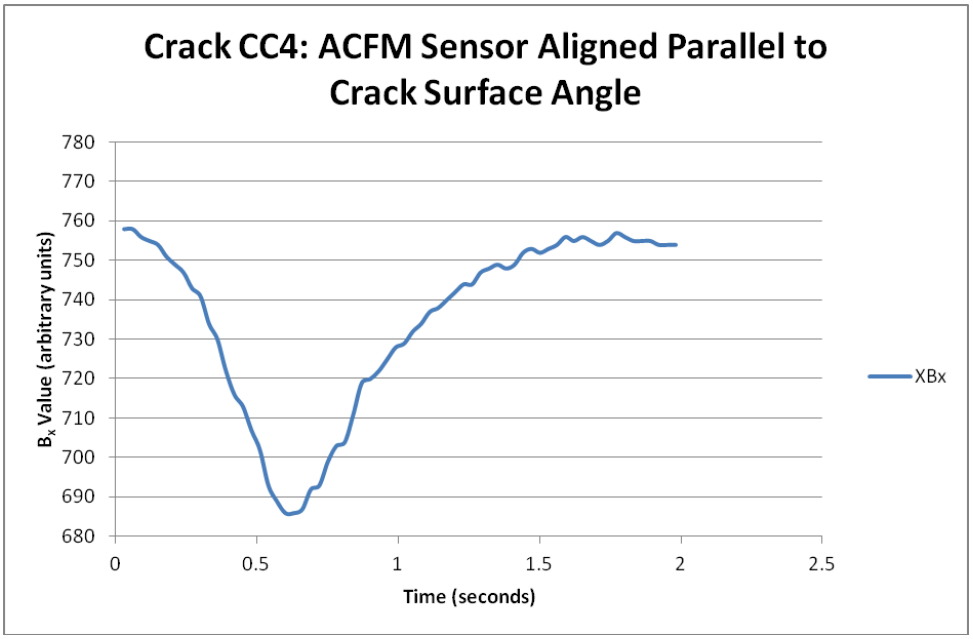

Figure 9.3 ACFM scan across calibration plate crack CC4 with the sensor aligned parallel to the surface angle of the crack.

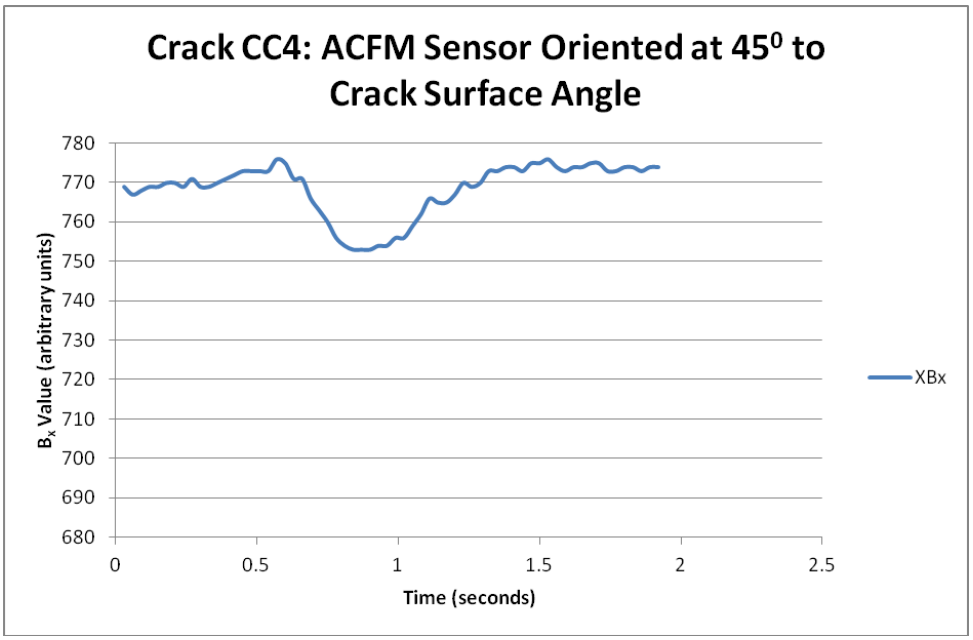

Figure 9.4 ACFM scan across calibration plate crack CC4 with the sensor at 450 to the surface angle of the crack.

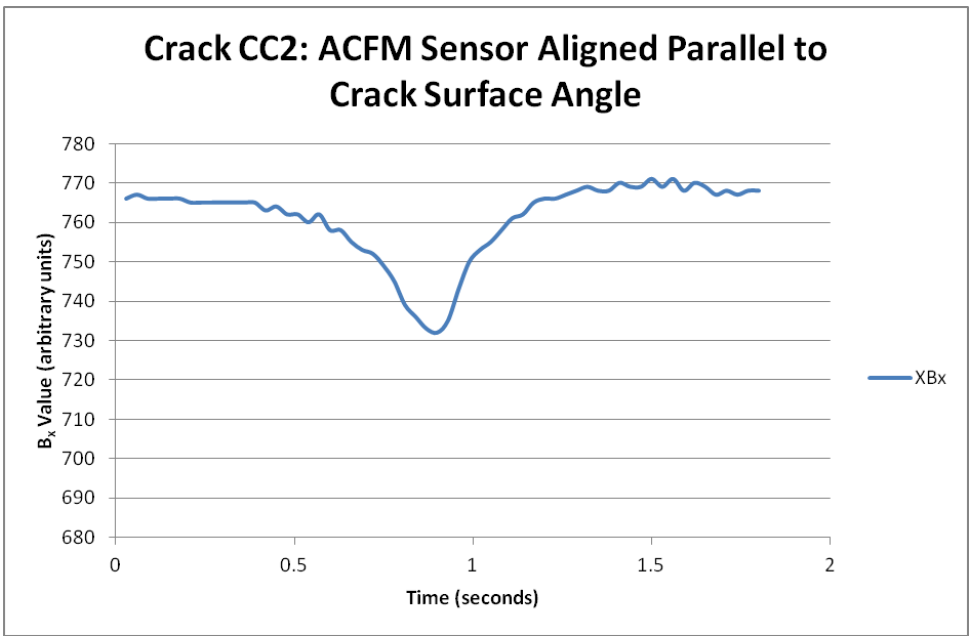

Figure 9.5 ACFM scan across calibration plate crack CC2 with the sensor aligned parallel to the surface angle of the crack.

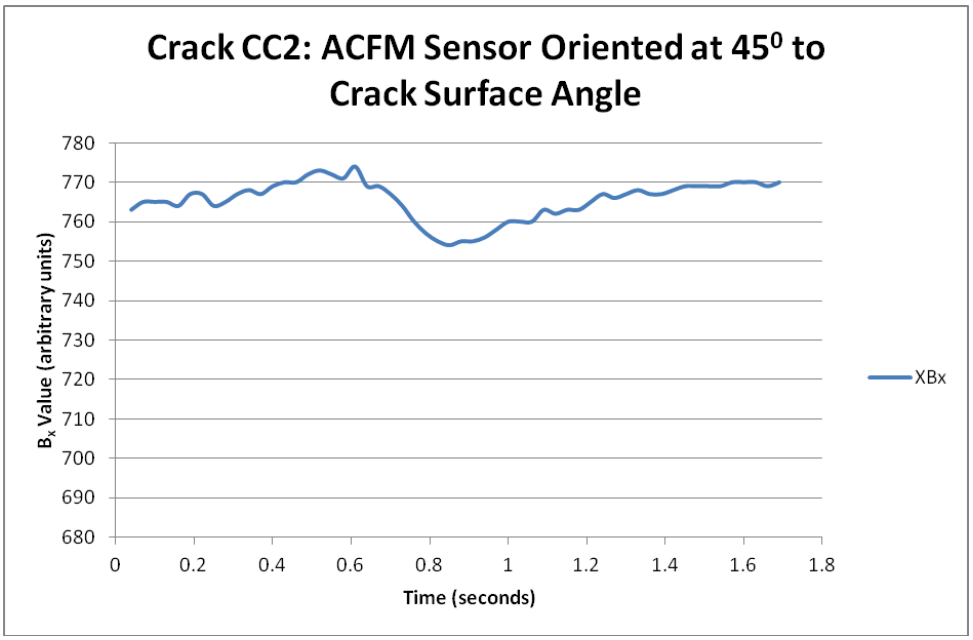

Figure 9.6 ACFM scan across calibration plate crack CC2 with the sensor oriented at 450 to the surface angle of the crack.

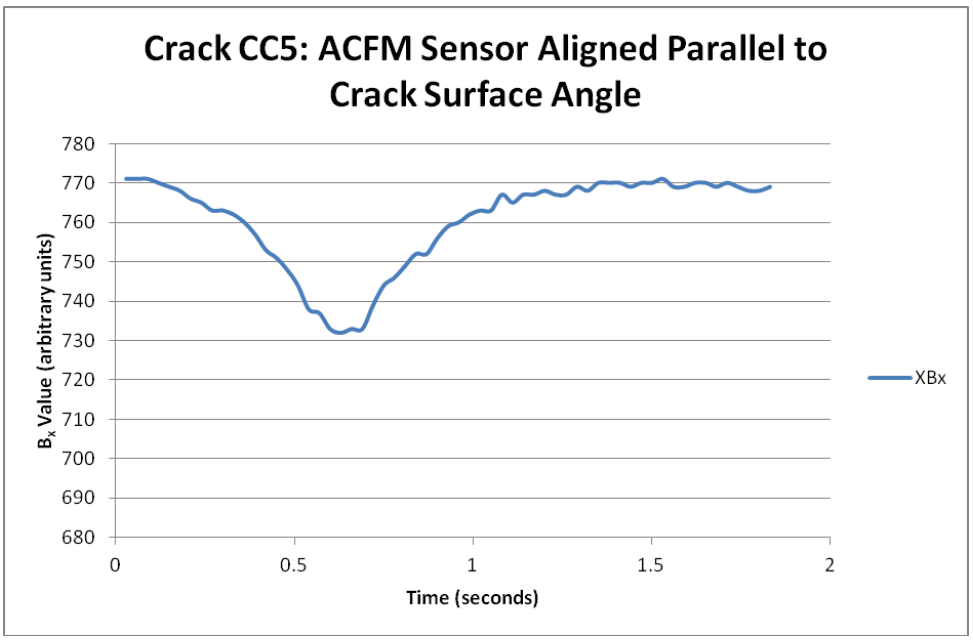

Figure 9.7 ACFM scan across calibration plate crack CC5 with the sensor aligned parallel to the surface angle of the crack.

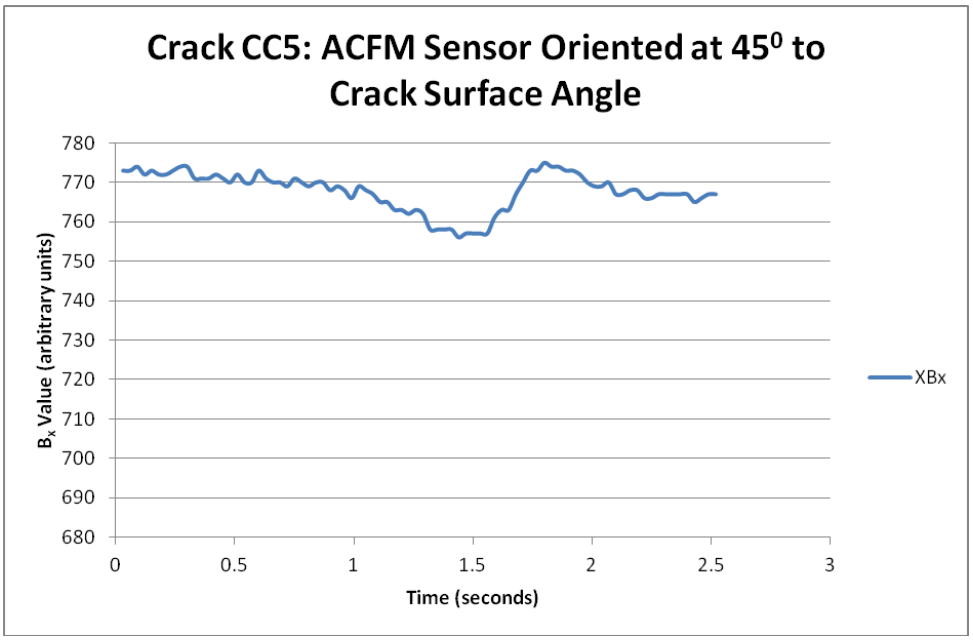

Figure 9.8 ACFM scan across calibration plate crack CC5 with the sensor oriented at 450 to the surface angle of the crack.

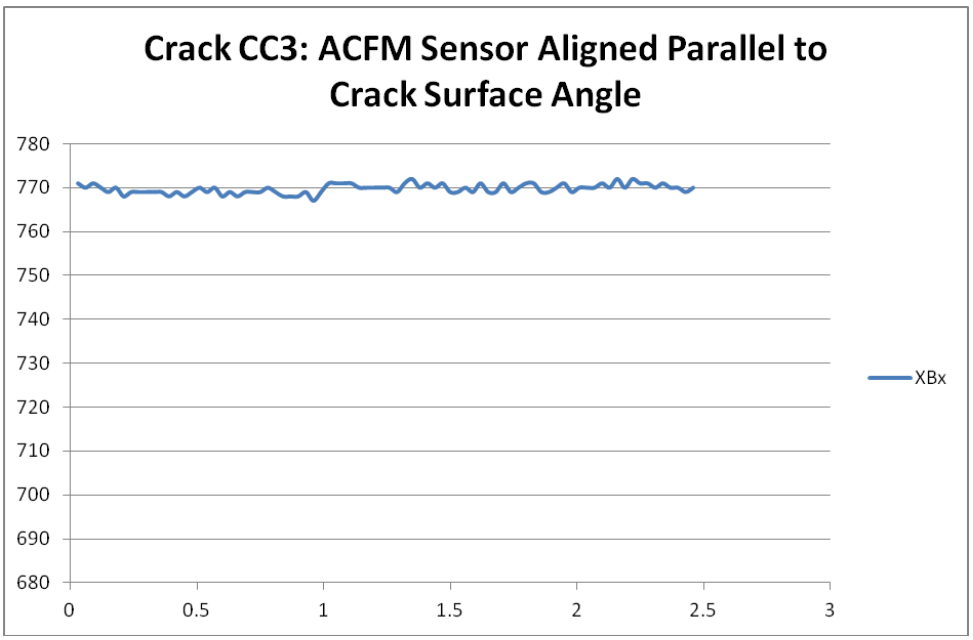

Figure 9.9 ACFM scan across calibration plate crack CC3 with the sensor aligned parallel to the surface angle of the crack.

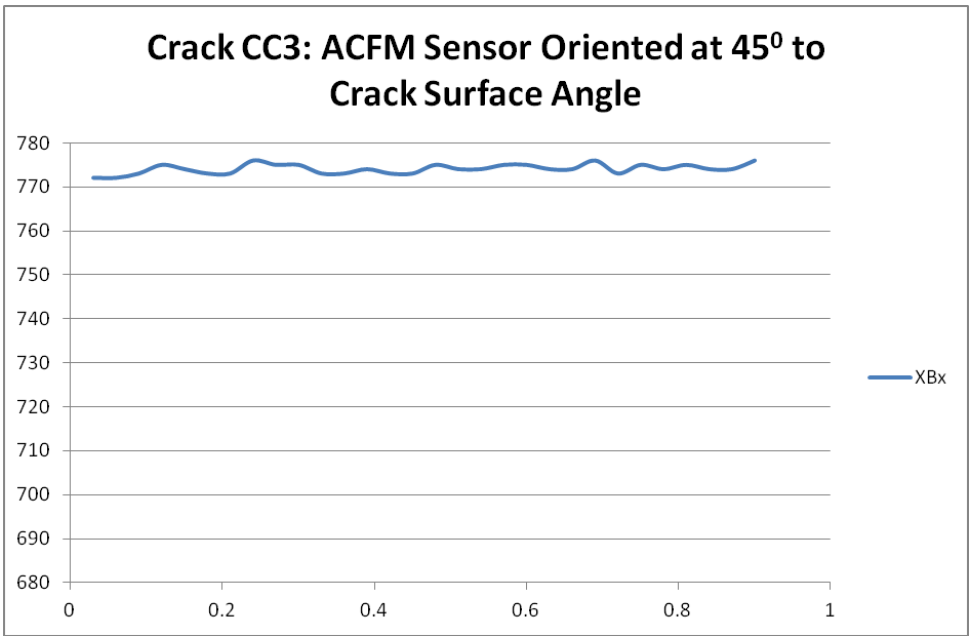

Figure 9.10 ACFM scan across calibration plate crack CC3 with the sensor oriented at 450 to the surface angle of the crack.

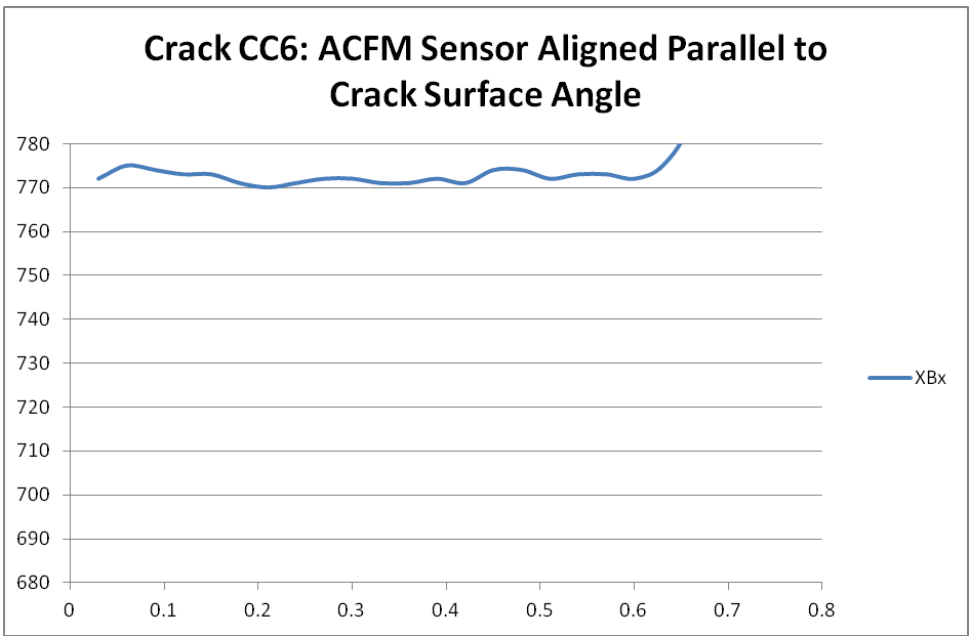

Figure 9.11 ACFM scan across calibration plate crack CC6 with the sensor aligned parallel to the surface angle of the crack.

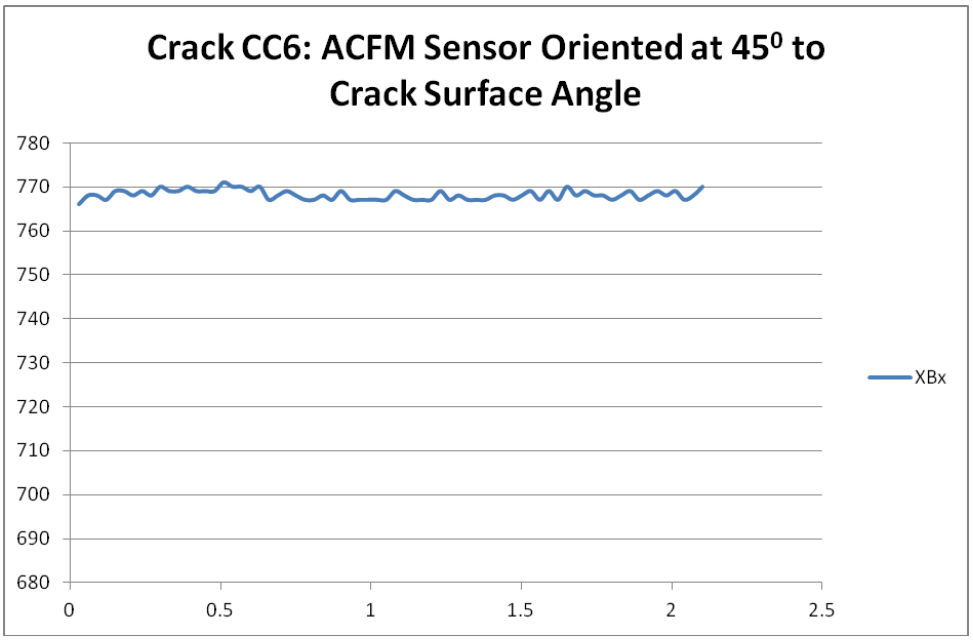

Figure 9.12 ACFM scan across calibration plate crack CC6 with the sensor oriented at 450 to the surface angle of the crack.

9.3 APPENDIX C: HSR1 RAILWAY WHEEL ACFM SCANS

Note: all horizontal and vertical axes on all plots shown in this appendix are Time (seconds) and B_x Values (arbitrary units), respectively.

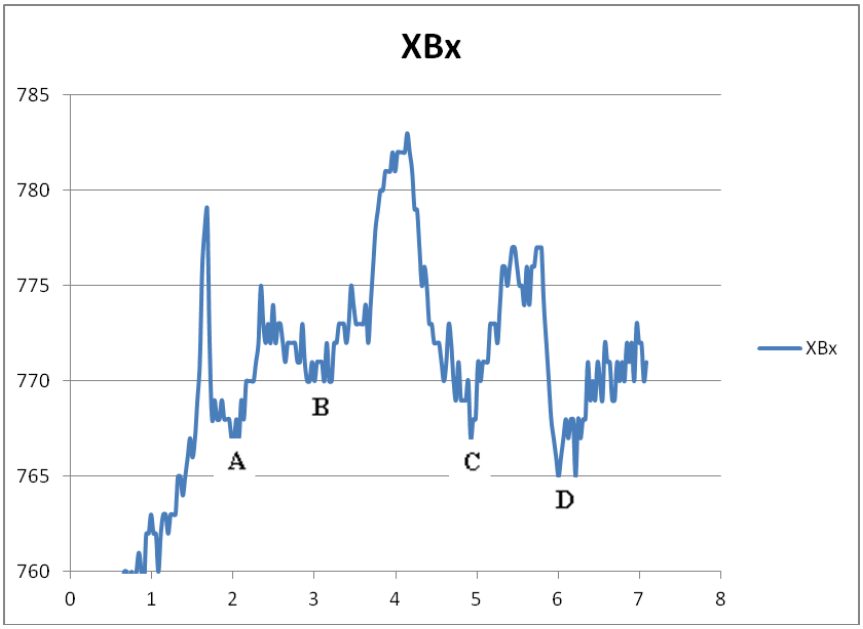

Figure 9.13 ACFM scan at position: 2.5 cm from the non-flange end of the HSR1 railway wheel tread at the maximum run-out position.

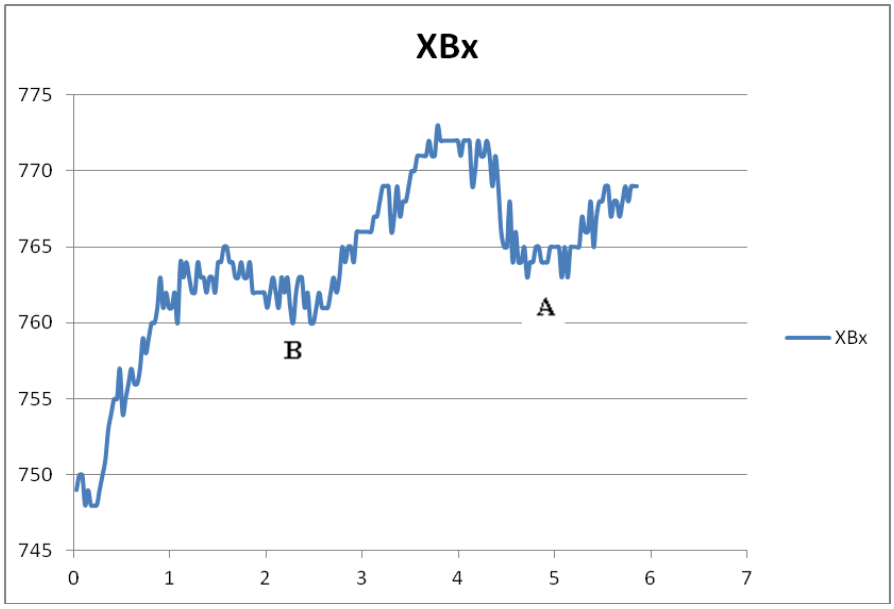

Figure 9.14 ACFM scan at position: 3 cm from the non-flange end of the HSR1 railway wheel tread at the maximum run-out position.

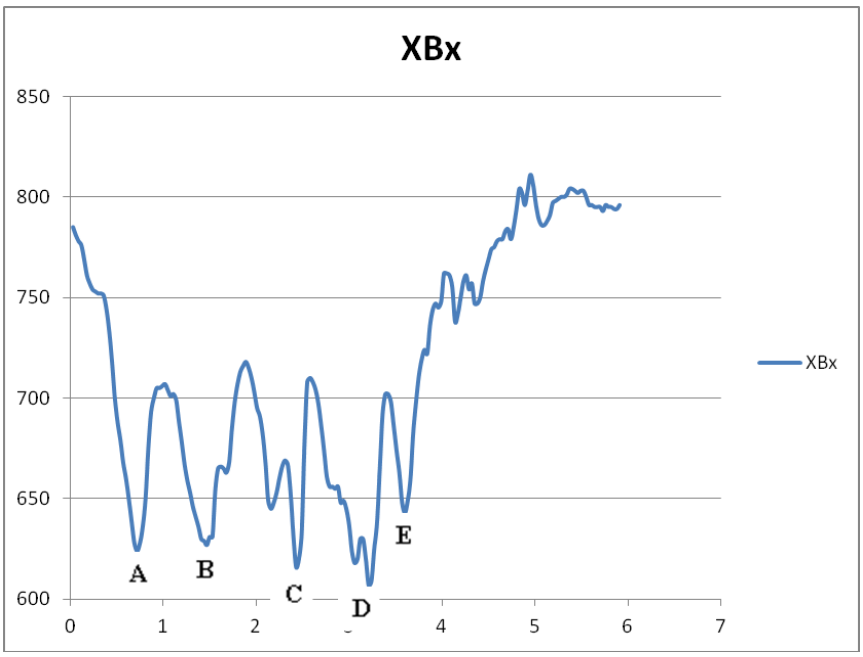

Figure 9.15 ACFM scan at position: 7 cm from the non-flange end of the HSR1 railway wheel tread at the maximum run-out position.

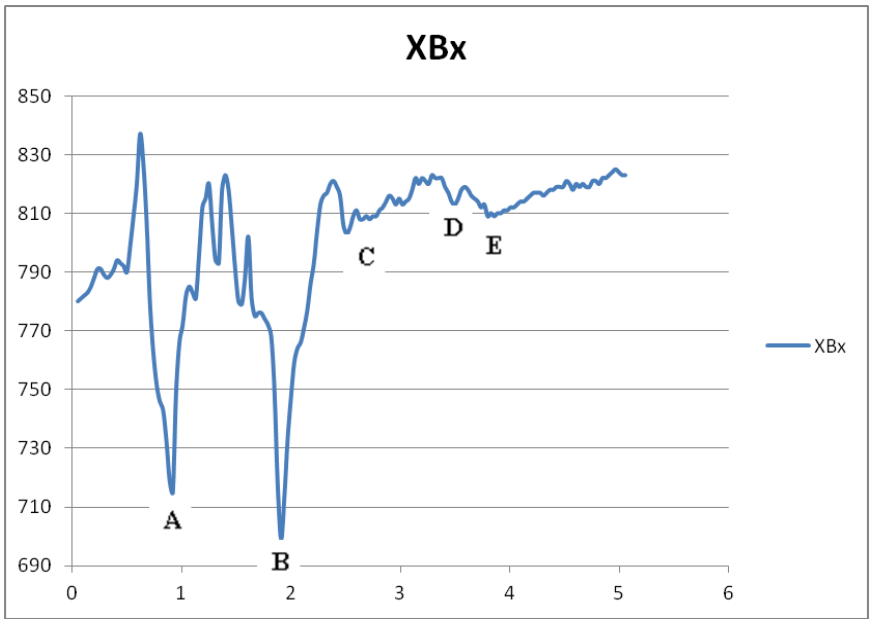

Figure 9.16 ACFM scan at position: 8 cm from the non-flange end of the HSR1 railway wheel tread at the maximum run-out position.

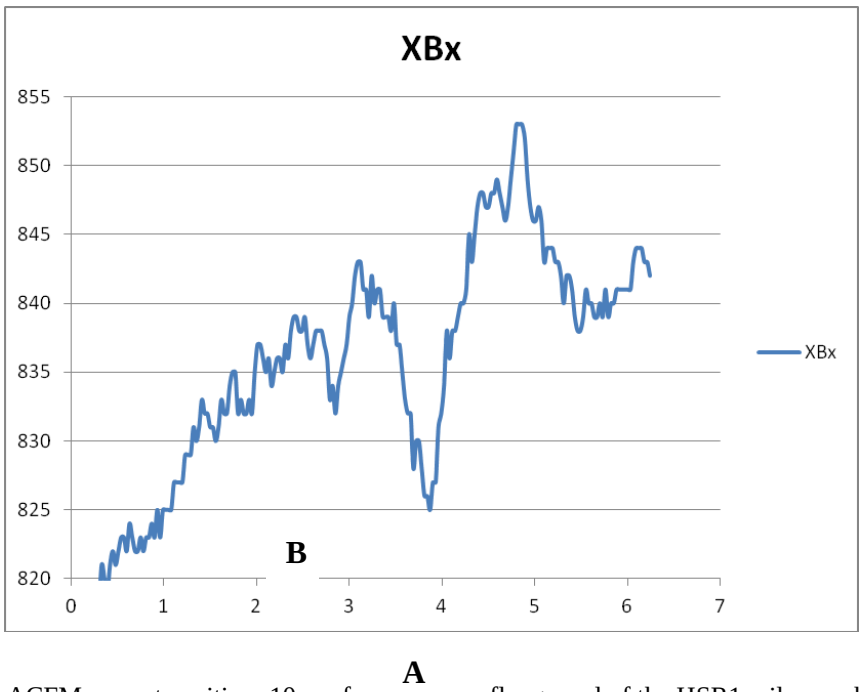

Figure 9.17 ACFM scan at position: 10 cm from the non-flange end of the HSR1 railway wheel tread at the maximum run-out position.

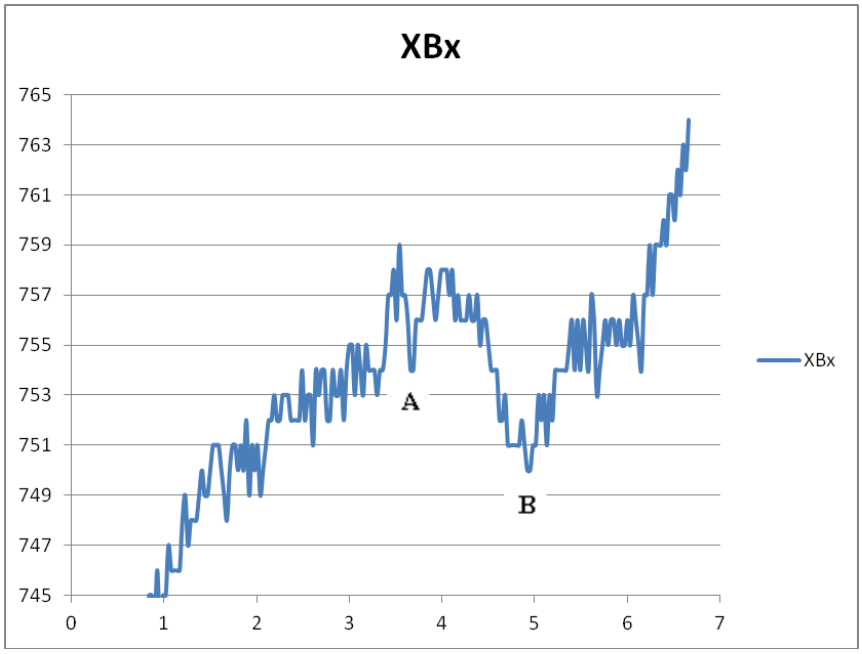

Figure 9.18 ACFM scan at position: 2.5 cm from the non-flange end of the HSR1 railway wheel tread at the minimum run-out position.

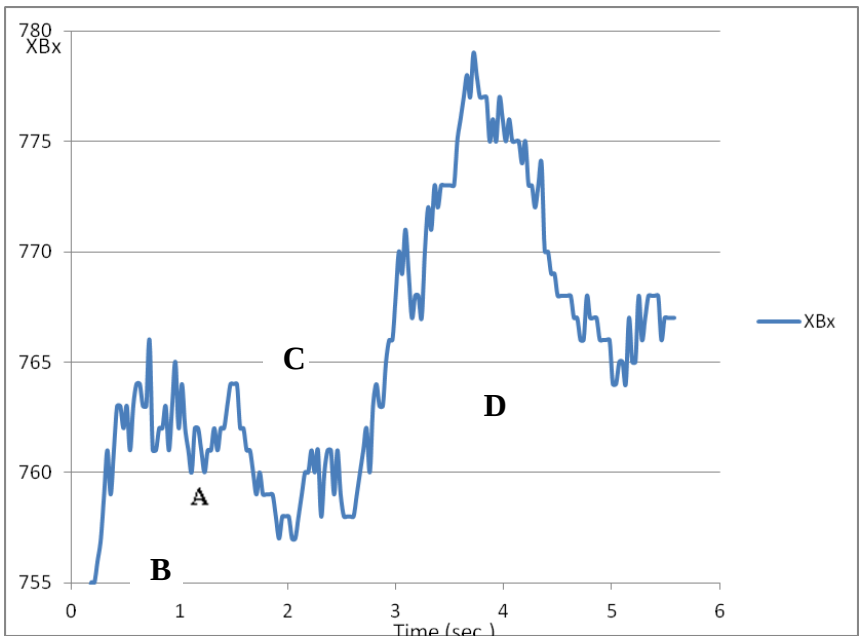

Figure 9.19 ACFM scan at position: 3 cm from the non-flange end of the HSR1 railway wheel tread at the minimum run-out position.

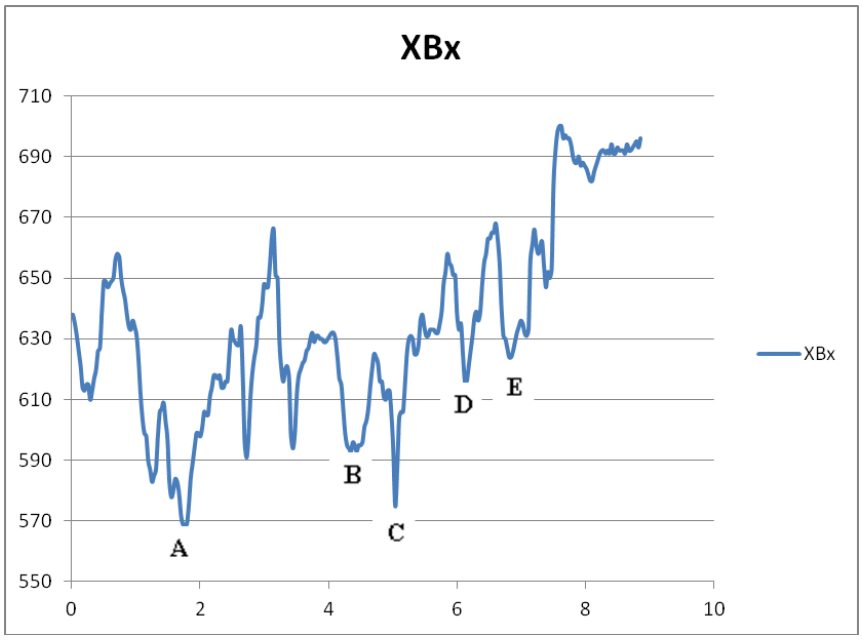

Figure 9.20 ACFM scan at position: 6 cm from the non-flange end of the HSR1 railway wheel tread at the minimum run-out position.

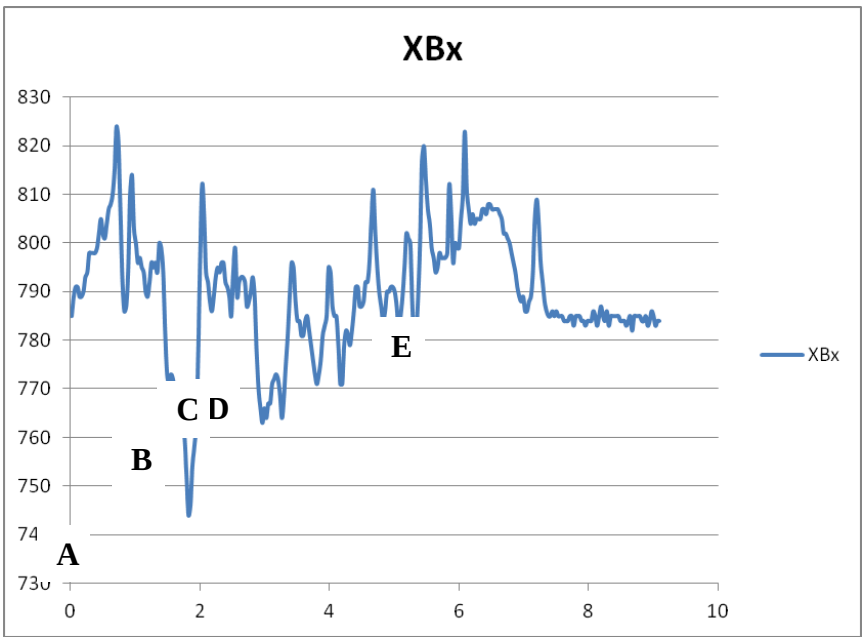

Figure 9.21 ACFM scan at position: 7 cm from the non-flange end of the HSR1 railway wheel tread at the minimum run-out position.

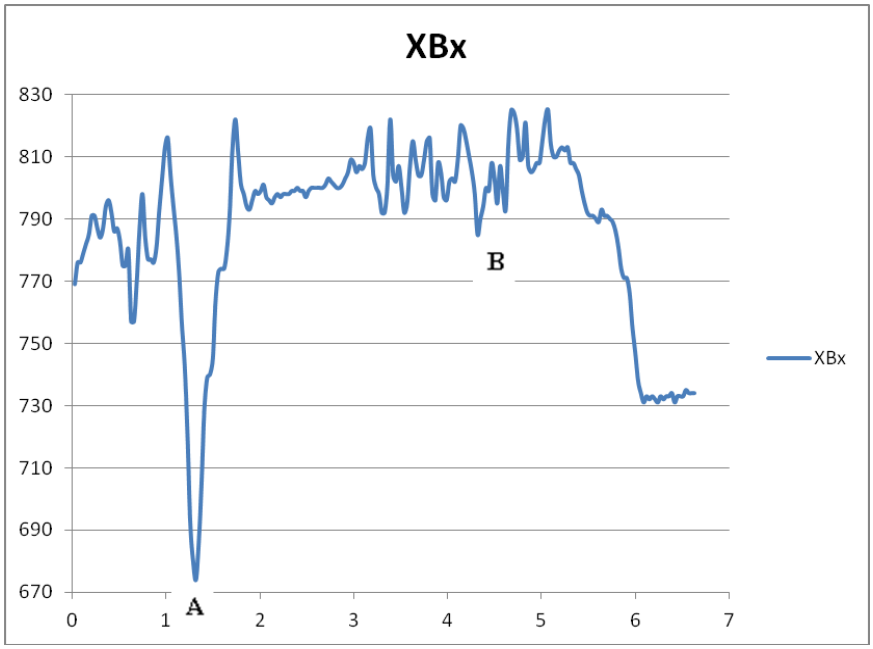

Figure 9.22 ACFM scan at position: 7 cm from the non-flange end of the HSR1 railway wheel tread at the minimum run-out position.

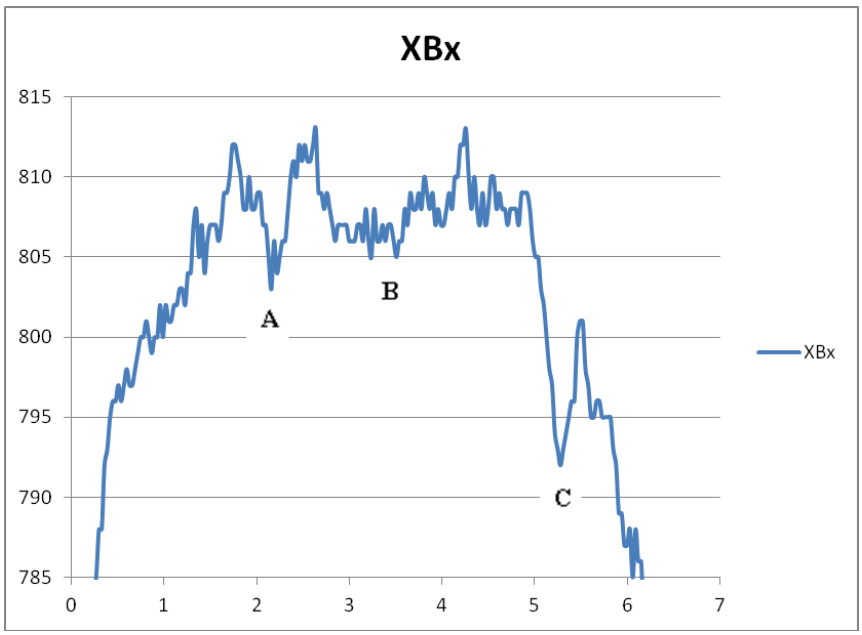

Figure 9.23 ACFM scan at position: 8 cm from the non-flange end of the HSR1 railway wheel tread at the minimum run-out position.

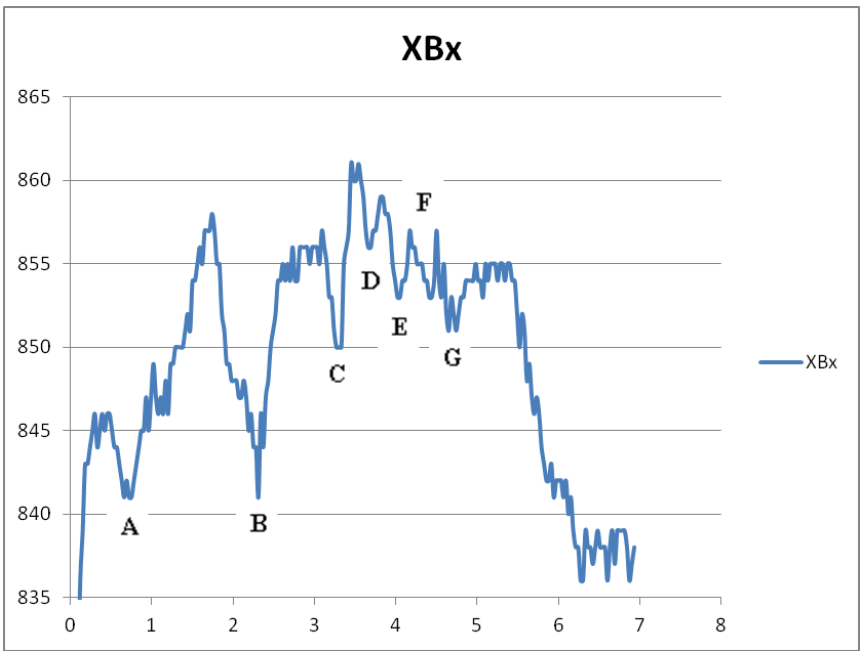

Figure 9.24 ACFM scan at position: 10 cm from the non-flange end of the HSR1 railway wheel tread at the minimum run-out position.

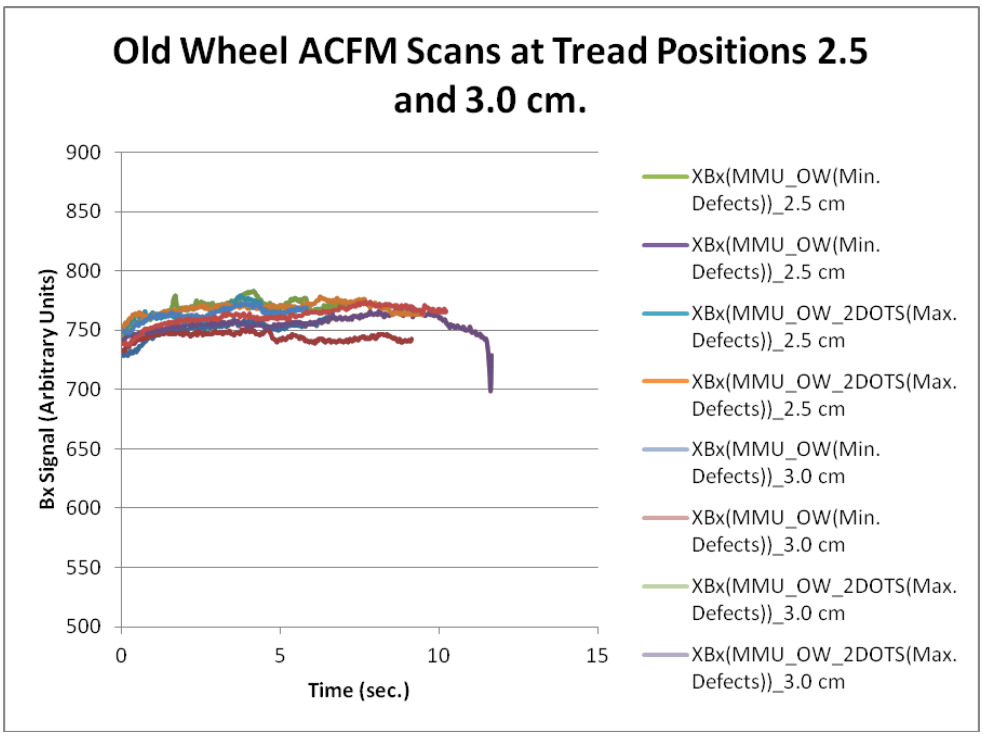

Figure 9.25 ACFM scans at positions: 2.5 and 3 cm from the non-flange end of the HSR1 railway wheel tread at the maximum (MMU_OW_2DOTS) and minimum (MMU_OW) run-out tread positions showing the variation in the background sensor signal at these tread positions.

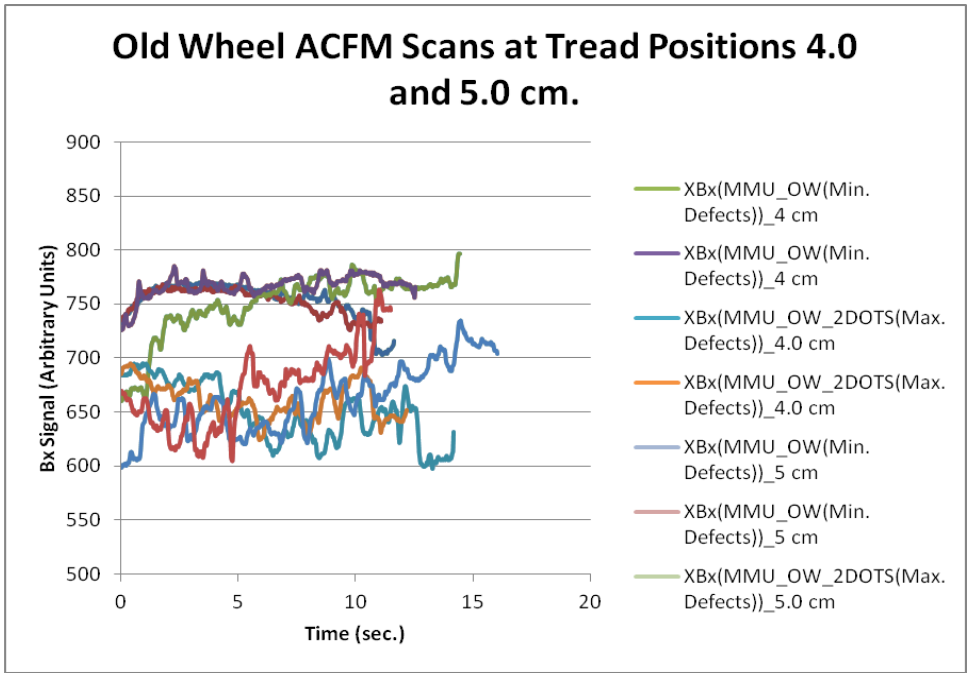

Figure 9.26 ACFM scans at positions: 4 and 5 cm from the non-flange end of the HSR1 railway wheel tread at the maximum (MMU_OW_2DOTS) and minimum (MMU_OW) run-out tread positions showing the variation in the background sensor signal at these tread positions.

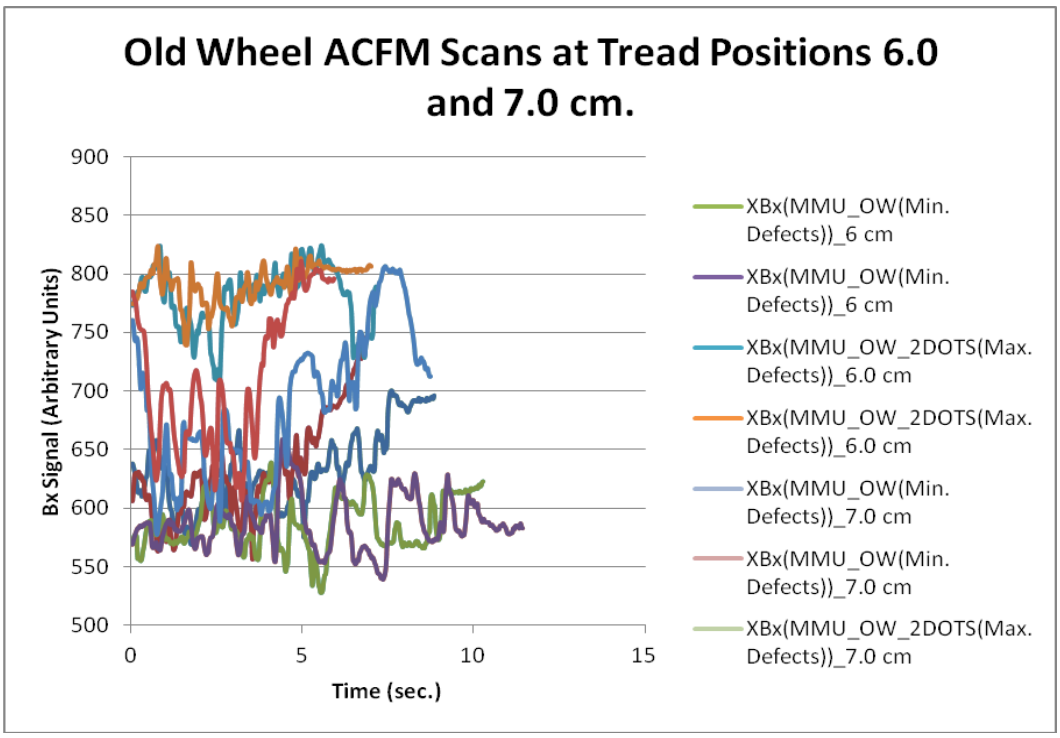

Figure 9.27 ACFM scans at positions: 6 and 7 cm from the non-flange end of the HSR1 railway wheel tread at the maximum (MMU_OW_2DOTS) and minimum (MMU_OW) run-out tread positions showing the variation in the background sensor signal at these tread positions.

9.4 APPENDIX D: HSR2 RAILWAY WHEEL ACFM SCANS

Note: all horizontal and vertical axes on all plots shown in this appendix are Time (seconds) and B_x Values (arbitrary units), respectively.

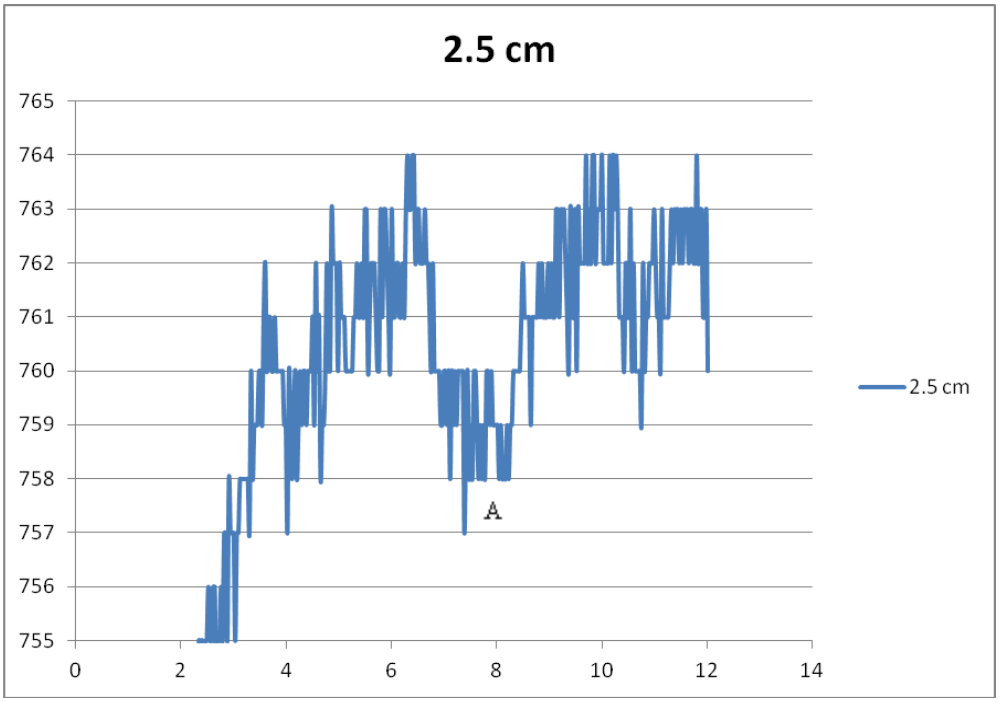

Figure 9.28 ACFM scan at position: 2.5 cm from the non-flange end of the HSR2 railway wheel tread.

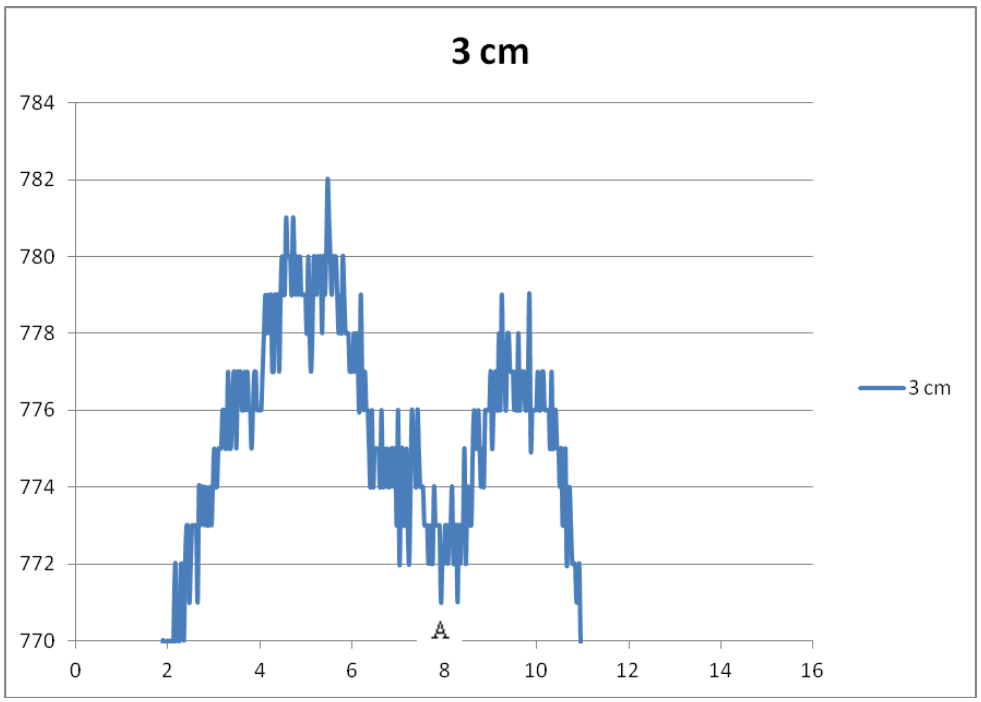

Figure 9.29 ACFM scan at position: 3 cm from the non-flange end of the HSR2 railway wheel tread.

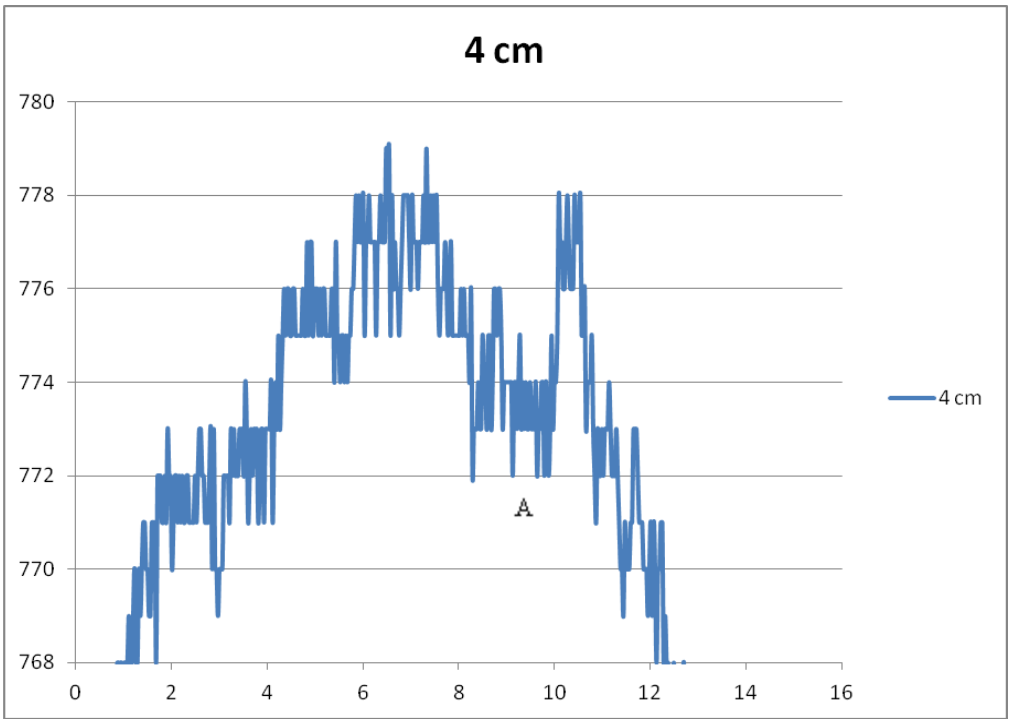

Figure 9.30 ACFM scan at position: 4 cm from the non-flange end of the HSR2 railway wheel tread.

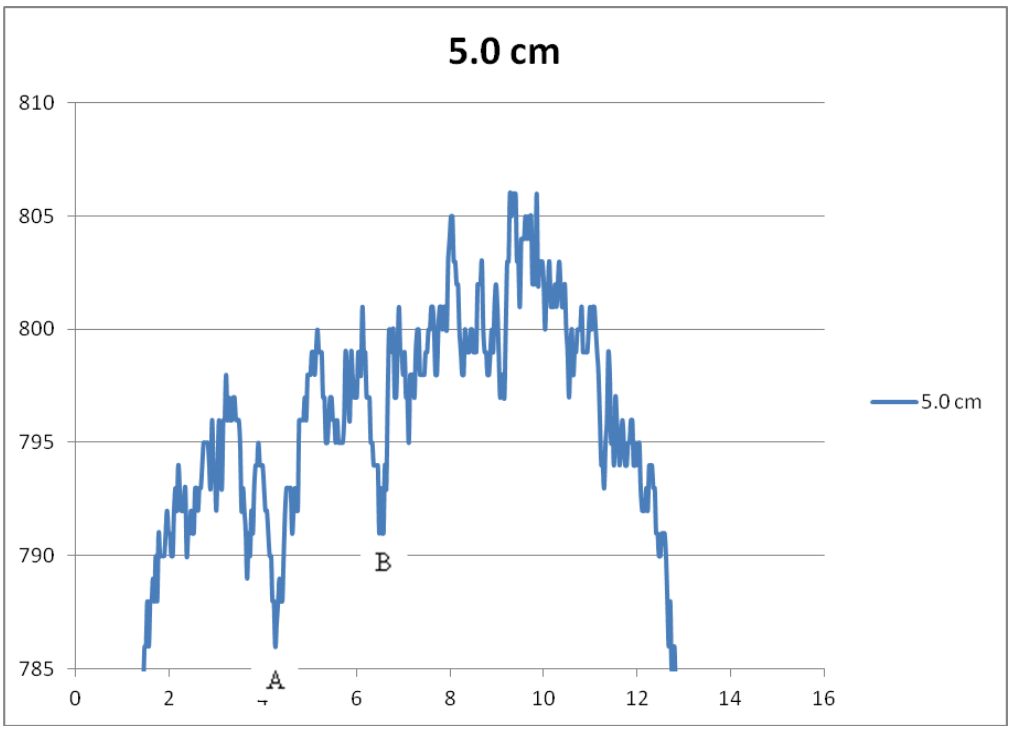

Figure 9.31 ACFM scan at position: 5 cm from the non-flange end of the HSR2 railway wheel tread.

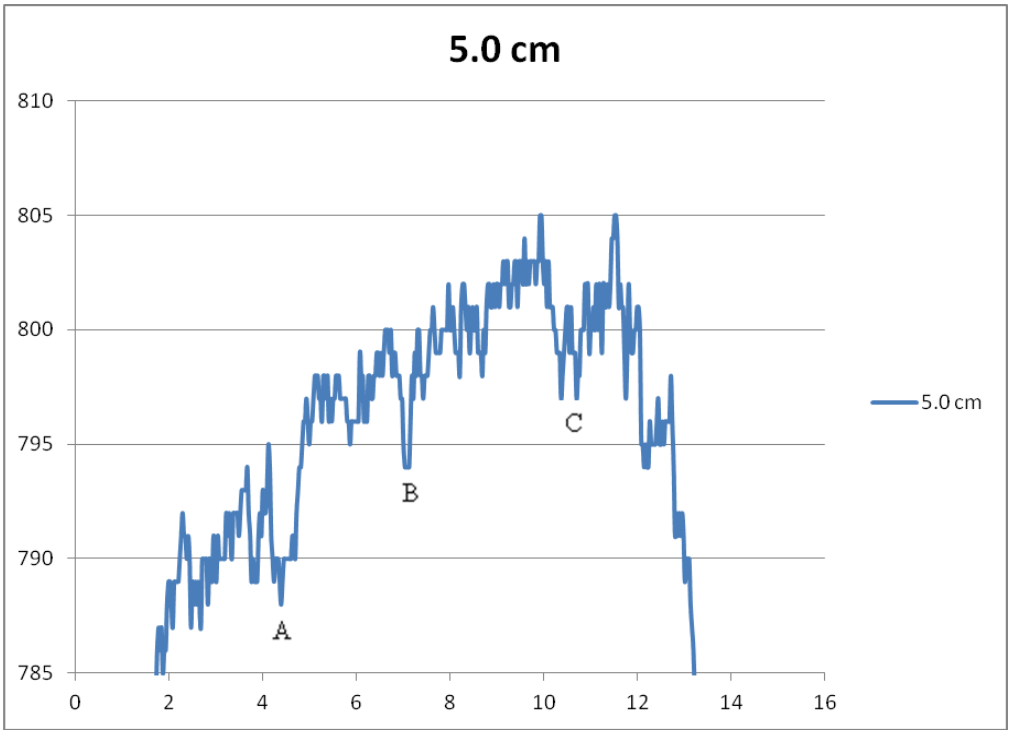

Figure 9.32 ACFM scan at position: 5 cm from the non-flange end of the HSR2 railway wheel tread.

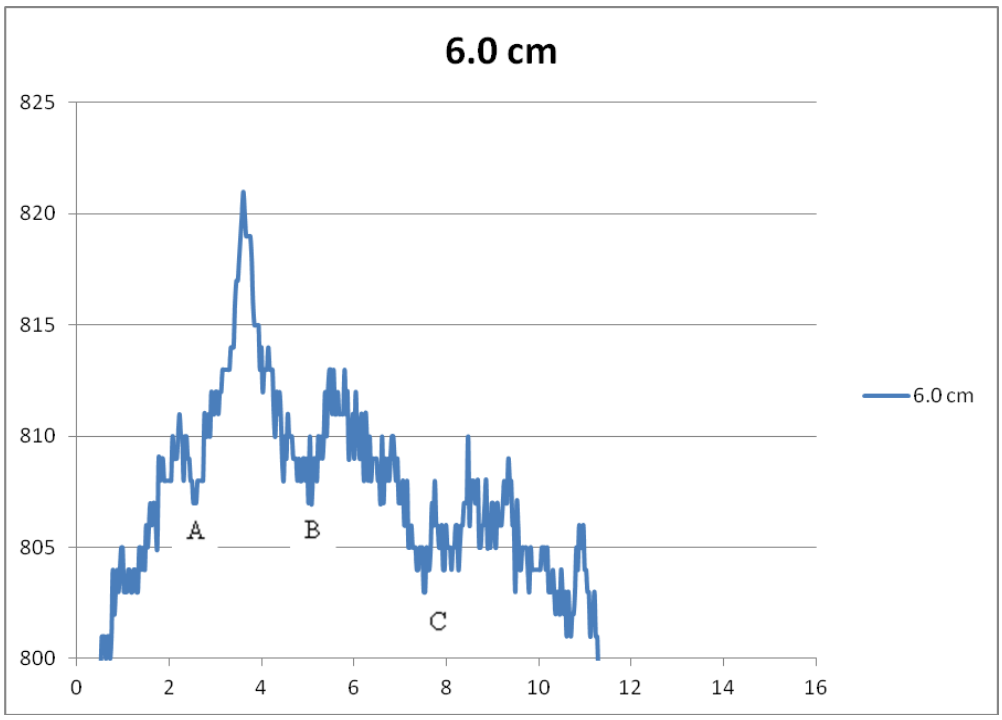

Figure 9.33 ACFM scan at position: 6 cm from the non-flange end of the HSR2 railway wheel tread.

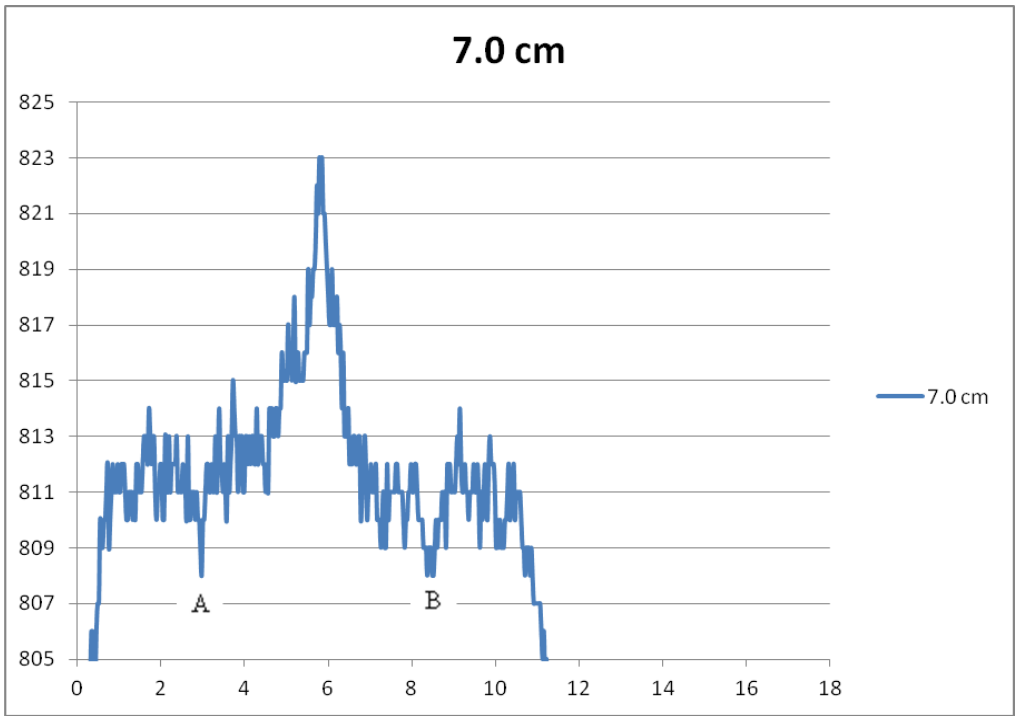

Figure 9.34 ACFM scan at position: 7 cm from the non-flange end of the HSR2 railway wheel tread.

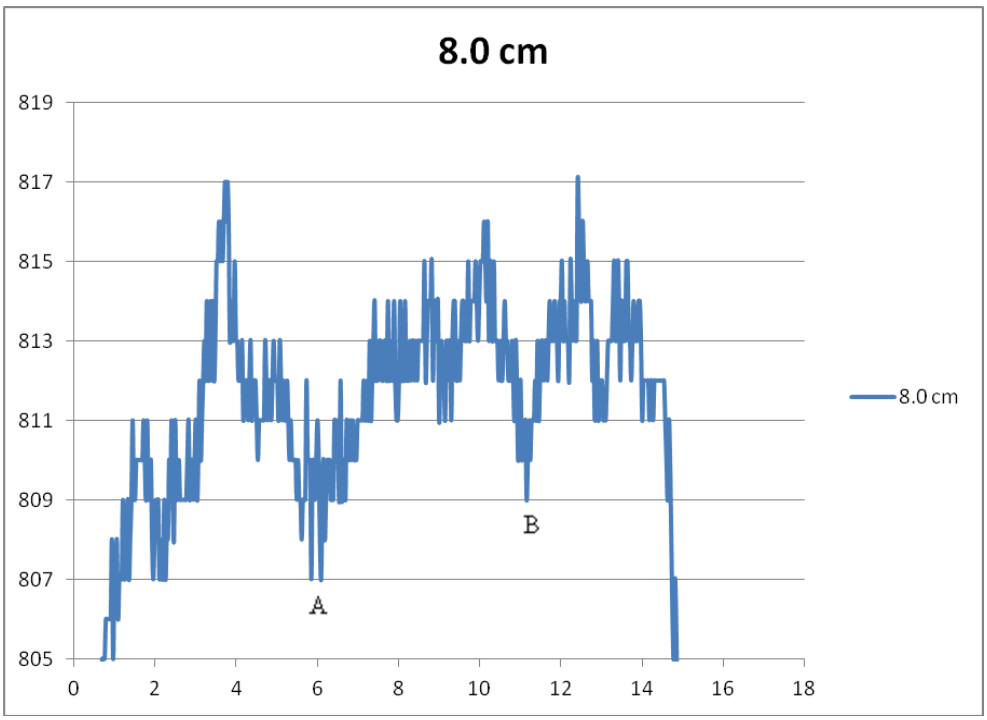

Figure 9.35 ACFM scan at position: 8 cm from the non-flange end of the HSR2 railway wheel tread.

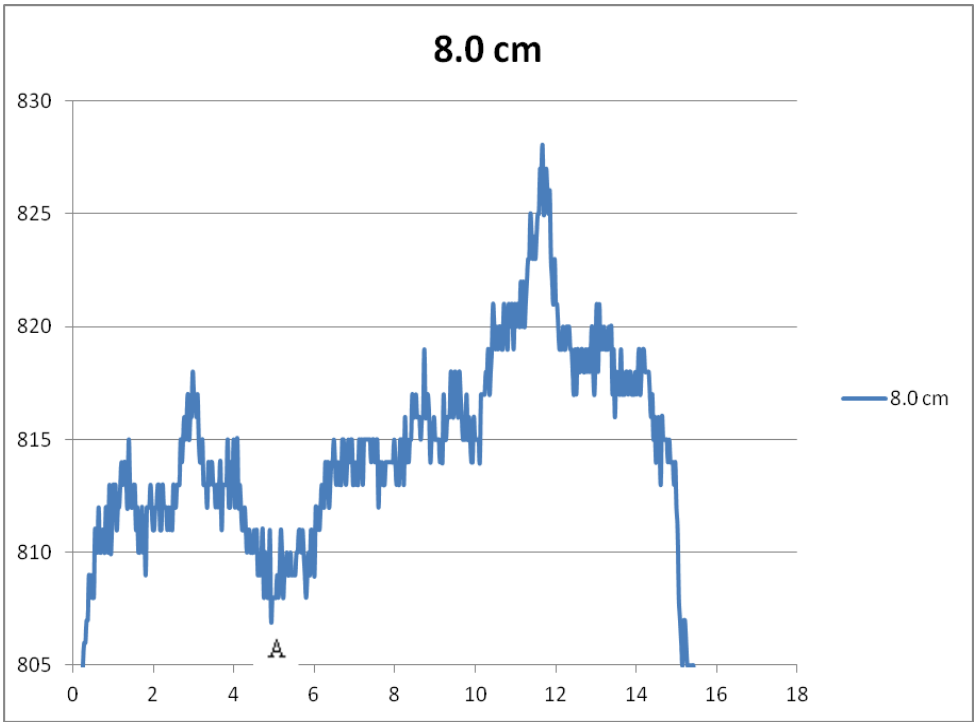

Figure 9.36 ACFM scan at position: 8 cm from the non-flange end of the HSR2 railway wheel tread.

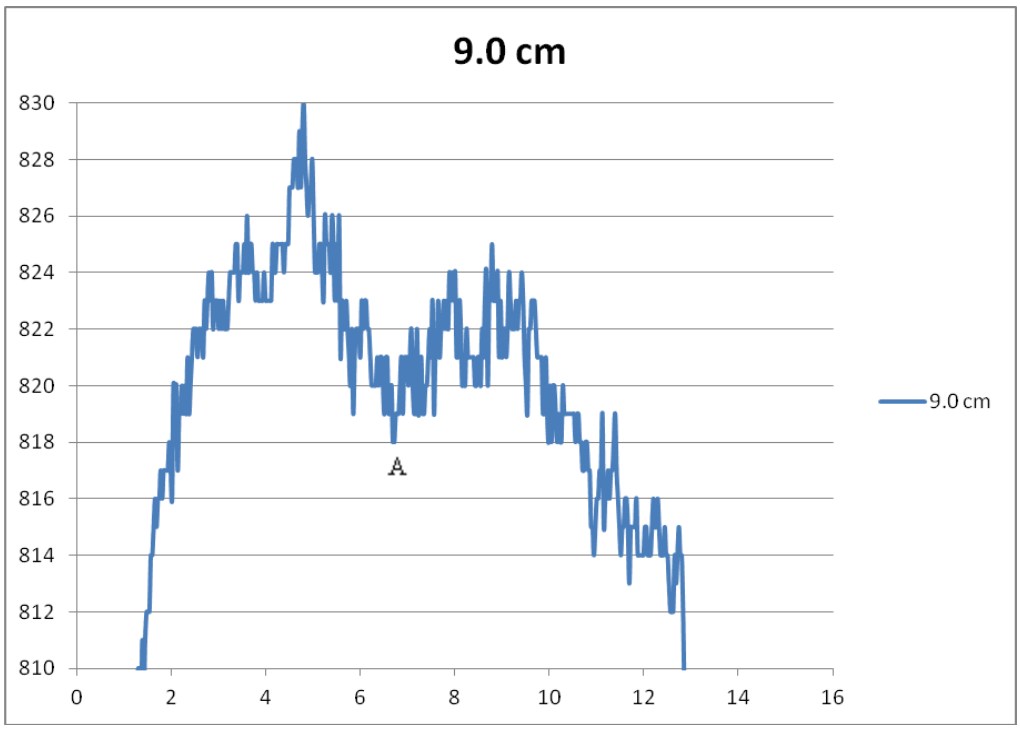

Figure 9.37 ACFM scan at position: 9 cm from the non-flange end of the HSR2 railway wheel tread.

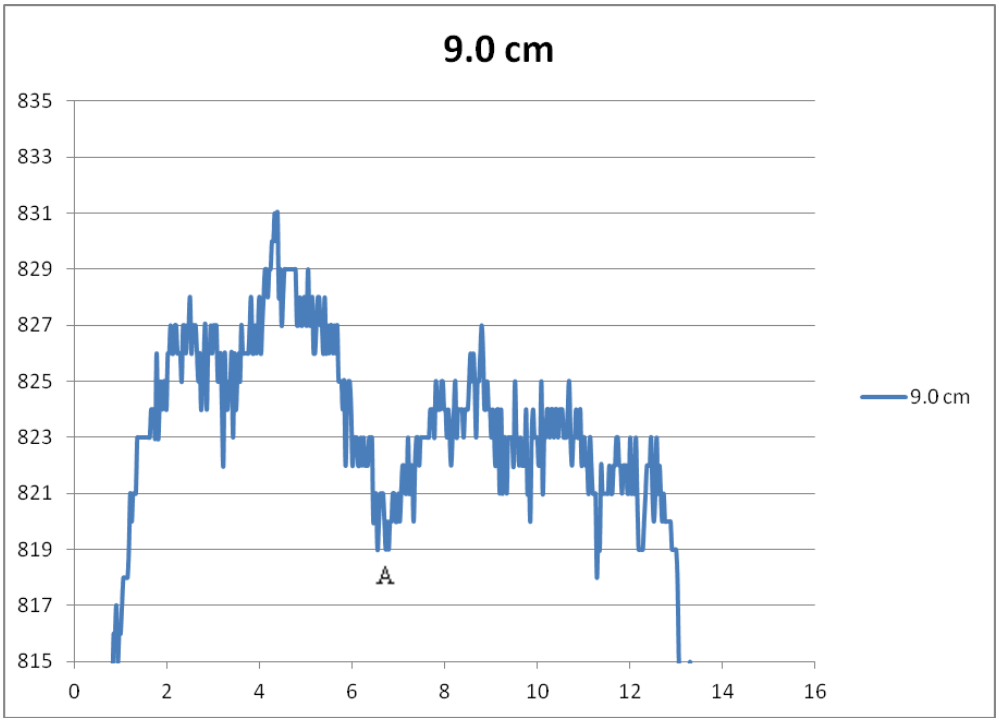

Figure 9.38 ACFM scan at position: 9 cm from the non-flange end of the HSR2 railway wheel tread.

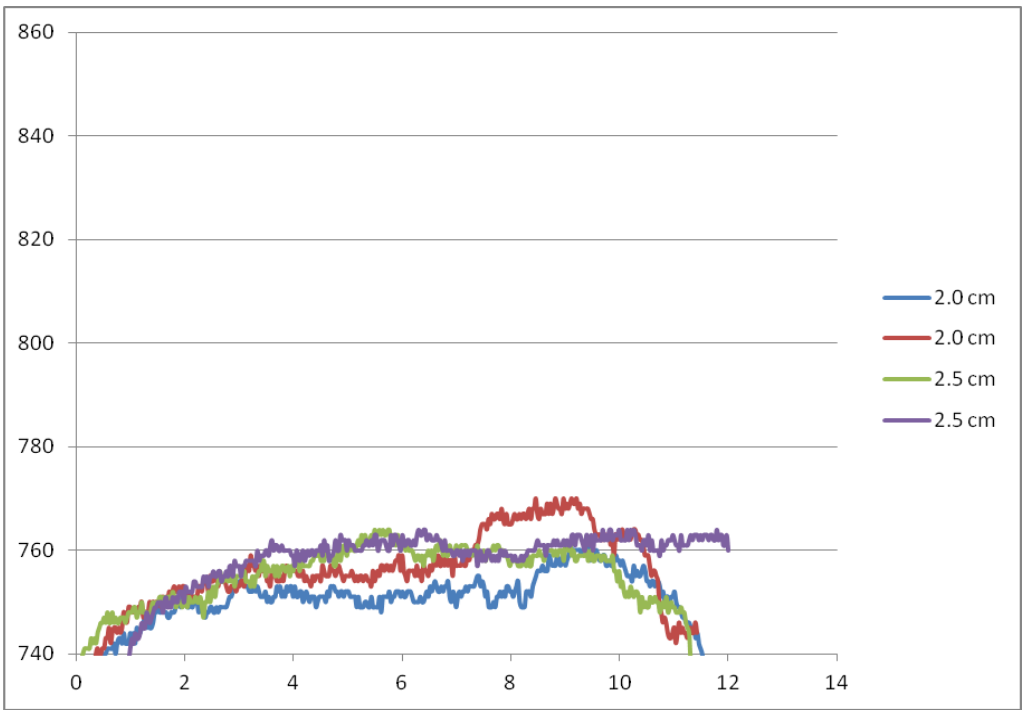

Figure 9.39 ACFM scans at positions: 2 and 2.5 cm from the non-flange end of the HSR2 railway wheel tread showing the variation in the background sensor signal at these tread positions.

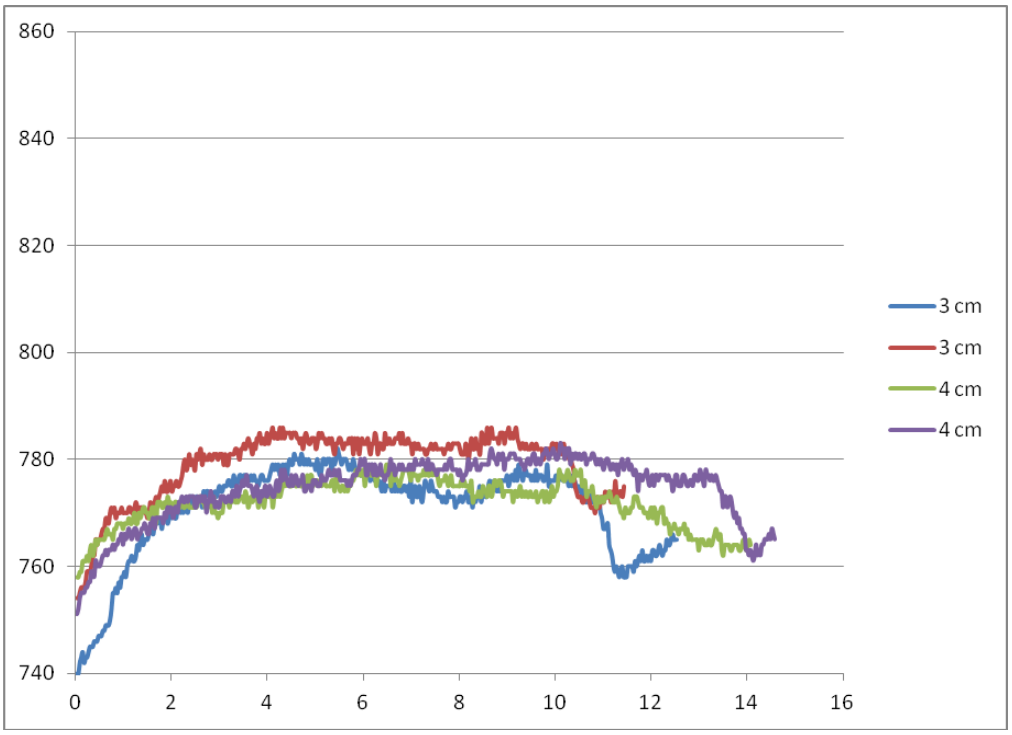

Figure 9.40 ACFM scans at positions: 3 and 4 cm from the non-flange end of the HSR2 railway wheel tread showing the variation in the background sensor signal at these tread positions.

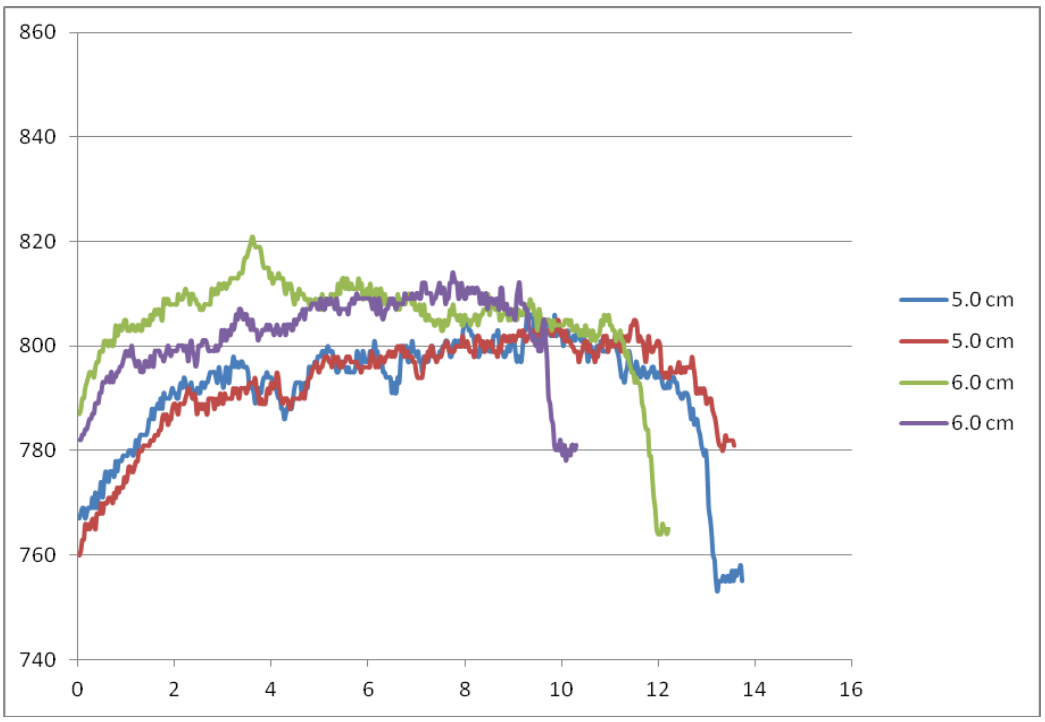

Figure 9.41 ACFM scans at positions: 5 and 6 cm from the non-flange end of the HSR2 railway wheel tread showing the variation in the background sensor signal at these tread positions.

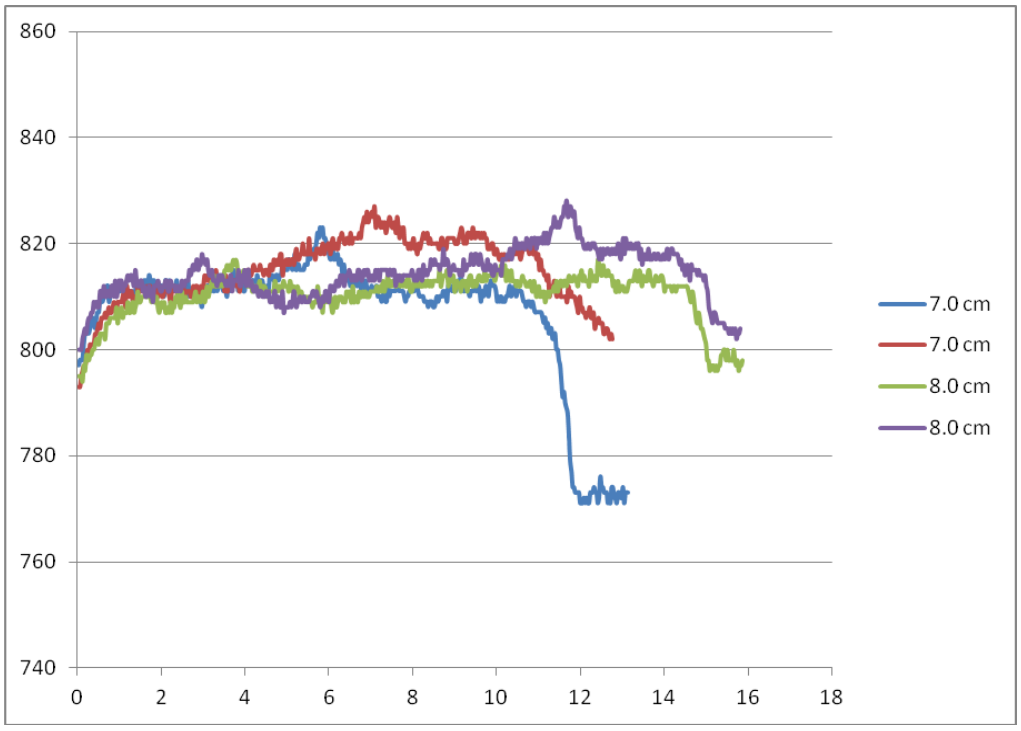

Figure 9.42 ACFM scans at positions: 7 and 8 cm from the non-flange end of the HSR2 railway wheel tread showing the variation in the background sensor signal at these tread positions.

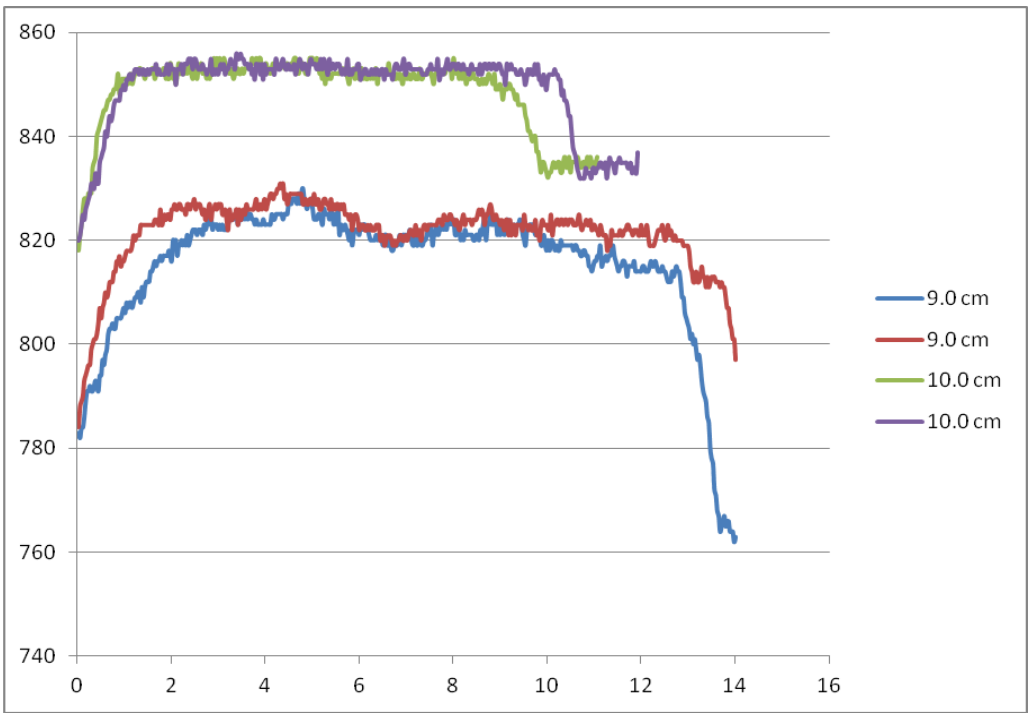

Figure 9.43 ACFM scans at positions: 9 and 10 cm from the non-flange end of the HSR2 railway wheel tread showing the variation in the background sensor signal at these tread positions.

9.5 APPENDIX E: HSR3 RAILWAY WHEEL ACFM SCANS

Note: all horizontal and vertical axes on all plots shown in this appendix are Time (seconds) and B_x Values (arbitrary units), respectively.

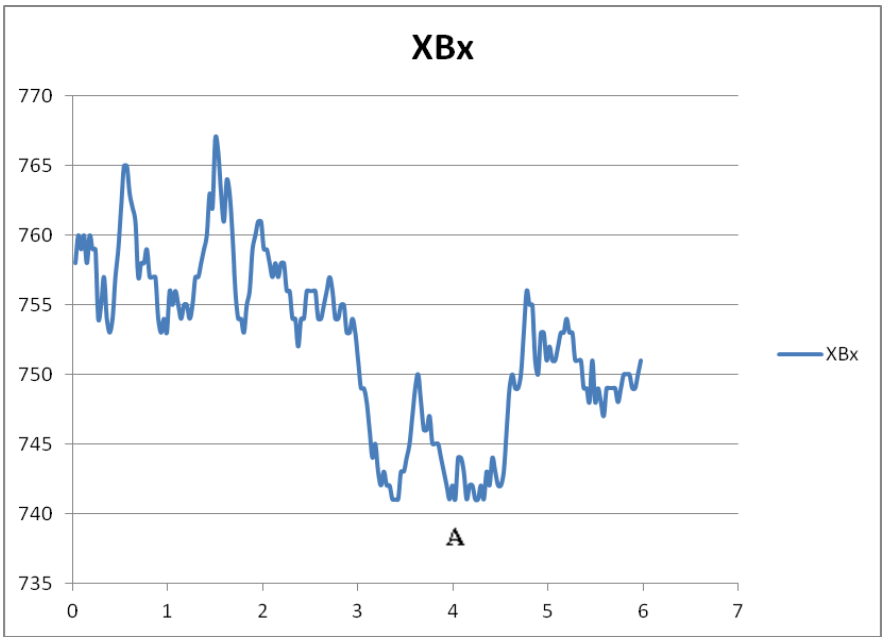

Figure 9.44 ACFM scan at position: 2.5 cm from the non-flange end of the HSR3 railway wheel tread.

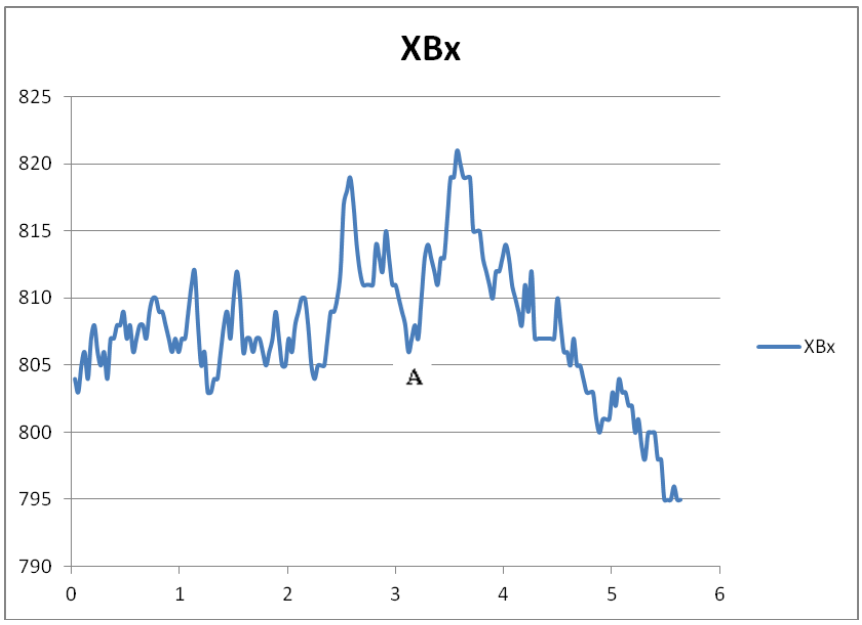

Figure 9.45 ACFM scan at position: 6 cm from the non-flange end of the HSR3 railway wheel tread.

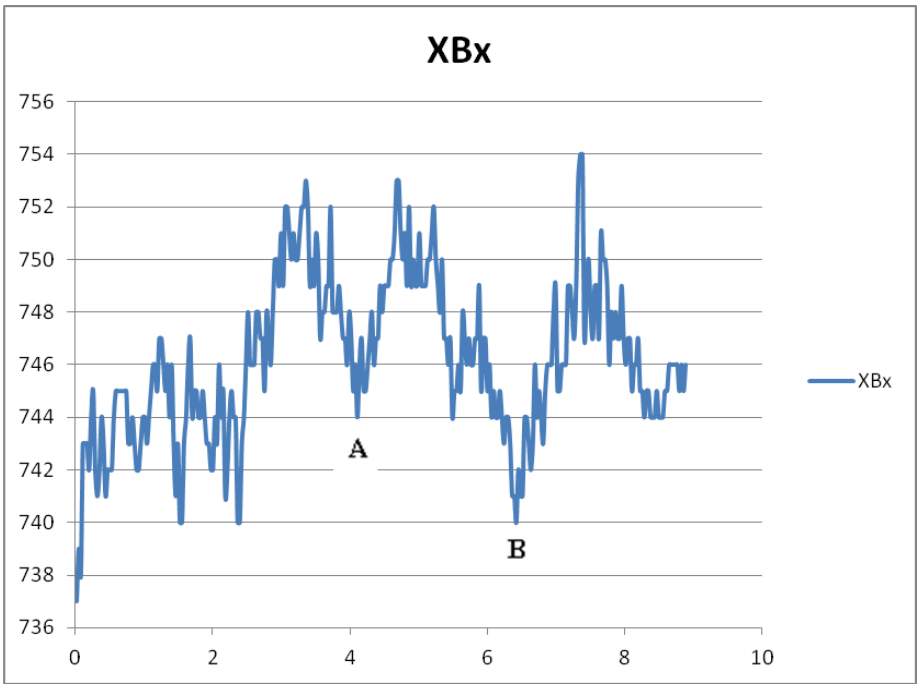

Figure 9.46 ACFM scan at position: 3 cm from the non-flange end of the HSR3 railway wheel tread.

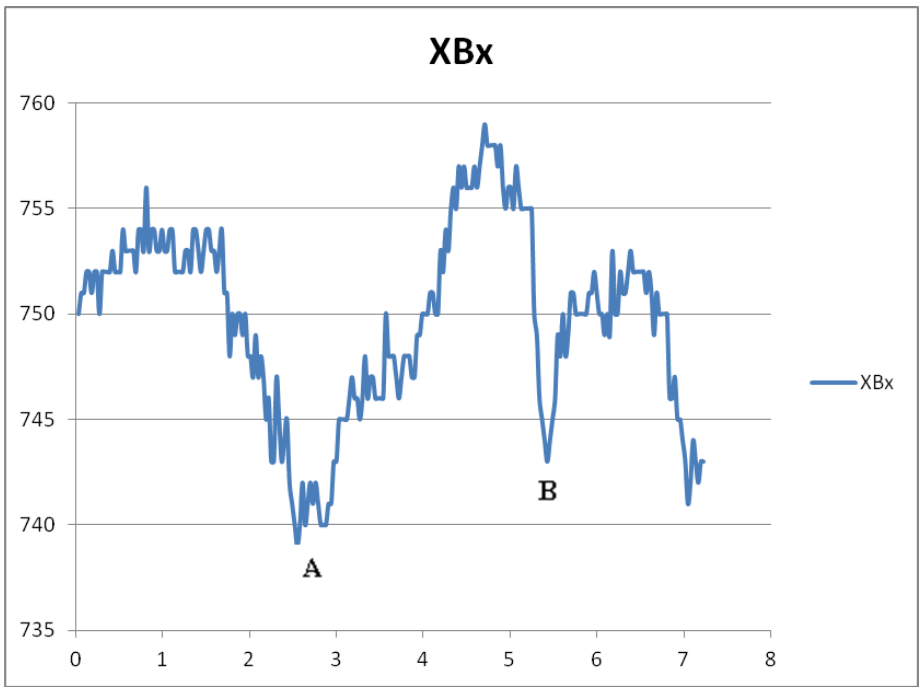

Figure 9.47 ACFM scan at position: 2.5 cm from the non-flange end of the HSR3 railway wheel tread.

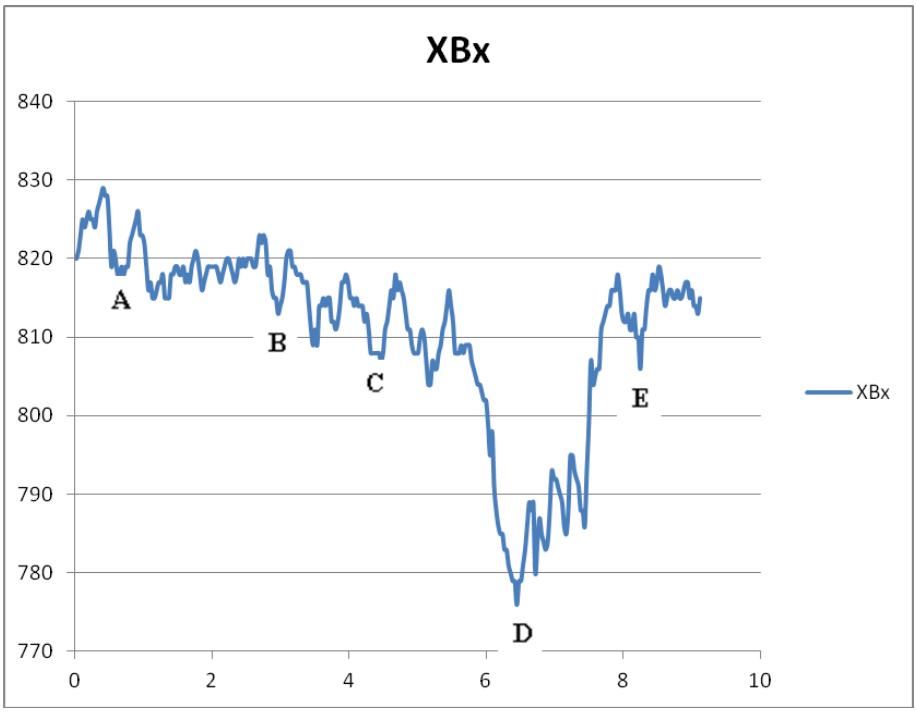

Figure 9.48 ACFM scan at position: 8 cm from the non-flange end of the HSR3 railway wheel tread.

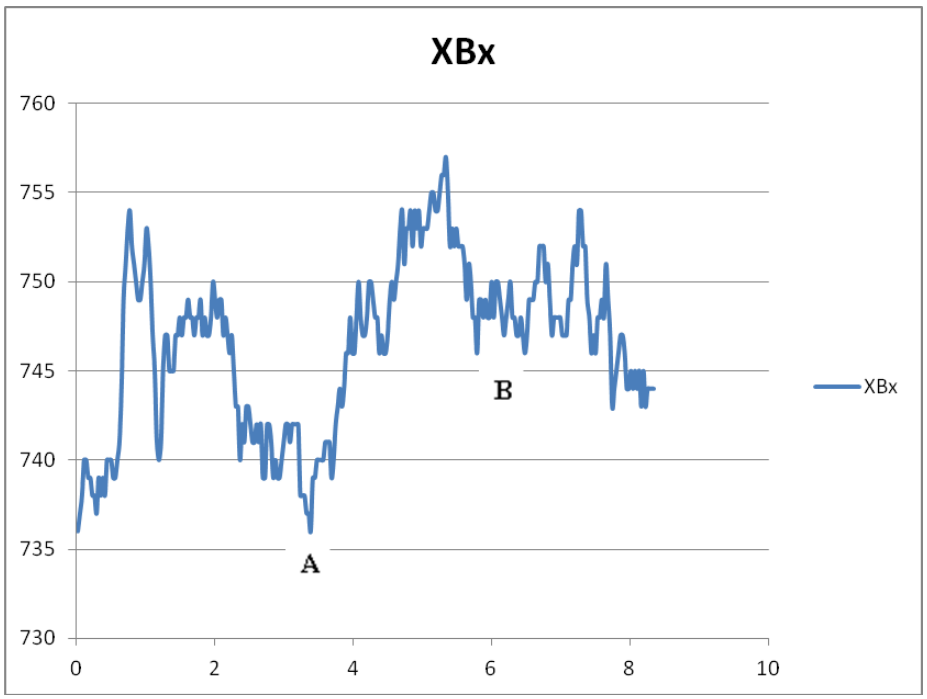

Figure 9.49 ACFM scan at position: 2.5 cm from the non-flange end of the HSR3 railway wheel tread.

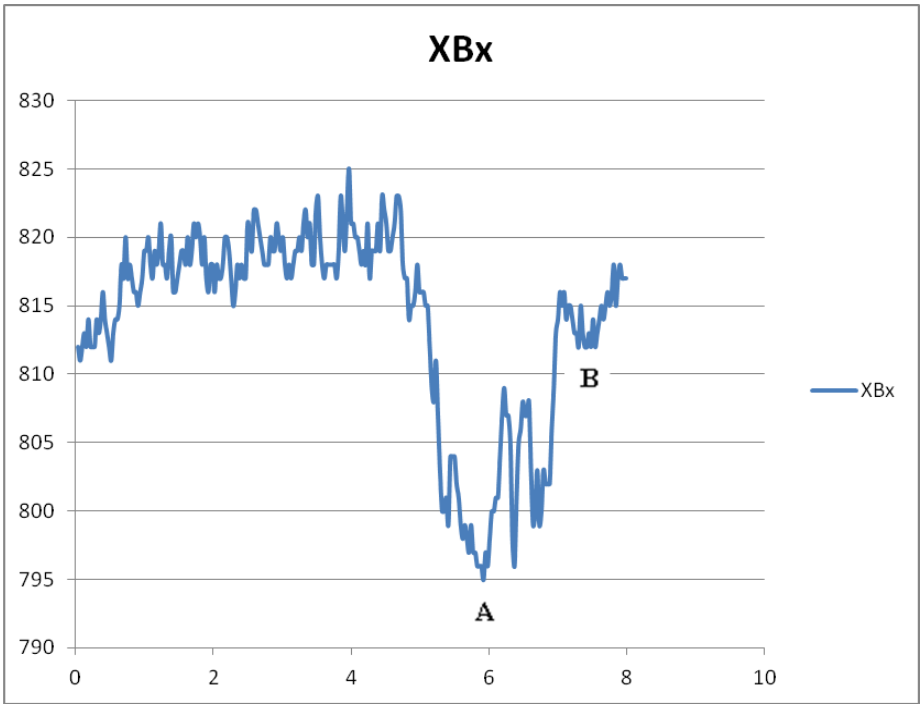

Figure 9.50 ACFM scan at position: 8 cm from the non-flange end of the HSR3 railway wheel tread.

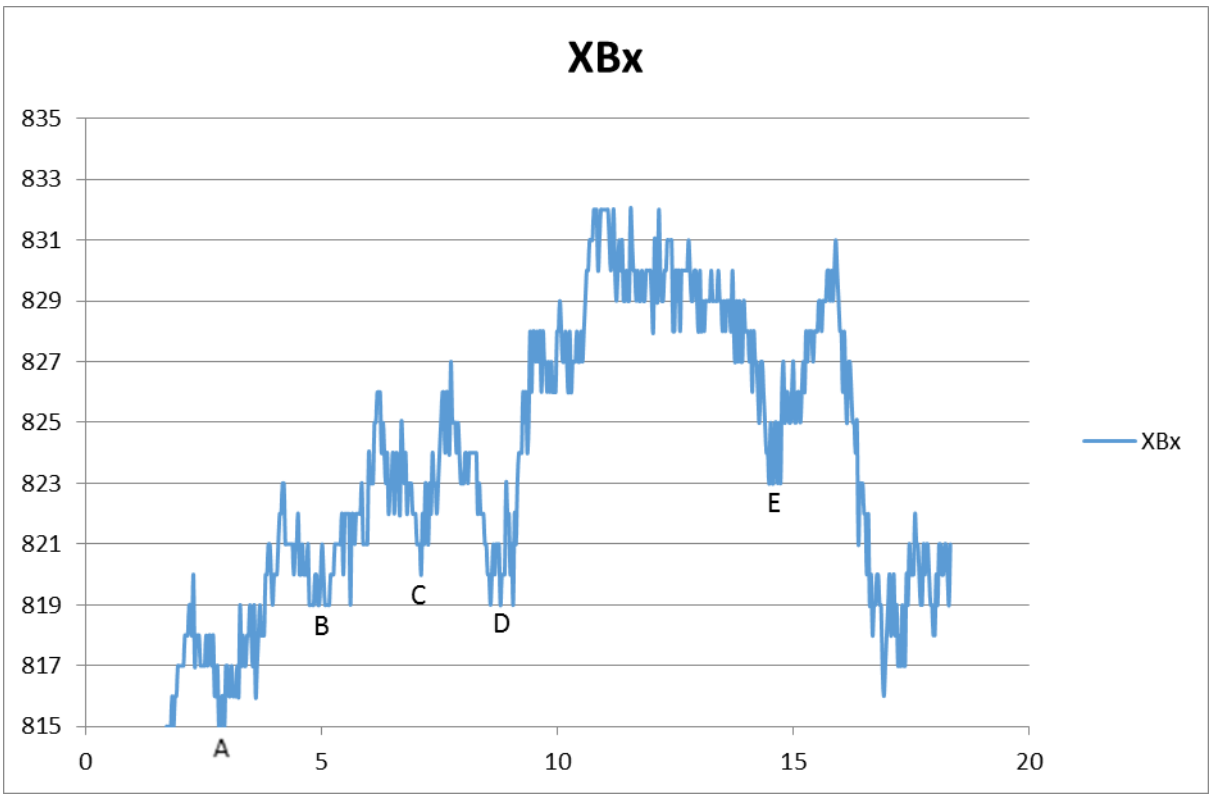

Figure 9.51 ACFM scan at position: 9 cm from the non-flange end of the HSR3 railway wheel tread.

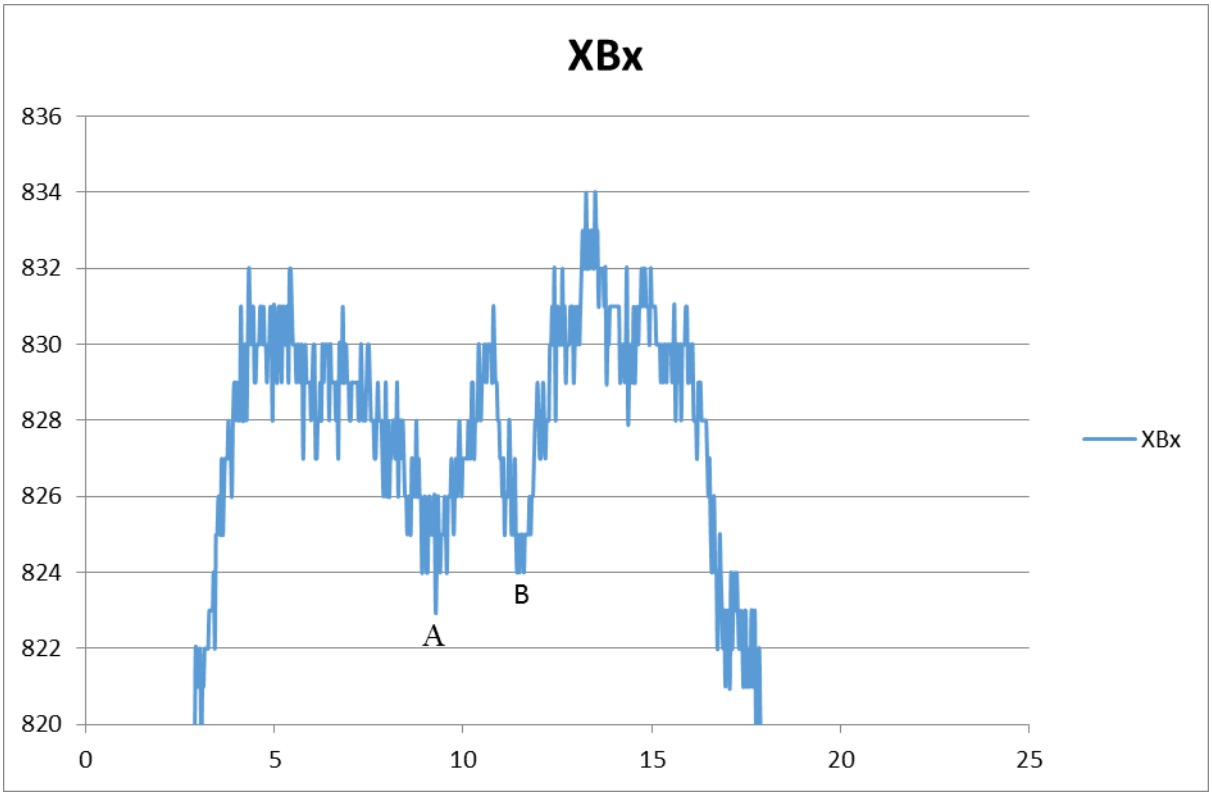

Figure 9.52 ACFM scan at position: 9 cm from the non-flange end of the HSR3 railway wheel tread.

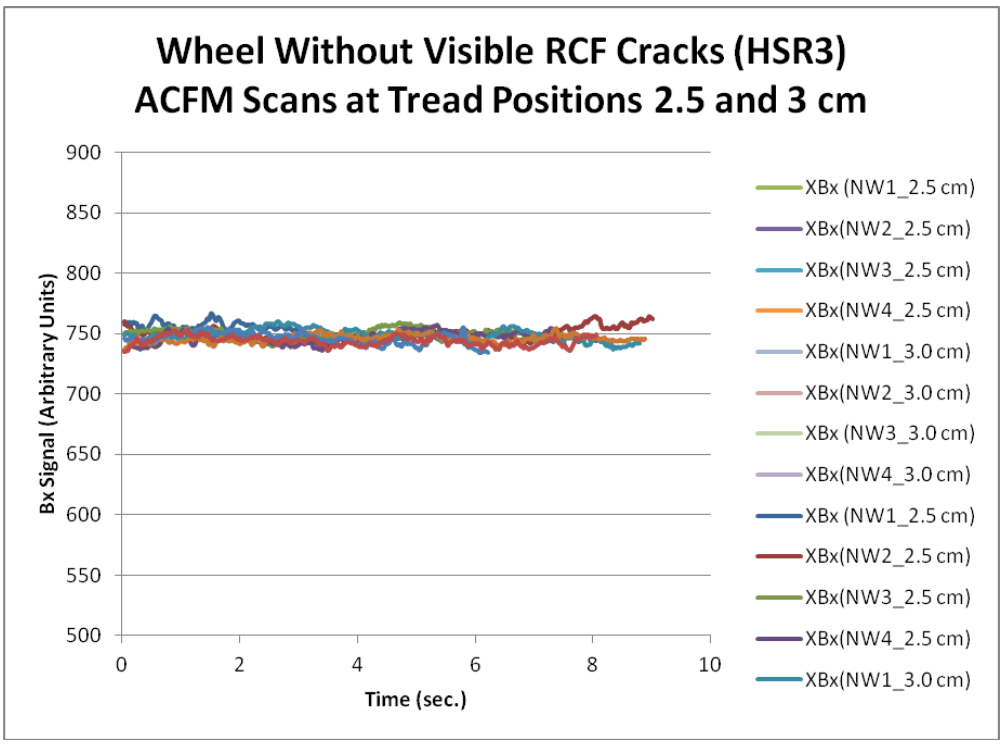

Figure 9.53 ACFM scans at positions: 2.5 and 3 cm from the non-flange end of the HSR3 railway wheel tread showing the variation in the background sensor signal at these tread positions.

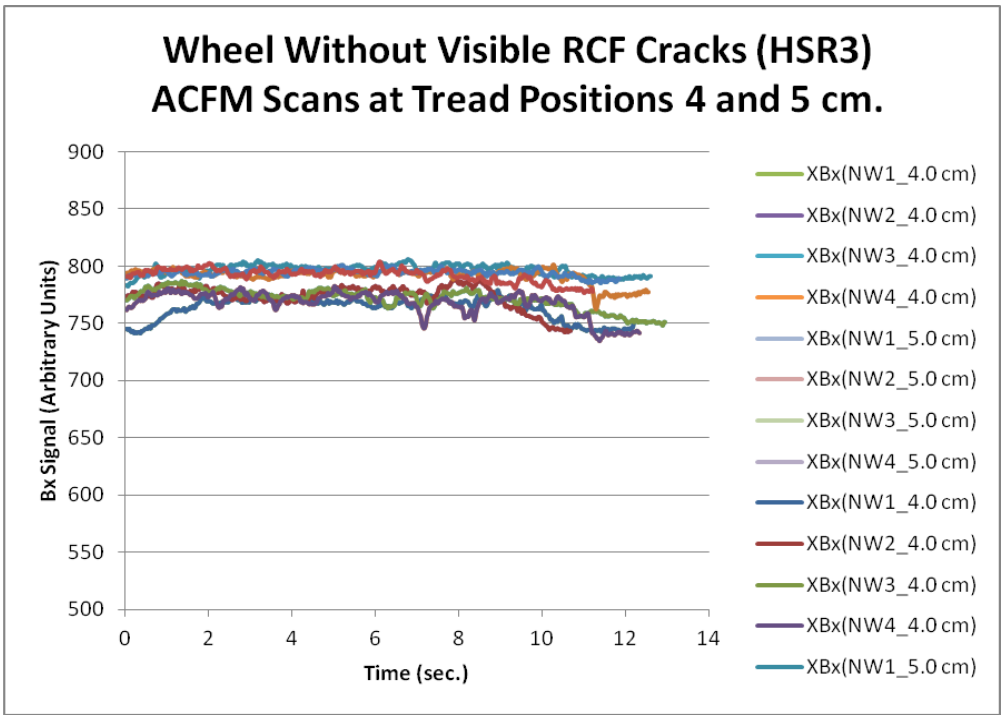

Figure 9.54 ACFM scans at positions: 4 and 5 cm from the non-flange end of the HSR3 railway wheel tread showing the variation in the background sensor signal at these tread positions.

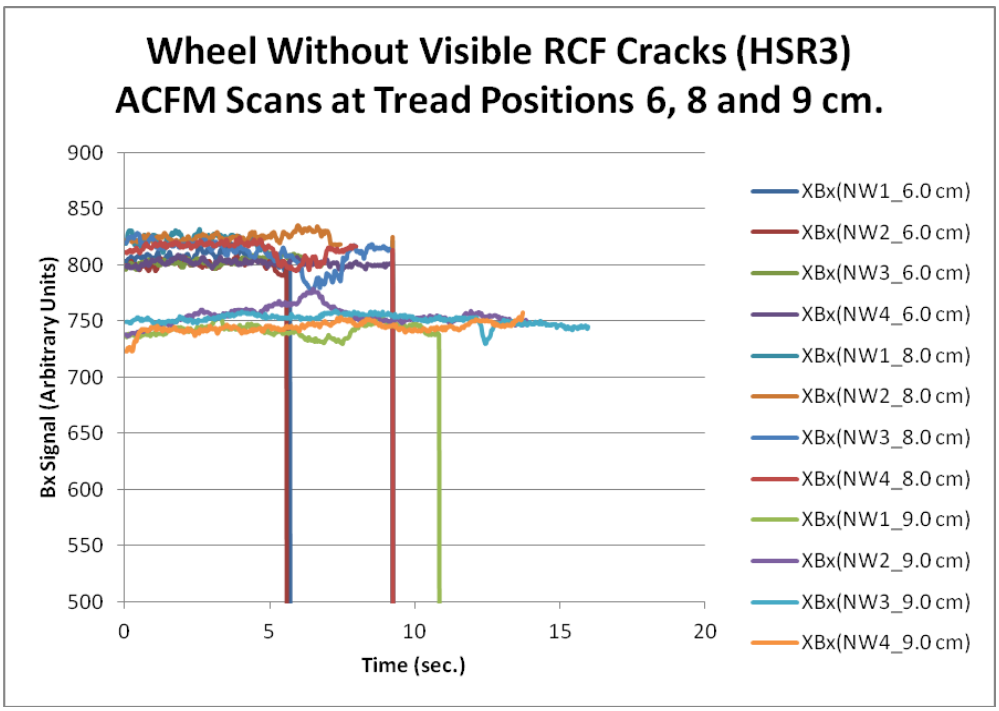

Figure 9.55 ACFM scans at positions: 6, 8 and 9 cm from the non-flange end of the HSR3 railway wheel tread showing the variation in the background sensor signal at these tread positions.

9.6 APPENDIX F: SELECTED ALTERNATING CURRENT FIELD MEASUREMENT (ACFM) RESULTS FOR WORN RAILWAY WHEELS HSR1 AND HSR2

Figure 9.56 Fine cracks found near the flange end and across most of the entire circumferential length of the HSR2 railway wheel at a position of 9.0 cm from the non-flange end.

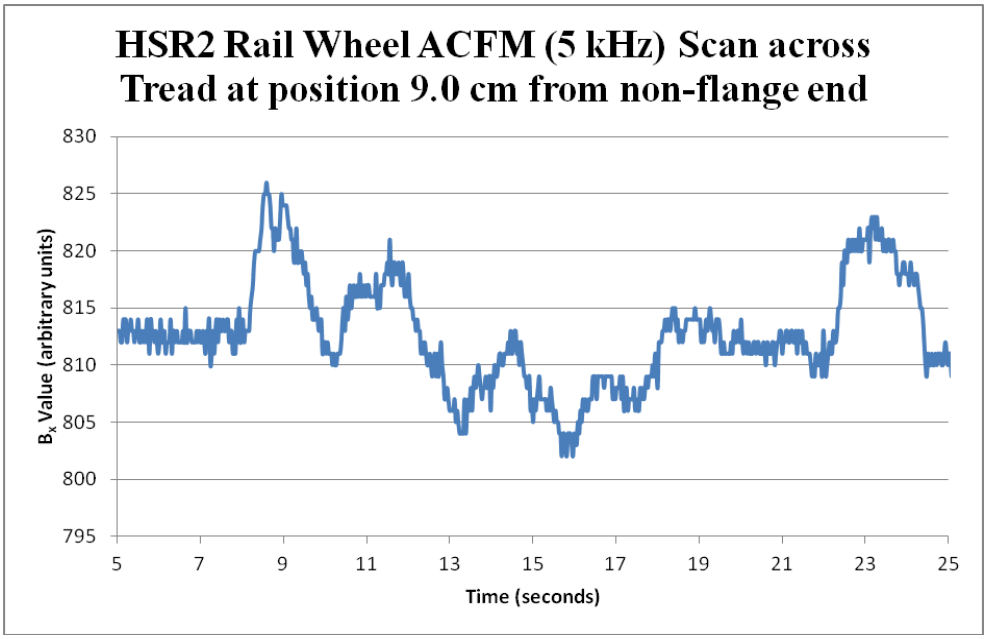

Figure 9.57 HSR2 Rail Wheel ACFM (5 kHz) Scan across the Tread at position 9.0 cm from non-flange end.

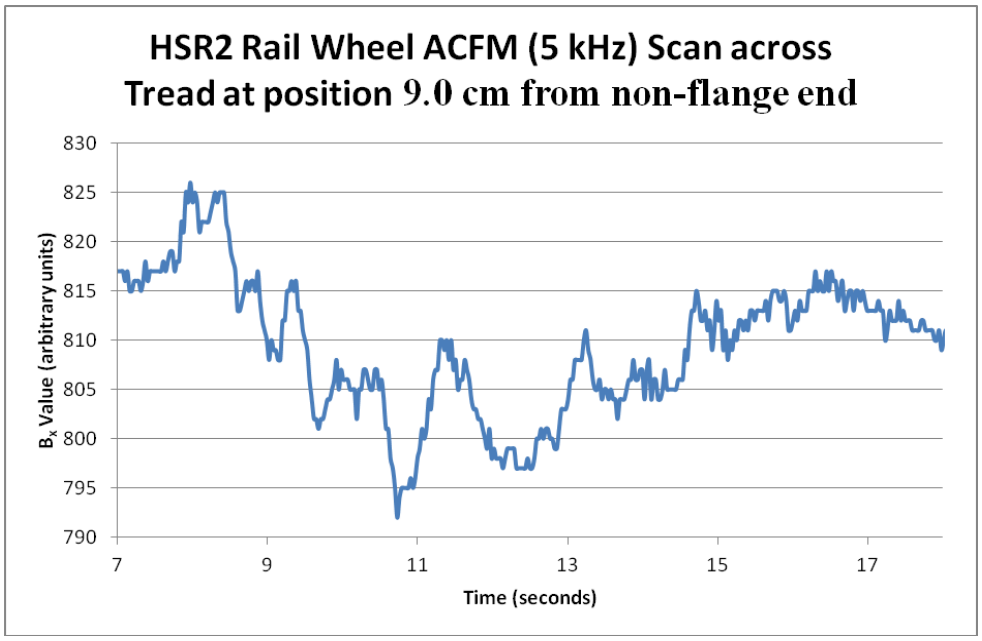

Figure 9.58 HSR2 Rail Wheel ACFM (5 kHz) Scan across the Tread at position 9.0 cm from the non-flange end.

Figure 9.59 shows closely spaced and shallow cracks found near the flange of the HSR2 railway wheel and oriented approx. at 60^0 to the circumference of the wheel tread surface and present across most of the entire circumferential length of the wheel.

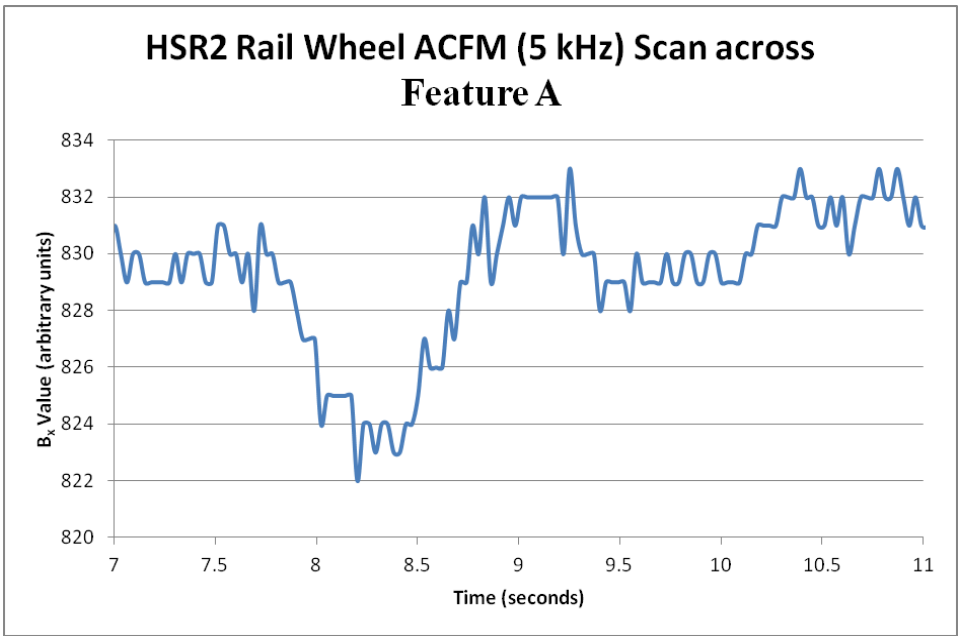

Figure 9.60 HSR2 Rail Wheel ACFM (5 kHz) Scan across Feature shown in A in figure 9.57.

Figure 9.61 shows fine cracks found near the non-flange end of the HSR2 railway wheel and oriented approx. at 90^0 to the circumference of the wheel tread surface and present across most of the entire circumferential length of the wheel at a position of 3 cm from the non-flange end.

Figure 9.62 Feature B on railway wheel HSR2 scanned by ACFM.

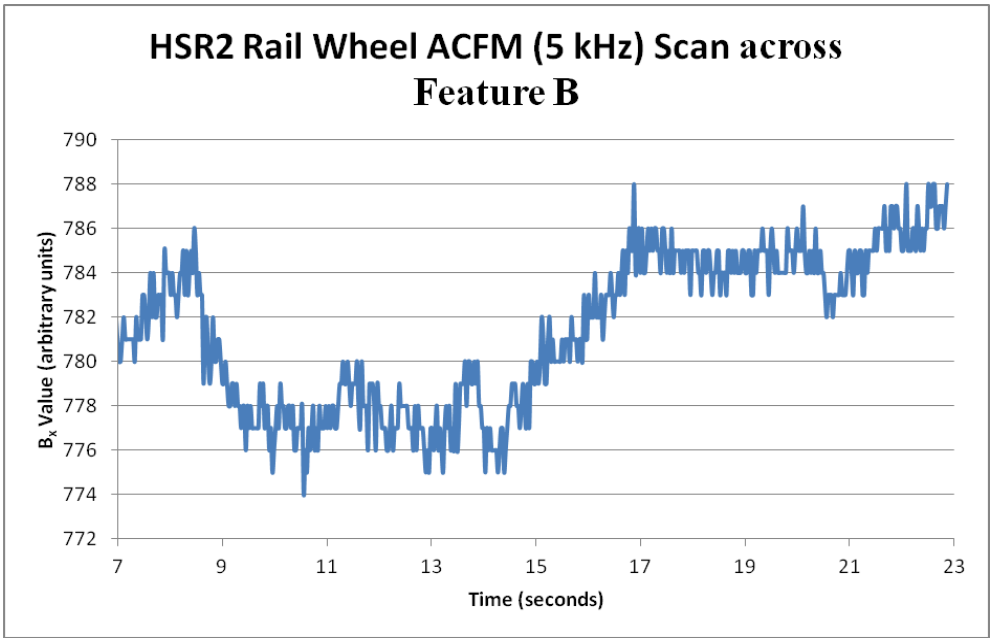

Figure 9.63 HSR2 Rail Wheel ACFM (5 kHz) Scan across Feature B.

Figure 9.64 Feature D found on the tread of railway wheel HSR2 scanned by ACFM.

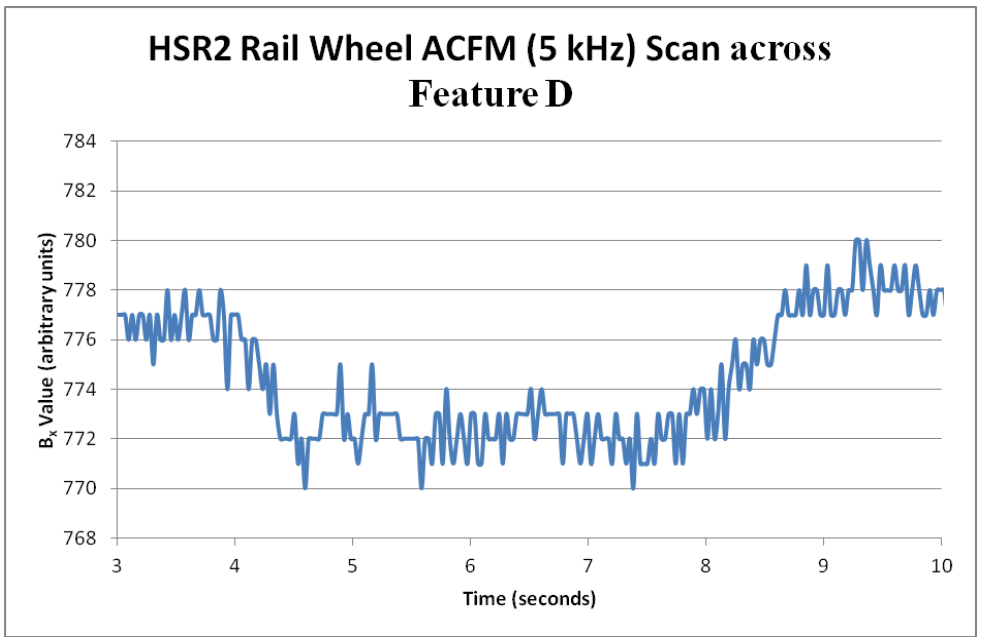

Figure 9.65 HSR2 Railway Wheel ACFM (5 kHz) Scan across Feature D.

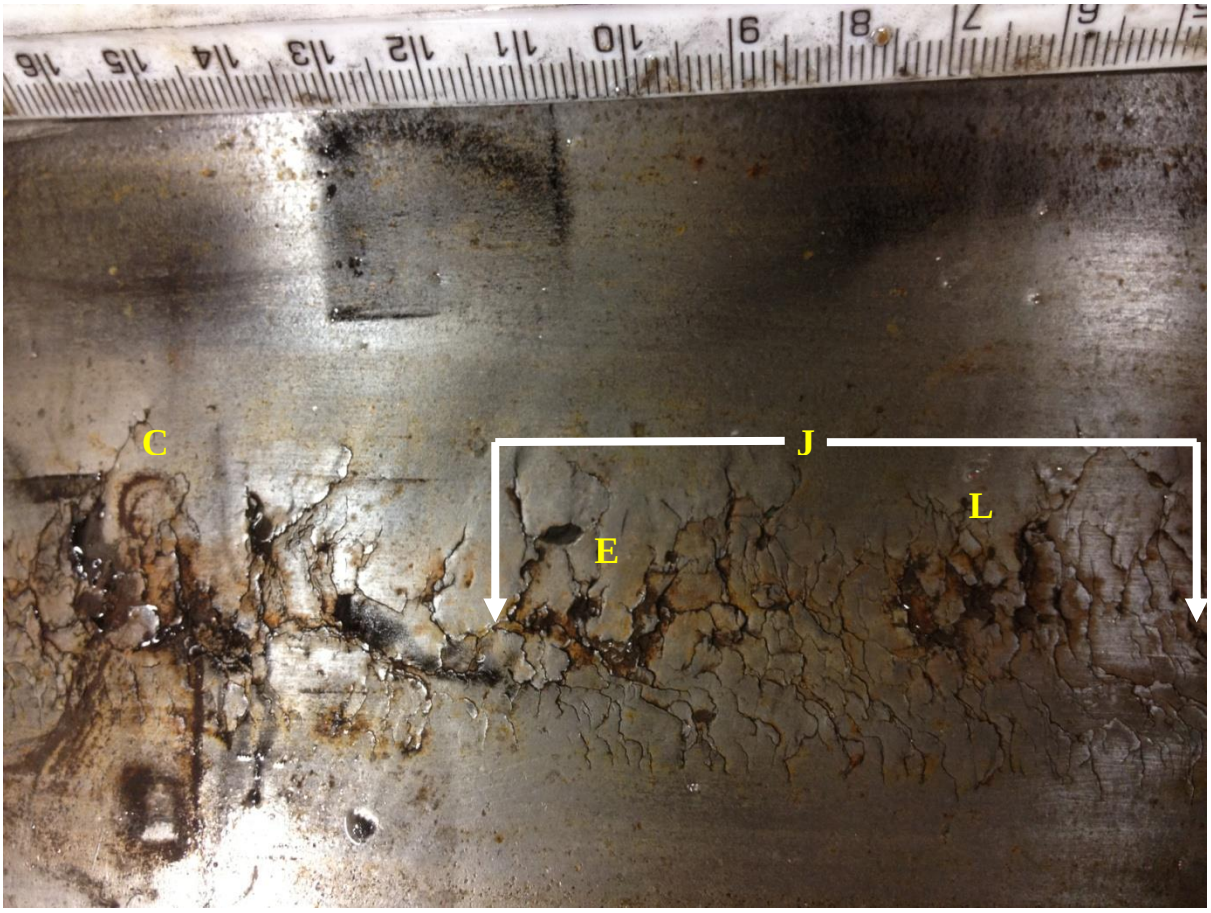

Figure 9.66 shows an image of the RCF prone region on the tread of wheel HSR1 showing the severe level of surface RCF damage that has occurred between 4 and 6 cm from the non-flange end of this wheel. Locations at which the subsequent ACFM scans (shown in the figures 9.65 and 9.66 below) conducted on this wheel tread have been clearly labelled on the photograph. Note that this figure is shown as figure 7.31 in chapter 7 of the PhD thesis above and has been reproduced here to keep it in context as it is part of this report and for the ease of the reader.

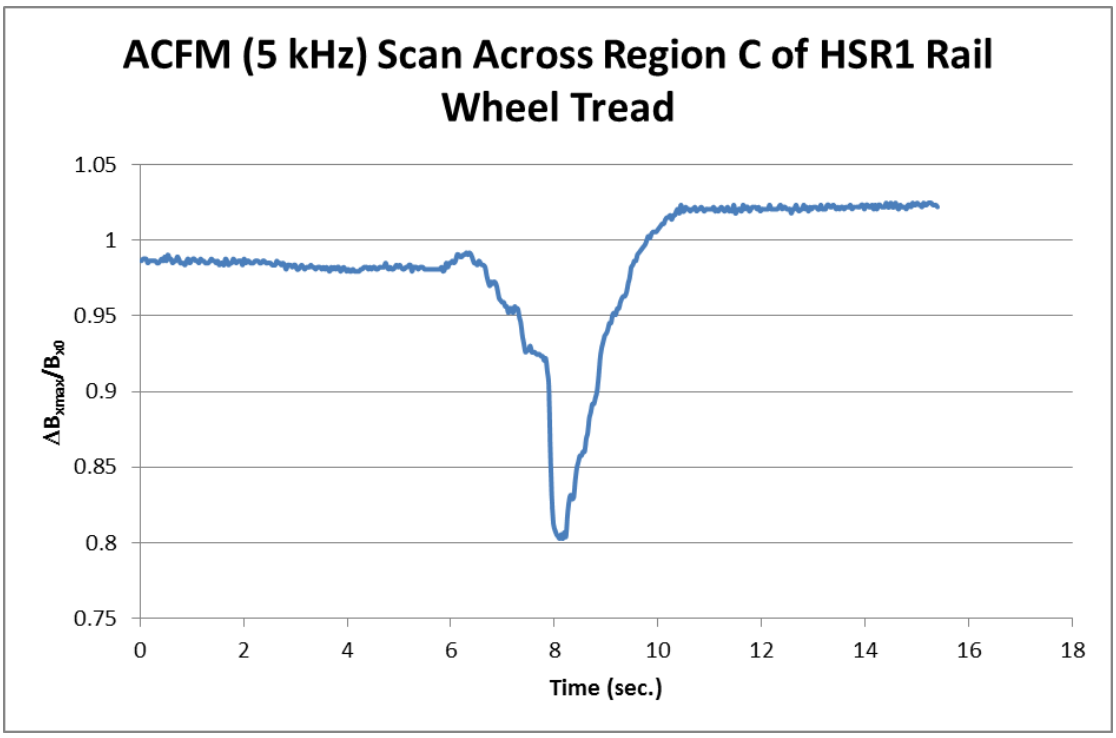

Figure 9.67 HSR1 Railway Wheel ACFM (5 kHz) Scan across Region C. Note that this figure is shown as figure 7.32(a) in chapter 7 of the PhD thesis above and has been reproduced here to keep it in context as it is part of this report and for the ease of the reader.

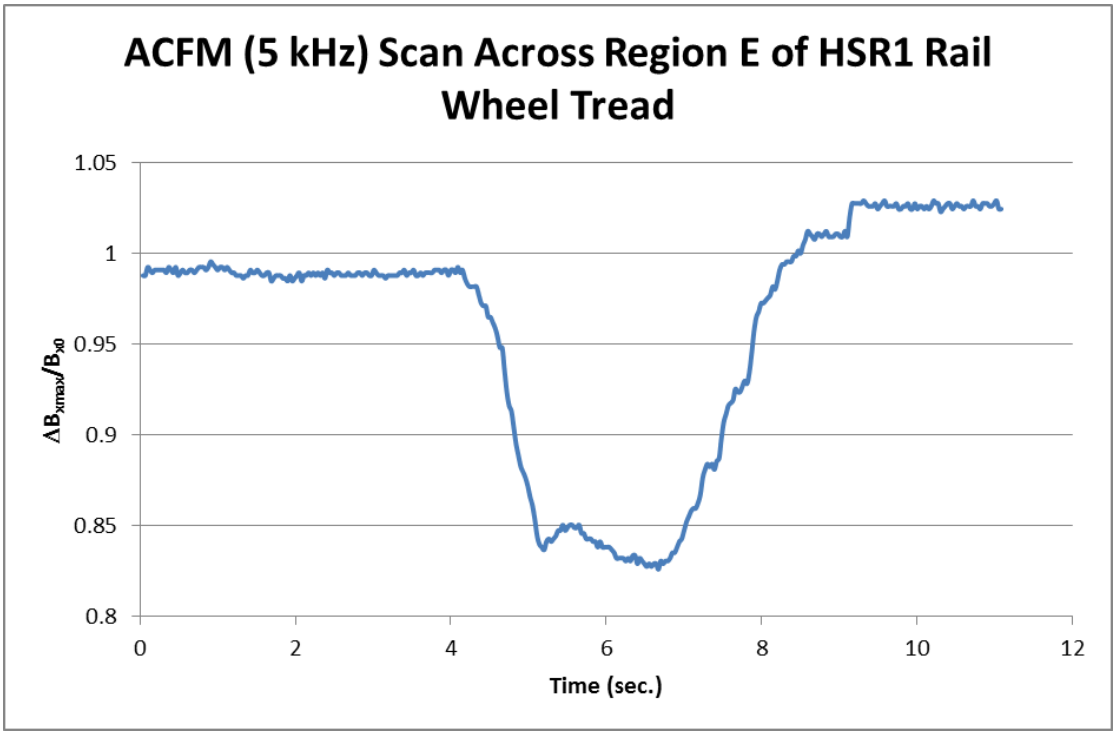

Figure 9.68 HSR1 Rail Wheel ACFM (5 kHz) Scan across Feature E (an 'E' shaped feature at an angle of approximately 45^0 to the circumferential direction of the railway wheel). Note that this figure is shown as figure 7.32(b) in chapter 7 of the PhD thesis above and has been reproduced here to keep it in context as it is part of this report and for the ease of the reader.

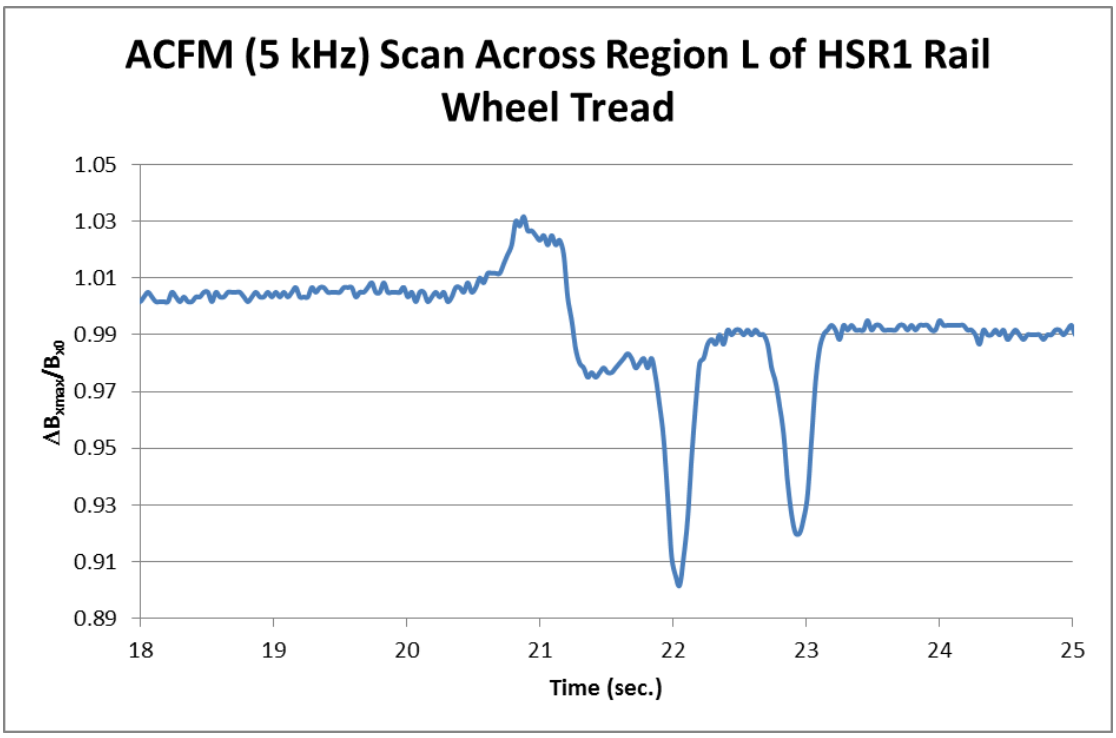

Figure 9.69 HSR1 Rail Wheel ACFM (5 kHz) Scan across Feature L; shows two separate troughs corresponding to adjacent individual cracks. Note that this figure is shown as figure 7.32(c) in chapter 7 of the PhD thesis above and has been reproduced here to keep it in context as it is part of this report and for the ease of the reader.

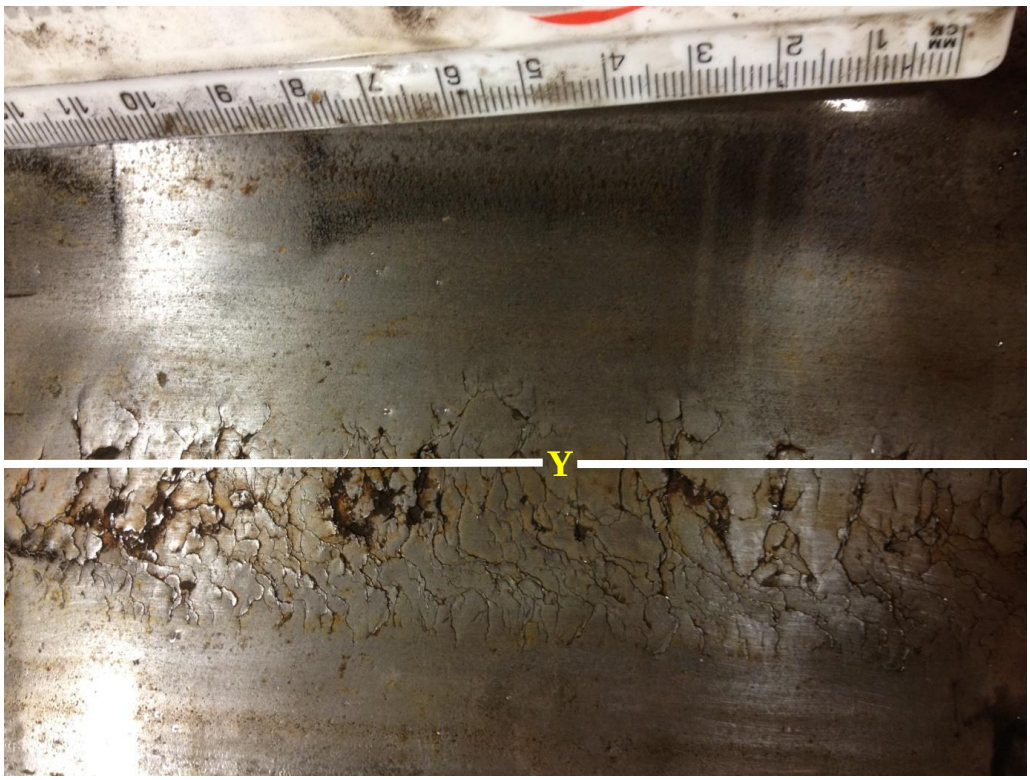

Figure 9.70 shows another image of the RCF prone region on the tread of wheel HSR1 showing the severe level of surface RCF damage that has occurred between 4 and 6 cm from the non-flange end of this wheel. Region Y across which the subsequent ACFM scan (shown in figure 9.69 below) conducted on this wheel tread has been labelled on the photograph.

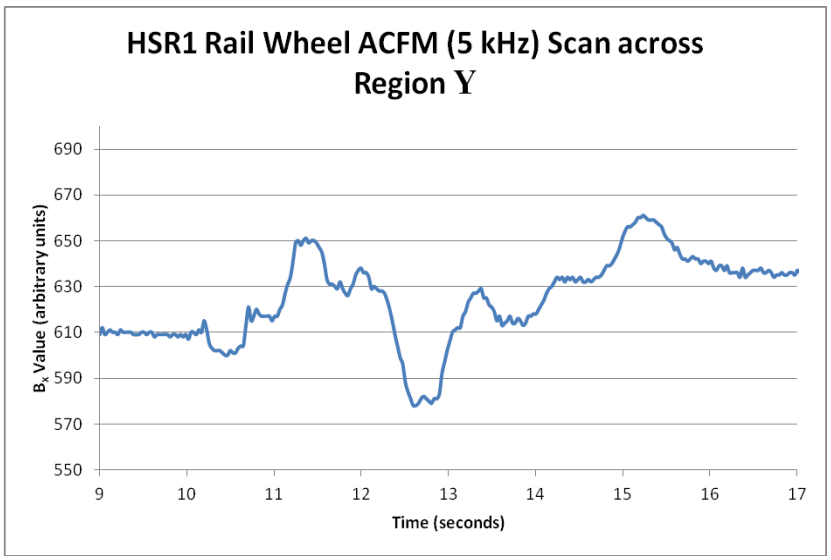

Figure 9.71 HSR1 Rail Wheel ACFM (5 kHz) Scan across Region Y.

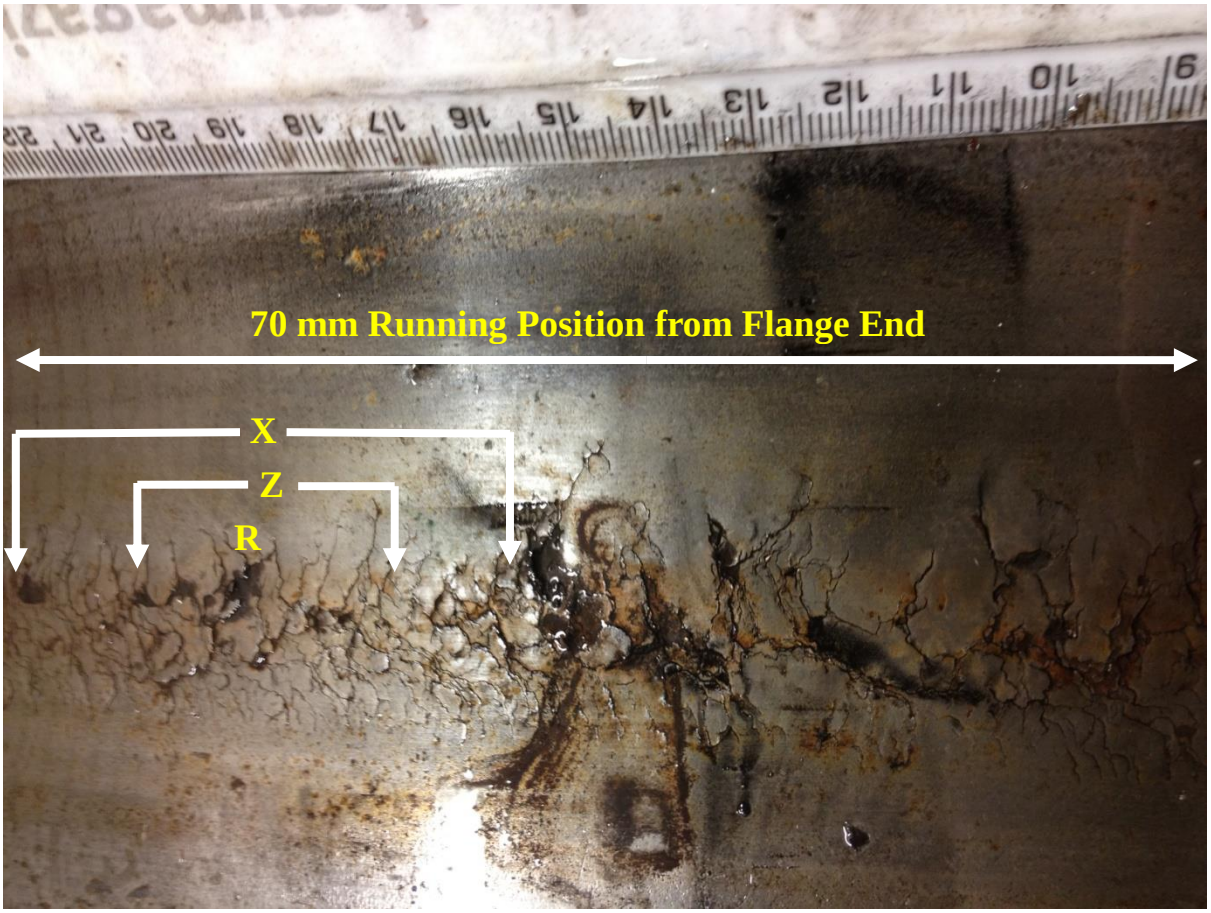

Figure 9.72 shows another image highlighting specific areas of the RCF prone region on the tread of wheel HSR1 showing the severe level of surface RCF damage that has occurred between 4 and 6 cm from the non-flange end of this wheel. Locations at which the subsequent ACFM scans (figures 9.71-9.73 incl. below) conduct+ed on this wheel tread have been clearly labelled on the photograph. Note that this figure is shown as figure 7.33 in chapter 7 of the PhD thesis above and has been reproduced here to keep it in context as it is part of this report and for the ease of the reader.

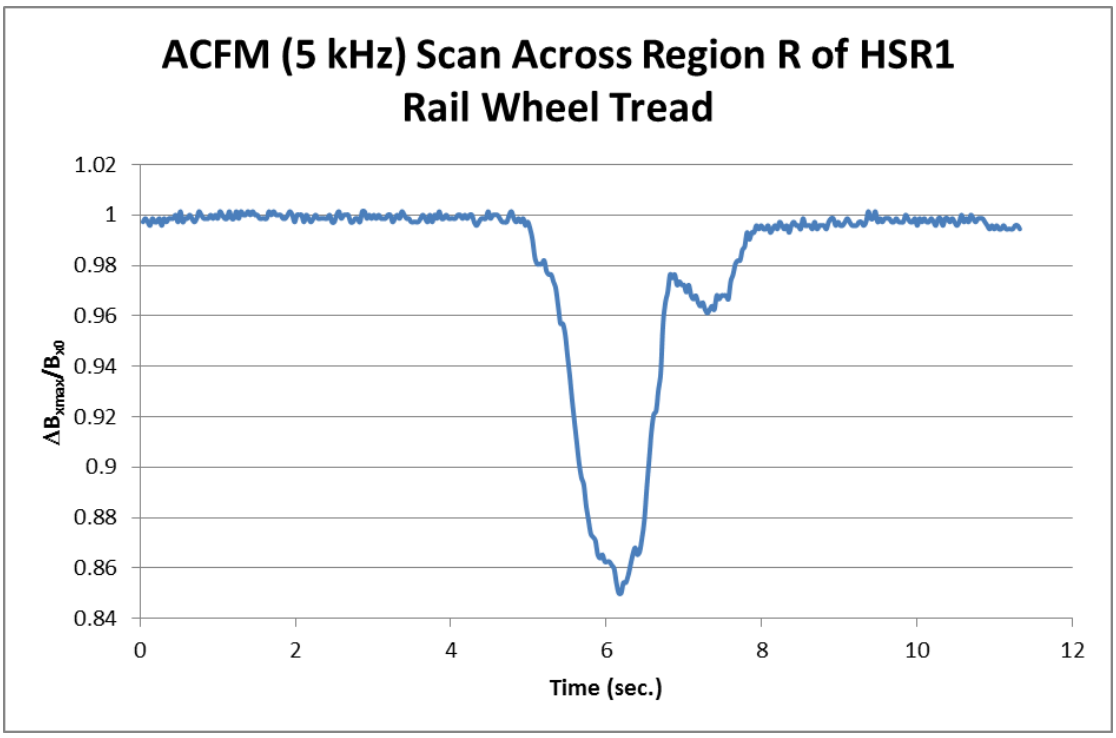

Figure 9.73 ACFM (5 kHz) scan across feature R in the downward direction, showing a large primary and an adjacent smaller subsidiary trough, corresponding to clusters of large and small cracks, respectively. Note that this figure is shown as figure 7.34(a) in chapter 7 of the PhD thesis above and has been reproduced here to keep it in context as it is part of this report and for the ease of the reader.

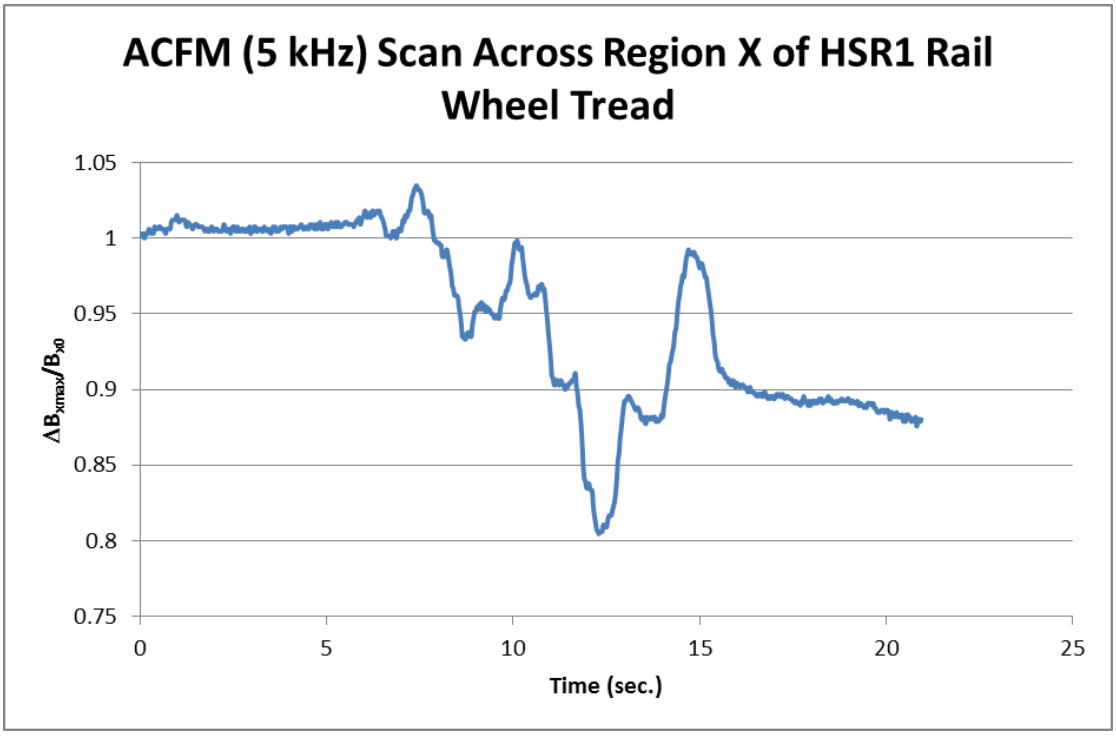

Figure 9.74 HSR1 railway wheel ACFM (5 kHz) scan across region X. Note that this figure is shown as figure 7.34(b) in chapter 7 of the PhD thesis above and has been reproduced here to keep it in context as it is part of this report and for the ease of the reader.

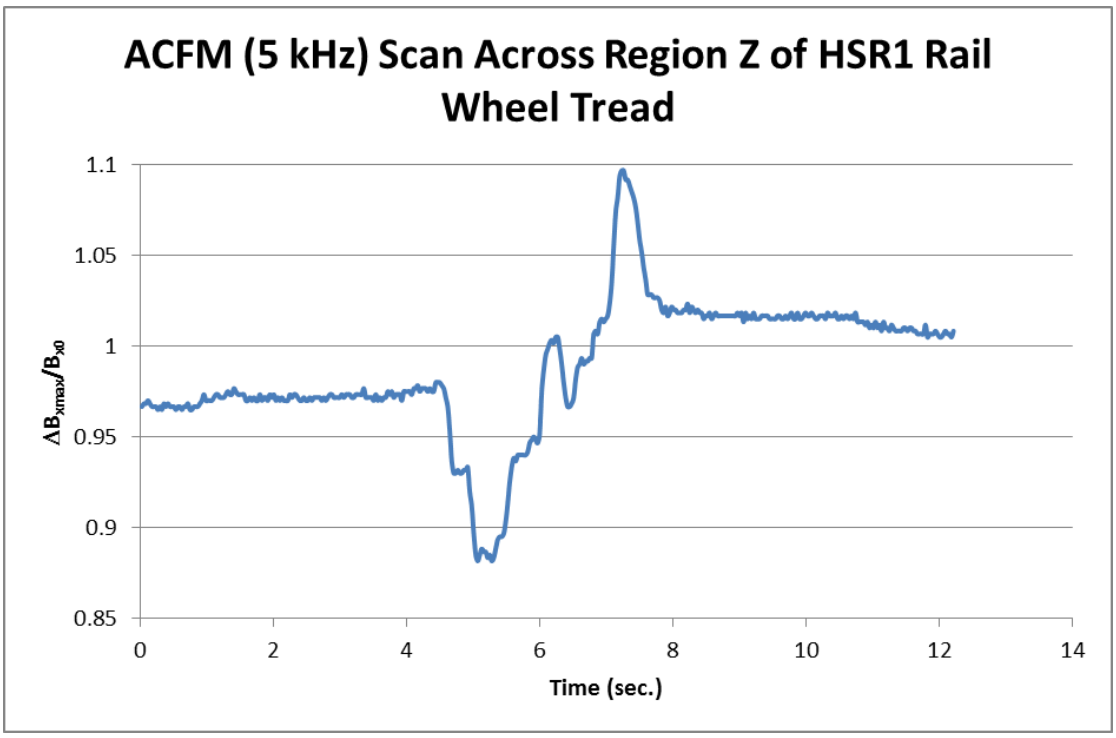

Figure 9.75 HSR1 railway wheel ACFM (5 kHz) scan across region Z. Note that this figure is shown as figure 7.34(c) in chapter 7 of the PhD thesis above and has been reproduced here to keep it in context as it is part of this report and for the ease of the reader.

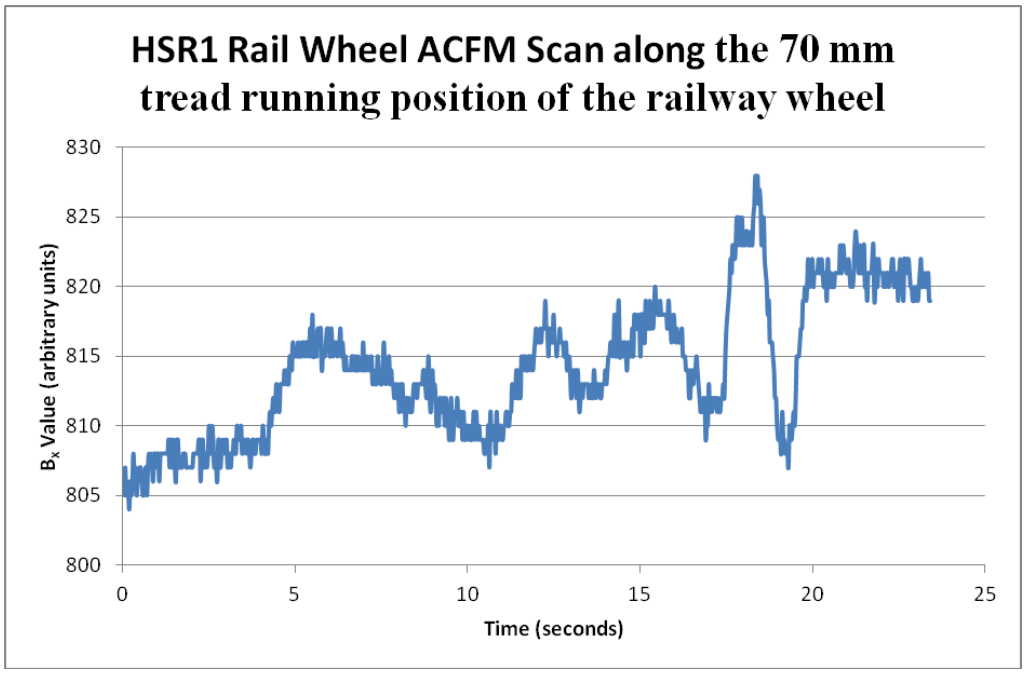

Figure 9.76 HSR1 rail wheel ACFM (5 kHz) scan along the 70 mm tread running position of the railway wheel.

REFERENCES

1. Allstrom, J., Karlsson, B., Modified Railway Wheel Steels: Production and Evaluation of Mechanical Properties with Emphasis on Low-Cycle Fatigue Behaviou, Metallurgical and Materials Transactions A, Vol. 40A, July 2009, pp. 1557-1567.
2. Lunde´n, R., Wear, 1991, Vol. 144, pp. 57–70.
3. Ahlstrom, J., Karlsson, B., Wear, 1999, Vol. 232 (1), pp. 1–14.
4. Ahlstrom, J., Karlsson, B., Wear, 1999, Vol. 232 (1), pp. 15–24.
5. Ahlstrom, J., Karlsson, B., Fatigue ‘99, Beijing, China, 1999, pp. 2609–2614.
6. Nicholson, G.L., Kostryzhev, A.G., Hao, X.J, Davis, C.L., Modelling and Experimental Measurements of Idealised and Light-Moderate RCF Cracks in Rails Using an ACFM Sensor, NDT&E International (2011), 44, pp. 427-437, doi: 10.1016/j.ndteint.2011.04.003.
7. Rowshandel, H., Nicholson, G.L., Roberts, C., Davis, C.L., A Robotic Approach for NDT of RCF Cracks in Rails Using an ACFM Sensor, Birmingham Centre for Railway Research and Education, University of Birmingham, Insight 2011; 53: pp. 368-371.
8. Liu, Y., et al., International Journal of Fatigue, 28 (2006), pp. 747–756.
9. AAR (Association of American Railroads), Manual of Standards and Recommended Practices: Section G-Wheels and Axles, Issue of 1998.
10. Tourney, H.M., Mulder, J.M., The Transition from The Wear to The Stress Regime, Wear 1996; 191: pp. 107-112.
11. Johnson, K.L., The Strength of Surfaces in Rolling Contact, Proc. Inst. Mech. Eng., 1989; 203: pp. 151-163.
12. Stone, D.H., Moyar, G.J., Wheel Shelling and Spalling – An Interpretive Review. In: Rail Transportation 1989, ASME; 1989, pp. 19-31.
13. Marais, J.J., Wheel Failures on Heavy Haul Freight Wheels Due to Subsurface Effects, Proceedings of 12th International Wheelset Congress, Qingdao, China; 1998, pp. 306-314.
14. Mutton, P.J., Epp, C.J., Dudek, J., Rolling Contact Fatigue in Railway Wheels Under Axle Loads, Wear 1991; 144, pp. 139-152.
15. Ekberg, A., Marais, J., Effects of Imperfections on Fatigue Initiation in Railway Wheels, IMechE J. Rail Rapid Trans., 1999; 214, pp. 45-54.

16. Gordon, J, Perlman, A.B., Estimation of Residual Stresses in Railroad Commuter Car Wheels Following Manufacture, Proceedings of The International Mechanical Engineering Congress and Exhibition in Anaheim, CA, ASME RTD, Vol. 15; 1998.
17. Snyder, T., Personal Meeting; November 2003.
18. Moyar, G.J., Stone, D.H., An Analysis of The Thermal Contributions to Railway Wheel Shelling, Wear 1991; 144: pp. 117–138.
19. Gimenez, J.G., Sobejano, H., Theoretical Approach to The Crack Growth and Fracture of Wheels, 11th International Wheelset Congress, Paris; 1995, pp. 15–20.
20. Marais, J.J., Pistorius, P.G.H., Terminal Fatigue of Tires on Urban Transport Service, 4th International Conference of Contact Mechanics and Wear of Rail/Wheel Systems (Preliminary Proceedings), Vancouver; 1994.
21. Stone, D.H., Majumder, G., Bowaj, V.S., Shattered Rim Wheel Defects and The Effect of Lateral Loads and Brake Heating on Their Growth, ASME International Mechanical Engineering Congress & Exposition, New Orleans, Louisiana; 1–4 November 2002.
22. Giammarise, A.W., Gilmore, R.S., Wheel Quality, A North American Locomotive Builder's Perspective, GE Research & Development Centre, CRD140; Sep. 2001.
23. Berge, S., Shattered Rim Fracture Research. Proceedings of 2000 Brenco Rail Conference, LaQuinta, California; October 19–20, 2000.
24. Stone, D.H., Geoffrey, E.D., The Effect of Discontinuity Size on The Initiation of Shattered Rim Defects, ASME Transportation Division, Vol. 19. New York: ASME; 2000. pp. 7–14.
25. Ekberg, A., Kabo, E., Andersson, H., An Engineering Model for Prediction of Rolling Contact Fatigue of Railway Wheels, Fatigue Fract. Eng. Mater. Struct. 2002, 25, pp. 899–909.
26. Papadopoulos, I.V., Davoli, P., Gorla, C., Filippini, M., Bernasconi, A., A Comparative Study of Multiaxial High-Cycle Fatigue Criteria for Metals, Int. J. Fatigue 1997; 19(3): pp. 219–235.
27. Johnson, K.L., Contact Mechanics, Cambridge, Cambridge University Press; 1985.

28. Guo, Y.B., Barkey, M.E., Modelling of Rolling Contact Fatigue for Hard Machined Components with Process-induced Residual Stress, Int. J. Fatigue 2004; 26(6): pp. 605–613.
29. Fatemi, A., Socie, D.F., A Critical Plane Approach to Multiaxial Fatigue Damage Including Out-of-Phase Loading, Fatigue Fract. Eng. Mater. Struct. 1988, 11, pp. 149–165.
30. Sraml, M., Flasker, J., Potrcˇ, I., Numerical Procedure for Predicting The Rolling Contact Fatigue Crack Initiation. Int. J. Fatigue 2003; 25(7), pp. 585–95.
31. Ahlstrom, J., Karlsson, B., Modified Railway Wheel Steels: Production and Evaluation of Mechanical Properties with Emphasis on Low-Cycle Fatigue Behaviour, Metallurgy and Materials Transactions A, Vol. 40A, July 2009, pp. 1557.
32. Railway Wheelsets, Railway Group Standard, GM/RT2466, Issue One, June 2003, published by: Rail Safety and Standards Board, Copyright 2003 Rail Safety and Standards Board.
33. Dover, W.D., Dharmavasan, S., Topp, D.A., Lugg, M., 'Fitness for Purpose' Using ACFM for Crack Detection and Sizing and FACTS/FADS for Analysis, Paper Presented at the Marine Structural Inspection, Maintenance and Monitoring Symposium, Sheraton National Hotel, Arlington, Virginia, March 18-19, 1991.
34. Murawa, F., Radsätze für Schienenfahrzeuge –grundsätzliche Gedanken zur Dimensionierung; EI – Eisenbahningenieur (55) 1/2004, pp. 40-47.
35. Heat Treatment Process and Facility for Railway Wheels, I. Poschmann LVQ WP Werkstoffprüfung GmbH, Mülheim an Der Ruhr, Germany, E. Tschapowetz & H. Rinnhofer Maerz-Gautschi Industrieofenanlagen GmbH, Düsseldorf, Germany.
36. Weidemann, C., Gumbiowski, M., Poschmann, I., Laufflächenreaktionen – zum Verhalten des Rades im System Fahrzeug-Radsatz-Fahrweg; EI-Eisenbahningenieur (52) 3/2001, pp. 34-37.
37. EN 50126 (1999) Railway Applications – Specification and Demonstration of Reliability, Availability, Maintainability and Safety; CEBELEC, Brussels.

38. UIC 812-3V (1984), Technical Specification for The Supply of Solid Wheels in Rolled Non-alloy Steel for Tractive and Rolling Stock, Editions Techniques Ferroviaires, Paris.
39. GOST 10791 (2004) All Rolled Wheels – Specification; Ministry of Railway, Traffic and Communication, Moscow.
40. AAR M-107-84 (1988) Standard Wheels, Wrought Carbon Steels; Association of American Railroads, Mechanical Division, Washington.
41. EN 13262 (2004) Railway Applications – Wheelsets and Bogies – Wheels – Product Requirements; CEBELEC, Brussels.
42. Poschmann, I., Heermant, C., Werkstoffe für Rollendes Bahnmaterial – Gefüge und Mechanische Eigenschaften; EI – Eisenbahningenieur (53) 8/2002, pp. 47-50.
43. Papaelias, M.Ph., Roberts, C., Davis, C.L., A Review on Non-destructive Evaluation of Rails: State-of-the-art and Future Development, Proc. IMechE. Vol. 222 Part F: J. Rail and Rapid Transit, JRRT209 © IMechE. 2008.
44. Weise, V., Waite, G., Developments of Rail Flaw Inspection Techniques within The UK Rail Industry. In The Proceedings of The 7th International Conference on Maintenance and Renewal of Permanent Way; Power and Signalling; Structures and Earthworks, London, UK, 6–7 July 2004.
45. Mair, C., Fararooy, S., Practice and Potential of Computer Vision for Railways. In IEE Seminar on Condition Monitoring for Rail Transport, 10 November 1998.
46. Marino, F., et al., A Real Time Visual Inspection System for Railway Maintenance: Automatic Rail Detection and Tracking. Internal Report DEE–Politecnico diPari, 2005.
47. Stella, E., Mazzeo, P.L., Nitti, M., Cicirelli, G., Distante, A., and D'Orazio, T., Visual Recognition of Missing Fastening Elements for Railroad Maintenance. In Proceedings of the IEEE-ITSC International Conference on Intelligent Transportation systems, Singapore, 2002, pp. 94–99.
48. Mazzeo, P.L., Nitti, M., Stella, E., Distante, A., Visual Recognition of Fastening Bolts for Railroad Maintenance, Pattern Recognit. Lett., 2004, 25(6), pp. 669–677.
49. Deutsch, W.A.K., Automated Ultrasonic Inspection. In Proceedings of the WCNDT Conference, Rome, Italy, October 2000.

50. Deutschl, E., Gasser, C., Niel, A., Werschonig, J., Defect Detection on Rail Surfaces by a Vision Based System. In Proceedings of the IEEE Intelligent Vehicles Symposium 2004, University of Parma, Parma, Italy, 14–17 June 2004.
51. Deutschl, E., Gasser, C., Tschabuschnig, K., DIRIS – Pseudo 3D Realtime Inspection of Rail Surfaces. In Advance Computer Vision Seminar, Graz, Austria, June 2001.
52. Eklund, B., Crocker, B., Inspecting Welds in Rail. Inspect. Trends, 2005.
53. Offereins, G.A., Mutton, P.J., Recent Experiences with The Performance of Alumina-thermic Rail Welds Under High Axle Loads. In Proceedings of the 13th International Rail Track Conference, Canberra, Australia, 2001.
54. Rose, J.L., Afioli, M.J., Song, W.-J., Application and Potential of Guided Wave Rail Inspection. Insight, 2002, 44(6), pp. 353–358.
55. Hayashi, T., Song, W.-J., Rose, J.L., Guided Wave Dispersion Curves for A Bar with An Arbitrary Cross-section, A Rod and Rail Example. Ultrasonics, 2003, 41, pp. 175–183.
56. Cawley, P., Wilcox, P., Alleyne, D.N., Pavlakovic, B., Evans, M., Vine, K., Lowe, M.J.S., Long Range Inspection of Rail Using Guided Waves – Field experience. In Proceedings of the 16th World Conference on Non-Destructive Testing, Montreal, Canada, August– September 2004. Proc. IMechE Vol. 222 Part F: J. Rail and Rapid Transit JRRT209 © IMechE 2008 Non-destructive evaluation of rails 383
57. Wilcox, P.D., Pavlakovic, B.N., Evans, M.J., Vine, K.A., Cawley, P., Lowe, M.J.S., Alleyne, D.N., Long Range Inspection of Rail Using Guided Waves, Review of Progress in Quantitative NDE (Eds D. O. Thompson and D. E. Chimenti), 2003, Vol. 22, pp. 236–243 (Plenum Press, New York).
58. Bartoli, I., di Scalea, F.L., Fateh, M., Viola, E., Modelling Guided Wave Propagation with Application to The Long Range Defect Detection in Railroad Tracks. NDT&E Int., 2005, 38, pp. 325–334.
59. di Scalea, F., Rizzo, P., Coccia, S., Bartoli, I., Fateh, M., Viola, E., Pascale, G., Non-contact Ultrasonic Inspection of Rails and Signal Processing for Automatic Defect Detection and Classification, Insight, 2005, 47(6).
60. Waves in Solids PRISM System, available from www.wavesinsolids.com.

61. Rose, J.L., Lee, C.M., Hay, T.R., Cho, Y., Park, I.K., Rail Inspection with Guided Waves. In Proceedings of the 12th Asia-Pacific Conference on NDT, Aukland, New Zealand, 5–10 November 2006.
62. Kenderian, S., Djordjevic, B., Green, R.E., Laser Based and Air Coupled Ultrasound as Non-contact and Remote Techniques for Testing of Railroad Tracks, Mater. Eval., 2002, 60, pp. 65–70.
63. Kenderian, S., Cerniglia, D., Djordjevic, B., Garcia, G., Morgan, R., Sun, J., Snell, M., Rail Track Field Testing Using Laser/Air Hybrid Ultrasonic Technique, Mater. Eval., 2003, 61, pp. 1129–1133.
64. TTCI 12th Annual Research Review CD-ROM, Pueblo, Colorado, USA, 2007.
65. Utrata, D., Exploring Enhanced Rail Flaw Detection Using Ultrasonic Phased Array Inspection, Review of Quantitative Non-destructive Evaluation (Eds. D. O. Thompson and D. E. Chimenti), 2002, Vol. 21, pp. 1813–1818.
66. Utrata, D., Clark, R., Groundwork for Rail Flaw Detection Using Ultrasonic Phased Array Inspection, Review of quantitative non-destructive evaluation (Eds D. O. Thompson and D. E. Chimenti), 2003, Vol. 22, pp. 799–805.
67. Garcia, G., Zhang, J., Application of Ultrasonic Phased Arrays for Rail Flaw Inspection. TTCI Report for the US Department of Transportation, July 2006.
68. Coperet, P., FAAST: Fast Automated Angle Scan Technique. In Proceedings of the ECNDT 2006, Berlin, Germany, 2006.
69. Cawser, S.J., Hardy, A.E.J., Wright, C.E., Acoustic Track Monitoring. Phase 1: Initial data gathering analysis, AEA Report for RSSB, December 2002.
70. Bruzelius, K., Mba, D., An Initial Investigation on The Potential Applicability of Acoustic Emission to Rail Track Fault Detection. NDT&E Int., 2004, 37(7), pp. 507–516.
71. Thakkar, N.A., Steel, J.A., Reuben, R.L., Knabe, G., Dixon, D., Shanks, R.L., Monitoring of Rail-Wheel Interaction Using Acoustic Emission (AE), Adv. Mater. Res., 2006, 13–14, pp. 161–166.
72. Fateh, M., On-line High Speed Rail Defect Detection. Phase III. US Department of Transportation Report, October 2005, available from www.fra.dot.gov/downloads/ research/rr0507.pdf.
73. Cruby, C.B., Drain, L.E., Laser Ultrasonics Techniques and Applications, 1990 (Taylor & Francis).

74. TTCI 12th Annual Research Review CD-ROM, Pueblo, Colorado, USA, 2007.
75. Utrata, D., Exploring Enhanced Rail Flaw Detection Using Ultrasonic Phased Array Inspection, Review of Quantitative Non-destructive Evaluation (Eds. D. O. Thompson and D. E. Chimenti), 2002, Vol. 21, pp. 1813–1818.
76. Utrata, D., Clark, R., Groundwork for Rail Flaw Detection Using Ultrasonic Phased Array Inspection, Review of Quantitative Non-destructive Evaluation (Eds D. O. Thompson and D. E. Chimenti), 2003, Vol. 22, pp. 799–805.
77. Garcia, G., Zhang, J., Application of Ultrasonic Phased Arrays for Rail Flaw Inspection. TTCI Report for the US Department of Transportation, July 2006.
78. Operet, P., FAAST: Fast Automated Angle Scan Technique. In Proceedings of the ECNDT 2006, Berlin, Germany, 2006.
79. Chahbaz, A., Development of A Mobile Inspection System for Rail Integrity Assessment. Tektrend International Report for the Transportation Development Centre, Montreal, Quebec, Canada, June 2000.
80. Chabhaz, A., Brassard, M., Pelletier, A., Mobile Inspection System for Rail Integrity Assessment. In Proceedings of the 15th World Conference of Non-Destructive Testing, Roma, Italy, 2000.
81. Sebko, V.P., Suchkov, G.M., Malakhov, A.V., Using The Electromagnetic-Acoustic Method, Russ. J. Nondestruct. Test., 2004, 40(7), pp. 442–448.
82. Dixon, S., Edwards, R.S., Jian, X., Inspection of The Railtrack Head Surfaces Using Electromagnetic Acoustic Transducers, Insight, 2004, 46, pp. 326–330.
83. Edwards, R.S., Jian, X., Dixon, S., Rail Defect Detection Using Ultrasonic Surface Waves, Review of Quantitative Non-destructive Evaluation (Eds. D. O. Thompson and D. E. Chimenti), 2006, vol. 25, pp. 1601-1608.
84. Edwards, R.S., Dixon, S., Jian, X., Characterisation of Defect in The Railhead Using Ultrasonic Surface Waves, NDT&E Int., 2006, 39, pp. 468–475.
85. Edwards, R.S., Dixon, S., Jian, X., Depth Gauging of Defects Using Low Frequency Wideband Rayleigh Waves, Ultrasonics, 2006, 44, pp. 93–98.
86. Edwards, R.S., Fan, Y., Papaelias, M., Dixon, S., Davis, C.L., Roberts, C., Ultrasonic Detection of Surface Breaking Railhead Defects. In the Proceedings of RQNDE 2007 Conference, Colorado, USA, July 2007.

87. Fan, Y., Dixon, S., Edwards, R.S., Jian, X., Ultrasonic Surface Wave Propagation and Interaction with Surface Defects on Rail Track Head, NDT&E Int., 2007, 40, pp. 471–477.
88. Edwards, R.S., Papaelias, M., Holmes, C., Fan, Y., Dixon, S., Ultrasonic Detection of Surface-breaking Railhead Defects. In Proceedings of the BINDT 2007 Conference, Glasgow, UK, 2007.
89. Wheel Shelling and Spalling Research - Association of American Railroads Vehicle Track Systems Newsletter, Railway Age, December 1989, (http://findarticles.com/p/articles/mi_m1215/is_n12_v190/ai_8274767/).
90. Kube, K., Sperry Trucks Track Troubles Deep Inside Rails. Trains. Mag., 2005, 20–21 February.
91. Junger, M., Thomas, H.-M., Krull, R., Rühe, S., The Potential of Eddy Current Technology Regarding Railroad Inspection and its Implementation. In Proceedings of the 16thWorld Conference on Non-Destructive Testing, Montreal, Canada, August–September 2004.
92. Cawser, S.J., Hardy, A.E.J., Wright, C.E., Acoustic Track Monitoring. Phase 1: Initial data gathering analysis, AEA Report for RSSB, December 2002.
93. Bruzelius, K., Mba, D., An Initial Investigation on The Potential Applicability of Acoustic Emission to Rail Track Fault Detection, NDT&E Int., 2004, 37(7), pp. 507–516.
94. Thakkar, N.A., Steel, J.A., Reuben, R.L., Knabe, G., Dixon, D., Shanks, R.L., Monitoring of Rail-Wheel Interaction Using Acoustic Emission (AE), Adv. Mater. Res., 2006, 13–14, pp. 161–166.
95. Weise, V., Waite, G., Developments of Rail Flaw Inspection Techniques within The UK Rail Industry. In the Proceedings of the 7th International Conference on Maintenance and Renewal of Permanent Way; Power and Signalling; Structures and Earthworks, London, UK, 6–7 July 2004.
96. Jeong, D.Y., Progress in Rail Integrity Research. In Proceedings of the AREMA 2001 Conference, Chicago, IL, USA, 9–12 September 2001.
97. Eklund, B., Crocker, B., Inspecting Welds in Rail, Inspect. Trends, 2005.
98. Bray, D.E., Historical Review of Technology Development in NDE. In Proceedings of the 15th World Conference on NDT, Roma, Italy, 2000.
99. Pohl, R., Krull, R., Meierhofer, R., A New Eddy Current Instrument in a Grinding Train. In Proceedings of ECNDT 2006, Berlin, Germany, 2006.

100. Ireland, R.C. Torres, C.R., Limitations of The Circumferential MFL Technique in The NDE of Pipelines, In Proceedings of Magnetics in Non-destructive Testing Seminar, London, UK, April 2005.

101. Mandayam, S., Udpa, L., Udpa, S. S., and Lord, W., Invariance transformations for magnetic flux leakage signals, *IEEE Trans. Magn.*, 1996, 32(3), pp. 1577–1580.

102. Li,Y., Tian, G.Y., and Ward, S., Numerical simulation on magnetic flux leakage evaluation at high speed. *NDT&E Int.*, 2006, 39, pp. 367–373.

103. Thomas, H.-M., Junger, M., Hintze, H., Krull, R., and Rühe, S., Pioneering inspection of railroad rails with eddy currents, In Proceedings of the 15th World Conference on Non-Destructive Testing, Rome, Italy, 2000.

104. Pohl, R., Erhard, A., Montag, H.-J., Thomas, H.-M., and Wüstenberg, H. NDT techniques for railroad wheel and gauge corner inspection. *NDT&E Int.*, 2004, 37, pp. 89–94.

105. Junger, M., Thomas, H.-M., Krull, R., and Rühe, S., The potential of eddy current technology regarding railroad inspection and its implementation, In Proceedings of the 16thWorld Conference on Non-Destructive Testing, Montreal, Canada, August–September 2004.

106. Thomas, H.-M., Junger, M., Hintze, H., Krull, R., and Rühe, S. Pioneering inspection of railroad rails with eddy currents. In Proceedings of the 15th World Conference on Non-Destructive Testing, Rome, Italy, 2000.

107. Pohl, R., Erhard, A.,Montag, H.-J.,Thomas, H.-M., and Wüstenberg, H. NDT techniques for railroad wheel and gauge corner inspection. NDT&E Int., 2004, 37, 89–94. Junger, M., Thomas, H.-M., Krull, R., and Rühe, S. The potential of eddy current technology regarding railroad inspection and its implementation. In Proceedings of the 16thWorld Conference on Non-Destructive Testing, Montreal, Canada, August–September 2004.

108. Thomas, H.-M., Heckel, T., and Hanspach, G. Advantage of a combined ultrasonic and eddy current examination for railway inspection trains. In Proceedings of ECNDT 2006, Berlin, Germany, 2006.

109. CT Services-Overview. Jesse Garant & Associates. August 17, 2010. http://www.jgarantmc.com/ct-services.html.

110. [a,b] Hoffman, J., Flisch, A., Obrist, A., Adaptive CT scanning – mesh based optimisation methods for industrial x-ray computer tomography applications. NDT&E International (37), 2004, pp. 271-278.

111. Lambert, J., Chambers, A. R., Sinclair, I., Spearing, S.M., 2012. 3D Damage characterisation and the role of voids in the fatigue of wind turbine blade materials, Computer Science and Technology 72 (2): 337; doi: 10; 1016 / j.comp-scitech. 2011.11.023.

112. Maldague X. P. V., Jones T. S., Kaplan H., Marinetti S. and Prystay M. "Chapter 2: Fundamentals of Infrared and Thermal Testing: Part 1. Principles of Infrared and Thermal Testing," in Nondestructive Handbook, Infrared and Thermal Testing, Volume 3, X. Maldague technical ed., P. O. Moore ed., 3rd edition, Columbus, Ohio, ASNT Press, 2001, pp. 718.

113. Renshaw J., Chen J. C., Holland S. D., and Thompson R. B. 2011, "The sources of heat generation in vibrothermography," NDT&E International, 44(8): pp. 736-739.

114. Raine, A., The Development of Alternating Current Field Measurement (ACFM) Technology as a Technique for the Detection of Surface Breaking Defects in Conducting Materials and its Use in Commercial and Industrial Applications, , TSC Inspection Systems Limited, a web-based article: http://www.ndt.net/article/wcndt00/papers/idn644/idn644.htm

115. Alternating Current Field Measurement, a web-based article, The NDT Validation Centre Site: http://www.ndt-validation.com/technologies/pr_16.jsp?menu_pos=4.

116. SAFERAIL – An EU FP7 Research Project Providing Innovation in Railway Wheelset Inspection and Wayside Monitoring, a web-based article: http://www.saferail.net/publications/SAFERAIL_Flyer.pdf.

117. Rowshandel, H., Papaelias, M., Roberts, C., Davis, C., Development of Autonomous ACFM Rail Inspection Techniques, NDT 2010 Conference.

118. Lugg, M., Topp, D., Recent developments and applications of the ACFM inspection method and ACSM stress measurement method. In Proceedings of ECNDT 2006, Berlin, Germany, 2006.

119. Nielsen, J.C.O., Johansson, A., Out-of round railway wheels – a literature review, Proc. Instn. IMechE 2000, Vol. 214, Part F.

120. GM/GN2497, Guidance on Railway Wheelset Tread, Gauging and Damage, Issue 1, December 2007, Railway Group Guidance Note, Railway Safety and Standards Board Limited.

121. Evans, J. (AEA Technology Rail), Iwnicki, S. (Manchester Metropolitan University (MMU)), Vehicle Dynamics and Wheel/Rail Interface, Wheels on Rails – An Update, Understanding and Managing the Wheel/Rail Interface, IMechE Seminar, London, April 2002 (©2002 The Institution of Mechanical Engineering).

122. European Railway Research Institute Draft Report, ERRI D173 Lubrication Site Trial, May 1996.

123. Pearce, T.G., and Sherratt, N.D., "Prediction of Wheel Profile Wear", Wear, 144 (1991), 343-351.

124. Iwnicki, S., (ed.) "The Manchester Benchmarks for Rail Vehicle Simulation", Swets & Zeitlinger B.V. Lisse 1999, ISBN 90 265 15510.

125. Kik, W., and Piotrowski, J., "A fast approximate method to calculate normal load at the contact between the wheel and rail and creep forces during rolling", Proc. 2nd mini conf. On contact mechanics and wear of wheel/rail systems, ed. Zabory, TU Budapest 1996.

126. Bower, A.F., and Johnson, K.L., Proc. 3rd International Conference on Contact Mechanics and Wear of Rail/Wheel Systems, Cambridge, UK, July 1990.

127. "Railtrack Rail Head Checking Investigation Phase 2 – Final Report", Ove Arup International Ltd. & Transportation Technology Centre Inc., September 2001.

128. prEN 15313: 2007, CEN/TC: 256 Secretariat: DIN, Railway Applications – In-service wheelset operation requirements and in-service and off-vehicle wheelset maintenance, Einfuhrendes – Element – Haupt – Element / D:\NORME EUROP\NORME MAINTENANCE EN 15313\9c NORME FINALE\17 October 2007 derniere version €\TRAVAIL\EN_15313_(E)-25-07-07 master draft.doc STD Version 2.2, pp. 1-62.

129. Network Rail October 2009 Strategic Business Plan, Supporting Document, Rolling Stock Paper.

130. TTCI Part 1: The Importance of Wheel/Rail Interface Management on Energy Savings and Sustainability.

131. Dover, W.D., Collins, R., and Michael, D.H., The use of ac field measurements for crack detection and sizing in air and underwater, Phil. Trans. R. Soc. Lond. A 320, pp. 271-283 (1986).

132. Nicholson, G., Kostryzher, A., Rowshandel, H., Papaelias, M., Davis, C.L., Roberts, C., Sizing and tomography of rolling contact fatigue cracks in rails using NDT technology – potential for high speed applications, Challenge C: Increasing freight capacity and services, 9th World Congress on Railway Research, May 22-26, 2011, WCRR Lille 2011.

133. Gaynor, T.M., Roberts, D.L., Holman, E. and Dover, W.D., Reduction in fatigue failures through crack detection by alternating current field measurements, IADC/SPE35033, Presented at IADC/SPE Drilling Conference, New Orleans, 12-15 March, 1996.

134. Lugg, M.C., The first 20 years of the A.C. field measurement technique, 18th World Conference on Non-destructive Testing, 16-20 April 2012, Durban, South Africa.

135. TOTAL MATERIA THE WORLDS MOST COMPLETE DATABASE, http://www.totalmateria.com/page.aspx?ID=CheckArticle&site=kts&NM=443 , an article found on the internet at the above website address.

136. Mirshekar-Syakhal, D., Collins, R., Michael, D.H., The influence of skin depth on crack measurement by the AC field technique, Nondestruct. Eval. 1982,; 3(2): pp.65-76.

137. Dover, W.D., Monahan, C.C., The measurement of surface breaking cracks by the electrical systems ACPD/ACFM. Fatigue Fract. Eng. 1994; 17(12): pp. 1485-92.

138. Dover, W.D., Charlesworth, F.D.W., Taylor, K.A., Collins, R., Michael, D.H., AC Field Measurement - Theory and Practice, 1980; 22(3): pp.149-54.

139. Lugg, M.C., Data Interpretation in ACPD Crack Inspection, NDT Int. 1989; 22(3): pp.149-54.

140. Collins, R., Dover, W.D., Michael, D.H., The use of AC field measurement for NDT, 1985; 8: pp.211-65.

141. Collins, R., Dover, W.D., Ranger, K.B., The AC field around a plane semi-elliptical crack in metal surface, 1981; pp.470-9.

142. Dover, W.D., Collins, R., Michael, D.H., Review of Development in ACPD and ACFM. Br.J.NDT 1991; 33(3): pp.121-7.

143. Michael, D.H., Collins, R., The AC field around a plane crack in metal surface when the skin depth is large. Nondestruct. Eval. 1982; 3(1): pp.19-24.

144. Lugg, M.C., Shang, H.M., Collins, R. and Michael, D.H., The measurement of surface crack inclination in metals using AC electric fields, Journal of Physics D: Applied Physics, Volume 21, Number 12, 1814, November 2000.

145. Pedrosa, N., Leitao, D., Barros, P., Quintino, L., Advanced Ultrasonic System for Improved Efficiency in Pipelines Inspection, Welding and Material Testing, year XIX, no. 2/2010, pp.36-41

146. Sousa, J.P., Demony, F., Pedrosa, N., Santos, T.G., Vilaca, P., Quintino, L, Development of Automatic Systems for NDT Inspection of Wheels and Propeller Blades of Airplanes, EuroTehnika d.o.a., pp. 11-17, www.eurotehnika.hr.

147. Pinto, M., Pedrosa, N., Papaelias, M., Development of a Novel Integrated Inspection System for the Accurate Evaluation of the Structural Integrity of Rail Tracks, SCP8-GA-2009-234040, INTERAIL Consortium 2013, Document Reference: INRAIL/ISQ/FR-PS-27-v1, pp.2-44, www.interailproject.eu.

148. Nicholson, GL., Davis, C.L., Modelling of the response of an ACFM sensor to rail and rail wheel RCF cracks, NDT&E International 46 (2012), pp.107-114.

149. Pohl, R., Erhard, A., Montag, H-J., Thomas, H-M., Wustenberg, HNDT, Techniques for railroad wheel and gauge corner inspection, NDT&E Int. 2004; 37: pp.89-94

150. Tillberg, J., Larsson, F., Runesson, K., A study of multiple crack interaction at rolling contact fatigue loading of rails, Proc. Inst. Mech. Eng. Part F, J. Rail Rapid Transit. 2009, 223: pp.319-30.

151. Magel, E., Sawley, K-J., Rail surface condition alert-stage 1, Evaluation and calibration of surface crack measuring devices, National Research Council of Canada – Centre for Transportation Technology (CSTT), Report no. CSTT-RYV-CAT-090, 2006 [report available from E. Magel (CSTT)].

152. Garnham, J.E., Fletcher, D.I., Davis, C.L., Franklin, F.J., Visualisation and modelling to understand rail rolling contact fatigue cracks in three-

dimensions, Proceedings of the Institution of Mechanical Engineers, Part F: Journal of Rail and Rapid Transit, 225 (2), pp.165-178.

153. Zhong, W., Hu, J.J., Li, Z.B., Liu, Q.Y., Zhou, Z.R., A study of rolling contact fatigue crack growth in U75V and U71Mn rails, Wear 2011; 271: pp.388-92.

154. Xu, X., Cho, D-H., Chang, Y-S., Choi, J.B., Kim, Y-J., Jun, H-K., et al., Evaluation of slant crack propagation under RCF in railway rail, J. Mech. Sci. Technol. 2011; 25: pp.1215-20.

155. Zerbst, U., Madler, K., Hintze, H., Fracture mechanics in railway applications – an overview, Eng. Fract. Mech. 2005; 72: pp.163-94.

156. Graham, H.D., Hempelmann, K., Grob-Thebing, A., A new type of RCF experimental investigations and theoretical modelling, Wear 2012; 253: pp.67-74.

157. Kumar, S., Study of rail breaks: associated risks and maintenance, Engineering, Lulea University of Technology, 2006, ISSN: pp. 1402-1536.

158. Topp, D, Smith, M, Application of the ACFM inspection method to rail and rail vehicles, Insight 2005; 47: pp354-7

159. Papaelias, M.P., Davis, C., Roberts, C., Blakeley, B., Lugg, M., INTERAIL: Development of a novel integrated inspection system for the accurate evaluation of the structural integrity of rail tracks – implementation of the ACFM rail inspection module: 10th European Conference on Non-Destructive Testing, Moscow, Russia 2010.

160. Tunna, J., Sinclair, J., Perez, J., A review of wheel wear and rolling contact fatigue Proc Inst Mech Eng Part F J-Rail Rapid Transit 2007, 221: pp271-89.

161. The development of a wheel wear and rolling contact fatigue model, Rail Safety and Standards Board, 2008.

162. Stow, J., Bevan, A., Trials of wheel and rail rolling contact fatigue control measures, Stage 1 Report: pre-modelling analysis and route simulations, V/T SIC Rolling Contact Fatigue Investigation: Phase 6: Vehicle Dynamics Rail Damage Modelling: Rail Safety and Standards Board, 2008.

163. Hyder, R., Girsch, G., Testing of HSH rails in high speed tracks to minimise rail damage, Wear 2005; 258: pp.1014-21.

164. Tillberg, J., Larsson, F., Runesson, K., A study of multiple crack interaction at rolling contact fatigue loading of rails, Proc. Inst. Mech. Eng. Part F. J. Rail Rapid Transit. 2009; 223: pp.319-30.

165. Magel, E., Sawley, K., J. Rail surface condition alert stage-1, Evaluation and calibration of surface crack measuring devices, National Research Council of Canada – Centre for Transport Technology (CSTT), Report no. CSTT-RYV-CAT-090; 2006 [report available from E. Magel (CSTT)].

166. SAFERAIL project website: www.saferail.net

167. Wei, Li., Guoming, C., Wenyan, L., Zhun, L., Feng, L, NDT&E International, 44 (2011), pp.324-328.

168. Yutiang, Q., Guoming, C., Yanting, Z., Digital simulation on ACFM and sensitivity analysis of detected signal, Journal of the University of Petroleum, China 2004; 28(3){ pp.65-8.

169. Ravan, M., Sadeghi Moin, R., Using a wavelet network for reconstruction of fatigue crack depth profile from AC field measurement signals, NDT&E International 2007; 40(7): pp.537-44.

170. Amineh Reza, K., Maryam Ravan, et al., Removal of probe lift-off effects on crack detection and sizing in metals by the AC field measurement technique, IEEE Transactions on Magnetics 2008; 44(8): pp.2066-73.

171. Bhangale, V. (Sr. DEN/N/Nagpur, C. Railway), Kumar, A. (DEN/Track/Delhi, N. Railway), Om Dwivedi (XEN/Const., N. Railway), A report presented by the above authors: On development of rolling contact fatigue (RCF) and its prevention.

172. Lugg, M.D., Dover, W.D., Assessment of factors that influence the skin depth in ACFM crack sizing, Copyright @ Controller HMSO ,London, 1985, pp.207-214.

173. Kittel, C., Rev. Mod. Phys., 21, 541 (1949).

174. Cullity, B.D., Introduction to Magnetic Materials (Addison-Wesley, New Yor, 1972).

175. Bozorth, R.M., Ferromagnetism (Van Nostrand, New York, 1951), Chaps 2 and 13.

176. Bozorth, R.M., Ferromagnetism (Van Nostrand, New York, 1951), Chap. 11.

177. Kwan, H., Burkhardt, G.L., Effects of grain size, hardness, and stress on the magnetic hysteresis loops of ferromagnetic steels, J. Appl. Phys. 61 (4), 187 American Institute of Physics, pp.1576-1579.

178. Langman, R., IEEE Trans. Mag. Mag-21, 1314 (1985).

179. Kwan, H., J. Mag. Mag. Mater. 49, 235 (1985).

180. Erdogan, M., Priestner, R., Effect of epitaxial ferrite on yielding and plastic flow in dual phase steel in tension and compression, Materials Science and Technology, Nov 1999, 15, 11, Pro Quest SciTech Collection.

181. CONFIDENTIAL REPORT: John Williams (Client: Confidential), Class High Speed Rail Wheel Investigation (Wheel Class: Confidential), Client: Confidential, 12 November 2010.

182. CONFIDENTIAL REPORT: Photographic Survey of RCF-Damaged Wheel from High Speed Rail Wheel Investigation (Wheel Class: Confidential), Rail Technology Unit (RTU), Manchester Metropolitan University, Client: Confidential, 26 November 2010.

183. Hao, X.J., Yin, W., Strangwood, M., Peyton, A.J., Morris, P.F., Davis, C.L., Scr. Mater. 2008; 58: pp.1033-6.

184. Hao, X.J., Yin, W., Strangwood, M., Peyton, A.J., Morris, P.F., Davis, C.L., Metall. Mater. Trans. A 2009; 40: pp.745-56.

185. Hao, X.J., Yin, W., Strangwood, M., Peyton, A.J., Morris, P.F., Davis, C.L., NDT E. Int. 2010; 43: pp.305-15.

186. Yin, W., Peyton, A.J., Strangwood, M., Davis, C.L., J. Mater. Sci. 2007; 42: pp.6854-61.

187. Looyenga, H., Physica 1965; 31: pp.401-6.

188. Birchak, J.R., Gardner, L.G., Hipp, J.W., Victor, J.M. Proc. EEEEE 1974; 62: pp.93-8.

189. Rumiche, F., Indacochea, J.E., Wang, M.L., Assessment of The Effect of Microstructure on The Magnetic Behaviour of Structural Carbon Steels Using an Electromagnetic Sensor, Journal of Materials Engineering and Performance (JMEPEG), 2008; 17: pp. 586-593.

190. Mesina, M.B., De Jong, T.P.R., Dalminj, W.L., Scrap Stainless Steel Detection Using a Pulsed Electromagnetic Field, Int. J. Miner. Proces. 76, pp. 21–31, 2005.

191. Haldane, R.J., W. Yin, W., Strangwood, M., Peyton, A.J., Davis, C.L., Multi-Frequency Electromagnetic Sensor Measurement of Ferrite/Austenite

Phase Fraction – Experiment and Theory, Scripta Mater. 54, pp. 1761–1765, 2006.

192. Papaelias, M.Ph., Strangwood, M., Peyton, A.J., Davis, C.L.: Effect of Microstructural Variations on Smart Inductive Sensor Measurements of Phase Transformation in Steel, Scripta Mater. 51, pp. 379–383, 2004.

193. Mohri, K., Uchiyama, T., Shen, L.P., Cai, C.M., Panina, L.V., Amorphous Wire and CMOS IC-based Sensitive Micro-magnetic Sensors for Intelligent Measurements and Controls, J. Magn. Magn. Mater. 249, pp. 351–356, 2002.

194. Taylor, R., An Online Grain Size Measuring System for Electrical Steel Production, J. Magn. Magn. Mater. 112, pp. 95–98, 1992.

195. Degauque, J., Astie, B., Porteseil, J.L., Vergne, R., Influence of The Grain Size on The Magnetic and Magnetomechanical Properties of High-Purity Iron, J. Magn. Magn. Mater. 26, pp. 261–263, 1982.

196. Anglada-Rivera, J., Padovese, L.R., Capo-Sanchez, J., Magnetic Barkhausen Noise and Hysteresis Loop in Commercial Carbon Steel, Influence of Applied Stress and Grain Size, J. Magn. Magn. Mater. 231, pp. 299–306, 2001.`

197. Tanner, B.K., Szpunar, J.A., Willcock, S.N., Morgan, L.L., Mundell, P.A., Magnetic and Metallurgical Properties of High-Tensile Steels, J. Mater. Sci. 23, pp. 4534–4540, 1988.

198. Yoshino, M., Tanabe, H., Sakamoto, T., Suzuki, N., Yaji, Y., Nondestructive Measurement of Grain Size in Steel Plates by Using Magnetic Coercive Force, Mater. Sci. Forum. 210–213, pp. 45–54, 1996.

199. Amini, A., Entezami, M., Papaelias, M., Onboard detection of railway axle bearing defects using envelope analysis of high frequency acoustic emission signals, Case Studies in Nondestructive Testing and Evaluation, 6 (2016), pp.8-16.

200. Anastasopoulos, A., et al. Acoustic emission on-line inspection of rail wheelsets, In: European Working Group on Acoustic Emission, 2010.

201. Papaelias, M., Effect of defective wheels on rail, Saferail report reference number: SCP7-GA-2008-218674, 2009.

202. Papaelias, M., et al., Condition monitoring of oil and gas pumps and their driving equipment based on acoustic emission techniques, presented at the non-destructive testing conference, Blackpool, 2009.

203. Tandon, N., Choudhury, A., A review of vibration and acoustic measurement methods for the detection of defects in rolling element bearings, Tribol. Int. 1999; 32: pp.469-80.

204. Miettinen, J., Salmenpera, P., Acoustic emission monitoring of grease lubricated rolling bearings, In: 13th international congress on condition monitoring and diagnostic engineering management, 2000, pp.21-30.

205. Yi, C., et al., Faults diagnostics of railway axle bearings based on IMF's confidence index algorithm for ensemble EMD. Sensors 2015; 15: pp.10991–1011.

206. Nondestructive Testing Handbook, Electromagnetic Testing, Third Edition, Volume 5, Technical Editor: Satish S. Udpa, Editor: Patrick O. Moore, ISBN 978-1-57117-046-0, American Society for Nondestructive Testing.

207. Private Report supplied by: Michael Smith (TSC Inspection Systems) and Stephen Ford (Daimler Chrysler Rail Systems (UK) Ltd.), ACFM Laboratory Tests (2001), Bombardier Transportation UK Ltd. 2001.

208. Railway Group Standard, GM/RT2466, Issue: Three, Date: February 2010.

209. Andy Doherty, Steve Clark, Robert Care and Mark Dembosky, Article: Why Rails Crack, Ingenia Magazine, Issue 23, June 2008, www.ingenia.org.uk.

210. Papaelias, M.Ph., Comments in a private communication received by email correspondence in August 2017.

211. Papaelias, M.Ph., Roberts, C., Davis, C.L., Blakeley, B., Lugg, M., Further developments in high-speed detection of rail rolling-contact fatigue using ACFM techniques, Insight - Non-Destructive Testing and Condition Monitoring, 07/2010, Vol.52(7), pp.358-360.

212. Papaelias, M.Ph., Roberts, C., Davis, C.L., Blakeley, B., Lugg, M., Further developments in high-speed detection of rail rolling-contact fatigue using ACFM techniques, Non-Destructive Testing 2009 Conference, Blackpool, UK, September 2009.

213. Girardi, L., Plu, J., Blakeley, B., Bredif, P., Davis, C., Lugg, M., Papaelias, M., Roberts, C., 'INNOTRACK SP4.4 – Detection of rolling contact fatigue in rails using electromagnetic and ultrasonic phased- array inspection techniques', 8th International Conference on Contact Mechanics and Wear of Rail/Wheel Systems, Firenze, Italy, September 15-18, 2009.

214. Papaelias, M.Ph., Roberts, C., Davis, C.L., Lugg, M., Smith, M., Detection and quantification of rail contact fatigue cracks in rails using ACFM technology, Journal of the British Institute of Non-Destructive TResting {Insight}, Number 7, July 2009.

215. Papaelias, M.Ph., Roberts, C., Davis, C.L., Lugg, M., Smith, M., Detection and quantification of rail contact fatigue cracks in rails using ACFM technology, Insight – Non-Destructive Testing and Condition Monitoring, Volume 50, Number 7, 1 July 2008, pp.364-368(5).

216. Papaelias, M.Ph., Lugg, M., Roberts, C., Davis, C.L., High-speed inspection of rails using ACFM techuiques, NDT&E, Volume 42, Issue 4, June 2009, pp.328-335.